

# Holographic Imaging of Cold Atoms



# Holographic Imaging of Cold Atoms

Lincoln David Turner

Submitted in total fulfilment of the requirements  
of the degree of Doctor of Philosophy.



SCHOOL OF PHYSICS • THE UNIVERSITY OF MELBOURNE  
AUGUST 2004 AUSTRALIA

Copyright © Lincoln David Turner 2004–2005.

This work is licensed under the Creative Commons *Attribution-NoDerivs 2.0 License (Australia)* <http://creativecommons.org/licenses/by-nd/2.0/au/>

You are free to copy, distribute and display this work, and to make commercial use of this work, provided that you give credit to the author Lincoln Turner. You may not alter, transform, or build upon this work. For any reuse or distribution, you must make clear to others the license terms of this work. Any of these conditions can be waived if you get permission from the copyright holder, Lincoln Turner. Your fair use and other rights are in no way affected by the above.

PDF edition.

*National Library of Australia Cataloguing-in-Publication entry:*

Turner, Lincoln David.

Holographic imaging of cold atoms.

Bibliography.

Includes index.

ISBN 0 7340 3060 6 (hardback print).

ISBN 0 7340 3075 4 (PDF).

1. Holography. 2. Imaging systems.

I. University of Melbourne. School of Physics. II. Title.

621.3675

This online version of this thesis is archived at the University of Melbourne ePrints Repository and is part of the Australian Digital Theses project. It has the Open Archives Initiative identifier oai:unimelb.edu.au:822, and is accessible at <http://errol.oclc.org/oai:unimelb.edu.au:822.resource>

*Frontispiece:* Stream on Taranaki, New Zealand.  
Fujichrome Velvia ISO 50, 1/90 s at f/4.8.

See colophon at back for production information.

*To Mum and Dad.*



# Holographic imaging of cold atoms

**Lincoln David Turner**

School of Physics  
University of Melbourne  
Australia.

A thesis submitted for the degree of Doctor of Philosophy.

*Chair of Supervisory Committee:* Associate Professor Robert Scholten.

## Abstract

THIS THESIS presents a new optical imaging technique which measures the structure of objects without the use of lenses. Termed *diffraction-contrast imaging (DCI)*, the method retrieves the object structure from a Fresnel diffraction pattern of the object, using a deconvolution algorithm. DCI is particularly adept at imaging highly transparent objects and this is demonstrated by retrieving the structure of an almost transparent cloud of laser-cooled atoms. Applied to transparent Bose-Einstein condensates, DCI should allow the non-destructive imaging of the condensate while requiring only the minimum possible apparatus of a light source and a detector.

The algorithm is derived from the free-space Fresnel diffraction integral under the assumption that the object is monomorphous (composed of a single material) and weakly absorbing. With a further assumption of slow spatial variation of the phase-shift, a linear expression is obtained relating the column density of the object to the diffraction-pattern contrast. Unlike previous derivations, I show that this *contrast transfer function (CTF)* formalism is *not* limited to weakly phase-shifting objects.

Diffraction-contrast imaging avoids the use of lenses to form images, and so is free of lens aberrations. The technique may be particularly useful at x-ray wavelengths where lenses are difficult to fabricate. Although lenses are avoided, magnification of the image is still possible if a point source of light projects an enlarged diffraction-pattern onto the detector. New validity conditions for the validity of this magnification are derived.

From the CTF expression, a retrieval algorithm is derived which returns a column density image given the diffraction pattern and the imaging parameters: wavelength, detector size, propagation distance and the object refractive index. This regularised deconvolution algorithm is fast and remains numerically stable even for objects with very weak absorption. An extension of the algorithm uses wavelet techniques to dramatically improve stability when the diffraction pattern has a low signal-to-noise ratio. Retrievals from exposures as low as 10 photons/pixel were successful in simulations.

Diffraction-contrast imaging was demonstrated by imaging a cloud of laser-cooled and trapped atoms illuminated with off-resonant laser light. A magneto-optical trap provided a cloud of  $^{85}\text{Rb}$  atoms. Diffraction patterns were obtained with a defocused lens system; focused absorption and fluorescence images were also taken for comparison. Retrieved column densities agreed quantitatively and visually with absorption images. Later, holographic diffraction patterns were imaged with no lens between the atom cloud and the CCD detector and column densities retrieved. Point projection magnification was demonstrated using a bare optical fibre source.

Diffraction-contrast imaging of cold atoms is expected to have a signal-to-noise ratio comparable with other off-resonant imaging techniques. Holographic depth-of-field has been demonstrated, removing the need to focus optical systems. The DCI apparatus is the simplest possible, requiring only a point-source of light and a detector. This lack of optical elements obviates most calibration uncertainties so that retrievals are highly accurate.

# **Declaration**

This is to certify that

- (i) this thesis comprises only my original work,
- (ii) due acknowledgement has been made in the text to all other material used,
- (iii) this thesis is less than 100,000 words in length, exclusive of tables, maps, bibliographies and appendices.

Lincoln Turner \_\_\_\_\_

Date \_\_\_\_\_



# Acknowledgments

One of the pleasures of being a scientist is communicating your enthusiasm with people who feel similarly. I have been fortunate to have in Robert Scholten a supervisor who has a visceral enthusiasm for physics and its applications. I'm very grateful to Rob for his guidance, support and friendship over the last five years.

My co-supervisors Professor Keith Nugent and Associate Professor Les Allen have always brought a fresh perspective to discussions and have followed my project with interest even when aspects have been distant from their own areas of research. My first supervisor, Professor Peter Teubner of Flinders University, has continued to be a wise mentor and a tireless advocate. I am also grateful to Associate Professor Peter Farrell for his wisdom and wisecracks.

It has been a privilege to work with some outstanding scientists during this project. Dr. David Paganin inspired me with his quiet but deeply incisive approach to physics and showed me that classical optics is not a closed book. Karl Weber's dedication and experimental skill provided the first demonstration that holographic cold-atom imaging actually works. Kenian Domen's adept experiments and his interest in the underlying theory have helped greatly in bringing this project to a conclusion. Recently, it has been pleasure to work with Dr. Andrew Peele on x-ray phase imaging; his hard work and good humour have been an example to me.

Further afield, I was fortunate to receive a Postgraduate Overseas Research Experience Scholarship from the University of Melbourne. This took me to the Technical University of Eindhoven, the Netherlands, where I worked in the research group of Professor Herman Beijerinck on a project led by Dr. Ton van Leeuwen. I am grateful to Herman and Ton for their professional hospitality and to all in Groep AQT for making my stay in Eindhoven enjoyable, and despite their best efforts in the Borrel, occasionally productive.

The experimental aspect of this work would not have been possible without the exemplary work of the Electronic and Mechanical Workshops of the School of

Physics. Zivko Jovanovski, Sandor Szilagy, Alex Slavec and Ad van Kempen (in Eindhoven) have mastered the art of looking at a tendered schematic, smiling politely and then producing something that works despite it. Similarly, Wayne Powrie, Ashley French and the other staff of the Mechanical Workshop fabricated components of the apparatus with a precision notably lacking in my drawings. Thanks also to Roland Szymanski for his advice on vacuum systems.

The atom optics lab has been a happy place to work thanks to the sanguinity and humour of my colleagues and friends Imogen, Luke, Karl, Colin, Phil, Tracey and Kenian. In the wider optics group, I have particularly enjoyed innumerable coffees with Adrian and Magda. Thanks to Eric, Gaby, James, Justine, Nick and Scott for being true friends.

I have been lucky to live with an amazing pseudofamily at Amess St. Justin, Katie, Sara and Tim have been the best housemates anyone could hope to have. Ook al mijn huisgenoten van Kettingstraat 30 in Eindhoven, en in het bijzonder Henk and Anke: mijn hartelijk bedankt!

My deepest thanks are for Penny, who sensibly disbelieved my deadlines, but did believe in me. Her humour, patience and love over the last year have been a constant inspiration.

I can blame Linnett, David and Marian for teaching me to ask questions. My family also taught me that the only worthwhile answer is a thorough one. There is, however, no questioning their support and love, nor how important this has been to me.

# Contents

<b>List of Figures</b>	<b>xvii</b>
<b>1 Introduction</b>	<b>1</b>
1.1 Cold atoms . . . . .	1
1.2 Imaging cold atoms . . . . .	2
1.3 Diffraction-contrast imaging . . . . .	3
1.3.1 Concept . . . . .	3
1.3.2 Forward and inverse problems . . . . .	4
1.3.3 Inline holography: phase, amplitude and the twin-image .	5
1.3.4 The monomorphous-object assumption . . . . .	6
1.3.5 Contrast transfer functions . . . . .	7
1.3.6 Retrieving the column-density . . . . .	9
1.3.7 Phase-advancing and phase-retarding objects . . . . .	10
1.3.8 Magnification by point-projection . . . . .	10
1.3.9 Benefits and restrictions of DCI . . . . .	12
1.4 Diffraction-contrast imaging of cold atoms . . . . .	14
1.4.1 A cold atom trap . . . . .	14
1.4.2 Optical properties of cold atoms . . . . .	15
1.4.3 Cold atom imaging results . . . . .	15
1.4.4 Comparison with other techniques . . . . .	16
1.5 A note on precedence and publications . . . . .	17
1.6 What's new? . . . . .	18
1.7 A note on image reproduction . . . . .	19
<b>2 Diffraction and contrast transfer</b>	<b>21</b>
2.1 Scalar optics in free space and in inhomogeneous media . . . . .	22
2.1.1 Intensity: the result of optical measurement . . . . .	22
2.1.2 The vector wave equation in an inhomogeneous medium .	23
2.1.3 The scalar wave equation in an inhomogeneous medium .	24
2.1.4 The Helmholtz equation for a monochromatic wave . . .	24
2.2 Propagation of light through a monomorphous object . . . . .	26
2.2.1 The eikonal equation . . . . .	26
2.2.2 Ray solutions to the eikonal equation . . . . .	27

---

2.2.3	Rays in absorbing media . . . . .	28
2.2.4	Projection through a monomorphous material . . . . .	28
2.2.5	Plane wave illumination . . . . .	29
2.2.6	Spherical wave illumination . . . . .	30
2.2.7	Ray optics and the Born and Rytov approximations . . . . .	30
2.3	Diffraction in free space and the Fresnel approximation . . . . .	33
2.3.1	The transverse Fourier transform . . . . .	33
2.3.2	The angular spectrum . . . . .	34
2.3.3	Diffraction as a linear shift-invariant system . . . . .	37
2.3.4	The Fresnel approximation . . . . .	39
2.3.5	Where is Fresnel diffraction a valid approximation? . . . . .	40
2.4	Diffraction and magnification by point-projection . . . . .	42
2.4.1	Diffraction with spherical-wave illumination . . . . .	43
2.4.2	A stationary phase analysis . . . . .	45
2.4.3	Validity of the isomorphism . . . . .	47
2.5	Contrast transfer . . . . .	48
2.5.1	The intensity spectrum of Fresnel diffraction patterns . . . . .	48
2.5.2	Contrast transfer of absorption and phase-shifts . . . . .	50
2.5.3	Validity of the CTF expression . . . . .	53
2.5.4	Previous use of contrast transfer functions . . . . .	53
2.5.5	Contrast transfer of monomorphous objects . . . . .	54
2.5.6	The slowly varying phase condition . . . . .	57
2.5.7	Breakdown of linearity for thick object diffraction . . . . .	61
2.6	Paraxial optics and space-frequency distributions . . . . .	61
<b>3</b>	<b>Solving the inverse problem</b>	<b>65</b>
3.1	Holography: Retrieving information from diffraction patterns . . . . .	66
3.1.1	Gabor in-line holography . . . . .	66
3.1.2	The twin image and the information deficit . . . . .	67
3.1.3	Recording half as much information . . . . .	69
3.1.4	Recording two holograms . . . . .	70
3.1.5	Two holograms: the Transport-of-Intensity solution . . . . .	71
3.1.6	Reconstruction of wavefields by iterative methods . . . . .	72
3.2	CTF deconvolution: overview and review . . . . .	73
3.2.1	The inverse problem for pure absorption objects . . . . .	74
3.2.2	The inverse problem for pure phase objects . . . . .	75
3.2.3	The inverse problem for monomorphous objects . . . . .	76
3.2.4	CTF deconvolution in electron microscopy . . . . .	80
3.2.5	Comparison of CTF deconvolutions: TEM and DCI . . . . .	82
3.3	A TIE solution for monomorphous objects . . . . .	84
3.3.1	Derivation from the ambiguity-function marginal . . . . .	84
3.3.2	Comparison with the deconvolution solution . . . . .	86
3.3.3	Hybrid and iterative solutions for monomorphous objects . . . . .	89
3.4	Fourier deconvolution of the inverse problem . . . . .	90

3.4.1	The Wiener filter . . . . .	91
3.4.2	Simple Tikhonov regularisation . . . . .	93
3.4.3	Partial Tikhonov regularisation . . . . .	98
3.4.4	Applicability of the partial-Tikhonov filter . . . . .	102
3.5	Alternative bases for deconvolution . . . . .	104
3.5.1	An optimal basis for deconvolution . . . . .	104
3.5.2	The Fourier basis is optimal for coloured noise . . . . .	108
3.5.3	A wavelet basis is optimal for real-world images . . . . .	109
3.6	Hybrid Fourier-Wavelet deconvolution . . . . .	112
3.6.1	Distribution of noise in the wavelet basis . . . . .	113
3.6.2	Filtering in the wavelet basis . . . . .	114
3.6.3	Determination of $\alpha$ . . . . .	115
3.6.4	Optimality of FORWARD . . . . .	116
3.6.5	Performance of the FORWARD algorithm . . . . .	116
3.6.6	Diffraction contrast versus Zernike phase contrast . . . . .	117
3.7	Further enhancements of the deconvolution solution . . . . .	119
3.7.1	Beyond white detector noise . . . . .	119
3.7.2	Better transforms: improved wavelets . . . . .	119
3.7.3	Iterative enhancements . . . . .	121
3.7.4	New bases: beyond wavelets . . . . .	121
3.7.5	Deconvolving diffraction: Curvelets instead of wavelets? . .	123
3.7.6	Inverse problems and assumptions . . . . .	123
3.8	Optimising the propagation distance . . . . .	126
3.8.1	Intuitive view of optimal propagation distance . . . . .	126
3.8.2	A quantitative comparison with Zernike phase-contrast . .	128
3.8.3	A minimax approach to optimal propagation distance . .	129
3.8.4	Uncertainties in the propagation distance . . . . .	134
3.8.5	Propagation distance and red-detuned imaging . . . . .	135
4	<b>Atom trapping and imaging apparatus</b>	<b>137</b>
4.1	Design of the apparatus . . . . .	137
4.1.1	Cold atomic beams . . . . .	138
4.1.2	Design for a cold atomic beam . . . . .	138
4.1.3	Design for a magneto-optical trap . . . . .	140
4.2	Vacuum system . . . . .	141
4.2.1	Chamber design . . . . .	141
4.2.2	Mechanical design . . . . .	143
4.2.3	Windows . . . . .	143
4.2.4	Pumps and gauges . . . . .	145
4.2.5	Pump-down and bakeout . . . . .	146
4.2.6	Rubidium source . . . . .	147
4.3	Magnetics . . . . .	148
4.3.1	Coil design . . . . .	148
4.3.2	Coil construction . . . . .	149

---

4.3.3	Coil operation . . . . .	149
4.4	External-cavity diode laser system . . . . .	149
4.4.1	Mechanical design . . . . .	150
4.4.2	Optical design . . . . .	151
4.4.3	Environment isolation . . . . .	151
4.4.4	Temperature and current controllers . . . . .	152
4.5	Laser-frequency servocontrol systems . . . . .	154
4.5.1	Linewidth reduction . . . . .	154
4.5.2	Approaches to laser locking . . . . .	155
4.6	An electronic laser servo . . . . .	158
4.6.1	Overview . . . . .	158
4.6.2	Zeeman-modulated saturated-absorption spectrometer . .	160
4.6.3	Photodetector and input stage . . . . .	161
4.6.4	Phase-sensitive detector . . . . .	161
4.6.5	Post-filter . . . . .	162
4.6.6	Gain control . . . . .	162
4.6.7	Injection current actuator . . . . .	163
4.6.8	Piezoelectric disc actuator . . . . .	164
4.6.9	Compensator design . . . . .	166
4.7	Trap optical system . . . . .	167
4.7.1	Cooling and repumping lasers . . . . .	168
4.7.2	Optical fibres . . . . .	169
4.7.3	Beam diameter and beam quality . . . . .	169
4.7.4	Alignment and operation . . . . .	170
4.7.5	Future work . . . . .	170
4.8	Imaging system . . . . .	172
4.8.1	Imaging laser . . . . .	172
4.8.2	Imaging optics . . . . .	172
<b>5</b>	<b>Column-density retrieval from cold atom images</b>	<b>177</b>
5.1	Interaction of light with cold atoms . . . . .	178
5.1.1	Resolution of imaging and non-imaging measurements . .	178
5.1.2	Refractive index of a two-level atomic gas . . . . .	179
5.1.3	Refractive index of a multi-level atomic gas . . . . .	181
5.1.4	Refractive index for a dilute Bose gas . . . . .	182
5.1.5	Weak and strong absorption by MOTs and BECs . . . . .	182
5.1.6	Photon absorption destroys BEC . . . . .	183
5.1.7	The promise of off-resonant imaging . . . . .	185
5.1.8	Optimising probe beam detuning, intensity and pulse length	186
5.1.9	Superradiant Rayleigh scattering limits probe intensity . .	188
5.1.10	Coherent recoil and backaction . . . . .	189
5.2	Column-density retrieval for cold-atom objects . . . . .	190
5.2.1	Non-destructive imaging and diffraction contrast . . . . .	190
5.2.2	Diffraction contrast due to cold atoms . . . . .	191

---

5.2.3	Hyperfine transition strengths . . . . .	192
5.2.4	Circularly-polarised probe light . . . . .	194
5.2.5	Linearly-polarised probe light far off resonance . . . . .	195
5.3	Experiments with defocus-contrast imaging . . . . .	197
5.3.1	Why image a MOT off-resonance? . . . . .	197
5.3.2	Obtaining defocused images of the MOT . . . . .	198
5.3.3	Analysis of defocused MOT images . . . . .	201
5.3.4	Equivalence of single-lens defocus and propagation . . . . .	201
5.3.5	Equivalence of telescope defocus and propagation . . . . .	206
5.3.6	Negative defocus and red detuning . . . . .	208
5.3.7	Implementing the algorithms . . . . .	209
5.3.8	Retrieving column-density from defocus-contrast images .	211
5.3.9	Comparison with absorption & fluorescence imaging . .	214
5.4	Experiments with holographic imaging . . . . .	217
5.4.1	Removing the imaging lens . . . . .	217
5.4.2	Focusing images at retrieval time . . . . .	222
5.4.3	Magnification by point-projection . . . . .	224
5.5	Resolution limits in diffraction-contrast imaging . . . . .	230
5.5.1	Pixel resolution limit . . . . .	230
5.5.2	Diffraction limit: intuitive view . . . . .	231
5.5.3	Diffraction limit: Abbe theory . . . . .	231
5.5.4	Diffraction limit: PSWFs, sampling, Wigner distributions .	233
5.5.5	The diffraction limit in practice . . . . .	233
5.5.6	Fresnel-approximation limit . . . . .	235
5.6	Comparison with other imaging techniques . . . . .	237
5.6.1	Near-resonant absorption . . . . .	237
5.6.2	Dark ground . . . . .	238
5.6.3	Zernike phase-contrast . . . . .	239
5.6.4	Spatial heterodyne imaging . . . . .	242
5.6.5	Comparison with diffraction-contrast imaging . . . . .	243
5.7	Imaging signal-to-noise and destructivity . . . . .	247
5.7.1	Non-destructive SNR independent of detuning and power .	247
5.7.2	Technical noise: sources and solutions . . . . .	248
5.7.3	Fundamental limits to non-destructive SNR . . . . .	250
5.7.4	Prospects for non-destructive DCI . . . . .	252
<b>6</b>	<b>Conclusion</b>	<b>253</b>
6.1	DCI: a new phase imaging technique . . . . .	253
6.2	Diffraction-contrast imaging of cold atoms . . . . .	254
6.3	Future work on diffraction-contrast imaging . . . . .	255
6.4	Future work on cold-atom imaging . . . . .	256
<b>References</b>		<b>259</b>

<b>Author index to references</b>	<b>293</b>
<b>Appendices</b>	
<b>A Intensity: the result of optical measurement</b>	<b>301</b>
<b>B Rays in absorbing media</b>	<b>303</b>
<b>C Origin of the twin-image in Gabor in-line holography</b>	<b>305</b>
<b>D Wavelets in ten minutes</b>	<b>307</b>
D.1 What is a wavelet? . . . . .	307
D.2 The Continuous Wavelet Transform . . . . .	308
D.3 Discrete sets of wavelets . . . . .	310
D.4 Wavelet bases . . . . .	310
D.5 Choosing a wavelet . . . . .	314
D.6 The Discrete Wavelet Transform . . . . .	314
D.7 Wavelets in two dimensions . . . . .	316
<b>E Power dissipated in anti-Helmholtz coils</b>	<b>321</b>
<b>Publications</b>	
<b>F Noninterferometric phase imaging of a neutral atomic beam</b>	<b>323</b>
<b>G Frequency noise characterisation of narrow linewidth diode lasers</b>	<b>329</b>
<b>H Off-resonant defocus-contrast imaging of cold atoms</b>	<b>337</b>
<b>I X-ray phase imaging: Demonstration of extended conditions</b>	<b>341</b>

# List of Figures

1.1	A conceptual view of diffraction-contrast imaging . . . . .	3
1.2	The monomorphous contrast transfer function . . . . .	8
1.3	Magnification by point-projection . . . . .	11
1.4	Zernike phase-contrast imaging . . . . .	13
1.5	A diffraction-pattern and retrieved column-density . . . . .	16
2.1	Optical rays defined . . . . .	27
2.2	Plane wave illumination . . . . .	31
2.3	Spherical wave illumination . . . . .	31
2.4	Magnification by point projection . . . . .	43
2.5	The contrast transfer functions for absorption and phase-shift . . .	52
2.6	The monomorphous column-density CTF . . . . .	56
2.7	The slowly-varying phase condition . . . . .	59
3.1	Gabor in-line holography is a two step process . . . . .	68
3.2	Several phase CTFs . . . . .	76
3.3	The monomorphous CTF and its inverse . . . . .	78
3.4	Cryo-electron microtomography of biomolecules . . . . .	81
3.5	Normalised transfer functions for TIE and CTF solutions . . . . .	87
3.6	TIE retrieval applied to a weakly-absorbing object . . . . .	88
3.7	Incoherent imaging compared to CTFs . . . . .	94
3.8	Simple-Tikhonov regularisation for small and large $\alpha$ . . . . .	95
3.9	Distortion and noise in Tikhonov retrievals . . . . .	97
3.10	Comparison of spectra: column-density, noise and inverse filter . .	99
3.11	Wiener and partial-Tikhonov filters compared . . . . .	101
3.12	Retrievals using Wiener and partial-Tikhonov filters . . . . .	101
3.13	Fourier deconvolution fails at low SNR . . . . .	107
3.14	Signal and noise energies and the minimum possible MSE . . . . .	108
3.15	Wavelets are more economical than sinusoids for real-world images	111
3.16	Wavelet spectra of signal and coloured noise . . . . .	114
3.17	Wavelet denoising of diffraction-contrast and Zernike-phase images	118
3.18	Zernike versus DCI for three exposure values . . . . .	120
3.19	Hybrid curvelet-wavelet removal of white noise . . . . .	125

3.20	Retrievals from 10 photon/pixel diffraction patterns at 3 $z$ values . . . . .	130
3.21	Retrievals from 1000 photon/pixel diffraction patterns at 3 $z$ values . . . . .	132
4.1	The Thomann cold atomic beam . . . . .	139
4.2	MOT chamber side view showing ports . . . . .	142
4.3	MOT chamber plan view showing coils, pumps and gauges . . . . .	142
4.4	Vacuum system and support structure . . . . .	144
4.5	The Melbourne ECDL design . . . . .	150
4.6	Vibration isolation for the ECDL system . . . . .	153
4.7	Frequency dither demodulates to an error signal . . . . .	157
4.8	Schematic of laser lock by Zeeman modulation . . . . .	159
4.9	Injection current FM response of an AlGaAs diode . . . . .	164
4.10	Bode plot of the laser current FM response . . . . .	165
4.11	Bode plot of the PZT disc FM response . . . . .	166
4.12	Lower table optical schematic . . . . .	169
4.13	Vertical table optical schematic . . . . .	171
4.14	Optical layout for a future cold atomic beam . . . . .	173
4.15	Optical layout for collimated-illumination defocus contrast . . . . .	174
5.1	The refractive index for a two level atom . . . . .	180
5.2	Multiple non-destructive images of BEC taken at MIT . . . . .	185
5.3	Refraction and diffraction by a thick object . . . . .	187
5.4	Hyperfine structure of $^{85}\text{Rb}$ . . . . .	193
5.5	Contrast calculation from raw images . . . . .	199
5.6	MOT diffraction patterns as function of detuning and defocus. . . . .	204
5.7	Equivalence of simple-lens defocus and propagation . . . . .	205
5.8	Focused and defocused imaging with a two-lens telescope . . . . .	207
5.9	Retrieval techniques compared for MOT images . . . . .	214
5.10	Retrieved column-densities: Gaussian peak height . . . . .	215
5.11	Configuration for lensless imaging of a MOT . . . . .	218
5.12	Holographic diffraction pattern of a MOT . . . . .	219
5.13	Column-densities retrieved from a holographic image . . . . .	221
5.14	Focusing at reconstruction time . . . . .	223
5.15	Configuration for point-projection imaging of a MOT . . . . .	225
5.16	Point-projection magnified diffraction-contrast imaging . . . . .	228
5.17	Lens-magnified absorption and fluorescence images . . . . .	229
5.18	Diffraction limit of a lens . . . . .	232
5.19	Possibility for point-projection imaging of a BEC . . . . .	234
5.20	Imaging at wavelength resolution and below . . . . .	235
5.21	Off-resonant imaging techniques demonstrated on cold atoms . . . . .	240
5.22	Spatially-coherent noise (SCN) on a CCD . . . . .	249

D.1	A closed-form wavelet . . . . .	309
D.2	The wavelet transform of an unsmooth function . . . . .	309
D.3	Space-frequency tiling by dyadic sampling of wavelets . . . . .	311
D.4	Three dilations and scalings of the Haar wavelet . . . . .	312
D.5	Four Daubechies wavelets . . . . .	313
D.6	The Discrete Wavelet Transform . . . . .	315
D.7	The 2D Discrete Wavelet Transform . . . . .	317
D.8	Separable two-dimensional DWT of <i>Lena</i> . . . . .	318
E.1	Geometry of a single coil former . . . . .	322



# Chapter 1

## Introduction

THIS THESIS DESCRIBES a new method of seeing transparent, microscopic objects. No optics need be used and only the coherent-light diffraction pattern is recorded. A regularised-deconvolution algorithm extracts the structure of the object from the diffraction pattern.

The objects of interest in this work are clouds of laser-cooled atoms. The coldest such clouds, Bose-Einstein condensates, are destroyed by the absorption of light and must be imaged when transparent. This thesis presents images of the diffraction patterns produced by transparent clouds of cold atoms, and demonstrates the retrieval of detailed structural information from these patterns.

### 1.1 Cold atoms

Early work on laser-cooling of atomic beams led to the first demonstration of magneto-optical trapping of an atomic gas in 1987 [1]. This achievement revitalised the field of atomic physics and stimulated advances in areas as diverse as metrology and microfabrication. Fundamental new processes were discovered in the interaction of light with free atoms. The first Bose-Einstein condensate (*BEC*) in an atomic gas was created in 1995 [2–4]: a gas of millions of weakly-interacting atoms all in the same internal *and* external quantum states. This novel state of matter offered an unprecedented level of control over interactions, exposing familiar condensed-matter physics to new experiments and revealing entirely new physical processes. Interest in cold atom physics, and BEC in particular, continues to grow as the theoretical possibilities of quantum entanglement and teleportation of atoms become experimental realities. Perhaps the most interesting prospect of all is that atoms cooled in

optical lattices could form the substrate for a scalable quantum computer [5].

## 1.2 Imaging cold atoms

Almost everything we know about Bose-Einstein condensates comes from optical observation. Cold atoms in general show conventional optical behaviour: they absorb and phase-shift light passing through them. BECs are no exception. The act of observing a Bose-Einstein condensate, however, is quite capable of destroying it. If the illuminating radiation is resonant with an atomic transition, the BEC will become opaque, absorbing all incident light. Even though absorbed photons are re-emitted, carrying away almost all of their energy, the *momentum* recoil from absorbing a single photon is enough to eject an atom from the condensate. For alkali condensates, imaging the dark shadow of a condensate is destructive: if enough photons are scattered to form an image, the condensate will be destroyed in the process.

It *is* possible to image a condensate without also destroying it. If illuminated with laser light far-detuned from atomic resonances, absorption falls to negligible levels. Such transparent BECs may still have a measurable effect on the *phase* of the optical wave, and it is then an *optical problem* to make the phase-variations visible. Non-destructive imaging was demonstrated only a year after the first BEC was produced and several new dynamic processes were observed as a consequence. Despite the demonstrated success of non-destructive imaging, all but two of the more than 35 BEC experiments worldwide continue to use destructive absorption imaging. Presumably, this is due to the considerable complexity of fabricating and aligning the phase-imaging optics.

This thesis presents a phase-imaging method, termed *diffraction-contrast imaging* (DCI), which uses much simpler apparatus than methods currently employed for non-destructive imaging of cold atoms. Diffraction-contrast imaging retrieves the structure of the object from an image of its diffraction pattern. DCI should be capable of non-destructive imaging of a BEC, while using the same optics as destructive absorption imaging. An extension of the method offers high-resolution imaging with no lenses at all: only a light source and a detector are required. DCI is not limited to cold-atom imaging: it has also been applied to x-ray point-projection microscopy and femtosecond imaging of laser-induced plasmas. These extensions of DCI are not discussed in this thesis. A journal article concerning x-ray theory and experiments is included as Appendix I.

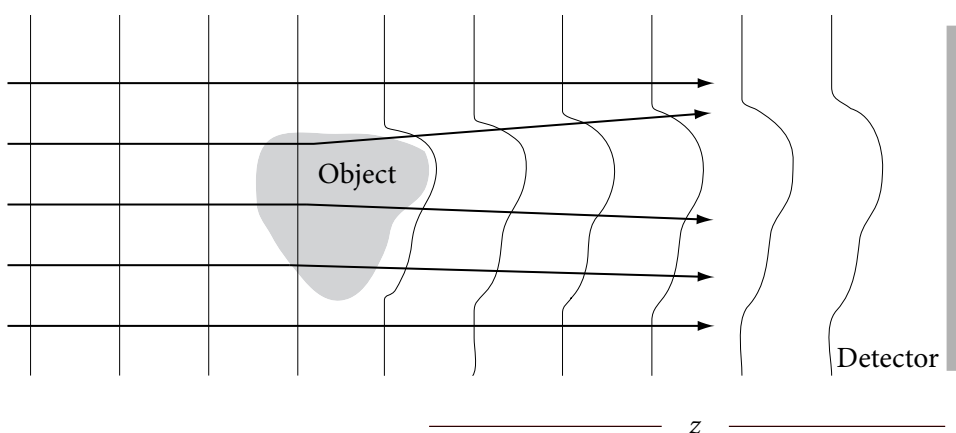


**FIGURE 1.1 A conceptual view of diffraction-contrast imaging.** A plane-wave of light is incident on an object, which absorbs and phase-shifts the light. The light propagates in free-space and is measured by a spatially-resolved detector. The second step of diffraction-contrast imaging is retrieving the column-density of the object from the measured diffraction pattern. This is done computationally.

Chapters 2 and 3 describe diffraction-contrast imaging as a general optical technique. Chapters 4 and 5 apply DCI to imaging of cold atoms in a magneto-optical trap (MOT). Prospects for future work are discussed in Chapter 6.

### 1.3 Diffraction-contrast imaging

Perceiving a transparent object is an old problem. Our ancestors must have wondered at the tangibility of the clear but turbulent air above a fire, and at how the gentle ripples on the surface of a pool render violent caustics on its bed.

The invention of new ways of seeing brought new transparent objects into view. Newton cursed the air, transparent but ‘in perpetual Tremor’, that lay between his telescope and the stars [6]. The first microscopists found the translucency of the microcosm allowed its observation in transmitted light. They saw, however, that the smallest things were so transparent as to be hardly visible.

#### 1.3.1 Concept

Diffraction-contrast imaging combines the oldest phase-contrast method with the newest mathematical tools for recovering the object structure. The principle is depicted in Figure 1.1. A plane-wave of light passes through a transparent, or almost-

transparent, object and after propagating through a distance  $z$  of free-space, the intensity is measured by a spatially-resolved detector, in particular a CCD camera. In the absence of the object, a constant intensity would be recorded. If the propagation distance is zero, we have a *contact image* which shows only absorption-contrast.

A contact image of a completely transparent object shows nothing but the constant background intensity. The *wavefield* will have been phase-shifted by the object, but the wave amplitude is unchanged and so the intensity is unchanged. As the detector is moved away from the object, refraction and diffraction cause amplitude variations in the wavefield and so variations in the measured intensity. Ripples of light on a river-bed are diffraction-contrast images of the water surface, although there the contrast is blurred by the limited spatial and temporal coherence of sunlight.

It does not seem possible to construct a simpler system than DCI which records an ‘image’. In the limit of small propagation distances, the image will resemble an outline of the object which a single bright and dark fringe pair outlining edges of the object. If the light is coherent, images at greater distances develop more diffraction fringes until the object is an unrecognisable mass of fringes (see left-hand column on p 88). To be an *imaging* technique, DCI must be able to recover a meaningful image of the object from this diffraction-pattern. This thesis shows that quantitative images *can* be recovered, subject to certain conditions on the object’s composition, thickness and on the propagation distance. The recovery process is termed *diffraction-contrast retrieval* (*DCR*).

### 1.3.2 Forward and inverse problems

An important theme of this thesis is the distinction between *forward* and *inverse* problems [7]. Leaving aside the finer points of etiology, we can describe the light passing through the object as a *cause*, and the detected diffraction-pattern as its *effect*.

The *forward problem* is predicting the effect of a known cause: in our case, the forward problem is predicting the diffraction-pattern of a known object. After introducing the scalar optics framework used in this thesis (§2.1), Chapter 2 describes the steps for solving the forward problem:

1. Determine the wavefield incident on the object. Usually this is well approximated by a spherical or plane wave.

- 
2. Given information about the object, such as refractive index and thickness, calculate the wavefield immediately after the object (§2.2).
  3. Propagate this exit-surface wavefunction a distance  $z$  to the imaging plane (§2.3), using either the *Rayleigh-Sommerfeld diffraction integral* (§2.3.3) or the *angular-spectrum transfer function* (§2.3.2), which are formally equivalent.
  4. Square the amplitude of this propagated wavefield to obtain the intensity at the detector.

Solving the forward problem is relatively simple. It is obviously *unique*: there is only one diffraction pattern for a given object, and the solution is *stable*: small changes to the object result in only small changes of the diffraction pattern.

Diffraction-contrast retrieval demands that we solve the *inverse problem*: given an effect (the diffraction pattern), we want to know as much as we can about its cause (the object). An example of the difficulty in solving this inverse problem is the well-known *Talbot effect*.

Imagine that the object to be imaged is a phase grating. It has been known since 1836 that the intensity following a grating shows periodic vanishings and reappearances of ‘images’ of the grating [8]. Equivalently, for any given propagation distance  $z$ , there are a countably infinite number of different grating periods which produce exactly zero contrast. Any combination of these gratings oriented in any direction in the plane could be added to any object and produce *no change* in the diffraction pattern. The inverse problem is thus not unique. Chapter 3 presents a solution to the non-uniqueness of a similar inverse problem.

### 1.3.3 Inline holography: phase, amplitude and the twin-image

We assumed in the previous discussion that the object was a *phase object*: one that is completely transparent and affects only the phase of the wavefield. If the object could be a phase-grating *or* an amplitude grating, it would not be possible to tell which from a diffracted image.

One way of viewing this problem is that we need *two* numbers at every point to specify the amplitude and phase of the wavefield after the object. The detector measures intensity, and so yields *one* number at each point. In a sense there is twice as much information in the wavefield than there is in the measured image. This generates a much deeper inverse problem than the vanishing contrast problem: rather

than missing information only at exact spatial frequencies, one-half of the information is gone. If using a  $1000 \times 1000$  pixel detector, recovering the full wavefield would be analogous to finding a unique solution to 1 million equations in 2 million unknowns! The general inverse problem of reconstructing the full wavefield from a diffraction pattern cannot be solved.

The first attempt to recover a wavefield from a diffraction pattern was made by Denis Gabor in 1947. He recorded a diffraction pattern on photographic film, and showed that illuminating the developed film reconstructed a wavefield which approximated the original wavefield incident on the film. We just saw, however, that there isn't enough information to reconstruct the full wavefield, and Gabor's method – which he termed *holography* – always produces a wavefield corrupted by an out-of-focus *twin-image* (§3.1).

#### 1.3.4 The monomorphous-object assumption

DCI has much in common with Gabor holography. Both techniques record diffraction-patterns, but Gabor holography attempts to reconstruct the full wavefield either optically, or by a digital simulation of optical propagation. Diffraction-contrast imaging assumes that the object is *composed of a single material*. Under this assumption, the phase and amplitude of the exit-surface wavefield are no longer independent quantities and both are simply related to the thickness of material the light has travelled through. There is then enough information to retrieve this *thickness* – a single number at each point – from the diffraction-pattern.

While the concept of thickness is sensible for conventional materials, it must be modified slightly for cold-atom imaging. I define the neologism *monomorphous* to describe an object composed of a single material. A monomorphous object is defined here to have a refractive index  $n$  with deviation from unity proportional to its density  $\rho$ :

$$n(\mathbf{r}) = 1 + \rho(\mathbf{r})(\delta + i\beta). \quad (1.1)$$

$\beta$  is termed the *absorption coefficient* and  $\delta$  the *phase coefficient*. A conventional material has a constant density, and therefore has a constant refractive-index: it is *homogeneous*. A cold-atom cloud does *not* have a constant density or refractive index, but still has a refractive index of the monomorphous form (1.1) if composed of a single species. The idea of thickness is then replaced by the *column-density*: the integral of the density  $\rho(\mathbf{r})$  along the direction of light propagation. For plane-

wave illumination as in Figure 1.1 the column-density is

$$\rho(\mathbf{x}) = \int_{-\infty}^0 \rho(\mathbf{r}) dz, \quad (1.2)$$

where  $\mathbf{r} = (x, y, z)$  and  $\mathbf{x} = (x, y)$ . The wavefield after the object is then  $\exp(-\mu) \exp(i\phi)$  with phase-shift  $\phi$  and absorption-coefficient  $\mu$  given by

$$\phi(\mathbf{x}) = k\delta\rho(\mathbf{x}) \quad \text{and} \quad \mu(\mathbf{x}) = k\beta\rho(\mathbf{x}). \quad (1.3)$$

Here we must assume that light rays are not refracted so much by the object that they are significantly transversely-displaced over its length. The derivation and validity of these expressions forms Section 2.2.

Diffraction-contrast imaging seeks to retrieve the column-density  $\rho(\mathbf{x})$  from the diffraction-pattern intensity  $I(\mathbf{x})$ . It seems that there is enough information to do this, but for our results to be meaningful the object must be monomorphous and we must know the phase and absorption constants  $\beta$  and  $\delta$ .

The monomorphous object assumption *includes* two commonly-used assumptions in optics. The *phase object* assumption of a purely-transparent object corresponds to  $\beta = 0$ , while the *real object* assumption of a purely-absorbing object corresponds to  $\delta = 0$ . Pure phase-objects are particularly unrealistic: transparent materials have a small residual absorption which can be accounted for with (1.1). We will see in §3.2.3 that doing so offers great advantages when retrieving the column-density.

### 1.3.5 Contrast transfer functions

It is all very well to use information theory to argue that this retrieval is *possible*. These arguments tell us nothing about *how* to carry out such a retrieval. This thesis presents a *direct solution* to this inverse problem: we incorporate our assumptions (1.1) into the forward problem and after further assumptions and approximations we obtain an expression for the diffraction-pattern intensity which can be solved for the column-density. Finding this expression is the subject of the Sections 2.5.

Section §2.5 shows that if the rigorous Rayleigh-Sommerfeld diffraction is approximated by *Fresnel diffraction* (a good approximation for objects significantly larger than a wavelength) then a simplified expression may be written for the measured diffraction-pattern *intensity* in terms of the object's phase-shift and absorp-

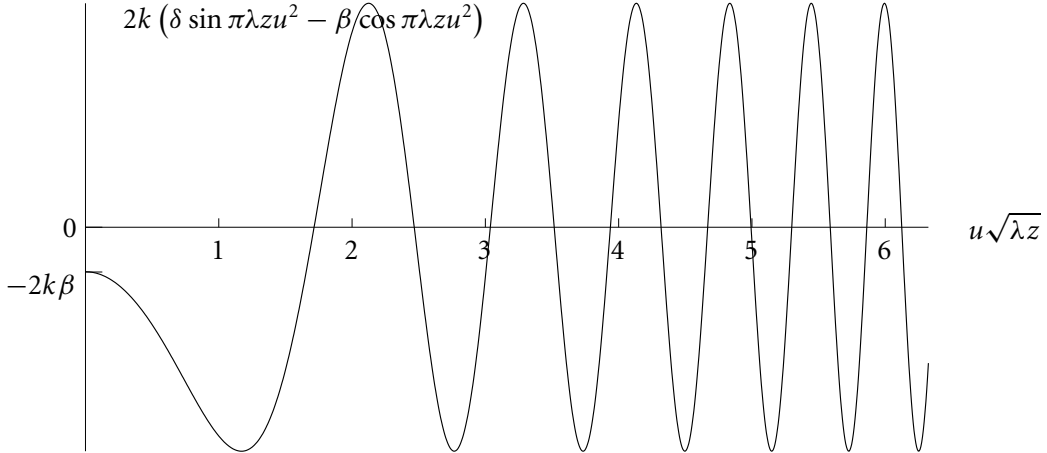


FIGURE 1.2 The monomorphous contrast transfer function. The object is assumed to be phase-advancing.

tion. Further assuming that the object absorbs weakly and causes limited phase-shifts leads to a *linear shift-invariant relationship* between the diffraction-pattern contrast  $I(\mathbf{x})/I_0 - 1$  and the phase and absorption:

$$\mathcal{F} \left\{ \frac{I(\mathbf{x}) - I_0}{I_0} \right\} = 2 \sin \pi \lambda z u^2 \mathcal{F}\{\phi(\mathbf{x})\} - 2 \cos \pi \lambda z u^2 \mathcal{F}\{\mu(\mathbf{x})\}, \quad (1.4)$$

in which  $I_0$  is the illumination intensity,  $\mathcal{F}\{\cdot\}$  indicates a Fourier transform and  $u^2 = u_x^2 + u_y^2$  is the spatial frequency. This expression makes it particularly clear that phase and absorption contribute to the diffraction pattern in a fundamentally inseparable manner. The factor  $\sin \pi \lambda z u^2$  is known as the phase *contrast transfer function (CTF)* and  $\cos \pi \lambda z u^2$  as the amplitude CTF.

Substituting the monomorphous-object expressions (1.3) for absorption and phase-shift yields

$$\mathcal{F} \left\{ \frac{I(\mathbf{x}) - I_0}{I_0} \right\} = 2k (\delta \sin \pi \lambda z u^2 - \beta \cos \pi \lambda z u^2) \mathcal{F}\{\rho(\mathbf{x})\}. \quad (1.5)$$

The term in parentheses, plotted in Figure 1.2, is termed the *monomorphous CTF*. This equation can be solved for column-density  $\rho$ , suggesting that it can be used to recover column-density images from diffraction contrast.

### 1.3.6 Retrieving the column-density

Re-arranging for  $\rho$  yields

$$\rho(\mathbf{x}) = \frac{1}{2k} \mathcal{F}^{-1} \left\{ \frac{1}{\delta \sin \pi \lambda z u^2 - \beta \cos \pi \lambda z u^2} \mathcal{F} \left\{ \frac{I(\mathbf{x}) - I_0}{I_0} \right\} \right\}. \quad (1.6)$$

This *formal solution* to the inverse problem is no use at all unless it can be made numerically stable and also fast enough to execute in a realistic period of time. We can already see that there is a profound problem with stability: for some spatial-frequencies  $u$  the denominator will be zero! It should be no surprise that these spatial frequencies are exactly those of the Talbot gratings for which there is no contrast.

Section 3.4 begins by discussing the conventional *Tikhonov regularisation* method used to stabilise many inverse problems. Unfortunately, this method retrieves column-density images that are either too noisy or too distorted. The theoretically-optimal retrieval method is known as a *Wiener filter*, but it cannot be implemented in practise as it assumes prior knowledge of the object structure. I show that a *partial-Tikhonov* filter more closely approximates the Wiener optimum without making strong assumptions about the object structure. Simulated retrievals with this filter display lower noise and less distortion.

When imaging the smallest Bose-Einstein condensates, every photon counts. Non-destructive imaging may require exposures of fewer than 50 photons per pixel. Under these conditions, shot-noise is high enough that even the ‘optimal’ Wiener filter does not yield satisfactory retrievals. The Wiener filter is really only the optimum for *stationary* objects, such as crystals, which look similar at all locations in space. It is far from optimal for finite-sized objects. Formulating a better filter requires moving away from the Fourier basis, which is good at representing crystals but very bad at representing compact objects with sharp edges. Section 3.5 shows that a *wavelet* basis is better for representing finite-sized objects, but not well-suited to deconvolving the contrast transfer function. In Section 3.6, I extend a hybrid Fourier-wavelet deconvolution algorithm known as `FORWARD` to use the partial-Tikhonov filter. Simulations suggest that this solution to the inverse problem is capable of retrieving accurate column-density images from diffraction-patterns with only a few photons per pixel exposure. Some possible further enhancements of the diffraction-contrast retrieval algorithm are considered in §3.7.

If we know the propagation distance  $z$ , the wavelength  $\lambda$  and the absorption

and phase coefficients  $\beta$  and  $\delta$ , these algorithms are capable of retrieving an image of a monomorphous object from a single diffraction-pattern. How do we select the propagation distance to use? A propagation distance of zero clearly renders the least contrast for an almost-transparent object, while in the far-field the pattern simply spreads out over a greater area of detector but with a concomitant reduction in contrast. Somewhere inbetween the contact and far-field images there must be a point of optimal contrast. Section 3.8 shows that integrated contrast is higher at larger distances where the diffraction-pattern is *holographic*: an unrecognisable tangle of fringes with all but the largest structures highly diffracted.

### 1.3.7 Phase-advancing and phase-retarding objects

Diffraction-contrast imaging suffers from a fundamental instability when applied to *phase-retarding* objects. Phase-retarding materials have refractive indices with real part greater than one, equivalently, they have positive  $\delta$  in the monomorphous refractive index expression (1.1). Conventional translucent materials at visible wavelengths are phase-retarding, for example glass has  $n \approx 1.5$ .

The instability is clear if we imagine a lens-shaped object made of phase-retarding material with some finite absorption, a piece of coloured glass for example. The phase effect of the object tends to focus light towards the optical axis, however this is where absorption is strongest and the absorption and phase effects cancel and contrast is lost. More rigorously, when  $\delta$  is positive the first zero of the monomorphous CTF in (1.6) is at a much lower spatial-frequency than for negative  $\delta$  materials and a much wider interval of the spatial-frequency spectrum is lost (see also Figure 3.3 on p 78).

This instability is less of a restriction than might be imagined: conventional objects of interest, such as biological cells, are not monomorphous and so do not fall within the ambit of DCI in any case. The highest-energy electronic resonance in light atoms lies in the soft x-ray region and so these materials are phase-advancing at hard x-ray wavelengths. Cold atoms are imaged in the visible, but by tuning to the blue of strong atomic resonances, they too become phase-advancing materials suitable for diffraction-contrast imaging.

### 1.3.8 Magnification by point-projection

One important advantage of diffraction-contrast imaging over focal phase imaging techniques, such as Zernike phase-contrast, is the absence of imaging optics. Re-

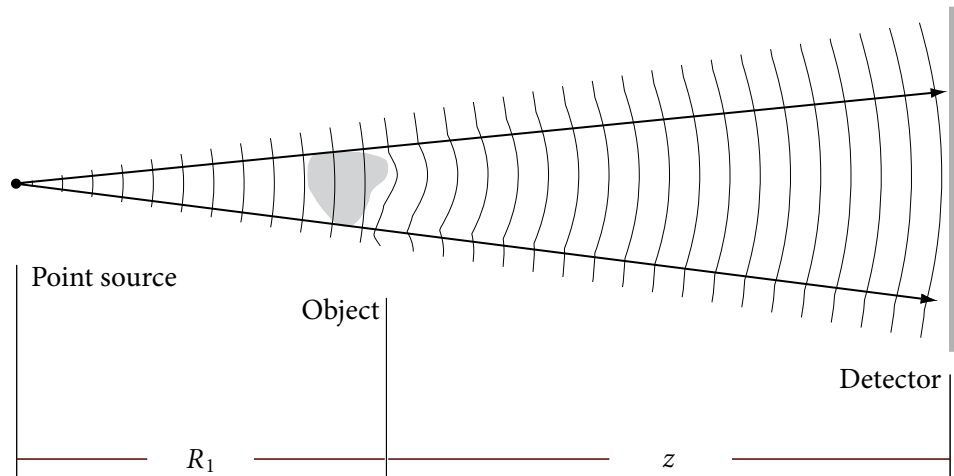


**FIGURE 1.3 Magnification by point-projection.** A point-source of light is located a distance  $R_1$  before the object, and the detector is a distance  $z$  after.

moving lenses removes lens aberrations, reduces losses from optical surfaces and removes image noise due to dust and imperfections on the lens surface. But removing lenses also removes magnification – or does it?

Figure 1.3 shows how lensless magnification can be achieved by *point projection*. The effect must be amongst the oldest known optics: the looming, enlarged shadows thrown by a fire on a distant wall must have been noticed millennia before the first lenses were ground. From geometry it is clear that the magnification is  $M = (R_1 + z)/R_1$ . With coherent light, the image will naturally not be a shadow, but a diffraction pattern.

What is less obvious is that the diffraction pattern will be magnified but otherwise identical to the diffraction pattern observed with collimated illumination (Figure 1.1) at an effective propagation distance  $z_{\text{eff}} = R_1 z / (R_1 + z)$ . A careful proof of this isomorphism is given in §2.4, and a novel and simple validity-bound is derived. The result assures us that we can retrieve a column-density from a point-projection magnified diffraction-pattern simply by using the effective propagation distance  $z_{\text{eff}}$  in place of  $z$  in the retrieval algorithm.

The ‘apparatus’ of Figure 1.3 may be even simpler than Figure 1.1 as it is often easier to produce a point-source of radiation than a well-collimated beam. In x-ray imaging, for example, a point source is readily produced by focusing an electron beam to a very small spot-size on a metal target. X-ray point-projection microscopes using this method have achieved magnifications of  $1000\times$  with no x-ray

TABLE 1.1 Benefits and restrictions of diffraction-contrast imaging.

Benefits	Restrictions
Simplest possible apparatus	Object must be monomorphous
Single image sufficient	Unstable for phase-retarding objects
Holographic depth-of-field	Absorption must be weak.
Lenses not required	Phase must be slowly-varying.
Uses full CCD resolution	Lower SNR than Zernike imaging
Residual absorption stabilises retrieval	
Stable, fast retrieval algorithm	
Temporal coherence not critical	
Minimal calibration	
No optical alignment	
Low sensitivity to vibration	

lenses required. Diffraction-contrast imaging has the potential to increase the resolution of these microscopes by deconvolving diffraction in the projected image.

### 1.3.9 Benefits and restrictions of DCI

The relative merits of phase-imaging techniques depend greatly on the object to be imaged. If imaging stained biological cells, any one of the first four restrictions given in Table 1.1 would be enough to rule out DCI. On the other hand, when imaging cold atoms these four restrictions are not a concern, as we will soon see.

Other methods for retrieving information from diffraction-patterns are discussed in §3.1 and compared with DCI. There are, of course, non-holographic methods of phase imaging which rely on optics – phaseplates, prisms, aperture-stops – placed between the object and the detector. These methods tend to be less general. For example, a prism with substantial refraction angle is a trivial device to make at visible wavelengths but quite impractical at x-ray wavelengths.

The benchmark non-holographic method used for comparisons in this thesis is the *Zernike phase-contrast* method depicted in Figure 1.4. An image of the object is focused on the detector by a telescopic lens system. A transparent object would produce no image if it was not for a *phase-plate* placed between the lenses. The phase-plate has a small bump at the focal point of the lens system so that the incident plane-wave component is phase-shifted and interferes with the component of the wavefield phase-shifted by the object. The result is a bright-field image with intensity

$$I(\mathbf{x}) = I_0(1 + 2\phi(\mathbf{x})) \quad (1.7)$$

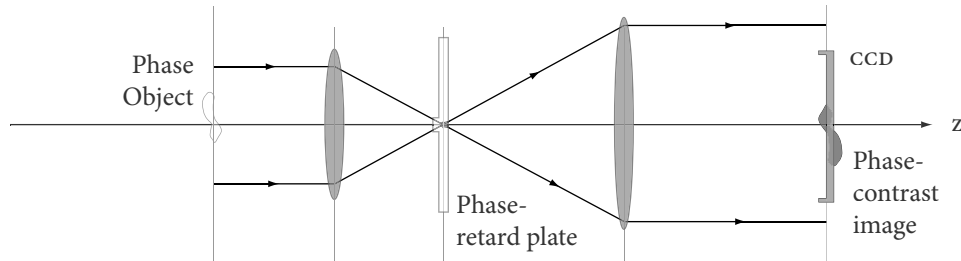


**FIGURE 1.4 Zernike phase-contrast imaging.** A standard telescopic imaging system is modified by placing a *phase-plate* in its Fourier plane. The incident plane-wave (grey) is phase-shifted by the central bump of the phase-plate. The scattered wave (black) is little affected. Superimposing the two components on the detector yields phase-contrast.

for small phase-shifts  $\phi$ . A more thorough description of the Zernike method is given in §5.6.3.

An advantage of the Zernike method is that the phase-contrast is directly visible and does not require a retrieval algorithm. Signal-to-noise is also the highest of all in-line imaging methods.

On the other hand, phase-contrast imaging requires fabrication and alignment of the phase-plate. The measured phase is highly sensitive to the phase-plate thickness and alignment. Lens aberrations ultimately limit the imaging resolution. These drawbacks are avoided using DCI. Zernike phase-contrast assumes a completely transparent object, although it can be corrected for absorption in a monomorphous objects.

One fundamental advantage of DCI over non-holographic methods such as Zernike imaging is its *holographic depth-of-field*. As no lenses are necessary, there is no focusing step when recording the diffraction-pattern. Setting the propagation distance in the retrieval is equivalent to focusing a lens system in a non-holographic method. It is *impossible* to record an out-of-focus diffraction-pattern, it is merely possible to retrieve at an incorrect distance. The retrieval distance can be adjusted at leisure, even after the apparatus has been dismantled. Further, if the diffraction-pattern was due to multiple objects at different distances from the detector, it is possible to ‘focus’ on them individually by retrieving at different propagation distances.

Diffraction-contrast imaging and Zernike phase-contrast are simulated for few-photon exposures and compared in §3.6.6 and a signal-to-noise analysis is given in §3.8.2. The relative merits of Zernike, DCI and other cold-atom imaging systems

are discussed in §5.6.



THE FIRST TWO Chapters of this thesis describe diffraction-contrast imaging, a phase imaging technique based on recording diffraction-patterns without the use of optics. Restricting Fresnel diffraction theory to consider only monomorphous objects generates a retrieval algorithm which can be stabilised by inverse-problem techniques. Diffraction-contrast imaging offers the depth-of-field of inline holography, but avoids the twin-image problem of holographic reconstruction.

## 1.4 Diffraction-contrast imaging of cold atoms

The latter part of this thesis applies diffraction-contrast imaging to imaging of cold atoms. Chapter 4 describes the design and construction of a magneto-optical trap (MOT) which produces a cloud of cold atoms. The cloud is larger, less dense and less cold than a BEC, and consequently is not as sensitive to heating when imaged. Nevertheless, the MOT makes an excellent test object for DCI experiments; the results of these are presented in Chapter 5.

### 1.4.1 A cold atom trap

The magneto-optical trap was originally designed to also function as a cold-atom *beam*; §4.1 describes the design decisions for this dual-use system, and the vacuum system is detailed in §4.2. The restoring force that confines atoms in a MOT is provided by Zeeman-adjustment of the optical spontaneous force. A spherical-quadrupole magnetic field traps atoms in three dimensions and is produced by anti-Helmholtz coils (§4.3).

The viscous cooling force is generated by an *optical molasses* of counter-propagating laser beams. Laser light was produced by *external-cavity diode lasers (ECDLs)*. Design and construction of these lasers was a major component of this project. The lasers themselves are described in §4.4. Stabilising lasers to an atomic transition requires electronic or optical feedback. Stabilisation techniques are reviewed in §4.5, and the controller design is described in detail in §4.6. Optics for the trapping beams are described in §4.7. Finally, the arrangement of the imaging system is given in §4.8.

### 1.4.2 Optical properties of cold atoms

Chapter 5 begins with a derivation of the refractive index of cold atoms. It is shown that cold atom clouds behave as monomorphous objects, and even the transition to BEC does not significantly alter this behaviour. They are phase-advancing objects when the probe light is detuned blue of the atomic resonance.

The destructive effects of photon absorption are considered in §5.1.6 and then an example is given of how off-resonant imaging can be non-destructive. Resolution of the imaging system is shown to be optimal when the atom cloud phase-shifts the probe beam by around one radian (§5.1.8).

It follows that a BEC imaged off-resonance is a weakly-absorbing object which confers a moderate phase-advance on the probe radiation. Typically, atoms in a BEC are in a single internal quantum state and the cloud is then a monomorphous object. With reference to Table 1.1 it is clear these are just the conditions needed for a DCR to be valid. Indeed, it is not an exaggeration to say that the diffraction-contrast method is ideally suited to imaging cold-atoms.

### 1.4.3 Cold atom imaging results

Alkali atoms have rich hyperfine structure. The interaction of this structure with the probe field determines the absorption and phase coefficients  $\beta$  and  $\delta$ . This spectroscopy is the subject of §5.2.3ff.

Although DCI is capable of imaging without lenses, the first series of results presented in §5.3 were taken with a re-imaging lens. This allowed a continuum of images to be taken including in-focus absorption images and diffraction-contrast images with arbitrarily small propagation distance. Isomorphism between a defocused lens systems and free-space propagation are elucidated in §5.3.4 and §5.3.5. Of particular interest is that defocusing towards the object is equivalent to a *negative* propagation distance, and that this can be used to render the diffraction-pattern of a phase-retarding object identical to that of the equivalent phase-advancing object (§5.3.6).

Column-density images retrieved with the partial-Tikhonov filter and with the hybrid Fourier-wavelet filter are shown on p 213. The retrievals are of comparable quality and resolution to fluorescence and absorption images. A quantitative comparison with absorption imaging (§5.3.9) shows that DCI is *more* precise.

A second series of experiments demonstrated diffraction-contrast retrievals without the reimaging lens (§5.4.1) and with point-projection magnification (§5.4.3).

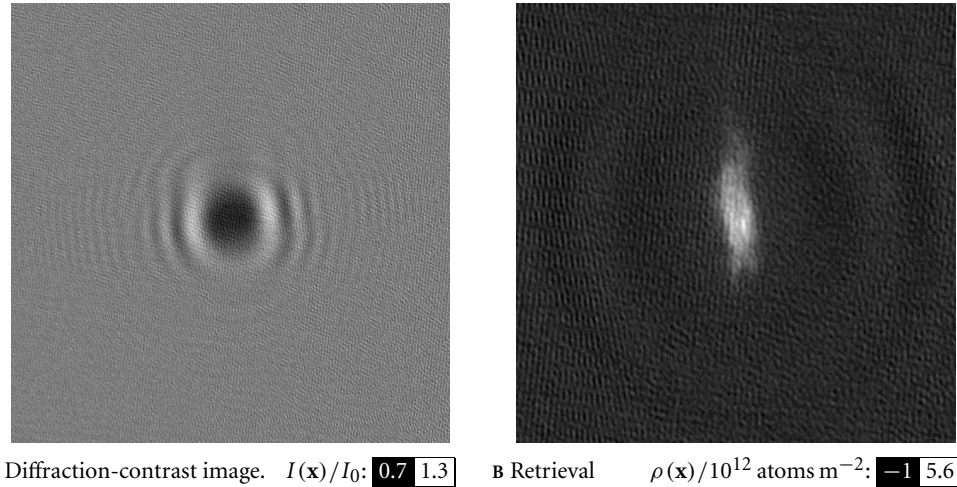


**FIGURE 1.5 A diffraction-pattern and retrieved column-density.** The diffraction-pattern section shown is  $4 \times 4 \text{ mm}$  and the retrieval is  $2 \times 2 \text{ mm}$ . The number on the black background corresponds to the black level in the image, the number on the white background to the white level. See Figures 5.12 and Figure 5.13 for details of the retrieval.

Considerable detail in the atom cloud is visible, and distortions introduced by the retrieval process are negligible. A diffraction-pattern (A) and retrieved column-density (B) are reproduced in Figure 1.5.

Section §5.5 comments on resolution limits in focal phase-imaging (i.e. Zernike phase-contrast) and in diffraction-contrast imaging. Re-imaging is shown to be advantageous when optical access is poor and the effective f-number of a bare detector limits the resolution. When optical access is good – such as imaging BECs held in UHV glass cells – resolution down to a few micrometres should be possible. An example geometry achieving  $3.7 \mu\text{m}$  resolution with a standard commercial CCD detector is given in Figure 5.19. Even better resolutions may be possible with in-vacuum fibre point-sources. The Section concludes by discussing obstacles to realising wavelength-resolution, and potential paths around them.

#### 1.4.4 Comparison with other techniques

Prior to this thesis, three techniques had been demonstrated for off-resonant phase-imaging of cold atoms: dark-ground imaging, Zernike phase-contrast and spatial-heterodyne imaging. The first two are standard microscopy techniques, the latter is more commonly known as *off-axis image holography*.

Section 5.6 presents a thorough critical comparison of the three techniques with diffraction-contrast imaging, summarised in a table on p 244. While the ultimate signal-to-noise ratio of DCI is somewhat lower than other techniques, there is no question that it is the simplest. I also argue that the simplicity of DCI and its lack of adjustable parameters to calibrate should make it more accurate than any other technique. Further, DCI has holographic depth-of-field, unlike the focal Zernike and dark-ground techniques. Spatial-heterodyne imaging also has holographic depth-of-field, but is the most elaborate of all techniques and has never been used for non-destructive imaging.

The final Section of the thesis is a quantitative analysis of signal-to-noise ratio in off-resonant imaging and its relation to destructive heating of BEC. The minimum heating of the condensate depends only on its density and on the signal-to-noise ratio of the measurement. Additionally, the SNR cannot be improved by exploiting coherences in the condensed atoms. I note, however, that non-destructive image sequences presented to date have been limited by technical considerations rather than heating of the condensate.

This thesis does not *demonstrate* that DCI is non-destructive. Nevertheless, I believe that the arguments advanced in the final two Sections show that a sequence of several diffraction-contrast images of a BEC should be possible without destroying the condensate. The next step is clearly to demonstrate DCI for Bose-Einstein condensates. In concluding, I comment on some other possible extensions of this work.



TWO ATTRIBUTES distinguish diffraction-contrast imaging from all other imaging techniques: *no optics* are needed, and only a *single image* is required. The lack of optics simplifies apparatus and removes technical variables from the imaging process. Diffraction-contrast imaging is uniquely suited to the requirements of cold-atom measurement. I hope that this new way of seeing will lead to new understandings in atomic and optical physics.

## 1.5 A note on precedence and publications

The course of this project has not, of course, followed the linear and coherent trajectory outlined in this precis. Initially the aim of the project was to make a

---

non-interferometric measurement of the phase of an atomic beam by Transport-of-Intensity techniques. I contributed to some early experiments with a thermal atomic beam; these are described in the article included as Appendix F. Seeking to improve these results led to the design of the cold atomic beam apparatus discussed in §4.1.

It became clear, however, that the atomic physics community would be more interested in non-interferometric measurements of *optical* phase-shifts, in particular the phase-shifts due to cold atom clouds illuminated off-resonance. Standard Transport-of-Intensity solutions require *two* images, but a single-image solution for monomorphous objects was described by David Paganin in early 2001 (see §3.3). The cold beam system was set up as a magneto-optical trap, and defocused images of the MOT were processed with the monomorphous TIE algorithm. These results were published in the article included as Appendix H. In considering the resolution limits of the TIE method, I derived the CTF-deconvolution solution, and later found that a similar expression was used by electron microscopists.

It was clear to me that the CTF deconvolution would be a powerful technique in x-ray point-projection microscopy. I sought a provisional patent on the solution, in particular the partial-Tikhonov regularisation procedure, and was granted Australian Provisional Patent number 2003903870 on 27 June 2003. I presented a poster describing this work at the Second International Workshop in Non-Crystallographic Phase Retrieval [9] on 30 June 2003. The following day, Timur Gureyev gave a talk outlining the same CTF deconvolution method [10]. As this was a genuine case of scientific coincidence, I decided that it was improper to proceed with the patent application.

## 1.6 What's new?

This work extends the deconvolution of optical diffraction patterns in a number of fundamental ways. A formally similar solution to (1.6) was derived in the electron microscopy literature as long ago as 1971. The derivation from the ambiguity functional marginal given in §2.5 is new, however, as is the consequent determination of extended validity conditions. The application of the monomorphous CTF outside electron microscopy is also novel. Electron and optical methods are compared and contrasted in §3.2.5.

Previous optical work on deconvolving the diffraction patterns due to pure phase objects (§3.2.2) came chiefly from particle holography literature. None of

these results demonstrate retrieval of the detailed structure in an object.

This thesis rigorously analyses of the inverse problem, and its relationship to the Wiener filter. A partial-Tikhonov filter follows from this; it is a new results and is carefully justified. More generally, the spectral analysis of signal and coloured noise (for example Figure 3.10 and accompanying discussion) has not previously been attempted. The wavelet-enhanced deconvolution of holograms is completely new.

This work is the first investigation of diffraction-based imaging of cold atoms. One 1997 article describes analysis of cold-atom diffraction patterns by regression method. As discussed in §5.2.1, only the mean size of the cloud (Gaussian width) was recovered. This thesis presents the first retrieval of an image of an atom cloud from its diffraction pattern. The demonstration of holographic depth-of-field is novel, as is point-projection magnification of the diffraction pattern.

The design and assembly of the atom trap was my work. I also derived, coded and applied the retrieval algorithms, with the exception of the Fourier-wavelet regularised deconvolution (`FORWARD`) algorithm described in §3.6 which was modified from published source code as cited.

All of the images presented in this thesis were taken by two colleagues, who were also responsible for constructing the imaging apparatus. Karl Weber obtained the first set of defocus-contrast images in 2002, taking data before I had debugged the `TIE` retrieval code. Despite this ‘blind’ data collection, the images form a meticulous set of data, more than sufficient to demonstrate the quantitative nature of `DCI` and its relative insensitivity to focusing errors. In 2004, Kenian Domen greatly enhanced the imaging apparatus, synchronising rapid, computer-controlled switching of the trapping and imaging lasers with the electronic camera shutter. Kenian obtained the first holographic diffraction patterns and performed the first point-projection imaging experiments.

I am deeply grateful to Karl and Kenian for their careful work and their interest and enthusiasm. Their results have rendered the ideas of this thesis into a demonstrated and useful technique.

## 1.7 A note on image reproduction

Many images are presented in this thesis, both simulations and data. I have presented them in linear greyscale rather than false colour; it appears to be the con-

sensus in the signal processing community that this best facilitates the comparison of results.

In this PDF version of this thesis, images have been embedded without compression or resampling. On-screen viewing of images allows comparison without the artifacts introduced by the printing process.

## Chapter 2

# The forward problem: Diffraction and contrast transfer

IN THIS CHAPTER I consider the forward problem: given a monomorphous object with known column-density, illuminated by a collimated or point source, what is the diffraction pattern measured by an optical detector some distance after the object? The problem separates into two parts: propagating light through the inhomogeneous medium (§2.2) and through free-space (§2.3).

The problem of diffraction through free-space can be solved exactly. This Chapter presents two equivalent and exact solutions: the angular spectrum and the Rayleigh-Sommerfeld integral. Although useful for simulating diffraction patterns, neither yields an invertible expression relating the object structure and the intensity of its diffraction pattern. Section §2.5 gives a novel derivation of a *contrast transfer function* expression which yields the desired simple and invertible relationship between object structure and diffraction contrast.

Point-projection of light through an object onto a detector achieves magnification without lenses. The point-projection magnification pattern is isomorphic to the magnified plane-wave pattern at a related propagation distance. An incidental result of this Chapter is a new extended validity condition for this isomorphism given in Section 2.4.

Both the ray optics approximations used inside the object, and the diffraction solutions used in free-space are derived from the scalar Helmholtz equation. This Chapter begins by summarising the provenance of the scalar Helmholtz equation and relating its scalar wavefield to the measured intensity.

## 2.1 Scalar optics in free space and in inhomogeneous media

The forward problem of diffraction-contrast imaging breaks into four sequential physical processes. First, the illuminating radiation must be generated, although the physical process involved is irrelevant. This Chapter considers two useful forms of illumination arriving at the object: plane-wave (collimated) and spherical wave (point-source). Second, the light propagates through the object and is attenuated and phase-shifted in the process. This disturbed wave then propagates through free-space and its amplitude and phase are altered by the process of *diffraction*. Finally, the intensity of the wavefield is measured on the detector.

Different models are used for propagation in the object and propagation in free space. Ray optics is used to describe the light inside the object (§2.2) while Fresnel diffraction describes propagation over a longer distance in free space (§2.3). Both models are based on *scalar optics*, which is only an approximation to the full Maxwell theory which governs the behaviour of classical fields. This Section is a brief discussion of the approximations involved in the underlying theory of scalar optics, and its connections to the measured intensity and the fundamental Maxwell theory of classical fields.

### 2.1.1 Intensity: the result of optical measurement

Diffraction-contrast imaging measures the *intensity* of light. Optical experiments in general measure intensity, even if this measurement is often interpreted as a measurement of wavelength, phase, polarisation or some other quantity of interest. An example is the spectrometer, which indirectly measures the wavelength of light but directly measures intensity as a function of the grating angle.

But what *is* intensity? Many texts define it in terms of the Poynting vector, either its magnitude or its projection onto a surface normal. The intensity is better defined in terms of the magnitude of the electric field vector  $\mathbf{E}$  as

$$I = \sqrt{\frac{\epsilon}{\mu}} \langle \mathbf{E} \cdot \mathbf{E} \rangle \quad (2.1)$$

where  $\epsilon$  is the dielectric permittivity,  $\mu$  is the magnetic permeability and the brackets  $\langle \cdot \rangle$  denote a time-average over many optical cycles. This is the same intensity as the Poynting vector definition *for a plane wave*, but in more complicated cases (2.1) is consistent with the measured intensity while the Poynting vector definiton is not. Appendix A discusses this further.

The electric field  $\mathbf{E}$  of an optical wave is a rapidly-oscillating vector quantity. The next two Articles show how the oscillations and polarisation information can be factored out. But we must start with the knowledge that the intensity is the square-magnitude of the electric field vector.

### 2.1.2 The vector wave equation in an inhomogeneous medium

The electric field vector obeys the Maxwell equations. In a medium composed of atoms, some of the microscopic interactions of electrons with the field are accounted for by introducing the *displacement field*  $\mathbf{D} = \epsilon \mathbf{E}$  where  $\epsilon$  is the *permittivity* of the medium. If  $\epsilon$  is allowed to be a complex number, then absorption by the medium is accounted for. This model assumes that the medium is linear, isotropic, uncharged, non-conducting, non-magnetic and does not vary over time. The macroscopic Maxwell's equations [11] yield:

$$\nabla^2 \mathbf{E} - \nabla (\nabla \cdot \mathbf{E}) = \frac{\epsilon}{c^2} \frac{\partial^2 \mathbf{E}}{\partial t^2}, \quad (2.2)$$

where  $c$  is the speed of light in vacuum. In free-space, the second term vanishes (absence of charges was assumed) leaving the familiar vector wave equation.

In a material, the induced polarisation must be included. It is useful to define here the *refractive index*  $n \equiv \sqrt{\epsilon}$  and substitute it into Gauss's Law yielding

$$\nabla \cdot \mathbf{D} = \nabla \cdot (n^2(\mathbf{r}) \mathbf{E}(\mathbf{r})) = 0, \quad (2.3)$$

where the spatial variation of the refractive index has been made explicit by showing  $n$  as a function of the position vector  $\mathbf{r} = (x, y, z)$ . Expanding and solving for  $\nabla \cdot \mathbf{E}$ , the source term in (2.2) may be written

$$\nabla (\nabla \cdot \mathbf{E}) = -2\nabla(\mathbf{E} \cdot \nabla \ln n). \quad (2.4)$$

Strohbehn [12] has considered a perturbative expansion of this expression for small deviations  $\delta n$  of the refractive index from unity, and found that it may be neglected if the refractive index varies slowly compared to the wavelength. Ignoring this source term leaves the *vector wave equation*

$$\nabla^2 \mathbf{E}(\mathbf{r}, t) = \frac{n^2(\mathbf{r})}{c^2} \frac{\partial^2 \mathbf{E}(\mathbf{r}, t)}{\partial t^2}, \quad (2.5)$$

which is identical to the free-space wave equation except for the spatially-varying

refractive index. Just like the free-space equation, it separates into its Cartesian components, implying that radiation initially polarised along the  $x$ -direction will remain so polarised after propagating through the material. The source term (2.4) couples the Cartesian components and so *depolarises* the field if the material is structured at the wavelength scale.

### 2.1.3 The scalar wave equation in an inhomogeneous medium

If the incident radiation is indeed linear polarised, then we can ignore the wave equation components in  $E_y$  and  $E_z$  and solve only the equation in  $E_x$ . For generality, write the *scalar wavefield* as  $f(\mathbf{r}, t)$  and identifying  $f$  with  $E_x$  we have the *scalar wave equation*

$$\nabla^2 f(\mathbf{r}, t) = \frac{n^2(\mathbf{r})}{c^2} \frac{\partial^2 f(\mathbf{r}, t)}{\partial t^2}. \quad (2.6)$$

The electric field is a real quantity. It is, however, a universal convention to use a complex representation for the scalar wavefield. This greatly simplifies the mathematics: for example, a phase-shift  $\phi$  of the wavefield is expressed as multiplication by  $\exp i\phi$  while there is no equivalent for a wave written as a cosine. The convention dictates that the electric field component  $E_x$  is recovered from the *real part* of the complex wavefield:  $E_x = \Re f$ . This convention was formalised by Gabor as the *analytic signal transform* for conversion of a real value such as  $E_x$  to a complex equivalent such as  $f$  [13, §3.1]. For monochromatic light the transform is just the familiar expedient of replacing  $\cos \phi$  with  $\exp i\phi$ .

For the purposes of this thesis, the assumption of linear polarisation is no great restriction. More generally, both components  $E_x$  and  $E_y$  are needed to describe a transverse wave. Monochromatic field with arbitrary polarisation can also be represented in free-space by a scalar complex wavefield [14] as can completely incoherent fields such as cavity radiation [15]. Further, the scalar wave equation can also be used to propagate the correlation functions of partially-coherent light. Scalar optics does not replace full vectorial optics in *all* circumstances and there is no general ‘scalarisation’ procedure for vector fields [16, p 275]. Scalar optics is, however, sufficient for our purposes.

### 2.1.4 The Helmholtz equation for a monochromatic wave

The wave equation can be further simplified by factoring out the time-dependence of the wavefield. For a monochromatic wavefield of frequency  $\nu$  the spatial and

temporal factors separate:

$$f(\mathbf{r}, t) = f(\mathbf{r}) \exp(-2\pi i \nu t), \quad (2.7)$$

and substituting into the scalar wave equation (2.6) yields the *Helmholtz equation*

$$\nabla^2 f(\mathbf{r}) + k^2 n^2(\mathbf{r}) f(\mathbf{r}) = 0. \quad (2.8)$$

The wavenumber  $k$  and wavelength  $\lambda$  of the monochromatic wave are related by

$$k = \frac{2\pi}{\lambda} \equiv \frac{2\pi\nu}{c}. \quad (2.9)$$

Solving (2.8) determines the wavefield  $f$  at all points in space. Finding the intensity from the wavefield requires stepping back to find the electric field and then using (2.10). However, it can be shown that the intensity can be found directly from the square-amplitude of the *scalar* wavefield  $f(\mathbf{r})$  [17, p 74]:

$$I(\mathbf{r}) \propto |f(\mathbf{r})|^2. \quad (2.10)$$

As we will only be dealing with intensity ratios, from now on we omit the constants and define the *dimensionless intensity*, or just *intensity* to be  $I = |f|^2$ .

The Helmholtz equation can readily be extended to non-monochromatic fields by replacing (2.7) with a temporal Fourier integral over spectral amplitudes  $f(\mathbf{r}, \nu)$ . Complications arise when calculating the intensity however, and assumptions of ergodicity and stationarity of the fields are necessary. In practice, there is no problem integrating over spectral densities  $I(\mathbf{r}, \nu)$  to form a total intensity of a polychromatic wave.

In free space, the refractive index is exactly one and the *free-space Helmholtz equation* is just

$$\nabla^2 f(\mathbf{r}) + k^2 f(\mathbf{r}) = 0. \quad (2.11)$$

∞

IN THE FOLLOWING analysis of the forward problem, we will use the scalar Helmholtz equation rather than the vector wave equation and use complex numbers to represent the amplitude and phase of the wavefield, although it is fundamentally a real quantity. This simplifies the algebra but the measured intensity remains the square-amplitude of the wavefield.

Although we expedited the derivation by assuming a monochromatic, linearly-polarised wavefield, the same scalar optics applies to polychromatic wavefields and arbitrary pure polarisation states in free space, and even is useful for partially-coherent radiation. Diffraction-contrast imaging is based on scalar optics, and is definitely valid for non-laser sources. Although not a subject of this thesis, the paper included in Appendix I demonstrates DCI with synchrotron x-rays of limited spatial and temporal coherence.

## 2.2 Propagation of light through a monomorphous object

Given an incident wavefield, either planar or spherical, arriving at the object, and knowing the object's density, we want to find the wavefield immediately after the object. This Section uses the formalism of ray optics to approximate the propagation of light in an inhomogeneous medium.

### 2.2.1 The eikonal equation

In inhomogeneous media, the asymptotic expansion

$$f(\mathbf{r}) = A(\mathbf{r}) \exp(ikS(\mathbf{r})) = \exp(ikS(\mathbf{r})) \sum_{m=0}^{\infty} \frac{A_m(r)}{(ik)^m}, \quad (2.12)$$

known as the Debye expansion<sup>1</sup> is a solution<sup>2</sup> of the inhomogeneous Helmholtz equation (2.8). We refer to  $A(\mathbf{r})$  as the amplitude, although it is a complex quantity, but refer to  $S(\mathbf{r})$  as the *eikonal*. In the short wavelength  $k \rightarrow \infty$  limit,  $f$  reduces to the plane wave solutions of the free-space Helmholtz equation. Substituting  $f$  into the inhomogeneous Helmholtz equation and equating coefficients in equal powers of  $k$  yields:

$$(k^0) \quad |\nabla S|^2 = n^2(r); \quad (2.13)$$

$$(k^1) \quad 2\nabla A_0 \nabla S + A_0 \nabla^2 S = 0, \quad (2.14)$$

$$(k^m) \quad 2\nabla A_m \nabla S + A_m \nabla^2 S = -\nabla^2 A_{m-1}. \quad (2.15)$$

Equation 2.13 is a first-order Hamilton-Jacobi equation known as the *eikonal equation* and the equations (2.14) and (2.15) are known as the *transport equations*.

---

<sup>1</sup> Also known as the Luneburg-Kline expansion and the WKB expansion.

<sup>2</sup> Proving that it is a *general* solution has not been done, although special cases have been proven [18, §2.9].

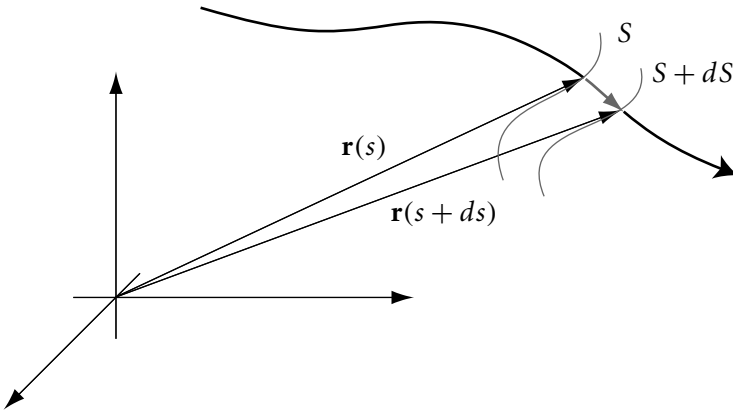


FIGURE 2.1 **Optical rays defined.** An optical ray  $\mathbf{r}(s)$  is a trajectory everywhere perpendicular to surfaces of constant eikonal  $S$ . The grey vector is the quantity in Equation (2.16).

### 2.2.2 Ray solutions to the eikonal equation

Born and Wolf [19, §3.1.2] consider only the first term in an asymptotic expansion for the electric field vectors, and show that the Poynting vector is everywhere orthogonal to surfaces of constant  $S$ . Thus we interpret these surfaces as *geometrical wavefronts* and the orthogonal trajectories as geometrical *lighthrays*. Integrating the eikonal equation is the mathematical analog of ‘ray-tracing’; the transport equations then provide the link between the amplitude of the field and the eikonal, allowing the full wavefunction to be propagated.

We define a ray, or trajectory,  $\mathbf{r}$  as a position vector parameterised by a scalar arclength  $s$ . A unit vector along a ray orthogonal to surfaces of constant eikonal must then obey

$$\frac{d\mathbf{r}}{ds} = \frac{\nabla S}{n}, \quad (2.16)$$

as depicted in Figure 2.1. Two important results follow immediately from using this definition of rays in the eikonal equation (2.13). The first is Fermat’s expression for the optical path length along a ray:

$$S(P_2) - S(P_1) = \int_{P_1}^{P_2} n \, ds. \quad (2.17)$$

Traditional derivations of ray optics take Fermat’s expression as an ansatz and define the optical ray as the extremal path that minimises the optical path length. We

have seen that the eikonal equation is in fact the more fundamental, and may be obtained from the wave equation. The optical path length is of interest to us as it relates the wavefield after propagation through the object to a integral along a ray through the object; it forms a projection.

The second result eliminates the eikonal function yielding a differential equation for light rays,

$$\frac{d}{ds} \left( n \frac{d\mathbf{r}}{ds} \right) = \nabla n. \quad (2.18)$$

This equation can be used to determine the path of rays in an inhomogeneous object, or at least to quantify the error in assuming that rays remain undeviated. In conventional materials the refractive index changes only at the edges: the refractive index is not continuous. This is accounted for in the ray model by *Snell's law of refraction*, which is readily derived from (2.16) [19, §3.2.2].

### 2.2.3 Rays in absorbing media

The summary of geometrical optics presented above was derived for real  $n$ , i.e. in the absence of absorption. The problem of propagation in inhomogeneous absorbing media has attracted comparatively little attention; a recent review is Reference 20, §4.11.

Ray optics is little affected by moderate levels of absorption. Simply replacing the refractive index (2.17) with the complex refractive index yields a *complex eikonal*  $S$  in (2.12), and accounts for absorption along the ray. The real part of the refractive index suffices when finding the ray direction using (2.18). Pure absorption does not deflect rays unless it is significant over wavelength-scale distances. Appendix B presents a mathematical justification for these comments.

### 2.2.4 Projection through a monomorphous material

The wavefield  $f(P_2)$  at a point  $P_2$  on a ray is related to the wavefield at an earlier point  $P_1$  on the ray by

$$f(P_2) = A(P_2) \exp(ikS(P_2)) = \frac{A(P_1)}{\sqrt{\mathcal{J}}} \exp \left( ikS(P_1) + ik \int_{P_1}^{P_2} n ds \right), \quad (2.19)$$

where we have used the eikonal definition (2.12) and Fermat's expression (2.17). The ray divergence  $\mathcal{J}$  would be one for collimated illumination and  $r^{-2}$  for point-source illumination; it is inessential to this argument.

We have defined a *monomorphous material* as one with refractive index

$$n(\mathbf{r}) = 1 + \rho(\mathbf{r})(\delta + i\beta) \quad (2.20)$$

with  $\rho(\mathbf{r})$  the density distribution. Now we make a central assumption of this section: that refraction in the object is sufficiently weak that rays in the object deviate negligibly from the straight line paths taken in the absence of the object.

For such a weakly refracting monomorphous material, the wavefield at point  $P_2$  after the object becomes:

$$\begin{aligned} f(P_2) &= \frac{A(P_1)}{\sqrt{\mathcal{J}}} \exp\left(ik\left(S(P_1) + \int_{P_1}^{P_2} ds\right)\right) \exp\left(ik(\delta + i\beta) \int_{P_1}^{P_2} \rho(\mathbf{r}) ds\right) \\ &= f^0(P_2) \exp\left(ik(\delta + i\beta) \int^{P_2} \rho(\mathbf{r}) ds\right) \end{aligned} \quad (2.21)$$

where  $f^0$  represents the wavefield in the absence of the object, and the integration takes place over the ray passing through  $P_2$  in the absence of the object. We are thus at liberty to deduce the ray trajectories and the free-space wavefunction  $f^0$ , for example by symmetry arguments, and then employ the *aperture function* – the factor in the preceding equation – to account for the effect of the object. The three-dimensional density distribution  $\rho(\mathbf{r})$  enters as its projection along the rays onto the exit-surface; we define the *column density*  $\rho(\mathbf{x})$  by

$$\rho(P) = \int^P \rho(\mathbf{r}) ds. \quad (2.22)$$

where  $P$  is a point on the surface with transverse position vector  $\mathbf{x} = (x, y)$  and the integration is performed along the ray passing through  $P$ .

This column-density  $\rho(\mathbf{x})$  represents the maximum amount of information we can hope to extract from a single image of a monomorphous object. The subject of this thesis is the retrieval of this column-density from a single diffraction pattern.

### 2.2.5 Plane wave illumination

We now consider two specific illuminating wavefields. Plane wave illumination propagating along the  $z$ -axis is depicted in Figure 2.2. Rays are parallel to the  $z$ -axis, and the osculating surface is the  $z = 0$  plane. The unperturbed wavefunction

is  $f^0 = \exp(ikz)$ , and so the wavefield after the object on the  $z = 0$  plane is

$$f(x, y, z = 0) = \exp(ik(\delta + i\beta)\rho(x, y)) \quad (2.23)$$

where

$$\rho(\mathbf{x}) = \int_{-\infty}^0 \rho(x, y, z) dz. \quad (2.24)$$

This case is known as the *eikonal approximation*.

### 2.2.6 Spherical wave illumination

We place a point source of radiation at  $z = -R_1$ . By symmetry, rays radiate outward from the point and the wavefronts are spherical; the osculating surface is the sphere centred on  $z = -R_1$  of radius  $R_1$  (or at least the right half of it!). The unperturbed wavefunction is  $f^0 = \exp(ikr)/r$  with  $r^2 = x^2 + y^2 + (z + R_1)^2$ . The wavefield on the  $z = 0$  plane is then

$$f(x, y, z = 0) = \exp(ik(\delta + i\beta)\rho_s(x, y)) \frac{\exp(ik\sqrt{R_1^2 + x^2 + y^2})}{\sqrt{R_1^2 + x^2 + y^2}}, \quad (2.25)$$

where  $\rho_s(x, y)$  is the column-density projected along the *diverging* rays. For thin objects with transverse extent much less than  $R_1$ , to a good approximation  $\rho_s \approx \rho$ . Figure 2.3 shows the case of an object very close to the point source. The ray formalism remains capable of determining the wavefield on the  $z = 0$  plane, but geometric distortions are introduced. The problem of correcting for such distortions is a problem of *interpreting* the column-density, and so lies outside the scope of this thesis.

### 2.2.7 Ray optics and the Born and Rytov approximations

The reader might be forgiven for thinking that the introduction of the full apparatus of ray optics to obtain the above relationships is not justified. After all, we have assumed rays propagate undeviated from their free space paths. Indeed, the results may be obtained rather more directly from the Helmholtz equation by expanding it in a Liouville-Neuman series [19, §13.1]. For plane wave incidence, the first term in the series is known as the *first Born approximation* and our collimated illumination result follows rather directly. The *Rytov ‘series’* – actually a product

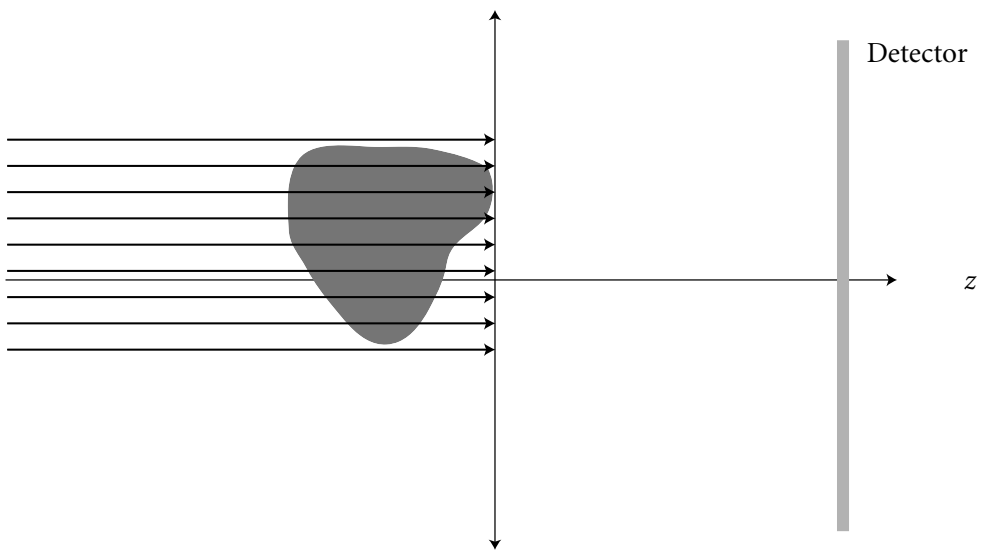


FIGURE 2.2 **Plane wave illumination.** The rays are parallel rays.

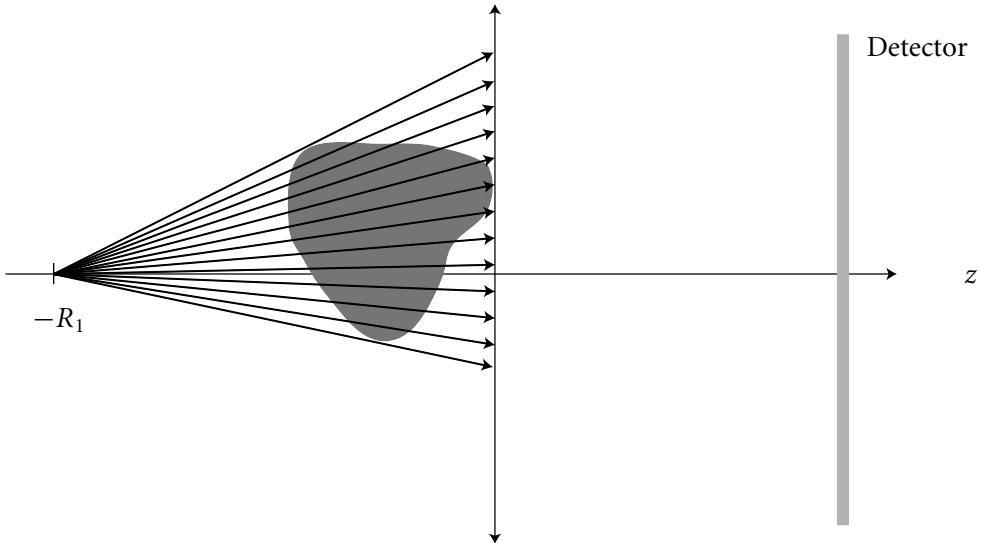


FIGURE 2.3 **Spherical wave illumination.** The rays diverge from a point source at  $z = -R_1$ .

of wavefunctions rather than a sum – is an extension of the Born series applicable to non-planar incident waves [19, §13.5]. Nieto-Vesperinas derives the eikonal approximation from the Rytov approximation [21, §13.10.3]; his derivation is readily extended to confirm our point-source illumination result (2.25). Reference 22 presents an excellent summary of the equivalence of ray optics and the Rytov approximation.

The great distinction between the Born and Rytov scattering formalisms on the one hand, and ray optics on the other, arises when considering the *validity* of the approximations made. Within the ray optics framework, the accuracy of the eikonal approximation is assessed by estimating the deviation of the supposedly undeviated ray, using the straightforward ray tracing formula (2.16), or Snell’s Law for discontinuous media. The scattering formalisms do not offer any such simple estimates of validity, and the available global conditions tend to be unnecessarily stringent [21, p 104].

One further distinction between these solutions of the inhomogeneous wave equation is that the Born approximation requires *weak* scattering: phase-shifts through the object must be much less than one radian. The Rytov and ray-optics approaches do not, and require only that refractive index vary slowly at wavelength scales [22]. This assumption was already made in obtaining the Helmholtz equation. A significant and novel result of this thesis is the extension of the monomorphous contrast-transfer function to non-weak objects. Avoiding the Born approximation assures us that the column-densities of such non-weak objects remain related to the exit-surface wavefield by eikonal-approximation expressions such as (2.23).



THE LIGHT IS half way on its journey having propagated from the source and then through the monomorphous object. We have seen that the wavefield is phase-shifted and attenuated along optical rays. The result is a simple expression relating the phase and amplitude of the wavefield to the column-density of the monomorphous object. The next step is to propagate this wavefield through free-space to the detector.

## 2.3 Diffraction in free space and the Fresnel approximation

Now that the light has propagated through the object, we must abandon the ray formalism. Propagation from the object to the detector occurs in free-space. The wave equation can be solved exactly in free-space, and this Section presents two equivalent solutions: a Fourier-domain transfer function (the angular spectrum, §2.3.2) and a real-space convolution (the Rayleigh-Sommerfeld integral §2.3.3). Deriving the contrast-transfer function expressions (§2.5) requires the Fresnel approximation to the exact solution. The Fresnel approximation and its validity are discussed at the end of this Section.

### 2.3.1 The transverse Fourier transform

At this point we introduce the Fourier transform definitions used in this thesis. Having assumed monochromatic radiation, we won't need the temporal Fourier transform. Note however, that our choice of positive phasors,  $\exp ikz$  for a wave propagating in the  $+z$  direction and  $\exp ikr$  for an outgoing spherical wave, implies a choice of *negative* temporal frequency component, i.e.  $f(\mathbf{r}) = f(\mathbf{r}, -\nu)$ . The authors of Reference 17 take the positive component  $f(\mathbf{r}, \nu)$  with the same phasors by altering the Fourier sign convention for the temporal transform. Considerable care must be taken when comparing the literature. The use of phasors and Fourier conventions in general in this thesis is consistent with Goodman's use in *Introduction to Fourier Optics* [23] and with that used in the online Reference 24.

The two-dimensional Fourier transform is used extensively in this thesis. The Fourier transform of a function  $f(x, y)$  is given by

$$\tilde{f}(u_x, u_y) = \iint_{-\infty}^{\infty} f(x, y) \exp(-2\pi i(xu_x + yu_y)) dx dy, \quad (2.26)$$

and the inverse transform by

$$f(x, y) = \iint_{-\infty}^{\infty} \tilde{f}(u_x, u_y) \exp(2\pi i(xu_x + yu_y)) du_x du_y. \quad (2.27)$$

The *spatial frequencies*  $u_x$  and  $u_y$  have units of cycles per unit length, rather than radians per unit length. The factor of  $2\pi$  in the exponent also allows the transforms to be written without pre-factors. This has become the convention in the recent

optics *and* signal processing literature, although there are exceptions, notably the books by Born and Wolf [19] and Mandel and Wolf [13].

The expressions may be written more compactly if we introduce the *transverse position vector*  $\mathbf{x} \equiv (x, y)$  and the *transverse spatial frequency vector*  $\mathbf{u} \equiv (u_x, u_y)$ . The vector forms of the forward and inverse transverse Fourier transforms are then

$$\tilde{f}(\mathbf{u}) = \int_{-\infty}^{\infty} f(\mathbf{x}) \exp(-2\pi i \mathbf{u} \cdot \mathbf{x}) d\mathbf{x} \quad (2.28)$$

and

$$f(\mathbf{x}) = \int_{-\infty}^{\infty} \tilde{f}(\mathbf{u}) \exp(2\pi i \mathbf{u} \cdot \mathbf{x}) d\mathbf{u}. \quad (2.29)$$

We will write the magnitude of the transverse spatial frequency vector  $|\mathbf{u}|$  as  $u$ , but note that  $x$  is always the  $x$ -coordinate and the real space lengths are always written  $|\mathbf{x}|$ .<sup>3</sup> The Fourier transform is a linear operator; it will occasionally be convenient to denote it alternatively in operator form:

$$\tilde{f}(\mathbf{u}) = \mathcal{F}\{f(\mathbf{x})\}; \quad f(\mathbf{x}) = \mathcal{F}^{-1}\{\tilde{f}(\mathbf{u})\}. \quad (2.30)$$

Although we won't need the following definitions until Chapter 3, here is also a good place to define the Hermitian *inner product*  $\langle f, g \rangle$  of two functions  $f$  and  $g$  as

$$\langle f, g \rangle = \int_{-\infty}^{\infty} f(\mathbf{x})g(\mathbf{x}) d\mathbf{x}. \quad (2.31)$$

The  $L^2$ -norm, denoted  $\| \cdot \|$  which is a measure of the total 'energy' in a signal [25]:

$$\|f(\mathbf{x})\|^2 = \langle f, f \rangle = \int_{-\infty}^{\infty} |f(\mathbf{x})|^2 d\mathbf{x} = \int_{-\infty}^{\infty} |\tilde{f}(\mathbf{u})|^2 d\mathbf{u}. \quad (2.32)$$

The equality of this norm in real and Fourier space is known as *Parseval's theorem*.

### 2.3.2 The angular spectrum

This Article describes the *angular spectrum* approach to solving the Helmholtz equation in free space (hereafter just the Helmholtz equation). The solution is both easier to derive and easier to implement than the Rayleigh-Sommerfeld in-

---

<sup>3</sup> By this asymmetry, we avoid both the attaching of  $\perp$  subscripts to every second symbol, and the false expedient of carrying out all derivations in one dimension.

tegrals considered in the next Article. It is rather curious then that the angular spectrum approach was not formulated until 1950, more than 50 years after the integral solutions were derived. The angular spectrum is still not explained in some standard optics text such as Born & Wolf. This derivation follows that of Reference 17. Greater rigour at the expense of some clarity is provided by Goodman [23, §3.10] and Mandel and Wolf [13, §3.2]. Absolute rigour and opacity may be found in Reference 26.

Consider the *plane waves*

$$f_{\text{PW}} = \exp(i\mathbf{k} \cdot \mathbf{r}) = \exp(i(k_x x + k_y y + k_z z)), \quad (2.33)$$

which are readily shown to be solutions of the Helmholtz equation provided that the magnitude of the wavevector  $\mathbf{k}$  equals the wavenumber  $k$ . Recall that for a given monochromatic component  $k^2 = k_x^2 + k_y^2 + k_z^2$  is a constant, and so we may eliminate  $k_z$  and obtain, for waves propagating in the  $+z$  direction,

$$f_{\text{PW}}(x, y, z) = \exp\left(i\left(k_x x + k_y y + z\sqrt{k^2 - k_x^2 - k_y^2}\right)\right). \quad (2.34)$$

It may be seen that waves with  $k_x^2 + k_y^2 < k^2$  propagate ad infinitum while waves otherwise are *evanescent*, decaying exponentially. In the plane  $z = 0$ , the plane waves take the form

$$f_{\text{PW}}(x, y, z = 0) = \exp(i(k_x x + k_y y)). \quad (2.35)$$

Making the substitution  $k_x = 2\pi u_x$ ,  $k_y = 2\pi u_y$  in the preceding two expressions, it is clear that equation (2.35) is a Fourier component of an arbitrary wavefield in the  $z = 0$  plane (compare (2.27)). This suggest a solution to the diffraction problem whereby a wavefield  $f(x, y, z = 0)$  known on the  $z = 0$  plane is Fourier decomposed into elements of the form of (2.35). Each such element propagates trivially as (2.34), and so a Fourier reassembly of elements so propagated should yield the wavefield  $f(x, y, z)$  at any given propagation distance  $z$ .

We Fourier decompose the wavefield in the  $z = 0$  plane

$$f(x, y, z = 0) = \iint_{-\infty}^{\infty} \tilde{f}(u_x, u_y, z = 0) \exp(2\pi i(xu_x + yu_y)) du_x du_y \quad (2.36)$$

but consider it as a weighted sum over basis elements of the form (2.35) with weighting  $\tilde{f}(u_x, u_y, z = 0)$ . Each such element propagates as (2.34) and so, by the linearity

of the wave equation, we may write down the wavefield at a subsequent plane  $z > 0$ :

$$\begin{aligned} f(x, y, z) &= \iint_{-\infty}^{\infty} \tilde{f}(u_x, u_y, z=0) \\ &\quad \times \exp\left(2\pi i \left(xu_x + yu_y + z\sqrt{1/\lambda^2 - u_x^2 - u_y^2}\right)\right) du_x du_y \end{aligned}$$

or, rearranging:

$$\begin{aligned} &= \iint_{-\infty}^{\infty} \tilde{f}(u_x, u_y, z=0) \exp\left(2\pi iz\sqrt{1/\lambda^2 - u_x^2 - u_y^2}\right) \\ &\quad \times \exp\left(2\pi i(xu_x + yu_y)\right) du_x du_y \end{aligned} \quad (2.37)$$

which is clearly itself a Fourier integral of the form of (2.36). This result, known as the *angular spectrum* of the wavefield lets us relate the Fourier transform of the wavefield on a plane  $z > 0$  to the Fourier transform of the wavefield on  $z = 0$ :

$$\tilde{f}(u_x, u_y, z) = \exp\left(2\pi iz\sqrt{1/\lambda^2 - u_x^2 - u_y^2}\right) \tilde{f}(u_x, u_y, z=0). \quad (2.38)$$

This is exactly the solution suggested above, and forms a complete theory of diffraction in scalar optics. The wavefield at an arbitrary plane  $z > 0$  is found by Fourier transforming the two-dimensional wavefield at  $z = 0$ , multiplying by the *transfer function*

$$\tilde{h}_{\text{as}}(u; z) = \exp\left(2\pi iz\sqrt{1/\lambda^2 - u^2}\right) \quad (2.39)$$

and taking the inverse Fourier transform. I use exactly this algorithm to produce the simulated diffraction patterns used throughout Chapter 3. The transfer function  $\tilde{h}_{\text{as}}$  is essentially the spatial-frequency response of free-space diffraction. It has unit modulus for spatial-frequencies up to  $1/\lambda$  but rapidly falls at higher frequencies. Diffraction preserves information about structures larger than the wavelength, but sub-wavelength variations in the wavefield quickly die out.

It bears re-iteration that this angular spectrum approach to diffraction is formally complete, in the sense that it solves the Helmholtz equation in the right half-space. Note however that the absence of explicit boundary values considerations is illusory and must be treated in a rigorous derivation [26].

### 2.3.3 Diffraction as a linear shift-invariant system

The construction of the theory of linear spaces was a major achievement of mathematics in the first half of the twentieth century. During the 1960s it was realised that a very broad class of problems in fields as diverse as optics, electronics, communications and control could be understood in terms of linear systems. Although concerned with very different phenomena, the underlying physics of these fields is characterised by linear differential equations, time and space invariance and causality. This confluence of ideas has formed a new field now known as *signal processing*. A theme of this thesis is the use of signal processing techniques to extract information from observed intensity patterns. Reference 23 is an introduction to the signal processing approach in optics, while a more rigorous approach to the field may be found in Reference 27.

In this section, the propagation of a wavefield in free space is placed in the framework of linear systems. Section 2.5 shows that subject to certain restrictions a further linear relationship exists between measured intensity and the column density of a monomorphous object.

Equation (2.38) relates the Fourier-transform of the diffracted wavefield  $\tilde{f}(u_x, u_y, z)$  to that of the initial wavefield  $\tilde{f}(u_x, u_y, z = 0)$  by multiplication in Fourier space by a transfer function  $\tilde{h}_{\text{AS}}$ . This transfer function depends only on the transverse Fourier co-ordinates  $(u_x, u_y)$  and is *not* a function of the real-space co-ordinates  $(x, y)$ . Systems meeting this criterion are termed *linear shift-invariant*.<sup>4</sup> In this case, the *convolution theorem* [28, p 115], a standard result readily derived from the Fourier transform relation (2.26), relates the wavefields in real space by a *convolution*, denoted  $*$

$$f(x, y, z) = \iint_{-\infty}^{\infty} f(x', y', z = 0) h_{\text{AS}}(x - x', y - y', z) dx' dy' \quad (2.40)$$

$$\equiv f(x, y, z = 0) * h_{\text{AS}}(x, y, z). \quad (2.41)$$

Convolution is a multiplication-like operation being associative, commutative and bilinear. The *impulse response*  $h_{\text{AS}}$  is the inverse Fourier transform of the transfer function  $\tilde{h}_{\text{AS}}$ . The linearity of the system is a natural consequence of the linearity of the wave equation. The shift-invariance is made explicit in the convolution relation, where the impulse response is seen to depend only on the separation  $(x - x', y -$

---

<sup>4</sup> Also *space-invariant* and *isoplanatic*. Signal processing literature betrays its time-domain origins, often referring to ‘linear time-invariant’ or LTI systems.

$y'$ ) and not on absolute position in space. Shift-invariance is a natural consequence of the homogeneity of free space.

The question now arises of whether the impulse response  $h_{AS}$  of free space propagation may be written in a closed form. If such a representation exists, then equation (2.40) will be an alternative formalism to the angular spectrum for describing diffraction. It has been shown [26] that the Weyl representation of a spherical wave<sup>5</sup> may be used to write

$$\begin{aligned} h_{AS}(x, y, z) &= \mathcal{F}^{-1} \left\{ \exp \left( 2\pi iz \sqrt{\frac{1}{\lambda^2} - u_x^2 - u_y^2} \right) \right\} \\ &= \frac{1}{2\pi} \left( \frac{1}{r} - ik \right) \frac{z}{r} \frac{\exp(ikr)}{r}, \end{aligned} \quad (2.42)$$

where  $r^2 = x^2 + y^2 + z^2$ . This result allows us to express diffraction as a convolution [31]

$$f(x, y, z) = \frac{1}{2\pi} \iint_{-\infty}^{\infty} f(x', y', z=0) \left( \frac{1}{l} - ik \right) \frac{z}{l} \frac{\exp(ikl)}{l} dx' dy', \quad (2.43)$$

where  $l^2 = (x - x')^2 + (y - y')^2 + z^2$ .

While the linear systems interpretation of this expression as convolution with an impulse response function is relatively recent, the expression itself is exactly the first Rayleigh-Sommerfeld diffraction integral originally written in 1896. The same expression may be derived by using Green's theorem to solve the Dirichlet problem of the scalar wave equation in the  $z > 0$  half-space [13, §3.2.5].

It is interesting to note that the impulse response  $h_{AS}$  takes the form of a spherical wave with cosine obliquity factor for  $z \gg \lambda$ . The convolution is then the addition of the effects of such spherical wavelets originating at each point in the  $z = 0$  plane. Although he was likely unaware that he was describing complex amplitudes in the analytic signal representation, this is exactly the concept introduced by Christiaan Huygens in 1678. More recently, it has been shown that  $h_{AS}$  is a wavelet in the sense of multiresolution analysis (see Appendix D), raising the possibility of diffraction calculations without employing the non-compact Fourier basis [32].

Free space propagation is equivalently described by a transfer function modulating the propagation of plane waves, or by convolution with spherical wavelets. The two forms of linear shift-invariant system analysis correspond to angular spec-

---

<sup>5</sup> H. Weyl (1919) [29], a simplified derivation has been given by Marathay [30], a summary with references to rigorous derivations may be found in Mandel & Wolf [13, §3.2.4].

trum and Rayleigh-Sommerfeld diffraction respectively. While the two are formally equivalent, the numerical implementations are very different. Convolution is *much* slower than Fourier methods. The use of rapid discrete Fourier transform algorithms such as the FFT permits fast transition to and from the Fourier representation, in which angular spectrum propagation is merely multiplication by the transfer function. Thus angular spectrum propagation is numerically expedient, although the question of sampling of the transfer function arises and is in general not a simple problem to resolve. An alternative free-space propagation algorithm has been proposed which uses the fractional Fourier transform. It predicts only diffracted intensities, but does so at near and far propagation distances [33].

#### 2.3.4 The Fresnel approximation

The preceding discussion describes both a direct real-space diffraction theory, and a computationally efficient Fourier-space method, both derived without approximation. Why should we impose approximations on these methods? Standard references refer to the approximation of Fresnel diffraction as being a ‘more simple and usable’ expression [23, p 66], and the angular spectrum or Rayleigh-Sommerfeld forms as ‘difficult to evaluate’ [34]. These comments seem somewhat unfair until one tries to repeat the derivations of the following two sections using the Rayleigh-Sommerfeld formula instead of the Fresnel one. In this section, I describe the Fresnel approximation and discuss its regime of validity.

Consider the binomial approximation of the surd in the angular spectrum transfer function, rewritten for the wavevector components  $k_x = 2\pi u_x$  and  $k_y = 2\pi u_y$

$$\tilde{h}_{\text{AS}}(k_x, k_y, z) = \exp\left(ikz\sqrt{k^2 - (k_x^2 + k_y^2)}\right) \quad (2.44)$$

$$= \exp\left(ik\sqrt{1 - \frac{k_x^2 + k_y^2}{k^2}}\right). \quad (2.45)$$

The second term under the surd is now  $\sin^2 \theta = (k_x^2 + k_y^2)/k^2$ , where  $\theta$  is the angle between the wavevector  $\mathbf{k}$  and the  $z$ -axis. We now make the *paraxial* approximation that this angle is small, and expand the surd

$$\tilde{h}_{\text{AS}}(k_x, k_y, z) = \exp\left(ikz\left(1 - \frac{1}{2}\frac{k_x^2 + k_y^2}{k^2} - \dots\right)\right). \quad (2.46)$$

Truncating the expansion obtains the *Fresnel transfer function*

$$\tilde{h}_{\text{Fr}}(u_x, u_y, z) = \exp(ikz) \exp\left(-i\pi\lambda z \left(u_x^2 + u_y^2\right)\right), \quad (2.47)$$

written again in terms of spatial frequencies.

Finding an associated impulse-response function is much easier than for the full angular spectrum transfer function. Taking the inverse Fourier transform is easily shown to result in:

$$h_{\text{Fr}}(x, y, z) = \frac{i}{\lambda z} \exp(ikz) \exp\left(ik\frac{x^2 + y^2}{2z}\right) \quad (2.48)$$

and so the convolution, or direct, expression that approximates the Rayleigh-Sommerfeld integral is the *Fresnel diffraction integral*

$$f(x, y, z) = \frac{i}{\lambda z} \exp(ikz) \iint_{-\infty}^{\infty} f(x', y', z=0) \times \exp\left(\frac{i\pi}{\lambda z}(x-x')^2 + (y-y')^2\right) dx' dy'. \quad (2.49)$$

Conventionally,  $k$  is written instead of  $\lambda$  in the constant phase factor to emphasise that  $\exp(ikz)$  is the phase shift accumulated by an undiffracted wave propagating from  $(x, y, 0)$  to  $(x, y, z)$ . The spherical wavefronts of Rayleigh-Sommerfeld diffraction have been approximated by parabolic wavefronts, in a manner superficially analogous to how a spherical lens approximates the desired parabolic thickness of glass.<sup>6</sup>

There is no reason to use the Fresnel diffraction integral (2.49) to propagate wavefields. For computational effort of the same order, the Rayleigh-Sommerfeld integral (2.43) yields an exact solution to the Helmholtz equation, rather than the approximate solution offered by the Fresnel expression. Notwithstanding this, Section 2.5 derives expressions for the propagated *intensity* starting with the Fresnel diffraction integrals. Equivalent forms cannot be obtained from the full Rayleigh-Sommerfeld integrals.

### 2.3.5 Where is Fresnel diffraction a valid approximation?

The question of at which distances from the diffracting object the Fresnel approximation is valid has received much attention, but has not been definitively re-

---

<sup>6</sup> This analogy should not be taken too far, see References 35, 36.

solved. From the consideration of paraxiality, it is clear that if the initial wavefield  $f(x, y, z = 0)$  is band-limited, that is that there is a maximum spatial-frequency  $(u_x, u_y)$  above which the Fourier representation  $\tilde{f}$  vanishes, then there is a maximum angle  $\theta$  of diffraction and so a maximum error for the Fresnel approximation may be determined. In practice, the detector may subtend a limited angle as viewed from the object, ensuring that steeply diffracted components are not detected (see §5.5).

More formally, the Uncertainty Principle of Fourier analysis [28, p 177] states that a function may not be limited in both spatial and frequency representations: a band-limited function has infinite spatial extent, while a compactly-supported (spatially finite) function is not band-limited. While the concept of Fresnel validity in the paraxial limit is sound, it does not yield a formal condition for finite objects.

Some authors consider instead the expansion of Rayleigh-Sommerfeld impulse-response function (2.42). A series of approximations are necessary, first removing the  $1/r$  term by the approximation that  $z \gg \lambda$ , and then approximating  $r \approx z$  in all but the exponential factor. There  $r$  is multiplied by the large quantity  $k$ , and so even a very small relative error in approximating  $r$  can yield an absolute error of more than one radian in evaluating the Fresnel integrand. Expanding

$$\begin{aligned} r &= z \sqrt{1 + \left(\frac{x - x'}{z}\right)^2 + \left(\frac{y - y'}{z}\right)^2} \\ &\approx z + \frac{(x - x')^2 + (y - y')^2}{2z} - \frac{((x - x')^2 + (y - y')^2)^2}{8z^3} + \dots \end{aligned} \quad (2.50)$$

and retaining the first *two* terms for  $r$  in the exponent recovers the Fresnel diffraction formula (2.49) derived above. Goodman argues that the error made in discarding higher-order terms is well approximated by the magnitude of the third term and so a sufficient condition for the Fresnel approximation to be valid is [23, §4.2.2]

$$z^3 \gg \frac{\pi}{4\lambda} ((x - x')^2 + (y - y')^2)_{\max}^2. \quad (2.51)$$

This condition is suitable for objects of finite extent, and indeed all of the results in this thesis satisfying this inequality at least marginally. It has long been observed, however, that Fresnel diffraction accurately predicts patterns closer to the object where this inequality does not apply. Goodman explains this in terms of a *stationary phase* argument<sup>7</sup> whereby oscillatory error components in the exponential

---

<sup>7</sup> The principle of stationary phase is briefly discussed and references given on page 45.

partially cancel, but does not derive a rigorous condition. Some problems with this argument are pointed out in Referencegaskill-1978 (§10.3).

Given these arguments, several authors conducted purely numerical studies of the regime of validity of Fresnel diffraction, their results confirming that agreement with rigorous diffraction theory is maintained closer to the diffracting object than indicated by simple analyses [37, 38]. Recently, a very thorough investigation by G W Forbes [39] yielded analytic error bounds for Fresnel diffraction from an aperture of maximum extent  $2R$  in an opaque screen, and confirmed the form of (2.51) and that it need only be weakly satisfied:  $z \approx 4(R^4/\lambda)^{1/3}$  being accurate to 1%.

In closing this discussion, there are two points salient to our use of the Fresnel approximation. The first is that we are not concerned with the diffraction pattern very close to the object, and the propagation-distance bound (2.51) is not of great concern. Second, most studies of Fresnel validity consider an aperture in an infinite opaque plane. This almost certainly leads to more stringent conditions than necessary for our case of a weakly-absorbing, limited phase-shift object perturbing an infinite plane wave. Of more concern is the paraxial restriction to small angles and the consequent limit on resolution. Extending the work of this thesis to near-wavelength resolution imaging (discussed in §5.5.6) would test this limit of the Fresnel approximation.

## 2.4 Diffraction and magnification by point-projection

I now consider diffraction from an object illuminated by a point source. I show that there is an isomorphism between the Fresnel diffraction intensity of an object illuminated with plane waves and of same object illuminated with a point-source of radiation. The point-source diffraction patterns is a *magnified* version of a plane-wave pattern at certain effective propagation distance.

Some approximations must be made in deriving this isomorphism from the Rayleigh-Sommerfeld diffraction integrals. When using point-projection for magnification in DCI, it is important to know if these approximations are valid. I find that range of validity of the isomorphism is larger than previous derivations would suggest, and give more accurate error bounds that have not been reported elsewhere.

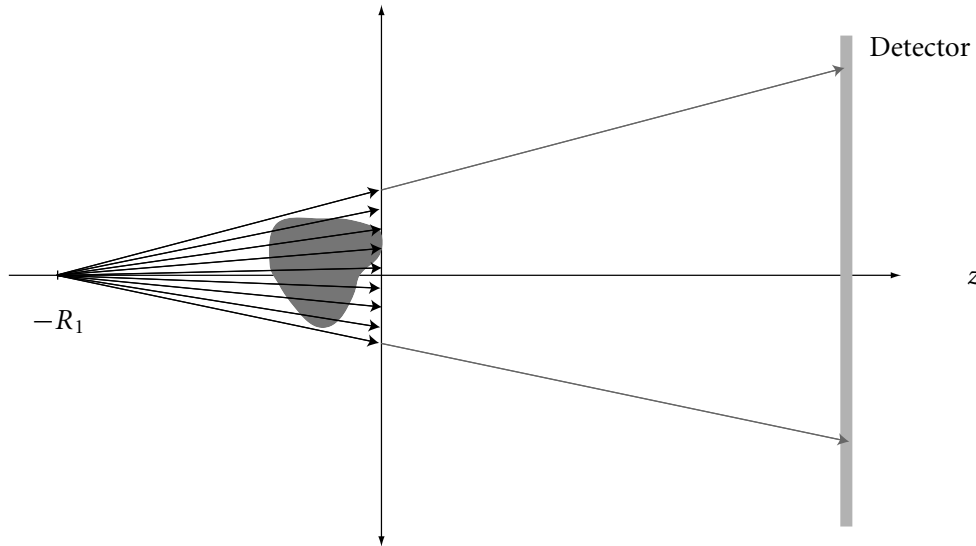


FIGURE 2.4 **Magnification by point projection.** The diffraction pattern after an object illuminated by a point source is magnified. Only extremal rays are shown beyond the object

#### 2.4.1 Diffraction with spherical-wave illumination

Figure 2.4 depicts diffraction with point-source illumination. In the limit of  $\lambda \rightarrow 0$ , diffraction effects disappear and the image is a magnified shadow of the object, known as the *geometric shadow*. The magnification  $M$  is clearly given by:

$$M = \frac{R_1 + z}{R_1}. \quad (2.52)$$

Diffraction naturally leads to the pattern extending beyond the geometric boundary. Nevertheless, we shall see that the geometric magnification  $M$  plays an important role in calculating the diffraction pattern.

Equation (2.25) describes the wavefield in the  $z = 0$  plane when an object on the left of the plane is illuminated by a point-source at  $z = -R_1$ . Substituting it into the Rayleigh-Sommerfeld diffraction integral (2.43) yields an expression for the spherical wave diffracted field  $f_s$

$$f_s(x, y, z) = \frac{i}{\lambda} \iint_{-\infty}^{\infty} q(x', y') \frac{\exp(ik\sqrt{R_1^2 + x'^2 + y'^2})}{\sqrt{z^2 + x'^2 + y'^2}} \frac{z \exp(ikl)}{l} dx' dy', \quad (2.53)$$

where

$$l^2 = z^2 + (x - x')^2 + (y - y')^2, \quad (2.54)$$

and we have assumed  $z \gg \lambda$  and denoted the aperture function by  $q(x, y)$  to preserve both generality and ink. We further make zeroth order approximations for all amplitude terms, but not for the exponent where, as we have seen, the integral is most sensitive. The problem now takes the form

$$f_s(x, y, z) = \frac{i}{\lambda z R_1} \iint_{-\infty}^{\infty} q(x', y') \exp(i k \phi(x, x', y, y')) dx' dy', \quad (2.55)$$

with

$$\phi(x, x', y, y') = \sqrt{R_1^2 - x'^2 - y'^2} + \sqrt{z^2 + (x - x')^2 + (y - y')^2}. \quad (2.56)$$

The algebra below becomes quite involved, and is simplified somewhat by considering the problem for one transverse dimension:

$$f_s(x, z) = \frac{i}{\sqrt{\lambda z}} \int_{-\infty}^{\infty} q(x') \exp(i k \phi(x, x')) dx', \quad (2.57)$$

with phase

$$\phi(x, x') = \sqrt{R_1^2 - x'^2} + \sqrt{z^2 + (x - x')^2}. \quad (2.58)$$

The approach taken by Cowley [40, p 17], Papoulis [41, 42, p 329], and Pogany et al. [43] is to retain only the first two terms in the expansion of the spherical wave phase-factor

$$\sqrt{R_1^2 - x'^2} = R_1 - \frac{x'^2}{2R_1} + \frac{x'^4}{8R_1^3} + \dots \quad (2.59)$$

approximating spherical wave illumination by parabolic wave illumination just as Fresnel diffraction approximates spherical Huygens wavelets by parabolic wavelets. Indeed, making the Fresnel approximation in the other term of  $\phi(x, x')$ , these authors refactor the resulting quadratic expression for  $\phi(x, x')$  and arrive at the result (2.69) derived below by somewhat different means. For this derivation to be valid however, the third term in the expansion (2.59) must contribute much less

than one radian, that is

$$\frac{ka^4}{8R_1^3} \ll 1 \text{ or } a \ll \sqrt[4]{\lambda R_1^3}, \quad (2.60)$$

for an object of half-width  $a$ . Such arguments are only directly applicable for a finite region of transmittance in an opaque screen. Further, the condition (2.60) is more stringent than is necessary, as I now show.

In considering the parabolic wave error in approximating the first term of  $\phi(x, x')$  separately from the Fresnel error in approximating the second term, we have overlooked a significant cancellation of errors. This cancellation was pointed out by Southwell, who compared the numerical propagation of spherical or parabolic wavefields with spherical or parabolic propagators. My analysis extends Southwell's in that I consider diffraction by an arbitrary object  $q(x)$  rather than an aperture, I provide a full derivation of the Fresnel isomorphism, and I quantify the Fresnel approximation errors in that derivation. A recent asymptotic analysis of the Fresnel approximation for *converging* spherical waves [44] expresses errors only in terms of derivatives of the diffracted field and does not seem to yield conditions analogous to those derived below.

#### 2.4.2 A stationary phase analysis

Although the sum-of-surds form of  $\phi(x, x')$  is off-putting, we may expand it in the same manner as we expanded the individual terms, albeit with somewhat greater algebraic effort. The *principle of stationary phase*<sup>8</sup> asserts that the greatest contribution to the diffracted wavefield (2.57) occurs around extremal points where  $\phi$  is slowly varying. Outside a finite region around these points,  $\phi(x, x')$  varies more rapidly than  $q(x')$  and so the exponent oscillates rapidly and contributions to the integral tend to cancel. The extremal points occur where

$$\frac{\partial \phi(x, x')}{\partial x'} = 0. \quad (2.61)$$

Omitting some unenlightening algebra, the solution is:

$$x'_0 = \frac{xR_1}{R_1 + z} = \frac{x}{M}. \quad (2.62)$$

---

<sup>8</sup> A useful overview, with references to the rigorous literature, is given in [13, §3.3]. Here I do not take the expression to the asymptotic limit, but rather use the principle to guide an appropriate expansion.

The Taylor expansion in  $x'$  of  $\phi(x, x')$  about  $x'_0$  is then (recall (2.61))

$$\phi(x, x') = \phi\left(x, \frac{x}{M}\right) + \frac{1}{2} \left(x' - \frac{x}{M}\right)^2 \frac{\partial^2 \phi}{\partial x'^2} + \frac{1}{6} \left(x' - \frac{x}{M}\right)^3 \frac{\partial^3 \phi}{\partial x'^3} + \dots \quad (2.63)$$

For two transverse dimensions the mixed partial derivative enters the expansion, but can be obviated by an appropriate rotation of the  $(x' - x'_0, y' - y'_0)$  coordinate system [13, §3.3.3a]. Evaluating the partial derivatives with Mathematica (Wolfram Research, Champaign IL, USA) yields

$$\phi\left(x, \frac{x}{M}\right) = (R_1 + z) \left(1 + \frac{x^2}{(R_1 + z)^2}\right)^{\frac{1}{2}} \quad (2.64)$$

$$\frac{\partial^2 \phi}{\partial x'^2}\left(x, \frac{x}{M}\right) = \frac{R_1 + z}{R_1 z} \left(1 + \frac{x^2}{(R_1 + z)^2}\right)^{\frac{3}{2}}, \quad (2.65)$$

$$\frac{\partial^3 \phi}{\partial x'^3}\left(x, \frac{x}{M}\right) = \frac{3x(R_1 - z)}{R_1^2 z^2} \left(1 + \frac{x^2}{(R_1 + z)^2}\right)^{-2}. \quad (2.66)$$

It can be shown that for when the magnification  $M$  is significantly larger than one, that is, when  $z \gg R_1$ , the error in approximating the second derivative by

$$\frac{\partial^2 \phi}{\partial x'^2}\left(x, \frac{x}{M}\right) \approx \frac{R_1 + z}{R_1 z} = \frac{M}{z} \quad (2.67)$$

is less than the error in dropping the cubic term by a factor very close to  $M$ . The quadratic approximation to  $\phi(x, x')$  is now

$$\phi(x, x') = R_1 + z + \frac{M(x' - x/M)^2}{2z}, \quad (2.68)$$

and so the diffraction integral (2.57) is approximately

$$f_s(x, z) = \frac{i \exp(ik(R_1 + z))}{\sqrt{\lambda z}} \int_{-\infty}^{\infty} q(x') \exp\left(ik \frac{(Mx - x')^2}{2z/M}\right) dx'. \quad (2.69)$$

This is the same formula obtained if the quadratic expansion is made on the two terms of  $\phi(x, x')$  independently. Extrapolating to two transverse dimensions, we arrive at the primary result of this Section: the above approximation for the spherical wave diffracted field  $f_s$  is related to the plane wave Fresnel diffracted field  $f_p$  from the same object by

$$f_s(x, y, z) = \frac{\exp(-ikR_1)}{M} f_p\left(\frac{x}{M}, \frac{y}{M}, \frac{z}{M}\right). \quad (2.70)$$

The point-source wavefield at distance  $z$  is therefore identical (up to a constant factor) to the plane-wave illuminated wavefield a distance  $z/M$  beyond the object, magnified by the geometric magnification  $M$ . The plane wave case is recovered in the limit  $R_1 \rightarrow \infty$  of an infinitely remote point source.

For  $z \gg R_1$ , the effective propagation distance  $z/M$  is to a good approximation equal to the point-source to object distance  $R_1$ . Varying the object to detector distance  $z$  changes only the magnification of the diffraction pattern, a somewhat counterintuitive result. A corollary is that point source diffraction never reaches the far field, and so a point projection microscope will always produce a Fresnel, not Fraunhofer, diffraction pattern.

#### 2.4.3 Validity of the isomorphism

This isomorphism will be valid provided the cubic term in the expansion (2.63) contributes much less than one radian to the phase of the oscillatory function. Considering the behaviour of (2.66) in the geometric shadow of the aperture leads to the condition:

$$a^4 \ll \frac{\lambda}{6\pi} \frac{R_1^2 z^2}{R_1 - z} \quad (2.71)$$

for a one-dimensional object of half-width  $a$ . In the large magnification limit of  $z \gg R_1$ , this condition is well approximated by the convenient expression

$$2a \ll \sqrt[4]{\lambda z R_1^2}. \quad (2.72)$$

Comparison with the overly stringent condition (2.60) shows that this new condition extends the validity of the isomorphism (2.70) to objects larger by a factor of approximately  $M^{1/4}/2$ . The astute reader may note that deriving this condition in one dimension avoids the vexing issue of third-order mixed partial derivatives in the expansion of  $\phi(x, x')$ . The naive condition (2.60) is valid for two transverse dimensions, and the fact that condition (2.72) differs from it by a function of the magnification – approximated by  $z/R_1$  in both one *and* two dimensions – lends support to a hypothesis that (2.72) is valid in two-dimensions.

Future work on this result would seek to confirm (2.72) in two dimensions by further algebraic analysis. This extension of validity conditions may be important in x-ray projection microscopy at high magnifications.

## 2.5 Contrast transfer

We have now considered the propagation of the complex amplitude  $f$  through the object, and diffraction in the space beyond. The light then falls on an optical detector, which measure the intensity, which we have seen is proportional to the square modulus of the complex amplitude. In this Section, I show how a result due to J-P Guigay yields a linear shift-invariant system connecting the measured Fresnel diffraction pattern to the column-density of a monomorphous object.

### 2.5.1 The intensity spectrum of Fresnel diffraction patterns

It is convenient to use vector notation in the following derivations. Note that *one* integral sign is used for each *vector* variable. This derivation follows Guigay's, but note that Guigay used the opposite Fourier sign convention [45].

The dimensionless intensity measured at a plane in the right half-space is

$$I(\mathbf{x}; z) = f^*(\mathbf{x}; z)f(\mathbf{x}; z). \quad (2.73)$$

Inserting the Fresnel diffraction integral (2.49) and naming the dummy variables  $\mathbf{x}_1$  and  $\mathbf{x}_2$  yields

$$I(\mathbf{x}; z) = \frac{1}{(\lambda z)^2} \iint_{-\infty}^{\infty} f^*(\mathbf{x}_1)f(\mathbf{x}_2) \exp\left(i\pi \frac{|\mathbf{x} - \mathbf{x}_2|^2 - |\mathbf{x} - \mathbf{x}_1|^2}{\lambda z}\right) d\mathbf{x}_1 d\mathbf{x}_2, \quad (2.74)$$

where it is understood that  $f(\mathbf{x}_1) = f(\mathbf{x}_1; z = 0)$ . This expression is rather unenlightening and there are no obvious simplifications to be made. Consider instead its Fourier transform

$$\begin{aligned} \tilde{I}(\mathbf{u}; z) &= \int_{-\infty}^{\infty} I(\mathbf{x}; z) \exp(-2\pi i \mathbf{x} \cdot \mathbf{u}) d\mathbf{x} \\ &= \frac{1}{(\lambda z)^2} \iiint_{-\infty}^{\infty} f^*(\mathbf{x}_1)f(\mathbf{x}_2) \exp\left(i\pi \frac{|\mathbf{x} - \mathbf{x}_2|^2 - |\mathbf{x} - \mathbf{x}_1|^2}{\lambda z}\right) \\ &\quad \times \exp(-2\pi i \mathbf{x} \cdot \mathbf{u}) d\mathbf{x} d\mathbf{x}_1 d\mathbf{x}_2. \end{aligned} \quad (2.75)$$

Expanding the quadratic terms and rearranging yields

$$\begin{aligned}\tilde{I}(\mathbf{u}; z) &= \iint_{-\infty}^{\infty} f^*(\mathbf{x}_1) f(\mathbf{x}_2) \exp\left(i\pi \frac{|\mathbf{x}_2|^2 - |\mathbf{x}_1|^2}{\lambda z}\right) \\ &\quad \times \underbrace{\frac{1}{(\lambda z)^2} \exp\left(\frac{2\pi i \mathbf{x}}{\lambda z} \cdot (\mathbf{x}_1 - \lambda z \mathbf{u} - \mathbf{x}_2)\right)}_{\delta(\mathbf{x}_1 - \lambda z \mathbf{u} - \mathbf{x}_2)} d\mathbf{x} d\mathbf{x}_1 d\mathbf{x}_2,\end{aligned}\quad (2.76)$$

where as indicated the integration over  $\mathbf{x}$  generates a delta function [28, p 95]. Carrying out the integration of  $\mathbf{x}_2$ , the delta function sets  $\mathbf{x}_2 = \mathbf{x}_1 - \lambda z \mathbf{u}$  leaving, after some cancellations:

$$\tilde{I}(\mathbf{u}; z) = \exp(i\pi \lambda z u^2) \int_{-\infty}^{\infty} f^*(\mathbf{x}_1) f(\mathbf{x}_1 - \lambda z \mathbf{u}) \exp(-2\pi i \mathbf{x}_1 \cdot \mathbf{u}) d\mathbf{x}_1,\quad (2.77)$$

where  $u = |\mathbf{u}|$ . For some simple aperture functions such as a circular aperture, slit, or phase-shifting half-plane, this expression may be directly evaluated, expediting the derivation of these standard results [46]. A more symmetric form results from the change of variable  $\mathbf{x}_1 \rightarrow \mathbf{x} + \lambda z \mathbf{u}/2$ :

$$\tilde{I}(\mathbf{u}; z) = \int_{-\infty}^{\infty} f^*\left(\mathbf{x} + \frac{\lambda z \mathbf{u}}{2}\right) f\left(\mathbf{x} - \frac{\lambda z \mathbf{u}}{2}\right) \exp(-2\pi i \mathbf{x} \cdot \mathbf{u}) d\mathbf{x}.\quad (2.78)$$

This is an odd looking expression! While it superficially resembles a Fourier transform, it is not, as  $\mathbf{u}$  is present outside the exponent. Equation (2.78) may instead be understood as a slice of a particular space-frequency representation<sup>9</sup> known as the *ambiguity function* [47, 48]. The ambiguity function  $A[f](\mathbf{u}, \mathbf{a})$  of a function  $f$  may be defined as<sup>10</sup>

$$A[f](\mathbf{u}, \mathbf{a}) = \int_{-\infty}^{\infty} f^*\left(\mathbf{x} - \frac{\mathbf{a}}{2}\right) f\left(\mathbf{x} + \frac{\mathbf{a}}{2}\right) \exp(-2\pi i \mathbf{x} \cdot \mathbf{u}) d\mathbf{x}\quad (2.79)$$

and so is a four-dimensional representation of a two-dimensional function. Comparing (2.78) with the ambiguity function definition, it is apparent that:

$$\tilde{I}(\mathbf{u}; z) = A[f](\mathbf{u}, -\lambda z \mathbf{u}),\quad (2.80)$$

<sup>9</sup> Space-frequency representations are also known as time-frequency representations by the signal processing community, and phase-spaces by physicists. Space-frequency distributions are briefly discussed in the next section, see p 63.

<sup>10</sup> There does not seem to be a standard convention for the ambiguity function. This definition is consistent with our Fourier transform definition (2.26) and with that of Mallat [49, p 117].

that is, the Fresnel-diffracted intensity spectrum may be found on a slice through the origin of the ambiguity function of the initial wavefield. The ambiguity function is also very closely related to the mutual intensity function of partially coherent light, and a straight-forward generalisation of (2.78) describes the diffracted intensity when the wavefield is quasimonochromatic and spatially partially coherent.

Equation (2.78) is already a much simpler expression than equation (2.74) and was derived without further approximation. In the next Section, I show that further simplifications result for weakly-absorbing and limited phase-shift objects. These simplifications are the *a posteriori* justification for making the Fresnel approximation; to my knowledge no similar forms have been obtained for the intensity of unapproximated wavefields propagated with Rayleigh-Sommerfeld diffraction.

### 2.5.2 Contrast transfer of absorption and phase-shifts

Equation (2.78) is a more compact expression for calculating intensities, but does not have any intrinsic advantages over the convolution form (2.49) or transfer function form (2.47) of Fresnel diffraction. This Article shows that certain assumptions about the absorption and phase-shift due to the object produce a dramatically simpler expression for the diffraction-pattern intensity. This *contrast-transfer function* relation is the core of the solution to the inverse problem described in the next Chapter.

The wavefield at  $z = 0$  due to a thin object with absorption  $\mu(\mathbf{x})$  and phase-shift  $\phi(\mathbf{x})$  is

$$f(\mathbf{x}) = f_0 \exp(-\mu(\mathbf{x})) \exp(i\phi(\mathbf{x})), \quad (2.81)$$

where  $f_0$  is the amplitude of the incident plane-wave, giving an incident intensity of  $I_0 = |f_0|^2$ . Substituting into (2.78) and combining the exponentials gives

$$\begin{aligned} \tilde{I}(\mathbf{u}; z) &= I_0 \int_{-\infty}^{\infty} \exp\left(-\mu(\mathbf{x} + \lambda z \mathbf{u}/2) - \mu(\mathbf{x} - \lambda z \mathbf{u}/2)\right. \\ &\quad \left.+ i(\phi(\mathbf{x} - \lambda z \mathbf{u}/2) - \phi(\mathbf{x} + \lambda z \mathbf{u}/2))\right) \\ &\quad \times \exp(-2\pi i \mathbf{x} \cdot \mathbf{u}) d\mathbf{x}. \end{aligned} \quad (2.82)$$

We now make the central approximation of diffraction-contrast imaging: the entire argument to the first exponential is assumed to be small, and so the exponential is expanded to first order,  $\exp \epsilon \approx 1 + \epsilon$ . The implications of this approximation are

discussed below. The approximated expression is now

$$\begin{aligned}\tilde{I}(\mathbf{u}; z) = I_0 \int_{-\infty}^{\infty} & \left( 1 - \mu(\mathbf{x} + \lambda z \mathbf{u}/2) - \mu(\mathbf{x} - \lambda z \mathbf{u}/2) \right. \\ & \left. + i(\phi(\mathbf{x} - \lambda z \mathbf{u}/2) - \phi(\mathbf{x} + \lambda z \mathbf{u}/2)) \right) \\ & \times \exp(-2\pi i \mathbf{x} \cdot \mathbf{u}) d\mathbf{x}.\end{aligned}\quad (2.83)$$

which is clearly the Fourier transform of the sum of five terms. This breaks up as

$$\begin{aligned}\frac{\tilde{I}(\mathbf{u}; z)}{I_0} = & \mathcal{F}\{1\} - \mathcal{F}\{\mu(\mathbf{x} + \lambda z \mathbf{u}/2)\} - \mathcal{F}\{\mu(\mathbf{x} - \lambda z \mathbf{u}/2)\} \\ & + i(\mathcal{F}\{\phi(\mathbf{x} - \lambda z \mathbf{u}/2)\} - \mathcal{F}\{\phi(\mathbf{x} + \lambda z \mathbf{u}/2)\}).\end{aligned}\quad (2.84)$$

The Fourier shift theorem relates the Fourier transforms of shifted and unshifted functions by [28, p 111]

$$\mathcal{F}\{f(\mathbf{x} - \mathbf{a})\} = \exp(-2\pi i \mathbf{u} \cdot \mathbf{a}) \mathcal{F}\{f(\mathbf{x})\}. \quad (2.85)$$

Applying the Fourier shift theorem to (2.84) yields

$$\begin{aligned}\frac{\tilde{I}(\mathbf{u}; z)}{I_0} = & \delta(\mathbf{u}) - \exp(i\pi\lambda zu^2) \mathcal{F}\{\mu(\mathbf{x})\} - \exp(-i\pi\lambda zu^2) \mathcal{F}\{\mu(\mathbf{x})\} \\ & + i(\exp(-i\pi\lambda zu^2) \mathcal{F}\{\phi(\mathbf{x})\} - \exp(i\pi\lambda zu^2) \mathcal{F}\{\phi(\mathbf{x})\}).\end{aligned}\quad (2.86)$$

which rearranges to

$$\frac{\tilde{I}(\mathbf{u}; z)}{I_0} = \delta(\mathbf{u}) - 2 \cos \pi\lambda zu^2 \mathcal{F}\{\mu(\mathbf{x})\} + 2 \sin \pi\lambda zu^2 \mathcal{F}\{\phi(\mathbf{x})\}. \quad (2.87)$$

This is a rather remarkable expression as it indicates a *linear shift-invariant* relationship between the diffracted intensity and both phase *and* absorption. The cosine factor is known as the absorption *contrast transfer function* (CTF) and the sine factor as the phase CTF; both are depicted in Figure 2.5. There is no special connection to the optical transfer function (OTF) which maps input *intensity* to output intensity for *incoherent* imaging systems.

While the graph has an appealing simplicity, it should be emphasised that the CTF parameter  $\pi\lambda zu^2$  confounds propagation distance  $z$  and spatial frequency  $u$  and so in general there are spatial frequencies at which contrast is due to both absorption and phase-shift. The phase and absorption contributions to a single image

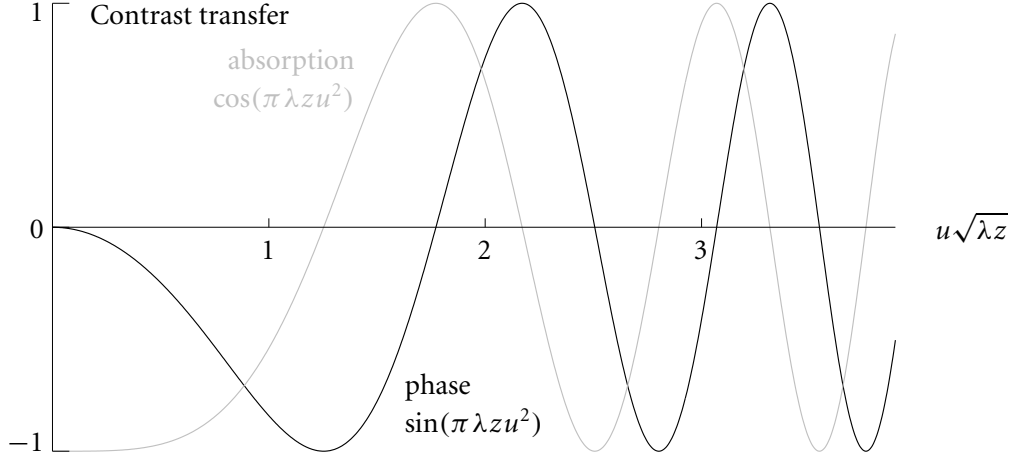


FIGURE 2.5 **The contrast transfer functions for absorption and phase-shift.** The CTFs are normalised and the phase CTF is shown for negative  $\delta$ , corresponding to a phase-advancing object.

cannot, in general, be separated.

The mixing of phase and absorption information is less complete, and is even beneficial, in the special case of small propagation distance  $z$ . For the contact image at  $z = 0$ , only absorption contrast contributes but as the propagation distance is increased phase effects become increasingly important. If  $\lambda z$  is small enough that the important spatial frequencies in the object satisfy  $\lambda z u^2 < 1/2$  then we need only consider the CTF curves up to the first zero-crossing. Over this range it is clear that loss of contrast due to absorption at higher spatial frequencies is more than compensated by increased phase contrast. The effect is particularly pronounced for almost-transparent objects where the phase term grows to be larger than the absorption term. This appears as the edge-enhancement effect familiar from the focusing of optical microscopes. The effect has recently been exploited to increase edge contrast in X-ray imaging when the absorption contrast is very low (see the review Reference 50).

Up to the first zero-crossing, no contrast reversal occurs and such images may be interpreted directly; they appear as standard absorption images with sharp, bright edges. In Section 3.8 I show that optimal signal-to-noise is obtained for greater propagation distances where the contrast reverses several times. Such *holographic* images cannot be interpreted directly. We will shortly see, however, that combining CTF formalism with the monomorphous object assumption yields an expression capable of retrieving information from holographic diffraction patterns.

### 2.5.3 Validity of the CTF expression

Before proceeding further with the contrast-transfer function expression, let us return to the linearising approximation made in obtaining it: explicitly that

$$\left| -\mu(\mathbf{x} + \lambda z \mathbf{u}/2) - \mu(\mathbf{x} - \lambda z \mathbf{u}/2) + i(\phi(\mathbf{x} - \lambda z \mathbf{u}/2) - \phi(\mathbf{x} + \lambda z \mathbf{u}/2)) \right| \ll 1. \quad (2.88)$$

This inequality is satisfied if both

$$\mu(\mathbf{x} + \lambda z \mathbf{u}/2) + \mu(\mathbf{x} - \lambda z \mathbf{u}/2) \ll 1 \quad (2.89)$$

$$\text{and } |\phi(\mathbf{x} + \lambda z \mathbf{u}/2) - \phi(\mathbf{x} - \lambda z \mathbf{u}/2)| \ll 1. \quad (2.90)$$

The first condition can only be satisfied everywhere if the absorption  $\mu$  is everywhere much less than one. The second condition, which we might call the *slowly-varying phase condition* (SVPC), does *not* require the phase-shift to be much smaller than one radian: it merely requires the phase-shift to vary by much less than one radian over a distance  $\lambda z u$ . Clearly, assuming weak-phase shift  $|\phi| \ll 1$  is *sufficient* to satisfy the SVPC, but it is not necessary.

The SVPC is a surprisingly complicated condition, depending on the phase structure of the object  $\phi(\mathbf{x})$  and on the propagation distance  $z$  and the spatial-frequencies imaged. It is discussed in more detail in §2.5.6, for now we simply note that the SVPC is more less restrictive than the weak-phase condition.

### 2.5.4 Previous use of contrast transfer functions

The above derivation of the contrast transfer relation (2.87) is new. The expression itself is not new; it was first written as part of early research on Fourier optics [51]. As a coherent-optics result, it attracted little attention until a related linear expression was derived by researchers seeking to improve the resolution of transmission electron microscopes (TEMs).

Electron optics suffer greatly from spherical aberration and until circa 2002 this aberration set the resolution limit of direct imaging in standard TEMs [52]. The first investigations of phase contrast in TEMs arising from spherical aberration and defocus were published by Scherzer in 1946 [53] and the so-called ‘linear imaging theory’ of contrast transfer described in this section was developed by 1970 [54–56]. In this theory, the electron microscope image has a contrast-transfer relation

$$\tilde{I}(\mathbf{u}; z) = \delta(\mathbf{u}) - 2 \cos \chi(u; z) \tilde{\mu}(\mathbf{u}) + 2 \sin \chi(u; z) \tilde{\phi}(\mathbf{u}), \quad (2.91)$$

where the *wave aberration*  $\chi$  is given by

$$\chi(u; z) = \pi\lambda zu^2 - 2\pi\lambda^3 C_s u^4 \quad (2.92)$$

and has a familiar term due to the defocus  $z$  but also one including the spherical aberration coefficient  $C_s$ . The form of (2.91) is familiar and reduces to the free-space case (2.87) in the absence of spherical aberration. The theory, however, assumes both weak absorption and weak phase-shifts from the outset.

The free-space case was not considered in detail until 1971, when J-P Guigay investigated Lorentz microscopes with negligible spherical aberration. Guigay's derivation was reproduced above in §2.5.1, but rather than substituting a wave-field of arbitrary absorption and phase-shift (2.81), Guigay considered only the pure-phase case and showed that the slowly-varying phase condition applies. Thus Guigay extended the linear imaging theory to non-weak objects. The novel result of the previous Article is that the CTF expression (2.87) applies also to weakly-absorbing objects with slowly-varying phase.

Interest in the contrast transfer theory has revived in recent years due to the demands of cryoelectron microscopy of biological materials. Much of the relevant literature on CTFs and their deconvolution concerns electron microscopy. This literature is reviewed when considering the inverse problem in §3.2.4.

### 2.5.5 Contrast transfer of monomorphous objects

The CTF expression adds the weighted effects of phase and absorption information in Fourier space, it does not assist us in separating them. Now consider the effect of assuming a monomorphous object. From (2.23), the wave-absorption and phase-shift due to a monomorphous material with column-density  $\rho$  are

$$\mu(\mathbf{x}) = k\beta\rho(\mathbf{x}) \quad \text{and} \quad \phi(\mathbf{x}) = k\delta\rho(\mathbf{x}). \quad (2.93)$$

Substituting these into the CTF expression (2.87) yields

$$\tilde{C}(\mathbf{u}; z) = 2k\tilde{\rho}(\mathbf{u}) (\delta \sin(\pi\lambda zu^2) - \beta \cos(\pi\lambda zu^2)), \quad (2.94)$$

where the *dimensionless contrast*  $C(\mathbf{x})$  is simply the normalised deviation of the diffraction intensity from the background:

$$C(\mathbf{x}) = \frac{I(\mathbf{x}) - I_0}{I_0}. \quad (2.95)$$

We now have a *single* transfer function  $\tilde{h}_{\text{mm}}$

$$\tilde{h}_{\text{mm}}(u, z) = 2k(\delta \sin \pi \lambda z u^2 - \beta \cos \pi \lambda z u^2) \quad (2.96)$$

relating, in the Fourier representation, the column-density  $\tilde{\rho}$  of a monomorphous object to the contrast of the diffracted image  $\tilde{C}$ .

The phase coefficient  $\delta$  may taken any value including zero, while the absorption coefficient may be zero (for a pure phase object) or greater. The transfer function may then be written in terms of a single trigonometric function as either

$$= -2k\sqrt{\beta^2 + \delta^2} \cos\left(\pi \lambda z u^2 + \arctan \frac{\delta}{\beta}\right) \quad (2.97)$$

or

$$= 2k \operatorname{sgn} \delta \sqrt{\beta^2 + \delta^2} \sin\left(\pi \lambda z u^2 - \arctan \frac{\beta}{\delta}\right) \quad (2.98)$$

where  $\operatorname{sgn}$  is the *signum* function which is one for positive argument, minus one for negative argument and zero when the argument is zero.

The normalised transfer function is plotted in Figure 2.6 for values of the *absorption ratio*  $\beta/\delta$  of 0.2 and  $-0.2$ . Notice that for  $\delta > 0$ , there is a contrast null at low spatial frequencies, and the more transparent the object, the lower the first frequency of vanishing contrast. At x-ray wavelengths all material have positive  $\beta$  and  $\delta$ , and this problem does not occur. For atomic gases,  $\beta/\delta$  is a function of the laser detuning, which can usually be adjusted so that the ratio is positive. At visible wavelengths, a lens may readily be used to re-image the diffraction pattern, and defocus *towards* the object has the effect of inverting the sign of  $\delta$ . This important effect is discussed in §5.3.4. The presence of zeros in the contrast transfer function corresponds to the loss of information at certain spatial frequencies. This is of critical importance to the inverse problem discussed in the next Chapter.

For completeness it is worth mentioning that this linear shift-invariant system may be written in the convolution form, that is a closed form for the impulse-

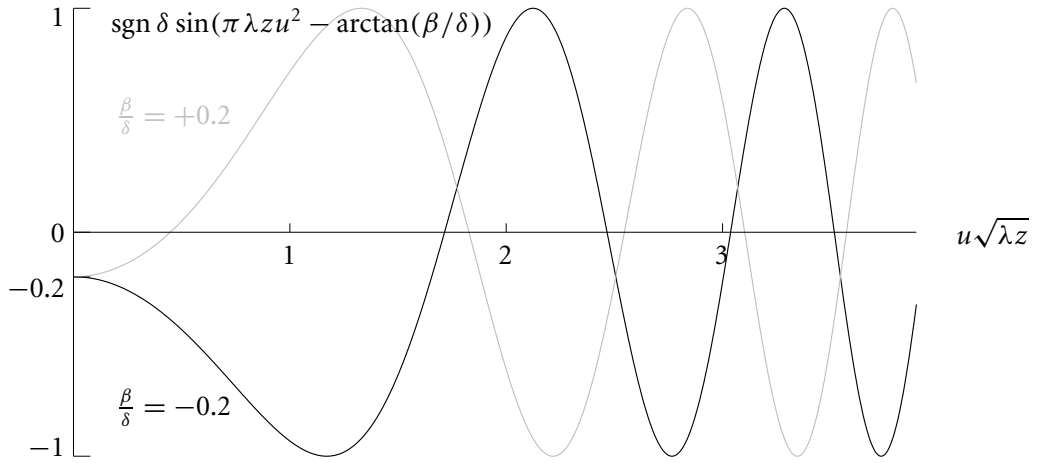


FIGURE 2.6 **The monomorphous column-density CTF.** The normalised CTF is shown for positive and negative values of the phase-coefficient  $\delta$ .

response function does exist. Taking the inverse Fourier transform of the transfer function  $\tilde{h}$  yields, after a modicum of trigonometry,

$$\begin{aligned} h_{\text{mm}}(\mathbf{x}, z) &= \mathcal{F}^{-1} \left\{ \tilde{h}(\mathbf{u}; z) \right\} \\ &= \frac{2k}{\lambda z} \operatorname{sgn} \delta \sqrt{\beta^2 + \delta^2} \cos \left( \frac{\pi |\mathbf{x}|^2}{\lambda z} + \arctan \frac{\beta}{\delta} \right). \end{aligned} \quad (2.99)$$

The convolution form of the system is then

$$C(\mathbf{x}; z) = \frac{2k}{\lambda z} \operatorname{sgn} \delta \sqrt{\beta^2 + \delta^2} \iint_{-\infty}^{\infty} \rho(\mathbf{x}') \cos \left( \frac{\pi |\mathbf{x} - \mathbf{x}'|^2}{\lambda z} + \arctan \frac{\beta}{\delta} \right) d\mathbf{x}'. \quad (2.100)$$

This form makes absolutely explicit the linear relationship between the column density  $\rho(\mathbf{x})$  of a monomorphous object, and the contrast  $C(\mathbf{x}; z)$  of the resulting diffraction-pattern. Note, however, that the impulse response function  $h_{\text{mm}}(\mathbf{x}; z)$  is infinite in extent, and so there is no obvious truncation of the impulse response that might allow efficient numeric implementation. The results of the next Chapter exploit the transfer function representation (2.94) rather than this convolution representation.

We have found the expression we sought: one that connects the column-density of a monomorphous object with the intensity of its diffraction pattern. Indeed, it even appears possible to solve (2.94) for the column-density. The zeros in the contrast-transfer function present a significant obstacle, however. Solving (2.94) for

column-density is the subject of Chapter 3. Before concluding this Chapter, a little further consideration of the SVPC is in order.

### 2.5.6 The slowly varying phase condition

The *slowly varying phase* condition (2.90) was written down by Guigay when he considered the spatial frequency spectrum of the diffraction pattern formed by a pure phase object. It is an oddly formed inequality, being non-local and depending on both spatial frequency  $\mathbf{u}$  and propagation distance  $z$ . It is perhaps best interpreted by considering the distance  $\lambda z \mathbf{u}$  for each spatial frequency from zero to a maximum spatial frequency set by, for example, the detector pixel size, or for the case of spherical illumination, the effective pixel sized after demagnification. The condition is that the phase must vary by much less than a radian over all separations  $\delta \mathbf{x} = \lambda z \mathbf{u}$  in the  $z = 0$  plane. For phase variations that are everywhere much less than one radian, the condition is satisfied at *all* spatial frequencies. For smoothly varying phase excursions of order one radian or larger, it is always possible to find a propagation distance  $z$  small enough that the condition is satisfied everywhere for spatial frequencies up to some desired maximum.

Of course, this upper bound on the spatial frequency must be high enough to include the structures of interest in the object! Consider the admittedly non-compact case of a sinusoidal phase grating of positive phase-amplitude  $\phi_0$

$$\phi(\mathbf{x}) = \phi_0 \cos(2\pi \mathbf{u} \cdot \mathbf{x}). \quad (2.101)$$

The slowly varying phase condition is then

$$\phi_0 |\cos(2\pi \mathbf{u} \cdot \mathbf{x} + \pi \lambda z u^2) - \cos(2\pi \mathbf{u} \cdot \mathbf{x} - \pi \lambda z u^2)| \ll 1, \quad (2.102)$$

and using trigonometric identities allows us to write

$$\begin{aligned} & \phi_0 |\cos(2\pi \mathbf{u} \cdot \mathbf{x} + \pi \lambda z u^2) - \cos(2\pi \mathbf{u} \cdot \mathbf{x} - \pi \lambda z u^2)| \\ &= 2\phi_0 |\sin(\pi \lambda z u^2)| |\sin(2\pi \mathbf{u} \cdot \mathbf{x})| \\ &\leq 2\phi_0 |\sin(\pi \lambda z u^2)| \end{aligned} \quad (2.103)$$

as  $z$  is positive. Hence the slowly varying phase condition (2.90) is satisfied when

$$\sin(\pi \lambda z u^2) \ll \frac{1}{2\phi_0}. \quad (2.104)$$

Recall from Figure 2.5 and ensuing discussion on page 52 that the phase CTF is  $\sin(\pi \lambda z u^2)$ . Thus the slowly varying phase condition requires that thick phase gratings must be in the edge-contrast regime of diffraction, although as gratings don't have edges, a more appropriate term might be the *single fringe* regime.

Generalising this result to an arbitrary phase function by Fourier methods is not as simple a task as might be expected, essentially due to the Uncertainty principle for real-space and Fourier-space representations. A numerical consideration of the almost-compact case of a Gaussian phase-object of  $1/e$  half-width  $a$  and peak phase-shift  $\phi_0$  leads to

$$0.8 \frac{\lambda z u}{a} \ll \frac{1}{\phi_0}. \quad (2.105)$$

Selecting a maximum spatial frequency of  $u = 1/a$  includes essentially the entire spectrum of the Gaussian and makes the condition

$$0.8 \lambda z u^2 \ll \frac{1}{\phi_0} \quad (2.106)$$

which is clearly analogous to the grating case (2.104). If instead we solve for the characteristic object size  $a$ , the condition reduces to

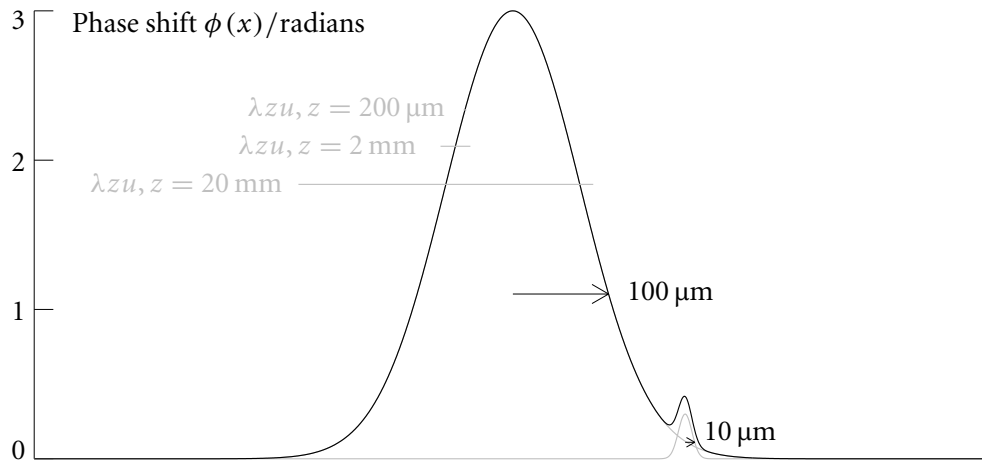
$$0.8 \frac{z}{z_R} \ll \frac{1}{\phi_0}, \quad (2.107)$$

where  $z_R$  is the *Rayleigh range* given by

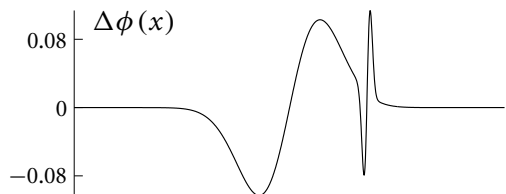
$$z_R = \frac{a^2}{\lambda}. \quad (2.108)$$

The Rayleigh range, and the associated dimensionless *Fresnel number*  $N_F = z_R/z$ , parameterise the extent of diffraction. For propagation distances  $z$  much smaller than  $z_R$ , only a single fringe is evident, while for  $z$  considerably greater than  $z_R$  there are multiple fringes. The Rayleigh range is a general parameter in Fresnel diffraction occurring, for example, in the analysis of diffraction from apertures, where contrast transfer theory is inappropriate. Hence the condition  $z/z_R \ll 1/\phi_0$  forms a useful approximation to the slowly varying phase condition for compact objects of characteristic size  $a$ .

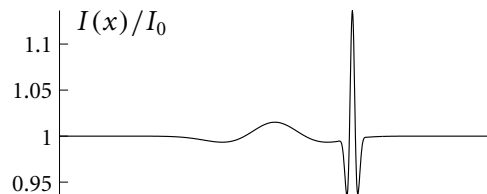
An example simulation is shown on the facing page in which a one dimensional phase object is illuminated with 780 nm radiation. The phase object, shown in Figure 2.7A, consists of a 3 radian high Gaussian of half-width 100  $\mu\text{m}$  on which is superposed a small Gaussian of one-tenth the height and width. Ninety-five



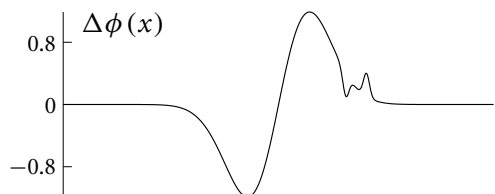
A A strong phase object with weak phase detail. The big Gaussian is 3 radian, the small 0.3 radian.



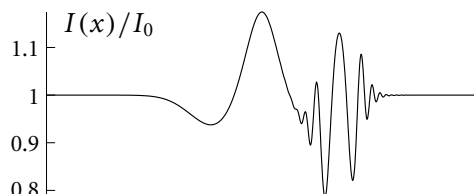
B Difference  $\Delta\phi(x)$  for  $z = 200 \mu\text{m}$ .



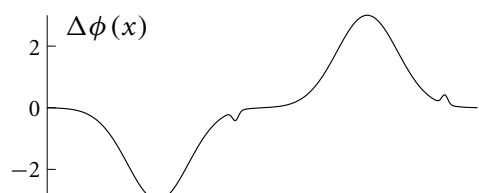
C Diffraction pattern at  $z = 200 \mu\text{m}$



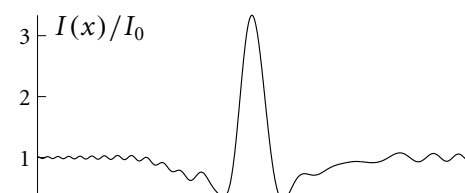
D Difference  $\Delta\phi(x)$  for  $z = 2 \text{ mm}$ .



E Diffraction pattern at  $z = 2 \text{ mm}$ .



F Difference  $\Delta\phi(x)$  for  $z = 20 \text{ mm}$ .



G Diffraction pattern at  $z = 20 \text{ mm}$ .

**FIGURE 2.7 The slowly-varying phase condition.** The SVPC (left column) and the diffraction-pattern intensity in one-dimension are shown for a non-weak phase object A. Three propagation distances are shown.

percent of the Fourier power spectrum of the *sharp* Gaussian, and essentially the entire spectrum of the large Gaussian, is contained in the spatial frequencies less than  $u = 31\,200 \text{ m}^{-1}$ . Three propagation distances are considered: 200  $\mu\text{m}$ , 2 mm and 20 mm. Depictions of the equivalent distances  $\lambda zu$  are shown superposed on the plot of the phase object. The left column of plots shows the phase difference  $\Delta\phi(x) = \phi(x + \lambda zu/2) - \phi(x - \lambda zu/2)$ , and the right column shows the diffracted intensity for the three propagation distances, calculated using the angular spectrum method described in §2.3.2.

At 200  $\mu\text{m}$ , the phase difference  $\Delta\phi(x)$  shown in Figure 2.7B is clearly much smaller than one for all values of  $x$  and so the slowly varying phase condition (2.90) is well satisfied. The diffraction pattern Figure 2.7C shows relatively strong single-fringe diffraction from the sharp Gaussian and a lower contrast single-fringe pattern due to the broad strong Gaussian. At 2 mm the phase condition is only marginally satisfied for the highest spatial frequencies, although is proportionally better satisfied for components less than the maximum  $u$ . The diffraction pattern shows many fringes due to the narrow Gaussian but still a single fringe due to the strong phase component. At 20 mm the slowly varying phase condition is clearly violated. There is very strong contrast due to the strong object; light has been partially focused. Note that the Rayleigh range  $a^2/\lambda$  for the large Gaussian is 13 mm, and so the 2 mm case marginally satisfies (2.107) while the 20 mm case clearly violates it.

The examples make clear that the slowly varying phase condition is neither a weak-phase condition nor a single-fringe condition. Notice, however, that for a grating, the condition reduces to (2.103), which on comparison with (2.94) is seen to be a requirement of weak phase *contrast*, that is  $\tilde{C}(\mathbf{u}; z) \ll 1$ . Similarly, in the Gaussian case the requirement  $\phi_0 \lambda zu^2 \ll 1$  is satisfied by the same weak contrast provision. This provision restricts the contrast in the Fourier representation, although by Parseval's theorem a similar relation might be expected to hold for the image contrast  $C(\mathbf{x}; z)$ .<sup>11</sup> Therefore I conjecture that the slowly varying phase condition is satisfied if the contrast in the diffraction pattern is small. For the monomorphous case, a complete proof would also require consideration of the absorption condition (2.89), which is of course a weak contrast condition for the *contact* image.

---

<sup>11</sup> Optimising the contrast as a function of propagation distance is discussed in §3.8 on page 126.

### 2.5.7 Breakdown of linearity for thick object diffraction

What can be said about the wavefield after a strong phase objects propagated beyond the slowly varying phase regime? Again, it is reasonable to consider phase gratings as they form a basis for arbitrary phase objects. The problem dates back to Talbot, who in 1836 observed contrast fluctuations behind a grating; the rich fractal structure of this simple system has only recently been appreciated [57]. Due to its crystallographic importance the problem was considered analytically some time ago [58, *et seqq.*], with a reasonably complete treatment in the Fresnel approximation published somewhat later [59].

This treatment considered a Jacobi-Anger expansion of the phase grating (2.101), and uses Graf's addition theorem on the resulting Bessel functions to simplify the double sum for the intensity to

$$I(\mathbf{x}; z) = I_0 + 2I_0 \sum_{m=1}^{\infty} \cos(2\pi m \mathbf{u} \cdot \mathbf{x}) J_m(2\phi_0 \sin(m\pi \lambda z u^2)). \quad (2.109)$$

For small  $\epsilon$ , the Bessel function of order  $m$  has leading term of order  $J_m(\epsilon) \simeq \epsilon^m$  and so we are lead naturally back to the condition (2.103). In this case, only the first term in the sum is significant, and the first order Bessel function may be approximated as  $J_1(x) \approx \frac{1}{2}x$  to recover the linear system result for the grating. This analysis makes it plain that configurations that violate the slowly varying phase condition yield a fundamentally non-linear relation between the phase-shift  $\phi_0$  through the object and the diffracted intensity. Furthermore, even determining the phase shift through a thick object is complicated by propagation effects within the object [60]; the undeviated ray approximation of §2.2.4 may well not apply.

## 2.6 Paraxial optics and space-frequency distributions

In this Chapter some connections between Fresnel diffraction, point projection, the ambiguity function and contrast transfer have been explored in a detailed, if necessarily ad-hoc, manner. In concluding, this section places some of these ideas within the unifying framework of modern theoretical optics.

If the  $\exp(ikz)$  phase-factor is excised from the expression for the Fresnel diffracted wavefield (2.49), the resulting function varies only slowly as a function of  $z$ .

It may be shown to be a solution of the *paraxial wave equation*

$$\left( \frac{\partial^2}{\partial x^2} + \frac{\partial^2}{\partial y^2} - 2ik \frac{\partial}{\partial z} \right) f(x, y; z) = 0, \quad (2.110)$$

which alternatively may be obtained from the Helmholtz equation by assuming variation of the wavefield in the  $z$ -direction is primarily of the form  $\exp(ikz)$  [61, Appendix A1,A2]. The paraxial wave equation is a *parabolic PDE* while the Helmholtz equation is *elliptic*. The eigenfunctions of the Helmholtz equation, the plane waves, have a continuous spectrum, while the eigenfunctions of the paraxial wave equation are the discrete, enumerable Gauss-Hermite functions [27]. We have seen that paraxial optics is, in many cases, an excellent approximation to the full scalar diffraction theory. The mathematical structures of the two systems are, however, profoundly different.

Comparing the transfer function formulation of Rayleigh-Sommerfeld diffraction (2.38) to that of Fresnel diffraction (2.47), it is clear that the Fresnel case is a unitary transform whereas the full Rayleigh-Sommerfeld transform is *not* unitary. A unitary although not shift-invariant generalisation of the Fresnel transform known as the *linear canonical transform*<sup>12</sup> and denoted  $\mathcal{L}$  is given by

$$(\mathcal{L}f)(\mathbf{x}) = \frac{i}{B} \iint_{-\infty}^{\infty} f(\mathbf{x}') \exp\left(\frac{i\pi}{B} (D|\mathbf{x}|^2 - 2\mathbf{x} \cdot \mathbf{x}' + A|\mathbf{x}'|^2)\right) d\mathbf{x}'. \quad (2.111)$$

The Fresnel transform<sup>13</sup> is the special case of  $A = D = 1$ ,  $B = \lambda z$ . The LCT also includes among its special cases the Fourier transform, geometric magnification (scaling) and propagation through a thin parabolic lens. If the LCT parameters are packed into a  $2 \times 2$  matrix of elements  $A$ ,  $B$ ,  $C$  and  $D$  with  $C$  such that  $AD - BC = 1$  then the action of successive LCTs may be conflated by multiplication of the associated matrices.<sup>14</sup> Further, the set of all possible LCTs forms a group known as the *metaplectic group*  $Mp(2, \mathbf{R})$ . [65, 66] [27, p 111]. Viewed through this formalism, the isomorphism of Fresnel diffraction under the change from plane-wave to point source illumination is a simple matrix or operator relation. I shall use this elegant

<sup>12</sup> Rediscovering this form is a popular pastime for workers in theoretical optics, verging on the popularity of rediscovering the fractional Fourier transform. The LCT is also known as the *quadratic phase system*, the *extended fractional Fourier transform*, the *generalised Fresnel transform* and other names. An excellent discussion is in [27, §2.4].

<sup>13</sup> For discussion of the Fresnel transform as an operator, see [62].

<sup>14</sup> The process is formally equivalent to the *operator optics* introduced by van der Lugt [63] and optimised by Nazarathy and Shamir [64]. See Goodman [23, §5.4] for a tutorial and Ozaktas [27, p 190] for recent references.

---

matrix calculus in §5.3.4 when I consider the reimaging of a diffraction pattern by defocusing a simple lens.

The linear canonical transform is also intimately connected with space-frequency representations, such as the Wigner distribution function [67] and the ambiguity function. Linear canonical transforms correspond to identical geometric distortions of both the Wigner and ambiguity functions, in fact the transition matrix in  $(\mathbf{x}, \mathbf{u})$  coordinates is the ABCD-matrix [27, p 95].

There is also a deep and very close relationship between paraxial optics and ray optics. The relationship is not germane to the discussion of general inhomogeneous media in §2.2, as it concerns only optical systems composed of thin lenses and quadratic-graded index media. It is nevertheless remarkable that the ABCD-matrix of the LCT is *exactly* the ABCD-matrix of classical ray optics [27, §4.6].

The paraxial optics formalism is not sufficient to explain the higher-order error cancellation in the Fresnel isomorphism described in §2.4. The extension of the paraxial theory described in this section to full Rayleigh-Sommerfeld scalar diffraction is currently incomplete. Alonso, Forbes and K B Wolf have described a *angle-impact Wigner distribution* for solutions of the two-dimensional Helmholtz equation [68]. A recent article describes non-paraxial diffraction using Wigner distributions [69]. There is little doubt that much remains to be discovered about the mathematical structure of optics, and in particular the mathematical representation of finite objects and wavefields.



OUR STUDY OF THE FORWARD PROBLEM is now complete. We have seen that a weakly-refracting monomorphous object imprints its phase and amplitude on the wavefield. Both quantities are simply related to the column-density summed along the rays of the radiation. We then considered the diffraction of the resulting wavefield in free space. The problem of scalar wavefield diffraction is solved exactly by either the angular spectrum or Rayleigh-Sommerfeld methods; the former is computationally efficient and is used in simulating diffraction patterns in the next Chapter.

Finding a linear relationship between the diffraction-pattern *intensity* and the object phase and absorption required making the Fresnel approximation. After some algebra and the further approximations of weak absorption and slowly-varying phase, a linear relationship was obtained, based on the contrast transfer functions. This relationship applies more widely than was previously understood.

Applying the CTF relation to monomorphous objects resulted in a single transfer function relating the column-density of the object to the diffraction-pattern intensity. The relation appears to be invertible in a formal sense. The next Chapter discusses the inverse problem of retrieving column-densities from diffraction patterns using the monomorphous contrast transfer function.

## Chapter 3

# Solving the inverse problem

IN THIS CHAPTER I consider the inverse problem: given a single diffraction image measured by an optical detector, what information may be retrieved about the object? This is the problem of *in-line holography* and the first Section reviews holographic solutions to the inverse problem from a information-theoretic perspective. Section 3.2 reviews deconvolution solutions for pure absorption and pure phase objects and we arrive at the monomorphous object case in §3.2.3. Similar deconvolution methods have been used in cryoelectron microtomography; this work is compared to the x-ray and optical results of this thesis. A distinct Transport-of-Intensity solution to the inverse problem, advanced for x-ray applications, is considered in §3.3. I show that this solution may also be derived from the Guigay ambiguity-function marginal.

Returning to the deconvolution solution, §3.4 points out its formal similarity with the much-studied field of incoherent-image deblurring. Fourier methods for solving the inverse problem are discussed, and a *partial-Tikhonov* filter is derived providing successful retrievals of column-density when diffraction pattern SNR is relatively high. X-ray and cold atom images typically have low exposure values and hence low SNR. In §3.5 I show that under these conditions, Fourier deconvolution produces a distorted and noisy retrieval. A hybrid Fourier-wavelet deconvolution algorithm, taken from the image deblurring literature, is modified in §3.6 to suit our diffraction-contrast retrieval. Simulated experiments show that this algorithm performs much better than any Fourier method on noisy diffraction patterns, approaching the quality of Zernike phase-contrast images. Other deconvolution algorithms are reviewed in §3.7 and I outline how some current research in computational harmonic analysis might enhance the hybrid algorithm. In many

experiments, the propagation distance is adjustable. The final Section discusses the optimal propagation distance from the inverse problem perspective.

### 3.1 Holography: Retrieving information from diffraction patterns

This thesis is concerned with retrieving information from diffraction patterns. The study of wavefield reconstruction from diffraction or interference patterns is known as *holography*. In this Section, methods for retrieving information from diffraction patterns are reviewed in terms of the *information content* of the pattern. The *information deficit* implicit in retrieval a full wavefield from a single, unmodified diffraction pattern can be resolved either by additional optics, or a obtaining a second diffraction pattern. This review elucidates the close relationship between holography and the problem of this thesis; but shows that traditional holographic methods cannot yield a solution.

#### 3.1.1 Gabor in-line holography

The early crystallographers Bragg and von Laue first considered the problem of retrieving structure information from a diffraction pattern. The first attempted retrieval of a non-crystallographic object was reported by Denis Gabor in 1948 [70].

Gabor was attempting to solve the problem of severe aberration in early electron lenses, which was then the limit on electron microscope resolution. His ‘new microscopic principle’ was a two-step process, and consisted of first removing the lens altogether and magnifying the object by point-projection onto a photographic plate, as depicted in Figure 3.1A. The image recorded was, of course, a Fresnel diffraction pattern as discussed in §2.4.

Gabor was awarded the Nobel prize in 1971 nominally for his attempt at retrieving an image of the object from this measured diffraction pattern. He demonstrated that if the developed plate is illuminated by a point source of light and the object removed, the optical wavefield beyond the plate is, in part, a magnified equivalent of the original wavefield in the same region of space (Figure 3.1B). An imaging system such as a lens and detector, or an eye, looking through the plate towards the point source sees the object suspended in space as if at its original location: the full depth of field and parallax are apparent. Gabor was interested in particular in recording an electron diffraction pattern and reconstructing the pattern with visible light.

This ‘method of reconstructed wavefronts’ was soon termed *holography*, with the recording of the diffraction pattern termed a *hologram*.

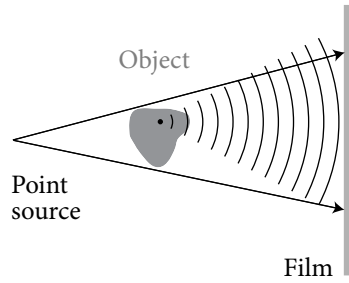
Many forms of holography have been described over the last half-century; all are concerned with reconstructing a wavefield. In some applications, the aim is to generate a known wavefield. This is the regime of *computer-generated holography*, where the first step of generating a hologram is performed in a computer. Other applications are more closely allied to the problem of this thesis, seeking as Gabor did to extract information from a wavefield. Here the hologram may be digitised and the *second* step of propagating light through the hologram to form a reconstructed wavefield is simulated by computer; this process is known as *digital holography* [71]. The following Articles review several methods for retrieving information from holograms. It should be noted that any optical apparatus used in the first step (recording the hologram) is essential, while any optical processing in the second step (reconstruction) may alternatively be performed in a digital computer.

### 3.1.2 The twin image and the information deficit

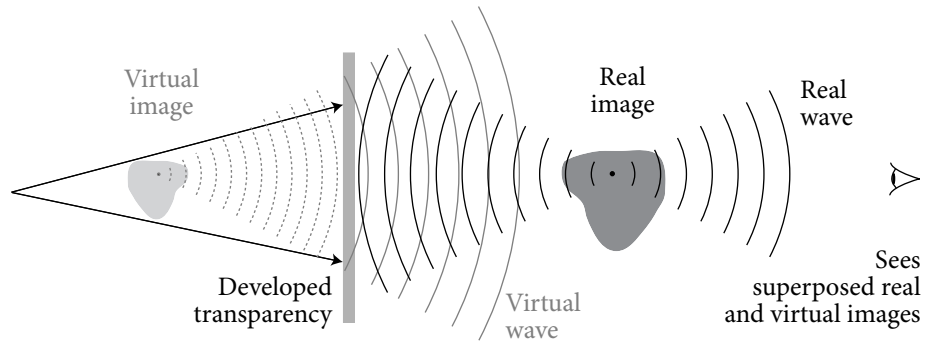
The reconstructed wavefront of Gabor holography is fundamentally flawed. As shown schematically in Figure 3.1B, and algebraically in Appendix C, the reconstructed wavefield is always accompanied by a second superposed wavefield proportional to the *conjugate* of the first. The real, conjugate image which results is widely known as the ‘twin image’, the term perhaps implying the inseparability of the superimposed image. A series of attempts were made to separate or remove the twin image in the years after Gabor’s announcement [72–74]. The requisite photographic information processing was awkward and interest in holography waned.

In 1962, Leith and Upatnieks [75] exploited the long coherence length of the recently invented laser to record holograms with an off-axis reference beam. The method thus records an *interferogram* of microscopic fringes modulated by the object aperture function, rather than the diffraction pattern recorded by Gabor’s geometry. Upon reconstruction, holograms so produced yield non-overlapping real and virtual images off-axis to the reconstruction beam. This solution of the twin image problem initiated a revolution in optics; some 30 000 papers mentioning holography in their abstracts have been published since 1970.

Leith and Upatnieks’ solution to the twin image problem is not, however, germane to this thesis. The method requires beam splitting optics, placing it outside the predicates of this work. It further requires high longitudinal coherence to en-



**A** Recording an in-line hologram is nothing more than photographing the diffraction pattern.



**B** Illuminating the developed transparency produces a wave proportional to the original wavefield (grey) and a conjugate wave (black). The real image is *pseudoscopic* or reversed.

**FIGURE 3.1 Gabor in-line holography is a two step process.** Curves depict the scattered wavefronts from an arbitrary point, see Appendix C for discussion.

sure interference fringes are formed with the off-axis reference, and high spatial resolution detectors are needed to record fringes with wavelength-order spacings.

Many other methods for wavefield reconstruction have been developed; whether these are ‘holography’ or ‘phase retrieval’ is an essentially epistemological distinction. In the following Articles I classify some of these methods by considering the information content of the problem. An in-line hologram is an intensity image, and so may be represented by one real number for each resolution element of the detector. The wavefield at the detector, however, is represented by a complex number at each resolution element. Even without entering into the vexed discussion on the nature of information, it is apparent that there is twice as much information in the wavefield as in the measured intensity. From this point of view, the twin-image problem of Gabor in-line holography is the result of attempting a reconstruction with inadequate information. This *information deficit* may be resolved by three

general classes of solution:

**Record only half of the available wavefield information** for example, by recording half the spatial-frequency spectrum of the object.

**Record twice as much intensity information** for example, by recording two holograms at different propagation distances, or at different wavelengths.

**Assume that the object is described by a real image** for example, by assuming the object is transparent and is therefore fully described by a real phase image.

Some previous methods of wavefield reconstruction are discussed in the remainder of this Section in terms of either the first or second class of solution. The assumption of a monomorphous object, on which this thesis is predicated, is a case of the third class of solution and is discussed as such in §3.2.3.

Finally, although the presence of the twin image in the Gabor technique makes it unsuitable in many applications, it has found a niche in the analysis of particle fields [76]. If a hologram is made of a very small object, or more precisely, the object-detector distance is much larger than the Rayleigh range, then the twin-image observed on reconstruction will be very far out of focus. The twin-images of many small particles tend to add to form a featureless background. In-line holography has thus been used to analyse aerosols [77] and even to image plankton in volumes of sea water [78]. This regime of application is, however, orthogonal to the microscopy with which we are concerned: we wish to see details in a single finite object, not to measure the distribution of many featureless objects.

### 3.1.3 Recording half as much information

One of the earliest attempts at solving the twin-image problem was the method of *single sideband holography* described by Lohmann in 1956 [72]. Rather than recording the diffraction pattern directly, a 4-f lens system with a schlieren knife records a diffraction pattern with one half of the spatial frequency plane removed. The reconstruction, performed through an identical system with the opposite half-plane occluded, is found to be free of the twin-image. Early analyses of the system concluded that only purely absorbing objects could be imaged [79, 80], but a recent reconsideration [81] shows that arbitrary wavefields are reconstructed without twin-images. The information deficit is balanced by the intuitive result that recording only half of the angular spectrum results in a reconstruction visible from only one side of the optical axis.

The off-axis holography method of Leith and Upatnieks also corresponds to the removal of half of the angular spectrum. An off-axis hologram is only successful if the fringes formed by the interference of the reference and scattered waves are resolved on the detector. Nyquist's theorem requires two resolution elements to resolve one cycle of the interference pattern, and so the spatial bandwidth available for encoding information about the scattered wave is halved. A similar loss of resolution must occur for a recently proposed 'in-line' technique where a reference wave is created on-axis but with a different curvature to the illumination [82].

### 3.1.4 Recording two holograms

Off-axis holography requires beam splitting optics, and single sideband holography requires a telecentric lens system. The use of optical elements may be avoided and the information deficit resolved by obtaining *two* in-line holograms.

Gabor's first attempt at eliminating the twin-image *did* require the use of a quarter-wave plate to record two holograms in quadrature [73] which could be added so that the twin-image canceled. The extension of Gabor's idea to all four quadrature phases has recently been shown to eliminate the autocorrelation term as well [83]. A proposal contemporaneous with Gabor's by W L Bragg and G L Rogers employed photographic subtraction of two holograms taken at distances  $z$  and  $2z$  for plane-wave illumination [74, 84], or analogous distances for point-source illumination [85]. Although not requiring optical elements, the photographic subtraction of the two images presented a prohibitive technical challenge and the technique was forgotten. Rogers re-proposed the technique in the light of digital image processing [86], and simulations of the algorithm with a view to x-ray experiments have been published recently [87, 88]. A similar method valid for arbitrary separations in  $z$  had been described previously in the electron microscopy literature [89] and much later in the optics literature [90], although the retrieval comes at the price of lower numerical stability.

New ideas for twin-image elimination continue to be advanced: an elegant method has been demonstrated whereby the stochastic variation in speckle between two images taken on identical apparatus provides enough information to reconstruct the wavefield without the conjugate contribution [91].

*Volume holograms* [23, §9.7] record information at many effective planes within the volume of a photographic emulsion, and hence over-satisfies the information deficit. An in-line volume hologram reconstructs the undistorted wavefield [92],

and may even reconstruct *spectral* information about a non-monochromatic incident wavefield. Solid-state detectors are, however, only sensitive to the intensity in a single plane. Volume holography is only relevant to photographic recording at visible wavelengths, and so falls outside the predicates of this thesis.

### 3.1.5 Two holograms: the Transport-of-Intensity solution

Although this thesis is predicated on the retrieval of object information from a *single* image, the work was inspired by a series of important results concerning *non-interferometric phase retrieval* from two closely-spaced images. I briefly introduce these developments in this Article.

The transport equation analogous to (2.14) for the paraxial wave equation (2.110) may be written as the *Transport of Intensity Equation* (TIE)<sup>1</sup>

$$\nabla \cdot (I(\mathbf{x}, z) \nabla \phi(\mathbf{x}, z)) = -k \frac{\partial I(\mathbf{x}, z)}{\partial z}, \quad (3.1)$$

where the vector derivative operator  $\nabla \equiv (\partial/\partial x, \partial/\partial y)$  acts in the transverse plane. The intensity derivative is approximated by the finite difference of two images separated by a small  $\Delta z$ , and their mean is used for the intensity  $I(\mathbf{x}, z)$ . A numerically efficient solution of the TIE derived by D Paganin and KA Nugent [94] returns the phase at a plane midway between the two images, and thus retrieves the full wavefield on this plane. The significance of this solution extends beyond the regime conventionally defined as in-line holography as, unlike most of the solutions described above, the TIE solution does *not* assume that the object scatters weakly, and is in fact valid for a very general class of wavefield.<sup>2</sup>

A novel concept of generalised phase valid for partially coherent wavefields is introduced and shown to reduce to the coherent definition of phase for monochromatic fields. The relaxed temporal coherence requirements of the TIE solution have led to applications to non-optical radiation for which high coherence sources are impractical or unavailable. TIE phase imaging has been demonstrated for electrons [98], x-rays [99], neutrons [100] and laser-cooled neutral atom beams [101–103]<sup>3</sup>, as well as for conventional optical microscopy with white light illumina-

<sup>1</sup> For a derivation of the TIE and thorough references see [93, §2.4.2].

<sup>2</sup> The wavefield must be free of optical vortices, a condition equivalent to the absence of intensity zeros. Refer [93, *passim*]; a recent comment on boundary value conditions is [95]. Extensions to non-linear [96] and inhomogeneous [97] media have been published recently.

<sup>3</sup> The paper [101] describes work that I contributed to in the early stages of this project, and is not otherwise discussed in this thesis. The paper is included in Appendix F, p 323.

tion [104]. While successful in many cases, the TIE solution must be regularised at low spatial frequencies; see comments in §3.2.3.

Early results during this project were processed with a TIE-based single-image solution for monomorphous objects. My study of the limitations of this solution led directly to the CTF methods presented in this Chapter. This antecedant TIE solution is discussed in §3.3.

### 3.1.6 Reconstruction of wavefields by iterative methods

The solutions hitherto described are in *closed form*, a direct and deterministic relation between holograms and wavefield is shown to exist for each method. A class of *iterative* solutions to the inverse problem has been developed, offering more general solutions but without a guarantee that the algorithm will converge to the correct solution. Iterative methods are also much more computationally intensive than direct methods.

In 1972, R W Gerchberg and W O Saxton published an iterative algorithm which retrieved the phase of a wavefield, given the intensity of the contact image and its Fourier transform [105]. Enhanced algorithms were soon developed that operate on a single far-field diffracted image and require only limited a priori information, known as the *constraints*, to be known about the object. An example of such a constraint is knowledge of the compact support of the object, although the method is very general and other convex and non-convex constraints have been used [106]. The uniqueness of the retrieved phase has been shown to be unique for all but ‘pathological rare’ cases [107]. Successful iterative retrieval from data has been published by one group [108] and results from a number of iterative phase retrieval experiments were presented recently at the Second International Workshop in Non-Crystallographic Phase Retrieval [9].

These algorithms are directly applicable only to phase retrieval from *far-field* diffraction patterns. Iterative methods for Fresnel regime phase retrieval were suggested by D L Misell [109, 110] soon after Gerchberg & Saxton’s original publication. Misell’s method likewise requires two intensity measurements, but unlike the holographic techniques is not limited to weak scattering. The iterative method is found to work better at larger separations of the imaging planes [111] and is thus complementary to the closed-form TIE method.

Later the technique was extended to a single-image iterative method where only a support constraint is used in the object plane. At first, only results for purely ab-

sorbing objects were presented [112, 113]. More recently, iterative retrieval of wave-fields propagated through realistic objects which both absorb and phase-shift has been simulated in one [114, 115] and two [116, 117] dimensions. Few experimental results have been presented. An attempted retrieval from a single image of a contaminated electron microscope aperture was only partially successful [118].

This apparent ability of the iterative techniques to extract both amplitude and phase from a single image is *not* a violation of the information theoretic limits discussed. On the contrary, R Vincent [119] describes how, even in the two-image case, phases may only be recovered at half the image sampling interval; here the information deficit is *over*-compensated.

A hybrid method has recently been proposed [120] in which a TIE retrieved phase is used as the initial guess for a Gerchberg-Saxton-Fienup iteration. While the method undoubtedly accelerates convergence of the iterative method in the near-Fresnel regime, it has only been demonstrated for pure phase objects, and it is not clear if it offers any advantages when attempting to retrieve information about objects which are also absorbing.

Mathematical understanding of the far-field algorithm is now quite sophisticated [121, 122]. In contrast, the question of uniqueness of retrieved phases in the Fresnel regime, first raised by Gerchberg [123] in response to Misell's original suggestion, has only been addressed for special cases [117]. In summary, while the far-field iterative method seems to have come of age thirty years after it was invented, the same cannot yet be said of iterative methods in the Fresnel regime.

## 3.2 CTF deconvolution: overview and review

We have seen that the information deficit may be resolved by methods which limit the bandwidth of the information recorded, or by incorporating a second image. Preprocessing methods which reduce bandwidth require some form of optical intervention between the object and the detector, either an additional reference beam, or manipulation of the wavefield with a Fourier processor. This thesis is concerned with extracting information from a *single* diffraction pattern *without* the use of imaging optics.

If the object is such that its aperture function can be parameterised by a purely real function, then there is not, in theory, an information deficit: both aperture function and diffraction pattern are described by a real image. This raises the possi-

bility of finding a solution to the single-image inverse problem for such a particular parameterisation.

Hitherto the discussion has been in terms of holography and wavefield reconstruction. We are now considering retrieval of a real image which is explicitly *not* the full complex wavefield, and as in the previous two Articles, the retrieval is performed in a computer rather than by physically reconstructing and imaging a wavefield. The problem is better thought of in terms of information retrieval and inverse problems than in terms of holography and wavefield reconstruction. The holographic advantages of great depth-of-field and absence of imaging optics remain pertinent, however.

The simplest parameterisation is a *purely absorbing* object, for which the aperture function is already real. A more useful approximation for many materials is *transparency*: the effect of the object on the wavefield is then parameterised by its phase-shift  $\phi$ .

### 3.2.1 The inverse problem for pure absorption objects

We first consider the case of purely absorbing objects. If the absorption is weak, then the expression for image contrast (2.87) is simply

$$\tilde{C}(\mathbf{u}; z) = -2\tilde{\mu}(\mathbf{u}) \cos(\pi\lambda zu^2), \quad (3.2)$$

which is recognisable as a linear shift-invariant system written in transfer function form. It may be solved trivially for the absorption function  $\mu$  by

$$\mu(\mathbf{x}) = -\frac{1}{2}\mathcal{F}^{-1} \left\{ \frac{1}{\cos(\pi\lambda zu^2)} \mathcal{F}\{C(\mathbf{x}; z)\} \right\}, \quad (3.3)$$

where we have written out the Fourier transform of the image contrast  $C$ , and taken an inverse transform overall. This form of inversion, known as *deconvolution*, obviously applies to *any* linear shift-invariant system, although it is most useful when a closed-form exists for the transfer function. Equation 3.3 may only be considered a formal solution to the inverse problem, as in general the denominator may be zero and direct implementation of (3.3) will produce wildly inaccurate results. Modifying retrieval algorithms to avoid such divergences is known as *regularising the inverse problem*, and is the subject of §3.4 and §3.5.

A regularised retrieval for purely-absorbing weak objects was demonstrated for particle field holography applications [124]. These authors comment on the prob-

lem of phase-shifting by supposedly purely absorbing objects. This problem does not arise if the diffraction object is *binary*: at any point either completely transparent or completely opaque. Binary objects are not weak, however iterative methods have been quite successful in retrieving binary structures at optical [113] and x-ray [125] wavelengths. Recent wavelet [126] and ambiguity function [127] methods allow the location in three dimensions of purely absorbing small particles to be extracted from a single hologram.

The development of nanotip field emitters [128] has revived interest in electron projection microscopy [129] for low radiation damage imaging [130, 131]. Operating at very low electron energies, these microscopes may produce almost pure absorption-object diffraction patterns. To date, the only reports are of simulations of iterative retrieval from electron projection microscopes [132].

### 3.2.2 The inverse problem for pure phase objects

Considerably more work has been done on pure phase objects. Again, the contrast expression (2.87) reduces to a transfer function, this time for the phase-shift through the object

$$\tilde{C}(\mathbf{u}; z) = -2\tilde{\phi}(\mathbf{u}) \sin(\pi \lambda z u^2), \quad (3.4)$$

which can be similarly inverted to

$$\phi(\mathbf{x}) = -\frac{1}{2} \mathcal{F}^{-1} \left\{ \frac{1}{\sin(\pi \lambda z u^2)} \mathcal{F}\{C(\mathbf{x}; z)\} \right\}. \quad (3.5)$$

The sine denominator also is zero at infinitely many discrete points along a radius in the Fourier plane, and so too must be regularised in any numerical implementation.

In transmission electron microscopy, thin biological objects absorb (inelastically scatter) on the order of 10% of incident electrons when shifting phase by 1 radian, and so are phase objects to a reasonably good approximation. Traditional phase imaging techniques such as off-axis holography and Zernike phase-contrast are hard to apply to TEMS; this motivated work on interpreting the phase contrast resulting from defocus and spherical aberration. Electron microscopists experimented with CTF deconvolution almost 20 years before the technique was applied to optical problems. Although in practice the TEM work is quite divorced from the results of this thesis, the formal similarities are substantial. The relevant electron microscopy literature is reviewed in §3.2.4.

Retrieval from free-space diffraction patterns of the form of (3.5) was consid-

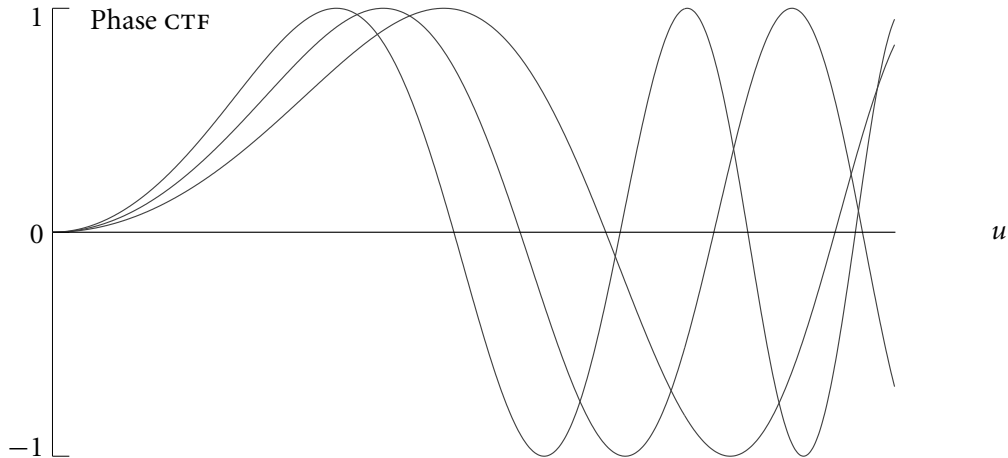


**FIGURE 3.2 Several phase CTFs.** By combining images taken at several difference propagation distances  $z$ , the loss of information at higher spatial frequencies can be avoided. Vanishing contrast at low frequencies remains a problem if objects are assumed to be purely phase-shifting.

ered much later for x-ray microscopy [133]. In this study, diffraction patterns were obtained at several propagation distances from an object assumed to be purely phase-shifting. This appears to be the first publication to point out that in free space, phase *retrieval* is possible from non-weak phase objects satisfying the slowly varying phase condition. Figure 3.2 shows the phase contrast transfer function for three values of  $z$ . Clearly there is contrast information at one propagation distance or another for every spatial frequency shown *except near  $u = 0$* . By appropriately weighting the images in the Fourier representation, these authors formed a composite image which was free of artefacts due to high-frequency zero-crossings in the phase CTF. In the limit of spatial frequency approaching zero, however, contrast vanishes in all of the images and so the retrieval was still unstable at low spatial frequencies [134].

Two of the iterative methods [118, 120] discussed in the previous Section attempted retrieval from an arbitrary pure phase object, without the restriction that the phase object be slowly varying. The fundamental instability of pure phase retrieval at low spatial frequencies is likely to remain a problem in any technique.

### 3.2.3 The inverse problem for monomorphous objects

No object is truly transparent. Many objects are better approximated by the assumption that they are monomorphous. We have seen in §2.2.4 that a thin mono-

morphous object has an aperture function parameterised by the real function  $\rho$ , the column-density. There is hence no information deficit in attempting to retrieve the column-density of a monomorphous object from a single diffraction pattern.

The principal result of Chapter 2 was the linear shift-invariant system (2.94) connecting the column-density of a monomorphous object to the contrast of the diffracted intensity, measured at a subsequent plane after propagation in free space. A formal solution to the inverse problem of retrieving the column-density  $\rho(\mathbf{x})$  is

$$\rho(\mathbf{x}) = \frac{1}{2k} \mathcal{F}^{-1} \left\{ \frac{1}{\delta \sin(\pi\lambda z u^2) - \beta \cos(\pi\lambda z u^2)} \mathcal{F} \left\{ \frac{I(\mathbf{x}; z)}{I_0} - 1 \right\} \right\}, \quad (3.6)$$

where the contrast  $C$  has been written out in terms of the diffraction pattern intensity  $I$  and background intensity  $I_0$ .

Figure 3.3A shows the CTF for a pure phase object in comparison with the CTF for a monomorphous object of  $\beta/\delta = \pm 0.2$ . Part B of the Figure compares the unregularised inverses of the phase-advancing (negative  $\delta$ ) case and the pure phase object case. At higher spatial frequencies the curves are similar, but the divergence at low spatial frequencies is severe.

I now anticipate an intuitive result that will be discussed in much more detail in the Section on regularisation (§3.4):

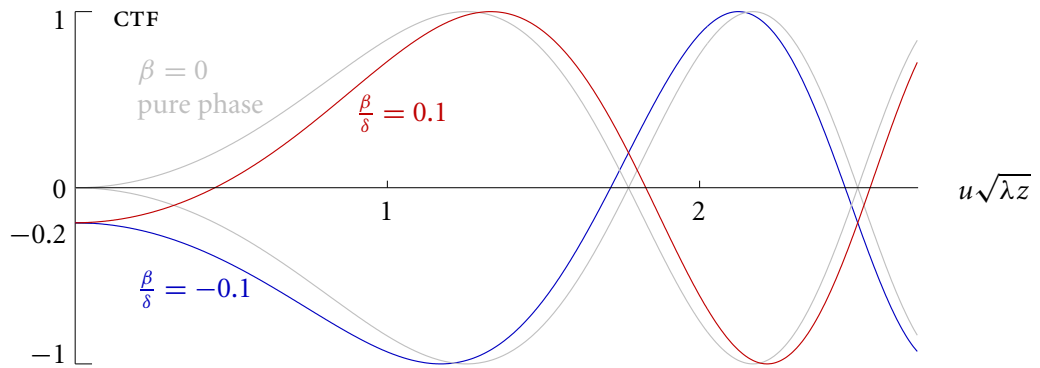
The column-density can be retrieved by multiplying by the inverse of the CTF in Fourier-space. At frequencies where this inverse is greater than the signal-to-noise ratio of the system<sup>4</sup>, we multiply instead by a *regularised* inverse which does not exceed the SNR.

In this example, the monomorphous CTF dictates an amplitude boost of 5 or less at low frequencies. Provided the SNR well above 5 there is no problem in performing the CTF correction at low frequencies. The inverse CTF still diverges at higher frequencies and so regularisation is necessary there. Clearly, the high-frequency regularisation affects only narrow bands of frequencies.

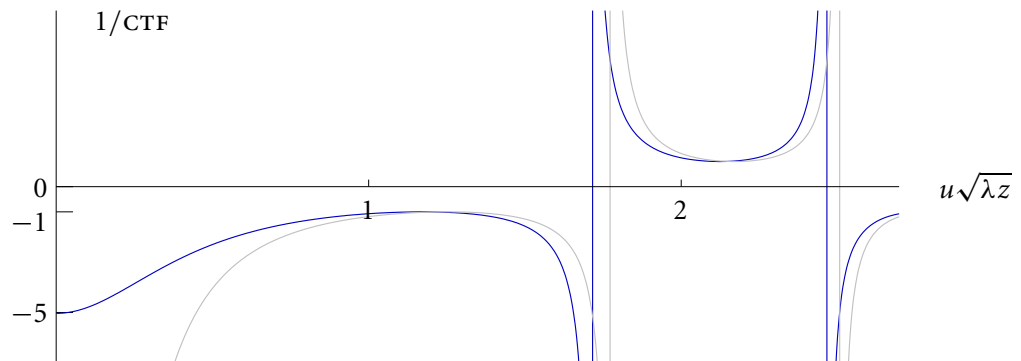
If a pure phase object is assumed, then some arbitrary regularisation procedure must be used to remove the divergence at  $u = 0$ . The retrieved information will be unquantitative for all spatial frequencies below a minimum value. Incorporating knowledge about the residual absorption of a monomorphous object has a profound stabilising effect at low frequencies.

---

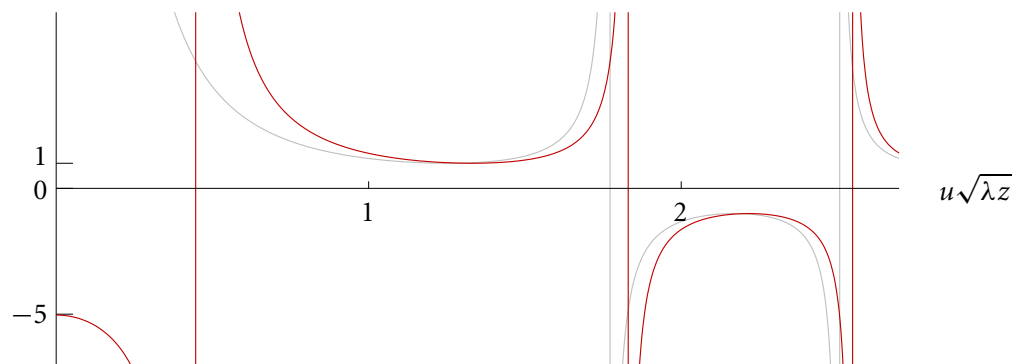
<sup>4</sup> The ‘system’ here is deliberately vague. A rigorous discussion is in §3.4.



A Contrast transfer functions for monomorphous objects with positive (blue) and negative (red) absorption ratios. The CTF for a pure phase object is shown in grey.



B The inverse of the CTF for negative absorption ratio.



C The inverse of the CTF for positive absorption ratio.

FIGURE 3.3 The monomorphous CTF and its inverse. Shown for positive and negative absorption ratio and compared with pure phase CTF.

Similar low frequencies divergences exist for more general methods. The *two* image TIE-based method is valid for any vortex-free wavefield, and so is clearly valid for the field after a weak monomorphous object. Nevertheless, the TIE retrieval algorithm has an analogous divergence at zero spatial frequency, and while it would be expected to yield better results than an erroneous assumption of a pure phase object, it must still be regularised at  $u = 0$  [93, §4.4.5d]. On the other hand, TIE retrieval does not require regularisation at higher frequencies. The catastrophe at zero spatial frequency is thus not limited to pure phase object imaging: it is the Achilles' heel of the TIE-based methods, and similar problems are expected for any *arbitrary wavefield* retrieval system operating on unmodified diffraction patterns. For weakly-absorbing monomorphous objects, CTF deconvolution avoids the catastrophe, and therefore has a fundamental advantage in stability, not only over single-plane pure-phase deconvolution but over two-plane arbitrary-wavefield methods as well.<sup>5</sup>

This optimistic result only applies when the real part  $\delta$  of the refractive index is negative. Figure 3.3C shows that for a phase-retarding (*positive*  $\delta$ ) material, the inverse CTF will exceed the signal-to-noise ratio for a broad range of low frequencies, and so retrieval will be unstable. An intuitive understanding of this contrast null follows from considering the focusing action of a lenticular piece of tinted glass. Glass has positive  $\delta$  and so focuses light towards the centre of the lens. This is where absorption is strongest, however, and so for a certain curvature of the lens, the two effects cancel and there is no contrast. In §5.3.4 I show that using a *negative* propagation distance converts the diffraction pattern of a phase-retarding object into that of the equivalent phase-advancing object. A negative propagation distance sounds absurd. I show in §5.3.4, however, that simple lens system is equivalent to negative propagation if defocused towards the object.

The remainder of this Chapter is predicated on the phase-advance form of CTF shown in Figure 3.3B, namely Equation 2.96 with  $\delta$  negative. While this case is free of contrast nulls at low frequencies, the nulls at high frequencies must still be regularised. Optimal regularisation turns out to be a rather deep problem and is discussed in §3.4 through 3.6.

---

<sup>5</sup> That the presence of absorption in the monomorphous case is formally equivalent to Tikhonov regularisation of TIE solutions was pointed out D Paganin et al., see discussion on p 89.

### 3.2.4 CTF deconvolution in electron microscopy

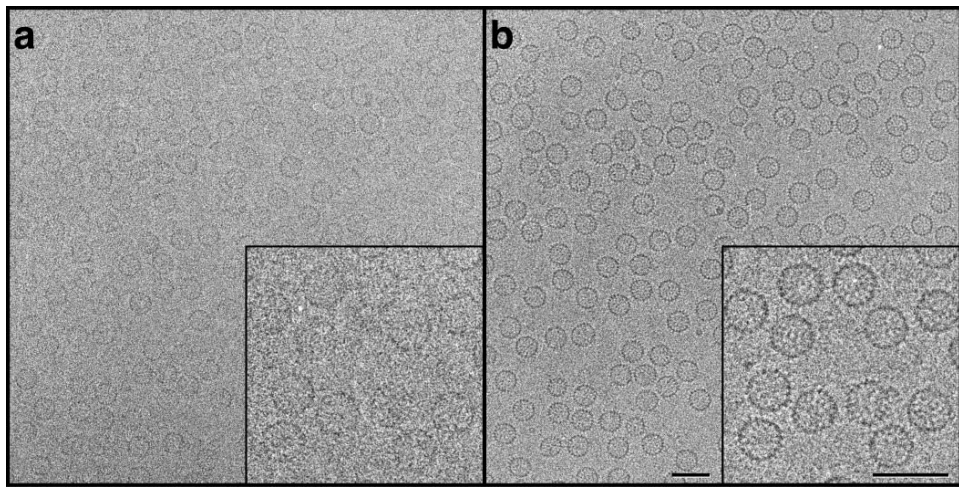
Most of the prior descriptions of phase CTF deconvolution, and *all* previous descriptions of monomorphous CTF deconvolution are for transmission electron micrographs.

Soon after the development of the linear imaging theory of electron microscopes, several authors experimented with processing electron micrographs of thin phase objects using analogs of (3.5) [135]. This work on deconvolution methods for in-line electron holography predicated by 20 years the optical holography deconvolutions described in §3.2.2. A discussion on the connection between contrast transfer theory and holography may be found in §6.4 of Reference 136.

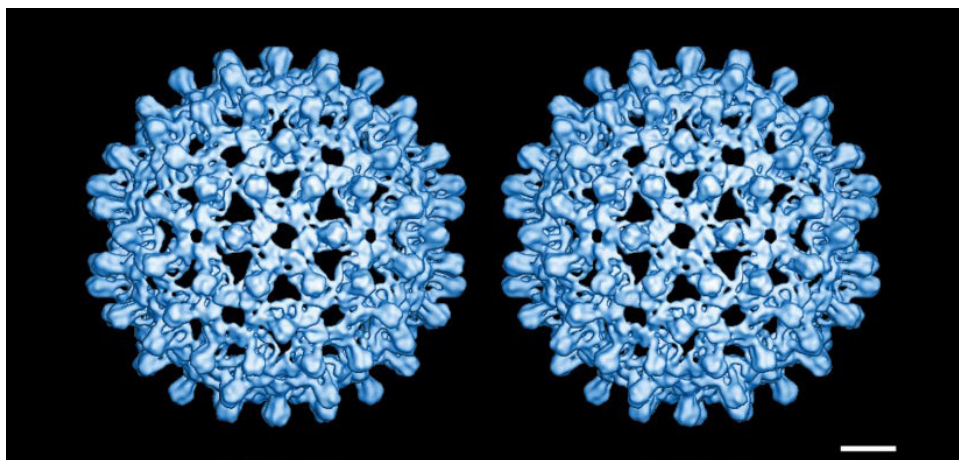
Calculating a Fourier transform of a reasonable sized image took many hours on early 1970s digital computers, and so most of the research effort was directed towards optical computing methods for retrieving phase images [137–140]. The system (3.5) was implemented as a Maréchal optical computer [23, §8.3] by intercalating a complex mask equivalent to  $\sin^{-1} \chi(u; z)$  in the Fourier plane of a 4-f lens system. The attendant description [141, p239] of producing the mask and installing it in the liquid gate of the optical computer makes soothing reading when one is feeling aggravated at a digital computer.

These technical obstacles appear to have been overwhelming. A detailed comparison published after a decade of work on optical and digital retrieval techniques [141, 142] showed similar quality images from both methods, but neither showed compelling enhancement in resolution over the unprocessed image. Exposure times in the TEM are relatively short, and focus is readily varied electronically, so that two or more images of a specimen may easily be obtained. As computing power increased, two image and focal-series [143] retrieval methods were preferred as they avoid the regularisation artefacts of the single image methods. Focal series methods are not limited to weak phase objects – a significant limitation of the linear theory for electron microscopes [144] – nor do they suffer the great sensitivity to focus and spherical aberration parameters [142] of single image retrieval.

Contrast transfer function fell from use, but was revived by the development of energy-filtered *cryoelectron microtomography* in the early 1990s. In this technique, biomolecules are embedded in vitreous ice and imaged at high magnification. Low electron doses reduce damage to the molecules so that resolution approaches that of crystallographic methods, while not requiring crystallisation [146]. The absorption contrast between unstained molecule and ice is, however, very low, and the



A Cryoelectron micrograph showing many randomly-oriented capsids. Scale bars are 50 nm. a: Close to focus. b: Greater defocus, contrast has increased.



B Stereo view of reconstructed capsid with resolution of 0.9 nm. Scale bar is 5 nm.

**FIGURE 3.4 Cryoelectron microtomography of biomolecules.** *Hepatitis B* virus capsids. The technique assembles a large number of noisy images a into a three-dimensional molecular structure b. CTF sign-correction was performed on images synthesised from near and far defocused image pairs. A value of 0.07 was assumed for  $\beta/\delta$  and the defocus  $z$  found by fitting to power spectra. Reprinted from Reference 145.

microscope must be defocused to render phase contrast. Early work assumed a pure phase object and retrieved the column-density – *projected potential* to electron microscopists – from focal series taken at each molecular orientation [147], but the preferred method became monomorphous CTF correction on the reconstructed tomogram [148, 149]. Figure 3.4A shows the enhancement of contrast due to defocus, and Figure 3.4B is a stereogram of the 3D reconstruction of the molecule.

The monomorphous object assumption was not completely new to TEM studies, having been used by Erickson and Klug in 1971 for a pseudo-crystallographic retrieval of the coarse structure of catalase [150].<sup>6</sup> The tomographic reconstruction and deconvolution steps were later combined into a single process in the Fourier representation [152]. While the three-dimensional structures of ribosomes [152], capsids [145] and other biological structures produced by these techniques are undoubtedly impressive, the only published retrieval from a *single* image is the original catalase crystal image of Erickson and Klug.

### 3.2.5 Comparison of CTF deconvolutions: TEM and DCI

These electron microscopy results, and the results of this thesis, are based on CTF deconvolutions of the form of (2.91). There is, however, little in common in the practical application of the techniques. This Article compares CTF deconvolution as applied to TEM with the diffraction-contrast imaging implemented in this thesis.

One major difference was discussed in §2.5.4: the electron microscopy solution must include the effects of spherical aberration and so is valid only for weak-absorption *and weak-phase objects*. The free-space solution is restricted to weak-absorption objects but the phase can be non-weak provided it is slowly varying in the sense of (2.90).

Another fundamental difference between the electron microscope, and optical or x-ray applications is how accurately the CTF parameters  $z$  and  $\beta/\delta$  are known. Although the defocus  $z$  is notionally a controlled parameter in an electron microscope, in practice the calibration is not sufficiently accurate for CTF calculation [145, p108]. The spherical aberration coefficient  $C_s$  is usually known somewhat better, but the absorption ratio  $\beta/\delta$  is now considered by electron microscopists to be a purely empirical parameter. Parameters are deduced from the power spectra of the defocused images [56, 152].

---

<sup>6</sup> In 1982 Klug received the Nobel Prize in Chemistry ‘for his development of crystallographic electron microscopy...’. His Nobel lecture places this work on CTF deconvolution in the context of the structural analysis of biomolecules [151].

TABLE 3.1 CTF deconvolution compared: TEM and free-space DCI.

	TEM	Free-space DCI
Optical process	Defocus + Sph. Ab.	Free-space propagation
Wave abberation $\chi(u, z)$	$\pi\lambda zu^2 - 2\pi\lambda^3 C_s u^4$	$\pi\lambda zu^2$
Absorption	$\mu \ll 1$	$\mu \ll 1$
Phase	Must be weak, $ \phi  \ll 1$	Slowly-varying OK
Coherence	Limited	Typically high
Diffraction pattern	Coherence limited	Holographic possible
Parameters $z, \beta/\delta$	Regressed from image	Measured
Image SNR	Usually very low	Reasonable
Application	Tomographic retrieval	Single-image retrieval
Quantitative?	Returns <i>structure</i>	Returns accurate $\rho$

This process is difficult enough for extracting defocus and  $C_s$  parameters. Extracting the absorption ratio from the low-frequency data is almost impossible. Usually a separate determination of the absorption ratio is required<sup>7</sup> [145]. Typke and Radermacher [153] deliberately enhanced the astigmatism of their microscope to obtain a distribution of CTF nulls more sensitive to the absorption ratio. Their experimentally determined values differed by more than 50% from electron diffraction calculations. The advent of cryo-electron techniques stimulated new attempts to measure  $\beta/\delta$  for frozen-hydrated specimens [149, 152, 154, 155] but results ranged from 0.07 to 0.14. Although CTF parameters are only known to low accuracy, electron tomography is typically an over-determined system and so contrast compensation errors are overwhelmed by the sheer weight of data.

TEM and DCI imaging are also distinguished by the coherence of their illumination. The limited longitudinal coherence of electron sources limits their defocus-contrast to the few-fringe regime.

CTF deconvolution in TEM is essentially an empirical technique. Advanced numerical models are now being used to extract the maximum *structural* information from micrographs [156–158]. The interest is in getting the *shape* of the molecule correct, not in knowing the electron density at every point to high accuracy.

In typical DCI applications, the parameters  $z, \beta$  and  $\delta$  are known to high accuracy. Errors in propagation distance are easily corrected (see §5.4.2). The retrieved column-density provides *quantitative* as well as structural information. Validity conditions are extended. This comparison is summarised in Table 3.1.

<sup>7</sup> Erickson and Klug achieved a fit *only* for  $\beta/\delta$ , and only because they had a very high  $\beta/\delta = -0.35$  due to negative staining.

### 3.3 A TIE solution for monomorphous objects

We have now reviewed the previous work on CTF retrieval, most but not all being by electron microscopy researchers. This Section discusses an alternative solution to the inverse problem for monomorphous objects [159]. The solution is based on the TIE (3.1), rather than on contrast transfer expression, and so is not limited to weakly-absorbing objects. This paper was the first to point out the utility of the monomorphous object assumption in optics and inspired the results of this thesis.

Here I present a novel derivation of this solution starting from Guigay's ambiguity-function marginal applied to a monomorphous object illuminated with collimated illumination.

#### 3.3.1 Derivation from the ambiguity-function marginal

Written down as (2.78), Guigay's ambiguity-functional marginal includes no approximations beyond the Fresnel approximation. In deriving the linear system in §2.5.5, I started from the same equation but proceeded by making a linear approximation to the exponential in (2.88). Instead, consider the refactoring for absorption and phase-shift

$$\begin{aligned} \tilde{I}(\mathbf{u}; z) &= I_0 \int_{-\infty}^{\infty} \exp \left( -k\beta \left( \rho(\mathbf{x} + \lambda z \mathbf{u}/2) + \rho(\mathbf{x} - \lambda z \mathbf{u}/2) \right) \right) \\ &\quad \times \exp \left( ik\delta \left( \rho(\mathbf{x} + \lambda z \mathbf{u}/2) - \rho(\mathbf{x} - \lambda z \mathbf{u}/2) \right) \right) \\ &\quad \times \exp(-2\pi i \mathbf{x} \cdot \mathbf{u}) d\mathbf{x}. \end{aligned} \quad (3.7)$$

This form suggest making a Taylor series approximation for the column-density sum and difference. Expanding

$$\begin{aligned} \rho \left( \mathbf{x} + \frac{\lambda z \mathbf{u}}{2} \right) &= \rho(\mathbf{x}) + \frac{\lambda z \mathbf{u}}{2} \cdot \nabla \rho(\mathbf{x}) + (\lambda z \mathbf{u}/2 \cdot \nabla)^2 \rho(\mathbf{x}) \\ &\quad + \frac{1}{6} (\lambda z \mathbf{u}/2 \cdot \nabla)^3 \rho(\mathbf{x}) + \dots \end{aligned} \quad (3.8)$$

which yields to first order

$$\rho(\mathbf{x} + \lambda z \mathbf{u}/2) + \rho(\mathbf{x} - \lambda z \mathbf{u}/2) \approx 2\rho(\mathbf{x}) \quad (3.9)$$

$$\text{and } \rho(\mathbf{x} + \lambda z \mathbf{u}/2) - \rho(\mathbf{x} - \lambda z \mathbf{u}/2) \approx \lambda z \mathbf{u} \cdot \nabla \rho(\mathbf{x}). \quad (3.10)$$

Recall that phase  $\phi(\mathbf{x}) = k\delta\rho(\mathbf{x})$ , and so if we further assume that  $\lambda z \mathbf{u} \cdot \nabla\phi(\mathbf{x}) \ll 1$  then the second exponential in (3.7) may be expanded to first order yielding

$$\begin{aligned}\tilde{I}(\mathbf{u}; z) &= I_0 \int_{-\infty}^{\infty} \exp(-2k\beta\rho(\mathbf{x})) (1 + ik\delta\lambda z \mathbf{u} \cdot \nabla\rho(\mathbf{x})) \\ &\quad \times \exp(-2\pi i \mathbf{x} \cdot \mathbf{u}) d\mathbf{x}.\end{aligned}\quad (3.11)$$

Making use of the identity

$$\exp(-2k\beta\rho(\mathbf{x})) \nabla\rho(\mathbf{x}) = -\frac{1}{2k\beta} \nabla \left( \exp(-2k\beta\rho(\mathbf{x})) \right) \quad (3.12)$$

and separating the integral yields

$$\begin{aligned}\tilde{I}(\mathbf{u}; z) &= I_0 \int_{-\infty}^{\infty} \exp(-2k\beta\rho(\mathbf{x})) \exp(-2\pi i \mathbf{x} \cdot \mathbf{u}) d\mathbf{x} \\ &\quad - \frac{i}{2\beta} I_0 \delta \lambda z \mathbf{u} \cdot \int_{-\infty}^{\infty} \nabla \left( \exp(-2k\beta\rho(\mathbf{x})) \right) \exp(-2\pi i \mathbf{x} \cdot \mathbf{u}) d\mathbf{x}\end{aligned}\quad (3.13)$$

Now we use the *Fourier derivative theorem* [28, p 124] [24]

$$\mathcal{F}\{\nabla f(\mathbf{x})\} = 2\pi i \mathbf{u} \mathcal{F}\{f(\mathbf{x})\} \quad (3.14)$$

to find

$$\begin{aligned}\tilde{I}(\mathbf{u}; z) &= I_0 \int_{-\infty}^{\infty} \exp(-2k\beta\rho(\mathbf{x})) \exp(-2\pi i \mathbf{x} \cdot \mathbf{u}) d\mathbf{x} \\ &\quad - I_0 \frac{\delta}{\beta} \pi \lambda z u^2 \int_{-\infty}^{\infty} \exp(-2k\beta\rho(\mathbf{x})) \exp(-2\pi i \mathbf{x} \cdot \mathbf{u}) d\mathbf{x}.\end{aligned}\quad (3.15)$$

Recognising that the integrals are Fourier transforms of the absorption function yields

$$\frac{\tilde{I}(\mathbf{u}; z)}{I_0} = \left( 1 - \frac{\delta}{\beta} \pi \lambda z u^2 \right) \mathcal{F}\{\exp(-2k\beta\rho(\mathbf{x}))\}, \quad (3.16)$$

and then re-arranging and taking inverse Fourier transforms as appropriate yields

$$\exp(-2k\beta\rho(\mathbf{x})) = \mathcal{F}^{-1} \left\{ \frac{\beta}{\beta - \delta \pi \lambda z u^2} \frac{\tilde{I}(\mathbf{u}; z)}{I_0} \right\}, \quad (3.17)$$

which is a linear shift-invariant system connecting the measured intensity ratio  $I/I_0$  with the contact image of the object given by  $\exp(-2k\beta\rho(\mathbf{x}))$ . Finally, taking the

logarithm, and writing  $\tilde{I}$  as an explicit Fourier transform results in

$$\rho(\mathbf{x}) = -\frac{1}{2k\beta} \ln \mathcal{F}^{-1} \left\{ \frac{\beta}{\beta - \delta\pi\lambda zu^2} \mathcal{F} \left\{ \frac{I(\mathbf{x}; z)}{I_0} \right\} \right\}, \quad (3.18)$$

which is Equation 23 of Reference 50 modulo the sign convention on  $\delta$ . Note that the original paper, Reference 159, measures spatial frequency ‘ $\mathbf{k}$ ’ =  $\mathbf{u}/2\pi$  in radians per unit length.

### 3.3.2 Comparison with the deconvolution solution

This result resembles a deconvolution, but isn’t due to the presence of the non-linear logarithm function. The solution may be thought of as deconvolving the effects of propagation to find the contact intensity, and then retrieving the column-density from the contact image by the Beer-Lambert law.<sup>8</sup> As the Beer-Lambert law is valid for strongly absorbing objects, it is clear that the TIE solution solution (3.18) is valid for strongly absorbing objects in the limit of small propagation distance, in contrast to the CTF solution which assumes weak absorption. The validity conditions for phase-shift are better analysed from the full TIE, and they appear to be broadly similar to the slowly-varying phase condition (see discussion in attached paper on p 343). We consider the weak-absorption limit of the TIE solution (3.18) to facilitate a comparison with the CTF solution discussed in the previous Article.

The exponential  $\exp(-2k\beta\rho(\mathbf{x}))$  on the left-hand side of (3.18) may be approximated by  $1 - 2k\beta\rho(\mathbf{x})$  if the object is weakly absorbing. A linear relation for column-density

$$\rho(\mathbf{x}) = \frac{1}{2k} \mathcal{F}^{-1} \left\{ \frac{1}{\delta\pi\lambda zu^2 - \beta} \mathcal{F} \left\{ \frac{I(\mathbf{x}; z)}{I_0} - 1 \right\} \right\} \quad (3.19)$$

then follows immediately. A moment’s consideration reveals that this expression may be obtained from the CTF solution (3.6) on the assumption that  $\pi\lambda zu^2 \ll 1$ . Figure 3.5 compares the inverse transfer functions for phase-advancing (negative  $\delta$ ) case of the CTF solution as shown in Figure 3.3B with the weak-absorption case of the TIE method (3.19). It is evident that the transfer functions agree for small  $\lambda zu^2$ , beginning to diverge at spatial frequencies just below the first contrast peak. Both solutions are predicated on the monomorphous object assumption, and both have the inherent low-frequency stability as a result. At higher spatial frequencies,

---

<sup>8</sup> The Beer-Lambert ‘law’ is simply the square-modulus of (2.23). See [13, §5.7.4] for the connection with radiometry.

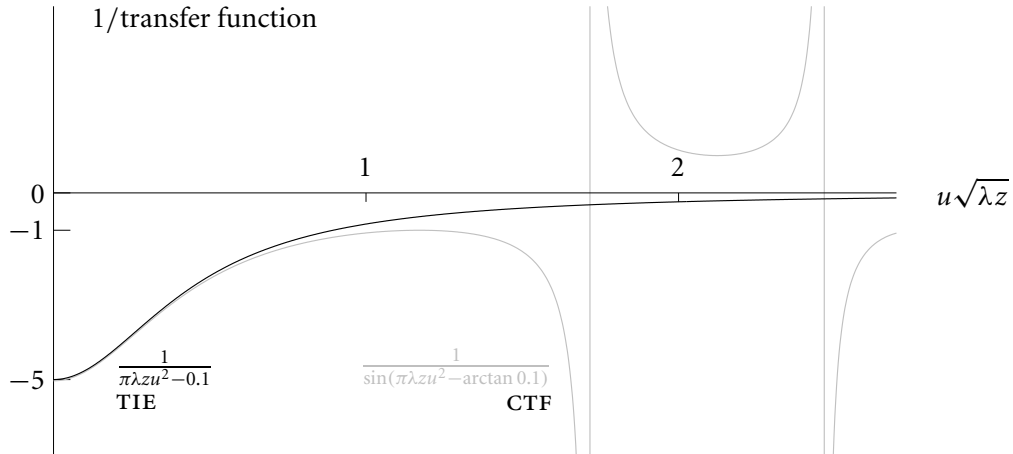


FIGURE 3.5 **Normalised transfer functions for TIE and CTF solutions.** Shown as inverse CTFs for the weak-absorption limit of the TIE solution (3.19) (black) and CTF solution (2.98) (grey). The TIE solution suppresses high-frequency information.

TIE retrieval strongly suppresses information. Consequently regularisation is not required: the TIE retrieval suppresses information where the contrast is reversed.

This unregularised solution comes at a significant price, however. It is clear from Figure 3.5 that for TIE solution to retrieve an unblurred column-density image, the propagation distance  $z$  must be *small* enough that all structure of interest in the object has spatial frequencies  $u$  satisfying  $\pi\lambda zu^2 \ll 1$ . Graphically, this requires that the object power-spectrum be contained within the first peak of the CTF plot. This is also equivalent to requiring only a single diffraction fringe for the smallest details in the object. Real-world objects typically have structure across more than a decade of spatial frequency. If the highest significant frequencies are to fall below the first maximum of the CTF, then the gross structure of the object will be rendered at little more than absorption contrast levels.

Figure 3.6 shows simulated diffraction patterns (left column) and column-densities retrieved with the TIE algorithm (right column). The simulations are for x-ray illumination of a thin metal foil, somewhat implausibly embossed with the *Lena* image. The simulation parameters (see caption) result in a peak absorption of 0.115 and a peak phase-shift of  $-0.6$  radian. This image has a real-world spatial-frequency power spectrum and a mix of detailed and empty areas; reconstruction artefacts are particularly easy to detect when viewing the image and it is widely used in the image processing community [160, 161]. Forward propagation was simulated

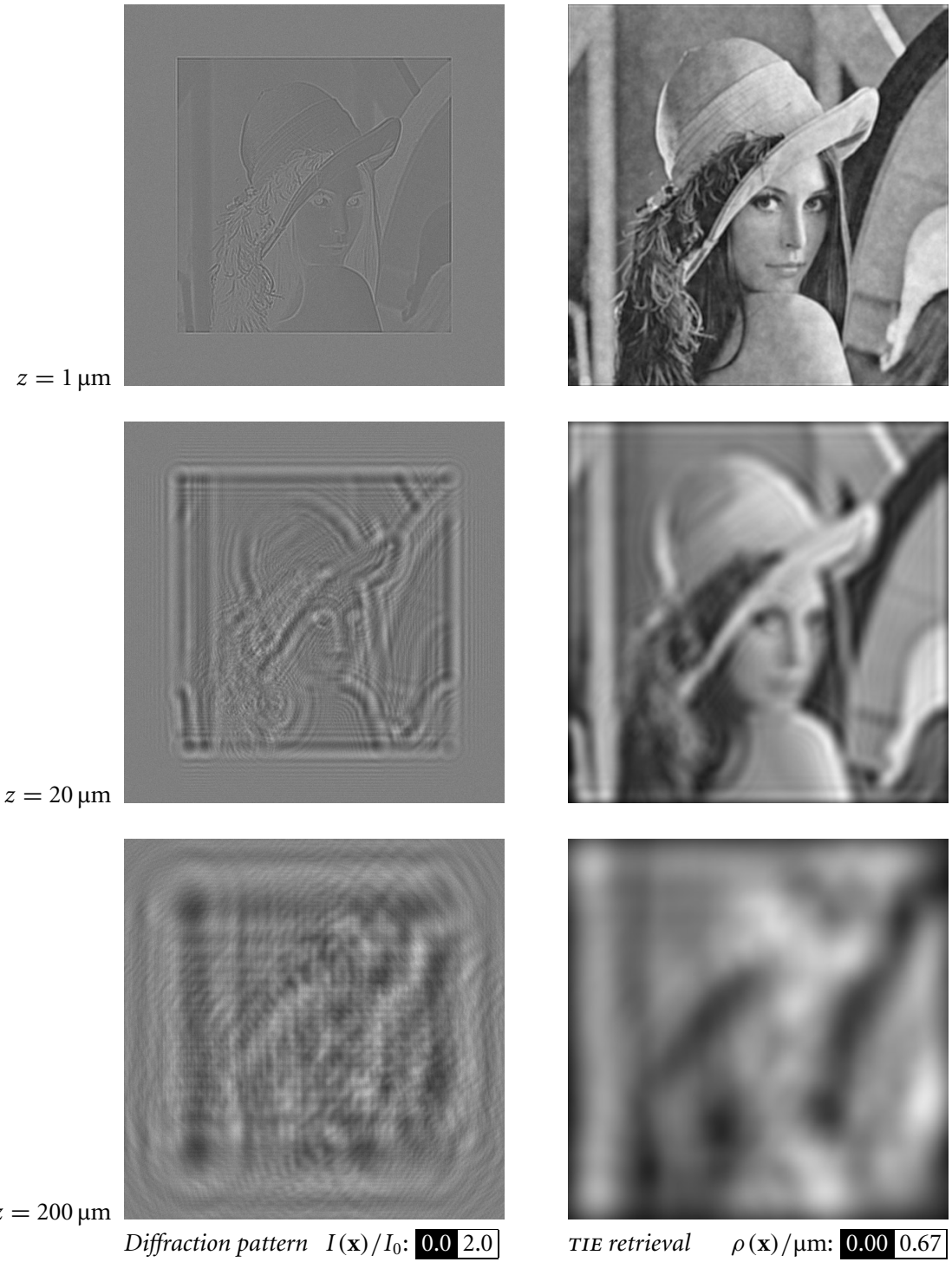


FIGURE 3.6 **TIE retrieval applied to a weakly-absorbing object.** Simulated object is a  $5 \times 5 \mu\text{m}$  Al foil, maximum thickness 670 nm, illuminated with 3 keV x-rays (nominally  $n = 1 - 6 \cdot 10^{-5} + i6 \cdot 10^{-6}$ ). Poisson noise is 1000 photons/pixel.

---

with the angular spectrum algorithm ([§2.3.2](#)).

The near-Fresnel image at top has most of the image spectrum below the first CTF maximum, and the diffraction pattern shows only edge-enhancement. The TIE-retrieved column-density is relatively sharp, but shows coarse noise as much of the coarse structure was retrieved from absorption contrast. The lower two diffraction patterns are more heavily diffracted and the retrievals are blurred.

Section [3.8](#) shows that the fidelity of the retrieved image is optimal at *large* propagation distances where there are many contrast reversals within the spectral support of the object. The single-fringe regime is thus far from optimal for imaging most weakly-absorbing objects. It must be said, however, that the TIE algorithm fails gracefully when applied to images with contrast beyond the first CTF maximum. The rapid but smooth roll-off of the TIE filter blurs detail at higher frequencies, but adds little ringing to images.

The TIE algorithm is generally valid for strongly-absorbing monomorphous objects at short propagation distances and is, in a sense, complementary to the CTF solution which is valid for weakly-absorbing objects at arbitrary propagation distances.

### 3.3.3 Hybrid and iterative solutions for monomorphous objects

In light of the complementarity of the TIE and CTF solutions, it is natural to ask if a more general solution may be found that reduces to the TIE solution in the limit of short propagation distance, and to the CTF solution in the limit of weak-absorption.

At the workshop on phase retrieval held in Cairns in July 2003<sup>9</sup>, T E Gureyev discussed a two-step algorithm which combined TIE-based retrieval with the CTF-deconvolution method [\[10\]](#). In simulations, a low frequency object structure was retrieved with TIE-based methods and a synthetic diffraction pattern formed from the difference between the ‘measured’ diffraction pattern and a calculated diffraction pattern due to the TIE-retrieved object. This weak-contrast synthetic pattern contained only high frequency information and so was amenable to processing with CTF deconvolution methods. Results of simulations were presented for strong phase objects. A subsequent paper published after this Chapter was written extends the idea to an iterative method involving an asymptotic series for the aperture function [\[162\]](#).

---

<sup>9</sup> The priority of these results is discussed in the Preface.

This paper, and a subsequent paper presenting experimental results [163], err in stating that the direct CTF deconvolution (which it refers to as the *Born solution*) is valid only for weak phase-shifts. Reconstruction artefacts were attributed to non-weak phase-shifts, but the artefacts appear to be due to regularisation. It would be very interesting to compare the suppression of these artefacts by their iterative technique with the artefact-suppression afforded by the wavelet methods discussed in §3.6 of this Chapter. Both basic CTF deconvolution, and the iterative extension of Gureyev et al. failed to retrieve information from a heavily-diffracted pattern of a strongly phase-shifting and strongly absorbing ( $\phi = -10$  radian,  $\mu = -2$ ) object.

Finally, recall that we saw in §3.2.3 that the assumption of monomorphicity solves the problem of vanishing diffraction phase-contrast at low frequencies which affects both pure-phase and arbitrary-wavefield retrieval algorithms. It is likely that such low-frequency instability also affects iterative algorithms. Although assuming a monomorphous object is a non-convex constraint, it would be most interesting to attempt an interactive retrieval where the phase is corrected by the log-amplitude in the object plane. In this manner, the gross structure of the object might be defined on the first iteration and convergence achieved as iteration corrects progressively higher spatial frequencies. An iterative method would be free of assumptions of slowly-varying phase and need not even assume paraxiality as unapproximated angular spectrum forward- and back-propagation may be employed.

We will see in Chapter 5 that the problem of imaging cold atoms demands *weak* absorption. In this case the SNR of TIE retrievals is much lower than CTF retrievals. Further, the ability to work at arbitrary propagation distances is a great practical advantage. CTF retrieval is a much better fit for cold atom imaging. We now turn our attention to the question of regularising the CTF solution.

### 3.4 Fourier deconvolution of the inverse problem

In *Methods of Mathematical Physics*, Courant and Hilbert wrote [164, p 227]:

Data in nature cannot possibly be conceived as rigidly fixed; the mere process of measuring them involves small errors. Therefore a mathematical problem cannot be considered as realistically corresponding to physical phenomena unless a variation of the given data in a sufficiently small range leads to an arbitrarily small change in the solution.

Even in the absence of noise, it is clear that any implementation of (3.6) fails this fundamental requirement that physical systems depend *continuously* on their inputs [165, 166, §6.1]. Regularisation is the search for a compromise between the stability and accuracy of a solution to an inverse problem.

This Section discusses the optimal *linear* solution to the inverse problem, known as the *Wiener filter*. The Wiener filter assumes prior knowledge of the *spectrum* of the column-density, which is usually not available. I derive an alternative *partial-Tikhonov* filter which assumes only a power-law form for the spectrum. The Wiener filter also assumes the statistical stationarity of the spectrum. Obviating this assumption is a harder problem and takes us beyond the familiar Fourier basis to wavelet bases; this extension is considered in the following Section.

### 3.4.1 The Wiener filter

We may explicitly introduce additive noise  $n$  to the forward problem (2.96) in convolution

$$C_{\text{meas}}(\mathbf{x}) = h(\mathbf{x}) * \rho(\mathbf{x}) + n(\mathbf{x}) \quad (3.20)$$

or transfer-function representations

$$\tilde{C}_{\text{meas}}(\mathbf{u}) = \tilde{h}(\mathbf{u})\tilde{\rho}(\mathbf{u}) + \tilde{n}(\mathbf{u}). \quad (3.21)$$

We are seeking the best possible retrieval *at a given propagation distance*, so we have dropped the explicit  $z$  dependence. The naive estimate  $\rho_{\text{est}}$  of the column-density is then

$$\tilde{\rho}_{\text{est}}(\mathbf{u}) = \tilde{h}^{-1}(\mathbf{u})\tilde{C}_{\text{meas}}(\mathbf{u}) = \tilde{\rho}(\mathbf{u}) + \tilde{h}^{-1}(\mathbf{u})\tilde{n}(\mathbf{u}), \quad (3.22)$$

and consists of the signal  $\tilde{\rho}$  which we wish to recover plus coloured noise  $\tilde{h}^{-1}\tilde{n}$ . It is clearly unstable at spatial frequencies where  $\tilde{h} \approx 0$ . The inverse problem is to recover an estimate of the column-density  $\rho_{\text{est}}$  which is as close as possible to the actual column-density  $\rho$ . We may quantify how close by the *mean square error*

$$\text{MSE} = \|\rho_{\text{est}}(\mathbf{x}) - \rho(\mathbf{x})\|^2 = \|\tilde{\rho}_{\text{est}}(\mathbf{u}) - \tilde{\rho}(\mathbf{u})\|^2, \quad (3.23)$$

by Parseval's Theorem identical in the spatial and Fourier representations. The  $L^2$ -norm  $\|\cdot\|$  was defined on p 34. It may be shown [165] that the solution which

mimimises the MSE is the *Wiener filter*<sup>10</sup>

$$\tilde{\rho}_{\text{est}}(\mathbf{u}) = \underbrace{\frac{\tilde{h}(\mathbf{u})}{|\tilde{h}(\mathbf{u})|^2 + \frac{|\tilde{n}(\mathbf{u})|^2}{|\rho(\mathbf{u})|^2}}}_{\text{Wiener filter}} \tilde{C}_{\text{meas}}(\mathbf{u}). \quad (3.24)$$

The general operation of the filter is clear: at frequencies where the SNR is high it closely approximates the simple inverse filter, but when the SNR tends to zero so too does the response of the Wiener filter, and it makes no attempt to retrieve information at these frequencies.

We can already see a significant problem with implementing the Wiener filter: we must know a priori the noise power spectrum  $|\tilde{n}|^2$  and the *original* signal power spectrum  $|\tilde{\rho}|^2$ . While the noise is usually estimable from a region of the image away from the object, obtaining the spectrum of the signal is rather more difficult: the spectrum is typically obtained from the signal, and the original signal is what we are trying to estimate with the Wiener filter in the first place! In addition, one must assume in deriving the Wiener filter that both the signal  $\rho$  and noise  $n$  are uncorrelated and also *wide-sense stationary*; their power spectra do not vary across the image. That noise is uncorrelated and stationary may reasonably be assumed for many systems, and is true of Poisson noise on a weak-contrast image.<sup>11</sup> Stationarity is *not* a reasonable assumption for many real-world images, which tend to have fairly homogeneous regions separated by distinct edges. The power spectrum within a homogeneous region will typically be quite different to that of a region containing an edge.

These manifest limitations of the theoretically-optimal Wiener filter have created a very sizable literature, under the moniker *digital image restoration*, describing improved algorithms for solving deconvolution problems of the form of (3.20). Reference 166 is a 1997 review of the field, although it predates much important work in the wavelet field discussed later in this Chapter. The subject draws heavily on the applied mathematical fields of inverse-problem theory and estimation theory, although the purview of these fields is much broader than convolution operators and includes more general linear and non-linear operators, and mappings between spaces of other than two dimensions [168].

Our deconvolution problem is quite vanilla by current digital image restoration

<sup>10</sup> The time-domain equivalent was derived by Norbert Wiener in 1942 for applications in anti-aircraft artillery tracking, but was not published in the open literature until 1949 [167].

<sup>11</sup> See §3.5.2 and §5.7.2 for discussions of the nature of noise in the imaging process.

standards: the ‘blur operator’  $h$ , which we call a contrast transfer function, is well characterised and noise is essentially additive, stationary and readily measurable. The only peculiarity is that unlike the blur operators typically considered in the literature, the contrast transfer function is not, in general, a low-pass filter. Of course, the physical interpretation of the convolution process is very different: our system relates column-density and contrast, two distinct physical quantities, while imaging systems relate intensity at one plane to intensity at another. This distinction is irrelevant to the mathematical problem; Figure 3.7 compares the form of spatial and Fourier representations of three standard blur operators with the monomorphous CTF. Both linear-motion and defocus blurring have multiple zero crossings in the Fourier representation. A solution suited to these incoherent image blurs is worth considering for CTF deconvolution.

### 3.4.2 Simple Tikhonov regularisation

The Wiener filter resulted from minimising the mean-square error  $\|\tilde{\rho}_{\text{est}} - \tilde{\rho}\|^2$ . It should be no surprise that this yielded a filter requiring both restrictive assumptions about the stochastic properties of  $\rho$ , and detailed knowledge of those properties. An actually implementable filter may be found by *admitting our ignorance* of the original signal  $\rho$ . Rather than the MSE, consider instead the error

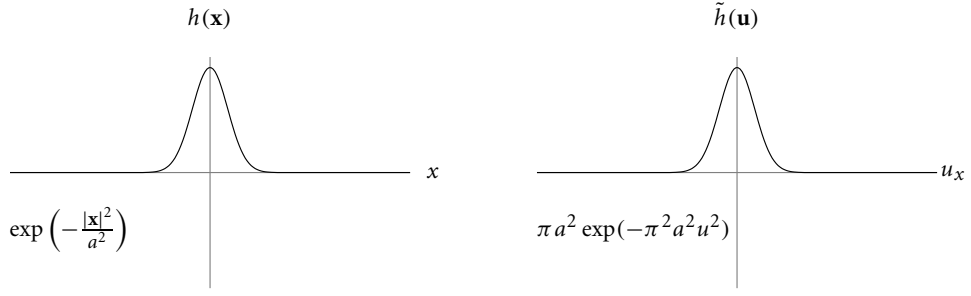
$$\|\tilde{C}_{\text{meas}} - \tilde{h}\tilde{\rho}_{\text{est}}\|, \quad (3.25)$$

which does *not* require knowledge of  $\rho$ , and simply seeks to minimise the residual between the observed contrast  $\tilde{C}_{\text{meas}}$  and the calculated contrast  $\tilde{h}\tilde{\rho}_{\text{est}}$  due to the estimated column-density  $\tilde{\rho}_{\text{est}}$ . Unfortunately, taking partial derivatives and finding the minimum takes us straight back to the naive inverse of (3.22).

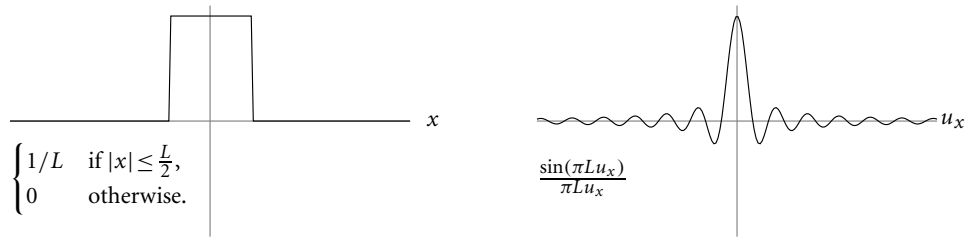
We have come up against the problem of *uniqueness*: we can take a very large sinusoid at a frequency where  $\tilde{h} = 0$ , add it to  $\tilde{\rho}_{\text{est}}$ , and it will not change the error (3.25). To distinguish amongst all the possible signals which yield the observed diffraction pattern, we must place some constraint on possible values of the signal. The Wiener filter used the very tight constraint of completely specifying the signal power-spectrum. Instead, we minimise the noise-aware error

$$\|\tilde{C}_{\text{meas}} - \tilde{h}\tilde{\rho}_{\text{est}}\| - \|\tilde{n}\| \quad (3.26)$$

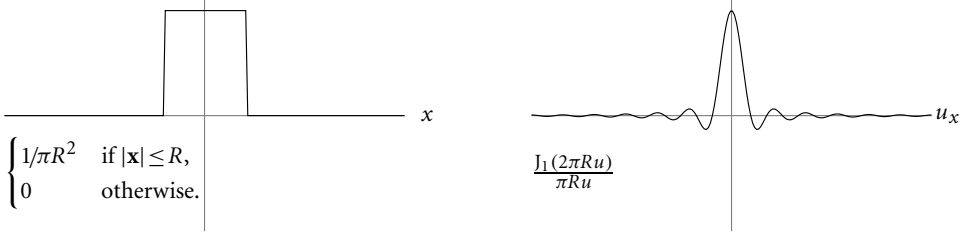
subject to the much weaker constraint that the signal norm  $\|\tilde{\rho}_{\text{est}}\|$  be as small as



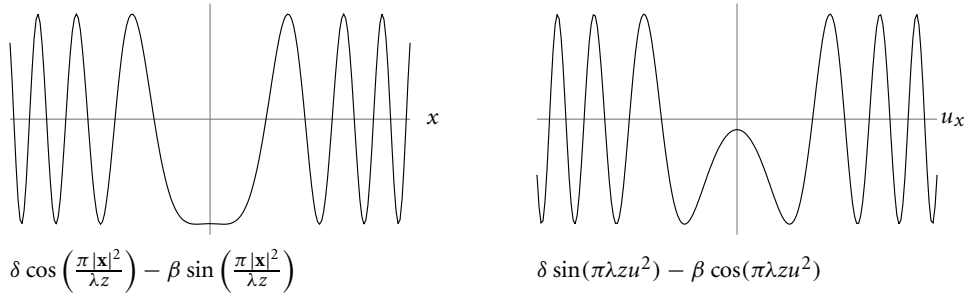
A Gaussian blur: has been used to model atmospheric turbulence.



B Linear motion blur: for an object traveling distance  $L$  along the  $x$  axis during an exposure.



C Defocus of lens with circular aperture: geometric optics limit of PSF is a disc. See also [169, 170].



D Diffracted contrast from monomorphous column-density,  $\beta/\delta = -0.1$ .

**FIGURE 3.7 Incoherent imaging compared to CTFs.** Three blurs used in image restoration for *incoherent* imaging systems, compared to our LSI system in d. Left column shows convolution kernel (point-spread function, PSF) and right column shows transfer function.

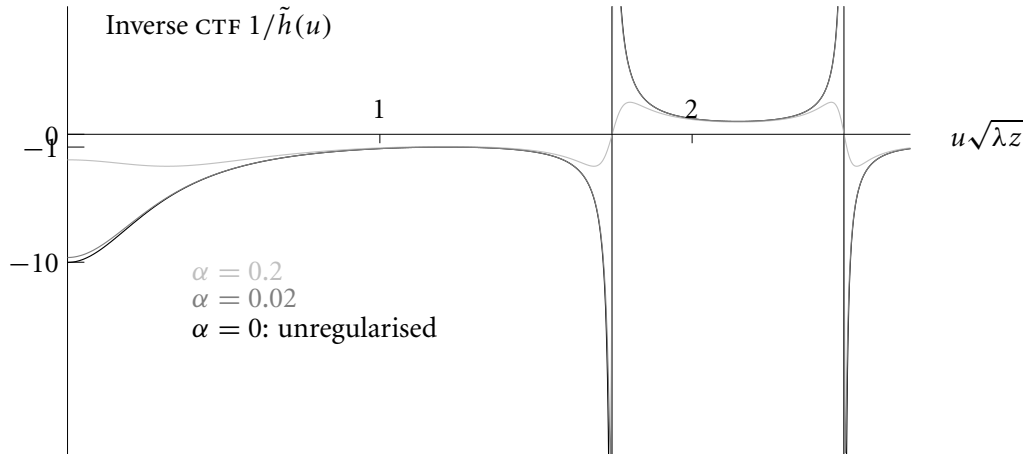


FIGURE 3.8 Simple-Tikhonov regularisation for small and large  $\alpha$ . Deconvolution filters (inverse CTFs) before regularisation (black) and after simple-Tikhonov regularisation for two values of  $\alpha$ . The absorption ratio was  $\beta/\delta = -0.1$ .

possible. Solving with the Lagrange multiplier  $1/\alpha$  yields the *method of Tikhonov regularisation*:<sup>12</sup>

$$\tilde{\rho}_{\text{est}}(\mathbf{u}) = \underbrace{\frac{\tilde{h}(\mathbf{u})}{|\tilde{h}(\mathbf{u})|^2 + \alpha^2}}_{\text{Tikhonov filter}} \tilde{C}_{\text{meas}}(\mathbf{u}). \quad (3.27)$$

This Tikhonov filter is a special case of the Wiener filter (3.24) when the signal-to-noise ratio does not vary with frequency ( $\text{SNR} = 1/\alpha$ ). The above derivation, however, emphasises the critical importance of prior information in solving ill-posed inverse problems. The error functional (3.26) measures agreement of the estimate with observation, while the constraint ensures the uniqueness and stability of the estimate by incorporating prior information or assumptions about the signal. Balancing the fidelity and stability of the retrieved signal is our goal.

Figure 3.8 compares unregularised and regularised forms of our example deconvolution filter for the somewhat arbitrary values of  $\alpha$  values of 0.2 and 0.02. In this and subsequent plots it is convenient to work with the *normalised CTF*  $\sin(\pi\lambda zu^2 - \arctan \beta/\delta)$ . Doing so doesn't change the analysis, it is simply equivalent to working with the dimensionless column-density  $2k\sqrt{\beta^2 + \delta^2}\rho(\mathbf{x})$  rather

<sup>12</sup> Also known as Phillips-Twomey, Miller and pseudo-inverse regularisation. Tikhonov's result [171, 172] applies *very* generally; essentially anywhere a norm is defined ie. any mapping between Banach spaces [173]. Chapter 18 of Reference 174 presents a readable summary is [174, Ch 18]. Note that the 'Wiener' filter in Ch 13 of this reference is not.

than  $\rho(\mathbf{x})$ .

It is clear that the Tikhonov filter mostly does what we want it to, tracking the simple inverse filter where contrast is high and departing only where the contrast falls to near the noise floor. Where the contrast vanishes, the filter makes no attempt to include non-existent information. And it does all this *smoothly*, satisfying the continuity requirement of Courant and Hilbert.

At higher frequencies, the regularised filter differs necessarily from the unregularised filter only in relatively narrow regions around the contrast nulls. Observe, however, that the  $\alpha = 0.2$  filter diverges from the unregularised filter at frequencies below the first contrast maximum and the divergence increases all the way to zero spatial frequency. This behaviour is unsurprising given that our example filter has a residual absorption contrast of 0.1, below the noise-floor assumed by  $\alpha = 0.2$ .

A simulated experiment exposes the limitations of simple Tikhonov regularisation. Figure 3.9A shows the column-density distribution *Spheres* used to calculate the aperture function. The plane-wave illuminated diffraction pattern 20  $\mu\text{m}$  after the object is shown in Figure 3.9B. The simulation approximates a 3 keV x-ray point-projection microscope image of micron-sized aluminium<sup>13</sup> spheroids, including a larger spheroid with spheroidal voids inside it. Maximum contact absorption was 8.5% and phase-shift  $-0.45$  radian. Poisson noise was included, equivalent to a mean exposure of 10 000 photons/pixel. Note that in this, and other images in thesis, the scale is indicated by a contrasting scale bar on the left-hand side. The scale-bar also indicates the position of a horizontal *lineout* which is plotted below. The scale bar is marked on the plot ordinate, while the plot abscissa corresponds to the grey range in the image: the bottom of the abscissa is black in the image and the top is white.

Figure 3.9C and D show column-density images retrieved from Figure 3.9B using the simple Tikhonov filters plotted in Figure 3.8. As we might expect, the more heavily regularised image C has lower noise and hence structures are more clearly visible, especially the detail within the large object. The lower noise has come at the price of significant image artefacts, manifest as dark fringes around the large object and in the vicinity of the regular array of spheres. Linescans show that the dark fringes correspond to regions of *negative* column-density, a clearly unphysical result. The artefacts are associated only with large-scale structures in the image and are absent in image D, lending support to the hypothesis that they arise from the

---

<sup>13</sup> At 3 keV, aluminium has  $\beta/\delta = -0.115$  [175]. The value  $\beta/\delta = -0.1$  was used in the simulation.

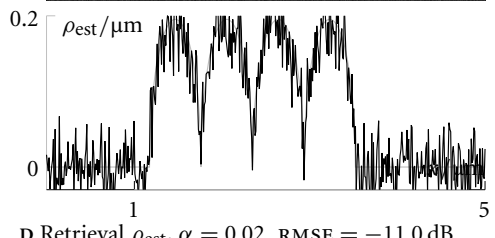
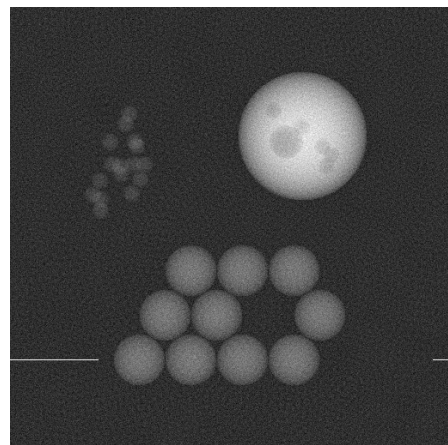
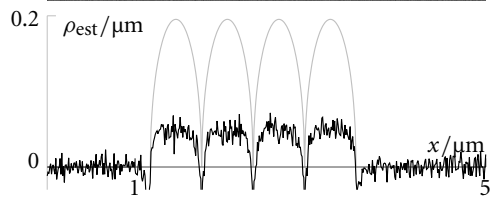
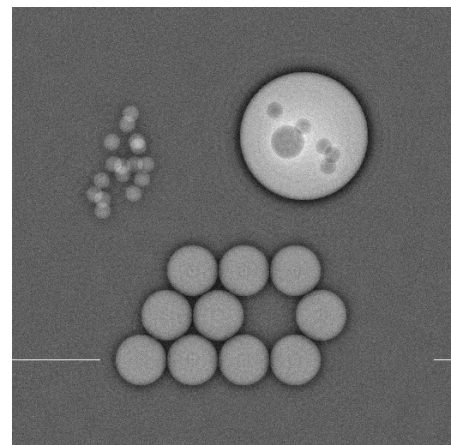
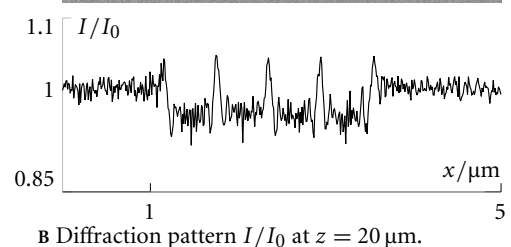
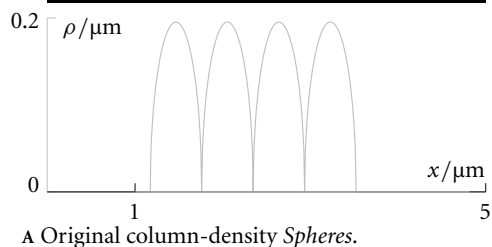
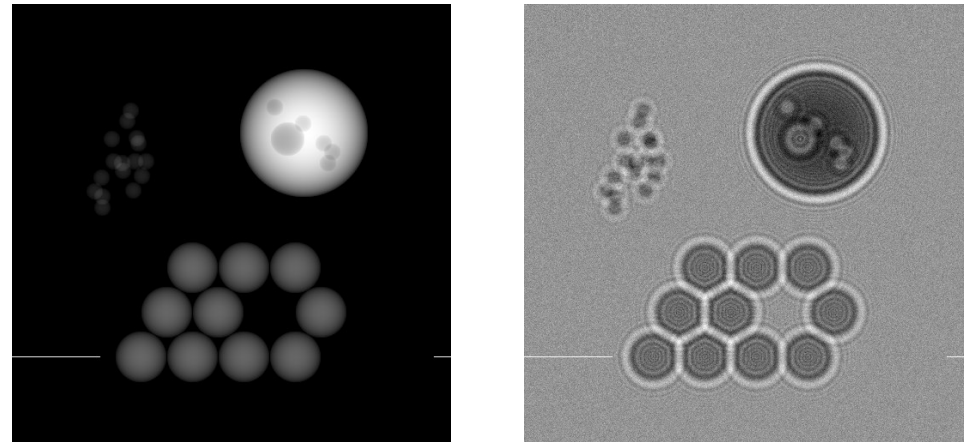


**FIGURE 3.9 Distortion and noise in Tikhonov retrievals.** Standard Tikhonov regularisation yields distorted (c) or noisy (d) retrievals. Actual column-density shown in plots in grey. See text for simulation parameters.

over-regularisation at low frequencies mentioned above.<sup>14</sup>

A degree of quantitativity may be introduced by comparing the *relative mean-square error*

$$\text{RMSE} = 10 \log_{10} \left( \frac{\|\rho_{\text{est}}(\mathbf{x}) - \rho(\mathbf{x})\|^2}{\|\rho(\mathbf{x})\|^2} \right) \quad (3.28)$$

which is simply the MSE normalised to the mean-square of the actual signal.<sup>15</sup> A failed estimate of zero, or of zero-mean noise, yields an RMSE of 0 dB. A uniform error of 1% of signal yields an RMSE of  $-40$  dB.

The trade-off between signal distortion and noise amplification may be expressed analytically by writing out the Tikhonov filter (3.27) in terms of the original signal  $\rho$  and coloured noise  $h^{-1}n$  (see (3.22)):

$$\tilde{\rho}_{\text{est}}(\mathbf{u}) = \underbrace{\frac{|\tilde{h}(\mathbf{u})|^2}{|\tilde{h}(\mathbf{u})|^2 + \alpha^2} \tilde{\rho}(\mathbf{u})}_{\text{Distorted signal}} + \underbrace{\frac{\tilde{h}(\mathbf{u})}{|\tilde{h}(\mathbf{u})|^2 + \alpha^2} \tilde{n}(\mathbf{u})}_{\text{Retained coloured noise}}. \quad (3.29)$$

It is clear that small values of  $\alpha$  lead to low distortion of the signal but large values of  $\alpha$  better suppress the noise. Our example indicated, however, that no value of  $\alpha$  yielded both low distortion *and* low noise. We will see in the next Article that this failure occurs because the simple-Tikhonov assumption of constant SNR is poorly suited to our particular deconvolution problem.

### 3.4.3 Partial Tikhonov regularisation

At this juncture, we ‘cheat’ and examine the spectrum of the input to our simulation, shown as the black trace in Figure 3.10. As for many images, the spectrum of the example behaves broadly as a power-law. Convolution with the CTF is manifest as the contrast curve (grey) falls below the column-density at low frequency, and in sharp contrast nulls at higher frequencies. Spectrally white Poisson noise is manifest where the contrast curve sinks into the noise floor after the first few contrast reversals. It is immediately apparent why simple Tikhonov regularisation is not very successful: the signal-to-noise ratio is by no means constant, indeed a power-law signal varies at the same logarithmic rate at all spatial scales and so is no more constant at low frequencies than at high frequencies.

<sup>14</sup> These artefacts are rendered more clearly by simulating retrievals of the simple image *Spheres* instead of the more detailed image *Lena* used elsewhere in this Chapter.

<sup>15</sup> This metric seems more appropriate than the **BSNR** and **ISNR** metrics commonly used in image restoration [166]. The non-logarithmic equivalent is used by Mallat [49, eg p 401].

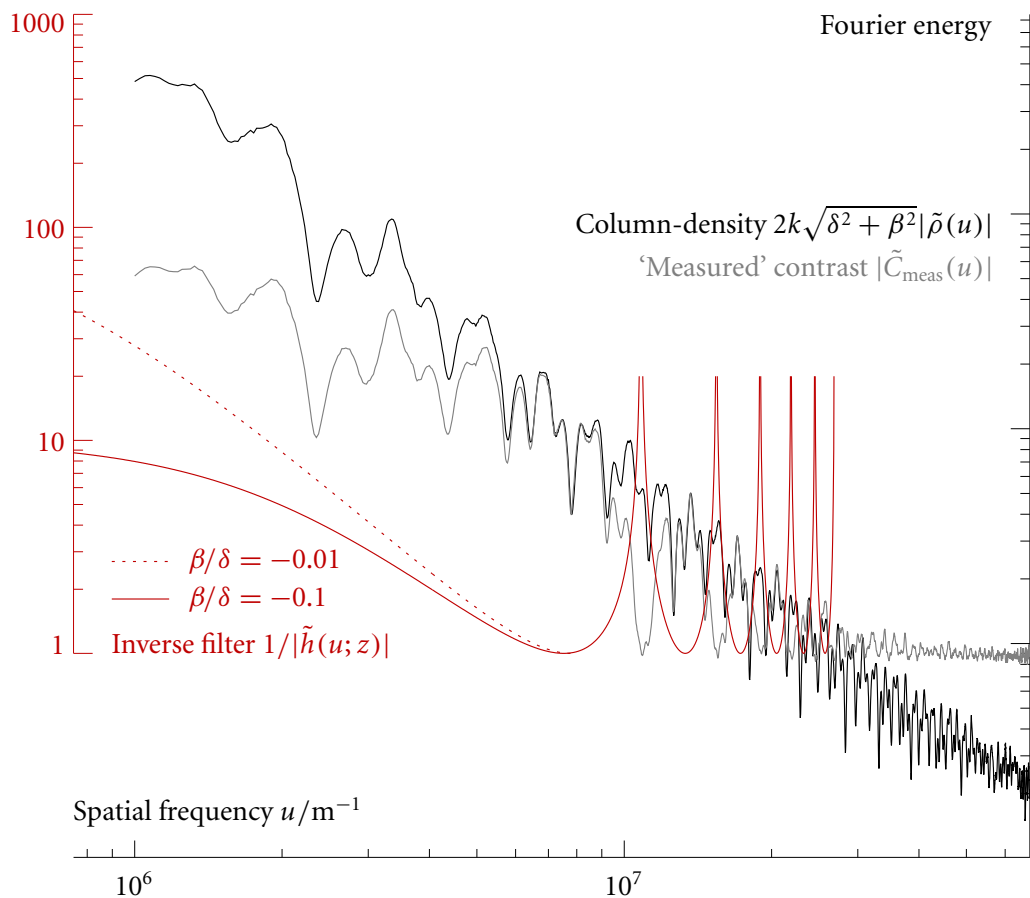


FIGURE 3.10 **Comparison of spectra: column-density, noise and inverse filter.** Azimuthally-averaged amplitude spectra are shown, with the column-density spectrum normalised for comparison with the dimensionless contrast. The contrast spectrum  $\tilde{C}_{\text{meas}} = \tilde{h}\tilde{\rho} + \tilde{n}$  includes simulated white noise. The inverse filter is positioned with  $\tilde{h} = 1$  coinciding with the mean noise level so that the red trace also represents the mean level of the coloured noise  $\tilde{h}^{-1}\tilde{n}$ .

The red trace on Figure 3.10 is the amplitude of the unregularised inverse filter  $1/\tilde{h}$ . The axes have been positioned so that  $\tilde{h} = 1$  coincides with the noise floor and the SNR  $\tilde{\rho}/\tilde{n}$  may be compared directly to the inverse filter. In the vicinity of the first contrast null, around  $u = 10^7 \text{ m}^{-1}$ , the SNR is of order 5, suggesting that *there* the choice of  $\alpha = 0.2$  is appropriate. It is clear from (3.24) that when the signal-to-noise ratio is significantly higher than the value of the inverse filter, the Wiener estimate is very close to the inverse filter value. This is the case for all frequencies below the first contrast peak: while the inverse filter increases through this range, it is outpaced by the object spectrum. The conclusion is that, at least for this form of

object spectrum, there is *no need for regularisation* for  $u$  less than  $u_{\min} = (2\lambda z)^{-1/2}$ .

On the other hand, by the third contrast null the SNR has fallen to 2. Maintaining a constant  $\alpha$  of 0.2 through this region yields less distortion of the signal, and greater amplification of noise than if an oracular Wiener filter had been employed.<sup>16</sup> The nett result is a higher mean-square error than the Wiener optimum, however there are two reasons why this may be desirable. Firstly, human vision is a decidedly non-linear system rather more tolerant of noise and less tolerant of blurred edges than the linear optimum. Secondly, the hybrid Fourier-wavelet regularisation described in the next Section is more adept at removing narrowband noise than it is at undoing signal distortion, and so benefits from an under-regularised Tikhonov filter in its initial Fourier-domain stage.

Our consideration of the column-density spectrum has lead to a *partial Tikhonov filter*

$$\tilde{g}_{\text{pTik}}(\mathbf{u}; z, \alpha) = \begin{cases} \frac{1}{\tilde{h}(\mathbf{u})} & \text{if } u < \frac{1}{\sqrt{2\lambda z}}, \\ \frac{\tilde{h}(\mathbf{u})}{|\tilde{h}(\mathbf{u})|^2 + \alpha^2} & \text{otherwise,} \end{cases} \quad (3.30)$$

which is a simple inverse filter at low frequencies, and a Tikhonov filter for most of the detail in the image. This piecewise definition does not lead to significant discontinuities in the filter however, as the step from zero to finite  $\alpha$  occurs at the first contrast maximum where the effect of regularisation is least.

Figure 3.11 compares this partial-Tikhonov filter with  $\alpha = 0.2$  to the Wiener filter designed by an oracle knowing the column-density spectrum. Crucially, the curves overlap to better than the plotting resolution at low frequencies, and the first two contrast nulls are well-fitted. At higher frequencies, the partial-Tikhonov filter is somewhat more zealous than the Wiener filter in attempting to retrieve information as the SNR decreases. Figure 3.12 compares column-densities retrieved with an oracular Wiener filter with the partial-Tikhonov approximation. The retrieved images are essentially identical, although the lower RMSE of the Wiener retrieval is statistically significant, if barely perceptible in the image. The noise level is much lower than the under-regularised image of Figure 3.9B, but without the artefacts of Figure 3.9A.

---

<sup>16</sup> That is, a Wiener filter equipped with an oracle informing it of the noise-less and undistorted power spectrum of the signal.

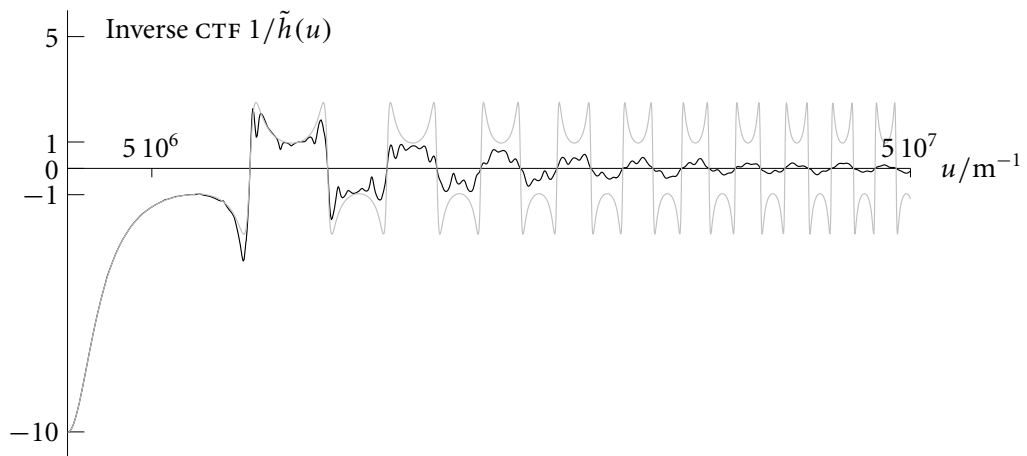


FIGURE 3.11 **Wiener and partial-Tikhonov filters compared.** The Wiener filter (black) was computed with full knowledge of the column-density spectrum. The partial-Tikhonov (grey) with  $\alpha = 0.2$  filter approximates it reasonably well up to around the 5th contrast null.

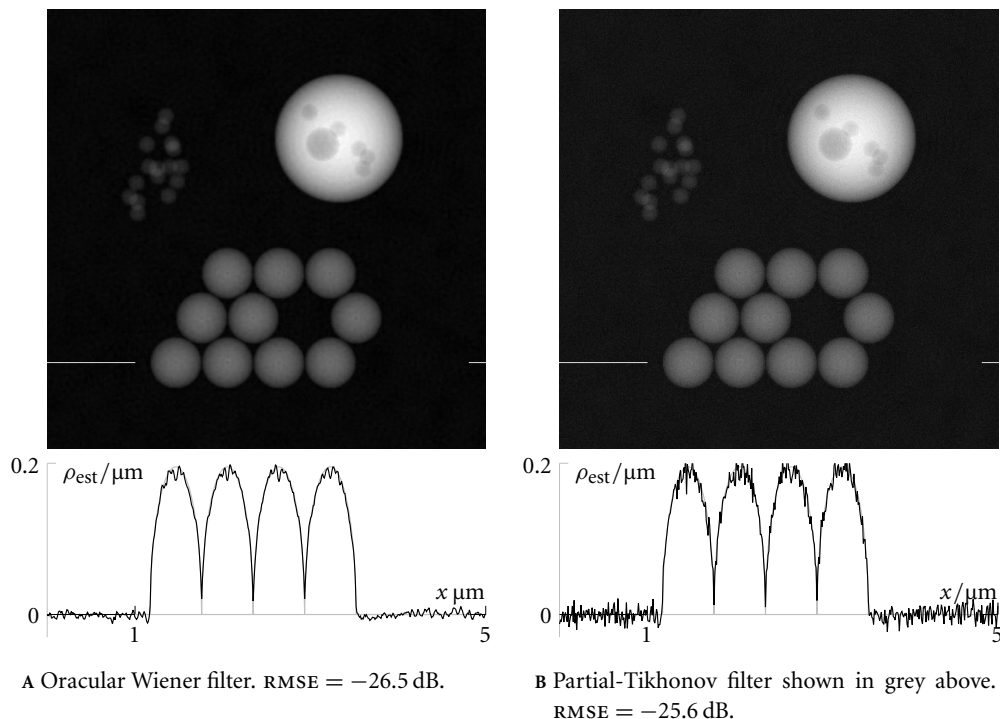


FIGURE 3.12 **Retrievals using Wiener and partial-Tikhonov filters.** Column-density images retrieved from Figure 3.9B using filters shown in Figure 3.11.

### 3.4.4 Applicability of the partial-Tikhonov filter

Formally,  $\alpha$  is determined by minimising the error (3.26). This method tends to over-smooth the signal and some more sophisticated variants [176] tend to assume rather ad-hoc smoothness constraints [177]. Still more advanced techniques employ full-image iteration and are formally similar to Projection Onto Convex Sets (*POCS*) iterations discussed in §3.1.6, only with less physical justification for the constraints.

In practice, the quality of the retrieval is remarkably insensitive to the value of  $\alpha$ , with values outside the range 0.03 to 0.3 seldom required. Larger values may be ‘optimal’ but yield unacceptably large distortion, and a noisier but less distorted estimate is usually preferred. Very small values are indicated when the SNR is high. As the Poisson SNR rises only as  $\sqrt{I_0}$ , the high SNR regime is seldom reached. In practice, it is often sufficient to search this range of  $\alpha$  manually for the best appearing image. We will see in the next Article that for the hybrid Fourier-wavelet extension there described, the Tikhonov parameter  $\alpha$  is readily optimised by a simple functional analogous to (3.26).

It is perhaps not so surprising that the partial-Tikhonov retrieval presented above is quite successful: after all, we cheated and looked at the spectrum of column-density, using this knowledge to design the filter! Is there any reason to believe that the filter (3.30) should apply to other images, or for that matter to other transfer function parameters?

Our test image has power-law behaviour  $|\tilde{\rho}| \propto u^{-\gamma}$  with slope  $\gamma$  very close to two for almost the full range of  $u$ .<sup>17</sup> At low frequencies,  $\tilde{h}^{-1}$  also rises as  $u^{-2}$  before eventually leveling off at  $\delta/\beta$ . The dashed curve on Figure 3.10 shows the case of  $\beta/\delta = -0.01$ ; it is apparent that as the inverse filter does not increase faster than the SNR, low frequency regularisation is not required for any value of  $\beta/\delta$  at this propagation distance  $z$ . Increasing  $z$  translates the red inverse filter curve to the left on Figure 3.10. This only improves the situation at low frequencies but does increase the range of SNRs for which the flawed Tikhonov assumption of constant SNR is in force. Decreasing  $z$  ultimately extends the first contrast peak at  $u_{\min}$  into the noise floor at the right-hand extreme of the plot, putting high-frequency structure below

---

<sup>17</sup> This is unsurprising as it follows from the zeroth-order Hankel transform [23, p 12] that the Fourier transform of the projection of a sphere  $\rho(\mathbf{x}) = 2\sqrt{a^2 - |\mathbf{x}|^2}$  is

$$\tilde{\rho}(\mathbf{u}) = \frac{1}{4\pi u^2} \frac{\sin(2\pi au) - 2\pi au \cos(2\pi au)}{2\pi au}, \quad (3.31)$$

which is absolutely bounded by  $u^{-2}$  for  $u > 1/2\pi a$ .

the inverse filter level. This corresponds to a fundamental loss of resolution when operating in the single-fringe regime where the TIE algorithm is valid.

A wide variety of images of ‘natural scenes’ – forests, mountains and even faces – have been shown to have amplitude power-laws with  $\gamma$  close to one [178]. Heuristically, such images are more ‘cluttered’ than our test image, and so have relatively greater spectral density at higher frequencies. Why ‘real’ images have such simple spectra has not yet been explained satisfactorily. Images with  $u^{-1}$  spectra are *scale invariant* or self-similar, but the phenomenon is not restricted to obviously fractal images of trees or snowflakes [179]. A recent analysis considered images which at all scales are composed of overlapping regions of constant intensity with sharp edges, not an unreasonable model for microscope images, and showed that a power-law spectrum resulted [180]. Even when the slope of the spectrum is not constant, it is almost always monotonic in its broad structure.<sup>18</sup> This remarkably consistent behaviour of real-world image spectra inspires confidence in the general applicability of the partial-Tikhonov filter. It is true that for slope  $\gamma < 2$ , the inverse filter  $1/\tilde{h}$  may slightly exceed the SNR at low frequencies; however, as the inverse filter eventually levels off at  $\delta/\beta$  it is likely that the important largest scale structures will be relatively clear. Ultimately, a larger propagation distance  $z$  may be required to keep the inverse filter below the SNR. Section 3.8 discusses optimisation of the propagation distance in some detail.



ONE MAJOR PROBLEM with implementing the Wiener filter was ignorance of the original signal spectrum. We have combined some very limited assumptions about the signal spectrum with our knowledge of the monomorphous column-density filter. The resulting partial-Tikhonov filter performed almost as well in a simulated experiment as the unrealisable oracular-Wiener filter.

We now have a solution to the inverse problem: partial-Tikhonov regularised deconvolution. Given a diffraction pattern due to a monomorphous object, such as Figure 3.9B, the solution retrieves the object’s column-density. Retrieval of cold-atom column-densities with this filter are presented in §5.3 and §5.4. The next three Sections describe an extension of this solution which substantially improves the quality of retrieved images, especially noisy image resulting from low exposures.

---

<sup>18</sup> Pathological examples may of course be constructed, but even regions of highly-periodic structure do not cause great anomaly in the overall spectrum provided they are isolated and relatively small.

### 3.5 Alternative bases for deconvolution

The simulation presented above used a mean exposure of 10 000 photons per pixel. We now consider a simulated retrieval with mean exposure of only 50 photons per pixel, a much more realistic model of x-ray and cold atom imaging. Figure 3.13B shows the diffraction pattern due to the monomorphous object with a column-density distribution following the *Lena* image A. *Lena* is arguably a more realistic object than the *Spheres* image, having a natural  $u^{-1}$  balance of coarse and fine detail. The simulation parameters are identical to those used in Figure 3.6, except that the absorption ratio is reduced from  $\beta/\delta = -0.1$  to a more demanding level of  $\beta/\delta = -0.005$ . For x-ray experiments, this corresponds to imaging a lighter element such as beryllium rather than aluminium.

The partial-Tikhonov filter described above yields either noisy (c, d) or distorted (e, f) retrievals. This time, however, the problem is *not* our inadequate knowledge of the SNR spectrum: the oracular Wiener retrieval i suffers from considerable ringing artefacts, despite being computed with full knowledge of the SNR spectrum. Pseudo-Wiener retrievals g and h, which use only observations, are much worse. Is this the best we can do with an image at realistic exposures?

In this Section we will see that the partial-Tikhonov filter represents an adequate approximation to the actual SNR spectrum and the retrieval quality of Wiener filtering is instead limited by the *non-stationarity* of the signal. I then show in the next Section that a combination of deconvolution in the Fourier basis with denoising in a *wavelet basis* yields a retrieved image Figure 3.13j with low noise and a remarkable absence of artefacts.

The hybrid Fourier-wavelet deconvolution algorithm discussed in the next Section is based on the PhD work of Ramesh Neelamani at Digital Signal Processing group at Rice University [181]. The discussion in this Section broadly follows Neelamani's development of the topic.

#### 3.5.1 An optimal basis for deconvolution

The Fourier basis was a natural choice for our first attempt at solving the deconvolution problem. The linear system  $h$  that connect column-density to contrast is *diagonal* in the Fourier basis, and so is trivially invertible. The Wiener filter exploits this inverse, but in doing so makes the assumption of stationarity which we now call into question.

Non-stationary extensions of the Wiener filter have a long history. In the time-domain, the Wiener filter has been displaced by the adaptive *Kalman filter*. Early uses included attitude control of the Apollo 11 lander, and the filter is now ubiquitous in servo control systems. It has had less success in processing *acausal* signals, such as most images, where there is no arrow of time to adapt along. In this Section, we search for a better deconvolution basis than the Fourier basis.

For maximum generality, let us consider solutions to the deconvolution problem over  $N$  discrete elements (pixels) in an *arbitrary orthonormal basis*  $\{b_k\}$ .<sup>19</sup> The Fourier basis corresponds to sinusoidal  $b_k$ , while various adaptive Fourier filters correspond to windowed sinusoidal bases [183]. The column-density  $\rho$  may be decomposed

$$\rho = \sum_{k=0}^{N-1} \langle \rho, b_k \rangle b_k. \quad (3.32)$$

In the spatial basis  $h$  is a convolution and in the Fourier basis, simply multiplication. In our arbitrary basis  $\{b_k\}$ , we cannot be more specific than taking  $h$  as a linear operator. A regularised retrieval in the arbitrary basis can be written:

$$\rho_{\text{est}} = \sum_{k=0}^{N-1} (\langle \rho, b_k \rangle + \langle h^{-1}n, b_k \rangle) \lambda_k b_k. \quad (3.33)$$

In this formalism, the regularisation process corresponds to re-weighting with filter  $\lambda_k$  the basis elements  $b_k$  (Neelamani refers to it as ‘shrinking’) for which the coloured noise coefficient  $\langle h^{-1}n, b_k \rangle$  exceeds the signal coefficient  $\langle \rho, b_k \rangle$ . As an example, the simple-Tikhonov filter corresponds to choosing the basis  $\{b_k\}$  to be the sinusoids, and choosing  $\lambda_k = h_k^2/(h_k^2 + \alpha^2)$ ; compare (3.29).

Of course, a regularisation procedure – a choice of  $\{\lambda_k\}$  – is dependent on the choice of basis  $\{b_k\}$ . Recall that in the Fourier basis the Wiener filter was the regularisation procedure which minimised the true mean-square error and the Tikhonov filter minimised an observation-based error. While we can’t actually find regularisation procedures in all possible bases, we *can* compare the ultimate success of the best possible regularisation procedure for each basis. It may be shown that in a given basis  $\{b_k\}$ , of all regularisation procedures  $\{\lambda_k\}$ , none yields a MSE less than

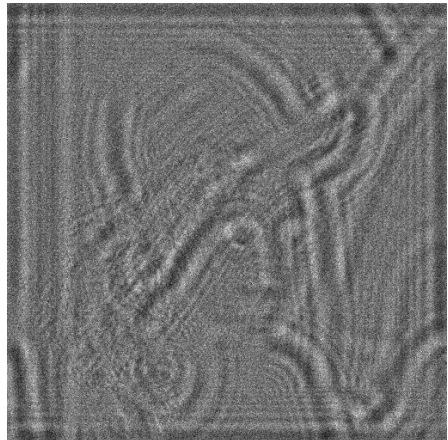
$$\frac{1}{2} \sum_{k=0}^{N-1} \min \left( |\langle \rho, b_k \rangle|^2, E |\langle h^{-1}n, b_k \rangle|^2 \right), \quad (3.34)$$

---

<sup>19</sup> Here  $k$  is a discrete enumerator and has no connection to spatial frequency or wavevector.



A Column-density image.  $\rho/\mu\text{m}$ : [0.0 2.0]



B Diffraction pattern,  $z = 20 \mu\text{m}$ .  $I/I_0$ : [0.26 1.9]



C partial-Tikhonov retrieval.  $\alpha = 0.1$ , no cutoff.  
RMSE = -6.0 dB.



D partial-Tikhonov retrieval.  $\alpha = 0.1$ .  
RMSE = -12.5 dB.



E partial-Tikhonov retrieval  $\alpha = 0.5$ , no cutoff.  
RMSE = -12.2 dB.



F partial-Tikhonov retrieval.  $\alpha = 0.5$ .  
RMSE = -14.8 dB.



G pseudo-Wiener retrieval using measured signal spectrum. RMSE = -0.7 dB.



H Iterative Wiener retrieval [182]. 30 iterations. RMSE = -6.9 dB



I oracular-Wiener retrieval.

RMSE = -15.8 dB.

$\rho_{\text{est}}/\mu\text{m}$ : 0.0 [2.0]



J Hybrid Fourier-wavelet retrieval.

$\alpha = 0.24$ , 5 decomp levels.

RMSE = -14.1 dB.

$\rho_{\text{est}}/\mu\text{m}$ : 0.0 [2.0]

FIGURE 3.13 Fourier deconvolution fails at low SNR. Simulated object is a  $5 \times 5 \mu\text{m}$  foil, maximum thickness  $2 \mu\text{m}$ , illuminated with 3 keV x-rays. Refractive index is  $n = 1 - 2 \times 10^{-5} + i10^{-7}$  (compare beryllium  $n = 1 - 3.9 \times 10^{-5} + i1.4 \times 10^{-7}$  [175]) yielding 0.3% contact absorption and -0.6 radian phase-shift. Poisson noise simulated at 50 photons/pixel.

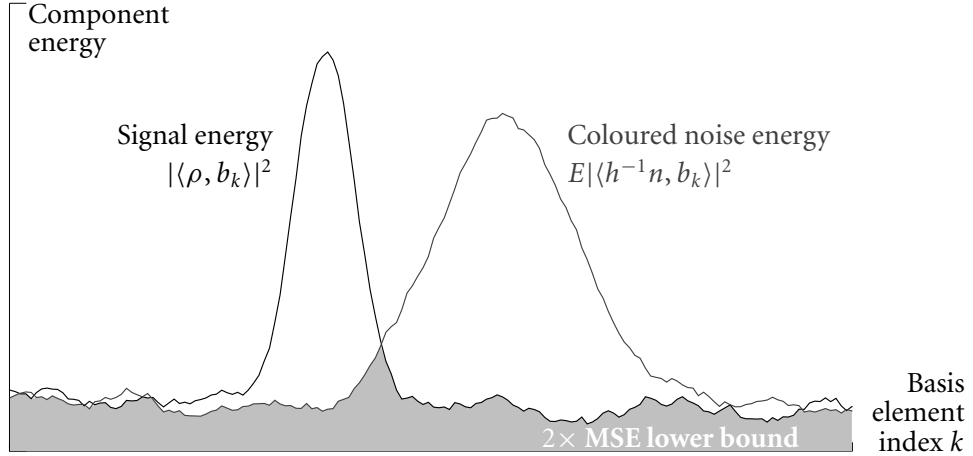


FIGURE 3.14 **Signal and noise energies and the minimum possible MSE.** The plot shows how signal and coloured noise coefficients might be distributed in a *fictitious* near-ideal basis.

where  $E|\cdot|$  indicates that some appropriately defined expectation value, or average, is to be taken over an ensemble of possible noises  $n$  [184] [185, Thm 3.3].<sup>20</sup> Clearly the best basis to use is one which minimises this minimum.

The schematic Figure 3.14 depicts the energy of signal and coloured noise coefficients in a near-ideal basis. The area under the minimum of the two traces is shaded, the MSE lower bound (3.34) is proportional to this area. Small MSEs are indicated when the signal and noise are concentrated in a small number of coefficients, and when those coefficients do not overlap. This is hardly surprising: for such an ideal basis, the regularisation procedure would consist of retaining ( $\lambda_k = 1$ ) the basis elements corresponding to the signal and discarding ( $\lambda_k = 0$ ) those other elements corresponding to coloured noise. Unfortunately, there is no guarantee that such an ideal basis exists.

### 3.5.2 The Fourier basis is optimal for coloured noise

We begin by searching for a basis that economically represents the coloured noise  $h^{-1}n$ . The *Karhunen-Loeve transform*<sup>21</sup> constructs the most economical basis for an image, given its autocorrelation [187, §3.1] [188]. It can be shown that for Gaus-

<sup>20</sup> This argument has been given in the language of minimax estimation, for a translation into linear algebra – SVD and eigenthings – see [186, §1.1–2].

<sup>21</sup> Also known as the *Hotelling transform* and closely related to the *singular value decomposition* of linear algebra and the *principal component analysis* of statistics.

sian noise, the Karhunen-Loëve transform asymptotes towards the Fourier transform as the image size  $N$  increases [187, §3.3–4]. It is not assumed that the noise is white: provided the noise  $n$  is Gaussian, the shift-invariant coloured noise  $h^{-1}n$  is also [189, §2]. The fundamental result is that stationary noise – noise unchanging in nature across the image – is optimally represented in the Fourier basis.

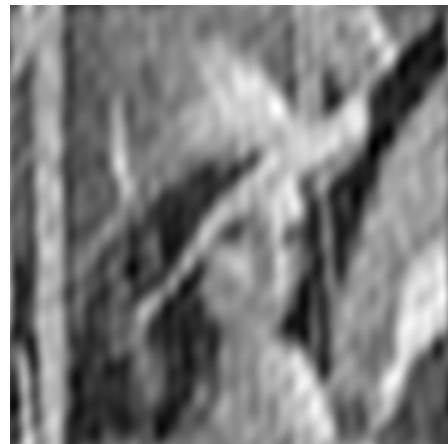
Our particular variety of coloured noise has an especially parsimonious Fourier representation. The great majority of the energy in  $h^{-1}n$  is concentrated in the few Fourier coefficients for which  $\tilde{h} \approx 0$ .

In the imaging systems considered in this thesis, the irreducible shot noise of photon counting is Poisson rather than Gaussian. A shot-noise limited image with strong variations in intensity will show substantial spatial variations in noise. In this case the Fourier basis is no longer optimal; some elegant wavelet techniques for Poisson denoising have already been demonstrated [190]. It was conjectured in §2.5.6, however, that our contrast transfer function model applies only to weak contrast images. Images with significantly non-stationary Poisson noise due to strong contrast are unlikely to be valid subjects for the current deconvolution algorithm. Poisson denoising might be required should it prove possible to extend retrieval to strongly-absorbing objects as hypothesised in §3.3.3.

### 3.5.3 A wavelet basis is optimal for real-world images

While the Fourier basis is near-optimal for stationary coloured noise  $h^{-1}n$ , it is far from optimal for most column-density images  $\rho$  which tend to be highly non-stationary. There are exceptions: a high-resolution electron microscope image of a crystal lattice appears as a regular array of fuzzy atoms, and is well-represented by a few Fourier coefficients. In the previous Section we saw that most real-world images have rather shallow power-law spectra and so are *uneconomically represented* in the Fourier basis.

Only in the last 15 years have mathematicians constructed alternative orthonormal bases better suited to unsMOOTH and discontinuous images. The field of *wavelet analysis* was created in the late 1980s around a remarkable confluence of ideas from fields as diverse as signal processing, computer vision, seismology, theoretical physics and harmonic analysis. A wavelet basis is composed of translations and dilations (scalings) of a *mother wavelet*: a function localised in space and having at least one zero-crossing so that it is also localised in frequency. Gabor realised the utility of decomposing a signal into such atoms in 1946 [191]. It was not until 1988



A 500 Fourier coefficients.



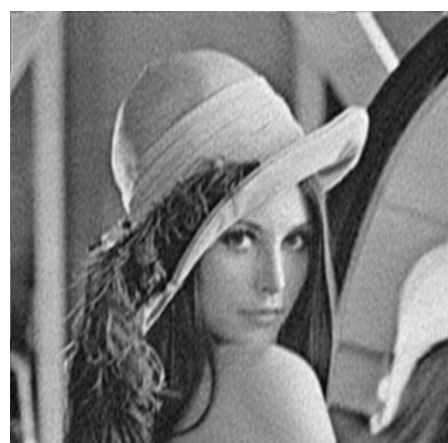
B 500 wavelet coefficients.



C 2000 Fourier coefficients.



D 2000 wavelet coefficients.



E 10 000 Fourier coefficients.



F 10 000 wavelet coefficients.

that I Daubechies found a class of such atoms which were compactly-supported, arbitrarily smooth and, most importantly, formed an orthonormal basis for finite-energy signals [192]. Appendix D gives an outline of wavelet properties with references and includes plots of the Daubechies mother-wavelets used in this Chapter. For the purposes of this discussion, it is entirely sufficient to consider wavelets as ‘just another orthonormal basis’.

On p 103 it was mentioned that the power-law spectra of real-world images might arise from their ‘edginess’. Heuristically, to approximate an edge in a region of an image, one need only translate the mother wavelet to the region and dilate it to an appropriate sharpness. Such a translation/dilation is already ‘on the shelf’ in the basis, and the sum of only a few such basis elements is sufficient to approximate an edge. As compactly-supported wavelets are available, the edge can be approximated without ringing through the rest of the image. In contrast, the Fourier spectrum of an edge falls off slowly as  $u^{-1}$ , and so approximating an edge requires a large number of basis elements. More precisely, the MSE of a largest- $N$ -coefficient approximation decays as  $N^{-1}$  for wavelets and only as  $N^{-1/2}$  for Fourier waves [186]. The *Lena* test image contains many edges of different contrasts: Figure 3.15 shows reconstructions from the largest  $N$  coefficients in both the Fourier basis and a wavelet basis, for three values of  $N$ . It is obvious that the wavelet basis is the more economic for this image.

Formally, it has been shown that wavelets form an *unconditional* [193], and therefore economic, basis for a class of functions known as a *Besov space*. A hand-waving definition of the Besov space  $B_{p,q}^s$  is that it contains all functions which may be differentiated  $s$  times and still have a finite  $L^p$ -norm [194].<sup>22</sup> In an even vaguer sense, the Besov space includes *piecewise polynomial* images: those having regions of polynomially smooth variation between discontinuities. While encouraging, it is a hard problem to show that *all* ‘natural images’ – or all images likely to be seen with a projection microscope – belong to a subset of a Besov space [196, 197].

Unfortunately, although wavelets are a promising basis for real-world images,

---

**FIGURE 3.15 (ON FACING PAGE) Wavelets are more economical than sinusoids for real-world images.** The test image 3.13A reconstructed from the largest  $N$  Fourier or Daubechies-6 wavelet coefficients. The image has  $512 \times 512$  pixels and so there are 262 144 distinct coefficients in the full transforms.

---

<sup>22</sup> The use of the  $L^p$ -norm [195] rather than the more usual finite-energy  $L^2$ -norm allows for rather more sharpness; there being no great significance attached to the energy of spatial derivatives.

they are a very bad basis for our coloured noise. For a small class of *dilation-invariant* transfer functions  $\tilde{h}(\mathbf{u}) \sim (1 + u)^{-\nu}$ ,  $\nu > 0$ , the coloured noise  $\tilde{h}^{-1}\tilde{n}$  is almost as economic in the wavelet domain as in the Fourier domain [184], and a *wavelet-vaguelette deconvolution* may be used. Tomographic data has been successfully deconvolved in the wavelet basis due to the dilation-invariance of the Radon transform [198]. Our transfer function, however, is *not* dilation-invariant as it has a characteristic scale  $\sqrt{\lambda z}$ . It is high-pass rather than low-pass, and the multitude of zero-crossings yield high-variance coloured noise at all locations and scales ensuring that the coloured noise is large in all wavelet coefficients.

### 3.6 Hybrid Fourier-Wavelet deconvolution

The result of §3.5.1 was that an optimal basis for deconvolution represents signal and coloured noise economically and separately. Our search for such an optimal basis has failed: the Fourier basis is optimal for the coloured noise, but poor for real-world images. Wavelet bases are much better suited to real-world images, but the coloured noise spreads itself across the wavelet coefficients.

Neelamani's idea is to use Fourier *and* wavelet bases in tandem to obtain a near-optimal deconvolution [199–202]. His **forward** (*Fourier-wavelet regularised deconvolution*) algorithm is a simple catenation of Fourier deconvolution and wavelet denoising:

1. **Deconvolve the transfer function** with a Tikhonov filter. The Tikhonov parameter  $\alpha$  is typically set lower than is optimal for Tikhonov retrieval, so that the signal is less distorted at the expense of higher levels of coloured noise.
2. **Apply a wavelet Wiener filter** to attenuate the coloured noise. After the Tikhonov step, the minimally-distorted signal remains well-represented by a small number of wavelet coefficients and the coloured noise remains spread across many wavelet coefficients but now at a much lower level due to the Tikhonov attenuation. A wavelet-domain Wiener filter retrieves the large signal coefficients which stand above the coloured noise floor.
3. **Compute a cost functional** assessing the success of the retrieval. Vary  $\alpha$  and retry the deconvolution until the functional is minimised.

The algorithm was developed for deblurring images degraded by motion or defocus blurs – such as those depicted in Figure 3.7 – where simple-Tikhonov regu-

larisation is appropriate. I have modified Neelamani's algorithm to use the monomorphous CTF and a partial-Tikhonov filter, making it applicable to our problem of retrieving column-density from a diffraction pattern.

### 3.6.1 Distribution of noise in the wavelet basis

Figure 3.16 illustrates the relative amplitude of the signal and partial-Tikhonov coloured noise (for two values of  $\alpha$ ) in the wavelet domain. This is the situation after deconvolution with the partial-Tikhonov filter, but before wavelet filtering. The Figure was calculated by separating the simulated diffraction pattern Figure 3.13B into pure signal and pure noise, and performing separate partial-Tikhonov retrievals on the pure components. This 'wavelet spectrum' of the pure components is somewhat analogous to the Fourier spectrum on p 99 which also shows the mean coloured noise as the red trace. We can see that the very largest signal wavelets are also large noise wavelets, but the vast majority of noise wavelets – all but the first few hundred out of  $2.6 \cdot 10^5$  – form a homogeneous background.

It is clear from the Fourier spectrum Figure 3.10 that the noise coloured by our partial-Tikhonov filter takes on large values across several octaves of low spatial frequencies, but beyond the first contrast maximum there are several coloured noise peaks in each octave. This explains the presence of a few large noise wavelets at coarse scales and broadly homogeneous wavelet amplitudes at finer scales of the coloured noise. In contrast, the coloured noise in the Fourier spectrum is far from homogeneous.

The dark red trace on Figure 3.16 on the next page shows coloured noise wavelet amplitudes when very little partial-Tikhonov regularisation is applied. Only the most significant 500 or so signal wavelets are above this noise floor. Even if these 500 wavelets were identified for us by an oracle, and even without the corrupting effects of the few noise wavelets that project above the signal level, we can see from Figure 3.15B that 500 wavelets are not enough to reconstruct *Lena*. When a somewhat greater degree of partial-Tikhonov regularisation is used ( $\alpha = 0.24$ ), the coloured noise shown in red results. The homogeneous noise floor is clearly lower, and now several thousand wavelet coefficients lie above the noise level. Reconstructions of *Lena* from this number of the most significant wavelets appears promising given Figure 3.15D and Figure 3.15F. The noise suppression comes at the expense of signal distortion; the hope is that the trade-off is more favourable using mutually optimal bases than it was when working solely in the Fourier basis.

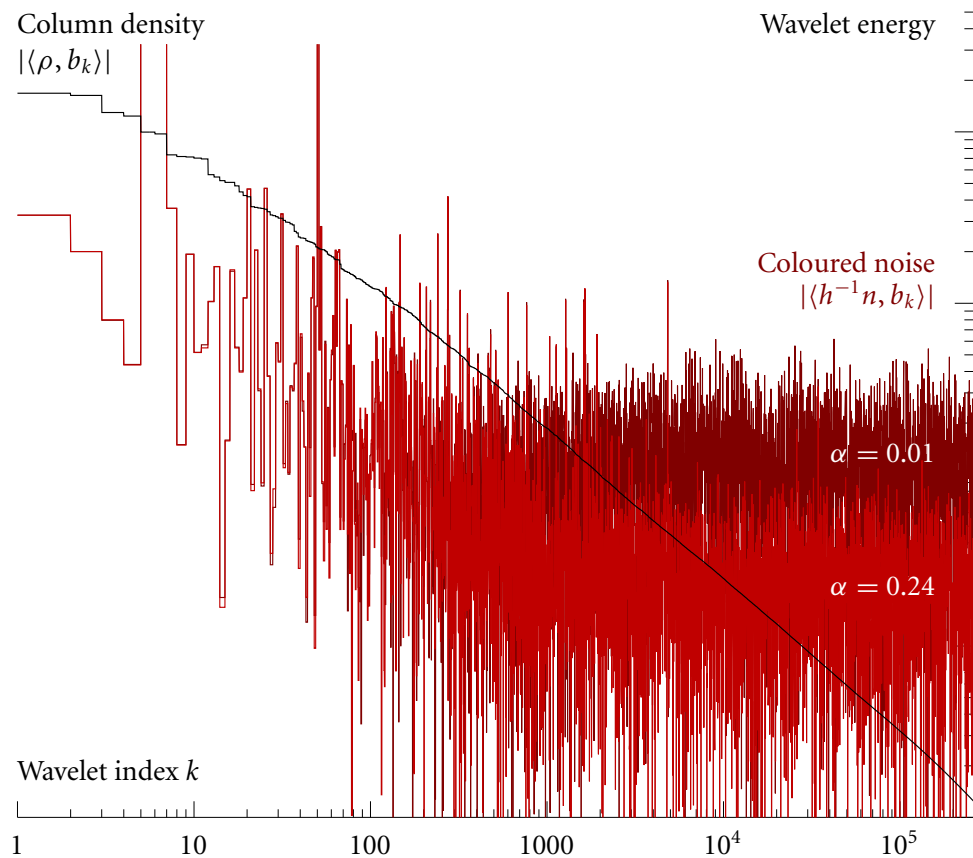


FIGURE 3.16 **Wavelet spectra of signal and coloured noise.** The wavelet indices are sorted in order of decreasing energy of the column-density components. Coloured noise is shown for two values of the partial-Tikhonov parameter  $\alpha$ . Compare the equivalent Fourier plot Figure 3.10 on p 99, although note that *all* wavelet coefficients are plotted here while only azimuth-averages of the Fourier coefficients are shown.

### 3.6.2 Filtering in the wavelet basis

The actual algorithm, of course, does not operate separately on the signal image and the coloured noise image, but on their sum. Figure 3.13C shows the noisy image resulting from partial-Tikhonov filtering with  $\alpha = 0.24$ . The second step of Neelamani's FORWARD algorithm is to filter this image in the wavelet domain: essentially to identify and retain as many of the uncorrupted signal wavelets which lie above the coloured noise floor and discard those below it. Just as in the Fourier domain, the optimal linear filter is a Wiener filter [203]. And, just as in the Fourier domain, the SNR-spectrum required by the Wiener filter is not known a priori.

There are two points in favour of wavelets, however. First, simplistic hard-thresholding is quite close to optimal in the wavelet domain [185], but produces ugly Gibbs phenomena in the Fourier domain as seen in Figure 3.13D. Second, there is more than one wavelet basis to play with. The forward algorithm exploits both points by using hard-thresholding in a first wavelet basis to obtain a reasonable estimate of the signal. The signal estimate is then used to *design* a Wiener filter in a sufficiently different second wavelet basis [203, 204].<sup>23</sup>

Both the initial hard-threshold and the Wiener filter require a noise estimate, which is provided by the median absolute deviation of the finest scale wavelets [205] [49, p 459]. This noise estimator is heuristic, but is considered robust for white noise and has been widely used. In many imaging applications we may sample ‘pure noise’ from an unoccupied region of the image plane should there be any doubt [206] about the validity of the noise estimator.

### 3.6.3 Determination of $\alpha$

In §3.4.3 we discussed the difficulty of finding the optimal value of the parameter  $\alpha$  in Tikhonov regularisation. Neelamani introduces the least-squares functional

$$\left\| \frac{\tilde{h}^*(\mathbf{u}; z)}{|\tilde{h}(\mathbf{u})|^2 + 1/\eta} \left( \tilde{C}_{\text{meas}}(\mathbf{u}) - \tilde{h}(\mathbf{u}) \tilde{\rho}_{\text{est}}(\mathbf{u}) \right) \right\| \quad (3.35)$$

with  $\eta$  a bootstrap SNR determined from the mean-square deviation of the measured contrast  $C_{\text{meas}}$  and the estimated noise.<sup>24</sup> The functional estimates an error value given the end result  $\rho_{\text{est}}$  of the Fourier-wavelet deconvolution. The Tikhonov parameter  $\alpha$  is varied until the error value is minimised. Neelamani shows [181, Fig 2.8] that the value of  $\alpha$  which results is very close to the optimal value which would be chosen by an oracle with full knowledge of the column-density and noise as separate quantities.

---

<sup>23</sup> Neelamani’s code uses Daubechies-2 and Daubechies-6 wavelets for the hard-threshold and Wiener filters, respectively, and performs a redundant shift-invariant discrete wavelet transforms. Mother wavelets are plotted in Appendix D.

<sup>24</sup> This is the form used in Neelamani’s *FORWARD version 2.0* code [207, RegParamSetup.m, Line 26], and is *not* the same as the *observation-based cost* given in his thesis [181, Eqn 2.25, §2.6.2], although the behaviour of the functionals should be similar.

### 3.6.4 Optimality of FORWARD

On first impression, Neelamani's FORWARD algorithm seems somewhat ad-hoc and even trivial, being a simple catenation of Fourier deconvolution and wavelet denoising. Only the Tikhonov parameter is optimised, and it is not used in designing the wavelet filter. Neelamani shows, however, that the mutual optimality of the Fourier and wavelet bases discussed in §3.5.2 and §3.5.3 renders FORWARD asymptotically optimal for Besov space signals [181, §2.5.4]. It seems reasonable to expect a similar optimality for the partial-Tikhonov modification of FORWARD used in this thesis; a full proof would be rather involved [181, App C, D].

### 3.6.5 Performance of the FORWARD algorithm

FORWARD retrieval was originally demonstrated for *boxcar blur*: convolution with a square top-hat function [181, §2.7]. This blur is not readily produced by a physical process, but approximates both linear motion blur and defocus blur in an incoherent imaging system.

I modified the original FORWARD code [207] which was written in MATLAB (The Mathworks, Natick MA, USA), replacing simple-Tikhonov regularisation with the partial-Tikhonov regularisation described in §3.4.3. The Tikhonov parameter  $\alpha$  is set to zero – no regularisation is performed – for spatial frequencies below the first contrast null. This code was run on the noisy diffraction pattern shown in Figure 3.13B with varying values of  $\alpha$ . Setting  $\alpha = 0.24$  minimised the error functional (3.35): the red trace in Figure 3.16 represents this *optimal* level of coloured noise. The output of the modified code is shown in Figure 3.13J.

It is obvious that the wavelet filter has removed almost all of the noise present after the partial-Tikhonov step (Figure 3.13C). In comparison with the oracular-Wiener filter, the FORWARD retrieval has fewer artefacts and lower noise. This is not reflected in the MSE, possibly due to the presence of two very large noise wavelets at large scales visible in Figure 3.16. Note in particular the diagonal ringing parallel to the brim of Lena's hat which corrupts the oracular-Wiener estimate Figure 3.13I. This distortion is particularly prominent on Lena's nose and cheek, and also superimposed on the tassels in the lower left corner. This artefact is completely absent from the FORWARD retrieval. Some of the detail of the tassels at centre-left of Lena's hat, and on her hat band, is just discernible in the Wiener retrieval and absent in the wavelet retrieval. Would an observer who had not seen the original image recognise it as detail? Close inspection of the wavelet retrieval does reveal tiny flecks

of *wavelet dust*, a characteristic artefact of undecimated discrete wavelet transform denoising [208]. In general, the wavelet retrieval *does not introduce spurious details* that could possibly be confused with genuine structure, and appears to substitute smooth patches where the signal is overwhelmed by noise. These are very desirable properties for image processing in microscopy applications.

The preceding comparison of **FORWARD** retrieval with oracular-Wiener retrieval is not a fair one. The **FORWARD** retrieval was calculated using only the ‘observed’ image Figure 3.13B while the oracular-Wiener calculation used full knowledge of the original signal power spectrum. A fair comparison with the partial-Tikhonov and iterative Wiener retrievals Figure 3.13C–H demonstrates the clear superiority of **FORWARD** retrieval over purely Fourier methods.

### 3.6.6 Diffraction contrast versus Zernike phase contrast

We are now in a position to compare diffraction-contrast imaging diffraction patterns with the established technique of Zernike phase-contrast imaging (see 5.6.3). Figure 3.17A shows a simulation of the Zernike phase-contrast image which would result from the same monomorphous *Lena* with the same mean exposure of 50 photons per pixel. The Zernike image was calculated with a full Fourier-optics propagation through an ideal lens system of infinite extent with a perfect  $\pi/2$ -bump phase plate.

Contrast is clearly higher in the Zernike image than in the diffraction pattern. Naturally, the raw Zernike image shows shot noise, and so a version of the Zernike image denoised with the same wavelet Wiener filter used in **FORWARD** is shown in Figure 3.17C. While the denoised Zernike image is slightly better than the **FORWARD**-retrieved image D, it is interesting to note that details in *Lena*’s tassels and hat band, visible in the raw Zernike image A, are absent in both denoised images C and D. The loss of such detail from the Zernike image as well suggests a limitation of wavelet-based deconvolution, rather than a fundamental limit of diffraction-contrast imaging. Possible improvements beyond wavelet bases are discussed in §3.7.4 and §3.7.5.

Figure 3.18 extends the comparison of denoised Zernike images and **FORWARD** retrievals to other exposure values. At an exposure of 50 photos per pixel we can see on Figure 3.16 that about eight of the first hundred wavelet coefficients are swamped by coloured noise. Reduction of the exposure to 20 photons per pixel increases the coloured noise with manifest instability at coarse spatial scales, and at 5 photons per

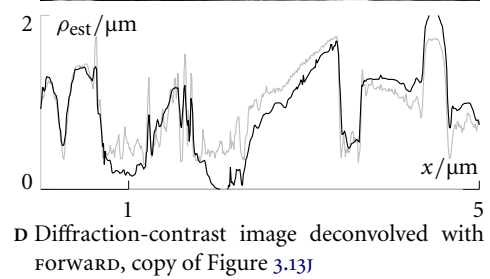
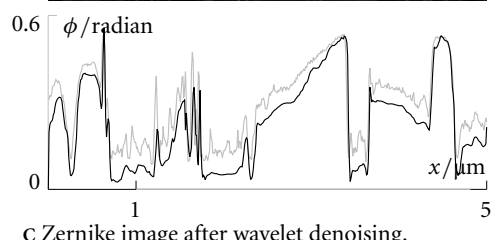
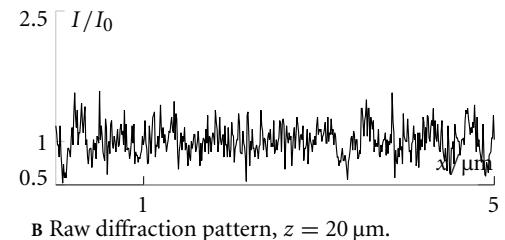
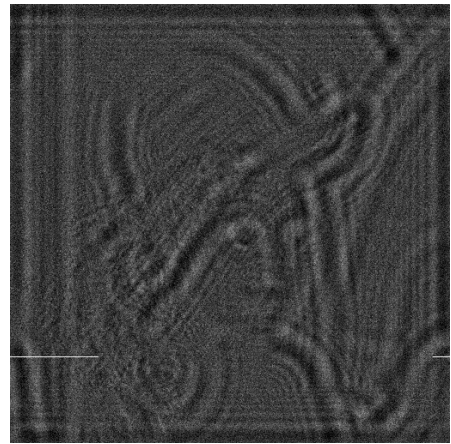
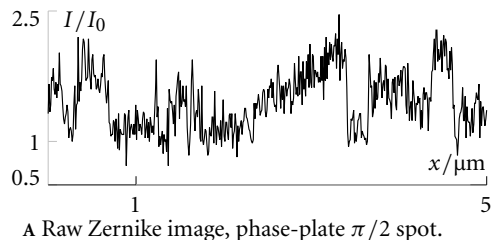


**FIGURE 3.17 Wavelet denoising of diffraction-contrast and Zernike-phase images.** Mean exposure 50 photons/pixel for both Zernike and diffraction images. Other simulation parameters as for Figure 3.13.

pixel the image is subsumed by coarse-scale noise. The Zernike image progressively loses detail only at the fine scales.

In §3.8.1 I show that successful retrievals are possible at exposures below 50 photons per pixel if the propagation distance is increased. Alternatively, low-frequency instability could be reduced if the absorption ratio  $\beta/\delta$  of the material was increased above the value of 0.005 used in this simulation. Even at 50 photons per pixel, these results demonstrated the applicability of the FORWARD algorithm when the SNR is very low. In comparison, Neelamani's examples correspond to Poisson noises equivalents of 10 000 photons per pixel [181, Fig 2.4].

## 3.7 Further enhancements of the deconvolution solution

In this Section, I review some alternative deconvolution techniques which have recently been described. An extension of wavelet analysis, known as *curvelets*, seem particularly promising for deconvolving real-world images (§3.7.5).

### 3.7.1 Beyond white detector noise

In an extension mentioned in his PhD thesis, Neelamani has modified the noise estimator to work across all scales, rather than only at the finest wavelet scale, and demonstrated enhanced retrievals for signals corrupted by off-white noise. Real-world image noise is seldom white, and in some systems has a  $u^{-1}$  technical component. Initial *experimental* results are impressive, although the blur operator was a relatively harmless Gaussian blur [181, §2.7.2].

In §5.7.2 I discuss the characteristic noise of *coherent* imaging systems. This noise tends to be localised at particular spatial frequencies, and it might be possible to alleviate its affects in the retrieval by injecting an estimated noise spectrum into the wavelet-Wiener filter stage of FORWARD.

### 3.7.2 Better transforms: improved wavelets

Discrete 2-dimensional wavelets are implemented as products of the one-dimensional functions (Appendix D). FORWARD already uses a *shift-invariant modification* [209, 210] of the standard Discrete Wavelet Transform (DWT). However, the preference of these separable wavelets for edges aligned with  $x$ - and  $y$ -axes causes characteristic horizontal and vertical distortions as in Figure 3.15D. Rotationally-invariant wavelet transforms have been advanced under the monikers *cycle spin-*

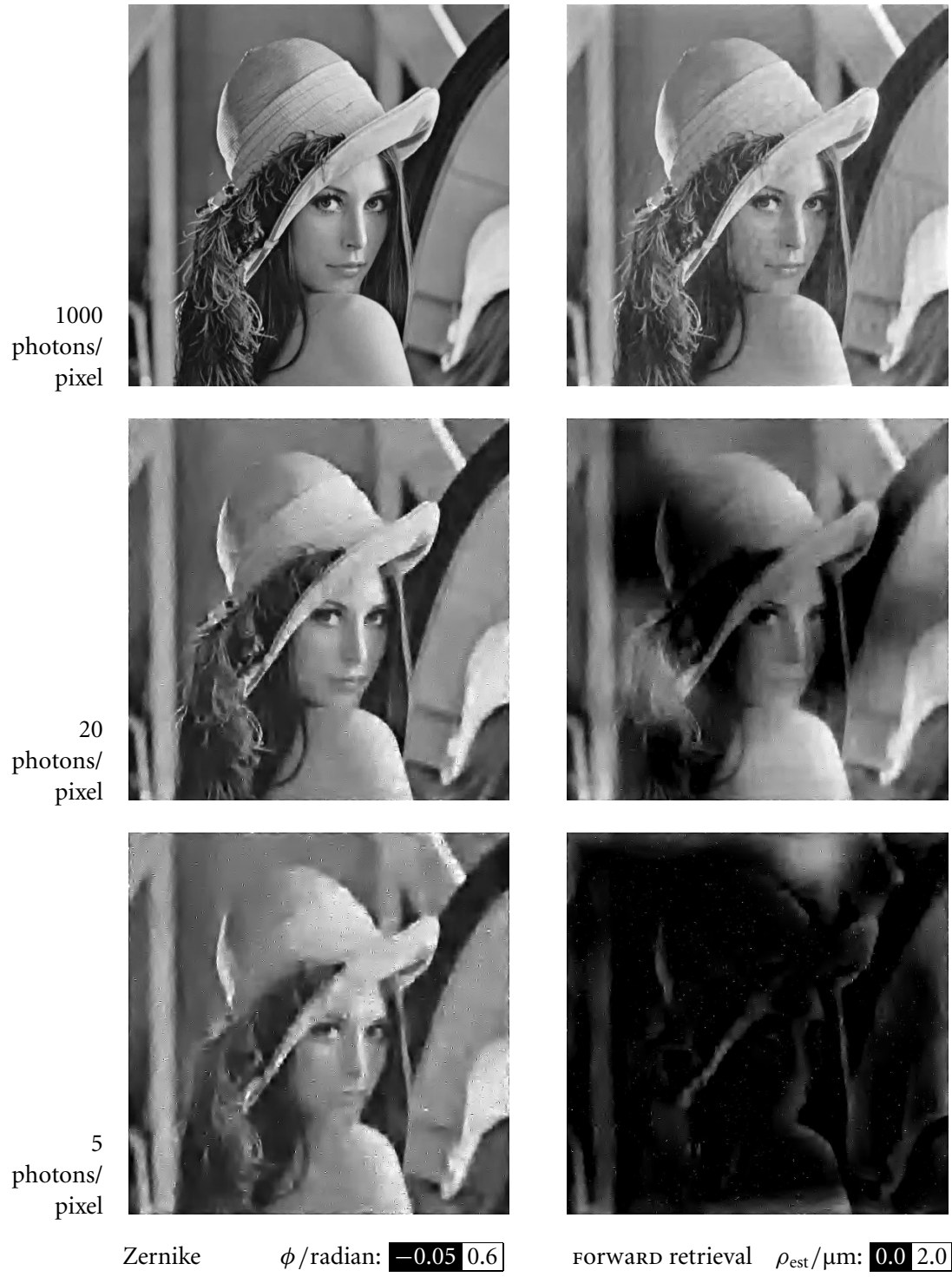


FIGURE 3.18 **Zernike versus DCI for three exposure values.** Other simulation parameters as for Figure 3.13. forward  $\alpha$  optimised for each retrieval.

*ning* [211] and *complex wavelets* [212]. They have recently been used to enhance denoising and deconvolution [213] algorithms, where small improvements beyond FORWARD performance were reported. Another very recent innovation is the use of overcomplete dictionaries of wavelets [214] but the extension of these impressive 1D results to 2D images has been judged difficult [215].

### 3.7.3 Iterative enhancements

While the two-basis wavelet-Wiener filter used by FORWARD performs quite well at low SNR, an iterative filter operating on *several* wavelet bases claims further reduced MSE at low signal-to-noise ratios [216]. The filter performs POCS onto surfaces in the different Besov spaces; it is presumably quite computationally intensive.

A very recent *expectation-maximisation (EM)* algorithm extends such iteration beyond the wavelet filter to the entire FORWARD process [217]. The observed signal is alternatively processed in the Fourier and wavelet bases. Results are encouraging, with performance very similar to FORWARD. Remember that the published FORWARD results used much higher SNRs and a more conventional low-pass filter than in our example, so comparisons with our particular inverse problem are merely suggestive.

One significant advantage of the FORWARD algorithm is that it is *not* iterative, and so is fast to execute and questions of convergence do not arise. If an iterative method is to be used, then it should probably include *physical constraints*, such as positivity of the column-density and possibly the compact support of the object. There are intriguing formal similarities between such iterative deconvolution methods and the iterative phase-retrieval methods discussed in §3.1.6: is there perhaps a role for convex wavelet constraints in POCS approaches to phase-retrieval?

### 3.7.4 New bases: beyond wavelets

The wavelet-Wiener filter produces impressively low noise and artefact-free images, but does tend to over-zealously suppress elongated fine structures: compare the feathers and Lena's hair in Figure 3.17A with Figure 3.17C. In §3.5.3 we introduced wavelets as a near-optimal basis for real-world images with edges. And indeed, we have seen that they perform well, at least much better than the Fourier basis. However, §3.7.2 discussed how translation and rotation invariance had to be ‘patched’ on to the wavelet transform. In an effort to represent real-world images even more economically than wavelets can, a panoply of ‘exoticlets’ have been devised:

*brushlets* [183], *edgelets* [218], *wedgelets* [219, 220], *beamlets* [221], *ridgelets* [222] and *curvelets* [223] among others.<sup>25</sup>

Curvelets are the most promising: they are atoms which have not only characteristic position and scale as wavelets do, but also *orientation* and *microlocation* [225]. A single curvelet looks rather like a brush-stroke. It is proved that wavelets are optimal only for *point discontinuities* in signals of any dimension, and so are truly optimal for ‘edgy’ signals only in one dimension where all discontinuities are point discontinuities. Curvelets are proved to be asymptotically optimal for line discontinuities in two-dimensions,<sup>26</sup> surface discontinuities in three-dimensions and so on [226]. Although some features of images, such as Lena’s eyes, are well modeled by point discontinuities, edges in images are essentially line discontinuities. Curvelets are mathematically attractive: they form a *tight frame* (an ‘almost-basis’), and computationally attractive: fast digital transforms have been devised [227]. It appears that just as wavelets have graduated from an image processing research tool to wide application in the JPEG-2000 image-compression standard [228], they are about to be overtaken by a new generation of multiresolution methods.

Naturally, as curvelets offer near-optimal economy in representing real-world images, they should be an excellent ‘basis’ for denoising. Complications arise due to non-orthogonality, but results are nevertheless impressive with much better preservation of edges than the undecimated wavelet transform [230]. A simulation by JL Starck et al. is reproduced as Figure 3.19 on page 124. Lena’s hair, tassels and hat band are all better restored by curvelet denoising (Figure 3.19B), but small point-like features – Lena’s eyes and nostrils – are still evident in the residual, motivating an iteration between wavelet and curvelet denoising [208] conceptually similar to the use of two distinct wavelet-bases in the FORWARD Wiener filter. The results (c) are truly impressive with no perceptible structure in the residual: it may be no exaggeration to say that this work closes the problem of denoising standard images in moderate levels of white noise.

---

<sup>25</sup> This area of research appears to be forming a subfield in its own right, the first conference on *multiscale geometric analysis* was held at UCLA in 2003 January. There is as yet no review article, but a lecture series is available online [224].

<sup>26</sup> The MSE in using only the largest  $N$  curvelets to represent step edge snaking its way  $C_2$ -smoothly across a plane falls as  $N^{-2} \log^3 N$ , faster than wavelets at  $N^{-1}$  and sinusoids at  $N^{-1/2}$ . No reasonable scheme, including adaptive schemes, can do better than  $N^{-2}$  [223].

### 3.7.5 Deconvolving diffraction: Curvelets instead of wavelets?

We saw in §3.5.1 that the deconvolution is analogous to denoising with coloured noise. In our case we had to first regularise the deconvolution so that the coloured noise has finite variance; nevertheless, the formal analogy is valid. The prospects are bright for a *Fourier-curvelet regularised deconvolution (ForCuRD?)*: curvelets seem to be even more economic than wavelets for representing the signal, and the coloured noise should be at least as homogeneous as in the wavelet basis. There the noise was homogeneous across position in the image, and flat at fine scales but boosted at coarse scales due to the high-pass nature of the convolution. Curvelets will show similar behaviour across position and scale, however the noise should be completely homogeneous across orientation and microlocation. In comparison to wavelets, we might reasonably expect the signal to be concentrated in fewer curvelets *and* the noise to be more evenly spread across the spectrum of curvelets. Simple denoising does not enjoy this additional benefit of further noise decorrelation as white noise remains white no matter how it is represented.

Two papers published in last six months consider curvelet deconvolution. The first shows that the curvelet frame almost diagonalises the Radon transform [186]. The second, published as I write this Chapter, discusses deconvolution by combined wavelet-curvelet methods [231]. Fourier inversion followed by wavelet-curvelet removal of the coloured noise is mentioned but discarded in favour of an iterative method. A deconvolution of Gaussian-blurred test image yields a much clearer result than a wavelet-only approach. In this example, and in one denoising example [230], noise levels were rather high with Poisson equivalents estimated at 20 photons per pixel or fewer. Such results augur well for applying curvelets to real-world diffraction patterns at low exposures. Regrettably, having outlined the potential of curvelet methods, development must be left for future work [232].

### 3.7.6 Inverse problems and assumptions

Our inverse problem can be approached from numerous formalisms: Fredholm integral equations, linear algebra SVD, minimax statistical estimation and information theory are examples. Here I briefly review the preceding solutions from the *variational* point of view, introduced in §3.4.2.

We seek optimal agreement between the estimated column-density  $\rho_{\text{est}}$  and the observed contrast  $C_{\text{meas}}$ . To render the estimate *stable* and *unique* we use some prior knowledge about the column-density, that is, we make *assumptions*. From the vari-



**A** Undecimated wavelet denoising. Performs least well on elongated sections: hat brim, background.



**B** Curvelet denoising. Performs least well on small point-like structures: eyes, nostrils etc.



**C** Hybrid wavelet-curvelet denoising. Residual shows no structure, denoising approaching optimal.

ational point of view, we minimise some measure of the error between the estimate and the observation, subject to a constraint representing the prior information.

The Fresnel iterative solution discussed in §3.1.6 is readily understood in this framework: the estimate is constrained to the observation in the diffraction plane and to the assumptions – positivity, compact-support etc – in the object plane. The Wiener filter was derived *explicitly* by optimisation, under the assumption of a *stationary and known* power spectrum. The simple Tikhonov filter was derived with a much weaker assumption – equivalent to assuming constant SNR – which was too far removed from reality to yield useful estimates for our inverse problem.

A much better assumption seems to be that the *column-density image is of the form of a real-world image*. Such images have spatial frequency spectra which broadly follow a power-law, and under this assumption we constructed a partial-Tikhonov filter with performance approaching the Wiener filter. The assumption has an inherent contradiction, however, as the power spectrum is not a well-defined quantity for a non-stationary real-world image. The hybrid Fourier-wavelet algorithm makes use of our assumption of real-world images *implicitly*. Wavelet filtering improves the estimate only of signals economically represented by wavelet bases. Translated into mathematics, our assumption of real-world images is an assumption that the image is a *member of a smoothness class of functions*.

The real-world image assumption is a rather imprecise one. A recent article [233] argues that several supposedly distinct features of natural images – non-Gaussian statistics and inter-scale correlations for example – are merely results of the *ubiquity of edges* in natural images. Suggestions that this ubiquity leads to power-law spectra were discussed in §3.4.4. The more precise description *images smooth apart from smooth edges* is perhaps justified.

In seeking enhancements to the elaborated partial-Tikhonov FORWARD method, we must be very careful in making further assumptions about the column-density image. An array of magneto-optically trapped atom clouds, for example, might have a column-density well described by a sum of Gaussians. These would be economically represented in one of the smoother wavelet bases, and it *seems* that

---

**FIGURE 3.19 (ON FACING PAGE) Hybrid curvelet-wavelet removal of white noise.** Denoised images (left column) and residuals (right column) for *Lena* image with approximately 10% white noise, similar to Figure 3.17A. See PDF version of thesis for clearer reproduction. Images reproduced from Reference 229, first published in Reference 208.

curvelets would do little worse than wavelets, but as there are no edges would probably do little better. Some prior and less able edge-based methods [234] [49, Figs 6.11,10.7], which work very well on *Lena*, would likely perform very poorly indeed on edgeless Gaussians.

This is the fundamental trade-off made in solving inverse problems: we must assume enough about the signal to ensure *stability* and *uniqueness* of the solution, but we must not assume so much that we *prejudice* the solution by excluding possible column-densities which fall outside an assumption. Our assumption – smooth column-density except for possible smooth edges – seems to strike a good balance.

One assumption which we have *not* made is that the *column-density is positive*. There is no question that this is an impeccably justified assumption: the solutions it excludes are unphysical. There is no risk of prejudicing our solution by including it, so why don't we? Unfortunately, there is no simple method for including this constraint in our direct algorithm, although it is readily incorporated into iterative solutions [231]. The assumption is desirable, but we have not the mathematical eloquence to express it.



THE INVERSE PROBLEM is solved. Although the Fourier-wavelet solution is not perfect, it is a definite advance on the unaugmented partial-Tikhonov filter. Images of cold-atom column-density retrieved with the Fourier-wavelet solution are presented in Chapter 5.

## 3.8 Optimising the propagation distance

So far we have discussed retrieving the most information possible from a diffraction pattern obtained *at a given propagation distance*. It is time to extend this discussion and consider the effects of varying the propagation distance.

### 3.8.1 Intuitive view of optimal propagation distance

Intuitively, there must be an optimal propagation distance for diffraction-contrast imaging. In the limit of zero distance, we have only absorption contrast. This represents optimal imaging only for purely absorbing objects, such as cold atoms imaged on resonance. Cold atoms off resonance, or any weakly absorbing x-ray object, are better imaged with some level of diffraction-contrast. Several considerations constrain the choice of propagation distance:

**Apparatus dimensions** It may not be possible to place the detector closer than some distance. For example, in the experiments described in Chapter 5, it is not realistic to place the camera inside the vacuum system.

**Far-field diffraction** The numerical aperture, and hence optical resolution, of a finite-sized detector falls as the propagation distance is increased. See §5.5.

**Slowly-varying phase condition (SVPC)** Recall from §2.5.6 that the CTF model is valid only when thick objects show a single diffraction fringe.

**Behaviour of the inverse problem** Further propagation yields higher contrast diffraction patterns, but a more oscillatory CTF.

This Chapter is concerned with the formal inverse problem, however, and so we assume that the detector may be placed at any distance from the object, and that the detector is infinitely large with infinitesimally small pixels. Further, the *Lena* simulation used in this Chapter has a maximum absolute phase-shift of 0.6 radian and so the SVPC is weakly satisfied regardless of propagation distance. In this Section, we consider only the *behaviour of the inverse problem* as a function of propagation distance.

Figure 3.20 shows our familiar simulation at three propagation distances, using an exposure of 10 photons per pixel. The propagation distances are those used in Figure 3.6: the short propagation distance shows only edge contrast and the retrieved signal is completely submerged in noise. The spectrum at right shows the coloured noise above the signal at all frequencies. The intermediate distance of 20 µm was used for most of the preceding simulations, in particular Figure 3.18 which showed 20 photons per pixel to be a lower limit for our simulated experiment at this propagation distance. Here, at 10 photons per pixel, coloured noise exceeds the signal across a broad band of low frequencies and this is manifest in the retrieved image. At 200 µm distance, the diffraction pattern is now full holographic with no recognisable structure. Increased SNR is obvious in the diffraction pattern, and the spectrum shows the signal remaining above the coloured noise up to mid-range spatial frequencies. The retrieval is unavoidably blurred but is free from coarse noise and artefacts.

Figure 3.21 simulates the same propagation distances, but with the much higher exposure of 1000 photons per pixel. These results may be compared with those re-

trieved with the TIE algorithm on p 88.<sup>27</sup> Again, the retrieval improves when  $z$  is increased from 1 to 20  $\mu\text{m}$ , however further increase to 200  $\mu\text{m}$  appears to degrade the quality of the retrieval. More quantitatively, the RMSE increases from  $-21.8 \text{ dB}$  at 20  $\mu\text{m}$  to  $-17.1 \text{ dB}$  at 200  $\mu\text{m}$ . The spectra make clear the improvement between near and mid-range images. They also show that further propagation only introduces additional contrast nulls, and moves the first contrast null to lower frequencies. As mentioned in §3.4.3, the partial-Tikhonov assumption – constant SNR above the first contrast peak – becomes less and less reasonable.

### 3.8.2 A quantitative comparison with Zernike phase-contrast

Let us consider briefly the increase in contrast visible with increasing propagation distance. We might quantify the total contrast by an RMS value of the dimensionless contrast  $C(\mathbf{x}) = I(\mathbf{x})/I_0 - 1$  taken over the entire image. For the sake of comparison with a Zernike phase-contrast system, consider a pure-phase object  $\phi(\mathbf{x})$ . The mean-square diffraction contrast is given by the norm

$$\begin{aligned} \|C_{\text{DCI}}(\mathbf{x}; z)\|^2 &= \|\tilde{C}_{\text{DCI}}(\mathbf{u}; z)\|^2 = \|2\tilde{h}(\mathbf{u})\tilde{\phi}(\mathbf{u})\| \\ &= \int_{-\infty}^{\infty} |\sin \pi \lambda z u^2|^2 |2\tilde{\phi}(\mathbf{u})|^2 d\mathbf{u}, \end{aligned} \quad (3.36)$$

and if the variation of  $\sin \pi \lambda z u^2$  is highly oscillatory across the spectrum  $\tilde{\phi}(\mathbf{u})$ ,

$$= \frac{1}{2} \|2\tilde{\phi}(\mathbf{u})\|^2 = \frac{1}{2} \|2\phi(\mathbf{x})\|^2; \quad (3.37)$$

as the mean-square value of  $\sin^2 x$  is one-half. Parseval's Theorem has been used *passim*. On the other hand, it follows from (1.7) that the mean-square Zernike phase-contrast is

$$\|C_{\text{ZPC}}(\mathbf{x})\|^2 = \|2\phi(\mathbf{x})\|^2. \quad (3.38)$$

Thus in the far propagation limit, the root-mean-square diffraction contrast is 71% of the RMS Zernike phase-contrast. In the Poissonian shot-noise limit, a DCI exposure would need to be twice as long as a Zernike exposure to have the same RMS contrast-to-noise ratio.

---

<sup>27</sup> The propagation distance and exposure values are the same, although the material used in the TIE simulation was more absorbing. A more stable retrieval, particularly at  $z = 1 \mu\text{m}$  would be obtained if the more absorbing material had been simulated.

This limit corresponds to propagation much further than even the holographic diffraction patterns at  $z = 200 \mu\text{m}$  shown in Figure 3.20 and 3.21. Diffraction patterns at more reasonable propagation distances must have much lower RMS contrast, but still yield retrievals of quality comparable to Zernike methods. The additional Zernike contrast is ‘wasted contrast’ at low frequencies where the signal already exceeds the coloured noise. Root-mean-square measures of *contrast* do not take this into account, and thus give a very incomplete picture of the RMS *error* in retrieval.

Contrast and signal-to-noise are more powerfully represented as functions of frequency, which has been the approach throughout this Chapter. Indeed, we have seen that increasing propagation distance reduces low-frequency instability, but further increases *degrade* retrieval quality. There must therefore be an *optimal propagation distance*, even from the formal perspective of this Chapter.

### 3.8.3 A minimax approach to optimal propagation distance

Here I mention how the variational approach to the inverse problem used in deriving the Tikhonov filter might be extended to optimising for the propagation distance. Rewriting the minimum-energy least-squares functional (3.26) with explicit dependence on propagation distance  $z$  yields

$$W(\tilde{\rho}; z) = \|\tilde{C}_{\text{meas}}(\mathbf{u}; z) - \tilde{h}(\mathbf{u}; z)\tilde{\rho}_{\text{est}}(\mathbf{u})\|^2 - \|\tilde{n}\|^2 + \frac{1}{\alpha} \|\tilde{\rho}_{\text{est}}(\mathbf{u})\|^2. \quad (3.39)$$

If  $z$  is assumed constant, minimising this functional over  $\tilde{\rho}$  yields the simple-Tikhonov regularisation formula (3.27). We would seek to minimise jointly over  $\tilde{\rho}$  and  $z$ , noting that the first engenders a variational derivative and the second a standard partial derivative. Recall, however, that the simple-Tikhonov filter proved ill-suited to our problem, and was modified to regularise only at frequencies above the first contrast peak.

A full solution to the problem of optimal propagation distance would be a significant exercise in approximation theory. Inspection of the spectra suggests that a good rule of thumb is to set the propagation distance so that the first contrast peak (the first minimum in  $\tilde{h}^{-1}\tilde{n}$ ) falls at a frequency 2–3 octaves below the intersection of the signal spectrum with the noise floor. For more absorbing objects, the gap could be somewhat less. The resulting diffraction patterns have more than two but less than, say, ten visible fringes around the largest scale structures in the object. Finally, it should be noted that the RMSE does not seem to be a very sensi-

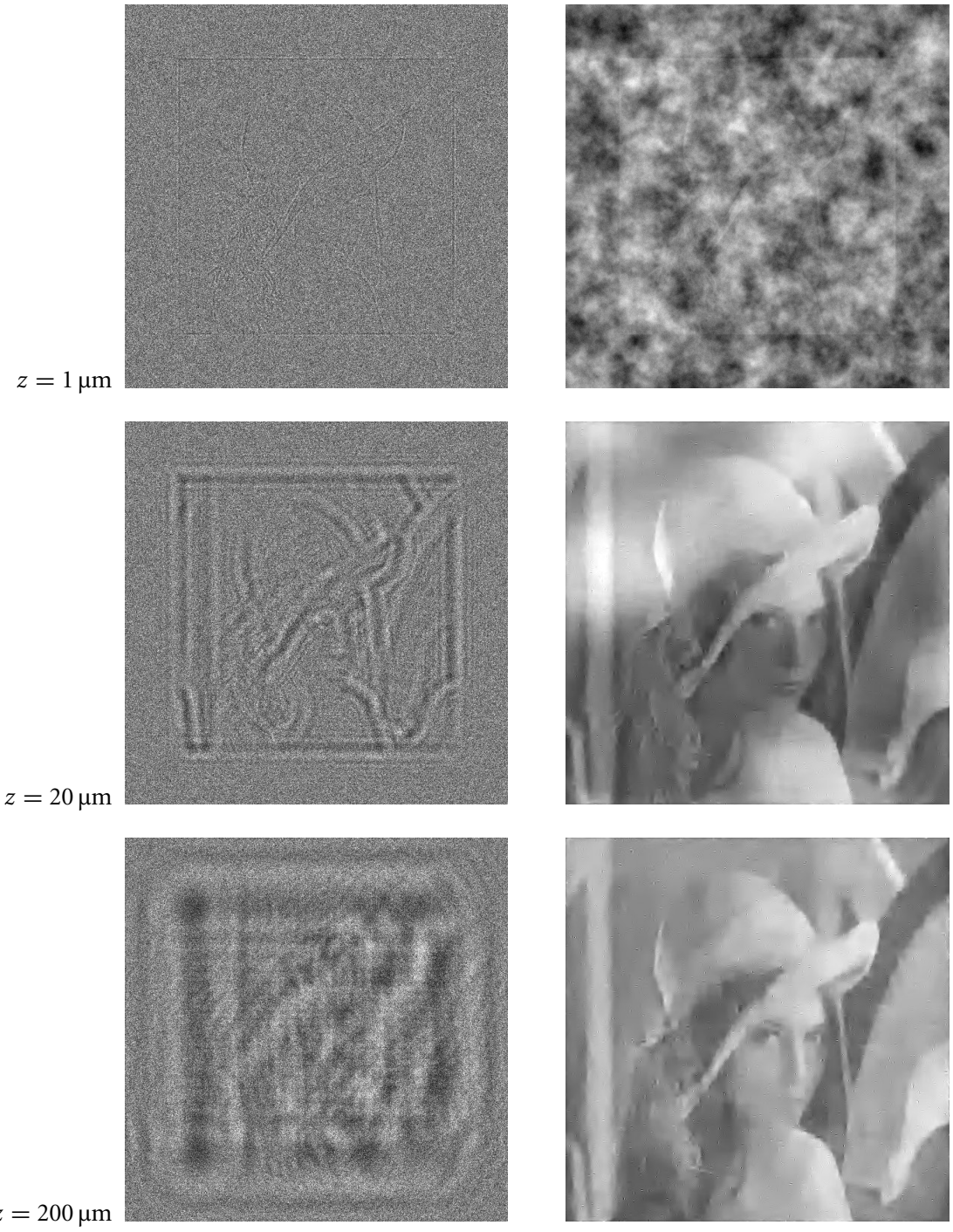
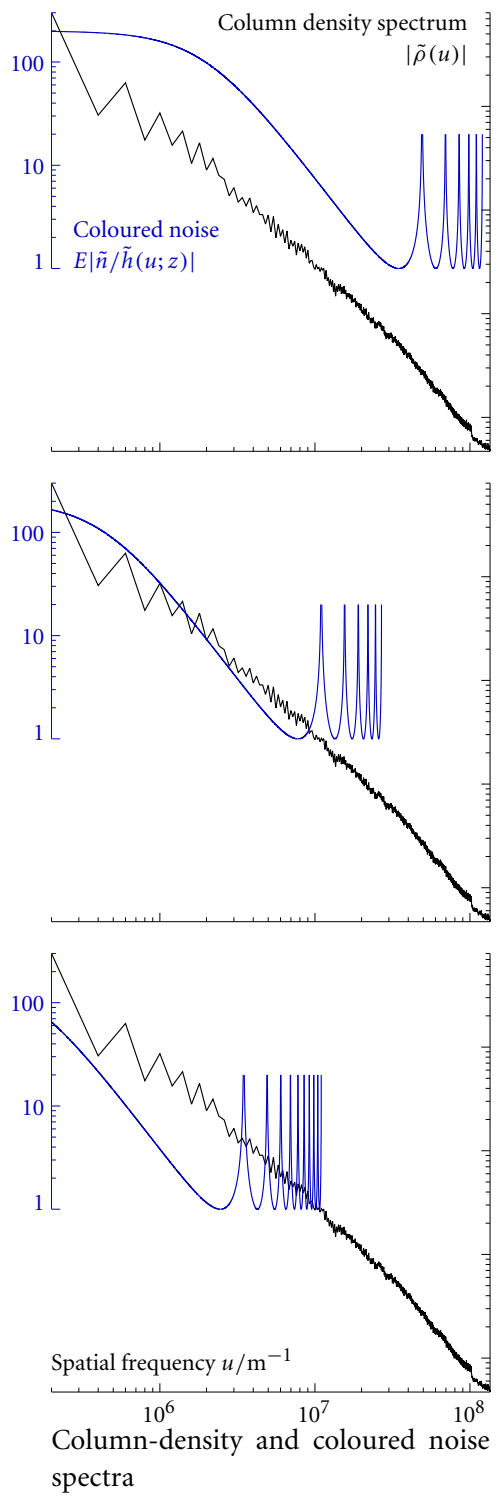
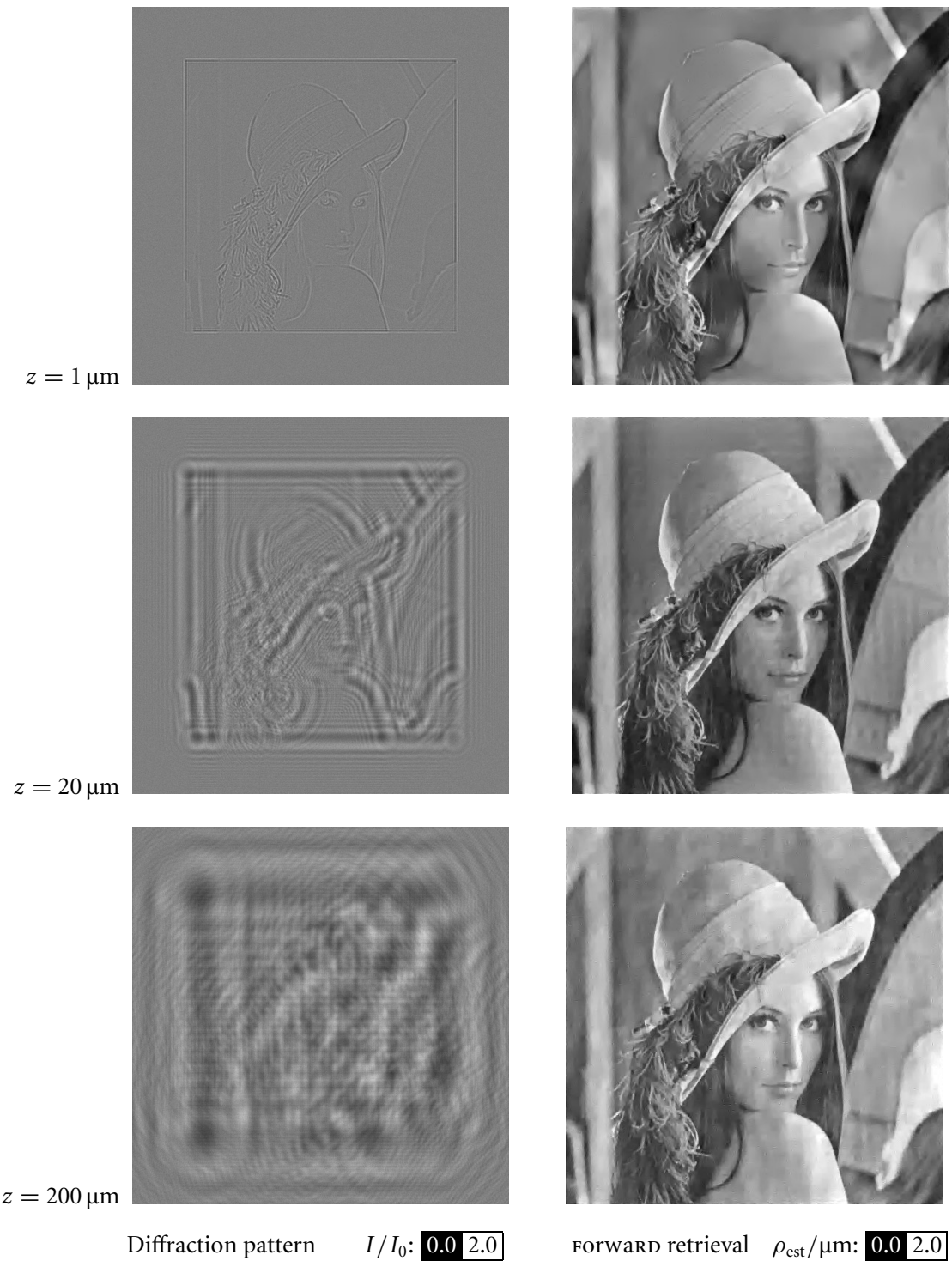
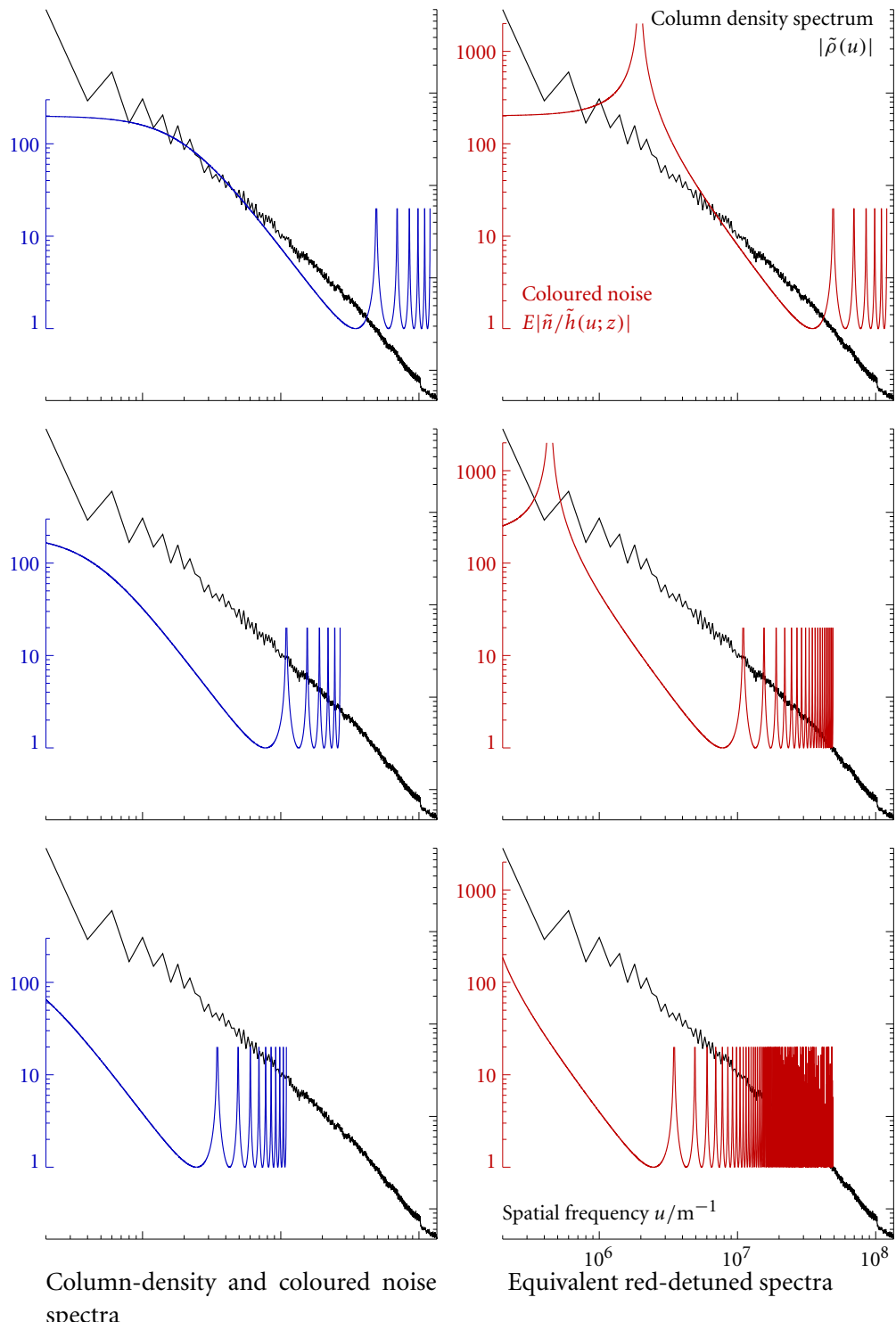


FIGURE 3.20 **Retrievals from 10 photon/pixel diffraction patterns at 3  $z$  values.**  
 Other simulation parameters as for Figure 3.13. forward  $\alpha$  optimised for each retrieval.





**FIGURE 3.21 Retrievals from 1000 photon/pixel diffraction patterns at 3  $z$  values.**  
 Other simulation parameters as for Figure 3.13. forward  $\alpha$  optimised for each retrieval.



tive function of propagation distance. We will see in Chapter 5 that apparatus and diffraction limits often determine the propagation distance in practice.

### 3.8.4 Uncertainties in the propagation distance

The propagation distance is an experimental variable and subject to measurement error. The effect of such error on retrievals is readily quantified by considering the CTFS for a correct value of  $z$  and an erroneous value  $z + \Delta z$ . The sinusoids will dephase as  $u$  increases. At the point where the arguments  $\pi\lambda zu^2$  differ by  $\pi/2$ , a contrast null frequency containing only noise is passed with unit amplitude, and a contrast peak is eliminated. Selecting  $\pi/4$  as a reasonable cutoff, the maximum frequency  $u_{\max}$  passed with acceptable distortion is found by

$$\pi\lambda(z + \Delta z)u_{\max}^2 - \pi\lambda zu_{\max}^2 = \frac{\pi}{4} \quad (3.40)$$

and so

$$u_{\max} = \frac{1}{2\sqrt{\lambda\Delta z}}, \quad (3.41)$$

or, equivalently, structures larger than  $\sqrt{\lambda\Delta z}$  are minimally distorted. This is merely the *depth of field* of any coherent imaging system.

In practice, fine adjustments to the measured propagation distance may be made in software. The distance is adjusted until fringes or halos in the retrieved image have disappeared. This is an example of the holographic nature of the retrieval process, introduced in §3.1. Such an adjustment might be used initially to calibrate the absolute distance from object to detector, with subsequent offsets of a translation stage being sufficiently precise that further numerical focusing is not required.

Finally, recall from §3.2.4 that electron microscopists have developed spectral estimation techniques for extracting propagation distance information from the diffraction pattern. Very recently, similar methods have been suggested by workers from the optics and signal processing community [235]. These methods might be useful for automated retrieval, but robust estimation is difficult, and less relevant to our case where a good initial measurement of propagation distance is available and numerical fine focusing is readily achieved.

### 3.8.5 Propagation distance and red-detuned imaging

The low-frequency instability when retrieving objects made of phase-retarding (positive  $\delta$ ) materials was discussed in §3.2.3, and thereafter phase-advancing materials have been assumed.

The right-hand column on p 133 breaks with this assumption and shows the signal and coloured noise spectra for a material with equal but opposite  $\delta$  to that used in all other simulations in this Chapter. At  $z = 1\text{ }\mu\text{m}$ , a broad range of low frequencies are well below the coloured noise level and any retrieval (not shown) is heavily distorted. At  $z = 20\text{ }\mu\text{m}$ , only a narrow band of the very lowest frequencies in the image is affected, and by  $z = 200\text{ }\mu\text{m}$  the low frequency null occurs at a frequency lower than any component of the image, and a successful retrieval is possible.

Formally, the low-frequency null for positive  $\delta$  occurs when the argument to sine in the CTF is zero, that is when

$$\pi\lambda z u^2 - \arctan \beta/\delta = 0. \quad (3.42)$$

Solving for spatial frequency yields

$$u^2 = \frac{\arctan \beta/\delta}{\pi\lambda z}. \quad (3.43)$$

If the image size is  $D$ , then the lowest spatial frequency in its transform is  $1/2D$  and so if we choose a propagation distance

$$z > \frac{4D^2 \arctan \beta/\delta}{\pi\lambda} \quad (3.44)$$

the low-frequency contrast null will not affect the retrieval. As will be shown in §5.5, the diffraction limit due to finite detector size is  $2\lambda z/D$  and so if  $z$  is chosen to just satisfy (3.44) then the diffraction-limited resolution is

$$a = \frac{8}{\pi} D \arctan \frac{\beta}{\delta}. \quad (3.45)$$

The clear corollary is that this fix is only viable for phase-retarding materials which are highly transparent with small absorption ratio  $\beta/\delta$ .

This Article has considered the effect of errors in the propagation distance. Errors in the other transfer function parameter – the absorption ratio  $\beta/\delta$  – have

a much less significant effect on retrieval, affecting only low frequencies. In x-ray and cold atom imaging,  $\beta/\delta$  is likely to be known to high accuracy. Of course, the presence of materials with differing absorption ratios is quite possible, and would cause substantial artefacts in the retrieval. This would, however, be a violation of the monomorphous object assumption on which this thesis is predicated, and is not further considered.



THIS COMPLETES the theoretical component of this thesis. In Chapter 2, a linear shift-invariant system was derived, which takes the column-density of a monomorphous object and returns the dimensionless contrast of its diffraction pattern. In this Chapter, I have shown how the inverse problem may be solved and the column-density retrieved from the diffraction pattern. The following Chapters describe how this solution was applied to specific experiments in cold atom imaging, and simulated experiments in x-ray microscopy.

## Chapter 4

# Atom trapping and imaging apparatus

THIS CHAPTER DESCRIBES the magneto-optical trap and associated imaging apparatus that I constructed during 2001–2. Background to the trap design is covered in §4.1 and details of the vacuum (§4.2) and coil (§4.3) systems follow. An external cavity diode laser system was a major component of this apparatus. Section 4.4 to 4.6 on pages 149–158 describe the mechanical and electronic design of this laser system in detail. The final Section describes an imaging system for producing off-resonant defocus-contrast images. Retrieval of column-density information from these images is discussed in the next Chapter.

### 4.1 Design of the apparatus

The original motivation for building the apparatus was not to provide a trapped sample of cold atoms for optical imaging experiments, but rather to provide a slow, cold atom beam for matter-wave phase imaging experiments. Preliminary results on matter-wave phase imaging were obtained by Phil Fox in 2000–1, using a thermal atomic beam (see Appendix F beginning p 323). Imogen Colton and I modelled the phase imaging process and determined that to obtain phase resolution approaching that of standard atom interferometers would require an atom beam with much higher transverse and longitudinal coherence – *spectral brilliance* in beam parlance – than the velocity-selected thermal beam. It was decided that a cold atom beam would be developed to pursue non-interferometric phase measurement of matter waves. The beam may also be employed in investigations of light fields for atom

focusing and lithography.

#### 4.1.1 Cold atomic beams

The first high spectral brilliance atomic beams were derived from standard effusive oven or discharge sources. The beam is typically collimated with a one or two-dimensional optical molasses transverse to the beam, before entering a Zeeman slower which greatly reduce the longitudinal velocity of the beam, at the expense of its angular divergence. The resulting beam is well-suited to loading atoms into magneto-optical traps, and such apparatus is employed in many laboratories. Loading magnetic guides [236], and other applications such as atom interferometry [237], place more stringent demands on the coherence of the beam.

Coherence may be improved by further magneto-optical compression and focusing stages [238–240]. The background of thermal atoms inadequately slowed by the Zeeman slower may be removed by spatial filtering [241] or by deflection of the cold atoms from the initial beam axis [242]. While the coherence of such cold atomic beam is very high, the apparatus is elaborate: the cesium beam of the Meschede group [242] is over 4 m long and the metastable helium beam of the Beijerinck group [241] is over 15 m with multiple lasers and vacuum pumps required.

Early versions of the magneto-optical trap (*MOT*) [1] were loaded with effusive beams. It was soon shown that a MOT could be loaded quite rapidly from a thermal vapour [243], and this has become the standard loading method for atom traps. Over the last decade, such vapour-cell MOTs have been developed as *sources* of cold atoms, initially with pulsed ejection of atoms from the trap and later [244] with continuous ejection; a review may be found in [245]. The apparatus is much more compact than effusive beamlines – a recently described source occupies less than  $20\text{ cm}^{-3}$  – and there is a concomitant reduction in laser power requirements.

In early 2000 it was decided that I would develop a vapour-cell trap source for phase imaging applications and that a separate Zeeman-slowed oven source would be developed by Anton Barty and Luke Maguire for atom lithography applications.

#### 4.1.2 Design for a cold atomic beam

A literature review in January 2000 identified a cold beam source [246] constructed by the Thomann group as the most appropriate design for matter-wave phase measurement. In its simplest form, the Thomann source consisted of a three-dimensional *optical molasses* (*OM*) [247, §7] in which two pairs of beams were detuned to

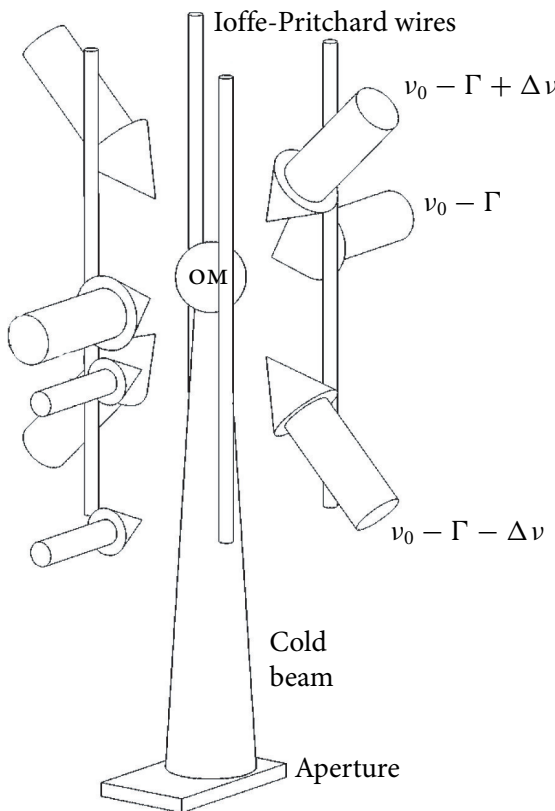


**FIGURE 4.1 The Thomann cold atomic beam.** The Ioffe-Pritchard current-carrying bars are not required when operating in moving optical-molasses (OM) mode. Adapted from Reference 246.

form a *moving molasses*, ejecting slowed atoms into a beam of well-defined velocity. A conventional MOT consists of a 3D OM with a concentric spherical-quadrupole magnetic field generated by anti-Helmholtz coils [247, §11.4]. The apparatus may therefore be operated as a standard MOT with stationary molasses and the anti-Helmholtz coils on, or as a cold beam source with moving molasses and coils off.

The geometry of this beam apparatus is shown in Figure 4.1. Upwards propagating beams are detuned  $-\Delta\nu$ , and downward beams  $+\Delta\nu$ , from the optimal OM frequency used for the lateral beams, which is typically around 2 natural linewidths  $\Gamma$  red of the cooling transition. Atoms are cooled in the reference frame moving downwards along the bisector of the detuned beams at a velocity of  $v = \sqrt{2}\lambda \Delta\nu$ . At small beam velocities of a few metres per second, the beam is usually oriented vertically upward (fountain configuration) or downward; in this

TABLE 4.1 Beam parameters of the Thomann source.

Longitudinal velocity $v_l$	Nominally 1–12 m/s
Min $v_l$	Flux falls below $10^7$ atoms/s for $v_l < 1$ m/s
Max $v_l$	Flux falls for $v_l > 8$ m/s due to capture rate
Longitudinal temperature	70 $\mu$ K or 0.15 m/s FWHM velocity spread
Transverse temperature	70 $\mu$ K, representing the OM Doppler limit
Angular divergence	15 mrad at $v_l = 10$ m/s
Beam area	Above fluxes through $5 \times 3$ mm aperture
Flux	Peak of $1.3 \times 10^8$ atoms/s at $v_l = 8$ m/s.

case, a falling beam was chosen.

Although the apparatus described in this Chapter has not yet been used to generate a cold beam, the Thomann apparatus produced a cesium beam with the properties tabulated in Table 4.1, and similar results would be expected from a rubidium source.

The very low longitudinal velocity and longitudinal velocity spread, as well as the low transverse temperature, make the source attractive for non-interferometric phase measurements. Much lower ‘beam’ temperatures, as low as 200 nK and below the photon recoil limit, have been achieved by Raman sideband cooling in a moving optical lattice. These pulsed sources are not continuous beams, however. Since 2000, the 2D-MOT seems to have become the preferred trap source [248]. A 2D-MOT constructed by the group of Pfau achieves a flux of  $6 \times 10^{10}$  atoms/s, approaching that of Zeeman-slowed oven systems [245]. The source used by Prentiss’ group produces a slow beam with longitudinal velocity 2 – 15 m/s at a somewhat lower flux of  $8 \times 10^9$  atoms/s [236]. Neither system attains the cold longitudinal temperature available with optical molasses sources.

While the cold beam was designed for matter-wave phase imaging, its likely coherence properties would also make it an excellent beam for atom lithography: a recent quantum-mechanical analysis of atom lithography cites the Thomann design, commenting ‘...the beam properties are nearly ideal...’ [249]. The low velocity would potentially be useful for arbitrary pattern deposition, and the low longitudinal temperature would reduce chromatic aberration.

#### 4.1.3 Design for a magneto-optical trap

Preliminary research during 2001 sparked interest in optical imaging of cold atoms using non-interferometric methods. The project was reoriented towards non-inter-

ferometric analysis of *optical* wavefields passing through cold atom objects.

It was resolved to construct the vacuum system and optical mounting hardware for the cold atomic beam, but initially to operate the apparatus as a conventional MOT. This MOT provided the cold atom sample for the diffraction-contrast imaging experiments discussed in the next Chapter.

A downward pointing cold-atom beam was preferred over an upward ‘fountain’ configuration. This required elevating the MOT chamber above the optical table, and building vertical breadboards to mount the trap optics. The trap chamber was designed for the best possible optical access consistent with welded construction.

The next two Sections describes the MOT vacuum system and magnetics and the following Sections describe the laser and optical systems for the MOT and for diffraction-contrast imaging.

## 4.2 Vacuum system

This Section discusses the design of the MOT vacuum system, bakeout of the vacuum system prior to the experiment, and the getter source of rubidium.

### 4.2.1 Chamber design

For reasons of flexibility and cost, the vacuum system was constructed from standard ultra-high vacuum (*UHV*) vacuum fittings made from 306 stainless steel. Figure 4.4 shows the system. A custom chamber (Figure 4.2) was constructed from a CF-600<sup>1</sup> nipple with eight radial CF-275 flanges on half-connectors to accommodate: the four diagonal trapping beams, a feedthrough for the getter source, a beam exit port and two additional optical accesses for a probe beam or imaging system. The half-connectors for the trapping beams are 35 mm inside diameter (*ID*), while the other flanges are on 25 mm *ID* half-connectors.

The chamber is connected to a CF-600 T-piece providing 100 mm unobstructed diameter of optical access for the horizontal trapping beams and potentially for other purposes. Three additional CF-275 flanges were welded to the T-piece, at present one accommodates a cold cathode ionisation gauge, another a metal-bonnet angle-valve for initial pump down (see §4.2.4). The stem of the T-piece connects to an ion pump via a 800 mm CF-600 connector.

---

<sup>1</sup> Industry-standard Conflat metal knife-edge flanges, CF-xxx, where xxx is the outer diameter of the flange in hundredths of an inch.

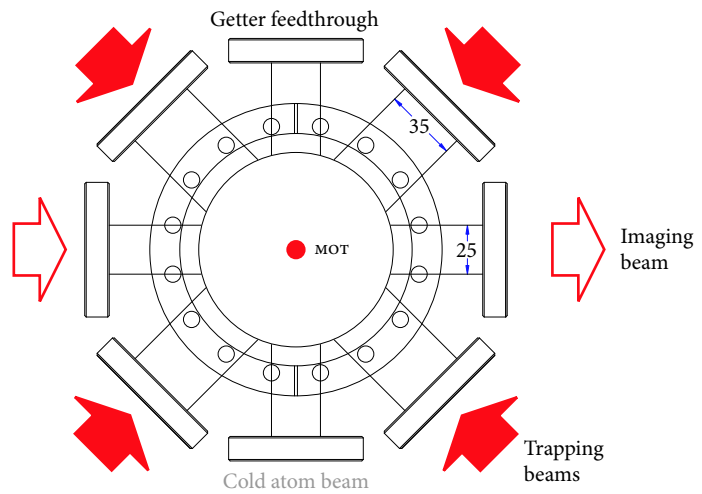


FIGURE 4.2 MOT chamber side view showing ports.

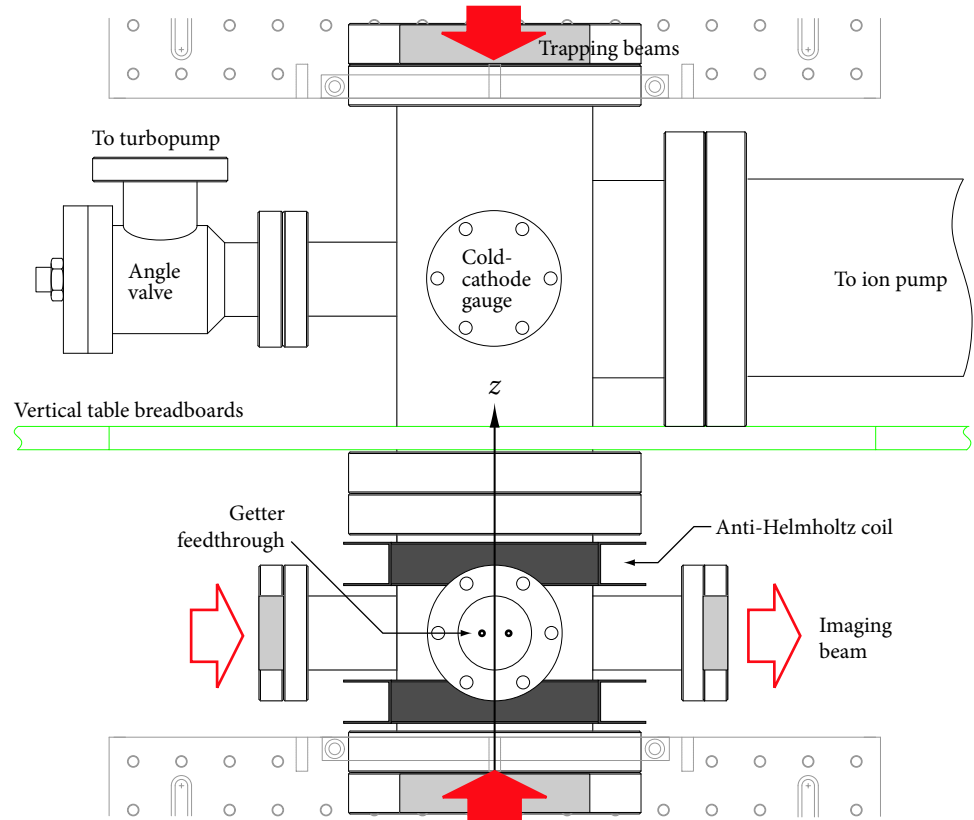


FIGURE 4.3 MOT chamber plan view showing coils, pumps and gauges.

### 4.2.2 Mechanical design

The entire system (Figure 4.4) is mounted so that the trap centre is 700 mm above the optical table. A modular system of optical breadboards surrounds the vacuum system and supports the trap optics, imaging optics and has provision for optical access to a downward propagating cold beam (Figure 4.4). Both support structures are rigid, but particularly strong cross-bracing with viscoelastic vibration damping connects the optical breadboards to the optical table (see §4.4.3). The vacuum and optical support structures are mechanically connected only through the optical table. Vibration of the more massive vacuum system is thus not coupled to the cold atom sample through movement of the trapping beams. As currently constructed, however, the anti-Helmholtz coils and the horizontal trapping beam mirrors *are* attached to the vacuum support rather than the optical support.

In practice, this level of vibration isolation is only required for very high precision measurements, such as atom interferometry, and is not of concern for the imaging experiments described in this thesis.

### 4.2.3 Windows

It is desirable to have anti-reflection (*AR*) coated, optically flat windows to admit trapping and probe beams to the vacuum chamber. The glass of conventional vacuum viewports is bonded to the stainless steel flange in a high temperature brazing process which distorts the glass; wedge distortion and surface undulations of several wavelengths are typical. Of even greater concern for imaging work are any scratches or point imperfections – bubbles, inclusions and the like – on the surface or in the volume of the glass. When illuminated with coherent laser light these produce prominent diffraction rings which are one of the major sources of image noise.

A paper by M Kasevich describes a technique for forming a bakeable UHV seal between a glass window and a conflat knife-edge [250]. The windows used were 12 mm thickness *AR*-coated borosilicate glass optical flats. I attempted to seal these to the MOT chamber using the Kasevich technique. A knife-edge was machined into a standard copper gasket; the copper knife seals against the glass and the stainless-steel flange knife seals against the other, unworked, side of the copper gasket. A precision torque wrench was used to increase the bolt torque gradually to 4 Nm at which point gross leaking stopped. Unfortunately, one or two of the eight windows cracked on each of three successive bakeouts.

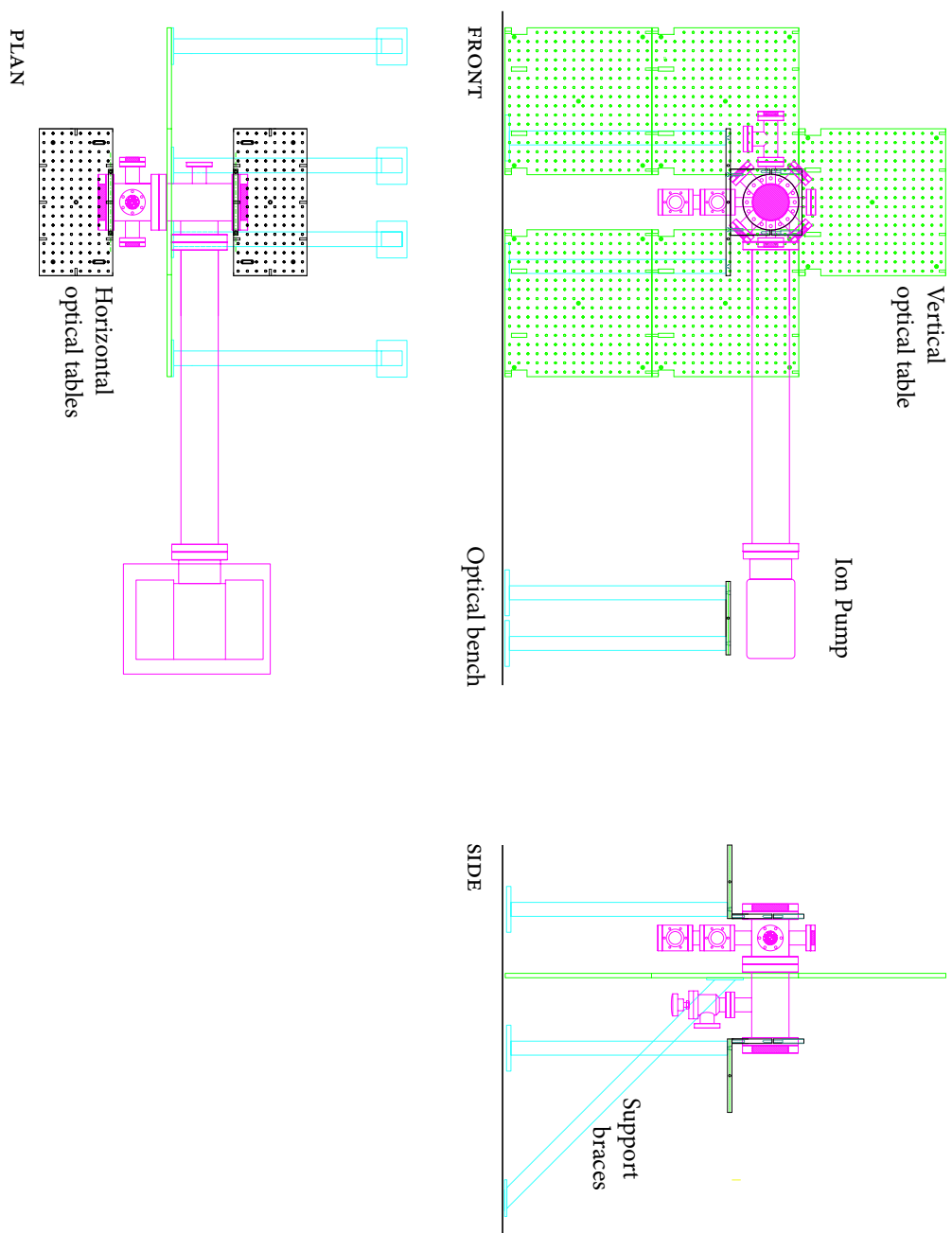


FIGURE 4.4 **Vacuum system and support structure.** The short cold beamline shown descending below the MOT chamber was not implemented.

Standard Viton fluoroelastomer gaskets were used instead to seal the optical flats to the vacuum chamber. Viton is generally eschewed in UHV due to outgassing and limits on bakeout temperature. The maximum temperature was already limited to 200 °C by other components (see §4.2.5). It has been shown that baking Viton gaskets *in situ* at 150 °C for 4 hours reduces the outgassing rate by a factor of one thousand to around the level of unbaked metal gaskets [251]. The pressure is then limited by air *permeation* through the elastomer seals [252].

The horizontal trapping beams enter through standard uncoated CF-600 viewports. This does not seem to adversely affect operation of the trap.

A rebuilt experiment might use Helicoflex seals [253], although users have noted that special preparation of flange faces is required [254, p 35]. Recently, a bakeable seal to glass has been reported using lead solder [255]. This seems a promising and simple approach should future experiments require substantially lower background pressure.

#### 4.2.4 Pumps and gauges

Ion pumps are ideal for vapour cell experiments. Getter sources outgas much less than oven sources, and so the relatively slow pumping speed of ion pumps is not a problem. Ion pumps are clean, vibration free, reliable and relatively inexpensive with base pressures below 10<sup>-10</sup> mbar possible. Although pumps as small as 2 L/s have been employed [256], a relatively high capacity 60 L/s Varian 911-5034 triode pump was selected. A Varian 921-0062 controller supplies -5800 V. If the getter source is switched off, the pump has sufficient capacity to reduce the background pressure for experiments requiring long trap lifetimes.

There was some concern that the substantial magnetic fields surrounding the ion pump could disturb cold beam experiments. Field compensation would be required in any case, however magnetic shielding impedes optical access and so the pump was exiled more than one metre from the trap centre on the end of a 800 mm long 98 mm ID connector. The total magnetic induction 1 m from the pump is less than 3 mT. The conductance  $C$  in L/s of dry air at 20 °C through a long tube in the molecular flow regime is given by

$$C = 0.116 \frac{D^3}{L}, \quad (4.1)$$

where  $D$  is the tube diameter and  $L$  its length, both in millimetres [257]. The effective pump capacity is reduced to 45 L/s and so use of longer tubes is counterpro-

ductive.

Ion pumps must be started at pressures below  $10^{-4}$  mbar. A cold-cathode ionisation gauge (Pfeiffer IKR-270, all-metal construction) indicated when the starting pressure was reached and monitored the pump down. During bakeout, the gauge-head electronics must be removed, and during normal operation the strong magnet on the gauge is also removed to reduce perturbing fields. The ion pump current provides a rough measure of pressure in the chamber at these times.

#### 4.2.5 Pump-down and bakeout

All stainless steel components and copper gaskets were cleaned in an ultrasonic bath, first in water and detergent, then in distilled water, then in acetone and finally in ethanol. At atmospheric pressure, a turbomolecular pump (Pfeiffer TMU-261) was attached via a zero-length reducer to the angle valve. The turbomolecular pump was backed by a Pfeiffer DUO5 oil-sealed rotary pump via a zeolite foreline trap. The ion pump was started once a pressure of  $10^{-4}$  mbar was achieved and the angle valve closed. The turbomolecular pump could then be disconnected. After several days pumping, the pressure stabilised at  $1.8 \times 10^{-8}$  mbar.

A continuously loaded vapour-cell MOT is little affected by background gas at this pressure. With a view to future precision measurement experiments, it was decided to reduce the base pressure by baking the system. With the angle-valve knob removed, the temperature-critical components which remained were: the Viton seals (rated at 150 °C, but easily capable of 180 °C for extended periods [251]), the angle-valve (rated at 204 °C), and the enamel insulation of the wire used in the anti-Helmholtz coils. In a test, the polyester-imide insulation (rated 20 000 hour temperature index of 207 °C) discoloured at 220 °C and smoked at 260 °C. Type-K thermocouples were attached at the extremities of the apparatus and near one window. By maintaining the thermocouple readings below 150 °C, one would expect to maintain the maximum temperature below 200 °C. Glass-fibre insulated heating tape was firmly attached to the chamber, long connector and ion pump with glass-cloth bandages. The entire system was wrapped in rockwool insulation blankets (Fibretex 350, 25 mm thickness, aluminium foil backed. R-value: 0.74 m<sup>2</sup>K/W, rated to 350 °C. Bradford Insulation, Ingleburn NSW, Australia).

The successful bakeout with Viton window seals proceeded as follows. The heating power was increased over 2 days to 110 W, the temperature stabilising at 156 °C at the ion pump and 144 °C at the MOT chamber. This temperature was

maintained for 14 hours before ramping down the heating power over another day. During the cooling phase, the getter was heated with a current of 2.3 A to prevent condensation of contaminants on the reactive load. Ion pump current was 2 mA during the 14 hr bake period but fell to 2  $\mu$ A when cold. The remounted cold-cathode gauge read  $3.5 \times 10^{-9}$  mbar, rather better than might be expected from a Viton air-permeability model [252]. Over the following 18 months, the pressure has increased to of order  $3 \times 10^{-8}$  mbar, not high enough to be of concern for simple trapping experiments; this may be due to compression-setting of the Viton or progressive failure of the ion pump.

Finally, a cautionary note. During one bakeout attempt, the system was left unattended over night. The temperature had been stable at 65 °C for over an hour, and the pressure as measured by the ion pump current had been decreasing for 30 minutes having remained constant for three hours prior to that. On returning eight hours later, a considerable quantity of smoke was present in the laboratory, the ion pump current was over 100 mA and the ion pump thermocouple read 205 °C! The ion pump electrodes lose heat only through radiation or conduction down very narrow stainless steel supports. Thermal runaway may occur when outgassing contaminants on the electrodes increase the discharge current, heating the electrodes and stimulating further outgassing. I surmise that the reconditioned ion pump arrived with electrode contamination, and due to the poor thermal coupling between electrodes and the pump body, runaway occurred several hours after the pump body had come to thermal equilibrium. A high-current interlock on the ion pump controller failed, causing continuous operation of the ion pump at several hundred watts dissipation. The interlock was repaired and a thermal interlock installed in the heating circuit prior to the next bakeout. Install and test redundant interlock systems before leaving a bakeout unattended!

#### 4.2.6 Rubidium source

Early vapour-cell apparatus used the vapour pressure of liquid rubidium distilled into a glass cell and connected to the main chamber by a controlled leak [256]. We use a *getter source* (SAES Getters SpA, Lainate, Italy), a small oven containing rubidium chromate and a reducing agent equivalent to 3 mg Rb which emits rubidium vapour when heated with a few amperes of current [256, 258, 259]. The getters may be handled with only normal vacuum hygiene precautions.

The getter is attached to an electrical feedthrough with standard CuBe screw

connectors. It exhibited the expected threshold emission behaviour, although nearer to 3.5 A than the 2.5 A reported elsewhere [258]. Fluorescence from the MOT was brightest at getter currents around 4.5 A, with trapping beams only weakly visible due to fluorescence of the background vapour. The vapour became optically thick around 6 A. At 8 A a metallic layer of rubidium was visible on the stainless steel walls and the viewports took on a blue translucency. The deposited rubidium was evacuated after a few hours. These results are broadly consistent with other reports [259]. In normal operation, the getter current is maintained around 4.5 A for the duration of the experiment. Other groups have observed that getter performance is unchanged after several months of full-time equivalent operation.

### 4.3 Magnetics

In the simplest model of a MOT, the optical molasses provides a *damping force* on atoms proportional to their velocity, while a magnetic field provides a spring-like *restoring force* proportional to the atom's distance from the zero-field point [247, §11.4]. The appropriate magnetic field is created by two identical coils in anti-Helmholtz configuration: separated by one radius with equal but counter-circulating currents.

Very high magnetic field gradients have been used to trap a single atom in a MOT [260]. The more common goal is to trap as many atoms as possible, and here the required field gradients are modest. An axial gradient of around 1 mT/mm (10 G/cm) is optimal across a rather wide range of trapping beam sizes and intensities [261].

#### 4.3.1 Coil design

This gradient is readily achieved with anti-Helmholtz coils external to the vacuum system. It is a somewhat surprising result, however, that for a fixed gradient and cross-sectional area of the coil, the heat dissipated in the coils scales as the 5th power of the coil diameter; see Appendix E. By the simple expedient of winding the coils around the 100 mm OD of the connector rather than the 150 mm OD of the flange, the typical dissipated heat is reduced from 95 W to 14 W. Water cooling might be required for the former, but free convection is sufficient to cool a 14 W coil pair. A disadvantage is that once wound onto the vacuum tank, removal of the coils would require unwinding the entire coil.

### 4.3.2 Coil construction

Two split-ring U-section coil formers were placed around the MOT chamber, and the whole chamber rotated in a lathe to wind on the wire. A Teflon (PTFE) sheet was placed between the aluminium former and the chamber, allowing the coils to slide along the chamber for spacing adjustment. Aluminium tube was welded to one side of each half-ring to permit water cooling should much larger field gradients be required in future experiments. The coils consist of approximately 310 turns of 22-AWG (0.644 mm) wire yielding a nominal  $6\ \Omega$  resistance per coil. From (E.2) on p 321, the axial field gradient  $\partial B / \partial z$  in gauss per centimetre is given by

$$\frac{\partial B}{\partial z} = 1.48V \quad (4.2)$$

where  $V$  is the voltage across the coils if connected in parallel. For 10 G/cm gradients, currents close to 1 A are indicated, readily available from a standard bench supply. In practice, the coils are connected to independent supplies so that the field zero, and thus the atom cloud location, may be centred in the chamber.

### 4.3.3 Coil operation

Fluorescence from the MOT remained roughly constant as the coil current was varied from 1 A to 3 A, corresponding to 10–30 G/cm. At a nominal current of 1.5 A, the coils dissipate 13.5 W each, and the temperature of the coil inner windings stabilised at 46 °C after 30 min.

## 4.4 External-cavity diode laser system

The final essential component for the magneto-optical trap is a source of coherent light to create the optical molasses. Alkali metals have dominated laser cooling research partly due to their principle spectral line lying in the visible region of the spectrum. Rubidium is particularly attractive having its alkali doublet in the near infra-red. The  $^{85}\text{Rb}$  D<sub>2</sub> ( $4S_{\frac{1}{2}} - 5P_{\frac{3}{2}}$ ) line has a nominal centre frequency of 384.229 1815 THz corresponding to 780.24373 nm in vacuum [262]. Since the advent of compact-disc writers operating at 780 nm, relatively high power (over 120 mW cw) laser diodes<sup>2</sup> have been mass-produced and these may be used in

---

<sup>2</sup> *Laser diode* refers to the packaged semiconductor unit, while *diode laser* refers to a complete laser system based around such a diode, necessarily including a current source and potentially an external cavity, temperature control, servo electronics etc.

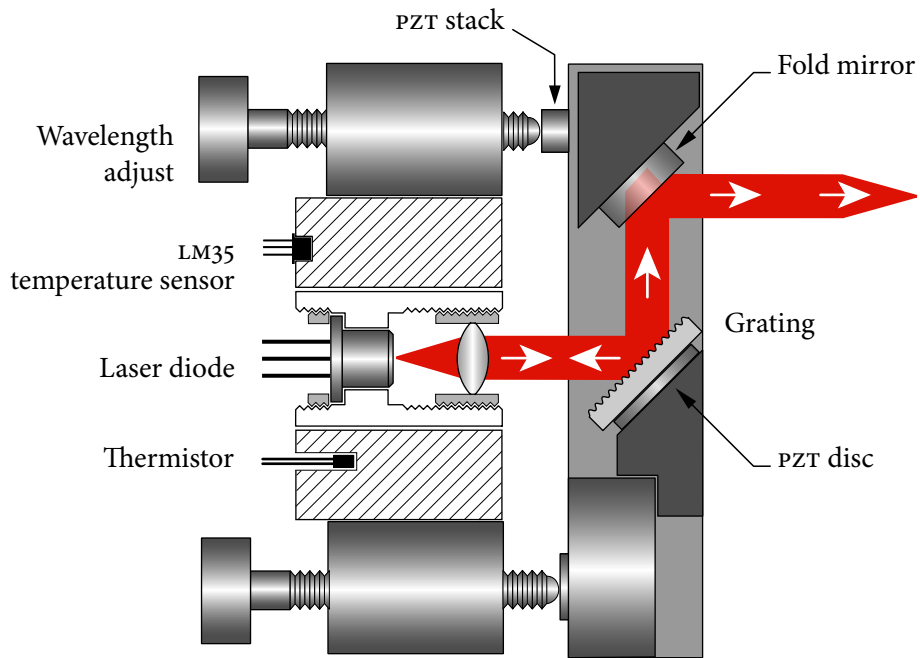


FIGURE 4.5 The Melbourne ECDL design. Adapted from Reference 265.

laser systems at much lower power consumption and cost than optically-pumped ring lasers. The laser system described in this Section augments these laser diodes with an external feedback grating and precision current and temperature control, yielding 80 mW of stable, single-mode laser light. An early review of the use of such diode lasers in atomic physics is Reference 263 while a more recent review may be found in the thesis of Phillip Fox [103, §2.4.1]. The next three Sections concentrate on enhancements to the basic laser diode system which I have developed as part of this project.

#### 4.4.1 Mechanical design

Our design (Figure 4.5) is a Littrow configuration in which an external cavity is formed with a holographic grating held on a modified optical mirror mount [264]. The laser diode and collimating lens are held rigidly in a focusing tube, and precision screws allow adjustment of the grating angle, and hence the wavelength. A fold mirror cancels angular deviation of the output beam as the laser wavelength is tuned [265].

This design is a compromise between simplicity of construction and mechanical stability (cf [266]). Co-axial mounting of the laser and lens obviates initial

alignment (cf [267]) and essentially eliminates thermal expansion effects transverse to the lens axis, which may tune the laser as much as 50 MHz per nanometre of lens displacement [268]. On the other hand, the design *is* susceptible to acoustic noise pickup due to springs forming high-Q mechanical resonances.

A detailed description of the mechanical mount, grating and the other components of the laser system is give in §2.4.2 of Reference 103. This Section concentrates on enhancements that I made to this mechanical design which provide *passive* stabilisation of the laser frequency. The following two Sections describe an *active* electronic stabilisation system.

#### 4.4.2 Optical design

Linewidth is reduced by the external cavity in proportion to the square of the cavity length [269, Fig 8]. A long cavity is indicated, except that the associated longitudinal mode spacing will eventually become smaller than the characteristic frequency of relaxation oscillations in the diode itself. Under such conditions, single-mode operation may be achieved only with anti-reflection coated diodes [267]. We choose instead a relatively short 15 mm cavity, well-suited to cheap, uncoated laser diodes and providing a free-running linewidth of 1–2 MHz at a typical mode spacing of 4 GHz, sufficient for a scan across the rubidium D<sub>2</sub> manifold.

#### 4.4.3 Environment isolation

A Peltier thermoelectric cooler is sandwiched between the mirror mount and an aluminium base plate; it is used in conjunction with a thermistor mounted close to the laser diode focusing tube to form a temperature servo-control loop (see next Article). The entire assembly is bolted to a 2 kg steel block with thermal transfer compound applied to the metal interfaces so that the block provides considerable thermal inertia.

While the addition of an external cavity reduces the laser sensitivity to thermal and current tuning, it *increases* sensitivity to vibration and acoustic pickup. I found that a viscoelastic polyether-based polyurethane known commercially as Sorbothane provided excellent vibration isolation and damping, and is readily attached to metal with cyanoacrylate adhesives [270].<sup>3</sup> Sorbothane pads were attached to the base of the steel block, the mass of the block providing near-optimal compression

---

<sup>3</sup> Known by trade names such as ‘superglue’.

for 4 mm thick 20 mm pads. Viscoelastics provide both vibration isolation (lowering of resonant frequency) and damping (dissipation of vibration energy as heat). Acoustic noise due to turbomolecular pumps, and impulsive shock due to doors closing or ball drivers dropped on optical tables, has most energy at frequencies above 1 kHz, much higher than most industrial vibration. Thin 4 mm isolation pads are indicated [271].

Vibrations coupled to the mirror mount change the length of the external cavity, and thus the frequency of the laser. Slight variation in the pressure of air in the cavity also alters the optical path length. The coefficients are  $-88 \text{ MHz/mbar}$  for air pressure and  $+300 \text{ MHz/K}$  for air temperature [268]. The pressure fluctuations due to someone walking past the optical bench is sufficient to move the laser frequency by more than 100 MHz. An inner aluminium box surrounding only the ECDL is supplemented with an acrylic box enclosing the laser block, optical isolator and saturated absorption spectrometer. Both covers rest on Sorbothane gaskets to reduce coupling of vibrations through the support. The arrangement is not hermetically sealed, however it would take an extreme drop in barometric pressure to induce a mode-hop, which would anyway be the least of our concerns in such circumstances. The double enclosure *does* prevent mode-hops due to air currents in the laboratory.

The entire apparatus was further isolated from the optical table by placing it on a  $400 \times 400 \text{ mm}$  breadboard which in turn rests on Sorbothane feet (Figure 4.6). The effect of these modifications is a dramatic reduction in the sensitivity of the laser to mechanically and acoustically coupled vibrations. Lasers may be operated on the same optical bench as a turbomolecular pump. Sharp rapping on the table with a screwdriver handle rarely unlocks the servoloop. This unusually high degree of stability is important in experiments using multiple lasers, the unlocking of any of which terminates the experiment.

#### 4.4.4 Temperature and current controllers

Laser diodes are highly sensitive to temperature fluctuations: AlGaAs diodes exhibit temperature tuning of order  $-30 \text{ GHz/K}$  [268]. Our external-cavity reduces this sensitivity considerably, and the measured temperature coefficient of order  $-1 \text{ MHz/mK}$  is probably dominated by expansion of the aluminium cavity support [268, Tbl 1]. To stabilise the temperature, the thermoelectric element and thermistor temperature sensor are closed into a servo-loop by a proportional-integral-

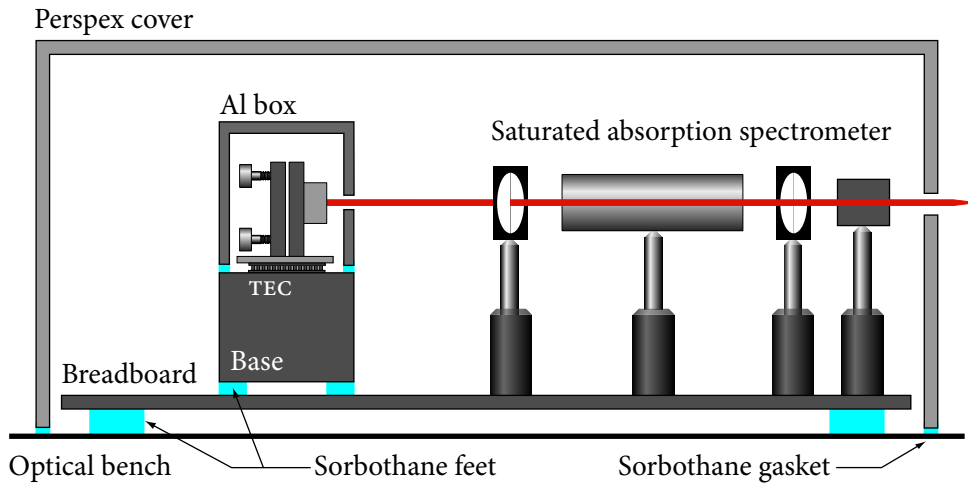


FIGURE 4.6 **Vibration isolation for the ECDL system.** Sorbothane feet and gaskets reduce acoustic coupling from the bench and the air.

derivative (*PID*) controller. This controller was designed by Bill Drury of the Flinders University Electronics Workshop based on a previously published design [272]. Temperature stability is better than 5 mK and the settling time is of order 5 min after which the laser may be locked. In normal use, the temperature controllers are left on even when the laser is off; the setpoint must be no more than a few degrees below room temperature else condensation promotes mould growth on the grating.

External cavity diode lasers are also highly sensitive to the injection current: the laser frequency shifts approximately  $-160$  MHz for a  $1\ \mu\text{A}$  increase in current. Our laser current source is based on a design [273] from JILA (Boulder CO, USA). A high-current transistor provides up to 200 mA to the laser diode with the voltage drop across a precision  $25\ \Omega$  resistor sensed by a precision, low-noise operational amplifier and fed back to the transistor. A more recent current controller design [274] improves the shielding, transient protection and current modulation capabilities while using the same current servosystem. Inadequate transient protection has been identified as the leading cause of premature diode demise [263]. Our diodes are protected when switched off by a shorting relay mounted close to the diode.

Luiten et al. [275] have shown that the JILA design outperforms two commercial current sources. They also found that the laser frequency noise at Fourier frequen-

cies<sup>4</sup> below 2 kHz was dominated by mechanical and acoustic effects, indicating that further reduction of noise in the current source is unnecessary.

## 4.5 Laser-frequency servocontrol systems

Our diode lasers are tuned to the appropriate atomic transition by adjusting the grating angle with a fine screw. Uncoated diodes render certain wavelength ranges inaccessible and the laser temperature may need to be adjusted. Despite the passive stabilisation described in the previous section, temperature and air pressure fluctuations cause the tuned laser to drift off a hyperfine resonance in a matter of minutes.

The lasers have two piezoelectric actuators which provide finer adjustment of the grating angle and cavity length. The range of these actuators is enough to keep the laser on resonance for many hours if they are actively controlled. Suitable control can be provided by an electronic servo which monitor the output of a spectrometer. A control bandwidth<sup>5</sup> of only a few Hertz will keep the laser on resonance. Substantially higher bandwidths are needed if a reduction in the ECDL linewidth is desired. The following Article discusses why linewidth narrowing might be desirable and I then review some approaches which have been used for optical and electronic servocontrol of diode lasers. The servo design used in this work is outlined in the next Section.

### 4.5.1 Linewidth reduction

The definition of linewidth is inevitably somewhat arbitrary; in this thesis it refers to the full width at half maximum of the optical-frequency power spectral density (*PSD*)  $S(\nu)$ . This measure still depends on the duration of the average; formally this is taken in the long-time average limit, but in practice non-stationary drifts distort results when averaged over much longer than 1 s. A linewidth measured over 1 s seems to include all significant Gaussian noise processes. Relations between frequency noise PSD, linewidth and the Allan variance (a time-domain measure of stability) are given in Reference 276, and in the paper included in Appendix G on p 332.

---

<sup>4</sup> The *Fourier frequency* refers to the frequency of modulation. Here the *carrier frequency*  $\nu(t)$  is the optical frequency of the laser (many THz) and the Fourier frequency  $f$  indexes the laser *frequency modulation spectrum*  $\tilde{\nu}(f)$ .

<sup>5</sup> In this thesis, *control bandwidth*  $f_b$  refers to the 0 dB point of the *open-loop* transfer function.

A bare laser diode has a linewidth of order 30 MHz, considerably broader than the 6.1 MHz natural linewidth of the rubidium D<sub>2</sub> line. The laser frequency noise power spectrum  $S_{\Delta\nu}(f)$  is typically  $1/f$  up to 100 kHz and white thereafter [277]. The white noise is a manifestation of the Schawlow-Townes spontaneous-emission limit in the very short internal cavity of the diode. Adding an external cavity, especially one formed with a dispersive element such as a grating [278], dramatically reduces the white noise and reduces the linewidth to of order 1 MHz. We have observed linewidths of this order as an RF beatnote of two free-running ECDLs.

For simple laser cooling and trapping experiments, a linewidth of one or two megahertz is marginally adequate. Precision laser cooling experiments, such as polarisation gradient cooling for nanodeposition [279], require a linewidth much narrower than the natural linewidth: 300 kHz is desirable. Even narrower linewidths are needed when locking lasers to high-finesse cavities. With the bare-diode white noise well-suppressed by the extended cavity, ECDL linewidths are dominated by  $1/f$  noise. Some authors have described this noise spectrum as consisting of a ‘fast’ linewidth (averaging time of order milliseconds) of around 50 kHz jittering across 1 MHz of optical frequency due to acoustic disturbances [280]. For general use in our atomic physics laboratory, we would be very satisfied if we could suppress these acoustic fluctuations and achieve a *slow* (1 s) linewidth of order 300 kHz. I now review some approaches to locking a diode laser to atomic resonances and narrowing linewidths, before describing the particular approach chosen for our ECDL design.

#### 4.5.2 Approaches to laser locking

In our laser design the grating acts as a frequency dispersive element in the external cavity, stabilising the lasing wavelength. A number of schemes have replaced the grating with a frequency dispersive atomic vapour and so achieved an *optical* lock to an atomic transition, among them: Faraday anomalous dispersion [276, 281–284], resonant phase conjugation [285], high-contrast saturated absorption [286], velocity-selective optical pumping [287] and sub-Doppler polarisation spectroscopy [288].

Optical locks have inherent high bandwidth, suppressing noise up to high Fourier frequencies, and so might be expected to narrow the laser linewidth considerably. However, the longer laser cavity with more optical elements inside it probably *increases* the sensitivity of optically-locked lasers to acoustic pickup, in comparison to short-cavity designs. Compounding the problem, optical noise suppression is

less effective at low Fourier frequencies [283].

The vast majority of ECDL systems in use are locked with purely electronic servosystems, which are generally simpler than optical locks of equivalent performance. Many electronic servos permit locking to any chosen saturated absorption peak, dip or cross-over, and electronic frequency-lock or phase-lock loops permit offset locking of lasers separated by several gigahertz. Notwithstanding, the narrowest reported linewidth for an atomic resonance-locked laser diode is 44 Hz, achieved with a hybrid electronic (slow) and optical (fast) lock [289].

An electronic servo must measure the intensity output of a spectrometer, process the resulting signal, and feed it back to an actuator which controls the laser frequency. A saturated-absorption spectrometer is a simple configuration providing sharp resonances. Resonances are typically symmetrical and must be *discriminated* to a zero-crossing *error signal* suitable for servo control, either by *baseband* or *modulation* methods.

Perhaps the simplest baseband method is *edge locking* where the measured absorption signal of an atomic resonance, less a DC offset, is fed back to control the laser frequency. Such a scheme clearly can lock to the side of a spectral line, but not to the peak. More advanced baseband methods modify the atomic spectrum to yield an error signal, for example using magnetically-induced dichroism [290]. Here, strong magnetic fields broaden the line and so the discriminator SNR is low. Other systems electronically subtract the signal from two photodiodes monitoring the same sharp resonance, but with centre-frequencies counter-shifted by acousto-optic modulators [291], incomplete Doppler cancellation [292], laser-induced birefringence [293–295] or even saturated interference methods [296]. Any imbalance in these differential methods causes the laser frequency to drift off the peak centre. Baseband methods in general are susceptible to technical  $1/f$  noise at low frequencies: for example, room lighting falling on photodiodes will introduce powerline harmonic noise into the laser frequency spectrum.

The simplest modulation method dithers the laser emission frequency, by adding a small amplitude sine wave to the laser injection current or tuning piezo. This results in a dither signal from the photodiode whose amplitude is symmetric on either side of a resonance, but the phase changes sign as shown in Figure 4.7. An electronic phase-sensitive detector synchronously demodulates the photodiode signal to an error signal, which closely approximates the derivative of the spectral line if the modulation is small compared to the linewidth [297].

Intrinsically immune to drifts, modulation methods also have an SNR advan-

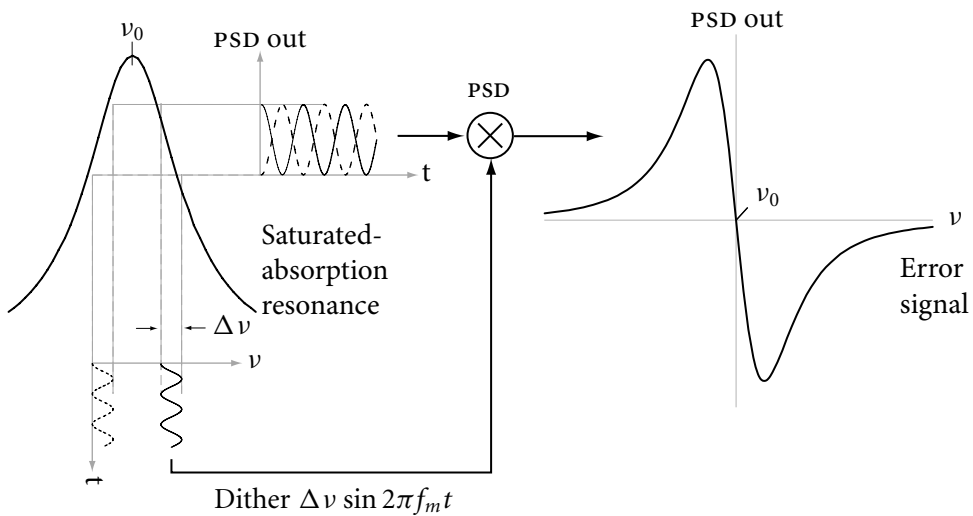


**FIGURE 4.7 Frequency dither demodulates to an error signal.** The solid-trace dither on the right-hand side of the peak yields a component on the photodiode at the dither frequency but  $180^\circ$  *out of phase* with the dither. The phase-sensitive detector (PSD) produces a negative signal there, resulting in a dispersion-shaped error signal as the laser is swept across the resonance at optical frequency  $\nu_0$ .

tage over baseband methods as photodetection occurs at the modulation frequency  $f_m$  which is usually above most technical noise. A typical modulated system with  $f_m = 100$  kHz can have more than 60 dB suppression of powerline harmonic signals picked up on the photodiode. These advantages come at the price of increased electronic complexity, especially as the dither frequency must be substantially higher than the desired bandwidth of the servosystem (see §4.6.5).

Direct modulation of the laser emission frequency is undesirable as it broadens the laser linewidth, and if injection current modulation is used then the intensity is also unavoidably modulated. These drawbacks are circumvented if instead only the fraction of the laser output picked off for locking is frequency modulated, using an acousto-optic [298, 299] or electro-optic [300, 301] modulator. These devices are expensive and require radio frequency electronics.

At high modulation frequencies  $f_m \approx 10$  MHz, the frequency deviation  $\Delta f$  over a modulation cycle is less than  $f_m$ . The resulting *wideband FM* spectrum has an unBroadened central peak with sidebands spaced by  $f_m$ . The signal may be synchronously demodulated by an RF mixer in a technique known as *Pound-Drever-*

*Hall (PDH)* locking [302] when used on a cavity resonance and *frequency modulation spectroscopy* when used on an atomic resonance [303, 304]. Shot-noise limited discriminator performance is possible [305]. Coupled with the greater available controller bandwidth, the PDH/FMS method offers the ultimate linewidth reduction of purely electronic methods. Such stability is seldom necessary for locking a laser to an atomic resonance [306], but is needed when the light must remain resonant with the much narrower resonance of a high-finesse Fabry-Perot cavity [280]. Much of the literature on cavity locks is relevant to atomic resonance locking, with the provisos that: cavity resonances are usually sharper and have higher contrast and so higher SNR, cavities store light and so have low-pass Fourier-frequency behaviour and cavity experiments are generally less sensitive to modulation sidebands.

A simpler alternative to modulating the laser is to modulate instead the resonant frequency of the atomic transition, for which the Zeeman effect is convenient. Here a dither current is applied to a solenoid surrounding the vapour cell in a saturated-absorption spectrometer [307]. The apparatus is simple, and RF-bandwidth detectors and electronics are not required. We have chosen this Zeeman modulation for our laser servocontrol system.

## 4.6 An electronic laser servo

The present controller design, used in the experiments described in the next Chapter, is known as *Claudius* and is described in §2.5.4 of Reference 103. A new design, termed *Augustus*, is currently being constructed, and its components are described in some detail in the following Articles. Both designs rely on the same modulated Zeeman spectrometer, and drive the same actuators. The differences are first in improvements in component choice and in the detailed electronics, and more importantly, the complete redesign of the compensator filters.

The remainder of this Section describes the components of the servo system. New compensators have been designed for the Augustus controller, but have not yet been tested. I comment briefly on compensator design at the end of the Section.

### 4.6.1 Overview

A schematic of the Melbourne laser controller is shown in Figure 4.8. The output of the saturated absorption spectrometer is measured on a photodiode connected by a low-noise analogue link to the demodulation circuit. An error signal is recovered by the phase-sensitive detector.

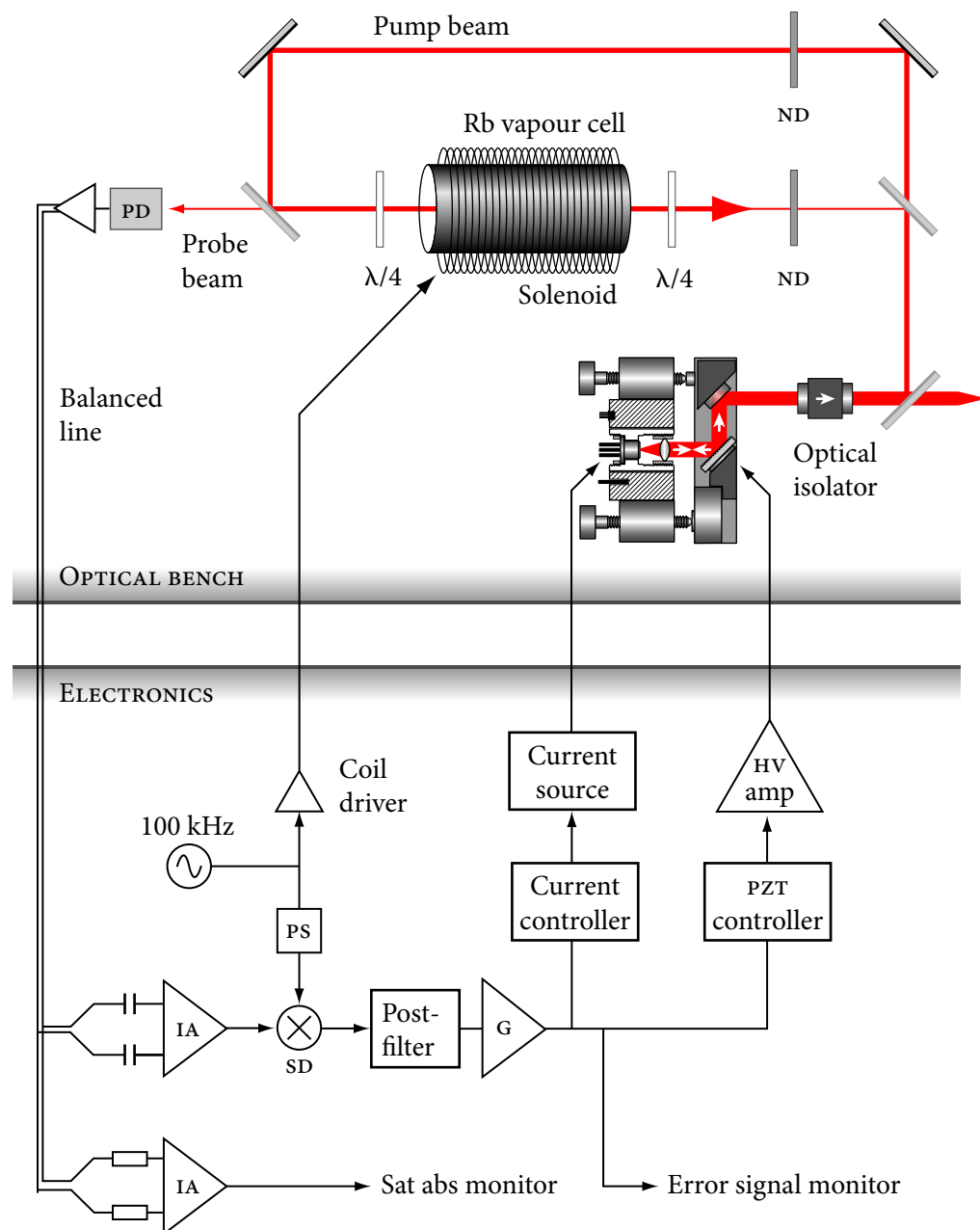


**FIGURE 4.8 Schematic of laser lock by Zeeman modulation.**  $\lambda/4$ : quarter-wave plates, ND: neutral density filters, PD: photodiode, IA: instrumentation amplifier, SD: synchronous demodulator, PS: phase shifter, G: master gain control. Sweep generator and temperature control circuits are not shown.

Feeding this error signal back to control the laser is not a simple matter. Three separate actuators are required to control the laser frequency: a wide-ranging but very slow *piezoelectric multilayer stack*, a faster but narrower-range *piezoelectric disc* and the laser current itself which effects very fast control of the laser frequency but has a very narrow mode-hop-free tuning range. The stack is used only for coarse manual tuning and is not part of the servo loop. The *compensator* electronics must split the error signal into a fast, low amplitude component to be fed to the current actuator and a slow, larger component to be fed to the piezo disc. A pair of linear compensators suffices, but both gain and phase responses of the compensators must be very carefully designed so that the resulting control system achieves high noise suppression, but remains stable against reasonable variations in parameters.

A significant early component of this PhD project was the development of a novel beatnote demodulation technique which measures a two-laser joint frequency noise spectrum with all-electronic discrimination. This work is described in the paper included as Appendix G on p 329. This work showed that acoustic noise is unambiguously the dominant contributor to the laser linewidth. The noise is broadly  $1/f$  and has substantial peaks in the 1–6 kHz band and at powerline harmonic frequencies. Analysis of these noise spectra suggested that a control bandwidth of 30 kHz would be sufficient to reduce the laser linewidth to the 300 kHz target. Achieving a control bandwidth of 30 kHz requires a dither frequency of at least 100 kHz.

#### 4.6.2 Zeeman-modulated saturated-absorption spectrometer

A bare glass plate picks off approximately 1 mW from the laser output beam after the Faraday isolator ( $> 35$  dB isolation) before variable attenuators set the pump and probe beam powers to approximately 100  $\mu\text{W}$  and 10  $\mu\text{W}$  respectively. Quarter-wave plates prepare the beams in identical circular polarisations. The beams overlap in a rubidium vapour cell (prepared at University of Melbourne [308, App G], nominal length 100 mm) mounted inside a solenoid. This *saturated-absorption spectrometer* produces hyperfine-structure resonances which are power-broadened to only slightly wider than the 6 MHz natural linewidth. Example spectra are on p 58 of Reference 308.

A single layer of winding on the solenoid achieves the lowest coil capacitance and hence raises the self-resonant frequency of the coil. A DC resistance of order  $10 \Omega$  is desirable and so fine winding wire is indicated. The coil is driven at 100 kHz

by a stable monolithic oscillator (Exar XR2206) via a high-current op-amp (Texas Instruments OPA547). There is provision for a DC current to be added, providing Zeeman tuning of the laser lock over  $\pm 30$  MHz and allowing stray field components along the propagation axis to be nulled for sharper saturated-absorption spectra.

The dither current amplitude, and thus the frequency deviation of the resonance, should be set to maximise the slope of the error signal after the phase sensitive detector. It can be shown that for a Lorentzian spectral line, this occurs when the dither peak-peak deviation is the line FWHM [297]. Harmonic distortion becomes substantial but only marginally distorts the linearity of the error signal at the line centre if standard phase-sensitive detection methods are used (see §4.6.4). Previous designs, including Claudio, operated with dithers 1 MHz or below, much narrower than the line FWHM of at least 6 MHz.

#### 4.6.3 Photodetector and input stage

The probe beam is detected by a pre-amplified photodiode (Burr-Brown OPT210, no longer in production) configured for 300 kHz bandwidth yielding a sensitivity of  $1\text{ V}/\mu\text{W}$ . Photodiode signals are conveyed to the electronics box over shielded twisted pair cable driven by a balanced line driver (Texas Instruments THS4130).

The photodiode input of the Augustus electronics box connects to a pair of instrumentation amplifiers, one ac-coupled [309–311] and high-bandwidth (INA103) with a fixed gain of 100 and the other (AD620) DC-coupled with unity gain. This novel input arrangement provides an immediate amplification of the dithered component and suppresses technical noise. The DC-coupled channel allows monitoring of the saturated-absorption spectrum as the laser is scanned. An optional filter in this channel rejects the dither frequency, allowing a clear view of the saturated-absorption spectrum when strong dithering is employed.

#### 4.6.4 Phase-sensitive detector

The dither signal is demodulated by a switched multiplier (Analog Devices AD630) synchronised to the dither oscillator via an op-amp based phase-shifter. As the switched multiplier effectively multiplies by a square wave, it also demodulates any ‘signals’ present at odd harmonics [312]. While we would expect little technical noise in windows around 300, 500, 700 . . . kHz, nonlinearities in the optical discriminator may cause harmonic components at the discriminator input.

Attempting to suppress dither harmonics at the multiplier input by bandpass or notch-array filters is likely to fail; the significant differential phase-shifts produced on either side of 100 kHz translate to substantial phase shifts of the baseband error signal after demodulation. These additional phase-shifts complicate the design of a stable compensator.

#### **4.6.5 Post-filter**

Ignoring harmonic contamination, the multiplication of the modulated dither from the photodiode with the pure reference yields the demodulated error signal at baseband *plus* an image component at  $2f_m$  [313, p 221–2]. Any noise making it through the initial high-pass filter (the ac-coupling of the instrumentation amplifier) is ‘demodulated’ to sidebands around  $f_m$ . In a standard lock-in amplifier, the multiplier output is heavily low-pass filtered and the  $2f_m$  image as well as the noise around  $f_m$  are greatly suppressed.

Such a filter is inappropriate for control applications. Deep attenuations at high frequencies induce large phase-shifts below the corner frequency. Large phase-shifts within the control bandwidth of the filter make compensator design very difficult. In Pound-Drever-Hall laser controllers, the modulation frequency is so much higher than the controller bandwidth that passive low-pass filters and notches can sufficiently attenuate the modulation harmonics without significant delay of the baseband signal.

We seek a filter which has a small phase-shift below the corner frequency but retains good attenuation around 100 kHz and particularly around 200 kHz. The low-frequency phase-shift may be reduced if the stop-band response is allowed to be non-monotonic. The Augustus filter<sup>6</sup> has notches at 100 kHz and 200 kHz superimposed on a basic 24 dB/oct rolloff. It offers strong noise and image frequency attenuation with minimal phase-shifts below 25 kHz. Full details will be published after the Augustus system has been tested.

#### **4.6.6 Gain control**

The filtered output passes through a master gain control and is buffered and made available on a front-panel BNC so that the dispersion-shaped error signal may be viewed as the laser sweeps. Overall loop gain may vary from day to day due to changed laser power output, the strength of selected hyperfine transitions, and the

---

<sup>6</sup> Designed by Alex Slavec, School of Physics Electronics Workshop, University of Melbourne.

sensitivity of the current and piezo actuators varying within a laser mode. Adjusting the master gain control so that the error signal has a predefined amplitude corrects for the first two of these variations. Measuring variations in actuator sensitivity is more difficult, however actuators variations should be small enough to fall within the gain margin of the controller.

At this point we have a clean error signal: a voltage proportional to the optical frequency deviation from line centre. This signal must be shaped by *compensators* before it is fed back to the actuators. The compensator must be designed so that the total open-loop transfer function – the compound effect of the optics, demodulator, filter, compensator and actuators – provides the maximum possible feedback gain, and hence the maximum possible noise suppression, while remaining stable. The next two Articles investigate the transfer functions of the laser current and PZT disc actuators; once these are measured we have the information we need to design the compensator.

#### 4.6.7 Injection current actuator

Two physical effects link the frequency of laser diode emission with the injection current. An increase in current naturally increases the charge carrier density in the semiconductor and this affects the refractive index of the gain medium [314, §2.3.4]. Changing the index changes the optical path length and hence the emission frequency. The charge carriers and photons come to equilibrium very rapidly, and so this effect has a flat Fourier frequency response up to the relaxation oscillation frequency, around 3 GHz [314, §7.6].

The second effect is less direct. An increase in current leads to greater Joule heating of the semiconductor and a consequent change in its refractive index with temperature [315]. The thermal effect is somewhat stronger than the carrier-density effect and *opposite in sign*, but its characteristic heating time is of the order of microseconds rather than nanoseconds. The nett FM transfer function therefore shows a significant change in amplitude as a function of Fourier frequency as shown in Figure 4.9, and undergoes a 180° phase-shift between 100 kHz and 1 MHz. Thermal resistances inside the diode determine the exact –90° point, and so it varies considerably with the design of the diode.

Accurate knowledge of the laser diode's FM transfer function is critical when designing a high-performance servo. We measured the current transfer function of our laser using the side of a Zeeman detuned saturated-absorption resonance as a

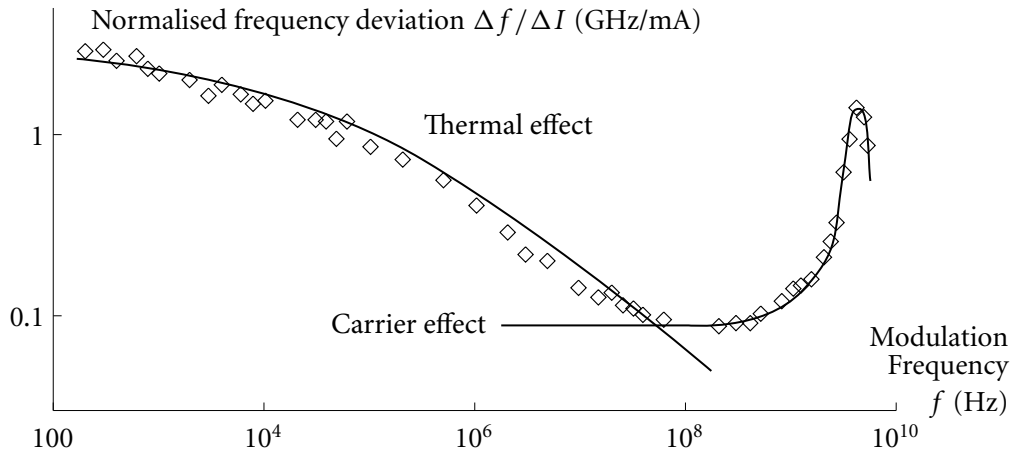


**FIGURE 4.9 Injection current FM response of an AlGaAs diode.** For this channelled-substrate planar (CSP) diode, the thermal effect dominates to around 10 MHz. Adapted from Figure 4 of Reference 315.

frequency discriminator to monitor the frequency deviation. A Fabry-Perot etalon could also have been employed as a frequency discriminator [316]. A DSP lock-in amplifier (Stanford Research SR850) swept the modulation signal and measured the amplitude and phase of the photodiode signal. Intensity modulation was negligible. Figure 4.10 shows that our current actuator has monotonically decreasing gain with the  $-90^\circ$  point at 65 kHz. This is at the lower end of expected values, but is consistent with the measured transfer function for a commercial ECDL system (Toptica TUI-DL100 at 870 nm) [317, Fig 1] [318].

While these linear characteristics of the current actuator are close to ideal, the actuator has a severe *saturation non-linearity*. The gain of the control input of the current source is set low enough that a full-scale input corresponds to a  $0.2\ \mu\text{A}$  current increment, or a 32 MHz shift, and so is unlikely to provoke a mode-hop. Once the current-control voltage is saturated at a supply rail, the laser is essentially uncontrolled and will soon unlock. We need another actuator channel to control for slow drifts over wide frequency ranges.

#### 4.6.8 Piezoelectric disc actuator

A second PZT actuator, a 1 mm thick disc glued between the grating and the mount, provides up to 2 GHz of tuning range. Varying the voltage across the piezoelectric disc changes the *external* cavity length and hence the ECDL emission frequency.

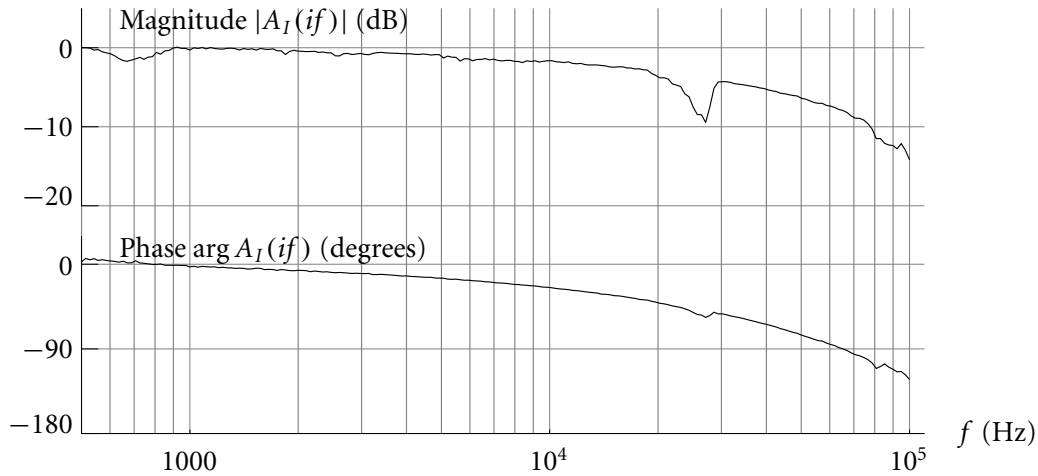


FIGURE 4.10 **Bode plot of the laser current FM response.** Deviations at 70 kHz and 25 kHz are due to the laser drifting off the shoulder of the atomic resonance and being manually corrected.

A high-voltage amplifier provides up to 150 V to the disc yielding a 1.3 GHz tuning range, much greater than that of the current actuator. However, the frequency response of the disc actuator, measured with the same discriminator described above and shown in Figure 4.11, is clearly more complicated than the current actuator. The fundamental mode determined by the disc elasticity and the grating mass is at 22 kHz, yet there are substantial phase and gain variations in the vicinity of 4 kHz. These are almost certainly due to mechanical resonances elsewhere in the laser, mostly likely the springs which hold together the kinetic mount (cf [319, §11]).

Designers usually take great pains to avoid including resonances in the control bandwidth of a servosystem. There are substantial difficulties in designing a stable resonant controller, and the frequencies and strengths of resonances tend to vary between systems and over time within a system [320, §4.3.6].

Many laser servo designs assume that the current modulation actuator is much faster than the piezo actuator. Our ECDL seems to have a particularly slow current response and a somewhat faster piezo response (ignoring the 4 kHz resonances) than others have reported [299, 321–323]. If the resonance problem could be solved, a pure piezo lock would achieve a similar control bandwidth to the parallel channel scheme but without the parasitic intensity modulation inherent in current-feedback schemes.

Two possible solutions to the resonance problem are *gain stabilisation*, in which

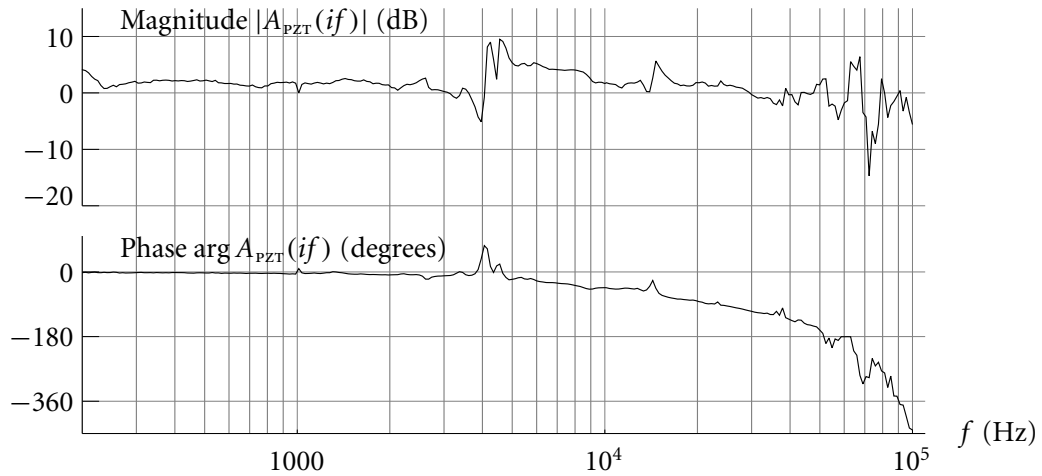


FIGURE 4.11 **Bode plot of the PZT disc FM response.** Laser drifts again render the gain profile inaccurate at decade spacings, however the magnitude of resonances at 4 kHz and 70 kHz is reliable.

a high-order controller boosts the loop gain well above the magnitude of the resonance [320, §4.3.6], and *reactuation* [320, p 417] [324]. A reactuator is a second piezo disc placed on the opposite side of the grating support arm with an attached dummy mass similar in dimension to the grating. The centre of mass of the system does not move when the piezos are driven with the same control signal, and resonance damping of 30–40 dB is readily achieved [319, p 152]. The technique has been used in high-performance dye [325] and CO<sub>2</sub> [326] laser servos.

Notwithstanding, gain stabilisation requires complex servo design while reactuation adds considerably to the mechanical complexity of the laser. We choose to implement the more conventional parallel channel servosystem described in the next Article.

#### 4.6.9 Compensator design

The Claudio controller used a simple compensator design. Piezo feedback was via an integrator, while current feedback was simply proportional to the error signal. An integrator has a gain of slope  $-6 \text{ dB/octave}$ , ensuring that at low frequencies the piezo disc is in control and the current channel is desaturated. The overall gain of this system, and hence its noise suppression capability, is much below the achievable maximum.

A better compensator applies an integrator to the current channel, and a double

integrator to the piezo channel. The piezo remains in control at low frequencies, but the overall gain is higher. Cross-over occurs at 7 Hz in the prototype, well below the region where there are resonances in the piezo response. Noise below 7 Hz is likely to be dominated by thermal drifts and pressure fluctuations, affecting the *external* cavity length. It is therefore desirable that this band is controlled by the external cavity piezo actuator.

In classical feedback control theory, the optimal slope for the open-loop transfer function is around  $-10 \text{ dB/octave}$  [320] and a compensating *Bode step* is introduced above the control bandwidth to preserve gain and phase margins.<sup>7</sup> In our case, however, the critical region of frequencies where the open-loop gain is near zero is dominated by phase-shifts due to the image-suppressing post-filter. The significant phase-shifts in the current actuator must also be considered. Careful loop-shaping is needed to maintain stability margins: accurate measurements of actuator responses, such as those shown above, are critical.

Testing of the Augustus system will also compare the merits of parallel and nested loop topologies. A full discussion of the loop-shaping process will be published with an evaluation of the Augustus controller.



THE DESIGN OF passive and active stabilisation systems for diode lasers has been described in some detail. For the purposes of trapping atoms in a MOT, the Claudius laser system was more than adequate. Future experiments planned in the research group, especially those applying quantum optics concepts to atomic physics experiments, will require lasers with narrower linewidths. I have outlined the design of the Augustus laser controller, which is currently in prototype assembly. The detailed design of the Augustus compensators will be published once the loop shapes have been optimised.

## 4.7 Trap optical system

The trap optical system is distributed over four optical breadboards. The laser systems sit on a standard optical table which also supports the MOT superstructure. Laser light is transported through single-mode, polarisation-maintaining optical

---

<sup>7</sup> For the sake of this discussion, gain and phase margins can be thought of as allowing for parameter variations in the system. Controller performance can be improved at the expense of robustness by reducing the margins.

fibres to vertical and horizontal breadboards surrounding the MOT. The fibres are convenient and reduce the system's sensitivity to misalignment. They also act as spatial filters, ensuring very high quality Gaussian beam profiles at the MOT.

#### 4.7.1 Cooling and repumping lasers

The MOT operates on the  $^{85}\text{Rb}$  isotope which constitutes 72.17% of the natural element. The MOT requires two ECDL systems: one providing *cooling* light red detuned from the  $^{85}\text{Rb} \ 4\text{S}_{\frac{1}{2}} (F = 3) \leftrightarrow 5\text{P}_{\frac{3}{2}} (F' = 4)$  transition at 384.229 2420 THz and one providing *repumping* light tuned to the  $F = 2 \leftrightarrow F' = 3$  transition 2915 GHz to the blue at a frequency of 384.232 1567 THz (frequencies from Reference 262).

Optimal red detuning of the cooling laser is typically 1 or 2  $\Gamma$ . We are able to take advantage of a strong  $F = 3 \leftrightarrow F' = (2, 4)$  cross-over resonance in the  $^{85}\text{Rb}$  saturated-absorption spectrum located 92.183 MHz to the red of the  $F = 3 \leftrightarrow F' = 4$  resonance. The beam picked off from the cooling laser diode is first blue-shifted an adjustable frequency  $f_{\text{AOM}}$  by an acousto-optic modulator (Isomet 1502C-2) before entering the saturated-absorption spectrometer. When the laser system is locked to the cross-over, the laser output is actually detuned  $f_{\text{AOM}} - 92.183$  MHz from the cooling transition. The indicated AOM drive frequencies of 65–85 MHz are easily achieved by a nominal 80 MHz AOM, and as only the locking beam is deflected by the AOM, the detuning may be adjusted over this range without re-aligning the modulator or using an awkward double-pass configuration.

A milliwatt of repump light is more than adequate to avoid hyperfine population trapping. The nominally 3 GHz separation of the hyperfine ground-state levels makes it awkward to generate repumping sidebands on the cooling laser, requiring an expensive resonant acousto- or electro-optic modulator, or direct current modulation near the diode's relaxation frequency [327]. Instead, we use a separate laser with the surplus repump power available for other rubidium experiments in the laboratory. The laser is locked using the same vapour cell as the cooling laser. Vale [328] and I [329] have observed the phenomenon of interactions between the spectrometers due to hyperfine-trapped atoms propagating between the laser beams in the cell. This small effect is noticeable when scanning the laser but does not seem to be adverse when the lasers are locked.

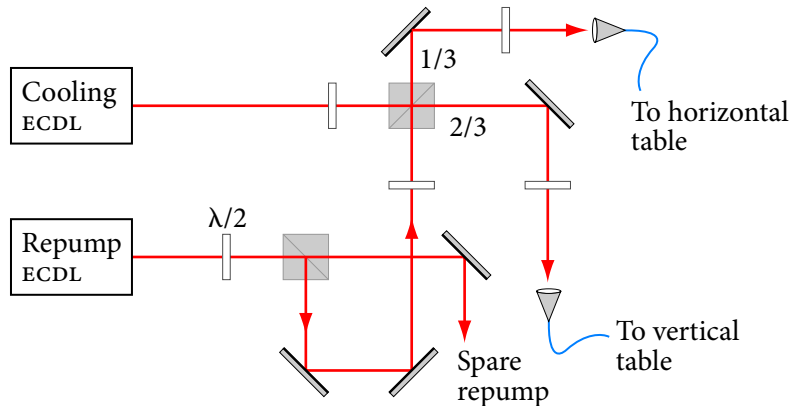


FIGURE 4.12 Lower table optical schematic.

### 4.7.2 Optical fibres

The lower table optical layout is shown in Figure 4.12. The cooling beam is split in a 2:1 ratio, the brighter component will be split 1:1 on the vertical table and become the vertical plane trapping beams. A fraction of the repump output – nominally 3 mW – is combined with this component on a polarising beamsplitter cube.

The two beams are then coupled into single-mode polarisation-maintaining fibres with integrated collimators as input couplers (OzOptics LPC-02-780-5/125-P-2.4-11AS-40-3A-3-10). Half-wave plates facilitate alignment of the beam polarisation with the fibre axis; agreement to within 2° is needed for the exit polarisation from the fibre to be stable against thermal and stress variations.

### 4.7.3 Beam diameter and beam quality

The fibres terminate in connectorised but bare ends, emitting a diverging Gaussian beam. Placing the fibre end at the focal point of a lens collimates the beam; the focal length determines the beam diameter. For a fixed total beam power, the number of trapped atoms has been found to increase linearly with beam diameter within reasonable limits [261]. We are, however, ultimately constrained by the 35 mm internal diameter of the half-connectors.

If the beam diameter<sup>8</sup> is of the same order as the internal diameter, then not only will power be wasted by clipping, but there will be substantial fluctuations in intensity across the trapping volume due to diffraction from the edges of the half-connector. We aim to keep the edge-diffraction contribution to these inten-

<sup>8</sup> All beam diameters are taken as the full width at the  $1/e^2$  (13.5%) intensity point.

sity fluctuations below 10% of the intensity; dust on optical surfaces and coating imperfections contribute spurious fringes of roughly this magnitude. A complete Fresnel-diffraction analysis of a truncated Gaussian beam has been published [330]. We use the result that for beam diameter  $w$  and aperture diameter  $a$ , intensity fluctuations are below the 10% level when  $w = a/1.5$  and below the 1% percent level when  $w = a/2$ .

The effective numerical aperture (the sine of  $1/e^2$ -cone half-angle) of the OzOptics 5  $\mu\text{m}$ -core fibre is 0.098 at 850 nm. Lenses of focal length  $f = 100$  mm were aligned by auto-collimation and yield a collimated beam diameter very close to 20 mm. All optical elements have clear diameters in excess of 38 mm, so we can be confident that intensity inhomogeneities due to edge-diffraction are negligible.

#### 4.7.4 Alignment and operation

The beam on the vertical table is split on a 40 mm polarising beamsplitter cube, while the horizontal beam passes through a cube merely to enforce a known linear polarisation. All beams then pass once though quarter-wave plates before entering the MOT chamber, and twice after exiting the MOT chamber due to retroreflection, as shown in Figure 4.13. This realises the  $\sigma^+ - \sigma^-$  configuration needed for polarisation gradient cooling in a MOT.

The retroreflected beams were aligned by observing the reflected spot focused on the fibre-chuck. When the alignment is near-perfect, back-coupling up the fibre destabilises the laser. We misalign slightly from this point until the laser is unperturbed.

A simple method described by Wieman [256, §IVb] was used to align the circular polarisations with the magnetic field gradient. With the getter running at 4 A, each anti-Helmholtz coil conducting 1 A and approximately 3 mW power in each beam (peak intensity of order  $I_{\text{sat}}$ ) a MOT appeared as soon as the coil polarities were set correctly.

A monochrome CCD video camera connected to a video monitor displayed the MOT fluorescence. Blocking the repump beam caused the MOT fluorescence to shrink and become much fainter.

#### 4.7.5 Future work

By this time, the project focus had moved to diffraction-contrast imaging of cold atoms. No diagnostic measurements were attempted, it being sufficient that cold

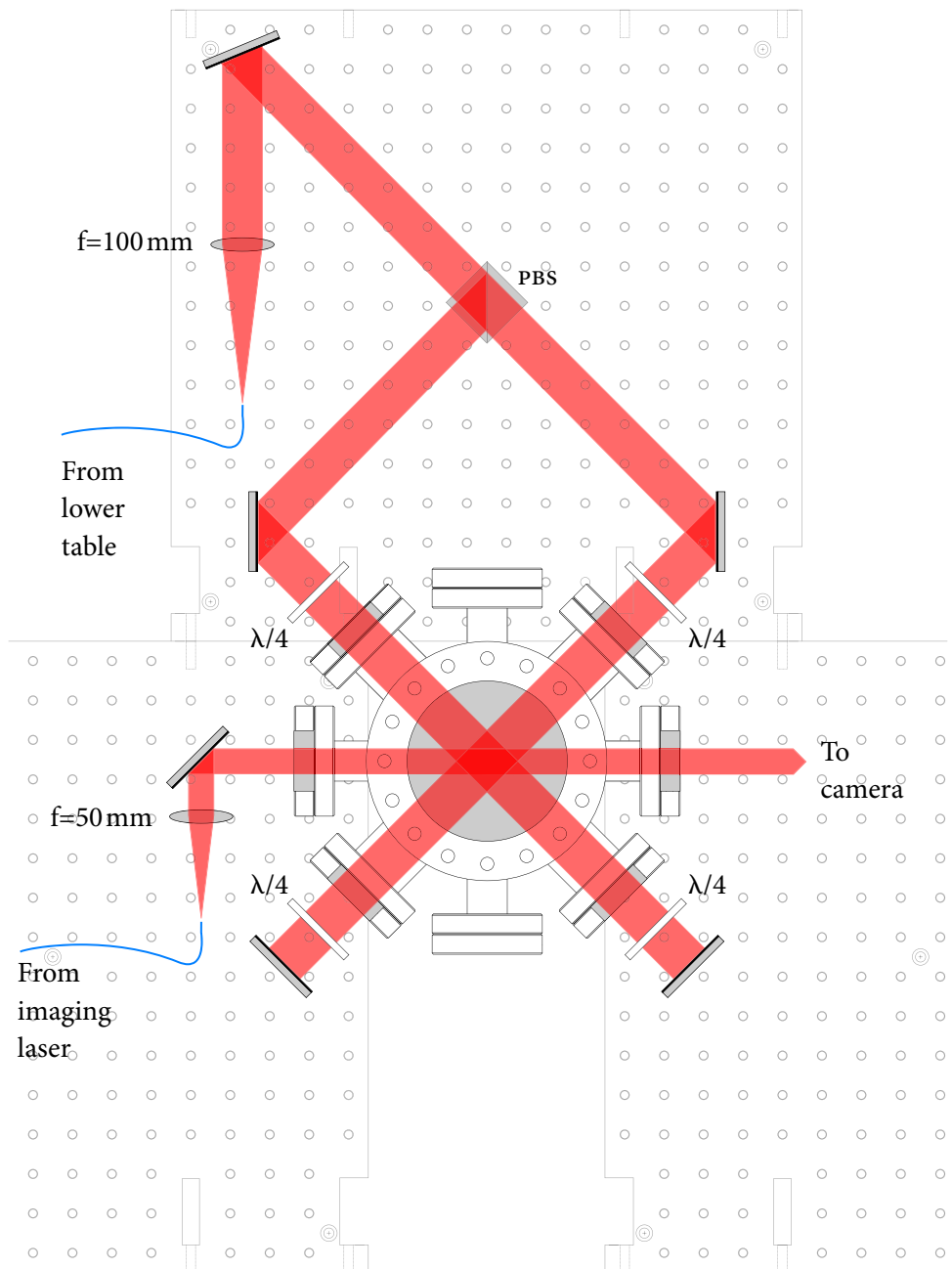


**FIGURE 4.13 Vertical table optical schematic.** The MOT beams propagating into and out of the plane of the page are not shown.

trapped atoms were available as an imaging target.

Recently, my coworkers have implemented a master-oscillator power-amplifier (*MOPA*) laser configuration using a tapered amplifier to produce up to 500 mW of cooling light. Figure 4.14 shows a possible optical schematic if it is desired to convert to a cold beam system such as the one described in §4.1.2. A third fibre is used to bring the upward-propagating beam onto the vertical table, while optical access to the horizontal ports is maintained.

## 4.8 Imaging system

The optical layout Figure 4.15 was used for the MOT imaging experiments described in the next Chapter.

### 4.8.1 Imaging laser

A third ECDL system on a separate optical bench provided probe light for absorption and diffraction-contrast imaging. The output was tunable  $-5\text{ }\Gamma$  to  $+5\text{ }\Gamma$  from the cooling transition resonance by a DC Zeeman shift applied to the vapour cell. More recently, an AOM shifting system has been introduced, providing more accurate and stable detuning and also allowing the probe beam to be shuttered in less than 1  $\mu\text{s}$ .

The probe beam passed through a variable attenuator (0.1–2.5 OD<sub>10</sub>) before entering another single-mode optical fibre.

### 4.8.2 Imaging optics

On the vertical MOT table, the beam expanded from the bare fibre end, before being collimated by a lens ( $f = 50\text{ mm}$ ) into a 10 mm diameter beam, which passed through the MOT chamber horizontally (Figure 4.13).

Imaging experiments conducted in July 2002 presumed that the Paganin algorithm would be used to retrieve the column-density of the atom cloud. For a nominally 250  $\mu\text{m}$  diameter MOT, the Rayleigh range is 80 mm while the MOT-to-window radius of the chamber is 160 mm. Reimaging the diffraction pattern onto the detector reduced the effective propagation distance below the Rayleigh range. Section §5.3.4 describes the equivalence between free-space propagation and defocused imaging.

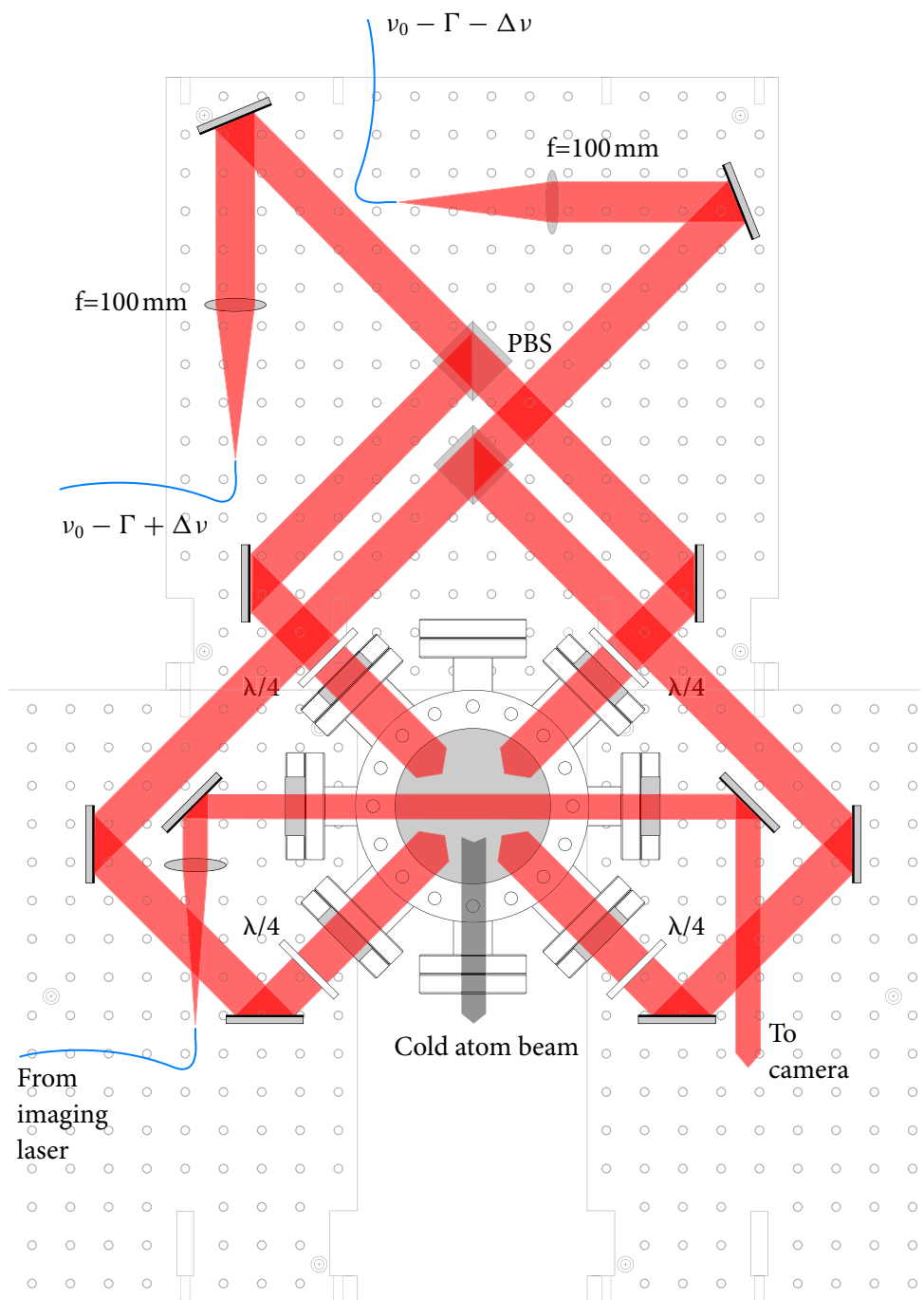
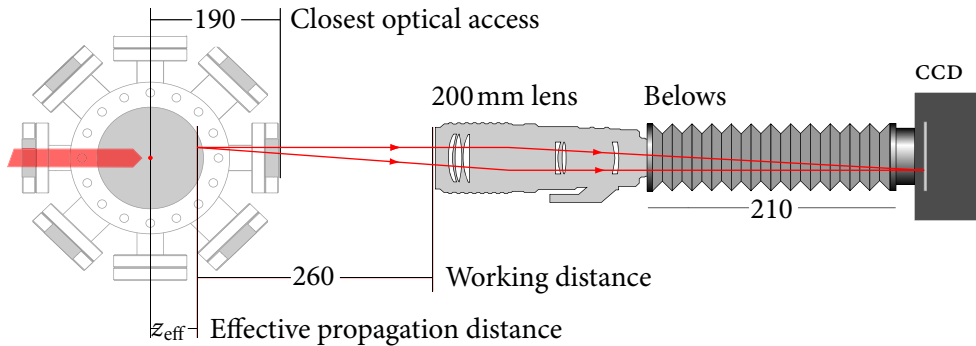


FIGURE 4.14 Optical layout for a future cold atomic beam.



**FIGURE 4.15 Optical layout for collimated-illumination defocus contrast.** The intensity of the wavefield at a distance  $z_{\text{eff}}$  from the MOT is reimaged onto the CCD detector. The *working distance* is the closest focal plane of the camera lens.

Reimaging was by a macrophotography system comprising a lens (Nikon micro-Nikkor AF 200 mm  $f/4$ ), bellows (Nikon PB-16) and a cooled 16-bit CCD camera (Roper VersArray 1300F, 1340  $\times$  1300 array of 20  $\mu\text{m}$  square pixels). The optical magnification of the system was 1.8.

When focused on the cloud, the system is in the standard absorption-imaging configuration. The entire macrophotography system was mounted on a rail assembly and could be translated more than 50 mm towards and away from the MOT relative to the in-focus position. This range was adequate given the Rayleigh range restrictions assumed during the MOT imaging experiments. Manual positioning of the camera was accurate to approximately 0.5 mm.

The retrieval algorithm described in the previous Chapter is *not* restricted by the Rayleigh range. Greater SNR is achieved at defocuses beyond the Rayleigh range. Recently the imaging systems has been modified by removing the reimaging lens and even removing the collimation lens for point-projection lensless imaging. This work was carried out by Kenian Domen, a short description of the modified apparatus is presented with the results of these experiments in §5.4.



THIS CHAPTER HAS discussed apparatus that produced a cloud of cold atoms. A major component of the apparatus was an external cavity diode laser system. I have outlined a design for an improved, narrow-linewidth diode laser system which is

currently being constructed. The diode laser system provided light for the atom trap and also for an absorption imaging system. The system was designed to be easily defocused to obtain diffraction-contrast images of the atom cloud.

The next Chapter describes the application of the column-density retrieval algorithms described in Chapters 2 and 3 to the problem of off-resonant imaging cold atoms. In particular, Section 5.3 demonstrates the retrieval of column-density maps from defocused images of the MOT, obtained with the apparatus described in this Chapter.



## Chapter 5

# Column-density retrieval from cold atom images

THIS CHAPTER PRESENTS diffraction-contrast images of cold atoms obtained with the apparatus of Chapter 4, and retrieves images of the atom column-density using the algorithm discussed in Chapter 3. We begin with the physics of light interacting with cold atoms in §5.1, and find that optically-speaking, cold atoms clouds are simply monomorphous objects. Cold atoms clouds are, however, much more fragile than most optical objects and sensitive to the mechanical action of light. In §5.2 it is shown that the conditions for non-destructive imaging of these object align closely with the validity conditions for diffraction-contrast imaging. Sections 5.3 and 5.4 present diffraction patterns due to light traveling through a cloud of cold atoms in a magneto-optical trap. Column-density images are then recovered from these patterns and compared qualitatively and quantitatively to those from fluorescence and absorption imaging. The optical resolution of diffraction-contrast imaging is compared with the resolution of conventional optics in §5.5, and then §5.6 compares the features, sensitivity and accuracy of DCI with other non-destructive imaging techniques.

The Chapter concludes by showing that, if applied to non-destructive imaging of Bose-Einstein condensates, diffraction-contrast imaging should have a signal-to-noise ratio comparable to the currently-used Zernike method. Diffraction-contrast imaging is likely to measurements column-density at higher resolution and with greater accuracy. The apparatus is much simpler and there is no need to physically focus lenses.

## 5.1 Interaction of light with cold atoms

In 1999 Ketterle et al. commented in a seminal review [331] that ‘everything we know about gaseous Bose-Einstein condensates has been obtained by optical diagnostics’. This is no longer completely true as in 2001 the signature of condensation in metastable helium was detected non-optically with a microchannel plate [332]. The observation by Ketterle et al. that any ‘contact probe’ measurement is impossible remains valid, and optical interaction provides the only means of measurement for the overwhelming majority of condensate and cold atom experiments.

After some comments on the fundamental resolution limits of imaging systems, this Section shows that the effect of cold atoms on near-resonant light is readily explained by the semi-classical theory of susceptibility. Unlike conventional materials, cold atom clouds may be heated and destroyed by even slight absorption of probe light. This Section goes on to show how off-resonant probe light allows non-destructive imaging of cold atoms, especially Bose-Einstein condensates (BEC).

### 5.1.1 Resolution of imaging and non-imaging measurements

For the purposes of this thesis we consider diagnostics which yield information on the *column-density* of the object. While some spectroscopic diagnostics may yield direct information on *velocities* [333], these are more usually inferred indirectly from *time-of-flight* measurements [334] in which the column-density is imaged after a known period of free expansion.

Column-density measurements may be partitioned into imaging and non-imaging methods. This Chapter is concerned with imaging methods, in which an image resolved in two dimensions is obtained instantaneously. The value of having an *image* of the column-density is clear, however there are limits on both the spatial and temporal resolution of imaging.

Imaging systems cannot resolve below one wavelength (§2.3.2). For imaging near alkali resonances, this corresponds to resolutions somewhat below one micrometer. Alkali metal BECs are typically 20–100  $\mu\text{m}$  in diameter. Interesting structures within them, such as vortex lattices, have spacings below a few micrometers or and so we desire resolution approaching the diffraction limit. The spatial resolution of imaging techniques are compared in §5.5.

The temporal resolution of imaging systems is limited in practice by technical considerations, such as the readout time of the detector. The standard scientific CCD cameras used in this work have readout times of several seconds. Scientific

quality cameras with video frame rates (30 frames/second) are available and frame rates may be extended to 640 Hz at the expense of reducing the dynamic range to 10 bits<sup>1</sup>. In §5.6.4 I propose the intriguing possibility of using holographic multiplexing to store multiple images in *one* CCD frame; if successful, the technique would obviate camera restrictions on frame-rate for short sequences of images.

Non-imaging methods offer higher spatial and temporal resolution than imaging techniques. Hybrid spatial-spectroscopic methods, such as magnetic resonance, may allow sub-wavelength *spatial* resolution but only in one spatial dimension [335]. The technique has not been demonstrated, but Fourier-limit and Stern-Gerlach effects would limit resolution to order  $0.5 \mu\text{m}$  for a  $50 \mu\text{s}$  measurement duration. Modulated spectroscopic methods, such as frequency [336] or phase [337, 338] modulation spectroscopy, offer very high *temporal* resolution but require fast (rf) photodetection. Arrays of fast photodetectors are not available, and so these techniques cannot make rapid spatially-resolved measurements.

In most experiments, such techniques will complement rather than replace imaging methods. We are concerned with imaging methods and we begin by discussing the interaction of the probe beam with the cold atom cloud.

### 5.1.2 Refractive index of a two-level atomic gas

The interaction of light with an atomic gas is a vast topic. Fortunately when imaging cold atoms, we are working with *weak, monochromatic* probe beams (and so can ignore conventional optical non-linearities) and exposure pulses which are long compared to the lifetime of the excited state (and so can assume time-independence).

The standard semi-classical approach considers a polarised, monochromatic traveling wave interacting with an electron bound at a radius much smaller than the radiation wavelength.<sup>2</sup> The interaction between the wave and the electron is modeled either implicitly by replacing the canonical momentum  $\mathbf{p}$  with  $\mathbf{p} - (e/c)\mathbf{A}$  in the *field-free* Hamiltonian, or explicitly by adding an *interaction* Hamiltonian  $\mathbf{d} \cdot \mathbf{E}$ , in which  $\mathbf{d}$  is the electronic dipole moment  $e\langle g|\mathbf{r}|e\rangle$  connecting a single ground state  $|g\rangle$  to a single excited  $|e\rangle$  and  $\mathbf{E} = \hat{\epsilon}\mathbf{E}_0 \exp(i\omega t)$  is the field polarised along  $\hat{\epsilon}$ . The two approaches have only recently been shown to be equivalent [339].

<sup>1</sup> For example the PCO 1200HS camera manufactured by PCO AG, Kelheim, Germany <http://www.pco.de/>

<sup>2</sup> This approximation is well-satisfied up to x-ray wavelengths, except for Rydberg atoms where atomic radii may approach optical wavelengths.

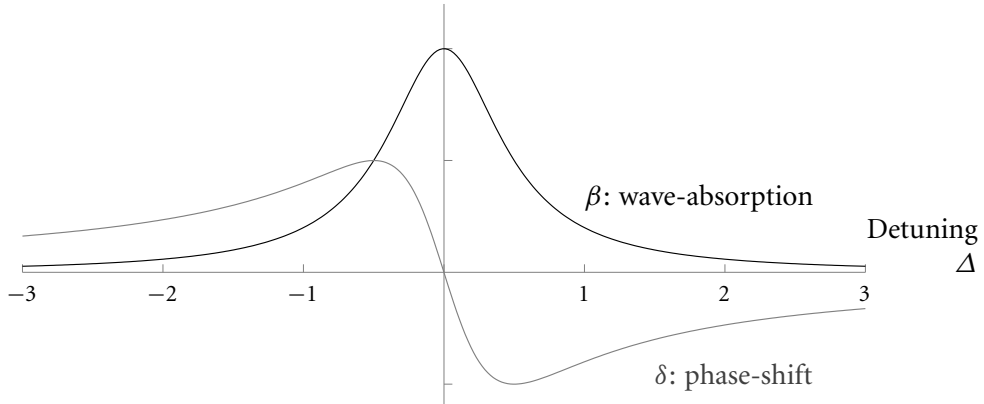


**FIGURE 5.1 The refractive index for a two level atom.** The grey trace is the real part of  $n - 1$  which corresponds to phase-shifting of the optical wavefield. The black trace is the imaginary part of  $n - 1$  which corresponds to absorption of the wavefield. The detuning is in full linewidths:  $\Delta = (\omega - \omega_0)/\gamma$ .

This latter *direct coupling* approach fits better with the classical description of dielectrics in §2.1.2. Indeed, the standard approach is to find the expectation value  $\langle g|\mathbf{d}(t)|e\rangle$  of the electronic dipole operator and average over the density of atoms to obtain a *macroscopic polarisation*  $P(t)$ . This polarisation is defined as an additive response to the applied field by  $\mathbf{D} = \mathbf{E} + \mathbf{P}$ , and in the linear limit the *polarisability*  $\chi_e$  is  $\mathbf{P} = \chi_e \mathbf{E}$ .

Extracting the temporal Fourier component of  $\langle g|\mathbf{d}(t)|e\rangle$  at the optical frequency  $\omega$  yields the polarisability  $\chi_e(\omega)$  of the atomic gas [340, §4] [341, §64]. This analysis correctly predicts that for the densities encountered in cold atom experiments, the refractive index  $n(\omega)$  is vanishingly small except near dipole-allowed resonances. However, the finite lifetime of the excited state is *not* included in the model and the refractive index diverges at resonance.

Spontaneous emission can be included phenomenologically in this semiclassical model [340, p 73–76], and is inherently accounted for by vacuum fluctuations when the radiation field is quantised [340, p 195–197]. For relevant atom densities, the susceptibility is small enough that the complex refractive index  $n$  is well-approximated by  $n = \sqrt{1 + \chi_e} \simeq 1 + \chi_e/2$ . The resulting refractive index for a cloud of two-level atoms is

$$n = 1 + \rho \frac{e^2 X_0^2}{2\epsilon_0 \hbar} \frac{i\gamma/2 - (\omega - \omega_0)}{(\omega - \omega_0)^2 + \gamma^2/4}, \quad (5.1)$$

with  $\rho$  the atom number density,  $\gamma = 2\pi\Gamma$  the natural linewidth,  $X_0 = \hat{\epsilon} \cdot \mathbf{d}$  the *atomic* dipole matrix-element of the transition,<sup>3</sup>  $\omega_0$  the resonant frequency of the transition and  $m$  the electron mass. In deriving this expression from, for example Eq 4.89 in Reference [340], the *rotating wave approximation* is made; this amounts to assuming  $\omega - \omega_0 \ll \omega_0$  which is a very well justified approximation in our case (but see [339, p 1144]). The refractive index is often written in terms of the resonant cross-section  $\sigma_0$  as

$$n = 1 + \rho \frac{\sigma_0 \lambda_0}{4\pi} \frac{i - 2\Delta}{1 + 4\Delta^2} \quad (5.2)$$

where we have also written the frequencies as *detunings* from resonance  $\Delta = (\omega - \omega_0)/\gamma$ . The resonant cross-section is defined in terms of the fundamental constants, wavelength  $\lambda_0$ , linewidth  $\gamma$  and the transition-strength  $X_0^2$  as [342, Eq 8.91]

$$\sigma_0 = \frac{4\pi e^2}{\hbar\epsilon_0} \frac{X_0^2}{\lambda_0\gamma}. \quad (5.3)$$

Calculation of  $X_0^2$  and thus  $\sigma_0$  for hyperfine transitions is described in §5.2.3. We will see that symmetries often allow a simple expression to be used for  $\sigma_0$ . Saturation effects may be included by a Rabi-frequency power-broadening term in the denominator of (5.2) [342, §2.9]. As we will see in §5.1.9, the effects of power-broadening will be negligible for typical non-destructive imaging parameters.

### 5.1.3 Refractive index of a multi-level atomic gas

If the energy levels of a multilevel atom are separated by many times their natural linewidths, then the refractive index is simply a sum of terms of the form of (5.2) [340, p 195–197]. If the levels are closely spaced, as is typically the case for the excited hyperfine states of alkali atoms, then the two-level atom assumption of the above derivation is invalid. A multilevel model using the density-matrix formalism can predict atomic polarisation when multiple optical frequencies and decay rates are involved [343]. The susceptibility and hence the refractive index are recovered in the manner described above [344]. The result should be of the monomorphous

---

<sup>3</sup> It is important to note that here we have simply added up the contribution of a density  $\rho$  of individual *atomic* matrix-elements  $X_0$ . The derivation is often cast in terms of *bulk* dipole matrix-elements  $d_0$  with an assumption that the atoms are randomly oriented. Under this assumption  $X_0^2 = \frac{1}{3}|d_0|^2$ . Cold atom traps often contain highly-oriented populations of atoms, and we will deal explicitly with orientation in terms of angular momentum states when considering the detailed spectroscopy in §5.2.3 to 5.2.5 on pages 192–195. The notation used here is consistent with that of Loudon [340, See esp p 51], except that Loudon's  $\gamma$  is a half-linewidth. This thesis uses full linewidths.

form  $n = 1 + \rho(\delta + i\beta)$ ; the coefficients  $\beta$  and  $\delta$  would typically have to be found numerically.

In the analysis of our experimental results, we will see that assumption of well-separated energy levels is marginally satisfied, and so we assume a two-level system correcting only for the hyperfine dipole transition-strength.

#### 5.1.4 Refractive index for a dilute Bose gas

The first observation of Bose-Einstein condensation (BEC) of an atomic vapour in 1995 made a macroscopic, long-lived quantum state available for study. Condensation occurs when the *phase-space density* of atoms is greater than 2.612, implying low temperatures (typically below 400 nK) but also high spatial densities.

Quantum statistical effects on the refractive index have been studied: a slightly dated review may be found in Reference [345]. Morice et al. determined corrections to the refractive index to second order in the density (per cubic wavelength), and found correlation and multiple scattering effects changed the index slightly for temperatures near the transition temperature [346]. Other studies confirm that refractive index effects of condensation are small [347, 348] and we should be confident that our results can be extended to imaging of Bose-Einstein condensates. The one exception is *superradiant scattering*, an effect which exponentially enhances absorption for bright probe-beams above a threshold intensity. Superradiant scattering is discussed in §5.1.9.

#### 5.1.5 Weak and strong absorption by MOTs and BECs

Equation 5.2 shows that on resonance, the atom cloud is purely absorbing with no phase shift. In the wings of the spectral line, the cloud both absorbs and phase-shifts but at larger relative detunings  $\Delta$  the absorption falls as the reciprocal-square of the detuning, while the phase-shift falls only as the reciprocal. The sign of the phase-shift is positive  $\delta$  for red-detuned light and negative  $\delta$  when the probe is detuned to the blue.

Given an estimate of the density  $\rho$  and the characteristic size of the atom cloud, we can estimate an exit surface wavefield for a spherical or Gaussian object using (2.23). For a MOT around 300 μm in diameter and with a density of order  $10^{16}$  atoms m<sup>-3</sup>, the on-resonant ( $\omega = \omega_0$ ) absorption is of order one optical density (OD:  $I = I_0 \exp(-\text{OD})$ ). Phase-shift at one linewidth  $\Gamma$  detuning is of order one radian. It is readily shown, using for example (2.18), that optical rays are neg-

ligibly displaced on propagating through such a medium, and so the use of (2.23) is justified. At a detuning of ten linewidths, the object interacts only very weakly with the probe light, with absorption below 1% and phase-shift below 0.1 radian. A MOT may be regarded as an *optically thin* object.

Although most alkali BECs have small diameters of order 20 µm, the number density is typically so high – at least  $10^{18} \text{ m}^{-3}$  – that on-resonant absorption is commonly *hundreds* of optical densities. For all practical purposes, a resonantly-imaged BEC is opaque.

Conventionally, BECs are imaged on-resonance by turning off the trapping magnetic fields and allowing the BEC to expand ‘ballistically’.<sup>4</sup> The cloud is then imaged when the opacity is low enough. Clearly such a process is incompatible with imaging an evolving Bose-condensed system in its trapping potential. Alternatively, the opaque cloud may be imaged in the trap with the desired data such as peak density and FWHM extracted from fitting to the steep sides of the absorption profile [349]. It is clear that this technique is numerically unstable, and cannot be used to image any detail except at the edges of the BEC.

There is a much more critical problem with absorption imaging. The imaginary part of the refractive index corresponds to *absorption* of photons by the atomic gas. Under our assumption of a weak probe beam, absorbed photons will be re-emitted after a characteristic period of the natural lifetime, 28.5 ns for  $^{85}\text{Rb}$ . The photon is emitted in a random direction<sup>5</sup> and so either misses the detector or forms an isotropic low-level background, negligible in comparison to the probe illumination. The problem with absorption is not the spontaneously emitted *photon* itself, but the *recoil* kick that spontaneous emission gives to the atom.

### 5.1.6 Photon absorption destroys BEC

The recoil of a single photon  $\hbar k$  – corresponding to a temperature of order 400 nK for rubidium – may be greater than the depth of the trapping potential. Any atom that absorbs a photon is kicked out of the trap by the photon momentum. For BECs containing  $1 \times 10^9$  atoms, such as the hydrogen BEC at MIT [350], many millions

---

<sup>4</sup> The condensed component does *not* expand ballistically in the classical sense, rather the wavefunction propagates but in a reversible manner, at least for the lowest Landau level. The process has been described as a ‘wavefunction microscope’ [344].

<sup>5</sup> Some anisotropy is expected due to the orientation and alignment of the atom cloud and the magnetic fields present, however spontaneous emission is typically into a much larger solid angle than the coherent, elastic scattering process responsible for the *real* part of the refractive index.

of atoms may be ejected without seriously perturbing the condensate. Absorption imaging *can* be non-destructive in such cases.

A discernible absorption image might be taken over  $30 \times 30$  pixels with 100 photons per pixel [331, p 28]. Such an image involves absorbing of order  $10^5$  photons, which would be an unacceptable perturbation of a typical alkali BEC containing  $10^6$  atoms. For alkali and metastable noble gas condensates, absorption imaging is a destructive process.

This model of condensate depletion by the ejection of individual atoms is rather simplistic. Close et al. point out that when the cloud is optically thick, the scattered photon is likely to be reabsorbed before it leaves the cloud. This process is known as *radiation trapping* and may be observed in thick vapours at any temperature [351]. In conventional atomic vapour experiments, radiation trapping manifests itself as a propagation delay of light diffusing out of the medium. In the case of ultracold atoms, it magnifies the depletion of the condensate as one photon may knock many atoms out of the condensate before it escapes. The photon's peregrination within the cloud is limited by its mean-free path, or ultimately by energy loss to the atoms which red-shifts the photon out of resonance after  $\omega_{\text{recoil}}/\gamma \approx 1000$  scatterings.

It is also possible for the recoiling atom to interact with other atoms in the condensate as it departs [352]. The cross-section for atom-atom scattering is *much* smaller than the resonant optical cross-section, however, and this effect contributes inconsequentially to destruction when the probe light is resonant. Shortly, we will consider imaging with off-resonant probe light where the optical cross-section is much reduced. In this case, collective atomic recoil effects *can* be significant, and we return to them in §5.1.9.

These additional effects of interactions of the emitted photon and interactions of the recoiling atom *enhance* the destructivity of resonant absorption. If the probe laser is detuned from resonance, the absorption (and thus the destructivity) falls off rapidly, but the phase-shift may remain substantial. Imaging the atom cloud with off-resonant light is potentially non-destructive, but at large detuning the atom cloud approaches a pure phase object. The next Article provides an argument for the plausibility of off-resonant imaging. A quantitative comparison of imaging techniques must consider the signal-to-noise ratio for a given number of absorbed photons. This analysis is given in the critical comparison of imaging techniques in §5.6.

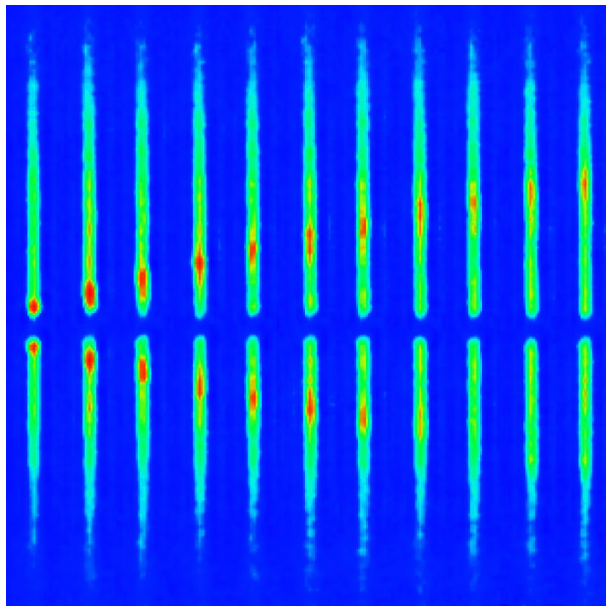


**FIGURE 5.2 Multiple non-destructive images of BEC taken at MIT.** Images were taken at 1.3 ms intervals, time advances to the right. Full length of condensate was 450  $\mu\text{m}$ . The images show a sound-wave propagating outwards from the centre, induced by an argon-ion laser pulse switched on 1 ms before the first image at left. Probe detuning was 1.7 GHz and a Zernike phase-plate with a 500  $\mu\text{m}$  spot was used (see §5.6.3); other details of imaging apparatus were not published. Reprinted from Reference 353.

### 5.1.7 The promise of off-resonant imaging

Consider a BEC with an *on-resonance optical density*  $D_0$  of 300. For probing on a closed transition (see §5.2.4), this corresponds to typical BEC parameters: a density of  $10^{20} \text{ m}^{-3}$  in a 20  $\mu\text{m}$  diameter cloud. It can be readily established from (5.2) and (2.23) that for a detuning of  $D_0/2\pi$  linewidths (around  $50 \Gamma$  or 300 MHz for this example), the peak phase shift through the cloud is  $\pi/2$  radians while the optical density decreases to  $\pi^2/D_0$ , in this case about 3%. The above-mentioned imaging pulse of 100 photons per pixel into a  $30 \times 30$  pixel array would now result in the absorption of only 2400 photons (and negligible radiation trapping): a small perturbation which would be non-destructive for most condensates.

The residual absorption of 3% is of the order of the technical noise on a carefully configured coherent imaging system, and so absorption imaging will result in very noisy images. The phase-shift, however, is easily detected: indeed,  $\pi/2$  is the optimal phase-shift for an interferometric detection scheme.

Off-resonant imaging of BEC was first demonstrated by the Ketterle group at MIT in 1996. They first used dark-ground imaging (§5.6.2) and subsequently a Zernike phase plate (§5.6.3) to render the phase-shift visible. Their sodium BEC had an on-resonant optical density of order 300 but was imaged 342 linewidths (1.7 GHz) red of resonance yielding a peak phase-shift of 0.2 radian and a residual absorption below  $10^{-3}$ . They demonstrated 11 consecutive non-destructive images of a sound-wave propagating through a BEC [353]; their published images are reproduced in Figure 5.2.

### 5.1.8 Optimising probe beam detuning, intensity and pulse length

While we defer a *quantitative* optimisation of the detuning and other parameters until Section 5.7, we can make some observations about the optical properties of an atom cloud imaged off-resonance.

We have seen that there are two problems with on-resonant imaging: the total opacity of the cloud and the destructivity. We might think that the first problem, although not the second, could be overcome by detuning by  $\sqrt{D_0}$  linewidths so that the optical density is of order unity and absorption imaging could then be used. The problem is that the residual phase-shift is approximately  $\sqrt{D_0}/2$  or more than 8 radian in our example. This strong phase gradient across the object will *refract* light, possibly beyond the aperture of the imaging system. Such lensing may even be strong enough to violate the eikonal approximation (see §2.2) for light propagating within the cloud.

More quantitatively, the angle of refraction  $\theta_r$  of initially axial ray is related to the transverse phase gradient by

$$\theta_r = \frac{\lambda}{2\pi} \nabla_{\perp} \phi, \quad (5.4)$$

which is readily verified by considering the phase-gradient of a plane wave. A cloud of diameter  $d$  has a gradient of approximately  $2\phi/d$ , yielding

$$\theta_r = \frac{\lambda}{\pi} \frac{\phi}{d}. \quad (5.5)$$

This can be compared to the angle of *diffraction*  $\theta_d = \lambda/2d$ . For us to be assured that a diffraction-limited imaging system will capture all of the light refracted *and*

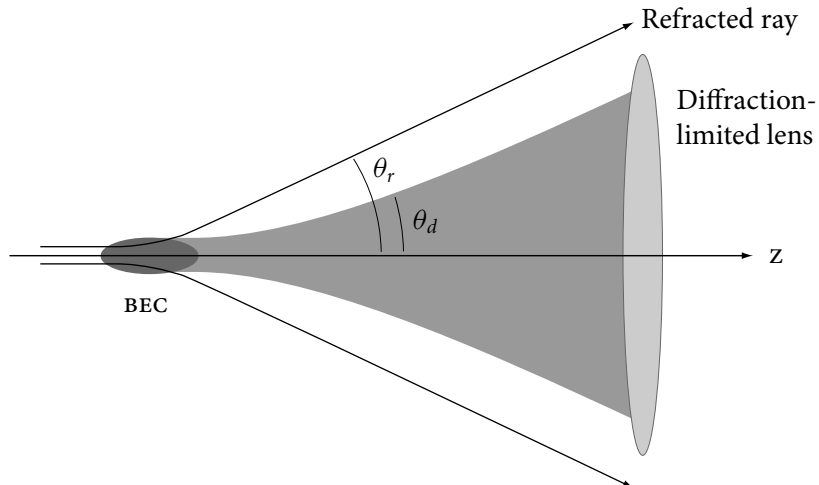


**FIGURE 5.3 Refraction and diffraction by a thick object.** The lens captures all light *diffracted* by the object and so the imaging system is *diffraction-limited* (see §5.5). But if the maximum phase-shift is  $> \pi/2$  then *refracted* rays will miss the lens and the image will be distorted.

diffracted by the object;<sup>6</sup>  $\theta_r$  must be less than  $\theta_d$ . Thus we require that the phase-shift through the object be less than  $\pi/2$ ; in a sense, the optimal phase-shift for very general phase-imaging system is the same as for an interferometer. In the previous Article we saw that this condition is satisfied if the detuning is more than  $D_0/2\pi$  linewidths. Naturally, increasing the detuning ad infinitum decreases the phase-shift, and hence the signal, and so in any practical system there must be an optimum detuning. This trade-off is further discussed in terms of quantitative signal-to-noise ratios in §5.7.

At such detunings, the cloud is optically *very* thin, and destructivity is a function only of the number of photons scattered  $N_s$ . For a fixed detuning this depends only on the *photon dose*, proportional to the product of intensity and exposure time. Higher photon doses are more destructive, but produce images with better signal-to-noise ratio (SNR). A balance must be found between the quality of the images and the number of images which can be taken before the object is too perturbed. The upper limit to exposure time is dictated by blurring due to the oscillation of the cloud in the trap, and is typically of order milliseconds. The lower limit of the exposure time is rather more involved.

Short exposure times of a few microseconds might be required to resolve extremely fast processes in BEC. Reducing the exposure time increases the intensity

<sup>6</sup> This argument is adapted from one in Reference 354.

necessary to create an image with the same photon dose and therefore the same SNR. If the probe intensity approaches the *saturation intensity*  $I_{\text{sat}}$  ( $1.64 \text{ mW cm}^{-2}$  for rubidium) then the effects of power-broadening must be considered. This is unlikely to be a major consideration as  $I_{\text{sat}}$  for rubidium corresponds to a flux of  $6.4 \cdot 10^9 \text{ photons cm}^{-2} \mu\text{s}^{-1}$ , enough to saturate a standard 12-bit CCD camera in a few microseconds.

There is, however, another effect which limits the probe beam intensity. In §5.1.6, we saw that for *resonant* light, radiation trapping magnified the effect of an absorbed photon whereas the cross-section for the recoiling atom to interact with another atom was negligible by comparison. For off-resonant light, the optical cross-section is reduced by a factor of  $1 + 4\Delta^2$  and radiation trapping ceases. Although the atom-atom cross-section is still very small, a subtle collective-atomic process has recently been discovered which is capable of amplifying the atom-atom interaction exponentially.

### 5.1.9 Superradiant Rayleigh scattering limits probe intensity

When Bose statistics are included in the atom-light interaction, a new *Bose-stimulated scattering* term appears in the cross-section [355]. Early discussions of this term identified it as being relatively unimportant [355], and Ketterle et al. ignore it in their analysis.

In 1999, the MIT group reported highly directional atom and light emission when a condensate was illuminated by a traveling, off-resonant laser beam. Their report [356] and later analyses [357–360] attributed the phenomena to an exponential gain process in which the strength of the Bose-stimulated recoil term is continually enhanced as more atoms recoil into the state. This *superradiant Rayleigh scattering* was found to have an onset-threshold scattering-rate set by the decoherence properties of the trap. Provided the scattering (absorption) rate is below the threshold, the Bose-stimulated contribution is indeed negligible. Once the absorption rate exceeds the threshold however, the run-away superradiant effect greatly perturbs the condensate.

In our example given above, we expected a successful off-resonant image with a few thousand absorbed photons in a condensate of a few million atoms: a per-atom absorption of about 0.001. A bright, short  $10 \mu\text{s}$  exposure with the same number of absorbed photons gives a scattering rate of 100 photons/sec, higher than the superradiant threshold of 50 photons/sec observed in the MIT experiment. This

estimate illustrates that Bose-enhanced recoil may set a lower limit for exposure times in non-destructive imaging.

### 5.1.10 Coherent recoil and backaction

We have so far considered atomic recoil for photons incoherently scattered (absorbed) by the atom cloud. Of course there must also be some back-action on the condensate by the coherent scattering (phase-shifting) process.

Coherently interacting photons are scattered into a diffraction cone of angle  $\lambda/2d$ , much smaller than the angles for incoherently scattered photons which are emitted isotropically. The atom recoil is correspondingly much less. Ketterle et al. have pointed out that if the imaging pulse is longer than the trap oscillation period, then atoms ‘sample’ the light from both sides of the cloud and the recoils cancel [354]. This Mössbauer-type effect couples the momentum to the entire trap, rather than the individual atoms. Imaging pulses shorter than the trapping period will impart a small recoil to individual atoms. This coherent recoil has less effect on the atom number than the residual incoherent absorption recoil, however [361–363].

Although off-resonant imaging of a condensate has only a small back-action on condensate number, it may have a larger back-action on the complimentary variable: the condensate phase [354]. The physical picture of this possible *quantum-nondemolition measurement* [364] is light-shifting of the condensate potential due to the probe beam. A recent study had to invoke an implausibly high probe intensity of  $100 \text{ mW cm}^{-2}$  to predict a measurable squeezing effect [365]. This perturbation may become more important as BEC are applied to the study of quantum information processing.



THIS SECTION has considered the effect of a cloud of cold atoms on a laser beam propagating through it, and found that a simple two-level atom refractive index accurately models the optical properties of the cloud over a wide range of parameters. We have also considered the effect of the laser beam on the atom cloud, including some unexpected collective effects due to the Bose statistics of the atoms. Bose-Einstein condensates are destroyed by the recoil of spontaneously-emitted photons, but by detuning off resonance the absorption can be reduced. The atom cloud becomes a weakly-absorbing phase object and sequences of many non-destructive images have been demonstrated by researchers using Zernike and other phase-imaging methods. In the next Section, we will see that these optical properties

TABLE 5.1 **Constraints on object parameters.** The requirements of optimal non-destructive imaging mesh very well with the approximations used in deriving the CTF solution linking column-density and diffraction-pattern contrast.

	BEC with $\Delta = D_0/2\pi$	Contrast transfer relation
Refractive index	$n = 1 + \frac{\rho(\mathbf{x})\sigma_0\lambda_0}{4\pi(1+4\Delta^2)}(2\Delta - i)$	$n = 1 + \rho(\mathbf{r})(\delta + i\beta)$
Absorption	$\pi^2/D_0$ , typically $< 0.03$ .	Must be $\ll 1$ .
Phase $ \phi $	$\pi/2$ , smaller at greater detuning.	Must be <i>slowly varying</i> , $ \phi(\mathbf{x}) - \phi(\mathbf{x} - \lambda z\mathbf{u})  \ll 1$ .
Phase (sign)	$\delta > 0$ for red detuning, $\delta < 0$ for blue detuning.	Low-frequency CTF null avoided when $\delta < 0$ .
Diffraction angles	$\theta_r < \theta_d$ Small for $d \gg \lambda$ .	Fresnel approx requires small angles $< \pi/6$ .

make cold atom clouds particularly well-suited to measurements with diffraction-contrast imaging.

## 5.2 Column-density retrieval for cold-atom objects

We have seen that for a broad range of imaging parameters, a cloud of cold atoms behaves as a classical, monomorphous object. The contrast transfer function theory of Chapter 2 should apply. In this Section, the constraints of that theory are compared with the destructivity constraints for off-resonant atom imaging. Quantitative retrieval of column-density requires accurate knowledge of the atomic transition-strength; these are given for linear and circularly-polarised probe light.

### 5.2.1 Non-destructive imaging and diffraction contrast

In Section 5.1 we saw how optimal and non-destructive imaging of cold atoms places constraints on the absorption and phase-shifts of light propagating through the cloud. In Section 2.5 we derived a linear shift-invariant system (LSI) relating column-density and diffraction contrast, also subject to constraints on the absorption and phase-shift.

Table 5.1 compares these constraints. First we see that the refractive index of an atomic gas fits the monomorphous template: the real and imaginary parts of  $n - 1$  are each proportional to the density. Next, it is unsurprising that off-resonant imaging satisfies the weak absorption constraint. Further, the imaging requirement that refraction angles be smaller than diffraction angles keeps phase shifts to around one radian, implying that the slowly-varying phase condition (SVPC) should be easily satisfied if propagation distances are moderate. Detunings of  $\Delta = D_0$  or more yield phase-shifts considerably less than one radian, and the SVPC is then satisfied at *any* propagation distance.

These constraints are sufficient to ensure the validity of the LSI relation between column-density and contrast. We saw in §3.2.3 that absorbing objects having a positive *real* part  $\delta$  of the refractive index produce diffraction patterns with a broad contrast null at low spatial frequencies. This loss of information makes the inverse problem much less stable. Fortunately, an atom cloud has negative  $\delta$  when the detuning is positive: that is, to the blue of the atomic transition.

It appears that cold atom clouds are ideal targets for diffraction-contrast imaging. Non-destructive imaging is inconvenient for standard imaging systems as absorption is vanishing and extra apparatus is needed to render phase-contrast. These are exactly the properties, however, which make non-destructive atom imaging an excellent subject for diffraction-contrast imaging.

There has been one prior investigation related to diffraction-imaging of cold atoms. In 1998 the group of D Meschede published images of diffraction patterns of a magneto-optical trap [366]. Although the authors recognised that this constituted a ‘holographic record’, they extracted information about the MOT by fitting diffracted-Gaussians to the diffraction pattern. This is not a robust or practical solution to the general inverse problem, and they recovered only the peak-height and width of the MOT. Experimental results presented in this Chapter show that the methods of this thesis recover detailed images of atom clouds. Our method is not restricted to Gaussian-shaped objects.

### 5.2.2 Diffraction contrast due to cold atoms

The two-level atom refractive index (5.2) matches the monomorphous template  $n = 1 + \rho(\delta + i\beta)$  with

$$\delta = -\frac{\sigma_0}{2k} \frac{2\Delta}{1 + 4\Delta^2} \quad \text{and} \quad \beta = \frac{\sigma_0}{2k} \frac{1}{1 + 4\Delta^2}. \quad (5.6)$$

Now substituting into the expression for diffraction contrast (2.94) yields

$$\tilde{C}(\mathbf{u}; z) = -\tilde{\rho}(\mathbf{u}) \frac{\sigma_0}{1 + 4\Delta^2} (2\Delta \sin \pi\lambda z u^2 + \cos \pi\lambda z u^2), \quad (5.7)$$

recalling that  $\tilde{C}(\mathbf{u}; z)$  is the Fourier transform of the diffraction contrast  $C(\mathbf{x})$  measured at distance  $z$  after the atom cloud. The important feature of this equation is that the cross-section  $\sigma_0$  appears only as an overall scaling factor and does *not* affect the *shape* of the transfer function.

This feature is important because the cross-section  $\sigma_0$  is seldom known with great precision. As we will see in the next Article, it depends on the hyperfine sub-level populations and is modified by magnetic fields and the orientation of atoms with respect to the probe laser polarisation axis  $\hat{e}$ . However, the form of (5.7) assures us that inaccuracies or variations in  $X_0^2$  are manifest in the retrieved image *exactly* as they would be in a traditional (focal plane) imaging system.

### 5.2.3 Hyperfine transition strengths

The refractive index (5.2) was derived under the assumption that any atomic orientation would be accounted for in the transition strength  $X_0^2$ .<sup>7</sup> Alkali gases have non-zero nuclear spin  $\mathbf{I}$  and so to analyse the orientation of atoms we must consider the coupling  $\mathbf{F} = \mathbf{I} + \mathbf{J}$  of the nuclear  $\mathbf{I}$  and total electron angular momentum  $\mathbf{J}$ . For alkali atoms, this in turn is the result of Russell-Saunders coupling  $\mathbf{J} = \mathbf{L} + \mathbf{S}$  of electron spin  $\mathbf{S}$  and orbital  $\mathbf{L}$  angular momentum.

The hyperfine structure of the  $^{85}\text{Rb}$  ground and excited states of the D<sub>2</sub> transition is shown in Figure 5.4. Often the atoms in the trap are optically pumped or otherwise selected into a single Zeeman substate of the ground state  $|Fm_F\rangle$ , where the quantum numbers  $F$ ,  $m_F$  and so on are the eigenvalues of the angular momentum operators defined above. Under our two-level atom assumption, probe light of polarisation<sup>8</sup>  $q$  couples this ground state to the excited state  $|F'm'_F\rangle$  with  $m'_F = m_F - q$  and the usual  $\Delta F = 0, \pm 1$  except  $F = 0 \rightarrow F' = 0$  selection rule applying. The transition strength is then

$$X_0^2 = |\langle Fm_F | r_q | F'm'_F \rangle|^2. \quad (5.8)$$

---

<sup>7</sup> This Article and the following two draw on the excellent set of unpublished notes by D A Steck, available online [367]. References in text are to the published literature.

<sup>8</sup> The index  $q$  identifies the spherical basis in which  $q = -1$  is right-handed circular, 0 linear and  $+1$  left-handed circular polarisation.

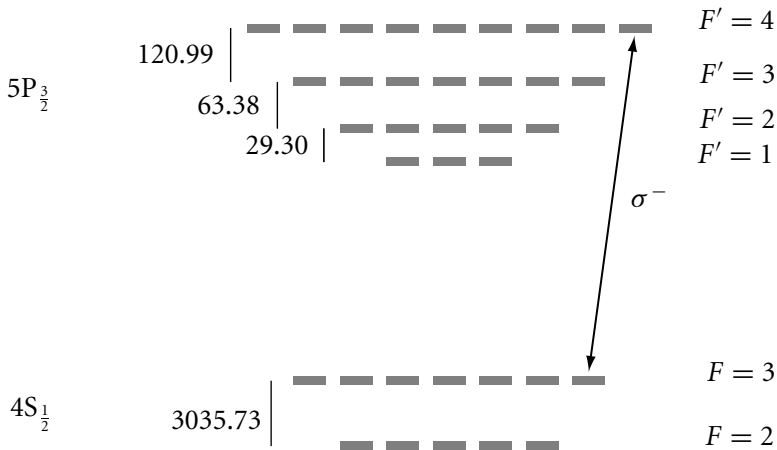


FIGURE 5.4 **Hyperfine structure of  $^{85}\text{Rb}$ .** The hyperfine ( $F$ ) and Zeeman ( $m_F$ ) sublevels of the  $4\text{S}_{\frac{1}{2}}$  ground-state and  $5\text{P}_{\frac{3}{2}}$  excited state are shown with separations in megahertz. Left-handed circularly-polarised ( $\sigma^-$ ) light drives the closed transition marked. Energy levels are from Reference 262.

The angular dependence may be factored out using the Wigner-Eckart theorem [368, p 77] and written in terms of the *Wigner 3-j symbol*, denoted by six parameters in parentheses:

$$X_0^2 = |\langle F \parallel \mathbf{r} \parallel F' \rangle|^2 (2F + 1) \begin{pmatrix} F' & 1 & F \\ m'_F & q & -m_F \end{pmatrix}^2, \quad (5.9)$$

and as the nuclear spin  $I$  is constant, the reduced hyperfine dipole element  $\langle F \parallel \mathbf{r} \parallel F' \rangle$  may in turn be factored [368, Eq 9.63] into a *Wigner 6-j symbol* (in braces) and a reduced fine-structure dipole element  $\langle J \parallel \mathbf{r} \parallel J' \rangle$  giving

$$X_0^2 = |\langle J \parallel \mathbf{r} \parallel J' \rangle|^2 (2F + 1)(2F' + 1)(2J + 1) \begin{pmatrix} F' & 1 & F \\ m'_F & q & -m_F \end{pmatrix}^2 \left\{ \begin{matrix} J & J' & 1 \\ F' & F & I \end{matrix} \right\}^2. \quad (5.10)$$

We could take this one step further and factor the  $J$  dependence, but we are working only with a single fine-structure transition, namely the D<sub>2</sub> line. The reduced transition strength can be found in terms of the transition wavelength  $\lambda_0$  and the natural linewidth  $\gamma$

$$|\langle J \parallel \mathbf{r} \parallel J' \rangle|^2 = \frac{2J' + 1}{2J + 1} \frac{3\gamma \hbar \epsilon_0 \lambda_0^3}{8\pi^2 e^2}. \quad (5.11)$$

For the D<sub>2</sub> transition, which couples the  $4\text{S}_{\frac{1}{2}}-5\text{P}_{\frac{3}{2}}$  states, the transition strength

takes the value [340, Eq 8.84]<sup>9</sup>

$$\left| \langle J = 1/2 \| \mathbf{r} \| J' = 3/2 \rangle \right|^2 = 17.85(6) a_0^2 = 5.003(5) 10^{-20} \text{ m}^2. \quad (5.12)$$

These expressions are sufficient for us to calculate the transition strength for circular or linear polarisations when all the atoms are in *any* single initial state. Care must be taken that the quantisation axes are consistent: the axis of the optical pumping or magnetic trapping process preparing the atoms in a particular state must agree with the propagation vector of the probe light. If the axes do not coincide, an appropriate change of basis is necessary. A change of basis is also required if the bias magnetic fields of the trap induces Zeeman shifts which are a substantial fraction of the detuning.

Fortunately, there are two experimentally-relevant cases which obviate the angular momentum algebra: oriented atoms imaged on-axis with circularly-polarised light, and arbitrarily-oriented atoms imaged with far off-resonant linearly-polarised light.

#### 5.2.4 Circularly-polarised probe light

Bose-Einstein condensates typically consist of atoms in a *maximally-oriented* ‘stretched’ state with  $F = I + J$  and  $m_F = \pm F$ . For light at the D<sub>2</sub> line, the appropriate choice of circular polarisation couples chiefly to the  $F' = F + 1$ ,  $m'_F = \pm F'$  extreme sublevel of the excited state from which atoms may only relax back to the maximally-oriented ground sublevel, as shown in Figure 5.4. This is known as a *closed transition*.

Symmetry rules for the Clebsch-Gordan coefficients yield a particularly simple value for the strength  $X_0^2$  of a closed transition. Summing over all the transitions which couple to a single excited sublevel reduces the transition strength to

$$\sum_{qF} \left| \langle F m_F | r_q | F' m'_F \rangle \right|^2 = \frac{2J+1}{2J'+1} \left| \langle J \| \mathbf{r} \| J' \rangle \right|^2, \quad (5.13)$$

where  $m_F = m'_F + q$  [367, Eq 40]. As only one of the extreme ground sublevel couples to the extreme excited sublevel, the sum vanishes for the closed transition,

---

<sup>9</sup> More rigorously, see Eq 9.47 of Sobelman [368] but note the use of CGS units and also the convention  $\langle J \| \mathbf{r} \| J' \rangle = \sqrt{2J+1} \langle J \| \mathbf{r} \| J' \rangle$ .

and on substituting (5.11) we have

$$X_{\text{closed}}^2 = \frac{3\gamma\hbar\epsilon_0\lambda_0^3}{8\pi^2 e^2}. \quad (5.14)$$

Substituting into the expression (5.3) for the resonant cross-section gives

$$\sigma_{\text{closed}} = \frac{3\lambda_0^2}{2\pi}. \quad (5.15)$$

From (5.2), the associated refractive index is then

$$n_{\text{closed}} = 1 + \rho(\mathbf{x}) \frac{3\lambda_0^3}{8\pi^2} \frac{i - 2\Delta}{1 + 4\Delta^2} \quad (5.16)$$

The expression contains no degeneracy parameters in  $J$  or  $J'$  and so applies to *any* closed transition.

For this expression to apply, the quantisation axis of the atoms must coincide with the imaging axis: the k-vector of the probe light. Typically this means imaging along the quadrupole axis of the trap.

Accurate measurements of BEC column-density are probably best performed with circular polarisation to ensure that only a single hyperfine transition contributes to the transition strength. When imaging a MOT, or other system where atoms do not have a strong common orientation, imaging is better performed with linearly-polarised light.

### 5.2.5 Linearly-polarised probe light far off resonance

An alternative simplification of the general expression (5.10) can be obtained when the light is detuned far from resonance in comparison to the splittings between upper hyperfine states. In  $^{85}\text{Rb}$ , this splitting is less than 200 MHz as shown in Figure 5.4, and so this simplification clearly applies to a typical BEC-imaging detuning of at least  $100\Gamma$ .

If the light is far-detuned then interactions with all possible excited-states contribute to the total transition strength with similar weightings. Hence we must sum over all possible excited states. If, in addition, the light is linearly-polarised then we have the sum [367, Eq 44]

$$X_{\text{linear}}^2 = \sum_{F'} |\langle F m_F | r_0 | F' m'_F \rangle|^2 = \frac{1}{3} |\langle J \parallel \mathbf{r} \parallel J' \rangle|^2, \quad (5.17)$$

which is independent of which ground-state  $|F m_F\rangle$  is chosen.

The proof of this simplification would require a long excursion into Racah algebra [369, §6.2], but the interpretation is straight-forward. The far-detuned light interacts with the whole excited-state manifold, and so for a single ground state, this is an interaction with the full  $J \rightarrow J'$  transition. The linearly-polarised light interacts with a single Cartesian component of the spherically-symmetric full transition and so the strength is reduced by a factor of one-third.

The resulting expression for the linearly-polarised resonant cross-section is

$$\sigma_{\text{lin}} = \frac{2J' + 1}{2J + 1} \frac{\lambda_0^2}{2\pi} \quad (5.18)$$

where the degeneracy parameter is 2 for D<sub>2</sub> lines and 1 for D<sub>1</sub> lines.

Off-resonant imaging with linear polarisation has the advantage that the cross-section (5.18) is *independent* of how the atomic population is distributed among hyperfine ground-states. The expression (5.16) for circularly-polarised light assumed the atoms were in the maximally-oriented ground state. This is very likely an excellent assumption for imaging a standard BEC along its quantisation axis, but not for other cases. Linearly-polarised imaging is more appropriate if the quantisation axis is expected to vary significantly across the object, or if the atom cloud isn't macroscopically oriented or aligned.

Atoms in the  $\sigma^+ - \sigma^-$  optical lattice of a MOT experience a linearly-polarised field with the polarisation axis varying on a wavelength scale. This results in an atomic population with at most slight overall alignment along the propagation-axes but no orientation [370]; we would expect this from the symmetry of the system. Linearly-polarised imaging is indicated, with the only caveat being that practical detunings for MOT imaging are unlikely to be greater than the excited-state hyperfine splitting for most of the alkalis. Nevertheless we might expect the linear-polarisation result (5.18) to be accurate to better than 10% given the relevant Clebsch-Gordan coefficients and the effect of the repumper in maintaining population in the upper ground state. This is the expression used for retrieving the column-density from diffraction images of the MOT in the experiments described in the next two Sections.



THE CONSTRAINTS of non-destructive imaging align very well with those for retrieval of column-density from diffraction patterns. Applying the contrast transfer

theory of Chapter 2 to imaging atoms required only the substitution of the refractive index components  $\delta$  and  $\beta$  appropriate for cold atoms. We saw that the diffraction contrast is no more sensitive to inaccuracies in the transition strength than other imaging methods. Uncertainties in the transition strength due to varying or unknown distributions in the Zeeman population appear to be minimised by the use of linear-polarised probe light. With the appropriate transition-strengths determined, (5.7) yields the diffracted intensity given an atom density distribution. The inverse-problem solving methods of Chapter 3 should retrieve this density distribution from the measured diffraction pattern. The next Section presents experimental demonstrations of such retrievals.

## 5.3 Experiments with defocus-contrast imaging

The first Section of this Chapter showed that off-resonant imaging allows non-destructive observation of Bose-Einstein condensates. A BEC was not available, however, so experiments on diffraction-contrast imaging were instead performed on a MOT. This Section presents defocused images of a MOT and shows that imaging with a defocused lens system is equivalent to free-space propagation. Column-densities are then retrieved from the defocus-contrast images and compared to column-densities obtained by conventional absorption imaging.

### 5.3.1 Why image a MOT off-resonance?

Only the very coldest or smallest atom traps are perturbed by resonant imaging. Alkali and metastable noble gas condensates are destroyed by resonant imaging, but most non-condensed systems are less sensitive. There is still a role for off-resonant imaging, however, if resonant absorption is greater than a few optical densities and the object is effectively opaque. This Section describes off-resonant imaging of a MOT: an object neither cold enough, small enough, nor opaque enough for off-resonant imaging to have any advantage over resonant absorption imaging in terms of SNR or destructivity. Despite this, we will see that the holographic nature of diffraction-contrast imaging offers a much greater depth-of-field than focal-plane imaging methods even when the non-destructivity advantage is negligible. We will also see that a product relationship exists between the signs of the defocus and the detuning, enabling stable retrievals even when the probe light is red-detuned from resonance.

The MOT trapping and imaging apparatus is an extremely good approximation to that used for BEC. Both systems have similar optical access constraints and technical noise sources. Successful diffraction-contrast imaging of a MOT would augur well for using the technique to image BECs non-destructively.

### 5.3.2 Obtaining defocused images of the MOT

The first experiments were based on a defocused absorption imaging system. The apparatus was depicted in Figure 4.15. When the first series of experiments were performed in 2002, I was unaware of the contrast transfer function formalism and intended to use Paganin's TIE-based method to retrieve column-densities from the diffraction patterns.

As described in §3.3, the TIE retrieves only weakly-diffracted details and so requires short propagation distances. Structures of size  $d \approx 50 \mu\text{m}$  are retrieved quantitatively at propagation distances smaller than  $d^2/\lambda \approx 3 \text{ mm}$ . The size of the vacuum chamber makes it impossible to place a detector closer than 190 mm from the MOT. A lens placed outside the chamber *reimages* the diffraction-pattern onto the detector, allowing images to be obtained at arbitrarily small *effective* propagation distances. Here I present images obtained at several defocuses and detunings; the following Articles give a full discussion of the equivalence of defocused imaging and free-space propagation and then column-densities are retrieved from the defocused images.

Real-world imaging deviates from the ideal in several ways. The illuminating wavefield incident on the object is far from uniform. On exiting the fibre it is, to a good approximation, Gaussian but diffraction from imperfections in the collimating lens and vacuum windows, and aperturing by the vacuum ports, induce substantial nonuniformity in the probe wavefield incident on the MOT. Etaloning in the detector adds further fringes to the detected intensity; these noise sources are discussed further in §5.7.2. Ironically, these inhomogeneities are termed the *flat-field*, visible when the MOT is turned off: an example is shown in Figure 5.5B. In this first series of experiments, the MOT trapping beams were not turned off while exposing the CCD. Fluorescence from the MOT (Figure 5.5C) was measured with the probe beams turned off. With both MOT trapping beams and the probe beam turned off, the detector registered residual stray light and thermal dark currents noise shown in Figure 5.5D. The raw diffraction pattern (Figure 5.5A) at the CCD contains contributions from all three effects.

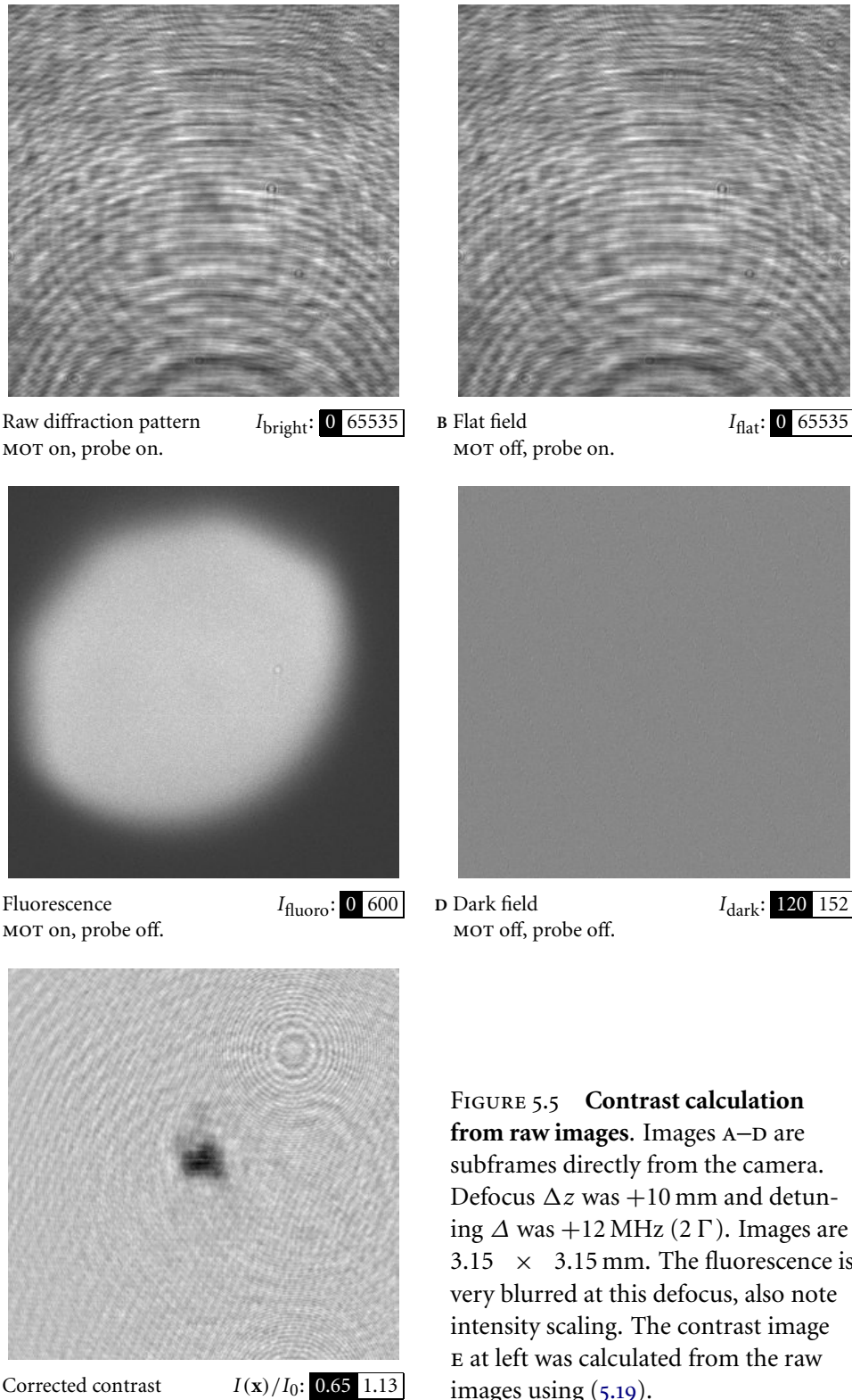


**FIGURE 5.5 Contrast calculation from raw images.** Images A–D are subframes directly from the camera. Defocus  $\Delta z$  was +10 mm and detuning  $\Delta$  was +12 MHz ( $2 \Gamma$ ). Images are  $3.15 \times 3.15$  mm. The fluorescence is very blurred at this defocus, also note intensity scaling. The contrast image E at left was calculated from the raw images using (5.19).

A better measurement of the dimensionless contrast  $C(\mathbf{x})$  is found from

$$C(\mathbf{x}) = \frac{I_{\text{bright}} - I_{\text{fluoro}}}{I_{\text{flat}} - I_{\text{dark}}} - 1; \quad (5.19)$$

the result for our example is Figure 5.5E, which is clearly an improvement over the raw image Figure 5.5A. This expression presumes that, to some degree of accuracy, the constant illumination intensity  $I_0$  in the derivation of the CTF relation can be replaced with a non-uniform intensity  $I_{\text{flat}}(\mathbf{x})$ . The general treatment of inline holography outlined in Appendix C can be shown to support this presumption, at least for weak objects.

For quantitative retrieval of the column-density, the trapping beams must be turned off so that there is no saturation of the probe transition. The somewhat complicated beam-gating and pulse sequencing apparatus needed to achieve this was not implemented for this first series of experiments. Instead, a neutral-density filter was placed in front of the imaging lens, reducing both the probe beam and the fluorescence by a factor of 4. The probe intensity was then increased to compensate. This approach was a poor substitute for gating the trapping beams but did enable the fluorescence contribution to be reduced to below 1% of the probe intensity (Figure 5.5C). If the trapping beams are turned off, or if imaging BEC or other non-dissipative systems, there is no fluorescence signal and the  $I_{\text{fluoro}}$  in the numerator should be replaced with  $I_{\text{dark}}$ .

Images were obtained for a range of defocuses and detunings, using the imaging apparatus which was described in §4.8.2. In this first series of experiments, the imaging apparatus was set up and images taken by Karl Weber.

Initially, the probe beam was turned off and the imaging system focused on the MOT fluorescence by adjusting the lens focusing collar until the peak pixel value was maximised. The imaging system was then translated through the defocus distance along an optical rail. Laser detuning was accomplished by Zeeman-shifting the saturated-absorption reference, calibrated by a beat-note measurement with an RF spectrum analyser.

The effective pixel size is the other critical parameter as it scales the spatial frequency matrix used to calculate the inverse filter. While the actual pixel size is determined by the photolithographic construction of the CCD chip, and is therefore known to better than 1%, the magnification of the imaging system must be accounted for. This was achieved by focusing the image system on a resolution target, measuring the effective pixel size to a few percent accuracy.

New fluorescence, flat-field and dark-frame images were obtained at each defocus. Exposure time was 15 ms with a probe intensity of  $5 \mu\text{W cm}^{-2}$  at the MOT. The CCD camera temperature controller was set to  $-15^\circ\text{C}$  and the readout rate to the minimum to reduce thermal and digitisation noise. Images were acquired using Roper Scientific WinView-32 software and stored as 16-bit TIFF files. At each detuning and defocus, the dimensionless contrast  $C(\mathbf{x})$  was calculated from the appropriate raw images using routines written in IDL (the Interactive Data Language, Research Systems Inc, Boulder CO, USA).

### 5.3.3 Analysis of defocused MOT images

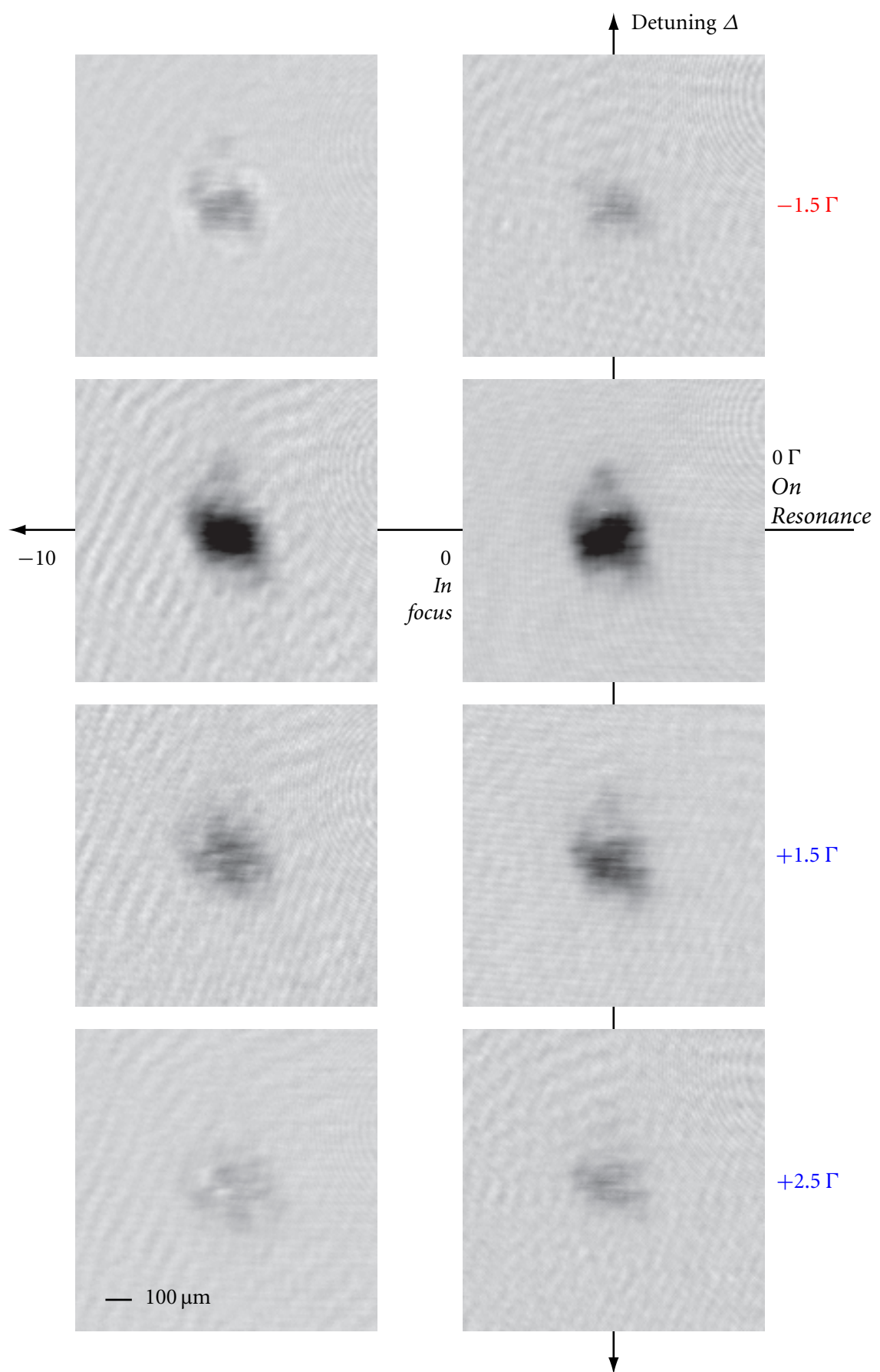
Partial frame images are displayed for an array of defocus and detuning settings in Figure 5.6. Note that the greyscale is the same for all images to facilitate comparison.

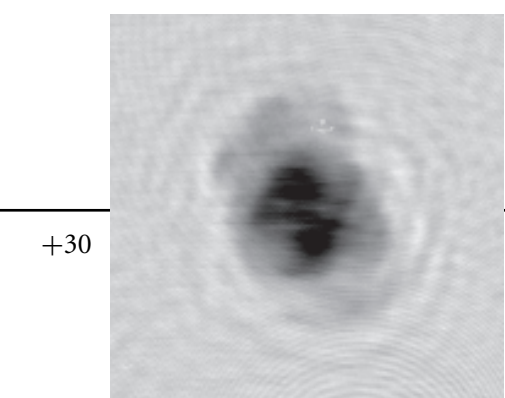
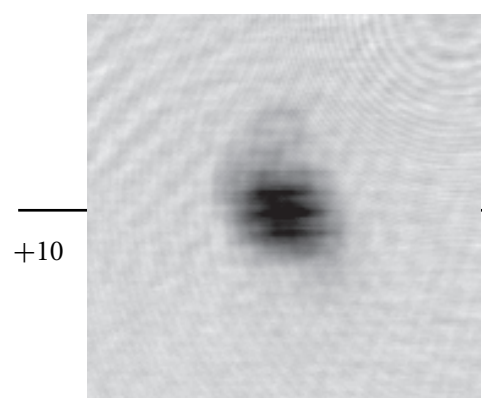
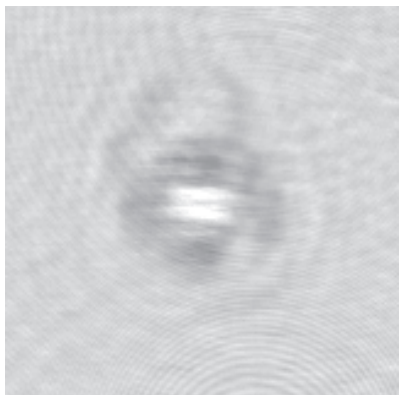
The second column shows images at zero defocus, that is, standard absorption images. The Lorentzian fall-off in absorption is clearly visible as the probe is detuned. For  $+9 \text{ MHz}$  ( $+1.5 \Gamma$ ) detuning, anti-lensing is visible at  $+10 \text{ mm}$  defocus and prominent at  $+30 \text{ mm}$ . Further to the blue at  $+15 \text{ MHz}$  detuning, the anti-lensing is less clear at  $+10 \text{ mm}$  but becomes obvious by  $+30 \text{ mm}$  defocus. When the probe is shifted 9 MHz to the red, lensing is discernible at  $+10 \text{ mm}$  and very clear at  $+30 \text{ mm}$ . On resonance, defocuses of  $\pm 10 \text{ mm}$  seem to have little effect, although spreading of the pattern due to diffraction is evident in the  $\Delta = 0, z = +30 \text{ mm}$  image.

Interestingly, the negatively-defocused and red-detuned image  $(\Delta, z) = (-1.5 \Gamma, -10 \text{ mm})$  in the upper-left corner closely resembles the positively-defocus and blue-detuned image at  $(+1.5 \Gamma, +10 \text{ mm})$ . The blue-detuned but negatively-defocused image at lower-right has bright spots towards its centre, indicating lensing. To understand the effects of negative defocus, we have to look more closely at the equivalence between a defocused imaging system and free-space propagation. The next two Articles consider this isomorphism before we return to the analysis of the defocused images using the retrieval techniques of Chapter 3 in §5.3.7.

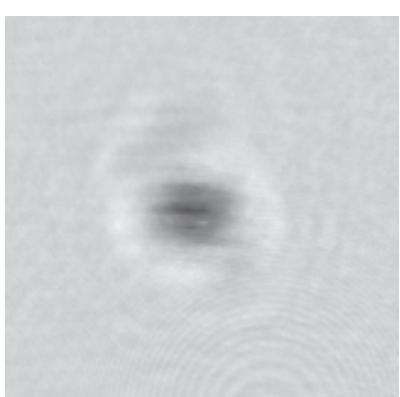
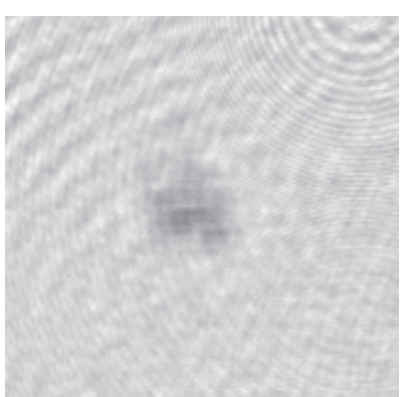
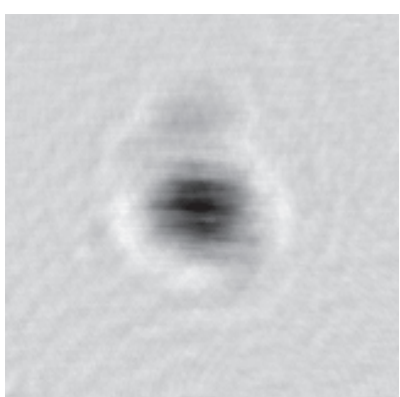
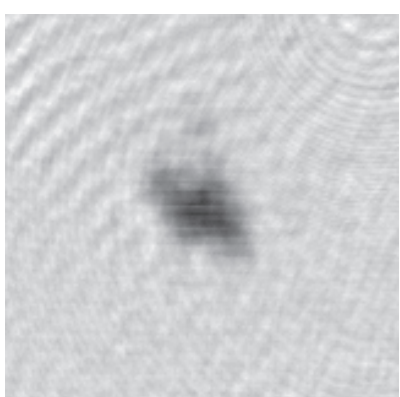
### 5.3.4 Equivalence of single-lens defocus and free-space propagation

The effect of the lens in reimaging a diffraction pattern is best understood using the matrix optics methods mentioned in §2.6. Figure 5.7A shows an imaging system composed of free-space propagation through a distance  $z_1$  followed by traversal of





Defocus  
(mm)



a lens with focal length  $f$  followed by a further free-space propagation of distance  $z_2$ . In the paraxial optics approximation, a lens imparts a phase-shift quadratic in the radial position vector. The matrices for the system are

$$\begin{aligned} \begin{pmatrix} 1 & \lambda z_2 \\ 0 & 1 \end{pmatrix} \begin{pmatrix} 1 & 0 \\ -\frac{1}{\lambda f} & 1 \end{pmatrix} \begin{pmatrix} 1 & \lambda z_1 \\ 0 & 1 \end{pmatrix} &= \begin{pmatrix} \frac{-z_2}{z_1} & 0 \\ -\frac{1}{\lambda f} & -\frac{z_1}{z_2} \end{pmatrix} \\ \text{Free space} & \text{Lens} \quad \text{Free space} \quad \text{provided } \frac{1}{f} = \frac{1}{z_1} + \frac{1}{z_2} \\ &= \begin{pmatrix} 1 & 0 \\ -\frac{1}{\lambda f M} & 1 \end{pmatrix} \begin{pmatrix} M & 0 \\ 0 & \frac{1}{M} \end{pmatrix}. \end{aligned} \quad (5.20)$$

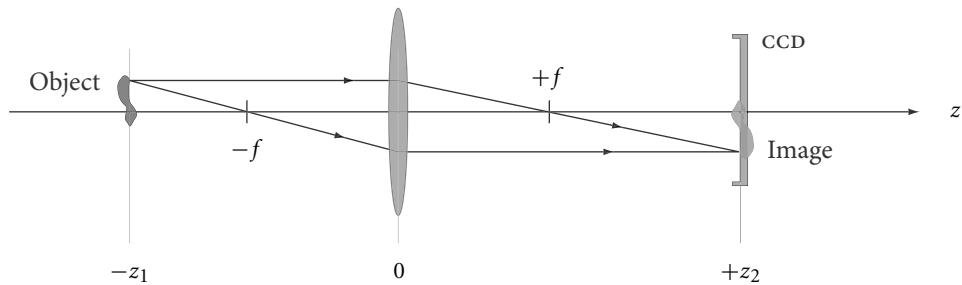
Chirp multiply      Magnification

Recall that we saw in §2.6 that the matrix elements correspond to parameters in a linear canonical transform of the wavefield. The product simplifies to the right-hand side of (5.20) provided the thin *lens equation*  $1/f = 1/z_1 + 1/z_2$  is satisfied; in this case the action of the system is a *magnification*  $M = -z_2/z_1$  followed by a *chirp multiplication*. This last operation is the same as traversing a lens with focal length  $Mf$ . Note, however, that the basic lens matrix assumes an infinitesimally thin lens which affects only the phase of the wavefield and does not displace rays. As our detector is sensitive only to the intensity of the wavefield, the phase-chirp multiplication has no effect on the measurement. This is proved formally in (5.23). We have proved the familiar result that a lens maps intensity from one plane to another with spacings satisfying the lens equation.

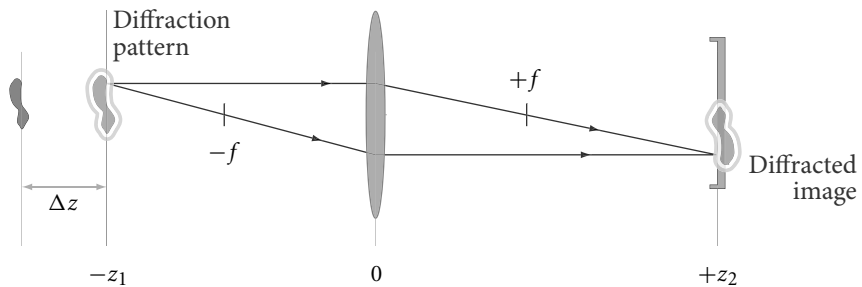
It is now straight-forward to analyse the defocused imaging case shown in Figure 5.7B. Consider moving the entire lens-and-camera assembly away from the object by a distance  $\Delta z$ . The propagation distance from the object to the first lens is  $z = z_1 + \Delta z$  and so we can write the right-most matrix in (5.20) as a propagation of  $\Delta z$  followed by a further propagation of  $z_1$ . Applying the result of (5.20) for the

---

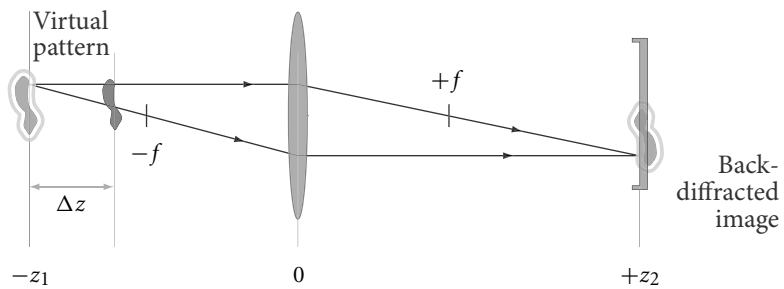
FIGURE 5.6 (ON PRECEDING SPREAD) The spread shows the measured contrast  $C(\mathbf{x})$  as a function of defocus (horizontal axis) and detuning (vertical axis). In-focus images lie along the vertical axis and on-resonance images along the horizontal axis. Each image is a  $160 \times 160$  pixel subframe with each pixel the equivalent of a  $7.15 \mu\text{m}$  square in the object-plane. All images are greyscaled identically, with black corresponding to a contrast of  $-0.4$  and white to  $0.15$ . The on-resonance images in particular have contrast beyond this range but this scaling was necessary so that structure could be discerned in the lower-contrast images while keeping the greyscale uniform.



A A single lens forming an imaging system.



B The imaging system has been moved away from the object a distance  $\Delta z$ . The diffraction pattern after this distance is imaged onto the detector.



C The imaging system moved *towards* the object. A virtual diffraction pattern behind the object is imaged onto the detector.

**FIGURE 5.7 Equivalence of simple-lens defocus and propagation.** Defocusing a simple imaging system A images the diffraction pattern at the input plane onto the detector (B). Focusing behind the object (C) is equivalent to diffraction over a negative propagation distance.

effective focused system yields

$$\begin{pmatrix} M & 0 \\ -\frac{1}{\lambda f} & M \end{pmatrix} \begin{pmatrix} 1 & \lambda \Delta z \\ 0 & 1 \end{pmatrix} = \begin{pmatrix} M & M\lambda \Delta z \\ -\frac{1}{\lambda f} & \frac{1}{M} - \frac{\Delta z}{f} \end{pmatrix}. \quad (5.21)$$

Focal system      Free space      Defocused system

This resulting ABCD-matrix has  $B \neq 0$  and so the associated LCT is found by inserting the  $A$ ,  $B$  and  $D$  elements into (2.111). Note, however, that the factor involving  $D$  does *not* involve the dummy variable  $\mathbf{x}'$  and so may be factored outside the integral. Inserting the  $A$  and  $B$  elements inside the integral yields

$$(\mathcal{L}f)(\mathbf{x}) = \frac{i}{B} \exp\left(\frac{i\pi}{B} D|\mathbf{x}|^2\right) \iint_{-\infty}^{\infty} f(\mathbf{x}') \exp\left(\frac{i\pi}{M\lambda\Delta z} (-2\mathbf{x} \cdot \mathbf{x}' + M|\mathbf{x}'|^2)\right) d\mathbf{x}'. \quad (5.22)$$

Finding the intensity after propagation through the imaging system,  $I = |\mathcal{L}f|^2$ , eliminates the factor involving  $D$ . Incorporating a further arbitrary phase factor, we find

$$I(M\mathbf{x}) = \frac{1}{(\lambda\Delta z M)^2} \iint_{-\infty}^{\infty} f(\mathbf{x}') \exp\left(\frac{i\pi}{\lambda\Delta z} |\mathbf{x} - \mathbf{x}'|^2\right) d\mathbf{x}', \quad (5.23)$$

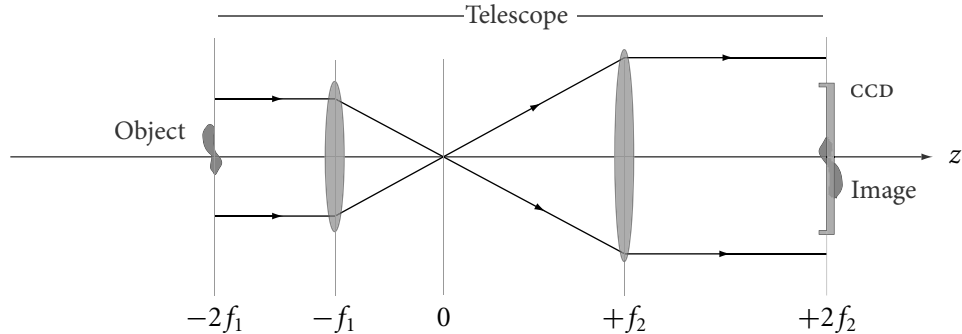
which is merely a magnification of the Fresnel equation for free-space propagation over the distance  $\Delta z$ .

In general, we have a single lens of focal length  $f$  positioned a distance  $z$  after the object and a distance  $z_2$  before the detector. The system is isomorphic to magnified free-space propagation. The effective magnification of the system is  $M = z_2/f - 1$  and the effective propagation distance is  $\Delta z = z - z_1 = z - fz_2/(z_2 - f)$ .

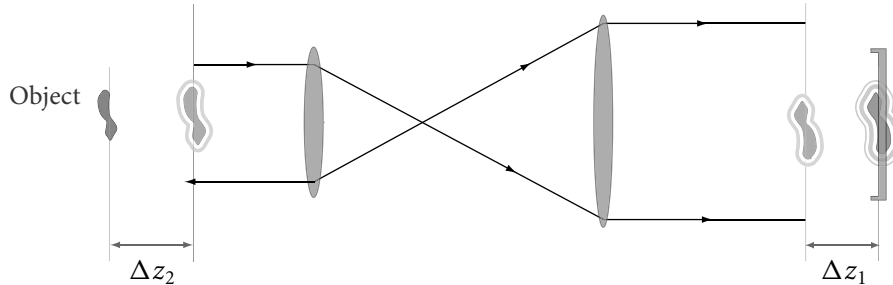
### 5.3.5 Equivalence of telescope defocus and free-space propagation

Most real-world imaging systems will use at least two lenses, enabling more compact configurations, cancellation of aberrations and simpler focusing, especially if SLR camera lenses are used. A less elaborate, but commonly used system is the simple telescope shown in Figure 5.8A.

Matrix calculations readily prove that the magnification of the whole system is  $M = -f_2/f_1$  with no residual curvature: the magnified wavefield is reproduced exactly at the exit plane. It then follows directly that if the object is placed a distance  $z_1$  before the entrance plane and the detector is placed a distance  $z_2$  after the exit



A A two-lens telescopic imaging system.

B The above telescope with front-defocus  $\Delta z_1$  and back-defocus  $\Delta z_2$ .

**FIGURE 5.8 Focused and defocused imaging with a two-lens telescope.** The telescope in A creates at  $+2f_2$  a magnified version of the wavefield at  $-2f_1$ . Additional propagation shown in B before or after the telescope is equivalent to sequential free-space propagation if magnification is accounted for by (5.24).

plane (Figure 5.8B), the effective propagation distance is

$$z_{\text{eff}} = \Delta z_1 + \frac{\Delta z_2}{M^2}. \quad (5.24)$$

The magnification is fixed by the focal lengths and, unlike for the single lens, is not changed by moving the detector. This insensitivity simplifies the correction of defocus errors, a topic we return to in §5.4.2.

In our MOT imaging case we use effective propagation distances of several centimetres with magnifications somewhat greater than one, and so it is more efficient to defocus the front focal-plane than the back. In other applications, this mode might be impractical or impossible. A very high resolution imaging system might

be formed by placing a microscope objective lens inside the vacuum system. Such a system could be conveniently defocused by moving the back-focal plane. At substantial magnifications back-focusing will also be less sensitive to focusing errors.

### 5.3.6 Negative defocus and red detuning

The immediate result is that, as expected, we can image the diffraction pattern arbitrarily close to the object simply by defocusing a standard absorption-imaging system. As the apparatus is identical, defocus imaging can be readily assessed against absorption imaging and fluorescence imaging.

A more subtle result follows if the imaging system is defocused *towards* the object and so  $\Delta z$  is negative (Figure 5.7c). Very naively, we might expect the flat intensity which would be measured by placing a detector before the object to be imaged onto the detector, resulting in a featureless image. The matrix analysis tells us that the intensity is a magnified version of the wavefield after propagating the *negative* distance  $\Delta z$ . Propagation over negative distances is unphysical but is perfectly valid mathematically: there is no harm in using a negative  $z$  in the diffraction integral (2.49) which corresponds to the free-space ABCD matrix.

The contrast transfer expression (2.94) followed from this Fresnel diffraction integral and so we can describe the defocus-towards-object case by substituting a negative  $z$  into that expression. Putting  $z = -|z|$  into (2.94) yields

$$\tilde{C}(\mathbf{u}; z) = 2k\tilde{\rho}(\mathbf{u}) \left( -\delta \sin \pi\lambda|z|u^2 - \beta \cos \pi\lambda|z|u^2 \right), \quad (5.25)$$

the only change being in the sign of the *phase* component  $\delta \sin \pi\lambda zu^2$ . In the case of cold-atom imaging (5.7), the *detuning*  $\Delta$  is multiplied by the sign of the defocus. The diffraction pattern measured for blue-detuning and positive defocus is *identical* to that measured for red-detuning and negative defocus. This isomorphism explains the similarity between the  $(-1.5 \Gamma, -10 \text{ mm})$  and  $(+1.5 \Gamma, +10 \text{ mm})$  images in Figure 5.6, which both show anti-lensing.

The lensing effect is less pronounced – a manifestation of the contrast null – but is visible in the negatively-defocused blue-detuned image at  $(+2.5 \Gamma, -10 \text{ mm})$ . A consequence of the isomorphism is that the particularly ill-posed inverse problem inherent in red-detuned imaging may be converted to the much better-behaved blue-detuned case by defocusing behind the object.

Why might this symmetry be useful? Red-detuning may be desirable due to the spectroscopy. In our case, we prefer to detune blue of the strong  $F = 3 \rightarrow$

$F' = 4$  transition as it lies at the blue extreme of the  $F = 3$  hyperfine structure manifold and so blue detuning better matches the two-level atom approximation. Different hyperfine structures may instead prefer red-detuning. Negative defocus may be desirable as it permits a more compact optical system. Moving the finite lens aperture closer to the object also increases the effective numerical aperture of the imaging system, potentially increasing the resolution (see §5.5.3).

### 5.3.7 Implementing the algorithms

This Article briefly discusses how the Fourier retrieval algorithm was implemented; the results are presented in the following Article.

Routines written in IDL were used for pre-processing, Fourier-regularised retrievals, analysis and plotting. MATLAB was used for wavelet retrievals. Implementing the Fourier algorithm is simple: the code is little more than a transliteration of the retrieval equation with appropriate regularisation included.

Fourier retrieval is performed by a routine `apqr`. Images are first checked for normalisation error due to exposure variation by dividing by an average contrast value taken over a region far away from the object. Equation 2.94 is then implemented: the Fourier transform is taken, multiplied by the regularised inverse CTF (3.30) and inverse transformed. In a high-level data language such as IDL, Fourier transforms are accomplished by a single function call and the few complexities in the routine involve initialising the matrix representing the spatial frequencies  $\mathbf{u}$  with the sample order expected by the Fourier transform routine.

IDL uses a version of the original Cooley-Tukey [371] decimation-in-space Fast Fourier Transform (FFT). The algorithm's speed is generally  $O(N \log N)$  when  $N$  is a power of 2, but is usually substantially slower for  $N$  not a power of 2. Consequently, there is usually a speed advantage in padding the contrast with zeros so that the array dimensions are powers of 2. After the Fourier-processing, we unpad, extracting the region of the original data from the centre of the processed array. This padding and unpading has a further advantage of ameliorating boundary effects.

Boundary effects were not apparent when considering continuous Fourier transforms in Chapter 3. Any machine transform must be discrete and finite. For the Fourier basis, this implies periodic boundary conditions: we may think of the image as ‘wrapping around’ between parallel edges. Non-white noise will be discontinuous at the boundary and will ‘ring’ in both directions. Regularisation distortions

centred on the object which ring over one boundary will wrap around and contaminate the other side of the image.

Zero-padding reduces these effects by providing a moat around the data into which distortions sink, instead of wrapping back into the data. An alternative view is that zeropadding better approximates a compactly-supported object. Indeed, compact support would be perfectly represented in the limit of an infinitely-wide zeropadding moat. In practice, padding by a factor of 2 in size gives substantial improvement while more than a factor of 4 shows marginal further improvement.

`IDL` executes a double-precision complex FFT of a  $1024 \times 1024$  array in 2.0 s on the 1.2 GHz Pentium-III machine used for data analysis. The FFT is clearly the rate-limiting step for retrievals, although most CCD cameras with 16-bit digitisers will take approximately this length of time to read out the CCD. Padding to  $4096 \times 4096$  increases the FFT time to 45 s. More highly optimised Fourier-transform algorithms exist. A popular library is `FFTW` [372] which has recently been interfaced to `IDL` [373]. Speed-up factors of 2–4 have been reported for large, complex 2D-FFTs. Even faster implementations [374] may be possible for deconvolution problems such as ours, in which the input and output data are real and only the intermediate step is complex. These customised FFTs outperform even purely-real transforms such as the Fast Hartley Transform [375]. For a CCD camera operating in a  $256 \times 256$  pixel subframe focusing mode even the standard `IDL` single-precision FFT is fast enough for 16 *retrievals* per second. Such retrievals would likely have sufficient quality for adjusting experimental parameters and the slower full-frame retrievals would then be employed when taking data.

By contrast, the wavelet-regularised retrieval algorithm (`FORWARD`) uses a slow undecimated wavelet transform. Retrievals take around 1 min on the data analysis machine and the iterative optimisation of the regularisation parameter described in §3.6.3 requires several such retrievals. `FORWARD` retrievals are more likely to be used at the analysis stage of an experiment rather than during acquisition and so longer execution time is of less concern. In concluding, it is notable that custom hardware such as digital signal processors (DSPs) and field-programmable gate arrays (FPGAs), are capable of full-frame deconvolution at video frame-rates and higher [376] and may offer similar performance for wavelet algorithms [377]. By the time camera technology produces full-frame images at video rates

### 5.3.8 Retrieving column-density from defocus-contrast images

Defocus-contrast images including those shown in Figure 5.6 were processed with three retrieval algorithms: monomorphous TIE, Fourier-only CTF deconvolution and Fourier-Wavelet (forward) CTF deconvolution. Two retrieved column-density images are shown in Figure 5.9 on page 213. The retrievals are from two defocuses at the one detuning, details are given in the caption. The left page of the spread shows (focused) absorption images, on- and off-resonance, and contemporaneous fluorescence images.

The fluorescence images are entirely free of the background fringes visible in the absorption images. Fluorescence arriving at the detector is much less spatially coherent than the probe beam, thus reducing the visibility of etalon fringes. Both resonant (C, D) and detuned E, F absorption column-densities show fringe-like horizontal banding structures, which are present neither in the fluorescence image nor the retrieved column-densities. The spacing of the bands is similar to the background fringe noise and it seems likely that they are due to incomplete cancellation of the fringe noise. Notwithstanding this possible contamination, the resonant absorption image does show the subtle change in MOT structure between the two days of image taking. This variation is much harder to discern in the off-resonant absorption images.

The Fourier retrievals I and J show essentially all of the structure visible in the fluorescence images (A and B respectively). The retrieval J from the image at greater defocus has less background noise than retrieval I. This is due to the greater diffraction contrast at the camera, visible in Figure 5.6. The Fourier-wavelet retrievals K and L are less noisy, albeit not dramatically so. They agree quantitatively with the non-wavelet retrievals and show no discernible loss of detail in comparison with the fluorescence image. On the other hand, the TIE retrievals G and H are clearly blurred. In particular, image H retrieved from the  $z = 30$  mm defocused image is missing most of the structure visible in the other column-density images at lower right and upper left of the MOT centre.

Figure 5.9 shows that spatially-resolved column-densities can be retrieved from defocused, off-resonant images. The retrievals have much higher SNR than the in-focus images at the same detuning, and approach the quality of in-focus images at zero detuning: that is, absorption imaging. At  $2.5 \Gamma$  detuning, the off-resonant images heat the MOT a factor of 7.25 less than the absorption images.

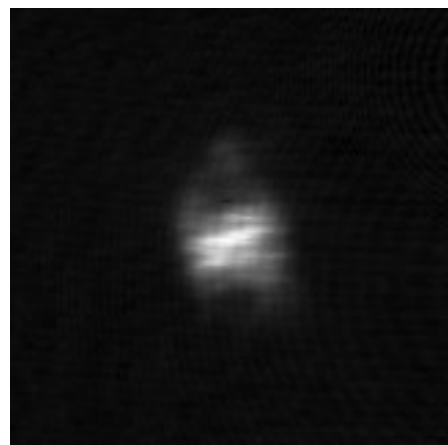
No images were taken at defocuses beyond 40 mm as the TIE algorithm avail-



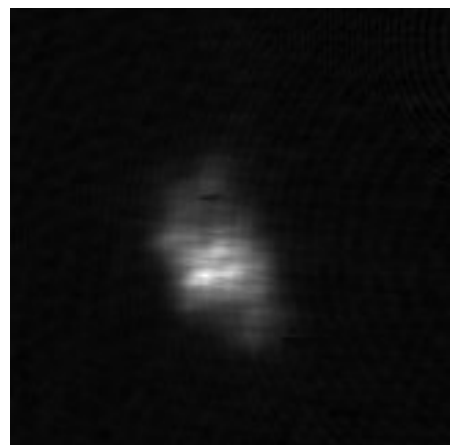
A Fluorescence image 2002-Jul-10



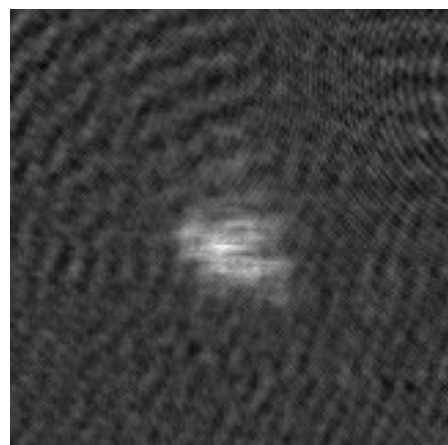
B Fluorescence image 2002-Jul-9



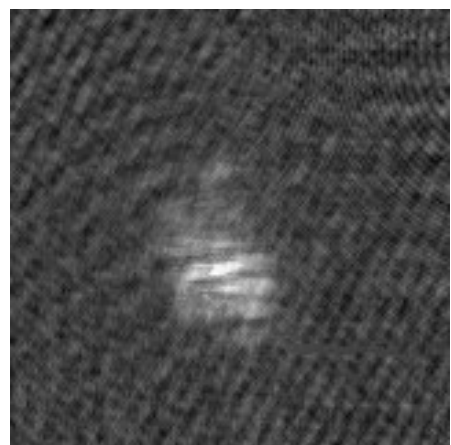
C Resonant absorption 2002-Jul-10



D Resonant absorption 2002-Jul-9

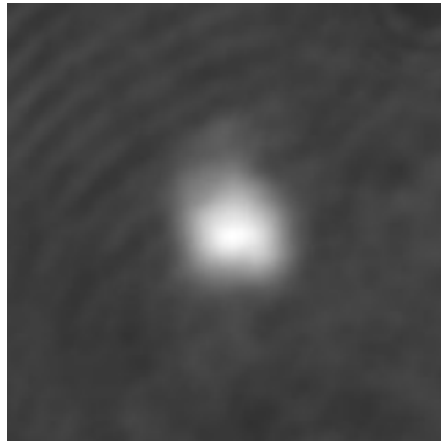


E Off-resonant absorption 2002-Jul-10



F Off-resonant absorption 2002-Jul-9

$z = 10 \text{ mm}$

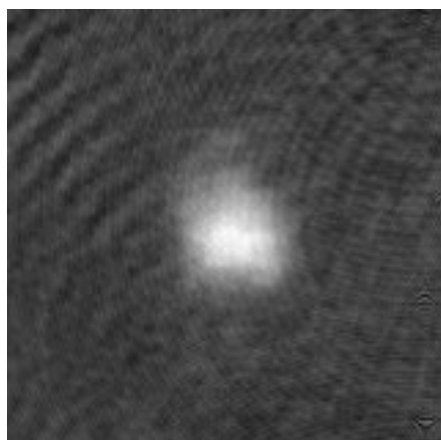


$z = 30 \text{ mm}$



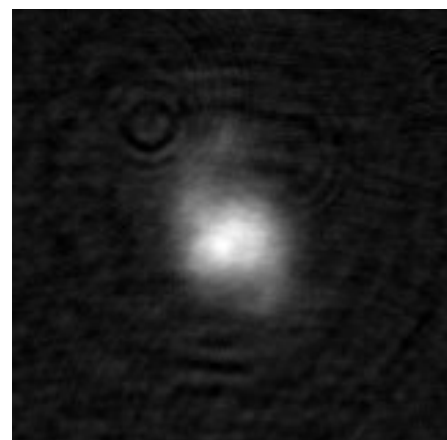
G TIE retrieval

$\rho(\mathbf{x})/10^{12} \text{ m}^{-2}: [-4 \ 10]$



H TIE retrieval

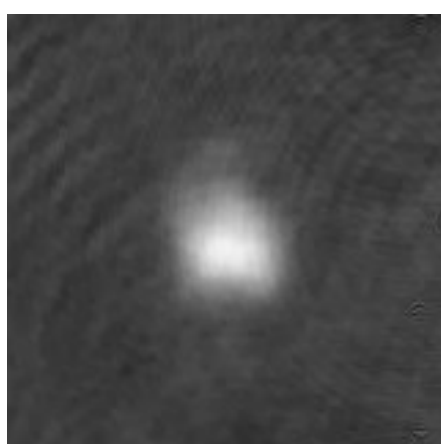
$\rho(\mathbf{x})/10^{12} \text{ m}^{-2}: [-1 \ 13]$



I CTF retrieval

$\alpha = 0.5$

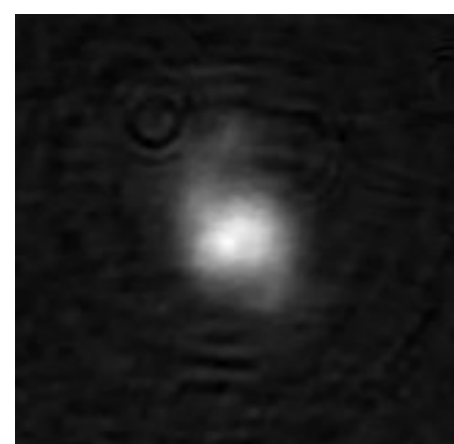
$\rho(\mathbf{x})/10^{12} \text{ m}^{-2}: [-4 \ 10]$



J CTF retrieval

$\alpha = 0.03$

$\rho(\mathbf{x})/10^{12} \text{ m}^{-2}: [-1 \ 13]$



K FORWARD retrieval

$\alpha = 0.32$

$\rho(\mathbf{x})/10^{12} \text{ m}^{-2}: [-4 \ 10]$

L FORWARD retrieval

$\alpha = 0.055$

$\rho(\mathbf{x})/10^{12} \text{ m}^{-2}: [-1 \ 13]$

able at the time retrieved highly blurred results at 40 mm defocus and beyond. Successful CTF retrievals from propagation distance of 165 mm are described in §5.4.

### 5.3.9 Quantitative comparison with absorption & fluorescence imaging

Defocus-contrast images were obtained at detunings from  $-2.5 \Gamma$  to  $+5 \Gamma$  and defocuses from  $-10 \text{ mm}$  to  $+40 \text{ mm}$ . Column-densities were retrieved from each image using the Fourier algorithm with regularisation parameter  $\alpha$  set to 0.2. This is likely to be higher than optimal for the higher contrast images at small detunings and large defocuses, while being lower than optimal for images with weak contrast. Nevertheless as all of these images have their broad structure in the first CTF peak and partial-Tikhonov regularisation was employed, retrievals are expected to be relatively insensitive to  $\alpha$ . A Gaussian peak was fitted to each retrieval using IDL's `gauss2dfit` routine with 7 free parameters (offset, height, minor-axis width, major-axis width,  $x$  centre,  $y$  centre and axis angle).

As a preliminary check, Gaussian fits to the *in focus* (absorption) images were plotted as a function of detuning. The expected Lorentzian profile was obtained, but centred on a detuning of 1.9 MHz rather than 0. This detuning offset likely resulted from bias in the laser servo, or uncompensated magnetic fields in the laser-locking cell or MOT chamber. There were insufficient data to perform separate fits for the two days of data collection. Images were reanalysed with correction for this detuning offset.

Ideally, we would expect to retrieve the same column-density peak-height re-

---

**FIGURE 5.9 (ON PRECEDING SPREAD) Retrieval techniques compared for MOT images.** The left-hand page shows fluorescence and absorption images of the MOT on two days. Figures A and B show in-focus fluorescence images which are free of fringes, C and D are column densities calculated from resonant-absorption images (such as the one shown at the intersection of the axes on p 202) using the Beer-Lambert law. Figures E and F are calculated from in-focus images, but with the same  $\Delta = +2.5 \Gamma$  detuning as the retrievals from defocused images on the right-hand page. As expected, the absorption is weaker.

The right-hand page shows retrievals from defocus-contrast images taken at  $\Delta = +2.5 \Gamma$  and defocuses of 10 (taken 2002-Jul-10) and 30 mm (taken 2002-Jul-9). The input images are the bottom row of p 203. Images were padded to  $2048 \times 2048$  pixels. The MOT was significantly different each day; the left and right columns of retrievals should be compared respectively with the left and right columns of fluorescence and absorption images on the opposite page.

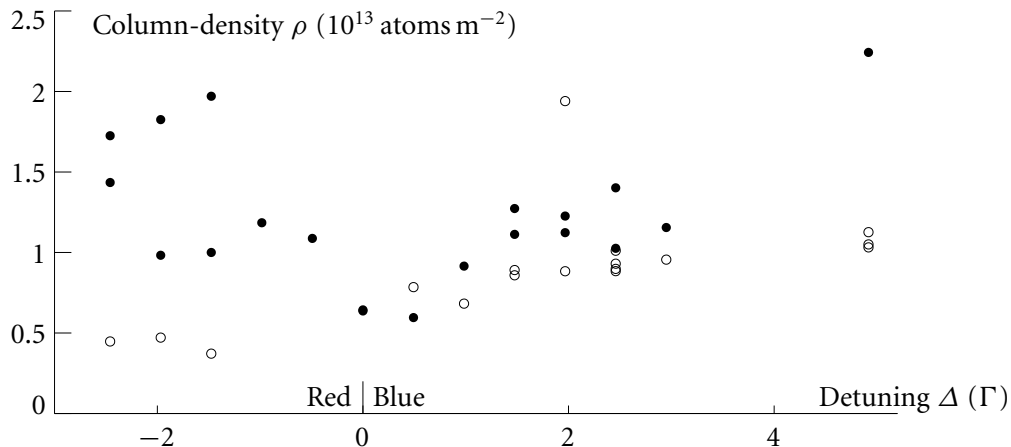


FIGURE 5.10 **Retrieved column-densities: Gaussian peak height.** Height of Gaussian peaks fitted to retrieved column-densities. Filled circles • are from fits to in-focus absorption images converted to column-densities with the Beer-Lambert equation. Open circles ○ are from fits to defocus-contrast retrievals using the Fourier CTF algorithm with  $\alpha = 0.2$ .

gardless of detuning or defocus. Realistically, the data are scattered by MOT fluctuations and detuning and defocus errors. No trends were discernible for peak height or widths as a function of defocus. The peak heights, but not the widths, *did* appear to differ for red-detuned, blue-detuned and resonant probe light as shown in Figure 5.10.

Each point corresponds to a separate configuration of detuning and defocus and so the number of points is relatively small: 14 defocus-contrast retrievals and 20 absorption images. I have used parametric statistics to infer some tentative conclusions from these data at the  $p = 0.05$  level of significance. One conclusion *not* requiring recourse to statistical tests is the dramatically greater variation apparent in the red-detuned data. This may to some extent be a selection bias, as red-detuned negatively-defocused data were only obtained at the small defocus of  $z = -10$  mm. But the in-focus absorption data (filled circles) are also widely scattered at red detunings. Further, the absorption data and – more arguably – the retrieval data, show a dip near resonance. I don't have a completely plausible explanation for the red-detuned scatter or the dip. Saturation by the probe beam can be ruled out: it was far too weak to saturate the transition. It also seems too weak to cause significant optical pumping, especially as the MOT trapping *and* repumping beams remained on during these exposures. The influence of the  $F = 3 \rightarrow F' = 3$

transition, 121 MHz to the red, seems unlikely to be sufficient to explain the discrepancy. Further experiments should include careful imaging at red detunings to verify and explain this potential systematic error.

Restricting the analysis to blue-detuned data leaves 13 defocus-contrast data<sup>10</sup> and 9 in-focus absorption data. From this modest data set, the following inferences can be made. First, the peak column-densities obtained from retrievals agree with those from absorption imaging.<sup>11</sup> The retrieved densities are less scattered than the absorption densities;<sup>12</sup> we will see in §5.6.1 that absorption imaging is fundamentally more sensitive to focus errors than defocused imaging.

The question remains of how much of the scatter of the retrieved data reflects true fluctuation in the MOT density, and how much is due to imaging errors such as errors in setting the defocus, technical image noise, fluctuations in the detuning and retrieval artefacts. In fluorescence imaging, the latter two imaging errors are obviated and we have seen that technical image noise is much lower. Obtaining calibrated atom density data from fluorescence images is difficult and no attempt was made to do so. However, we can compare the coefficient of variation<sup>13</sup> of the Gaussian peak-heights of *fluorescence* data (not plotted) with the coefficient of variation of the peak-heights retrieved from defocused images. In doing this, we are making the substantial assumption that if calibrated, the mean of the fluorescence data would coincide with the mean determined from defocused images. With this proviso, however, the variance of the blue-detuned retrievals is not significantly greater than the variance of the fluorescence data.<sup>14</sup> We can thus tentatively infer that much of the scatter in the defocus-contrast retrievals is actually a measurement of fluctuations in the MOT density. We saw that the absorption data were more scattered than the retrieved data, so it is not surprising that the variance of *absorption* peak-heights is very significantly greater than the fluorescence variance.<sup>15</sup>

In summary, this experiment showed that column-densities retrieved from defocus-contrast images agree with those calculated from absorption images, and I hypothesize that defocus-contrast imaging is less sensitive to defocus errors than absorption measurements. A first-order analysis of defocus errors which supports

<sup>10</sup> One outlier excluded at  $> 8$  standard deviations from the mean.

<sup>11</sup> Retrieval mean  $9.22 \times 10^{12}$  atoms m $^{-2}$  and absorption mean  $1.09 \times 10^{13}$  atoms m $^{-2}$  not significantly different (Welch Two Sample t-test [378, 343–4],  $p = 0.068$ ).

<sup>12</sup> Ratio of variances 0.252 significantly different from 1 (F-test [378, p 363–6],  $p = 0.032$ ).

<sup>13</sup> The *coefficient of variation* is the standard deviation divided by the mean.

<sup>14</sup>  $N = 20$  for fluorescence data. Ratio of variances 2.5 not significantly different from 1 (F-test,  $p = 0.072$ ).

<sup>15</sup> Ratio of variances 7.1 significantly greater than 1 (F-test,  $p < 0.0005$ ).

this hypothesis is given in §5.6.1. Retrievals using the CTF method were largely free of distortion and showed none of the blurring evident in TIE retrievals. The experiments were not powerful enough to measure errors introduced by the retrieval process: there is evidence that MOT fluctuations were the dominant uncertainty.

A future course of measurement should investigate the red-detuning anomaly. Use of a translation stage would increase the focusing precision. We saw in §3.8 that retrieval performance is likely to be optimal at substantial defocuses where even the gross structure of the object shows several diffraction fringes. The next Section shows retrievals from such highly-diffracted images of atom clouds.

## 5.4 Experiments with holographic imaging

This Section describes experiments where diffraction patterns are measured without an imaging lens. We established in §5.3.4 the formal equivalence between imaging with a defocused lens and lensless detection of diffraction patterns. In practice, however, the two configurations are not equivalent and we will see that lensless imaging opens up new possibilities. Removing the imaging lens maximises the holographic depth-of-field, and permits post-facto focusing in the computer. Removing the collimating lens leaves the divergent probe beam emanating from a bare optical fibre tip. We will see how this eliminates lens aberrations while magnifying the diffraction pattern. There are also limitations when imaging without lenses, in particular the diffraction limit on resolution due to the small size of CCD detectors, which will be discussed in the next Section.

### 5.4.1 Removing the imaging lens

This Article considers the imaging configuration depicted in Figure 5.11: the imaging lens is removed but the collimating lens remains. A plane wave is incident on the object, is perturbed by the absorption and phase-shift of the object and then propagates through free space to the detector.

Conceptually, this is the simplest form of diffraction-contrast imaging; the contrast transfer function relations were derived in §2.5 for such a configuration. The effects of imaging lenses (§5.3.4 and §5.3.5) and point-projection (§2.4) were analysed by showing their equivalence, up to a magnification, to an underlying system of plane-wave illumination followed by free-space propagation to the detector.

Because of the practical restrictions on placing the CCD detector, we first considered the defocused imaging case above. The continuum of defocuses included

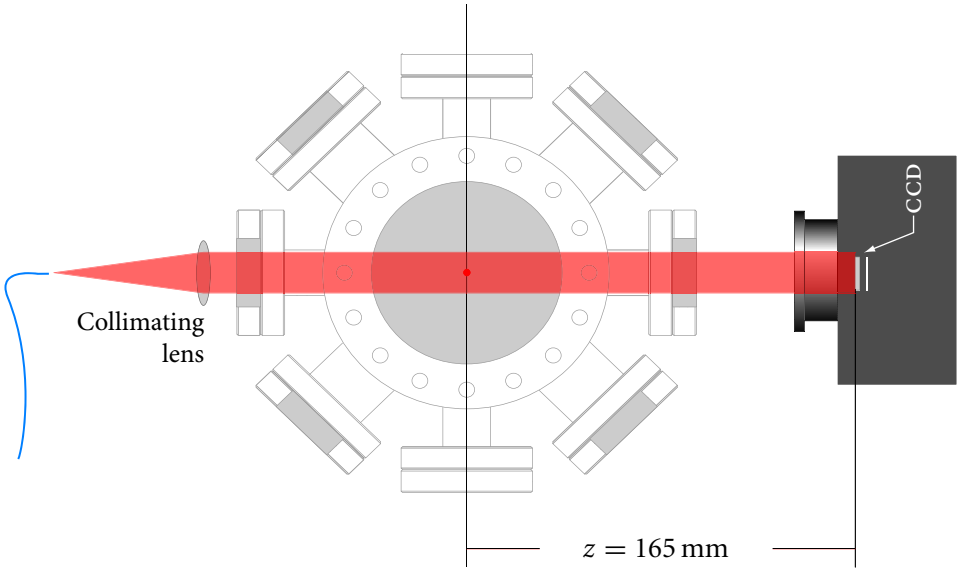
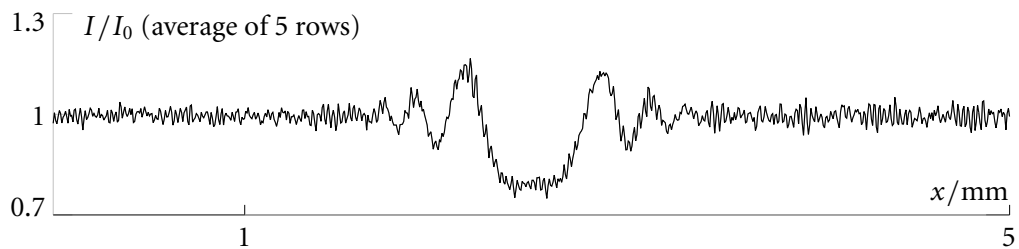
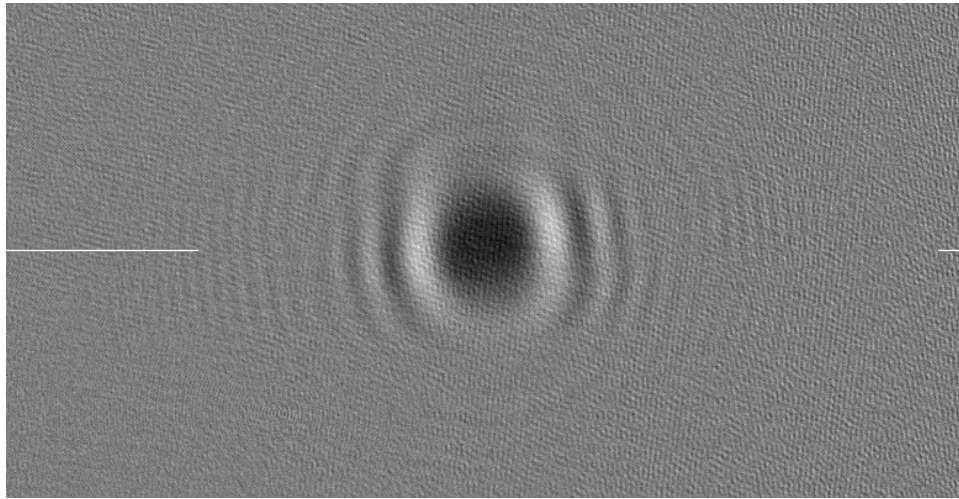


FIGURE 5.11 Configuration for lensless imaging of a MOT. The imaging lens is removed. The remaining lens serves only to collimate the beam.

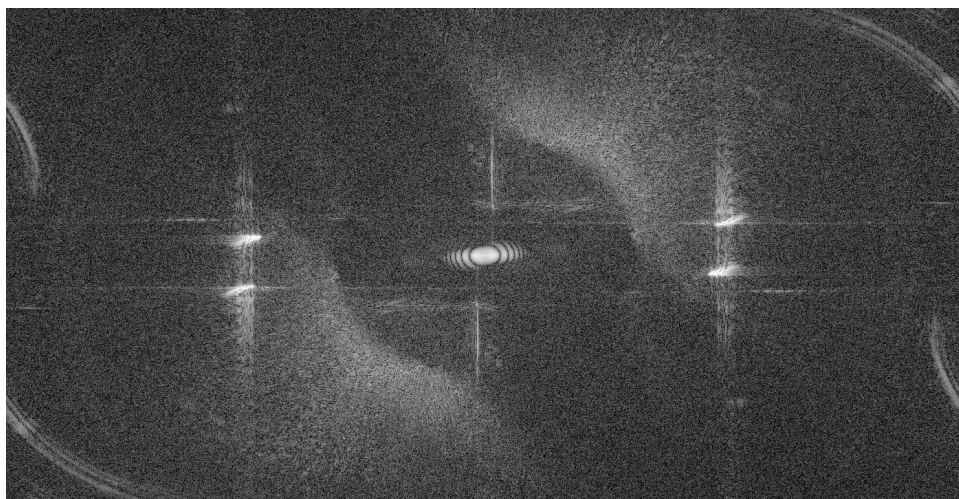
conventional absorption imaging at zero defocus. Now in this Article I show retrievals from the more heavily diffracted patterns detected when the wavefield propagates from the MOT to the detector outside the vacuum system, without an intervening reimaging lens. The next Article discusses how such diffraction patterns can be processed for different propagation distances, allowing the imaging system to be ‘virtually focused’ after the images have been taken.

The diffraction pattern shown in Figure 5.12 was taken by placing a bare CCD camera, without an imaging lens, as close as possible to the imaging viewport of the MOT. The detected diffraction pattern was normalised to yield contrast image shown using (5.19), just as for the defocused images in the previous Section.

These experiments were performed by Kenian Domen, on sabbatical from the Technical University of Eindhoven in the Netherlands. He also made a number of improvements to the apparatus, beyond the original MOT configuration described in Chapter 4. In particular, a tapered amplifier boosted trapping beam power to around  $8 \text{ mW cm}^{-2}$ , leading to a larger but not significantly more dense atom cloud. A Photometrics Coolsnap HQ camera detected the diffraction pattern. This camera has a  $1392 \times 1040$  array of pixels spaced by  $6.45 \mu\text{m}$  on both axes. Unlike the VersArray model used in 2002, the Coolsnap has a fast *electronic* shutter which can be externally triggered by a TTL pulse. As the CCD hardware is optimised for



A Diffraction-contrast image taken without an imaging lens.  $775 \times 400$  pixel subframe.



B Power spectrum  $|\tilde{I}(\mathbf{u})/I_0|^2$  of the above diffraction pattern.

Logarithmic greyscale.

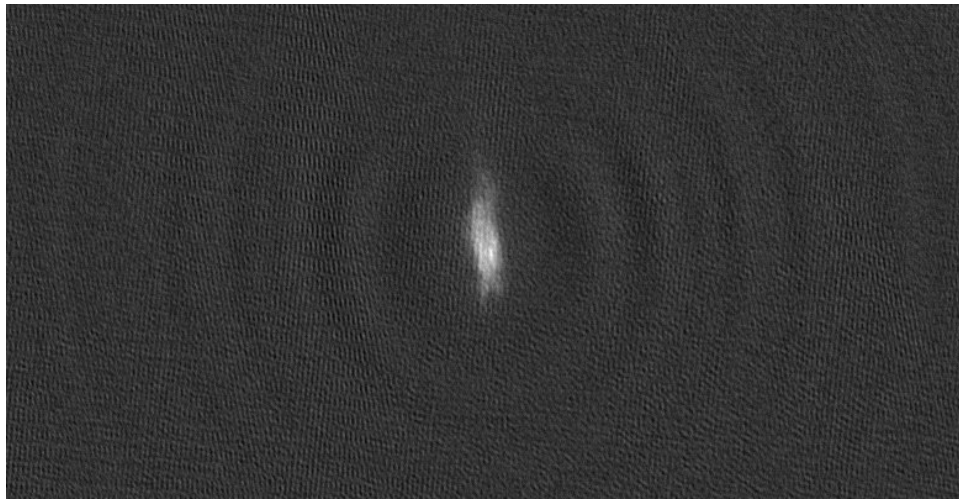
FIGURE 5.12 **Holographic diffraction pattern of a MOT.** Upper image A shows the significant portion of the normalised diffraction pattern  $I(\mathbf{x})/I_0$ . Lower image B is the power spectrum of image A. Zero spatial frequency is at centre, note the periodic boundary wraps arcs of high-frequency noise at the edges.

substantial frame rates, digitisation is only 12-bit. A computer-controlled delay generator (Measurement Computing PCI-CTR10) sequentially turned off the MOT trapping beams, opened the electronic shutter and turned on the probe beam. After an exposure delay, in this case  $300\ \mu\text{s}$ , the delay generator turned off the probe beam, closed the shutter and turned the trapping beams back on for the next cycle, before triggering the software to read out the CCD. This arrangement overcomes both the problem of MOT fluorescence contaminating the diffraction pattern and of saturation of the probe transition by the MOT trapping beams. Probe detuning was set to  $+8.4\ \text{MHz}$  and the MOT-to-CCD distance was  $165 \pm 2\ \text{mm}$ , the closest achievable given the camera housing and vacuum geometry. The probe intensity was of order  $1\ \text{mW cm}^{-2}$ .

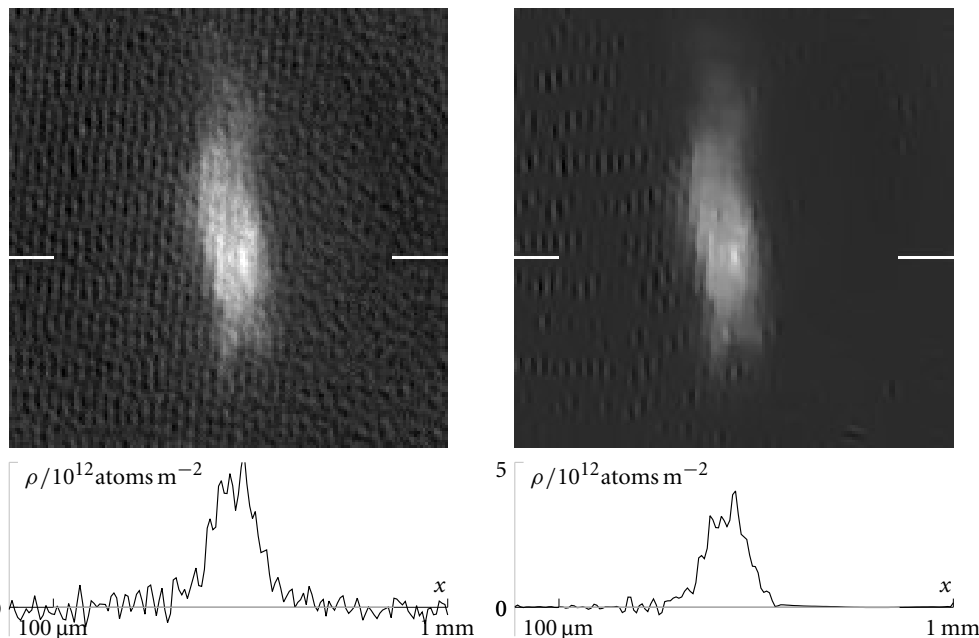
The diffraction pattern is clearly in the holographic regime: no object structure is discernible and at least 10 fringes are visible. The contrast level is moderate, deviating no more than 0.3 from the background. As a matter of incidental interest, Figure 5.12B shows the power spectrum of the diffraction pattern. The azimuthal averages of such spectra were discussed in §3.4; in particular, compare Figure 3.10 on p 99. The smooth elliptical object in the centre is the spectrum of the atom cloud, with CTF minima clearly visible as dark circles superimposed upon it. Weak noise fringes visible in the background of the diffraction pattern appear as prominent spots in the power spectrum. Well-targeted Fourier filtering could potentially reduce this coherent background without undue distortion of the retrieved image of the atom cloud.

Column-densities retrieved from Figure 5.12A are shown on p 221. The retrieval Figure 5.13A shows only very weak artefacts, manifest as wide and predominantly vertical ring-segments starting at a significant radius from the cloud and visible to the edge of the frame. Part B shows only the central section of the retrieval. The regularisation artefacts do not contaminate the atom cloud, but the image is marred by broadly-stationary fringe and white noises which have been coloured (amplified) by the retrieval. From the arguments of §3.5 we might expect wavelet denoising to attenuate this noise, and indeed the forward retrieval shown in Figure 5.13C confirms this expectation.

Both Fourier and Fourier-wavelet retrieval algorithms performed well on heavily-diffracted, noisy images. This Article has shown an example of CTF retrieval from a holographic-regime image at least as successful as that from single-fringe images obtained with the assistance of a re-imaging lens. The result is particularly important in light of the result of §3.8, which showed that holographic diffraction



A Fourier retrieval from holographic image Figure 5.12A.  $\alpha = 0.04$ ,  $775 \times 400$  pixel subframe.



B Zoom on above retrieval, with lineout.

C FORWARD retrieval,  $\alpha = 0.005$ .

FIGURE 5.13 Column-densities retrieved from a holographic image. The column-densities shown were retrieved from Figure 5.12A, assuming propagation distance  $z = 151.9$  mm and detuning  $\Delta = +0.44\Gamma$ . Images were padded to  $2048 \times 2048$  pixels. Residual regularisation artefacts are barely visible in A as partial rings well-separated from the retrieved cloud profile.

patterns yield the highest signal-to-noise ratio upon retrieval.

#### 5.4.2 Focusing images at retrieval time

The retrieval Figure 5.13A used the propagation distance  $z = 151.9$  mm, more than a centimetre less than the measured distance of 165 mm. The discrepancy is easily accounted for by a residual 2 m radius of curvature on the supposedly-collimated probe beam. This curvature is, in turn, accounted for by an entirely plausible 1.3 mm displacement of the  $f = 50$  mm probe collimating lens. The effective propagation distance used in the successful retrieval was found by retrieving at a range of  $z$ -values until the sharpest column-density image was obtained. Images retrieved from Figure 5.12A at several propagation distances are shown in Figure 5.14;  $z = 152$  mm is clearly the sharpest.

This minor discrepancy is not significant. However, the *focusing process* that was employed to find the best propagation distance points to a fundamental advantage of diffraction-contrast imaging over other techniques. At first glance, the use of a manual search to find the  $z$ -value yielding the sharpest image seems rather ad hoc. But consider that *all* focal imaging systems – absorption, fluorescence, Zernike phase-contrast and even spatial-heterodyne – require a manual focusing step. Furthermore, focusing these lens-based systems requires moving lenses around on the optical table. If it is later realised that the system was not correctly focused, or was focused on the wrong object, there is little that can be done to the data to correct it. By contrast, our search for the correct retrieval distance occurs *in the computer*. As there is no imaging lens, there is no imaging system to focus.

When column-densities are retrieved at an incorrect distance, the result is blurred in a manner similar to a defocused imaging system. Figure 5.14 shows how details in the retrieved column-density snap into ‘focus’. This virtual focusing process is best understood by reviving the analogy with holography considered in §3.1. Recall that holography is a two-step process: the first step is recording a diffraction (or interference) pattern, just as in diffraction-contrast imaging. Holography and retrieval differ in the second step: holography attempts to reconstruct the *entire wavefield*, while CTF-deconvolution retrieves the structure of the object directly. Setting the retrieval distance is equivalent to focusing on the virtual image produced by an inline hologram. Thus diffraction-contrast imaging has *holographic depth of field*: while any single retrieval has the limited depth-of-field of the equivalent focal system, the retrieval can be ‘refocused’ across a wide range of propagation

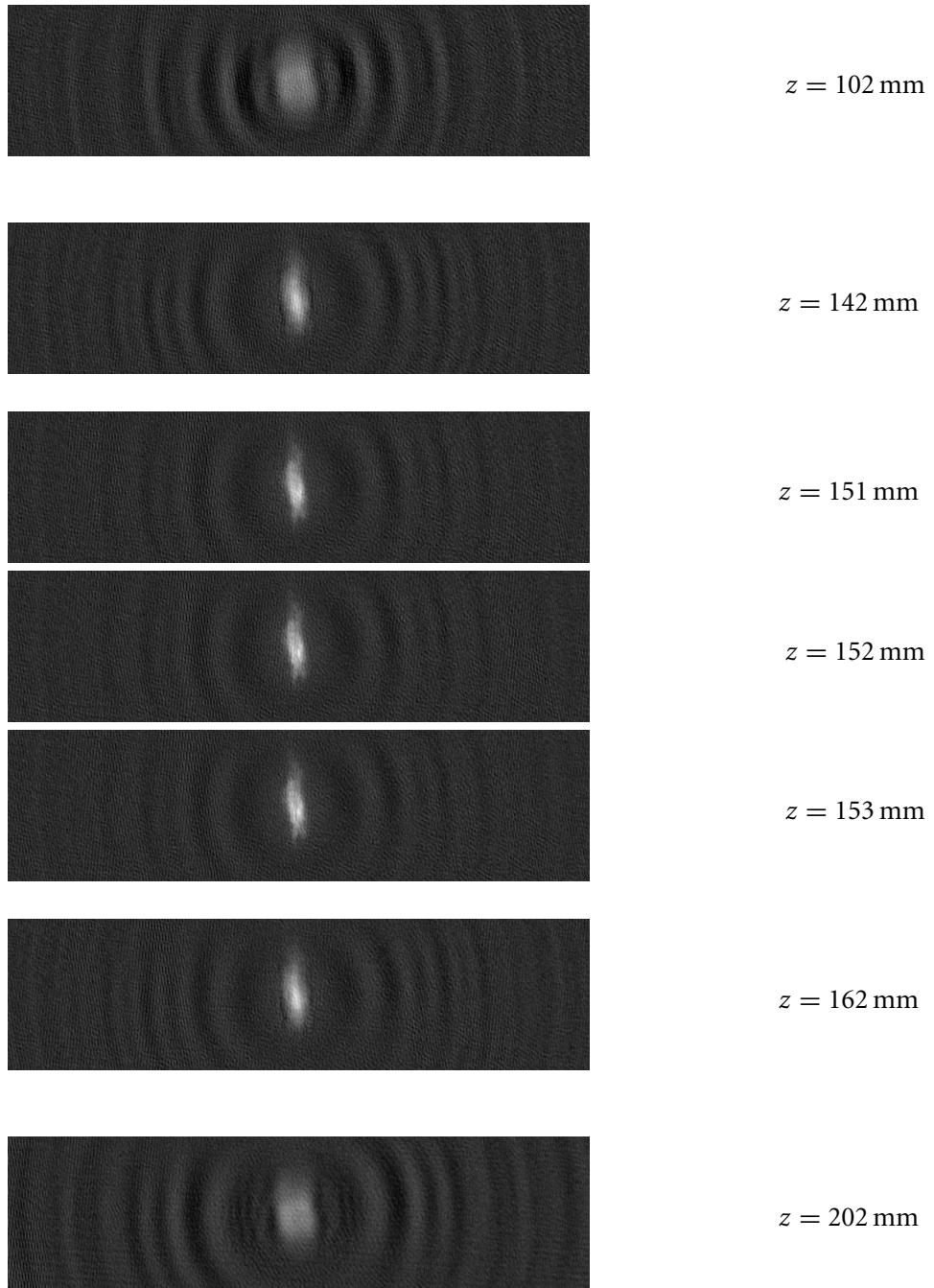


**FIGURE 5.14 Focusing at reconstruction time.** The single diffraction pattern Figure 5.12A was processed with Fourier CTF retrieval at several different reconstruction distances. Sharpest retrieval is at  $z = 152 \text{ mm}$  with a precision better than 1 mm.

distances.

Naturally, the defocused-lens system of the previous Section also has an extended depth-of-field over the focused system. For a pure phase object, however, there is no contrast when the object lies in the focal plane. For a fixed detuning, say to the blue of resonance, any objects closer to the lens than the focal plane will have a positive  $\delta$  coefficient in (5.25) and retrievals will be unstable at low spatial frequencies. Provided that the probe light is blue detuned, removing the lens obviates these problems: for the apparatus used to obtain Figure 5.12A, the central 20 mm of the MOT chamber lies between 150 and 170 mm from the CCD. Any atom cloud in this region will produce a diffraction pattern with holographic fringes.

It is, of course, impossible to reconstruct the full 3-dimensional atom-density distribution through the probe-beam volume: there is simply not enough information in a single diffracted image. When the retrieval is focused on one object of interest, other objects will show ‘defocus’ fringes which may overlap and contaminate the object of interest. If the objects are discrete atom clouds with non-overlapping compact support, there might be iterative means of disentangling the contaminating fringes. Simulated retrievals and results of imaging multiple atom clouds will be presented in a forthcoming paper [379].

It is also noteworthy that the image was retrieved with the detuning parameter set to  $\Delta = 0.44 \Gamma$ , when the detuning set with the acousto-optic modulator was  $\Delta = 1.4 \Gamma$ . The best detuning was found by a search procedure similar to the focusing procedure described above. The detuning discrepancy in the retrievals described in the following Article was much smaller. The origin of this discrepancy is not clear, but it may be due to inhomogeneous broadening of the transition. This discrepancy does appear to be easily corrected for. Nevertheless, current work is investigating its provenance and amelioration.

#### 5.4.3 Magnification by point-projection

Removing the imaging lens yields holographic diffraction patterns and great depth of field. It also eliminates any magnification provided by the imaging systems. Individual pixels are clearly visible in Figure 5.13B, and a bright spot in the lineout is only three pixels across. It is not clear if this spot is a spurious background fringe or genuine structure. This strongly suggests that the resolution of this retrieval is not limited by any optical process or by the retrieval algorithm, but by the pixel spacing, in this case  $6.45 \mu\text{m}$ .

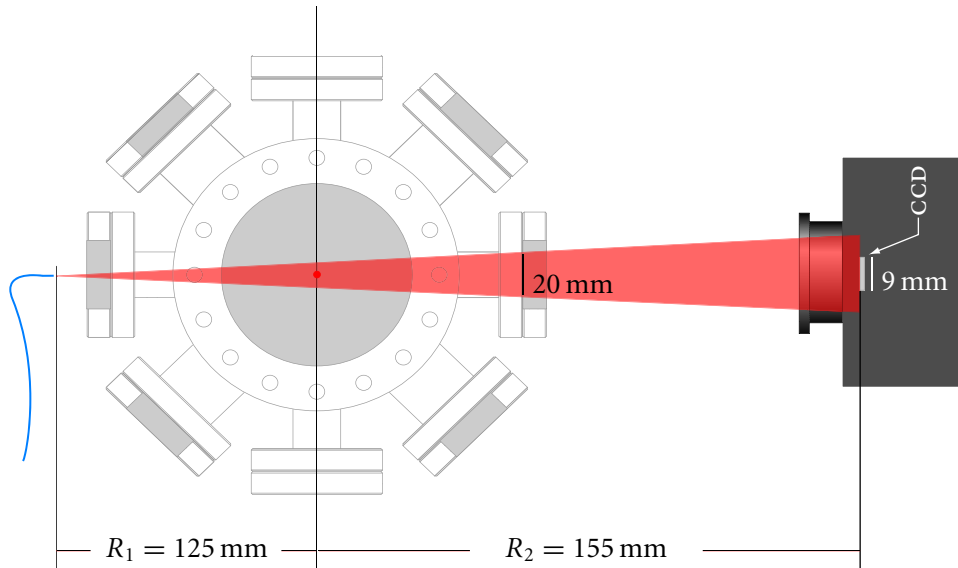


**FIGURE 5.15 Configuration for point-projection imaging of a MOT.** The two relevant apertures which set the diffraction-limited resolution are indicated. Note that in the experiment the beam is clipped substantially by the second vacuum connector. Diagram not to scale, magnification is exaggerated.

We saw in §2.4 that a diffraction pattern can be magnified by using point-source rather than plane-wave illumination. No lenses are required. An excellent and convenient point-source is the bare end of an optical fibre. Fibres are commonly used to transport probe light to atom-imaging systems, and in many cases the point-source may be realised simply by removing the collimating lens from the fibre. The beam emanating from a fibre is Gaussian and so corresponds to a spherical wave-front with varying radius of curvature [17, §3.1]. Beyond a few Rayleigh-ranges from the fibre, the radius of curvature is indistinguishable from the source-to-object distance: the fibre behaves as a point source. For typical fibre-core diameters of  $5\ \mu\text{m}$ , the fibre behaves identically to a point source provided it is at least a few hundred micrometres from the object.

If the dynamic range of the detector is ignored as a factor, there is no advantage in having effective pixel sizes much smaller than one wavelength. In our case, this corresponds to useful magnifications up to around  $8\times$ , or equivalently placing a fibre-end 20 mm before the atom cloud. This is inside our vacuum system, which is inconvenient but by no means impossible. Indeed, feeding through a fibre is much easier than placing a lens or CCD detector inside [380]. A plausible set-up for

imaging a BEC in a small glass cell is shown in Figure 5.19. The fibre-end is outside the vacuum and resolution down to a few wavelengths could be expected.

Using point-source illumination, we can remove the imaging lens without sacrificing magnification. Removing lenses also removes lens aberrations and optical losses from the additional interfaces. Technical noise due to surface imperfections and dust is obviated. Perhaps most importantly, the configuration is much less sensitive to alignment of optical axes: the only significant axis in the system is the wavevector itself.

A proof-of-principle experiment was carried out by Kenian Domen at the University of Melbourne, who placed a bare fibre-end abutting one imaging viewport and the CCD camera some distance from the opposite viewport. The relevant dimensions are shown in Figure 5.15. As the numerical aperture of the fibre is approximately 0.1, the probe beam diverges to more than 20 mm FWHM diameter before passing through the exit connector of the MOT tank. Careful aiming of the probe beam through the vacuum connectors is required to avoid bright caustics in the image. Obviously the better optical access of a configuration such as Figure 5.19 would solve this technical problem.

The probe beam was detuned +6 MHz from resonance. After normalisation, the measured diffraction pattern appeared as shown in Figure 5.16A on page 228. Magnification and effective defocus for the point-projection system are found by the expressions derived in §2.4:

$$M = \frac{R_1 + R_2}{R_1} = 2.24, \quad z_{\text{eff}} = \frac{R_2}{M} = 69.2 \text{ mm} \quad (5.26)$$

Accurate measurements of the distances  $R_1$  and  $R_2$  are not easily obtained as the MOT position can vary up to several millimetres. However, the magnification  $M$  and effective propagation distance  $z_{\text{eff}}$  are not independent in their effect on the contrast transfer function. Both enter only in the term  $\pi\lambda zu^2$ ; the magnification through the spatial frequency. Indeed, there is an *unmagnified propagation distance*  $z_{\text{UM}}$  given by

$$z_{\text{UM}} = \frac{R_2}{R_1} (R_1 + R_2) = 347 \text{ mm}, \quad (5.27)$$

valid where the spatial frequency discretisation is that for unit magnification. Varying this single parameter is sufficient to ‘focus’ a retrieval, although naturally for a fully quantitative interpretation of the retrieved column-density the magnification must be determined independently.

Retrieving with  $z_{\text{UM}} = 336$  mm yields the column-density image Figure 5.16B. The discrepancy with the predicted  $z_{\text{UM}}$  is well within the error range for a nominal 3 mm uncertainty in the propagation distances  $z_1$  and  $z_2$ .

Compare this retrieval with the collimated-illumination retrieval Figure 5.13A, which is scaled identically: the magnification is plain. The collimated-illumination image was taken several days earlier and the precise shape of the MOT had changed, presumably due to fine adjustment of the trap field.

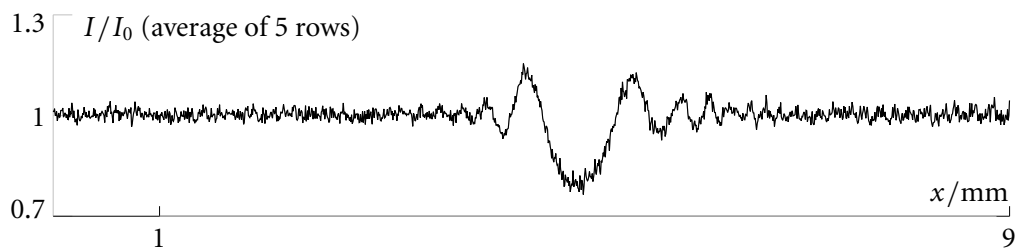
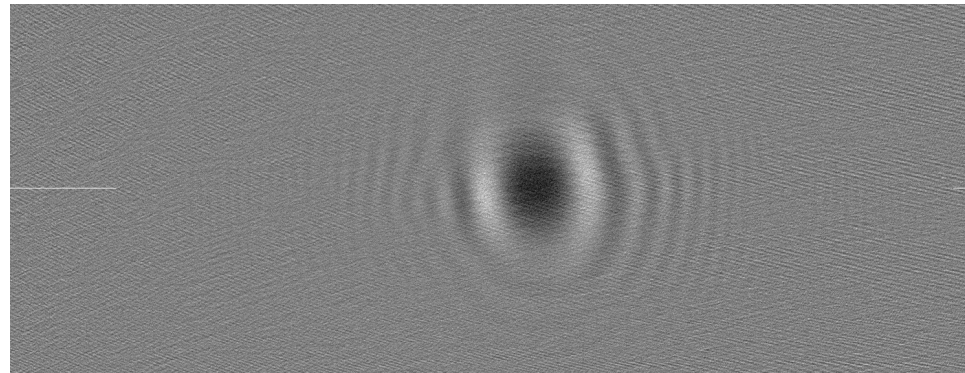
Fluorescence and absorption images taken on the same day as Figure 5.16B are shown facing in Figure 5.17. The fluorescence image B is overexposed, but does not show more detail than the DCI retrieval, and arguably shows less. There is no doubt that the retrieval has a higher level of coloured background noise, although *distortions* are well-separated from the cloud and would not be mistaken for details.

Figure 5.17A is retrieved (negative log) from a resonant absorption image. The absorption image is almost too opaque, reaching 2.5 OD, which may explain why it too appears somewhat overexposed. The horizontal bands in the absorption image are visible in the flat field: they arise from incomplete cancellation of fringe noise and are *not* structure in the MOT. Note that these bands are present neither in the fluorescence nor in the DCI retrieval. Interestingly, as in the quantitative comparison of the 2002 data, there is a disagreement in overall scale between absorption and DCI retrievals. This anomaly should be further investigated.

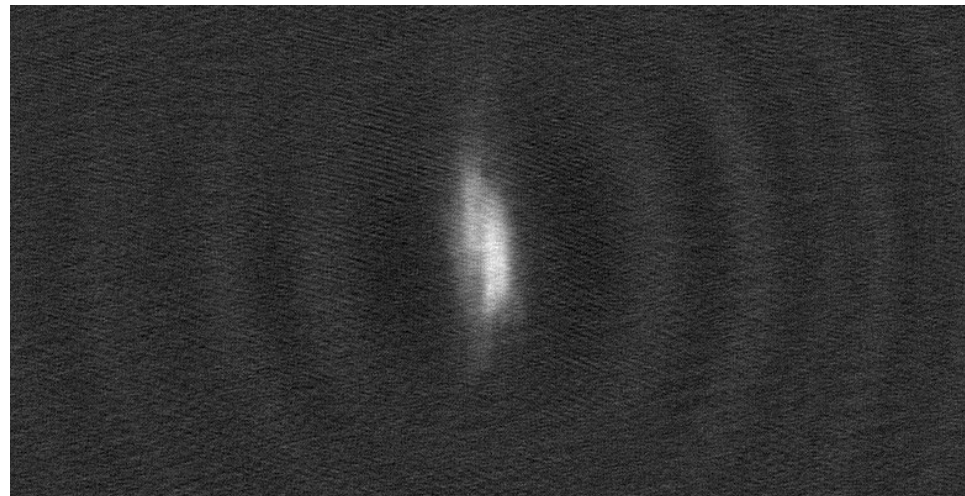
This qualitative comparison shows that point-projection can be used to add magnification to diffraction-contrast imaging. The quality of the retrieved image is qualitatively *better* than the absorption and fluorescence images. At the same time, this DCI image heated the MOT around 5 times less than the absorption image.



THESE LENSLESS PROJECTION-IMAGING experiments conclude the results section of this thesis. There is no simpler system than Figure 5.15 for interacting light, cold atoms and a spatially-resolved detector: indeed, the only essential elements are a point-source of light, the cold atoms and the detector! These experiments have demonstrated that such a system can magnify, and render phase-contrast. The system is inherently free of aberrations and requires no alignment beyond rough colinearity. Finally, the CTF retrieval algorithm proved robust under real-world conditions of technical noise and parametric variation.

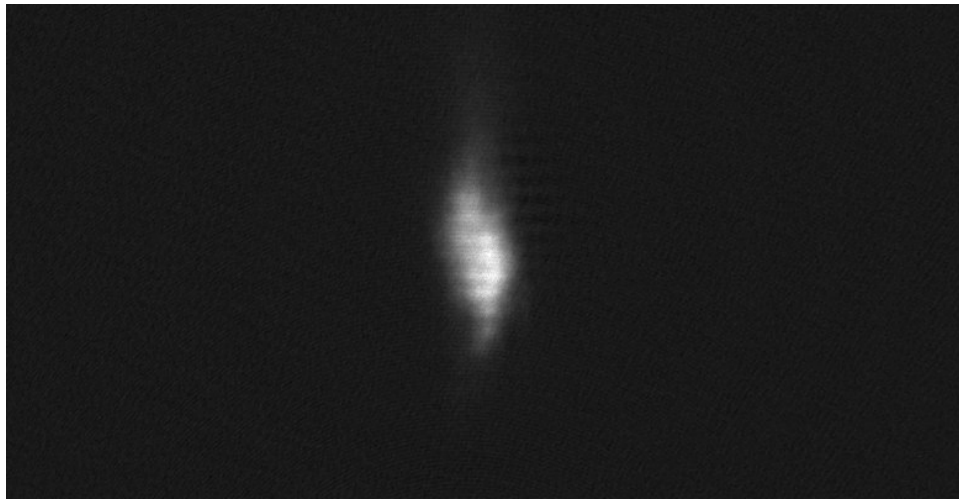


A Entirely lensless point-projected diffraction pattern.  $1392 \times 536$  pixel subframe.



B Fourier retrieval from A above,  $\alpha = 0.2$ .  $775 \times 400$  pixel subframe.  $\rho(\mathbf{x})/10^{12} \text{ atoms m}^{-2}$ : [-1 4]

FIGURE 5.16 Point-projection magnified diffraction-contrast imaging. Upper image A shows the full-width (cropped only in vertical direction) of the CCD recording of the diffraction pattern from the apparatus of Figure 5.15. Lower image B shows the column-density retrieved from A with effective unmagnified propagation distance  $z_{\text{UM}} = 336$  mm and detuning  $\Delta = 0.8 \Gamma$ . The scale is the same as Figure 5.13A; comparison demonstrates the magnification.



A Column-density from resonant absorption image.  $775 \times 400$  pixels.  $\rho(\mathbf{x})/10^{12} \text{ atoms m}^{-2}$ : [-1 9]



B Fluorescence image.  $775 \times 400$  pixel subframe. 50 ms exposure. Uncalibrated

FIGURE 5.17 **Lens-magnified absorption and fluorescence images.** The absorption image shows horizontal banding structure due to incomplete flat-fielding. The fluorescence image is saturated at centre. A long exposure time of 50 ms was necessary to collect enough fluorescence (300  $\mu\text{s}$  used for absorption and DCI). Image may be motion blurred over the long exposure.

## 5.5 Resolution limits in diffraction-contrast imaging

This Section considers the limits on the resolution of column-density information retrieved from diffraction patterns. The theory of optical resolution is connected to the idea of the information content of optical fields, an idea which is still evolving [381]. The resolution is limited by the weakest link in the optical chain, which may be the lens, the detector size or the pixel size. Focal imaging systems are not limited by detector size (except in field-of-view), while lensless-imaging obviously avoids the lens diffraction-limit.

### 5.5.1 Pixel resolution limit

The most obvious resolution limit in any imaging system is the pixel resolution of the detector itself. Optical resolution is conventionally defined by the closest peak-to-peak spacing  $a$  of lines which can be resolved. By Nyquist's sampling theorem, two pixels are required to just resolve one line cycle.

A CCD camera has a very well-defined pixel resolution due to the lithographic fabrication process used: the 6.45  $\mu\text{m}$  pixel-pitch of the Sony ICX285 CCD used in the Coolsnap HQ really does define the resolution to a few nanometers accuracy. Older film-based detectors have much higher resolutions, but are highly non-linear and much less sensitive. The resolution of CCD detectors continues to improve, with 2  $\mu\text{m}$  devices developed for the consumer digital camera market (i.e. Sony ICX432DQ).

Pixel resolution at the detector is magnified to the effective pixel resolution at the object. The magnification may be due to a lens system (§5.3.4) or due to point-projection (§2.4). The smallest resolved line spacing is then

$$a_{\text{pixel}} = \frac{2 \times \text{pixel-pitch}}{M}. \quad (5.28)$$

By increasing the magnification, it is quite possible to make the effective pixel resolution finer than a wavelength. Of course this does not extract sub-wavelength *detail* in the wavefield, but merely oversamples the wavefield. Over-sampling is useful, however, in increasing the SNR as the full-well capacity per unit object-area continues to increase even though the actual resolution does not. In other terms, we can use brighter illumination across the object and avoid saturating the detector if the image is magnified across a greater area of detector.

### 5.5.2 Diffraction limit: intuitive view

If we are imaging with infinite-sized, perfect lenses, or if we are recording diffraction patterns with infinite-sized detectors, then there is little more to consider. In reality, the finite size of lenses or detectors limits the resolution.

We can get an impression of the resolution limit by considering a featureless cloud of size  $a$ , as we did in §5.1.8. The scattered field varies significantly only within a cone of half-angle  $\theta = \lambda/a$  at distances far from the object compared to the Rayleigh range  $z_{\text{RR}} = a^2/\lambda$ . Focused imaging with a telescope requires placing the object at the focal-plane and so a lens of diameter  $D$  encompasses the scattered wave provided  $D/2f > \lambda/a$ . Thus the smallest resolvable object is roughly  $2\lambda f/D$ .

The equivalent holographic system consists of a *detector* of diameter  $D$  at distance  $z$  from the object. It seems reasonable to assume that there will be diffraction-contrast essentially only within the cone of the scattered wave and so the same diffraction-limited resolution applies, and the smallest object able to be retrieved from the diffraction pattern will be  $2\lambda z/D$  [382, §12.2].

### 5.5.3 Diffraction limit: Abbe theory

This intuitive view of the diffraction limit is unsatisfying for a number of reasons. We are not very interested in ‘featureless objects of diameter  $a$ ’ for a start. The scattering-angle assumption is rigorously valid for a Gaussian beam, but we work with bright-field diffraction patterns rather than beams. Further, Gaussian spots do not form a basis. A more rigorous approach to resolution arises from the angular spectrum of plane-waves, although even this approach is imperfect.

Figure 5.18 shows a plane wave incident on an object with column-density varying sinusoidally at spatial frequency  $u_{\max}$ . We saw in §2.3.2 that this generates an angular spectrum consisting of plane-waves at angles  $\theta = \arcsin \lambda u_x$ . Here we have added a telescope focused on the object, and the plane-wave shown is *just* captured by the first lens of the telescope. The diffracted wave from a finer grating at higher spatial frequency would miss the lens. We saw that the telescope is focused when the object is at the focal-plane so the angle  $\theta$  is also  $\arctan D/2f$  where  $D$  is the lens diameter. The lens is thus *diffraction-limited* to resolving line-pairs no closer than

$$a_{\text{diffrac}} = \frac{1}{u_{\max}} = \lambda \sqrt{1 + \left(\frac{2f}{D}\right)^2} \approx 2\lambda \times f\#, \quad (5.29)$$

where  $f\# = f/D$  is the *focal ratio* or *f-number* of the lens. High-resolution lenses

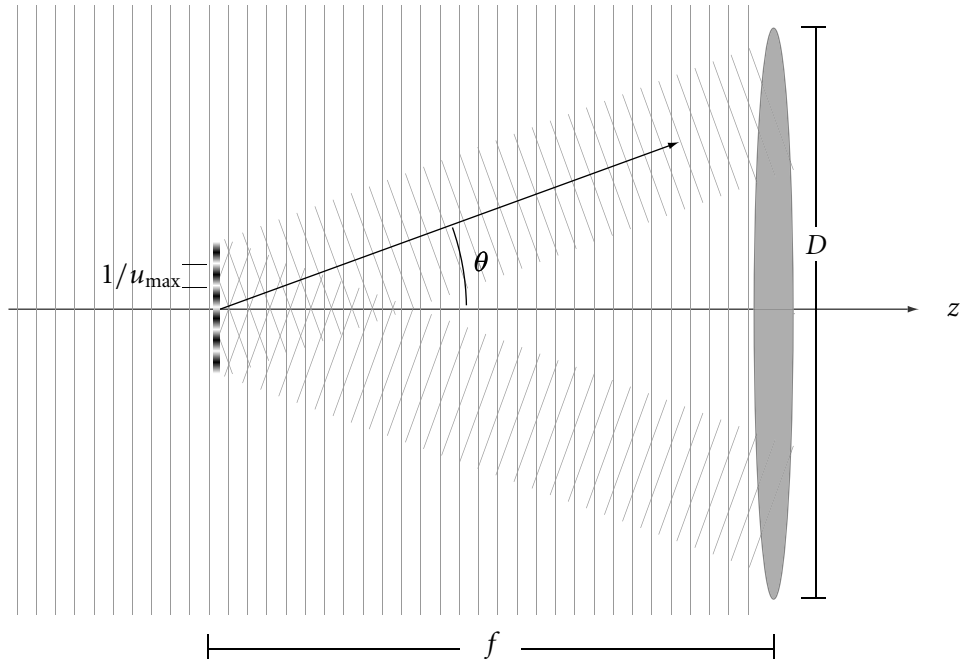


**FIGURE 5.18 Diffraction limit of a lens.** A finite grating diffracts two beams at angles  $\pm\theta$ , which are just captured by the lens. The grating spacing is the *diffraction limit* of the lens.

such as microscope objectives are often described by their *numerical aperture*  $\text{NA} = 1/(2 \times f\#)$  instead. Naturally, the second lens in the telescope must have an equal or smaller f-number to achieve diffraction-limited resolution.

This discussion is a simplification of *Abbe's theory of image formation* [383] [23, §6]. As emphasised by Walton [384], it is erroneous to talk about a plane-wave *missing* the lens: a plane-wave has infinite extent. Instead, we consider a finite-sized grating, smaller than the lens aperture but much larger than the fringe spacing, so that a narrow range of frequencies centred on  $u_{\max}$  are propagated. The net effect is the transport of the grating oscillation at the central angle  $\theta$  to the axis while its envelope diffracts only slowly [385, §8.1] [386]; this justifies the construction shown in Figure 5.18. It is then reasonable to talk about the diffracted beam missing the lens or detector, and it is clear that this quasigeometric condition applies both to an imaging lens and to a detector of the same diameter used in a holographic experiment.

Naturally, the net resolving power of the system is limited by the weakest step. In defocus-contrast imaging, it is no use applying a high-magnification high-resolution lens system if the resulting diffraction pattern is so large that it falls off

the sides of the detector. When reimaging, the *demagnified* detector size and the *effective* propagation distance must be used to find the detector diffraction-limit. If it is a greater size than the lens diffraction limit then the lens resolution serves only to enhance the saturation properties and not the resolution.

This model is still imperfect. In the limit of the grating becoming infinitely large, the diffracted beams enter the lens or, in the holographic case, interfere on the detector. In the correct Abbe theory, it can be shown [387] that the truncated beams after the lens fail to form an image if the resolution criterion (5.29) is not met and so the two views of the Abbe theory are consistent [384]. This must also be the case for a traditional holographic reconstruction of the wavefield. The result of diffraction-contrast retrieval on such a hologram is presumably equivalent, but has not been simulated.

#### 5.5.4 Diffraction limit: PSWFs, sampling and Wigner distributions

The manifest difficulty in explaining resolution limits may be attributed to the inappropriate use of the Fourier (plane-wave) basis. We are inquiring about the detail which can be retrieved within a *finite* object using a *finite* detector. It is then unsurprising that the spatially-infinite Fourier basis is unsuited.

A better basis may well be the *prolate spheroidal wavefunctions* (PSWFs) which are eigenfunctions of the Helmholtz wave equation in elliptical coordinates [388–392]. PSWFs have been applied to finite Fresnel transformation [393] and most interestingly to diffraction-limited imaging [394]. Some work has also been done on *communication modes* connecting diffracted intensities and PSWFs [395].

The question of resolution and information content is deeply connected to *sampling* of the diffracted field [396]. Wigner-space analyses of wavefields [397] and intensities [398] offer a unified view of sampling in the space-bandwidth domain [399]. It seems very likely that a rigorous theory of resolution in diffraction-contrast imaging could be built on these foundations; unfortunately, this must be left for future work.

#### 5.5.5 The diffraction limit in practice

In the experiments reported in this thesis, the atom cloud is much smaller than the detector. The lens diffraction-limit (5.29) then applies to DCI as discussed in §5.5.3. The detector used in the holographic imaging experiments was  $9.0 \times 6.7$  mm and due to the size of the vacuum chamber could not be placed closer than about

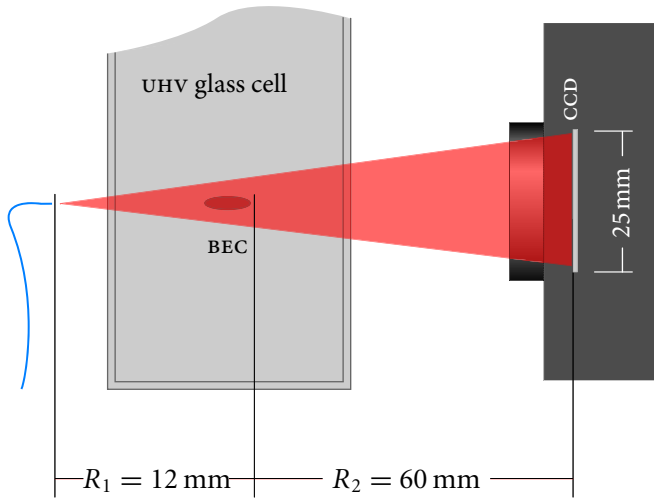


**FIGURE 5.19 Possibility for point-projection imaging of a BEC.** Given a CCD with  $9 \mu\text{m}$  pixel-pitch, this configuration yields a pixel resolution limit of  $3.0 \mu\text{m}$  and a diffraction-limited resolution of  $3.7 \mu\text{m}$ . The Gaussian beam profile of the fibre will have fallen off considerably at the edges of the detector, but likely not below the scattered-wave intensities so that Fresnel diffraction will still apply.

160 mm to the MOT. This was equivalent to an  $f/20$  imaging system or diffraction-limit of  $40\lambda = 31 \mu\text{m}$ . In comparison, an unremarkable 50 mm diameter lens placed in the same position constitutes an  $f/3.2$  system with  $5 \mu\text{m}$  resolution. If this lens was focused onto the same CCD, the resolution limit would be set by the  $6.45 \mu\text{m}$  pixel pitch unless the lens magnification was greater than one. In practice, the resolution of our system was limited to an equivalent of roughly  $f/6$  by the 20 mm diameter vacuum connector on the imaging port, which extended to around 120 mm from the trap centre.

The preceding comparison argues for defocus-contrast imaging over the lensless version. Note, however, that the CCD is particularly small and the optical access is particularly bad in these experiments. Much larger CCDs are available (ie. Kodak KAF-16801E,  $4096^2$  pixels,  $37 \times 37 \text{ mm}$ ) and better optical access (a few centimetres can be realistic) quickly bring the equivalent focal ratio for a lensless system down to  $f/2$ . At these resolutions, aberrations become hard to control in home-made optical systems. The diffraction limit is easily below the pixel-pitch of common CCDs and so point-projection magnification would be needed.

Figure 5.19 shows a possible configuration for imaging a BEC formed in a UHV glass cell of realistic size; see caption for details. Note that here the  $R_1$  distance from

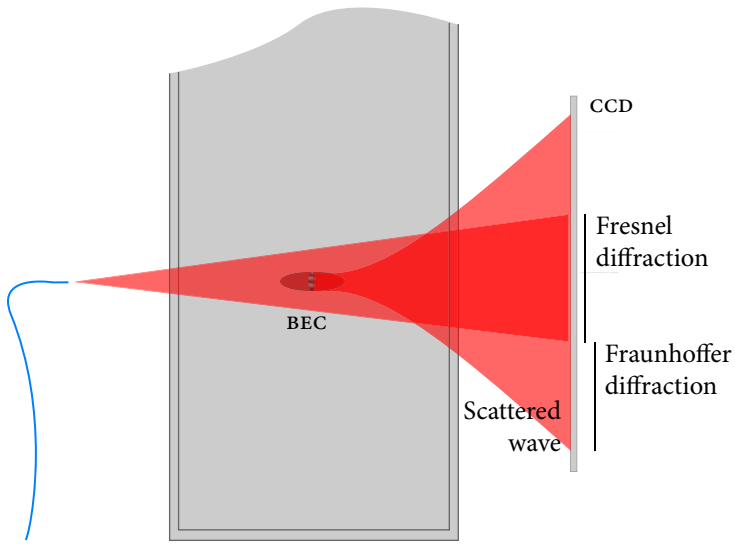


**FIGURE 5.20 Imaging at wavelength resolution and below.** A hypothetical wavelength-scale atom grating is shown diffracting into a wide-angled cone. The diffraction angle is wider than the illuminating beam from the fibre. Information on the wavelength-scale detail would appear as Fraunhofer-diffraction spots in the unilluminated area of the CCD.

fibre to BEC cannot be made smaller than half the cell-width. Changing only  $R_2$  has mixed effects: moving the CCD closer improves the diffraction-limit but reduces the magnification and thus the pixel-limit. Reducing  $R_1$  by using a narrower cell or moving the trap centre and using a yet-larger CCD would make a  $1.5\text{ }\mu\text{m}$  ( $2\lambda$ ) resolution system plausible, if expensive. Achieving such resolutions at working distances of order 30 mm would be essentially impossible with conventional lens optics.

### 5.5.6 Fresnel-approximation limit

There are two foreseeable obstacles to holographic imaging at near-wavelength resolution. First, conventional single-mode optical fibres illuminate only a cone equivalent to about  $f/5$ . Second, diffraction angles greater than  $\pi/6$  are really beyond the validity of the Fresnel (or paraxial) approximation and so we would expect the CTF relations to lose accuracy for features below  $2-3\lambda$  in size.

If the fibre illuminates an  $f/5$  cone, then information about structures smaller than about  $10\lambda$  is eventually scattered outside the illuminating wave and will appear as a *Fraunhofer diffraction pattern*: bright spots on a dark background (see Fig-

ure 5.20). One solution is to use a spatial filter to ensure a smaller effective source size, another is to place a diverging lens after the fibre. Optical fibres with tips tapering to sub-wavelength dimensions are manufactured for use in near-field scanning optical microscopy (*NSOM*). These fibre-tips are readily made as small as 20 nm. A tip of order 500 nm would radiate around one-tenth of 780 nm light coupled into the fibre, and would radiate it into a cone with half-angle of order 90°. For the purposes of diffraction-contrast imaging, these fibre tips may be the perfect point-source of light.

A more exotic solution would be to record the Fraunhofer pattern surrounding the illuminated region, and use an iterative retrieval technique to ‘fill in’ the wavelength-scale details missing in a CTF-retrieval from the illuminated region. Such a hybrid Fresnel-Fraunhofer image would likely circumvent the Fresnel-approximation resolution limit, as angular-spectrum propagation could be used at the iterative stage. Vortex lattices in a BEC might be imaged at wavelength or better resolution as Laue spots in the dark section of the detector.

Another alternative for wavelength resolution imaging would be to place a microscope objective inside the vacuum system. The objective would pre-magnify the wavefield and subsequent defocus of the *back* focal-plane would render defocus-contrast while propagation would remain paraxial.

These obstacles are likely to be serious only for resolutions approaching one wavelength. The Fresnel-approximation limit should not impede resolution of structures larger than about  $2\lambda$ , already a resolution extremely difficult to achieve with conventional imaging optics. Future work should include simulations of CTF retrievals at wavelength resolution to quantify this resolution limit.



OPTICAL RESOLUTION is not a simple quantity to assess. Pixel size, detector size and propagation distances interact to determine the resolution which can be retrieved from a diffraction-contrast image. In holographic DCI, the complete absence of lens aberrations should make possible the resolution of details separated by only two or three wavelengths. This extreme resolution is plausible even with realistic constraints on optical access.

## 5.6 Comparison with other imaging techniques

In Section §5.3 DCIs were compared with absorption and fluorescence images and shown to be of similar quality. Yet these two methods are *destructive* of Bose-Einstein condensates. This Section compares diffraction-contrast imaging with three other off-resonant imaging techniques that have been used to image cold atoms. While the ultimate SNR achievable with DCI is somewhat less than that achievable with Zernike phase-contrast or spatial heterodyne imaging, we will see that diffraction-contrast imaging has specific advantages over the other techniques. Most importantly, DCI has the simplest possible apparatus and alignment.

### 5.6.1 Near-resonant absorption

Although *not* a non-destructive imaging method, near-resonant absorption imaging is a tempting possibility when imaging atom clouds of moderate (several) optical densities [400, Ch 4]. Here residual absorption may still be appreciable at detunings where phase-shifts are less than several radians. The lensing condition discussed in §5.1.8 is roughly satisfied, and high-resolution absorption imaging is possible. Indeed, the detuned absorption images forming the right-hand column on p 202 are just such images, although the MOT was not quite dense enough for on-resonant absorption to be excessive.

If destructivity is not an issue, high-contrast absorption images can be obtained with detuned probe-light. While harmless in an accurately focused system, the off-resonant phase-shift makes the absorption imaging very sensitive to focusing errors. Elaborate procedures have been described for improving focus accuracy [401, p 120].

We can estimate the contrast error  $\Delta C(z)$  due to a focus error  $\Delta z$  from the Taylor expansion

$$C(z + \Delta z) \approx C(z) + \Delta z \frac{\partial C}{\partial z}. \quad (5.30)$$

As differentiation with respect to  $z$  commutes with the transverse Fourier transform, we can insert the CTF expression (2.94) obtaining for the error term

$$\begin{aligned} \Delta C(z) &= \Delta z \mathcal{F}^{-1} \left\{ 2k \frac{\partial}{\partial z} (\delta \sin(\pi\lambda zu^2) - \beta \cos(\pi\lambda zu^2)) \tilde{\rho}(\mathbf{u}) \right\} \\ &= \Delta z \mathcal{F}^{-1} \left\{ 2k\pi\lambda u^2 (\delta \cos(\pi\lambda zu^2) + \beta \sin(\pi\lambda zu^2)) \tilde{\rho}(\mathbf{u}) \right\}. \end{aligned} \quad (5.31)$$

It is clear that for in-focus (absorption) imaging where  $z = 0$ , this first-order error

vanishes for a purely absorbing object with  $\delta = 0$ ; *on-resonant* in-focus imaging is stable against focusing errors. On the other hand, the off-resonant phase contribution resulting from a focus error  $\Delta z$  is *maximal* at  $z = 0$ ; *off-resonant* in-focus imaging is sensitive to focusing errors.

The expansion (5.30) can be substituted into the retrieval expression (3.6) (or the regularised form thereof) to obtain a retrieval error  $\Delta\rho(\mathbf{x})$ . Consideration of this retrieval error, and simulations of misfocused retrievals, have confirmed that diffraction-contrast imaging is much less sensitive to focus errors than absorption imaging. This insensitivity may explain why the retrieved data are less scattered than the absorption data in Figure 5.10. Even if non-destructivity is unimportant, DCI might be preferred to absorption imaging due to its lower sensitivity to focusing errors.

### 5.6.2 Dark ground

The first BECs were observed with absorption imaging. Dark-ground imaging was used to obtain the first non-destructive images of BEC [354] only a year later. The dark-ground apparatus (Figure 5.21A) was first described by Toepler in 1864 [402]. An opaque mask is introduced in the Fourier plane of a telescope focused on the object; the simplest mask is a half-plane just occulting the central focal spot, a system known as *schlieren* imaging. A wire, or a dark spot on a transparent slide make more efficient use of the scattered light. The idea is to remove the central focused spot in the Fourier plane which corresponds to the unscattered component of the wavefield.

If imaging a weak pure-phase object, the field at the input plane is  $\exp(i\phi(\mathbf{x})) \approx 1 + i\phi(\mathbf{x})$  and so in the Fourier plane we have  $\delta(\mathbf{u}) + i\tilde{\phi}(\mathbf{u})$ . The mask removes the bright central spot which corresponds to the delta function, and so the output plane wavefunction is  $i\phi(\mathbf{x})$  and the measured intensity  $I_{DG}$  is approximately

$$I_{DG}(\mathbf{x}) \approx I_0 |\phi(\mathbf{x})|^2 \quad (5.32)$$

Clearly for weak, pure-phase objects the phase-shift is recovered from the square-root of the normalised intensity. This nonlinearity frustrates the subtraction of background phase signals measured with the atom trap empty, as cross-terms remain.

For stronger objects, the intensity becomes an oscillatory function of the phase. Note, however, that simple analytic expression for the dark-ground and phase con-

trast of stronger objects given in common references [331, §3.2, Fig. 9] have been shown to be flawed [403]. In general, there is no simple solution which extracts the phase for a strong object. So-called ‘2D phase unwrapping’ algorithms exist for extracting ‘wrapped’ information from such images: they are a research topic in their own right.

As the signal is on a dark background, the Poisson noise is just the square-root of the signal count and so the SNR in the shot-noise limit is

$$\left(\frac{S}{N}\right)_{\text{DG}} \propto \frac{I_0 \phi^2}{\sqrt{I_0 \phi^2}} = \phi \sqrt{I_0}. \quad (5.33)$$

As we will see in the next Section, dark-ground imaging is highly sensitive to technical noise and is inferior to Zernike phase-contrast in all cases [331, p 25], its only merit is its simplicity: one can create a dark-ground imaging apparatus simply by moving a needle or wire around in an existing telescope until the field goes dark.

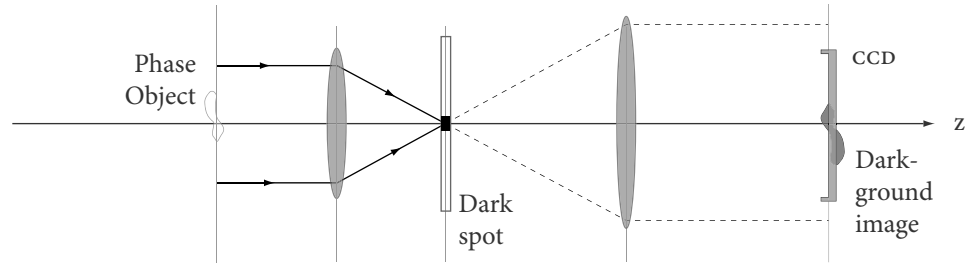
### 5.6.3 Zernike phase-contrast

The MIT group of Ketterle and co-workers soon upgraded their BEC imaging apparatus to the Zernike phase-contrast configuration depicted in Figure 5.21B. As in the dark-ground case, a mask is intercalated in the Fourier plane of the telescope but rather than blocking the unscattered component, it phase-shifts it by  $\pi/2$ . This is usually achieved by precisely etching a small depression or bump into a glass plate. The phase-shifted unscattered wave then interferes with the scattered wave in the image plane producing *phase contrast*: image contrast linear in the object phase-shift. The technique was discovered by Zernike in 1930 [404] but publication was delayed[405, 406]. Zernike received the Nobel Prize for this work in 1953, in recognition of how phase-contrast microscopy transformed biological imaging.

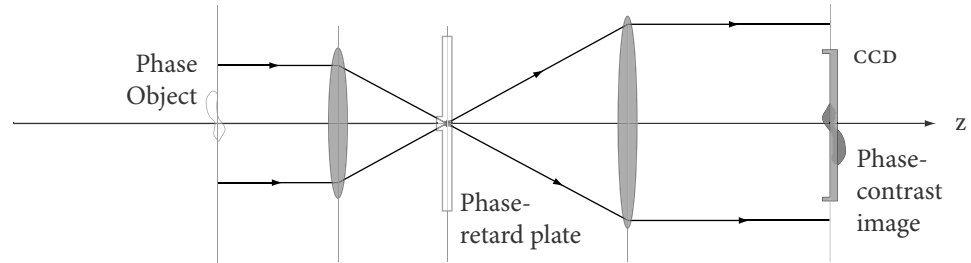
For a weak phase object, the measured intensity can be found with a similar argument to the dark-ground case. The phase plate shifts, rather than removes, the delta function in the Fourier plane yielding  $i\delta(\mathbf{u}) + i\tilde{\phi}(\mathbf{u})$  and so, neglecting terms of order  $|\phi|^2$  the Zernike phase-contrast signal is

$$I_{\text{ZPC}}(\mathbf{x}) \approx I_0 (1 \pm 2\phi(\mathbf{x})) \quad (5.34)$$

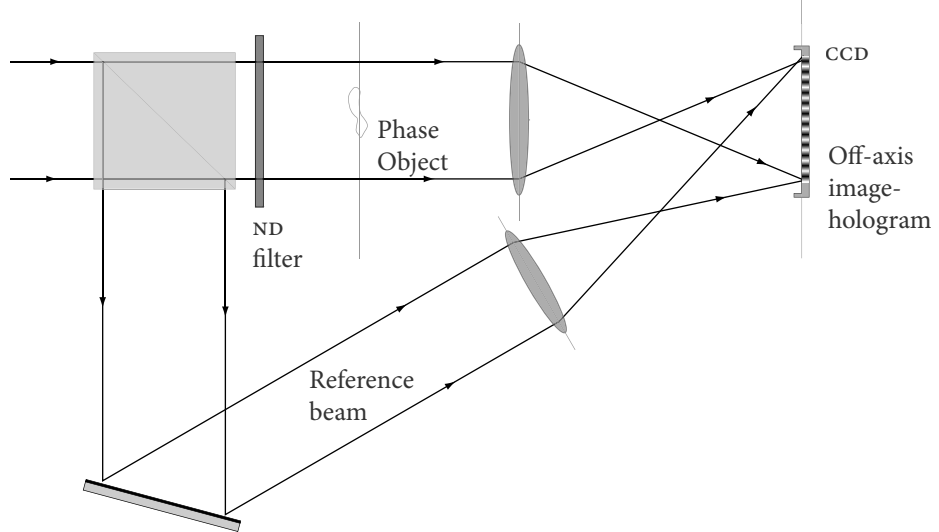
with the sign positive for a phase-retarding plate (bump) and negative for a phase-advancing plate (dip). This proportionality between contrast and phase makes Zernike images particularly easy to interpret, provided the phase-shifts are small.



**A DARK-GROUND IMAGING.** A dark spot blocks the illumination beam, allowing only the diffracted component to pass.



**B ZERNIKE PHASE-CONTRAST IMAGING.** A phase-bump (here shown as a phase-retarder) shifts the un-scattered wave for maximum interference contrast.



**C SPATIAL-HETERODYNE IMAGING.** A separate reference wave interferes with the re-imaged exit-surface wavefield on the detector.

**FIGURE 5.21 Off-resonant imaging techniques demonstrated on cold atoms.** Dark-ground A and Zernike phase-contrast B have been used for non-destructive imaging of BEC. Spatial-heterodyne imaging has been demonstrated on a dark-spot MOT.

A strong-object expression

$$I_{\text{ZPC}}(\mathbf{x}) = I_0 (3 + 2 (\sin \phi - \cos \phi)), \quad (5.35)$$

can be derived [19, §8.6.3c] which suggests that the Zernike intensity reaches a value  $5.8I_0$  before rolling over and is rather linear up to around  $5I_0$ , corresponding to  $\phi = 1.5$  radian. It has recently been shown, however, that the effects of finite lens size are important. While an excessively small phase bump reduces the peak contrast, an excessively large one leads to curvature of the shifted, unscattered field [403]. Choosing an optimum bump size is not a trivial process [407]. The Zernike bump sizes used in cold-atom imaging appear to have been chosen for convenience of alignment, rather than for quantitative phase measurement [400, p 72]. In any case, it seems that intensities up to  $5.8I_0$  could only be achieved, if at all, at the price of a vanishingly small region of *quantitative* contrast about the optical axis. Nevertheless, the dynamic range of phase-contrast is likely to be at least  $I_0$  to  $2I_0$  and so is larger than absorption imaging.

Being a focal, single-image technique, Zernike imaging cannot hope to give an independent measurement of absorption and phase. An object with residual absorption will yield inaccurate results if treated as a pure phase object. However, an appropriate modification of (5.34) can be derived which includes the effects of absorption [331, Eq. 25,26]. Under the monomorphous object assumption, the contrast remains proportional to the column-density. Absorption reduces the sensitivity and linear contrast range of Zernike imaging.

The Zernike contrast  $2\phi$  is larger than the dark-ground signal at small phase-shifts. Unlike dark-ground imaging, the background illumination remains and so the Poisson noise is also larger than the dark-ground noise being approximately  $2\sqrt{I_0}$ , where the factor of 2 arises from the subtraction of the background intensity. Zernike phase-contrast then has the shot-noise limit SNR

$$\left( \frac{S}{N} \right)_{\text{ZPC}} \propto \frac{2I_0\phi}{2\sqrt{I_0}} = \phi\sqrt{I_0}, \quad (5.36)$$

which is identical to dark-ground imaging. Note, however, that because both signal and noise are greater in absolute terms, Zernike phase-contrast is less sensitive to technical noise.

Ketterle's group first used phase-contrast imaging for quantitative, in-trap imaging of BEC [408] and shortly afterward exploited the non-destructive possibilities

of the technique to obtain 11 sequential images of sound propagation through a BEC [353]. Phase-contrast was critical to subsequent observation of bosonic stimulation in condensate formation [409], Feshbach resonances [410], collective excitations and second sound [411], surface excitations [412] and superfluid flow [413]. Phase-contrast also assisted in observing vortex nucleation [414] at MIT. Workers at JILA (Boulder CO, USA) continued phase-contrast imaging of superfluid effects [415] and vortex creation [416, 417], precession [418], lattices [419] and recently, vortex equilibrium properties [420].

Given this spectacular success of phase-contrast in illuminating dynamic processes in BEC, one might expect it to be widely used. However, none of the other 30-plus BEC groups have published non-destructive imaging results.<sup>16</sup> The reason seems to be the complexity in constructing and aligning a Zernike imaging set-up. While white-light Zernike phase-contrast microscopes have been available commercially for 50 years, Zernike phase-plates for coherent imaging are not commercially available. Manufacturing one requires custom-coating a layer (MgF for example) on an optical flat with precisely controlled size and thickness. Then comes the problem of alignment. M R Matthews of JILA commented that ‘In general it is not trivial to align the phase dot with the probe beam’ [400, p 74]. BEC researchers who have worked with phase-contrast imaging have described<sup>17</sup> how, while relatively large phase bumps can eventually be located, it is extremely difficult to distinguish phase bumps smaller than 200 µm from the effects of dust particles resting on the glass.

A recently proposed improvement to Zernike imaging is to use a non-linear photorefractive sheet to create a self-induced phase-bump [422–424]. Such a plate would obviate both fabrication and alignment problems, although accurate control of the phase-shift would still present some technical challenges.

#### 5.6.4 Spatial heterodyne imaging

Zernike imaging is a special case of ‘common-path interferometry’: the unscattered wave is shifted relative to the scattered wave by the phase-plate, maximising contrast when they interfere at the detector. A more traditional separated-path interferometer has also been demonstrated for cold-atom imaging. The group of Walker at the University of Wisconsin-Madison (Madison WI, USA) constructed the apparatus of Figure 5.21c, describing the method as ‘spatial heterodyne imaging’ [425].

<sup>16</sup> Hulet’s group at Rice have used Zernike phase-contrast but only in the destructive regime [421].

<sup>17</sup> Personal communication with Wilbert Rooijakers at University of Melbourne, 2004-Jul-26.

Alternatively, the configuration could be described as an *imaging Mach-Zehnder interferometer* or as *off-axis image holography*. One lens images the probe beam onto the detector as in absorption imaging. A second lens images the reference beam onto the detector at an angle to the probe beam. In the absence of an atom cloud, the field-curvatures are matched to produce a pattern of parallel fringes on the detector. Phase-shifts on the probe beam then manifest themselves as displacement of fringes while absorption reduces the fringe contrast.

### 5.6.5 Comparison with diffraction-contrast imaging

The recorded fringe pattern cannot be directly interpreted, and must first be demodulated by computer processing; the spectrum is obtained by FFT and then one sideband down-converted from the fringe carrier-frequency to baseband before it is inverse-transformed. This procedure returns the *full complex wavefield*, demonstrating the similarity with off-axis holography. Information theory arguments discussed in §3.1.3 dictate that retrieving the complex wavefield requires the loss of half of the spatial resolution. Here, this is reflected by the minimum of two pixels needed to resolve each fringe. In combination with a demodulation filter, Kadlec et al. reported a spatial resolution of 20 μm when the diffraction limit of their lens systems was 5 μm.

The need to resolve fringes must also make spatial heterodyne imaging particularly sensitive to vibration. While a blur of a few pixels might be relatively harmless for baseband imaging (including DCI and Zernike phase-contrast), it would be sufficient to blur the carrier fringes in spatial heterodyne imaging and destroy the interference pattern completely. Low vibration sensitivity is critical in BEC experiments as magnetostriction due to the sudden removal of trap fields can produce a strong mechanical shock in the apparatus. Non-destructive image sequences are usually taken after turning off the trap field, so that the magnetostrictive shock-wave arrives during the image sequence.

Retrieving the full wavefield yields holographic depth-of-field. Although not demonstrated by Kadlec et al., the retrieved wavefield could be forward- or back-propagated to an arbitrary plane of the probe beam. Zernike and dark-ground imaging have no such possibilities: there, accurate mechanical focus is essential, and imaging objects at different focal planes requires manual refocusing. A more exotic possibility, also not considered by Kadlec et al., is *multiplex holography*. Multiple reference waves at different angles to the probe beam can record the object

	Fluorescence	Absorption	Darkground	Zernike PC	Spatial-Het	Defocus DCI	Lensless DCI
Non-destructive?	No	No	Yes	Yes	Yes	Yes	Yes
Method of phase-contrast			— Fourier-plane filter —		Interference		Diffraction
Image processing?	Multiply	Log	Pixel maths only	Subtract	FFTS	FFTS, wavelets optional	
Algorithm			Sqrt		Demod		
$I$ linear in small $\phi^2$ ?			No, $\propto \phi^2$	Yes	Yes		
Min, max monotonic $\phi$			0, $\pi$	$-\pi/4, 3\pi/4$	$-\pi, \pi$		
Min, max intensity / $I_0$	0, $\ll 1$	0, 1	0, 4	0, 5.8	$\gg 1^b$	Possibly $> \pm 2\pi^a$	0.7, 1.3 <sup>c</sup>
Quantitativity <sup>d</sup>	Poor	Very good	Mediocre	Good	Very good	Excellent	
Shot-noise SNR / ZPC	$\ll 1$	1	1	1	1	$\lesssim 1$	
Tech noise SNR / ZPC	$< 1$	$\approx 1$	$\ll 1$	1	$> 1^b$	$\lesssim 1$	
Quantisation SNR / ZPC	$\ll 1$	1	$< 1$	1	$\gg 1^b$	1	
Pixel resolution	Full	Full	Full	Full	< Half <sup>e</sup>	Full	
Diffracton-limit by	Lenses	Lenses	Lenses	Lenses	Lenses	Lenses	Detector
Holographic DOF?	No	No	No	No	Yes	Yes	Yes
Red-detuning?	Yes	Yes	Yes	Yes <sup>f</sup>	Yes	Yes	Unstable <sup>g</sup>
Multiplexing?	No	No	No	No	Angular	No	No
Apparatus complexity	Simple	Simple	Moderate	Moderate	Elaborate	Simple	Simplest!
Optics	— Imaging only —	+ Darkspot	+ Phaseplate	Lots	Imaging	None!	
Alignment	Easy	Easy	Fairly easy	Difficult	Easy	Trivial	
Vibration insensitivity	High	High	Moderate	Moderate	Very low	Very high	
Lens Aberrations?	Yes	Yes	Yes	Yes <sup>h</sup>	Yes <sup>i</sup>	No	

<sup>a</sup> Large phases provided SVPC satisfied.<sup>b</sup> Reference intensity arbitrarily bright.<sup>c</sup> Weak contrast for max accuracy.<sup>d</sup> See §5.6.5.<sup>e</sup> Less when filtered [425].<sup>f</sup> Phase-advance filter needed to preserve dynamic range.<sup>g</sup> Stable at large  $z$ .<sup>h</sup> Lensless possible?<sup>i</sup> Spherical aberration potentially deconvolvable?

data modulated onto different spatial carrier frequencies [426]. The reference waves could have different detunings to probe other states, different wavelengths to probe other species, or could be sequenced to record object evolution at different times. In an unrelated application area, three separate images taken at sub-microsecond intervals have been reconstructed from one hologram recorded on a CCD [427]. Multiplex holography makes very stringent demands of detector resolution as the available spatial bandwidth, already half the focused-image bandwidth, is further divided between the images.

Separated-path interferometry has one clear advantage over all other techniques considered: a higher signal-to-noise ratio, at least in the presence of technical noise. In diffraction-contrast imaging, and in Zernike and dark-ground imaging, the un-scattered reference wave passes through the object. Dark-ground imaging is the most wasteful, absorbing the reference while Zernike makes optimal use of it. But with separated-path imaging, the reference can be made arbitrarily bright without additional heating of the atoms. The resulting SNR is identical to the Zernike and dark-ground SNRs (5.36) in the shot-noise limit but substantially better than the Zernike SNR in the presence of technical noise [425].

Spatial heterodyne imaging offers excellent SNR and holographic refocusing, while its resolution limit is inessential. Yet the technique has not been applied in other laboratories, nor has it been used for imaging BEC. Again, the likely explanation is the complexity of the apparatus and the alignment process. The optics are more complicated than Zernike optics and the interferometer must be carefully aligned. The reference beam must be routed around the trap chamber. Further, spatial heterodyne requires elaborate computer processing while Zernike offers a direct image with contrast proportional to phase-shift. The added complexity in apparatus *and* in processing seems to have outweighed the manifest advantages of the technique.

Table 5.2 compares four aspects of the techniques discussed with diffraction-contrast imaging: contrast generation, retrieval quality, imaging flexibility and implementation.

---

TABLE 5.2 (ON FACING PAGE) **Comparison of cold-atom imaging techniques.** Off-resonant techniques assumed to be operating at detunings  $> D_0/\pi$  so that phase-shifts are small. Resonant-absorption and fluorescence imaging are for a  $D_0 = 1$  cloud using the same probe intensity  $I_0$ . Signal-to-noise ratios are given relative to those for Zernike phase-contrast imaging.

Spatial-heterodyne imaging is the clear leader when comparing SNRs for various forms of noise. This fully-holographic method has the potential, albeit not yet demonstrated, for lensless imaging, extended depth-of-field and possibly even multiplexed imaging. This comes at the expense of easily the most complicated apparatus of the techniques considered.

Diffraction-contrast imaging appears to fall down on SNR, having the lowest shot-noise SNR of any technique except destructive fluorescence imaging. We saw in §3.8.2 that the RMS shot-noise SNR of diffraction-contrast imaging approaches half the Zernike phase-contrast value for substantially-diffracted images. After wavelet-denoising, the diffraction-contrast SNR should be much closer to that of the (denoised) Zernike image. Nevertheless, we must accept that an ideal diffraction-contrast retrieval will never equal the SNR of a similarly-denoised ideal Zernike image taken with the same detuning and exposure.

There is no question, however, that the diffraction-contrast apparatus is the simplest. For defocus-contrast imaging, the apparatus is just the imaging system for absorption or fluorescence imaging thrown out of focus. For lensless DCI, nothing more than a fibre-end and detector are needed, although the images are more interesting if there is an atom cloud present! While this simplicity reduces construction and alignment effort and reduces sensitivity to vibration, it also fundamentally reduces uncertainties in image analysis. For example, residual fringe curvature in the spatial heterodyne image will introduce artefacts in the retrieved image. In Zernike imaging, an incorrectly sized or aligned phase-bump or imperfectly aligned lenses will warp the reference, inducing errors in the measured phase. These are small errors, not gross distortions, and would not be obvious without optical bench testing of the imaging system. There are no parameters to adjust in DCI, except for the magnification and focus parameters inherent in all of the imaging systems. Further, we have seen that focus can be adjusted digitally. Thus I argue that DCI is likely to yield more *accurate* non-destructive measurements of column-density than the other phase-imaging techniques.



IF A CONDENSATE is small or otherwise particularly sensitive, the extra optics and processing required by spatial-heterodyne imaging may be the only way to obtain a measurement given the tenacity of technical image noise (see §5.7.2). For standard alkali condensates, diffraction-contrast imaging offers holographic depth-of-field with the simplest apparatus of all. The only advantages of Zernike phase-contrast –

the only method which has been used in multiple BEC experiments – are a slightly greater SNR and simpler image processing.

## 5.7 Imaging signal-to-noise and destructivity

Motivated by non-destructive imaging of cold atoms, this thesis has presented a new phase imaging technique and shown that its regime of operation is peculiarly well-adapted to cold-atom imaging. Although no experiments have been presented which *demonstrate* the non-destructive character of DCI, we can infer non-destructivity using the results of this Section. I consider two papers by JD Close, JJ Hope and JE Lye of the Australian National University (ANU, Canberra, Australia). The first shows that the minimum destructivity for a given experiment is set by the desired SNR of the measurement, and does *not* depend on the probe beam intensity or detuning [428]. These arguments are simplified somewhat and adapted to our spatially-resolved imaging case in the first Article, and technical SNR considerations are canvassed in §5.7.2. The second paper shows that this minimum destructivity is a rather stubborn limit, and cannot be circumvented by involving multiple atomic states and multiple lasers [429]. I conclude by discussing the implication of these results for diffraction-contrast imaging.

### 5.7.1 Non-destructive SNR independent of detuning and power

We will consider the *form* of the SNR: its dependence on detuning, probe intensity and column-density. The first ANU paper considers *dynamic* detection at a Fourier frequency whereas we are concerned with an instantaneous observation which is *spatially* resolved. Assuming unit quantum efficiency of the detector, we consider a probe pulse delivering  $N_p$  photons incident *on the object* in each pixel area. Further assuming a shot-noise Zernike SNR (5.36) we have the pixel SNR

$$\frac{S}{N} = \phi \sqrt{N_p}, \quad (5.37)$$

which is reasonable provided the object image covers a relatively small area of the detector. Of the  $N_p$  photons incident on the pixel area at position  $\mathbf{x}$ ,

$$N_s = N_p (1 - \exp(-2k\beta\rho(\mathbf{x})) = N_p \left( 1 - \exp \left( -\sigma_0 \rho(\mathbf{x}) \frac{1}{1 + 4\Delta^2} \right) \right) \quad (5.38)$$

are absorbed, or scattered, by the atom cloud. Provided Bose-stimulated scattering and such exotic effects are absent, the heating of the cloud may be represented simply by the number of scattered photons  $N_s$  (see §5.1.6).<sup>18</sup> We are about to substitute this expression into (5.37), but note that the phase is also a function of column-density  $\rho$  and detuning  $\Delta$ :

$$\phi = k\delta\rho(\mathbf{x}) = \frac{\sigma_0\rho(\mathbf{x})}{2} \frac{2\Delta}{1 + 4\Delta^2}. \quad (5.39)$$

Substituting both (5.38) and (5.39) into (5.37) yields the SNR

$$\frac{S}{N} = \frac{\sigma_0\rho\Delta}{1 + 4\Delta^2} \sqrt{\frac{N_s}{1 - \exp\left(\frac{-\sigma_0\rho}{1+4\Delta^2}\right)}}, \quad (5.40)$$

which asymptotes towards a limiting value for large detunings where  $\Delta^2 \gg \sigma_0\rho$ , taking the value

$$\frac{S}{N} \rightarrow \frac{1}{2} \sqrt{N_s \sigma_0 \rho}. \quad (5.41)$$

The quantity  $\sigma_0\rho$  is just the resonant optical density  $D_0$ , and so we see that, unsurprisingly, the SNR increases with heating and with density of atoms. This simple expression allows us to make a more quantitative assessment of the hypothetical image of §5.1.7. For those parameters, 2400 photons were scattered for an image subtending 900 pixels yielding  $N_s = 0.375$  photons scattered per pixel. Given the assumed resonant OD of 300, the shot-noise SNR should be

$$\frac{S}{N} \approx \frac{1}{2} \sqrt{0.375 \times 300} = 5.3. \quad (5.42)$$

This confirms that a meaningful image could be extracted under these conditions. A condensate of this density will contain many more than 2400 atoms, so this level of photon scattering is likely to be ‘non-destructive’.

### 5.7.2 Technical noise: sources and solutions

Technical noise has been ignored so far. While shot-noise limited detection is fairly easy to achieve with dynamic detectors by using RF techniques, these detectors are

---

<sup>18</sup> Note that in Reference 428 the analogous expression Eq 9 confuses optical power *scattered* by the BEC with power *absorbed*. As discussed in §5.1.6 the energy imparted to an optically thin cloud is one recoil energy  $\hbar\omega_r$  not one photon energy  $\hbar\omega_0$ . Their  $P_{ab}$  overestimates the heating by a factor of  $\omega_0/\omega_{\text{recoil}} = 2\lambda Mc/h \approx 10^{11}$ .

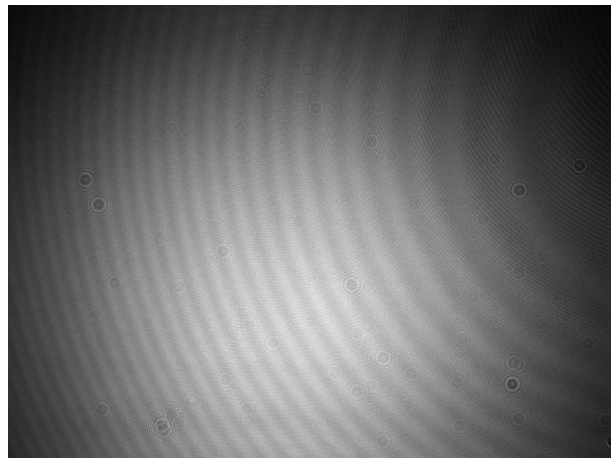


FIGURE 5.22 **Spatially-coherent noise (SCN) on a CCD.** This image is the result of illuminating a standard scientific CCD chip (Sony ICX285) with a single-mode laser beam emanating from a single-mode fibre. The fringes are likely due to etaloning in the 15  $\mu\text{m}$  thick silicon substrate of the thinned, back-illuminated CCD. Small circular fringes are due to dust on the cover window.

not currently available in spatially-resolved arrays. Furthermore, the chief source of contamination is *not* stationary noise: for modern, cooled cameras with low-noise digitisers the aggregate stationary noise – thermal ‘dark’ noise and read-out noise – is of order 10 electrons/pixel, below the shot-noise for exposures yielding more than 100 electrons. Quantum efficiencies of up to 75% at 780 nm are available in commercial detectors.

Illuminate a CCD with a coherent beam from a fibre-end and, rather than the featureless Gaussian intensity profile you would expect, you will likely see an amalgam of straight and circular fringe patterns superposed on the Gaussian background, rather like Figure 5.22. This mess which we might term *spatially coherent noise (SCN)* (in preference to the laboratory vernacular) is the major obstacle to reaching the shot-noise limit. While some of the features are due to inevitable dust particles on the CCD window, strong chip-wide fringes are likely caused by etaloning in the silicon, or in the coverglass or CCD vacuum window. The problem is particularly acute for the thinned, back-illuminated CCDs used to achieve high QE, as the opacity of silicon falls sharply through the near infra-red. With current technology, photon sensitivity and SCN immunity are anti-correlated at 780 nm. A recent study has shown that calibrating for pixel-to-pixel variation allows true shot-noise limited spatial imaging for incoherent and partially-coherent sources, but not for laser illumination due to etaloning [430].

Interposing vacuum windows and collimating and imaging lenses between the fibre and the camera only introduces more SCN, resulting in highly corrugated flat-fields such as Figure 5.5B. However, there is little point in improving coatings and zealously removing dust when the CCD chip itself is responsible for most of the noise. Although flat-fielding removes the majority of these fringes (Figure 5.5E), some noise is additive rather than multiplicative and the chip-etalon fringes move visibly on sub-second time-scales, presumably due to temperature fluctuations. The spatially coherent nature of the etalon fringes make them attractive targets for Fourier filtering (Figure 5.12B). Experiments with manual filtering have been quite successful. Circular diffraction fringes due to dust are harder to remove, being concentric in Fourier-space with the signal. Filtering using the fractional Fourier transform [431] or using space-frequency distributions such as the Wigner distribution function [432] or the ambiguity function [127] are current areas of research and may be particularly well-suited to removing localised coherent noise.

Assuming some SCN remains above the shot-noise floor, is there any setting of probe laser intensity or detuning which will minimise its effects? The probe detuning and intensity affect the *shot-noise* SNR only through the scattering rate  $N_s$ . For example, doubling the detuning from  $D_0/2\pi$  to  $D_0/\pi$  linewidths and quadrupling the probe intensity would leave  $N_s$  unchanged. It would also reduce both the phase-signal *and* the fractional shot-noise by a factor of two, leaving the shot-noise SNR unchanged. The amplitude of technical noise is unlikely to be affected by detuning or probe intensity and so the overall SNR will be optimal at smaller detunings where the signal is higher. The lower-limit on detuning set by the no-lensing condition of §5.1.8 is then the optimal detuning.

### 5.7.3 Fundamental limits to non-destructive SNR

Bose-Einstein condensates have been observed using species with negative scattering lengths, but they are limited to very small numbers of atoms [433]. The first alkali BEC created was probably in  $^7\text{Li}$ , which has negative scattering length, but the cloud was initially too small for unambiguous detection. Besides highlighting the need for high-resolution, this condensate also demonstrates the limits of non-destructive imaging. With around 1000 atoms in a  $3\ \mu\text{m}$  sized cloud, the resonant OD was of order 4: deep enough for unexpanded absorption imaging to lose accuracy. However, the shot-noise expression (5.41) shows that for a SNR of 5, there must be 25 scattered photons per pixel. Although the condensate is small, illu-

---

minating even a  $3 \times 3$  grid of pixels is enough to remove around one-quarter of the atoms from the condensate. Indeed, non-destructive imaging of this condensate was found to be impossible and only destructive phase-contrast images were obtained [421, 433].

The question arises: could a better imaging system transcend the above-derived SNR limit? In the above derivation, we assumed a single-frequency classical-light probe laser interacting with a two-level atom in a single-pass optical configuration. Experiments with *electromagnetically induced transparency* (*EIT*) have demonstrated that in a three-level atomic system, a strong non-resonant pump beam can induce a phase-shift on a weak-probe beam with no absorption whatsoever [434]. Such a scheme appears at first glance very promising for non-destructive imaging. However, the second ANU paper proves a theorem stating that

No single-pass optical technique using classical light, based on any number of lasers or coherence between any number of [atomic] levels, can exceed the [SNR] limit imposed by the two-level atom [model] [429].

The proof is quite intricate and is not elaborated here.

Close, Hope and Lye also describe two methods which *can* enhance the SNR for a given destructivity beyond the limit (5.41). One is to use non-classical *squeezed light*, which improves the SNR by the squeezing factor. Given the great technical difficulty in producing and detecting squeezed light and the modest squeezing factors obtained, this approach must be considered impractical at present.

The other method circumventing the limit is to *multipass* the probe light, by building a resonant cavity around the atom cloud. This too presents very substantial technical difficulties: the SNR is increased by a factor of the square-root of the cavity finesse, but the vibration sensitivity also increases. Active stabilisation would be required [428, §5b]. This published analysis of the potential of cavity-enhanced BEC measurement considered only dynamic measurement with a point detector. Extracting *spatially-resolved* information from light exiting a cavity containing a BEC would be even more complicated.

I have hypothesised that many laboratories have avoided phase-contrast and spatial-heterodyne imaging due to perceived optical complexity of the techniques. The complexity of squeezed-light or cavity-enhanced imaging is, by any assessment, orders of magnitude greater. The conclusion of this Article is that the shot-noise SNR limit (5.41) is robust: it seems most unlikely that any optical imaging technique will surpass it in the foreseeable future.

### 5.7.4 Prospects for non-destructive DCI

The MIT Zernike imaging experiments typically obtained 11 consecutive images. Sub-images were accumulated by interline-transfer on a covered section of the CCD. The imaging rate seems to have been set by the camera line clock, not by the probe beam heating the condensate. Further, the probe detuning of 1.7 GHz was likely chosen for convenient locking to a sodium hyperfine ground-state. For this condensate,  $D_0/2\pi \approx 500$  MHz and so we might expect a sequence of DCI images taken at this optimal detuning to have similar or better SNR to the published Zernike images.

In contrast to the  $^7\text{Li}$  BEC, most sodium and rubidium experiments do *not* face fundamental SNR limits when imaged off-resonance. Rather, the number of images appears limited by the hardware. Phase-contrast imaging has no real advantage over diffraction-contrast imaging in these circumstances.

The next generation of cold atom experiments is being constructed on *atom chips*: microstructured surfaces using either current-carrying wires to generate trap fields [435] or using ferromagnets [436]. These devices make it much harder to perform conventional destructive imaging by turning off the trap field and allowing the condensate to expand. Even if the field can be turned off, interactions with the surface blur structures in the expanding condensate. These devices may provide a new impetus to non-destructive *in situ* imaging. Interest in atom chips has been spurred by the possibility of manipulating multiple condensates, with a view towards quantum atom optics and quantum computation. The holographic depth-of-field available with diffraction-contrast imaging may be particularly useful for simultaneous imaging of multiple condensates on atom chips.



ALTHOUGH IT WAS not possible to demonstrate the non-destructive ability of diffraction-contrast imaging using only a MOT, it is clear that DCI can be applied to non-destructive imaging of BEC. A diffraction-contrast image can be recorded with an optical fibre point-source, a BEC and a CCD detector: the apparatus literally could not be simpler. Focusing is also simplified, being performed digitally rather than with translation stages. In practise, the SNR attained with diffraction-contrast imaging should be equivalent to the Zernike technique. The tight control of calibration factors should make DCI highly accurate. There seems to be little reason *not* to use DCI in the non-destructive imaging of cold atoms.

# Chapter 6

## Conclusion

THIS THESIS HAS presented a new imaging technique for monomorphous objects, termed diffraction-contrast imaging, and applied it to the measurement of the column-densities of cold atom clouds. Here I review some of the features of DCI and its application to cold atoms. The intention is not to summarise the development of the technique or the results; a precis of the work may be found in Chapter 1. I then speculate on some ideas for future work on the imaging method and its applications.

### 6.1 DCI: a new phase imaging technique

The first half of this thesis exposed a novel technique for optical imaging. Diffraction-contrast imaging records the diffraction pattern, or in-line hologram, of an object and retrieves the structure of the object using a numerical algorithm. Retrieving the full wavefield from this image is, in general, impossible. Instead, diffraction-contrast imaging assumes that the object is monomorphous, that is, made of a single material, so that the phase-shift and absorption through the object are correlated. The monomorphous object assumption includes purely absorbing and purely phase-shifting object as special cases. Further assuming weak absorption and slowly-varying phase shift resulted in a closed-form *linear* relation between the object column-density and the image contrast.

Diffraction-contrast imaging is not a general purpose imaging technique; it will return distorted results if applied outside its assumptions, for example to strongly absorbing objects, or multimorphous samples. For the price of working within the assumptions, we were able to obtain a *direct solution* to the inverse problem. The

solution is numerically fast and even very slight absorption is sufficient to ensure the stability of the solution. No other imaging technique has been demonstrated which can retrieve detailed information from a single diffraction image, obtained without use of optical elements.

Most previous work on deconvolution in optics has treated questions of stability and uniqueness as mathematical inconveniences. This thesis approached the deconvolution problem from the viewpoint of estimation theory, which provides a rigorous framework for solving the inverse problem. I have shown that the power-law characteristic of most object spectra can be exploited, leading to a new partial-Tikhonov filter. This filter yields stable retrievals even when the residual absorption is very small.

The mathematical and signal processing literature on deconvolution is extensive. Although the underlying physics is very different, our deconvolution problem is *mathematically* similar to a number of well-researched inverse problems, notably the removal of motion- and defocus-blurring from standard camera images. I adapted a hybrid Fourier-wavelet algorithm, originally developed for these traditional image-restoration problems, to serve our holographic deconvolution. This solution is capable of retrieving column-densities from noisy images without introducing the edge-ringing distortions characteristic of pure Fourier filters. Successful retrievals were demonstrated from simulated diffraction-patterns with exposures as low as 10 photons/pixel. This low-exposure capability makes DCI attractive in both cold-atom imaging and x-ray imaging applications where exposure of the sample to the illuminating radiation must be minimised.

## 6.2 Diffraction-contrast imaging of cold atoms

The second half of this thesis demonstrated diffraction-contrast imaging of a cloud of laser-cooled atoms. We saw that DCI made three core assumptions: weak absorption, slowly-varying phase and a monomorphous object. All three are satisfied by imaging the atom cloud off-resonance. Imaging off resonance also achieves optimal resolution and minimises the heating of a dense cloud.

An early series of experiments studied diffraction-contrast imaging of a MOT at small defocus distances. Quantitative comparison with absorption imaging suggested that DCI is less sensitive than absorption imaging to focusing errors. Residual scatter in the data was indistinguishable from the shot-to-shot fluctuation level.

A more recent series of experiments demonstrated diffraction-contrast imaging without a reimaging lens. Holographic diffraction patterns measured by the camera appeared as concentric fringes, bearing no resemblance to the MOT as viewed by fluorescence or absorption imaging. Detailed column-density images of the MOT were retrieved from these patterns. Further experiments showed that the diffraction pattern, and hence the retrieved image, could be magnified simply by point projection, for example using a bare optical fibre as the illumination source.

Other imaging techniques, holographic and focal, have previously been used to image transparent clouds of cold atoms. Diffraction-contrast imaging will always be the simplest optical technique, requiring only a point source of light and a detector to be placed on opposite sides of the cold atom object. The signal-to-noise performance of DCI is likely, in practise, to be similar to that of Zernike phase-contrast. Unlike Zernike phase-contrast, DCI offers holographic depth-of-field, obviating the need to focus an imaging system on the atom cloud. The lack of optical ‘variables’, including the removal of focusing, makes DCI an *accurate* technique for measurement of column densities.

### 6.3 Future work on diffraction-contrast imaging

In concluding, I make a few comments on possible extensions of the DCI algorithm. I consider only direct enhancements or alternatives to DCI: techniques capable of retrieving object information from a *single diffracted image*, without the necessary involvement of optics.

The major impediment to shot-noise limited imaging of cold atoms is the spatially coherent noise, or fringe noise, discussed in §5.7.2. The monomorphous CTF inverse-filter tends to amplify a few coherent noise components which are inevitably found near zeros in the transfer function. A particularly unfortunate alignment of noise and zeros can substantially degrade a diffraction-contrast retrieval. Fringe noise plagues all types of cold atom imaging, although the DCI algorithm is particularly sensitive to it. Sensitivity might be reduced by judicious modification of the inverse filter to correct only for the CTF sign above a threshold frequency. More generally, the noise should be decorrelated in the wavelet basis and might be substantially reduced by feeding an atom-free flatfield image to the noise estimator of the wavelet-Wiener filter. It seems very plausible that the *phase* of noise fringes evolves more rapidly than the amplitude and such coherent filtering is likely to be beneficial.

Possible extensions of DCI employing more exotic multiscale representations, such as curvelets, were considered in §3.7.5. It is notable that the most dramatic denoising results published were from hybrid wavelet-curvelet methods that *iterated* between wavelet and curvelet frames.

There is also no question that the iterative CTF deconvolution proposed by Gureyev (see §3.3.3) yields lower-noise images in simulations than a single step deconvolution. Although approaching from very different mathematical angles, these inverse problem solutions seem to be converging on an iterative solution which starts with the monomorphous object approximation. Incorporating constraints such as requiring positive column-density and finite support is effortless in an iterative solution. It seems likely that future algorithms will use some form of iterative refinement of an initial deconvolution retrieval.

Iterative solutions may also be of use in pushing the resolution limit of diffraction-contrast methods; there is no reason not to use the angular spectrum for forward- and back-propagation and so resolution may be pushed as far sub-wavelength as the detector aperture and SNR allow.

X-ray results have not been discussed in this thesis. The assumption of full optical coherence was eminently justified for the laser illumination used in cold atom imaging. Nevertheless, a partially-coherent extension of DCI follows quite naturally from the Guigay ansatz, and was given by Guigay as early as 1971 [437]. Spatial and temporal coherence modulation of the CTFs were considered in some detail by electron microscopists in the 1970s. Further work on x-ray DCI should investigate the estimation and deconvolution of coherence effects in the linear model. Such analyses would be particularly germane to diffraction patterns produced by point-projection microscopes based on laboratory (microfocus) x-ray sources.

## 6.4 Future work on cold-atom imaging

The obvious next step for DCI of cold atoms is to demonstrate non-destructive imaging of BEC. A quantitative comparison with Zernike phase-contrast would, hopefully, verify claims made here about the greater quantitativity of DCI. On a practical level, I intend to make an interactive version of the retrieval code available as bytecode for the IDL virtual machine. This will enable researchers to use the algorithm without requiring an IDL license. The code is available at  
<http://eprints.unimelb.edu.au/archive/00000835/>

Although I have presented results of holographic ‘focusing’ on a single object, the depth-of-field property of DCI would be better illustrated by focusing separately on two objects where one is defocused. Simulations of this process will be presented in a forthcoming paper [379].

An intriguing extension of the depth-of-field concept arises if imaging atoms trapped above a microstructured surface [435]. An imaging system focused on the atom cloud also sees the *reflection* of the atom cloud in the surface, which is usually polished to a mirror finish. The optical distance from the reflection to the detector is longer, however, and the reflection is typically out of focus. Diffraction-contrast imaging would be capable of focusing on either atom cloud. There seems little point in having two images of the same cloud, until one realises that the reflection is viewed along a different propagation axis. If the angle of incidence between the illumination and the chip is 45° then the reflection is viewed *orthogonally* to the direct image. Two orthogonal views may be sufficient to locate simple structures in the atom cloud in 3-dimensions. Additional or segmented mirrors raise the possibility of tomographic reconstruction from a single diffraction pattern.

Finally, the prospects seem bright for technical improvements to DCI apparatus. While lens designs have changed little in recent decades, detector technology and computer power continue to increase and the advantages of holographic imaging should grow in parallel. Ever larger CCDs are being designed with smaller pixels and faster readouts. Wavelength resolution imaging appears to be a realistic prospect. Perhaps a future generation of atom chip experiments will include integrated CCDs on the substrate, with optical fibres providing point-projection illumination. Diffraction contrast imaging would remove the need to integrate bulk optics into microstructured cold atom devices.



I HOPE THAT DCI will be lead to the wider use of phase imaging in cold-atom research. The technique works with the absorption imaging systems already in use in most cold atom laboratories, converting them to potentially non-destructive imaging systems by moving (or removing) a lens. It would most satisfying if this work contributed to the unveiling of new dynamic processes in this fascinating state of matter.



# References

Digital object identifiers (*DOIs*) are given where available. Back-references are given to the pages on which each entry was cited. The page numbers are hyperlinked in brackets at the end of the entry.

- 1 E. Raab, M. Prentiss, A. Cable, S. Chu and D. E. Pritchard. *Trapping of neutral sodium atoms with radiation pressure*. Physical Review Letters **59**(23) 2631–2634 (1987). DOI [10.1103/PhysRevLett.59.2631](https://doi.org/10.1103/PhysRevLett.59.2631). [pp 1 and 138]
- 2 K. B. Davis, M.-O. Mewes, M. R. Andrews, N. J. van Druten, D. S. Durfee, D. M. Kurn and W. Ketterle. *Bose-Einstein condensation in a gas of sodium atoms*. Physical Review Letters **75**(22) 3969–3973 (1995). DOI [10.1103/PhysRevLett.75.3969](https://doi.org/10.1103/PhysRevLett.75.3969). [p 1]
- 3 M. H. Anderson, J. R. Ensher, M. R. Matthews, C. E. Wieman and E. A. Cornell. *Observation of Bose-Einstein condensation in a dilute atomic vapor*. Science **269**(5221) 198–201 (1995). [p 1]
- 4 C. C. Bradley, C. A. Sackett, J. J. Tollett and R. G. Hulet. *Evidence of Bose-Einstein condensation in an atomic gas with attractive interactions*. Physical Review Letters **75**(9) 1687–1690 (1995). DOI [10.1103/PhysRevLett.75.1687](https://doi.org/10.1103/PhysRevLett.75.1687). [p 1]
- 5 I. H. Deutsch and G. K. Brennen. *Quantum computing with neutral atoms in an optical lattice*. Fortschritte der Physik **48**(9–11) 925–943 (2000). DOI [10.1002/1521-3978\(200009\)48:9/11<925::AID-PROP925>3.0.CO;2-A](https://doi.org/10.1002/1521-3978(200009)48:9/11<925::AID-PROP925>3.0.CO;2-A). [p 2]
- 6 I. Newton. *Opticks, or, A Treatise of the Reflections, Refractions, Inflections & Colours of Light (based on the Fourth Edition, London, 1730)*. Dover, New York (1952). [p 3]
- 7 C. W. Groetsch. *Inverse Problems in the Mathematical Sciences*. Vieweg, Braunschweig, Germany (1993). ISBN 3528065451. [p 4]
- 8 W. H. F. Talbot. *Facts relating to optical science. No. IV*. Philosophical Magazine (3rd Ser.) **9** 401–407 (1836). [p 5]
- 9 A. G. Peele and K. A. Nugent (eds.). *Proceedings of the Second International Workshop on Non-crystallographic Phase Retrieval*. Cairns QLD, Australia (2003). URL <http://optics.ph.unimelb.edu.au/cairnso3/cairnso3/proceedings.htm>. [pp 18, 72, 259 and 268]
- 10 T. E. Gureyev. *Composite techniques for phase retrieval and visualization in the near-Fresnel region*. In Peele and Nugent [9]. URL <http://optics.ph.unimelb.edu.au/cairnso3/cairnso3/proceedings.htm>. [pp 18 and 89]

- 11 J. D. Jackson. *Classical Electrodynamics*. John Wiley & Sons, New York, 3rd edn. (1995). ISBN 047143132X. [pp 23 and 321]
- 12 J. W. Strohben. *Line-of-sight wave propagation through the turbulent atmosphere*. Proceedings of the IEEE **56**(8) 1301–1318 (1968). [p 23]
- 13 L. Mandel and E. Wolf. *Optical Coherence and Quantum Optics*. Cambridge University Press, Cambridge, UK (1995). ISBN 0521417112. [pp 24, 34, 35, 38, 45, 46, 86 and 302]
- 14 H. S. Green and E. Wolf. *A scalar representation of the electromagnetic fields*. Proceedings of the Physical Society of London A **66**(12) 1129–1137 (1953). [p 24]
- 15 A. S. Marathay and G. B. Parrent. *Use of scalar theory in optics*. Journal of the Optical Society of America **60**(2) 243–245 (1970). URL <http://www.opticsinfobase.org/abstract.cfm?id=53946>. [p 24]
- 16 A. S. Marathay. *Elements of Optical Coherence Theory*. John Wiley & Sons, New York (1982). ISBN 0471567892. [pp 24 and 301]
- 17 B. E. A. Saleh and M. C. Teich. *Fundamentals of Photonics*. John Wiley & Sons, New York (1991). ISBN 0471839655. [pp 25, 33, 35 and 225]
- 18 V. M. Babic and V. S. Buldyrev. *Short-Wavelength Diffraction Theory: Asymptotic Methods*. Springer-Verlag, Berlin (1991). ISBN 3540191895/0387191895. Translation of *Asimptoticheskie methody v zadachakh difraktsii korotkikh voln*, Nauka, Moscow (1972). [p 26]
- 19 M. Born and E. Wolf. *Principles of Optics*. Cambridge University Press, Cambridge, UK, 7th (expanded) edn. (1999). ISBN 0521642221. [pp 27, 28, 30, 32, 34, 241, 301 and 305]
- 20 Y. A. Kravtsov, G. W. Forbes and A. A. Asatryan. *Theory and application of complex rays*. Progress in Optics **39** 1–61 (1999). [p 28]
- 21 M. Nieto-Vesperinas. *Scattering and Diffraction in Physical Optics*. John Wiley & Sons, New York (1991). ISBN 0471615293. [pp 32 and 301]
- 22 T. J. Davis. *A unified treatment of small-angle x-ray scattering, x-ray refraction and absorption using the Rytov approximation*. Acta Crystallographica A **50** 686–690 (1994). DOI [10.1107/S0108767394003478](https://doi.org/10.1107/S0108767394003478). [p 32]
- 23 J. W. Goodman. *Introduction to Fourier Optics*. McGraw-Hill, Boston, 2nd edn. (1996). ISBN 0070242542. [pp 33, 35, 37, 39, 41, 62, 70, 80, 102, 232, 305 and 306]
- 24 E. W. Weisstein. *Fourier transform*. Web document, Mathworld (2003). URL <http://mathworld.wolfram.com/FourierTransform.html>. [pp 33 and 85]
- 25 E. W. Weisstein. *L<sub>2</sub>-norm*. Web document, Mathworld (2003). URL <http://mathworld.wolfram.com/L2-Norm.html>. [p 34]
- 26 É. Lalor. *Conditions for the validity of the angular spectrum of plane waves*. Journal of the Optical Society of America **58**(9) 1235–1237 (1968). URL <http://www.opticsinfobase.org/abstract.cfm?id=75245>. [pp 35, 36 and 38]

- 27 H. M. Ozaktas and M. A. Kutay. *Wigner distributions, Linear Canonical Transforms and Phase-space Optics*. Tech. Rep. BU-CE-0006, Bilkent University, Department of Computer Engineering, TR-06533 Bilkent, Ankara, Turkey (2000). Sections published in Reference 438., URL <http://www.cs.bilkent.edu.tr/tech-reports/2000/BU-CE-0006.ps.gz>. [pp 37, 62 and 63]
- 28 R. N. Bracewell. *The Fourier Transform and its Applications*. McGraw Hill, Boston, 3rd edn. (2000). ISBN 0073039381. [pp 37, 41, 49, 51 and 85]
- 29 H. Weyl. *Ausbreitung elektromagnetischer wellen ueber einem ebenen leiter [Propagation of electromagnetic waves above a conducting plane]*. Annalen der Physik (Leipzig) Ser. 4 **60** 481–500 (1919). [p 38]
- 30 A. S. Marathay. *Fourier transform of the Green's function for the Helmholtz equation*. Journal of the Optical Society of America **65**(8) 964–965 (1975). [p 38]
- 31 G. C. Sherman. *Application of the convolution theorem to Rayleigh's integral formulas*. Journal of the Optical Society of America **57**(4) 546–547 (1967). [p 38]
- 32 L. Onural. *Diffraction from a wavelet point of view*. Optics Letters **18**(11) 846–848 (1993). URL <http://www.opticsinfobase.org/abstract.cfm?id=11723>. [p 38]
- 33 D. Mas, J. Garcia, C. Ferreira, L. M. Bernardo and F. Marinho. *Fast algorithms for free-space diffraction patterns calculation*. Optics Communications **164** 233–245 (1999). DOI [10.1016/S0030-4018\(99\)00201-1](https://doi.org/10.1016/S0030-4018(99)00201-1). [p 39]
- 34 J. D. Gaskill. *Linear systems, Fourier transforms and Optics*. John Wiley & Sons, New York (1978). ISBN 0471292885. [p 39]
- 35 V. N. Mahajan. *Aberrations of diffracted wave fields. I. Optical imaging*. Journal of the Optical Society of America A **17**(12) 2216–2222 (2000). URL <http://www.opticsinfobase.org/abstract.cfm?id=61937>. [p 40]
- 36 V. N. Mahajan. *Aberrations of diffracted wave fields. II. Diffraction gratings*. Journal of the Optical Society of America A **17**(12) 2223–2228 (2000). URL <http://www.opticsinfobase.org/abstract.cfm?id=61938>. [p 40]
- 37 F. D. Feiock. *Wave propagation in optical systems with large apertures*. Journal of the Optical Society of America **68**(4) 485–489 (1978). URL <http://www.opticsinfobase.org/abstract.cfm?id=56951>. [p 42]
- 38 W. H. Southwell. *Validity of the Fresnel approximation in the near field*. Journal of the Optical Society of America **71**(1) 7–14 (1981). URL <http://www.opticsinfobase.org/abstract.cfm?id=57921>. [p 42]
- 39 G. W. Forbes. *Validity of the Fresnel approximation in the diffraction of collimated beams*. Journal of the Optical Society of America A **13**(9) 1816–1826 (1996). URL <http://www.opticsinfobase.org/abstract.cfm?id=18827>. [p 42]
- 40 J. M. Cowley. *Diffraction Physics*. Elsevier Science, Amsterdam, 3rd rev edn. (1995). ISBN 0444822186. [p 44]
- 41 A. Papoulis. *Systems and Transforms with Applications in Optics*. McGraw-Hill, New York (1968). [p 44]

- 42 A. Papoulis. *Fresnel transforms with applications in diffraction theory*. In J. Fox (ed.), *Proceedings of the Symposium on Modern Optics*. Polytechnic Press, Interscience Publishers, Polytechnic Institute of Brooklyn, New York (1967), pp. 453–466. [p 44]
- 43 A. Pogany, D. Gao and S. W. Wilkins. *Contrast and resolution in imaging with a microfocus X-ray source*. Review of Scientific Instruments **68**(7) 2774–2782 (1997). DOI [10.1063/1.1148194](https://doi.org/10.1063/1.1148194). [p 44]
- 44 M. A. Alonso, A. A. Asatryan and G. W. Forbes. *Beyond the Fresnel approximation for focused waves*. Journal of the Optical Society of America A **16**(8) 1958–1969 (1999). URL <http://www.opticsinfobase.org/abstract.cfm?id=1243>. [p 45]
- 45 J.-P. Guigay. *Fourier transform analysis of Fresnel diffraction patterns and in-line holograms*. Optik **49**(1) 121–125 (1977). [p 48]
- 46 J.-P. Guigay. *Analyse spectrale (fréquences spatiales) d'une figure de diffraction de Fresnel [Spatial frequency spectral analysis of Fresnel diffraction patterns]*. Comptes Rendus hebdomadaires des séances de l'Académie des Sciences (Paris) B: Sciences Physiques **284** 193–196 (1977). In French. [p 49]
- 47 J.-P. Guigay. *The ambiguity function in diffraction and isoplanatic imaging by partially coherent beams*. Optics Communications **26**(2) 136–138 (1978). DOI [10.1016/0030-4018\(78\)90037-8](https://doi.org/10.1016/0030-4018(78)90037-8). [p 49]
- 48 A. Papoulis. *Ambiguity function in Fourier optics*. Journal of the Optical Society of America **64**(6) 779–788 (1974). URL <http://www.opticsinfobase.org/abstract.cfm?id=55331>. [p 49]
- 49 S. Mallat. *A Wavelet Tour of Signal Processing*. Academic Press, San Diego, 2nd edn. (1999). ISBN 012466606X. First chapter is available online, URL <http://www.cs.nyu.edu/cs/faculty/mallat/book.html>. [pp 49, 98, 115, 126, 307, 309, 310, 311, 312, 314, 315, 316, 317, 318 and 319]
- 50 S. C. Mayo, P. R. Miller, S. W. Wilkins, T. J. Davis, D. Gao, T. E. Gureyev, D. Paganin, D. J. Parry, A. Pogany and A. W. Stevenson. *Quantitative X-ray projection microscopy: phase-contrast and multi-spectral imaging in SEM*. Journal of Microscopy **207** 79–96 (2002). DOI [10.1046/j.1365-2818.2002.01046.x](https://doi.org/10.1046/j.1365-2818.2002.01046.x). [pp 52 and 86]
- 51 E. Menzel. *Die darstellung verschiedener phasenkontrast-verfahren in der optischen übertragungstheorie [A discussion of various phase-contrast techniques in the optical transfer theory]*. Optik **15**(8) 460–470 (1958). In German. [p 53]
- 52 M. Lentzen, B. Jähnen, C. L. Jia, A. Thust, K. Tillmann and K. Urban. *High-resolution imaging with an aberration-corrected transmission electron microscope*. Ultramicroscopy **92**(3–4) 233–242 (2002). DOI [10.1016/S0304-3991\(02\)00139-0](https://doi.org/10.1016/S0304-3991(02)00139-0). [p 53]
- 53 O. Scherzer. *The theoretical resolution limit of the electron microscope*. Journal of Applied Physics **20**(1) 20–29 (1948). DOI [10.1063/1.1698233](https://doi.org/10.1063/1.1698233). [p 53]
- 54 K.-J. Hanssen and B. Morgenstern. *Die phasenkontrast- und amplitudenkontrast-übertragung des elektronenmikroskopischen objektivs [The phase-contrast and amplitude-contrast transfer of electron microscope objectives]*. Zeitschrift für angewandte Physik **29**(3) 215–227 (1965). In German. [p 53]

- 55 H. P. Erickson. *The Fourier transform of an electron micrograph – first order and second order theory of image formation*. Advances in Optical and Electron Microscopy **5** 163–199 (1971). [p 53]
- 56 F. Thon. *Zur defokussierungsabhängigkeit des phasenkontrastes bei der elektronenmikroskopischen abbildung [On the defocusing-dependance of phase-contrast in electron microscope imaging]*. Zeitschrift für Naturforschung **21A** 476–478 (1966). [pp 53 and 82]
- 57 M. V. Berry and S. Klein. *Integer, fractional and fractal Talbot effects*. Journal of Modern Optics **43**(10) 2139–2164 (1996). DOI [10.1080/095003496154761](https://doi.org/10.1080/095003496154761). [p 61]
- 58 J. M. Cowley and A. F. Moodie. *Fourier images IV: The phase grating*. Proceedings of the Physical Society of London B **76**(3) 378–384 (1960). [p 61]
- 59 A. Reichelt, E. Storck and U. Wolff. *Near field diffraction pattern behind a sinusoidal phase grating*. Optics Communications **3**(3) 169–172 (1971). DOI [10.1016/0030-4018\(71\)90172-6](https://doi.org/10.1016/0030-4018(71)90172-6). [p 61]
- 60 W. Singer and H. J. Tiziani. *Born approximation for the nonparaxial scalar treatment of thick phase gratings*. Applied Optics **37**(7) 1249–1255 (1998). URL <http://www.opticsinfobase.org/abstract.cfm?id=43639>. [p 61]
- 61 M. R. Teague. *Deterministic phase retrieval: a Green's function solution*. Journal of the Optical Society of America **73**(11) 1434–1441 (1983). URL <http://www.opticsinfobase.org/abstract.cfm?id=58918>. [p 62]
- 62 F. Gori. *Why is the Fresnel transform so little known?* In J. C. Dainty (ed.), *Current Trends in Optics*, Academic Press, London, pp. 139–148 (1994). ISBN 0122007204. [p 62]
- 63 A. VanderLugt. *Operational notation for the analysis and synthesis of optical data processing systems*. Proceedings of the IEEE **54**(8) 1055–1064 (1966). [p 62]
- 64 M. Nazarathy and J. Shamir. *Fourier optics described by operator algebra*. Journal of the Optical Society of America **70**(2) 150–159 (1980). URL <http://www.opticsinfobase.org/abstract.cfm?id=57427>. [p 62]
- 65 H. Bacry and M. Cadilhac. *Metaplectic group and Fourier optics*. Physical Review A **23**(5) 2533–2536 (1981). DOI [10.1103/PhysRevA.23.2533](https://doi.org/10.1103/PhysRevA.23.2533). [p 62]
- 66 R. Simon and N. Mukunda. *Optical phase space, Wigner representation, and invariant quality parameters*. Journal of the Optical Society of America A **17**(12) 2440–2463 (2000). URL <http://www.opticsinfobase.org/abstract.cfm?id=61959>. [p 62]
- 67 D. Dragoman. *The Wigner distribution function in optics and optoelectronics*. Progress in Optics **37** 1–56 (1997). [p 63]
- 68 K. B. Wolf, M. A. Alonso and G. W. Forbes. *Wigner functions for Helmholtz wave fields*. Journal of the Optical Society of America A **16**(10) 2476–2487 (1999). URL <http://www.opticsinfobase.org/abstract.cfm?id=1301>. [p 63]
- 69 J. B. Almeida and V. Lakshminarayanan. *Wide angle near-field diffraction and Wigner distribution*. Optik **114**(7) 333–335 (2003). DOI [10.1087/0030-4026-00272](https://doi.org/10.1087/0030-4026-00272). URL <http://arxiv.org/abs/physics/0305026>. [p 63]

- 70 D. Gabor. *A new microscopic principle*. Nature (London) **161**(4098) 777–778 (1948). URL <http://www.nature.com/physics/lookingback/gabor/gabor.pdf>. [p 66]
- 71 U. Schnars and W. P. O. Juptner. *Digital recording and numerical reconstruction of holograms*. Measurement Science & Technology **13**(9) R85–R101 (2002). DOI [10.1088/0957-0233/13/9/201](https://doi.org/10.1088/0957-0233/13/9/201). [p 67]
- 72 A. W. Lohmann. *Optische einseitenbandübertragung angewandt auf das Gabor-mikroskop [Optical single-sideband application of the Gabor microscope]*. Optica Acta **3**(2) 97–99 (1956). In German. [pp 67 and 69]
- 73 D. Gabor and W. P. Goss. *Interference microscope with total wavefront reconstruction*. Journal of the Optical Society of America **56**(7) 849–858 (1966). URL <http://www.opticsinfobase.org/abstract.cfm?id=53063>. [pp 67 and 70]
- 74 W. L. Bragg and G. L. Rogers. *Elimination of the unwanted image in diffraction microscopy*. Nature (London) **167**(4240) 190–191 (1951). [pp 67 and 70]
- 75 E. N. Leith and J. Upatnieks. *Wavefront reconstruction with diffused illumination and three-dimensional objects*. Journal of the Optical Society of America **54**(11) 1295–1301 (1965). URL <http://www.opticsinfobase.org/abstract.cfm?id=52505>. [p 67]
- 76 C. S. Vikram. *Particle Field Holography*. Cambridge University Press, Cambridge, UK (1992). ISBN 0521411270. [p 69]
- 77 H.-J. Vossing, S. Borrmann and R. Jaenicke. *In-line holography of cloud volumes applied to the measurement of raindrops and snowflakes*. Atmospheric Research **49**(3) 199–212 (1998). DOI [10.1016/S0169-8095\(98\)00082-9](https://doi.org/10.1016/S0169-8095(98)00082-9). [p 69]
- 78 E. Malkiel, O. Alquaddomi and J. Katz. *Measurements of plankton distribution in the ocean using submersible holography*. Measurement Science & Technology **10**(12) 1142–1152 (1999). DOI [10.1088/0957-0233/10/12/305](https://doi.org/10.1088/0957-0233/10/12/305). [p 69]
- 79 O. Bryngdahl and A. W. Lohmann. *Single-sideband holography*. Journal of the Optical Society of America **58**(5) 620–624 (1968). URL <http://www.opticsinfobase.org/abstract.cfm?id=53377>. [p 69]
- 80 E. N. Leith and J. Upatnieks. *Reconstructed wavefronts and communication theory*. Journal of the Optical Society of America **52**(10) 1123–1130 (1962). URL <http://www.opticsinfobase.org/abstract.cfm?id=75894>. [p 69]
- 81 T. Mishina, F. Okano and I. Yuyama. *Time-alternating method based on single-sideband holography with half-zone-plate processing for the enlargement of viewing zones*. Applied Optics **38**(17) 3703–3713 (1999). URL <http://www.opticsinfobase.org/abstract.cfm?id=43925>. [p 69]
- 82 G. Pedrini, P. Froning, H. Fessler and H. J. Tiziani. *In-line digital holographic interferometry*. Applied Optics **37**(26) 6262–6269 (1998). URL <http://www.opticsinfobase.org/abstract.cfm?id=43288>. [p 70]
- 83 Songcan Lai, B. King and M. A. Neifeld. *Wave front reconstruction by means of phase-shifting digital in-line holography*. Optics Communications **173**(1-6) 155–160 (2000). DOI [10.1016/S0030-4018\(99\)00625-2](https://doi.org/10.1016/S0030-4018(99)00625-2). [p 70]

- 84 G. L. Rogers. *Experiments in diffraction microscopy*. Proceedings of the Royal Society of Edinburgh Section A (Mathematical and Physical Sciences) **63** 193–221 (1952). [p 70]
- 85 G. L. Rogers. *Two hologram methods in diffraction microscopy*. Proceedings of the Royal Society of Edinburgh Section A (Mathematical and Physical Sciences) **64**(II) 209–221 (1956). [p 70]
- 86 G. L. Rogers. *In-line soft-X-ray holography: the unwanted image*. Optics Letters **19**(1) 67 (1994). URL <http://www.opticsinfobase.org/abstract.cfm?id=12117>. [p 70]
- 87 Tiqiao Xiao, Hongjie Xu, Yingji Zhang, Jianwen Chen and Zhizhan Xu. *Digital image decoding for in-line X-ray holography using two holograms*. Journal of Modern Optics **45**(2) 343–353 (1998). DOI [10.1080/095003498152013](https://doi.org/10.1080/095003498152013). [p 70]
- 88 Y. Zhang and X. Zhang. *Reconstruction of a complex object from two in-line holograms*. Optics Express **11**(6) 572–578 (2003). URL <http://www.opticsinfobase.org/abstract.cfm?id=71671>. [p 70]
- 89 P. Schiske. *Focal series reconstruction*. In P. W. Hawkes (ed.), *Image Processing and Computer Aided Design in Electron Optics*, Academic Press, London, pp. 82–90 (1973). ISBN 0123333652. [p 70]
- 90 M. H. Maleki and A. J. Devaney. *Noniterative reconstruction of complex-valued objects from two intensity measurements*. Optical Engineering **33**(10) 3243–3253 (1994). [p 70]
- 91 N. Demoli, J. Mestrovic and I. Sovic. *Subtraction digital holography*. Applied Optics **42**(5) 798–804 (2003). URL <http://www.opticsinfobase.org/abstract.cfm?id=71197>. [p 70]
- 92 L. Onural and M. Kocatepe. *Family of scaling chirp functions, diffraction, and holography*. IEEE Transactions on Signal Processing **43**(7) 1568–1578 (1995). DOI [10.1109/78.398718](https://doi.org/10.1109/78.398718). [p 70]
- 93 David Paganin. *Studies in Phase Retrieval*. Ph.D. thesis, University of Melbourne, School of Physics, Victoria 3010, Australia (1999). [pp 71 and 79]
- 94 D. Paganin and K. A. Nugent. *Noninterferometric phase imaging with partially coherent light*. Physical Review Letters **80**(12) 2586–2589 (1998). DOI [10.1103/PhysRevLett.80.2586](https://doi.org/10.1103/PhysRevLett.80.2586). [p 71]
- 95 V. V. Volkov, Y. Zhua and M. D. Graef. *A new symmetrized solution for phase retrieval using the transport-of-intensity equation*. Micron **33**(5) 411–416 (2002). DOI [10.1016/S0968-4328\(02\)00017-3](https://doi.org/10.1016/S0968-4328(02)00017-3). [p 71]
- 96 D. Paganin and K. A. Nugent. *Phase measurement of waves that obey nonlinear equations*. Optics Letters **27**(8) 622–624 (2002). URL <http://www.opticsinfobase.org/abstract.cfm?id=68550>. [p 71]
- 97 M. Fernández-Guasti, J. L. Jiménez, F. Granados-Agustín and A. Cornejo-Rodríguez. *Amplitude and phase representation of monochromatic fields in physical optics*. Journal of the Optical Society of America A **20**(8) 1629–1634 (2003). URL <http://www.opticsinfobase.org/abstract.cfm?id=73747>. [p 71]

- 98 S. Bajt, A. Barty, K. A. Nugent, M. McCartney, M. Wall and D. Paganin. *Quantitative phase-sensitive imaging in a transmission electron microscope*. Ultramicroscopy **83**(1-2) 67–73 (2000). DOI [10.1016/S0304-3991\(99\)00174-6](https://doi.org/10.1016/S0304-3991(99)00174-6). [p 71]
- 99 B. E. Allman, P. J. McMahon, J. B. Tiller, K. A. Nugent, D. Paganin, A. Barty, I. McNulty, S. P. Frigo, Yuxin Wang and C. C. Retsch. *Noninterferometric quantitative phase imaging with soft X-rays*. Journal of the Optical Society of America A **17**(10) 1732–1743 (2000). URL <http://www.opticsinfobase.org/abstract.cfm?id=64562>. [p 71]
- 100 P. J. McMahon, B. E. Allman, K. A. Nugent, D. L. Jacobson, M. Arif and S. A. Werner. *Contrast mechanisms for neutron radiography*. Applied Physics Letters **78**(7) 1011–1013 (2001). DOI [10.1063/1.1347387](https://doi.org/10.1063/1.1347387). [p 71]
- 101 P. J. Fox, T. R. Mackin, L. D. Turner, I. Colton, K. A. Nugent and R. E. Scholten. *Noninterferometric phase imaging of a neutral atomic beam*. Journal of the Optical Society of America B **19**(8) 1773–1776 (2002). This paper is included as Appendix F, beginning on p 323., URL <http://www.opticsinfobase.org/abstract.cfm?id=69569>. [p 71]
- 102 K. A. Nugent and D. Paganin. *Matter-wave phase measurement: A noninterferometric approach*. Physical Review A **61**(6) 063614 (2000). DOI [10.1103/PhysRevA.61.063614](https://doi.org/10.1103/PhysRevA.61.063614). [p 71]
- 103 Phillip John Fox. *Non-interferometric Phase Imaging using Neutral Atoms*. Ph.D. thesis, University of Melbourne, School of Physics, Victoria 3010, Australia (2001). [pp 71, 150, 151 and 158]
- 104 A. Barty, K. A. Nugent, D. Paganin and A. Roberts. *Quantitative optical phase microscopy*. Optics Letters **23**(11) 817–819 (1998). URL <http://www.opticsinfobase.org/abstract.cfm?id=36754>. [p 72]
- 105 R. W. Gerchberg and W. O. Saxton. *A practical algorithm for the determination of phase from image and diffraction plane pictures*. Optik **35**(2) 237–246 (1972). [p 72]
- 106 U. Weierstall, Q. Chen, J. C. H. Spence, M. R. Howells, M. Isaacson and R. R. Panepucci. *Image reconstruction from electron and X-ray diffraction patterns using iterative algorithms: experiment and simulation*. Ultramicroscopy **90**(2-3) 171–195 (2002). DOI [10.1016/S0304-3991\(01\)00134-6](https://doi.org/10.1016/S0304-3991(01)00134-6). [p 72]
- 107 R. Barakat and G. Newsam. *Necessary conditions for a unique solution to two-dimensional phase recovery*. Journal of Mathematical Physics **25**(11) 3190–3193 (1984). DOI [10.1063/1.526089](https://doi.org/10.1063/1.526089). [p 72]
- 108 Jianwei Miao, P. Charalambous, J. Kirz and D. Sayre. *Extending the methodology of X-ray crystallography to allow imaging of micrometre-sized non-crystalline specimens*. Nature (London) **400**(6742) 342–344 (1999). DOI [10.1038/22498](https://doi.org/10.1038/22498). [p 72]
- 109 D. L. Misell. *A method for the solution of the phase problem in electron microscopy*. Journal of Physics D **6**(1) L6–L9 (1973). DOI [10.1088/0022-3727/6/1/102](https://doi.org/10.1088/0022-3727/6/1/102). [p 72]
- 110 D. L. Misell. *An examination of an iterative method for the solution of the phase problem in optics and electron optics. I. Test calculations*. Journal of Physics D **6**(18) 2200–2216 (1973). DOI [10.1088/0022-3727/6/18/305](https://doi.org/10.1088/0022-3727/6/18/305). [p 72]

- 111 R. H. Boucher. *Convergence of algorithms for phase retrieval from two intensity distributions*. In *Proceedings of the SPIE International Optical Computing Conference*. SPIE, Washington DC (1980), vol. 231, pp. 130–141. [p 72]
- 112 R. Rolleston and N. George. *Image reconstruction from partial Fresnel zone information*. Applied Optics **25**(2) 178–183 (1986).  
URL <http://www.opticsinfobase.org/abstract.cfm?id=29027>. [p 73]
- 113 G. Liu and P. D. Scott. *Phase retrieval and twin-image elimination for in-line Fresnel holograms*. Journal of the Optical Society of America A **4**(1) 159–165 (1987).  
URL <http://www.opticsinfobase.org/abstract.cfm?id=2619>. [pp 73 and 75]
- 114 G. Koren, D. Joyeux and F. Polack. *Twin-image elimination in in-line holography of finite-support complex object*. Optics Letters **16**(24) 1979–1981 (1991).  
URL <http://www.opticsinfobase.org/abstract.cfm?id=59848>. [p 73]
- 115 Wen-Xiang Cong, Nan-Xian Chen and Ben-Yuan Gu. *Phase retrieval in the Fresnel transform system: a recursive algorithm*. Journal of the Optical Society of America A **16**(7) 1827–1830 (1999). URL <http://www.opticsinfobase.org/abstract.cfm?id=1230>. [p 73]
- 116 G. Koren, F. Polack and D. Joyeux. *Iterative algorithms for twin-image elimination in in-line holography using finite-support constraints*. Journal of the Optical Society of America A **10**(3) 423–433 (1993). URL <http://www.opticsinfobase.org/abstract.cfm?id=59112>. [p 73]
- 117 M. H. Maleki and A. J. Devaney. *Phase-retrieval and intensity-only reconstruction algorithms for optical diffraction tomography*. Journal of the Optical Society of America A **10**(5) 1086–1092 (1993). URL <http://www.opticsinfobase.org/abstract.cfm?id=4618>. [p 73]
- 118 R. Vincent. *Phase retrieval in TEM using Fresnel images*. Ultramicroscopy **90**(2-3) 135–151 (2002). DOI [10.1016/S0304-3991\(01\)00135-8](https://doi.org/10.1016/S0304-3991(01)00135-8). [pp 73 and 76]
- 119 R. Vincent. *A comparative study of iterative and conjugate gradient methods for phase retrieval from Fresnel images*. In M. R. Howells, L. D. Marks, J. Miao and J. Spence (eds.), *Proceedings of the Workshop on New Approaches to the Phase Problem for Non-Periodic Objects*. Lawrence Berkeley National Laboratory, CA, USA (2001).  
URL <http://www-esg.lbl.gov/esg/meetings/phasing/viewgraphs/VincentPoster.pdf>. [p 73]
- 120 T. E. Gureyev. *Composite techniques for phase retrieval in the Fresnel region*. Optics Communications **220**(1-3) 49–58 (2003). DOI [10.1016/S0030-4018\(03\)01353-1](https://doi.org/10.1016/S0030-4018(03)01353-1). [pp 73 and 76]
- 121 H. H. Bauschke, P. L. Combettes and D. R. Luke. *Phase retrieval, error reduction algorithm, and Fienup variants: a view from convex optimization*. Journal of the Optical Society of America A **19**(7) 1334–1345 (2002).  
URL <http://www.opticsinfobase.org/abstract.cfm?id=69199>. [p 73]
- 122 H. H. Bauschke, P. L. Combettes and D. R. Luke. *Hybrid projection-reflection method for phase retrieval*. Journal of the Optical Society of America A **20**(6) 1025–1034 (2003).  
URL <http://www.opticsinfobase.org/abstract.cfm?id=72624>. [p 73]
- 123 R. W. Gerchberg and W. O. Saxton. *Comment on A method for the solution of the phase problem in electron microscopy*. Journal of Physics D **6**(5) L31–L32 (1973).  
DOI [10.1088/0022-3727/6/5/101](https://doi.org/10.1088/0022-3727/6/5/101). [p 73]

- 124 L. Onural and P. D. Scott. *Digital decoding of in-line holograms*. Optical Engineering **26**(11) 1124–1132 (1987). [p 74]
- 125 I. Kodama, M. Yamaguchi, N. Ohyama, T. Honda, K. Shinohara, A. Ito, T. Matsumura, K. Kinoshita and K. Yada. *Image reconstruction from an in-line X-ray hologram with intensity distribution constraint*. Optics Communications **125**(1-3) 36–42 (1996). DOI [10.1016/0030-4018\(96\)00755-9](https://doi.org/10.1016/0030-4018(96)00755-9). [p 75]
- 126 S. Soontaranon, J. Widjaja and T. Asakura. *Direct analysis of in-line particle holograms by using wavelet transform and envelope reconstruction method*. Optik **113**(11) 489–494 (2002). URL [10.1087/0030-4026-00197](https://doi.org/10.1087/0030-4026-00197). [p 75]
- 127 M. T. Ozgen. *Automatic kernel design procedure for Cohen's bilinear class of representations as applied to in-line Fresnel holograms*. Optics Communications **174**(1-4) 51–67 (2000). DOI [10.1016/S0030-4018\(99\)00571-4](https://doi.org/10.1016/S0030-4018(99)00571-4). [pp 75 and 250]
- 128 N. de Jonge, Y. Lamy, K. Schoots and T. H. Oosterkamp. *High brightness electron beam from a multi-walled carbon nanotube*. Nature (London) **420**(6914) 393–395 (2002). DOI [10.1038/nature01233](https://doi.org/10.1038/nature01233). [p 75]
- 129 G. A. Morton and E. G. Ramberg. *Point projector electron microscope*. Physical Review **56**(7) 705 (1939). DOI [10.1103/PhysRev.56.705](https://doi.org/10.1103/PhysRev.56.705). [p 75]
- 130 J. C. H. Spence, W. Qian and A. J. Melmed. *Experimental low-voltage point-projection microscopy and its possibilities*. Ultramicroscopy **52**(3-4) 473–477 (1993). DOI [10.1016/0304-3991\(93\)90063-4](https://doi.org/10.1016/0304-3991(93)90063-4). [p 75]
- 131 Vu Thien Binh, V. Semet and N. Garcia. *Nanometric observations at low energy by Fresnel projection microscopy: carbon and polymer fibres*. Ultramicroscopy **58**(3-4) 307–317 (1995). DOI [10.1016/0304-3991\(95\)00047-5](https://doi.org/10.1016/0304-3991(95)00047-5). [p 75]
- 132 A. L. Bleloch, A. Howie and E. M. James. *Amplitude recovery in Fresnel projection microscopy*. Applied Surface Science **111** 180–184 (1997). DOI [10.1016/S0169-4332\(96\)00707-6](https://doi.org/10.1016/S0169-4332(96)00707-6). [p 75]
- 133 P. Cloetens, W. Ludwig, J. Baruchel, D. van Dyck, J. van Landuyt, J. P. Guigay and M. Schlenker. *Holotomography: Quantitative phase tomography with micrometer resolution using hard synchrotron radiation X-rays*. Applied Physics Letters **75**(19) 2912–2914 (1999). DOI [10.1063/1.125225](https://doi.org/10.1063/1.125225). [p 76]
- 134 P. Cloetens, J.-P. Guigay, O. Hignette, W. Ludwig, M. Schlenker and S. Zabler. *Quantitative phase contrast tomography using coherent synchrotron radiation*. In Peele and Nugent [9]. URL <http://optics.ph.unimelb.edu.au/cairnso3/cairnso3/cairnso3/cloetens.ppt>. [p 76]
- 135 P. Schiske. *Zur frage der bilderkonstruktion durch fokusreihen [On questions of image reconstruction from defocused images]*. In D. S. Bocciarelli (ed.), *Electron Microscopy 1968*. Fourth European Regional Conference on Electron Microscopy, Rome (1968), vol. 1, pp. 145–146. In German. [p 80]
- 136 R. H. Wade. *Holographic methods in electron microscopy*. In P. W. Hawkes (ed.), *Computer Processing of Electron Microscope Images*, Springer-Verlag, New York, vol. 13 of *Topics in Current Physics*, pp. 223–255 (1980). ISBN 0387096221. [p 80]

- 137 K.-J. Hanssen. *Holographic reconstruction methods in electron microscopy and their contrast-theoretical interpretation I. In-line Fresnel-holography*. Optik **32**(1) 74–90 (1970). [p 80]
- 138 G. W. Stroke and M. Halioua. *Image improvement in high-resolution electron microscopy with coherent illumination (low-contrast objects) using holographic image-deblurring deconvolution. III A: Theory*. Optik **37**(2) 184–195 (1973). [p 80]
- 139 G. W. Stroke and M. Halioua. *Image improvement in high-resolution electron microscopy with coherent illumination (low-contrast objects) using holographic image-deblurring deconvolution. III B: Experimental implementations and applications to electron beam image holography*. Optik **37**(3) 249–264 (1973). [p 80]
- 140 G. W. Stroke, M. Halioua, F. Thon and D. Willasch. *Image improvement in high-resolution electron microscopy using holographic image deconvolution*. Optik **41**(3) 319–343 (1974). [p 80]
- 141 O. Kubler. *Optical and digital spatial frequency filtering of electron micrographs. II. Experimental results*. Optik **51**(3) 235–256 (1978). [p 80]
- 142 O. Kubler, M. Hahn and J. Seredynski. *Optical and digital spatial frequency filtering of electron micrographs. I. Theoretical considerations*. Optik **51**(2) 171–188 (1978). [p 80]
- 143 E. J. Kirkland. *Nonlinear high resolution image processing of conventional transmission electron micrographs. I. Theory*. Ultramicroscopy **9**(1-2) 45–64 (1982). DOI [10.1016/0304-3991\(82\)90228-5](https://doi.org/10.1016/0304-3991(82)90228-5). [p 80]
- 144 D. L. Misell. *On the validity of the weak-phase and other approximations in the analysis of electron microscope images*. Journal of Physics D **9**(13) 1849–1866 (1976). DOI [10.1088/0022-3727/9/13/006](https://doi.org/10.1088/0022-3727/9/13/006). [p 80]
- 145 J. F. Conway and A. C. Steven. *Methods for reconstructing density maps of ‘single’ particles from cryoelectron micrographs to subnanometer resolution*. Journal of Structural Biology **128** 106–118 (1999). DOI [10.1006/jsb.1999.4168](https://doi.org/10.1006/jsb.1999.4168). [pp 81, 82 and 83]
- 146 J. Dubochet, M. Adrian, J. J. Chang, J. C. Homo, J. Lepault, A. W. McDowall and P. Schultz. *Cryo-electron microscopy of vitrified specimens*. Quarterly Reviews of Biophysics **21**(2) 129–228 (1988). [p 80]
- 147 D. Typke, R. Hegerl and J. Kleinz. *Image restoration for biological objects using external TEM control and electronic image recording*. Ultramicroscopy **46** 157–173 (1992). DOI [10.1016/0304-3991\(92\)90012-9](https://doi.org/10.1016/0304-3991(92)90012-9). [p 82]
- 148 J. P. Langmore and M. F. Smith. *Quantitative energy-filtered electron microscopy of biological molecules in ice*. Ultramicroscopy **46** 349–373 (1992). DOI [10.1016/0304-3991\(92\)90024-E](https://doi.org/10.1016/0304-3991(92)90024-E). [p 82]
- 149 M. F. Smith and J. P. Langmore. *Quantitation of molecular densities by cryo-electron microscopy: Determination of the radial density distribution of tobacco mosaic virus*. Journal of Molecular Biology **226** 763–774 (1992). DOI [10.1016/0022-2836\(92\)90631-S](https://doi.org/10.1016/0022-2836(92)90631-S). [pp 82 and 83]

- 150 H. P. Erickson and A. Klug. *Measurement and compensation of defocusing and aberrations by Fourier processing of electron micrographs*. Philosophical Transactions of the Royal Society of London B **261** 105–118 (1971). [p 82]
- 151 A. Klug. *From macromolecules to biological assemblies*. In B. G. Malmström (ed.), *Nobel Lectures in Chemistry 1981–1990*, World Scientific, Singapore, vol. 5, pp. 77–109 (1993). ISBN 9810207883. URL <http://www.nobel.se/chemistry/laureates/1982/klug-lecture.pdf>. [p 82]
- 152 Jun Zhu, P. A. Penczek, R. Schröder and J. Frank. *Three-dimensional reconstruction with contrast transfer function correction from energy-filtered cryo-electron micrographs: Procedure and application to the 70S Escherichia coli ribosome*. Journal of Structural Biology **118** 197–219 (1997). DOI [10.1006/jsb.1997.3845](https://doi.org/10.1006/jsb.1997.3845). [pp 82 and 83]
- 153 D. Typke and M. Radermacher. *Determination of the phase of complex atomic scattering amplitudes from light-optical diffractograms of electron microscope images*. Ultramicroscopy **9**(1-2) 131–138 (1982). DOI [10.1016/0304-3991\(82\)90235-2](https://doi.org/10.1016/0304-3991(82)90235-2). [p 83]
- 154 C. Toyoshima and N. Unwin. *Contrast transfer for frozen-hydrated specimens: determination from pairs of defocused images*. Ultramicroscopy **25**(4) 279–292 (1988). DOI [10.1016/0304-3991\(88\)90003-4](https://doi.org/10.1016/0304-3991(88)90003-4). [p 83]
- 155 C. Toyoshima, K. Yonekura and H. Sasabe. *Contrast transfer for frozen-hydrated specimens. II. Amplitude contrast at very low frequencies (proteins)*. Ultramicroscopy **48**(1-2) 165–176 (1993). DOI [10.1016/0304-3991\(93\)90179-2](https://doi.org/10.1016/0304-3991(93)90179-2). [p 83]
- 156 J.-J. Fernandez, J. R. Sanjurjo and J. M. Carazo. *A spectral estimation approach to contrast transfer function detection in electron microscopy*. Ultramicroscopy **68**(4) 267–295 (1997). DOI [10.1016/S0304-3991\(97\)00032-6](https://doi.org/10.1016/S0304-3991(97)00032-6). [p 83]
- 157 J. A. Velazquez-Muriel, C. O. S. Sorzana, J. J. Fernandez and J. M. Carazo. *A method for estimating the CTF in electron microscopy based on ARMA models and parameter adjustment*. Ultramicroscopy **96**(1) 17–35 (2003). DOI [10.1016/S0304-3991\(02\)00377-7](https://doi.org/10.1016/S0304-3991(02)00377-7). [p 83]
- 158 M. van Heel, B. Gowen, R. Matadeen, E. V. Orlova, R. Finn, T. Pape, D. Cohen, H. Stark, R. Schmidt, M. Schatz and A. Patwardhan. *Single-particle electron cryo-microscopy: towards atomic resolution*. Quarterly Reviews of Biophysics **33**(4) 307–369 (2000). DOI [10.1017/S0033583500003644](https://doi.org/10.1017/S0033583500003644). [p 83]
- 159 D. Paganin, S. C. Mayo, T. E. Gureyev, P. R. Miller and S. W. Wilkins. *Simultaneous phase and amplitude extraction from a single defocused image of a homogeneous object*. Journal of Microscopy **206** 33–40 (2002). DOI [10.1046/j.1365-2818.2002.01010.x](https://doi.org/10.1046/j.1365-2818.2002.01010.x). [pp 84 and 86]
- 160 D. C. Munson. *A note on Lena*. IEEE Transactions on Image Processing **5**(1) 3 (1996). [p 87]
- 161 Anon. *Playmate of the month [photograph]*. Playboy **20**(11) (1972). [p 87]
- 162 T. E. Gureyev, A. Pogany, D. Paganin and S. W. Wilkins. *Linear algorithms for phase retrieval in the Fresnel region*. Optics Communications **231**(1–6) 53–70 (2004). DOI [10.1016/j.optcom.2003.12.020](https://doi.org/10.1016/j.optcom.2003.12.020). [p 89]
- 163 T. E. Gureyev, T. J. David, A. Pogany, S. C. Mayo and S. W. Wilkins. *Optical phase retrieval by use of first Born- and Rytov-type approximations*. Applied Optics **43**(12) 2418–2430 (2004). DOI [10.1364/AO.43.002418](https://doi.org/10.1364/AO.43.002418). [p 90]

- 164 R. Courant and D. Hilbert. *Methods of Mathematical Physics*. Interscience, New York (1962). Translation of *Methoden der mathematischen physik*. [p 90]
- 165 H. C. Andrews and B. R. Hunt. *Digital Image Restoration*. Prentice-Hall, Englewood Cliffs, NJ, USA (1977). ISBN 0132142139. [p 91]
- 166 M. R. Banham and A. K. Katsaggelos. *Digital image restoration*. IEEE Signal Processing Magazine **14**(2) 24–41 (1997). [pp 91, 92 and 98]
- 167 N. Wiener. *Extrapolation, Interpolation, and Smoothing of Stationary Time Series*. MIT Press, Cambridge, MA, USA (1949). ISBN 026223002x. First published as classified report to the National Defense Research Committee (1942). [p 92]
- 168 C. R. Vogel. *Computational Methods for Inverse Problems*. SIAM Publishing, Philadelphia (2002). ISBN 0898715075. [p 92]
- 169 I. Raveh, D. Mendlovic, Z. Zalevsky and A. W. Lohmann. *Digital method for defocus corrections: experimental results*. Optical Engineering **38**(10) 1620–1626 (1999). DOI [10.1117/1.602215](https://doi.org/10.1117/1.602215). [p 94]
- 170 C. J. R. Sheppard and M. Gu. *Approximation to the three-dimensional optical transfer function*. Journal of the Optical Society of America A **8**(4) 692–694 (1991). URL <http://www.opticsinfobase.org/abstract.cfm?id=4044>. [p 94]
- 171 A. N. Tikhonov. *Solution of incorrectly formulated problems and the regularization method*. Soviet Mathematics Doklady **4** 1035–1038 (1963). [p 95]
- 172 A. N. Tikhonov and V. Y. Arsenin. *Solutions of Ill-posed Problems*. V. H. Winston & Sons, Washington D.C. (1977). [p 95]
- 173 J. Cheng and M. Yamamoto. *One new strategy for a priori choice of regularizing parameters in Tikhonov's regularization*. Inverse Problems **16**(4) L31–L38 (2000). DOI [10.1088/0266-5611/16/4/101](https://doi.org/10.1088/0266-5611/16/4/101). [p 95]
- 174 W. H. Press, B. P. Flannery, S. A. Teukolsky and W. T. Vetterling. *Numerical Recipes in C*. Cambridge University Press, Cambridge, UK, 2nd edn. (1992). ISBN 0521431085. [pp 95 and 315]
- 175 B. L. Henke, E. M. Gullikson and J. C. Davis. *X-ray interactions: photoabsorption, scattering, transmission, and reflection at E=50–30 000 eV*. Atomic Data and Nuclear Data Tables **54**(2) 181–342 (1993). DOI [10.1006/adnd.1993.1013](https://doi.org/10.1006/adnd.1993.1013). URL [http://www-cxro.lbl.gov/optical\\_constants/](http://www-cxro.lbl.gov/optical_constants/). [pp 96 and 107]
- 176 N. P. Galatsanos and A. K. Katsaggelos. *Methods for choosing the regularization parameter and estimating the noise variance in image restoration and their relation*. IEEE Transactions of Image Processing **1**(3) 322–336 (1992). DOI [10.1109/83.148606](https://doi.org/10.1109/83.148606). [p 102]
- 177 Moon Gi Kang and A. K. Katsaggelos. *General choice of the regularization functional in regularized image restoration*. IEEE Transactions of Image Processing **4**(5) 594–602 (1995). DOI [10.1109/83.382494](https://doi.org/10.1109/83.382494). [p 102]
- 178 D. J. Tolhurst, Y. Tadmor and Tang Chao. *Amplitude spectra of natural images*. Ophthalmic and Physiological Optics **12** 229–232 (1992). [p 103]

- 179 B. B. Mandelbrot. *The Fractal Geometry of Nature*. W. H. Freeman, New York (1983). ISBN 0716711869. [p 103]
- 180 R. M. Balboa, C. W. Tyler and N. M. Grzywacz. *Occlusions contribute to scaling in natural images*. Vision Research **41**(7) 955–964 (2001). DOI [10.1016/S0042-6989\(00\)00302-3](https://doi.org/10.1016/S0042-6989(00)00302-3). [p 103]
- 181 Ramesh Neelamani. *Inverse Problems in Image Processing*. Ph.D. thesis, Rice University, Department of Electrical and Computer Engineering, Houston TX, USA (2003). URL [http://www.dsp.rice.edu/~neelsh/publications/phd\\_abs.html](http://www.dsp.rice.edu/~neelsh/publications/phd_abs.html). [pp 104, 115, 116 and 119]
- 182 A. D. Hillery and R. T. Chin. *Iterative Wiener filters for image restoration*. IEEE Transactions on Signal Processing **39**(8) 1892–1899 (1991). DOI [10.1109/78.91161](https://doi.org/10.1109/78.91161). [p 107]
- 183 F. G. Meyer and R. R. Coifman. *Brushlets: a tool for directional image analysis and image compression*. Applied & Computational Harmonic Analysis **4**(2) 147–187 (1997). DOI [10.1006/acha.1997.0208](https://doi.org/10.1006/acha.1997.0208). [pp 105 and 122]
- 184 D. L. Donoho. *Nonlinear solution of linear inverse problems by wavelet-vaguelette decomposition*. Applied & Computational Harmonic Analysis **2**(2) 101–126 (1995). DOI [10.1006/acha.1995.1008](https://doi.org/10.1006/acha.1995.1008). [pp 108 and 112]
- 185 D. L. Donoho. *De-noising by soft-thresholding*. IEEE Transactions on Information Theory **41**(3) 613–627 (1995). DOI [10.1109/18.382009](https://doi.org/10.1109/18.382009). [pp 108 and 115]
- 186 E. J. Candès and D. L. Donoho. *Recovering edges in ill-posed inverse problems: Optimality of curvelet frames*. Annals of Statistics **30**(3) 784–842 (2002). DOI [10.1214/aos/1028674842](https://doi.org/10.1214/aos/1028674842). Also available as Stanford University Department of Statistics Technical Report 2000-16 (2000 March) at <http://www-stat.stanford.edu/~emmanuel/papers/CurveInverse.pdf>. [pp 108, 111 and 123]
- 187 G. M. Davis and A. Nosratinia. *Wavelet-based image coding: An overview*. In B. N. Datta (ed.), *Applied and Computational Control, Signals, and Circuits*, Birkhauser, vol. 1, pp. 205–269 (1998). ISBN 0817639543. Available online at <http://www.geoffdavis.net/papers/accsc.pdf>. [pp 108 and 109]
- 188 M. Rosenblatt. *Random Processes*. Springer-Verlag, New York, 2nd edn. (1974). ISBN 0387900853. [p 108]
- 189 J. Kalifa and S. Mallat. *Thresholding estimators for linear inverse problems and deconvolutions*. Annals of Statistics **31**(1) 58–109 (2003). DOI [10.1214/aos/1046294458](https://doi.org/10.1214/aos/1046294458). [p 109]
- 190 R. D. Nowak and R. G. G. Baraniuk. *Wavelet-domain filtering for photon imaging systems*. IEEE Transactions of Image Processing **8**(5) 666–678 (1999). DOI [10.1109/83.760334](https://doi.org/10.1109/83.760334). [p 109]
- 191 D. Gabor. *Theory of communication*. Journal of the Institute of Electrical Engineers (London) **93**(III,26) 429–457 (1946). [p 109]
- 192 I. Daubechies. *Ten Lectures on Wavelets*. CBMS-NSF Regional Conference Series in Applied Mathematics. SIAM Publishing, Philadelphia (1992). ISBN 0898712742. [p 111]

- 193 D. L. Donoho. *Unconditional bases are optimal bases for data compression and for statistical estimation*. Applied & Computational Harmonic Analysis **1**(1) 100–115 (1993). DOI [10.1006/acha.1993.1008](https://doi.org/10.1006/acha.1993.1008). [p 111]
- 194 R. A. DeVore, B. Jawerth and B. J. Lucier. *Image compression through wavelet transform coding*. IEEE Transactions on Information Theory **38**(2) 719–746 (1992). DOI [10.1109/18.119733](https://doi.org/10.1109/18.119733). [p 111]
- 195 E. W. Weisstein and T. Rowland. *L<sup>p</sup>-Space*. Web document, Mathworld (2003). URL <http://mathworld.wolfram.com/Lp-Space.html>. [p 111]
- 196 H. Choi and R. G. G. Baraniuk. *Wavelet statistical models and Besov spaces*. In *Proceedings of SPIE Technical Conference on Wavelet Applications in Signal and Image Processing VII*. SPIE, Denver (1999), vol. 3813, pp. 489–501. DOI [10.1117/12.366806](https://doi.org/10.1117/12.366806). [p 111]
- 197 H. Choi and R. G. G. Baraniuk. *Information-theoretic analysis of Besov spaces*. In *Proceedings of SPIE Technical Conference on Wavelet Applications in Signal and Image Processing VIII*. SPIE, San Diego (2000), vol. 4119, pp. 675–685. DOI [10.1117/12.408657](https://doi.org/10.1117/12.408657). [p 111]
- 198 Nam-Yong Lee and B. J. Lucier. *Wavelet methods for inverting the Radon transform with noisy data*. IEEE Transactions on Image Processing **10**(1) 79–94 (2001). DOI [10.1109/83.892445](https://doi.org/10.1109/83.892445). [p 112]
- 199 R. Neelamani, H. Choi and R. G. G. Baraniuk. *Forward: Fourier-wavelet regularized deconvolution for ill-conditioned systems*. IEEE Transactions on Signal Processing **52**(2) 418–433 (2004). DOI [10.1109/TSP.2003.821103](https://doi.org/10.1109/TSP.2003.821103). URL <http://cmc.rice.edu/docs/info.pl?doc=Nee2002Sep1ForWaRDFou>. [p 112]
- 200 R. Neelamani, H. Choi and R. G. G. Baraniuk. *Wavelet-based deconvolution using optimally regularized inversion for ill-conditioned systems*. In *Proceedings of SPIE Technical Conference on Wavelet Applications in Signal and Image Processing VII*. Denver, co, USA (1999), vol. 3813, pp. 58–72. DOI [10.1117/12.366812](https://doi.org/10.1117/12.366812). [p 112]
- 201 R. Neelamani, H. Choi and R. G. G. Baraniuk. *Wavelet-domain regularized deconvolution for ill-conditioned systems*. In *Proceedings of the 6th IEEE International Conference on Image Processing*. IEEE, Kobe, Japan (1999), vol. 3, pp. 204–208. URL <http://cmc.rice.edu/docs/info.pl?doc=Nee1999Oct5Wavelet-do>. [p 112]
- 202 R. Neelamani, H. Choi and R. G. G. Baraniuk. *Wavelet-based Deconvolution for Ill-conditioned Systems*. In *Proceedings of the IEEE International Conference on Acoustics, Speech, and Signal Processing (ICASSP)*. Phoenix, AZ, USA (1999), vol. 6, pp. 3241–3244. URL <http://cmc.rice.edu/docs/info.pl?doc=Nee1999Mar5Wavelet-ba>. [p 112]
- 203 H. Choi and R. G. G. Baraniuk. *Analysis of Wavelet-domain Wiener filters*. In *Proceedings of the IEEE-SP International Symposium on Time-frequency and Time-scale Analysis*. Pittsburgh, PA, USA (1998), pp. 613–616. URL <http://cmc.rice.edu/docs/info.pl?doc=Cho1998Oct5Analysisof>. [pp 114 and 115]
- 204 S. P. Ghosh, A. M. Sayeed and R. G. G. Baraniuk. *Improved wavelet denoising via empirical Wiener filtering*. In *Proceedings of SPIE Technical Conference on Wavelet Applications in Signal and Image Processing V*. San Diego (1997), vol. 3169, pp. 389–399. DOI [10.1117/12.292799](https://doi.org/10.1117/12.292799). URL [http://dune.ece.wisc.edu/~akbar/papers/spie97\\_akira.ps.Z](http://dune.ece.wisc.edu/~akbar/papers/spie97_akira.ps.Z). [p 115]

- 205 D. L. Donoho and I. M. Johnstone. *Ideal spatial adaptation by wavelet shrinkage*. Biometrika **81**(3) 425–455 (1994). URL <http://citeseer.ist.psu.edu/donoho93ideal.html>. [p 115]
- 206 S. Beheshti and M. A. Dahleh. *Noise variance in signal denoising*. In *Proceedings of the International Conference Acoustic, Speech, and Signal Processing (ICASSP)*. Hong Kong (2003), vol. 6, pp. 185–188. URL [http://mit.edu/dahleh/www/Pubs/research\\_students/beheshti\\_cassp%2003.pdf](http://mit.edu/dahleh/www/Pubs/research_students/beheshti_cassp%2003.pdf). [p 115]
- 207 R. Neelamani. *Fourier wavelet regularized deconvolution: ForWaRD*. Matlab source code and MEX object files, Department of ECE, Rice University, Houston, TX, USA (2002). URL <http://www-dsp.rice.edu/software/ward.shtml>. [pp 115 and 116]
- 208 J.-L. Starck, D. L. Donoho and E. J. Candès. *Very high quality image restoration by combining wavelets and curvelets*. In A. Aldroubi, A. F. Laine and M. A. Unser (eds.), *Proceedings of SPIE Technical Conference on Wavelet Applications in Signal and Image Processing IX*. SPIE, San Diego, CA, USA (2001), vol. 4478, pp. 9–19. DOI [10.1117/12.449693](https://doi.org/10.1117/12.449693). URL <http://www.acm.caltech.edu/~emmanuel/papers/spie01.ps.gz>. [pp 117, 122 and 125]
- 209 R. R. Coifman and D. L. Donoho. *Translation invariant denoising*. In A. Antoniadis and G. Oppenheim (eds.), *Wavelets and Statistics*, Springer-Verlag Telos, New York, vol. 103 of *Lecture Notes in Statistics*, pp. 125–150 (1995). ISBN 0387945644. URL <http://www-stat.stanford.edu/~donoho/Reports/1995/TIDeNoise.ps.Z>. [p 119]
- 210 A. Chambolle and B. J. Lucier. *Interpreting translation-invariant wavelet shrinkage as a new image smoothing scale space*. IEEE Transactions of Image Processing **10**(7) 993–1000 (2001). DOI [10.1109/83.931093](https://doi.org/10.1109/83.931093). [p 119]
- 211 T. Yu, A. Stoschek and D. L. Donoho. *Translation- and direction-invariant denoising*. In M. A. Unser, A. Aldroubi and A. F. Laine (eds.), *Proceedings of SPIE Technical Conference on Wavelet Applications in Signal and Image Processing IV* (1996), vol. 2825, pp. 608–619. URL <http://www.rpi.edu/~yut/ImageDenoise.html>. [p 121]
- 212 N. Kingsbury. *Image processing with complex wavelets*. Philosophical Transactions of the Royal Society of London Series A **357**(1760) 2543–2560 (1999). DOI [10.1098/rsta.1999.0447](https://doi.org/10.1098/rsta.1999.0447). [p 121]
- 213 N. Kingsbury and P. de Rivaz. *Bayesian image deconvolution and denoising using complex wavelets*. In *Proceedings of the International Conference on Image Processing*. IEEE, Thessaloniki, Greece (2001), vol. 2, pp. 273–276. URL [http://www-sigproc.eng.cam.ac.uk/~ngk/publications/pfcd\\_icipo1.zip](http://www-sigproc.eng.cam.ac.uk/~ngk/publications/pfcd_icipo1.zip). [p 121]
- 214 P. L. Dragotti and M. Vetterli. *Wavelet footprints: theory, algorithms, and applications*. IEEE Transactions on Signal Processing **51**(5) 1306–1323 (2003). DOI [10.1109/TSP.2003.810296](https://doi.org/10.1109/TSP.2003.810296). [p 121]
- 215 S. Durand and J. Froment. *Artifact free signal denoising with wavelets*. In *Proceedings of the International Conference Acoustic, Speech, and Signal Processing (ICASSP)*. Salt Lake City, UT, USA (2001), vol. 6, pp. 3685–3688. URL <http://citeseer.csail.mit.edu/durando1artifact.html>. [p 121]

- 216 H. Choi and R. G. G. Baraniuk. *Multiple basis wavelet denoising using Besov projections*. In *Proceedings of 6th IEEE International Conference on Image Processing*. IEEE (1999), vol. 1, pp. 595–599. URL <http://cmc.rice.edu/docs/info.pl?doc=Cho1999Oct5Multipleba>. [p 121]
- 217 M. A. T. Figueiredo and R. D. Nowak. *An EM algorithm for wavelet-based image restoration*. *IEEE Transactions on Image Processing* **12**(8) 906–916 (2003). DOI [10.1109/TIP.2003.814255](https://doi.org/10.1109/TIP.2003.814255). [p 121]
- 218 D. L. Donoho and X. Huo. *Combined image representation using edgelets and wavelets*. In *Proceedings of SPIE Technical Conference on Wavelet Applications in Signal and Image Processing VII*. Denver, CO, USA (1999), vol. 3813, pp. 468–476. DOI [10.1117/12.366804](https://doi.org/10.1117/12.366804). [p 122]
- 219 D. L. Donoho. *Wedgelets: Nearly minimax estimation of edges*. *Annals of Statistics* **27** 859–897 (1999). DOI [10.1214/aos/1018031261](https://doi.org/10.1214/aos/1018031261). URL <http://www-stat.stanford.edu/~donoho/Reports/1997/Wedgelets.pdf>. [p 122]
- 220 J. Romberg, M. Wakin and R. G. G. Baraniuk. *Approximation and compression of piecewise smooth images using a wavelet/wedgelet geometric model*. In *Proceedings of the IEEE International Conference on Image Processing*. Barcelona (2003), vol. 1, pp. 49–52. URL <http://cmc.rice.edu/docs/info.pl?doc=Rom2003Sep5Approxima>. [p 122]
- 221 D. L. Donoho and X. Huo. *Beamlets and multiscale image analysis*. In T. J. Barth, T. Chan and R. Haimes (eds.), *Multiscale and Multiresolution Methods: Theory and Applications*, Springer-Verlag, Berlin, vol. 20 of *Lecture Notes in Computational Science and Engineering*, pp. 149–196 (2001). ISBN 3540424202. URL <http://www.isye.gatech.edu/~xiaoming/publication/Beam070901.pdf>. [p 122]
- 222 E. J. Candès and D. L. Donoho. *Ridgelets: a key to higher-dimensional intermittency?* *Philosophical Transactions of the Royal Society of London A: Mathematical, Physical and Engineering Sciences* **357**(1760) 1496–2509 (1999). URL <http://www-stat.stanford.edu/~emmanuel/papers/RoySoc.pdf>. [p 122]
- 223 E. J. Candès and D. L. Donoho. *Curvelets – a surprisingly effective Nonadaptive representation for objects with edges*. In A. Cohen, C. Rabut and L. L. Schumaker (eds.), *Curve and Surface Fitting: Saint-Malo 1999*, Vanderbilt University Press, Nashville, TN, USA, Innovations in Applied Mathematics, pp. 105–120 (2000). ISBN 0826513573. URL <http://www-stat.stanford.edu/~donoho/Reports/1999/curveletsprise.pdf>. [p 122]
- 224 D. L. Donoho. *Beyond wavelets*. In *National Science Foundation CBMS Lecture Series*. University of Missouri, USA (2000). Unpublished lecture series, URL <http://www-stat.stanford.edu/~donoho/Lectures/CBMS/CBMSLect.html>. [p 122]
- 225 E. J. Candès and D. L. Donoho. *Curvelets, multiresolution representation, and scaling laws*. In *Proceedings of SPIE Technical Conference on Wavelet Applications in Signal and Image Processing VIII*. SPIE, San Diego (2000), vol. 4119, pp. 1–12. DOI [10.1117/12.408568](https://doi.org/10.1117/12.408568). URL [http://www-stat.stanford.edu/~emmanuel/papers/spie\\_Curvelets.pdf](http://www-stat.stanford.edu/~emmanuel/papers/spie_Curvelets.pdf). [p 122]
- 226 E. J. Candès and D. L. Donoho. *New tight frames of curvelets and optimal representations of objects with  $c^2$  singularities*. *Communications on Pure and Applied Mathematics* **57**(2) 219–266 (2004). DOI [10.1002/cpa.10116](https://doi.org/10.1002/cpa.10116). URL <http://www.acm.caltech.edu/~emmanuel/papers/CurveEdges.pdf>. [p 122]

- 227 D. L. Donoho and M. L. Duncan. *Digital curvelet transform: Strategy, implementation and experiments*. In *Proceedings of SPIE Technical Conference on Wavelet Applications in Signal and Image Processing VII*. SPIE, Orlando, FL, USA (2000), vol. 4056, pp. 12–30.  
DOI [10.1117/12.381679](https://doi.org/10.1117/12.381679).  
URL <http://www-stat.stanford.edu/~donoho/Reports/1999/DCvT.pdf>. [p 122]
- 228 International Organisation for Standardisation. *JPEG 2000 image coding system, ISO/IEC 15444-1:2004*. ISO, Geneva, Switzerland (2004). [p 122]
- 229 J.-L. Starck. *The Curvelet Home Page*. Website, Department of Statistics, Stanford University (2003). Lena images at <http://www-stat.stanford.edu/~jstarck/comp.html>, URL <http://www-stat.stanford.edu/~jstarck>. [p 125]
- 230 J.-L. Starck, E. J. Candès and D. L. Donoho. *The curvelet transform for image denoising*. IEEE Transactions of Image Processing **11**(6) 670–684 (2002).  
DOI [10.1109/TIP.2002.1014998](https://doi.org/10.1109/TIP.2002.1014998). [pp 122 and 123]
- 231 J.-L. Starck, M. K. Nguyen and F. Murtagh. *Wavelets and curvelets for image deconvolution: a combined approach*. Signal Processing **83**(10) 2279–2283 (2003).  
DOI [10.1016/S0165-1684\(03\)00150-6](https://doi.org/10.1016/S0165-1684(03)00150-6). [pp 123 and 126]
- 232 D. L. Donoho, A. G. Flesia and X. Huo. *Beamlab 2000 for MATLAB 5.x or 6.x*. Software package / source code, Department of Statistics, Stanford University (2002).  
URL <http://www-stat.stanford.edu/~beamlab/>. [p 123]
- 233 D. L. Donoho and A. G. Flesia. *Can recent innovations in harmonic analysis ‘explain’ key findings in natural image statistics?* Network: Computation in Neural Systems **12**(3) 371–393 (2001). DOI [10.1088/0954-898X/12/3/308](https://doi.org/10.1088/0954-898X/12/3/308). [p 125]
- 234 S. Mallat and W. L. Hwang. *Singularity detection and processing with wavelets*. IEEE Transactions on Information Theory **38**(2) 617–643 (1992). DOI [10.1109/18.119727](https://doi.org/10.1109/18.119727). [p 126]
- 235 M. T. Ozgen and T. Tuncer. *Object reconstruction from in-line Fresnel holograms without explicit depth focusing*. Optical Engineering **43**(6) 1300–1310 (2004). DOI [10.1117/1.1737785](https://doi.org/10.1117/1.1737785). [p 134]
- 236 R. S. Conroy, Y. Xiao, M. Vengalattore, W. Rooijakkers and M. Prentiss. *Compact, robust source of cold atoms for efficient loading of a magnetic guide*. Optics Communications **226**(1-6) 259–266 (2003). DOI [10.1016/j.optcom.2003.09.012](https://doi.org/10.1016/j.optcom.2003.09.012). [pp 138 and 140]
- 237 P. R. Berman (ed.). *Atom Interferometry*. Academic Press, San Diego (1997). ISBN 0120924609. [p 138]
- 238 E. Riis, D. S. Weiss, K. A. Moler and S. Chu. *Atom funnel for the production of a slow, high-density atomic beam*. Physical Review Letters **64**(14) 1658–1661 (1990). DOI [10.1103/PhysRevLett.64.1658](https://doi.org/10.1103/PhysRevLett.64.1658). [p 138]
- 239 J. Nellessen, J. Werner and W. Ertmer. *Magneto-optical compression of a monoenergetic sodium atomic beam*. Optics Communications **78**(3-4) 300–308 (1990). DOI [10.1016/0030-4018\(90\)90365-Z](https://doi.org/10.1016/0030-4018(90)90365-Z). [p 138]
- 240 T. B. Swanson, N. J. Silva, S. K. Mayer, J. J. Maki and D. H. McIntyre. *Rubidium atomic funnel*. Journal of the Optical Society of America B **13**(9) 1833–1836 (1996). URL <http://www.opticsinfobase.org/abstract.cfm?id=33875>. [p 138]

- 241 R. M. S. Knops, A. E. A. Koolen, H. C. W. Beijerinck and K. A. H. van Leeuwen. *Design and construction of a high-precision atomic beam machine for quantum optics and atom optics experiments.* Laser Physics **9**(1) 286–292 (1999). [p 138]
- 242 F. Lison, P. Schuh, D. Haubrich and D. Meschede. *High-brilliance Zeeman-slowed cesium atomic beam.* Physical Review A **61**(1) 013405 (2000). DOI [10.1103/PhysRevA.61.013405](https://doi.org/10.1103/PhysRevA.61.013405). [p 138]
- 243 C. Monroe, W. Swann, H. Robinson and C. E. Wieman. *Very cold trapped atoms in a vapor cell.* Physical Review Letters **65**(13) 1571–1574 (1990). DOI [10.1103/PhysRevLett.65.1571](https://doi.org/10.1103/PhysRevLett.65.1571). [p 138]
- 244 Z. T. Lu, K. L. Corwin, M. J. Renn, M. H. Anderson, E. A. Cornell and C. E. Wieman. *Low-velocity intense source of atoms from a magneto-optical trap.* Physical Review Letters **77**(16) 3331–3334 (1996). DOI [10.1103/PhysRevLett.77.3331](https://doi.org/10.1103/PhysRevLett.77.3331). [p 138]
- 245 J. Schosser, A. Batar, R. F. Low, V. Schweikhard, A. Grabowski, Y. B. Ovchinnikov and T. Pfau. *Intense source of cold Rb atoms from a pure two-dimensional magneto-optical trap.* Physical Review A **66**(2) 023410 (2002). DOI [10.1103/PhysRevA.66.023410](https://doi.org/10.1103/PhysRevA.66.023410). [pp 138 and 140]
- 246 P. Berthoud, E. Fretel and P. Thomann. *Bright, slow, and continuous beam of laser-cooled cesium atoms.* Physical Review A **60**(6) R4241–R4244 (1999). DOI [10.1103/PhysRevA.60.R4241](https://doi.org/10.1103/PhysRevA.60.R4241). [pp 138 and 139]
- 247 H. J. Metcalf and P. van der Straten. *Laser Cooling and Trapping.* Springer-Verlag, Berlin (1999). ISBN 0387987282. A shorter but similar treatment is available online, see Reference 439. [pp 138, 139 and 148]
- 248 S. Weyers, E. Aucouturier, C. Valentin and N. Dimarcq. *A continuous beam of cold cesium atoms extracted from a two-dimensional magneto-optical trap.* Optics Communications **143**(1-3) 30–34 (1997). DOI [10.1016/S0030-4018\(97\)00312-X](https://doi.org/10.1016/S0030-4018(97)00312-X). [p 140]
- 249 Chang Jae Lee. *Quantum-mechanical analysis of atom lithography.* Physical Review A **61**(6) 063604 (2000). DOI [10.1103/PhysRevA.61.063604](https://doi.org/10.1103/PhysRevA.61.063604). [p 140]
- 250 A. Noble and M. Kasevich. *UHV optical window seal to conflat knife edge.* Review of Scientific Instruments **65**(9) 3042–3043 (1994). DOI [10.1063/1.1144604](https://doi.org/10.1063/1.1144604). [p 143]
- 251 R. R. Addiss, L. Pensak and N. J. Scott. *Evaluation of a new fluoroelastomer as a gasketing material for high vacuum systems.* In *Transactions of the Seventh National Symposium on Vacuum Technology.* American Vacuum Society (1960), pp. 39–44.  
URL <http://www.duniway.com/images/pdf/viton-out-gassed-orings.pdf>. [pp 145 and 146]
- 252 P. Danielson. *Gas loads from elastomer and metal seals.* Unreviewed Web article SA-3, VacuumLab.com (2002).  
URL <http://www.vacuumlab.com/Gas%20Loads%20Elastomer-Metal%20Seals.pdf>. [pp 145 and 147]
- 253 I. Sakai, H. Ishimaru and G. Horikoshi. *Sealing concept of elastic metal gasket ‘Helicoflex’.* Vacuum **32**(1) 33–37 (1982). [p 145]
- 254 Jan Grünert. *Ultracold Metastable Calcium Atoms in a Bichromatic Magneto-Optical Trap.* Ph.D. thesis, Universität Hamburg (2002).  
URL <http://www.sub.uni-hamburg.de/disse/705/dissertation.pdf>. [p 145]

- 255 S. G. Cox, P. F. Griffin, C. S. Adams, D. DeMille and E. Riis. *Reusable ultrahigh vacuum viewport bakeable to 240 degrees C.* Review of Scientific Instruments **74**(6) 3185–3187 (2003). DOI [10.1063/1.1574604](https://doi.org/10.1063/1.1574604). [p 145]
- 256 C. E. Wieman, G. Flowers and S. Gilbert. *Inexpensive laser cooling and trapping experiment for undergraduate laboratories.* American Journal of Physics **63**(4) 317–330 (1995). DOI [10.1119/1.18072](https://doi.org/10.1119/1.18072). [pp 145, 147 and 170]
- 257 Duniway Stockroom Corporation. *Conductance of a tube.* Web document, Mountainview, CA, USA (2003). URL <http://www.duniway.com/images/pdf/p-bo3-conductance.pdf>. [p 145]
- 258 U. D. Rapol, A. Wasan and V. Natarajan. *Loading of a Rb magneto-optic trap from a getter source.* Physical Review A **64**(2) 023402 (2001). DOI [10.1103/PhysRevA.64.023402](https://doi.org/10.1103/PhysRevA.64.023402). [pp 147 and 148]
- 259 J. Fortagh, A. Grossmann, T. W. Hansch and C. Zimmermann. *Fast loading of a magneto-optical trap from a pulsed thermal source.* Journal of Applied Physics **84**(12) 6499–6501 (1998). DOI [10.1063/1.369018](https://doi.org/10.1063/1.369018). [pp 147 and 148]
- 260 D. Haubrich, H. Schadwinkel, F. Strauch, B. Ueberholz, R. Wynands and D. Meschede. *Observation of individual neutral atoms in magnetic and magneto-optical traps.* Europhysics Letters **34**(9) 663–668 (1996). DOI [10.1209/eppli1996-00512-5](https://doi.org/10.1209/epl/i1996-00512-5). [p 148]
- 261 K. Lindquist, M. Stephens and C. E. Wieman. *Experimental and theoretical study of the vapor-cell Zeeman optical trap.* Physical Review A **46**(7) 4082–4090 (1992). DOI [10.1103/PhysRevA.46.4082](https://doi.org/10.1103/PhysRevA.46.4082). [pp 148 and 169]
- 262 A. Banerjee, D. Das and V. Natarajan. *Precise frequency measurements of atomic transitions by use of a Rb-stabilized resonator.* Optics Letters **28**(17) 1579–1581 (2003). URL <http://www.opticsinfobase.org/abstract.cfm?id=74095>. [pp 149, 168 and 193]
- 263 C. E. Wieman and L. W. Hollberg. *Using diode lasers for atomic physics.* Review of Scientific Instruments **62**(1) 1–20 (1991). DOI [10.1063/1.1142305](https://doi.org/10.1063/1.1142305). [pp 150 and 153]
- 264 A. S. Arnold, J. S. Wilson and M. G. Boshier. *A simple extended-cavity diode laser.* Review of Scientific Instruments **69**(3) 1236–1239 (1998). DOI [10.1063/1.1148756](https://doi.org/10.1063/1.1148756). [p 150]
- 265 C. J. Hawthorn, K. P. Weber and R. E. Scholten. *Littrow configuration tunable external cavity diode laser with fixed direction output beam.* Review of Scientific Instruments **72**(12) 4477–4479 (2001). DOI [10.1063/1.1419217](https://doi.org/10.1063/1.1419217). [p 150]
- 266 J. Lazar, O. Cíp and B. Ruzicka. *The design of a compact and tunable extended-cavity semiconductor laser.* Measurement Science & Technology **15**(1) N6–N9 (2004). DOI [10.1088/0957-0233/15/1/N02](https://doi.org/10.1088/0957-0233/15/1/N02). [p 150]
- 267 L. Ricci, M. Weidemuller, T. Esslinger, A. Hemmerich, C. Zimmermann, V. Vuletic, W. Konig and T. W. Hansch. *A compact grating-stabilized diode laser system for atomic physics.* Optics Communications **117**(5–6) 541–549 (1995). DOI [10.1016/0030-4018\(95\)00146-Y](https://doi.org/10.1016/0030-4018(95)00146-Y). [p 151]
- 268 H. Talvitie, A. Pietilainen, H. Ludvigsen and E. Ikonen. *Passive frequency and intensity stabilization of extended-cavity diode lasers.* Review of Scientific Instruments **68**(1) 1–7 (1997). DOI [10.1063/1.1147810](https://doi.org/10.1063/1.1147810). [pp 151 and 152]

- 269 S. Saito, O. Nilsson and Y. Yamamoto. *Oscillation center frequency tuning, quantum FM noise, and direct frequency modulation characteristics in external grating loaded semiconductor lasers.* IEEE Journal of Quantum Electronics **18**(6) 961–970 (1982). DOI [10.1109/JQE.1982.1071636](https://doi.org/10.1109/JQE.1982.1071636). [p 151]
- 270 Sorbothane Inc. *Sorbothane adhesive recommendations.* Web document, Sorbothane Inc., Kent, OH, US (2001). URL [http://www.sorbothane.com/PDF/sor\\_adh.pdf](http://www.sorbothane.com/PDF/sor_adh.pdf). [p 151]
- 271 D. I. G. Jones. *Handbook of Viscoelastic Vibration Damping.* John Wiley & Sons, Chichester, UK (2001). ISBN 0471492485. [p 152]
- 272 R. J. Miller and H. F. Gleeson. *A computer interfaced high-stability temperature controller and heating stage for optical microscopy.* Measurement Science & Technology **5**(8) 904–911 (1994). DOI [10.1088/0957-0233/5/8/006](https://doi.org/10.1088/0957-0233/5/8/006). [p 153]
- 273 K. G. Libbrecht and J. L. Hall. *A low-noise high-speed diode laser current controller.* Review of Scientific Instruments **64**(8) 2133–2135 (1993). DOI [10.1063/1.1143949](https://doi.org/10.1063/1.1143949). [p 153]
- 274 J. Lazar, P. Jedlicka, O. Cip and B. Ruzicka. *Laser diode current controller with a high level of protection against electromagnetic interference.* Review of Scientific Instruments **74**(8) 3816–3819 (2003). DOI [10.1063/1.1593783](https://doi.org/10.1063/1.1593783). [p 153]
- 275 J. J. McFerran, R. P. Kovacich and A. N. Luiten. *Wide bandwidth modulation techniques for laser diodes and current noise investigations of laser diode drivers.* Measurement Science and Technology (submitted) (2004). University of Western Australian preprint, URL <http://www.physics.uwa.edu.au/~mcferran/JJMMSTp3.pdf>. [p 153]
- 276 Y. Shevy, J. Kitching and A. Yariv. *Linewidth reduction and frequency stabilization of a semiconductor laser with a combination of FM sideband locking and optical feedback.* Optics Letters **18**(13) 1071–1073 (1993). URL <http://www.opticsinfobase.org/abstract.cfm?id=11790>. [pp 154 and 155]
- 277 Y. Salvade and R. Dandliker. *Limitations of interferometry due to the flicker noise of laser diodes.* Journal of the Optical Society of America A **17**(5) 927–932 (2000). URL <http://www.opticsinfobase.org/abstract.cfm?id=94>. [p 155]
- 278 A. Yariv, R. Nabiev and K. Vahala. *Self-quenching of fundamental phase and amplitude noise in semiconductor lasers with dispersive loss.* Optics Letters **15**(23) 1359–1361 (1990). URL <http://www.opticsinfobase.org/abstract.cfm?id=10313>. [p 155]
- 279 D. Meschede and H. J. Metcalf. *Atomic nanofabrication: atomic deposition and lithography by laser and magnetic forces.* Journal of Physics D **36**(3) R17–R38 (2003). DOI [10.1088/0022-3727/36/3/202](https://doi.org/10.1088/0022-3727/36/3/202). [p 155]
- 280 R. W. Fox, C. W. Oates and L. W. Hollberg. *Stabilizing diode lasers to high-finesse cavities.* In J. P. van Zee, J. P. Looney and R. van Zee (eds.), *Experimental Methods in the Physical Sciences: Cavity-Enhanced Spectroscopies*, Academic Press, vol. 40, chap. 2 (2002). ISBN 0124759874. [pp 155 and 158]
- 281 W. D. Lee and J. C. Campbell. *Optically stabilized Al<sub>x</sub>Ga<sub>1-x</sub>As/GaAs laser using magnetically induced birefringence in Rb vapor.* Applied Physics Letters **58**(10) 995–997 (1991). DOI [10.1063/1.105214](https://doi.org/10.1063/1.105214). [p 155]

- 282 P. Wanninger and E. C. Valdez. *Diode-laser frequency stabilization based on the resonant Faraday effect.* IEEE Photonics Technology Letters **4**(1) 94–96 (1992). DOI [10.1109/68.124888](https://doi.org/10.1109/68.124888). [p 155]
- 283 Y. Shevy, J. Iannelli, J. Kitching and A. Yariv. *Self-quenching of the semiconductor laser linewidth below the Schawlow-Townes limit by using optical feedback.* Optics Letters **17**(9) 661–663 (1992). URL <http://www.opticsinfobase.org/abstract.cfm?id=11137>. [pp 155 and 156]
- 284 K. Choi, J. Menders, P. Searcy and E. Korevaar. *Optical feedback locking of a diode laser using a cesium Faraday filter.* Optics Communications **96**(4-6) 240–244 (1993). DOI [10.1016/0030-4018\(93\)90268-A](https://doi.org/10.1016/0030-4018(93)90268-A). [p 155]
- 285 N. Cyr, M. Breton, M. Tetu and S. Theriault. *Laser-diode frequency control by resonant phase-conjugate reflection from an atomic vapor.* Optics Letters **16**(17) 1298–1300 (1991). URL <http://www.opticsinfobase.org/abstract.cfm?id=59830>. [p 155]
- 286 C. J. Cuneo, J. J. Maki and D. H. McIntyre. *Optically stabilized diode laser using high-contrast saturated absorption.* Applied Physics Letters **64**(20) 2625–2627 (1994). DOI [10.1063/1.111498](https://doi.org/10.1063/1.111498). [p 155]
- 287 M. Kozuma, M. Kourogi, M. Ohtsu and H. Hori. *Frequency stabilization, linewidth reduction and fine detuning of a semiconductor laser by using velocity-selective optical pumping of atomic resonance line.* Applied Physics Letters **61**(16) 1895–1897 (1992). DOI [10.1063/1.108381](https://doi.org/10.1063/1.108381). [p 155]
- 288 Zi Dong Liu, D. Bloch and M. Ducloy. *Absolute active frequency locking of a diode laser with optical feedback generated by Doppler-free collinear polarization spectroscopy.* Applied Physics Letters **65**(3) 274–276 (1994). DOI [10.1063/1.112369](https://doi.org/10.1063/1.112369). [p 155]
- 289 Y. Shevy and Hua Deng. *Frequency-stable and ultranarrow-linewidth semiconductor laser locked directly to an atomic-cesium transition.* Optics Letters **23**(6) 472–474 (1998). URL <http://www.opticsinfobase.org/abstract.cfm?id=36644>. [p 156]
- 290 K. L. Corwin, Zheng-Tian Lu, C. F. Hand, R. J. Epstein and C. E. Wieman. *Frequency-stabilized diode laser with the Zeeman shift in an atomic vapor.* Applied Optics **37**(15) 3295–3298 (1998). URL <http://www.opticsinfobase.org/abstract.cfm?id=60553>. [p 156]
- 291 C. I. Sukenik, H. C. Busch and M. Shiddiq. *Modulation-free laser frequency stabilization and detuning.* Optics Communications **203**(1-2) 133–137 (2002). DOI [10.1016/S0030-4018\(02\)01126-4](https://doi.org/10.1016/S0030-4018(02)01126-4). [p 156]
- 292 Sang Eon Park, Ho Seong Lee, Taeg Yong Kwon and Hyuck Cho. *Dispersion-like signals in velocity-selective saturated-absorption spectroscopy.* Optics Communications **192**(1-2) 49–55 (2001). DOI [10.1016/S0030-4018\(01\)01155-5](https://doi.org/10.1016/S0030-4018(01)01155-5). [p 156]
- 293 H. S. Moon, Do-Young Jeong, Kwang-Hoon Ko and E. C. Jung. *Laser-induced birefringence by using a linearly polarized field in Na D<sub>1</sub> line and its application to laser frequency stabilization.* Optics Communications **228**(1-3) 133–138 (2003). DOI [10.1016/j.optcom.2003.09.090](https://doi.org/10.1016/j.optcom.2003.09.090). [p 156]

- 294 C. P. Pearman, C. S. Adams, S. G. Cox, P. F. Griffin, D. A. Smith and I. G. Hughes. *Polarization spectroscopy of a closed atomic transition: applications to laser frequency locking*. Journal of Physics B **35**(24) 5141–5151 (2002). DOI [10.1088/0953-4075/35/24/315](https://doi.org/10.1088/0953-4075/35/24/315). [p 156]
- 295 Y. Yoshikawa, T. Umeki, T. Mukae, Y. Torii and T. Kuga. *Frequency stabilization of a laser diode with use of light-induced birefringence in an atomic vapor*. Applied Optics **42**(33) 6645–6649 (2003). URL <http://www.opticsinfobase.org/abstract.cfm?id=77954>. [p 156]
- 296 N. P. Robins, B. J. J. Slagmolen, D. A. Shaddock, J. D. Close and M. B. Gray. *Interferometric, modulation-free laser stabilization*. Optics Letters **27**(21) 1905–1907 (2002). URL <http://www.opticsinfobase.org/abstract.cfm?id=70327>. [p 156]
- 297 R. Arndt. *Analytical line shapes for Lorentzian signals broadened by modulation*. Journal of Applied Physics **36**(8) 2522–2524 (1965). DOI [10.1063/1.1714523](https://doi.org/10.1063/1.1714523). [pp 156 and 161]
- 298 A. G. Truscott, N. R. Heckenberg and H. Rubinsztein-Dunlop. *Frequency stabilised grating feedback laser diode for atom cooling applications*. Optical & Quantum Electronics **31**(5-7) 417–430 (1999). DOI [10.1023/A:1006962911229](https://doi.org/10.1023/A:1006962911229). [p 157]
- 299 F. Allard, I. Maksimovic, M. Abgrall and P. Laurent. *Automatic system to control the operation of an extended cavity diode laser*. Review of Scientific Instruments **75**(1) 54–58 (2004). DOI [10.1063/1.1634359](https://doi.org/10.1063/1.1634359). [pp 157 and 165]
- 300 M. Levesque, A. Michaud, M. Tetu, S. Theriault, P. Tremblay, N. Cyr and M. Chamberland. *Frequency locking of a laser diode to an atomic resonance by use of an external phase modulator*. In *Proceedings of the Lasers and Electro-Optics Society Annual Meeting* (1990), pp. 277–278. [p 157]
- 301 N. Beverini, E. Maccioni, P. Marsili, A. Ruffini and F. Sorrentino. *Frequency stabilization of a diode laser on the Cs D<sub>2</sub> resonance line by the Zeeman effect in a vapor cell*. Applied Physics B **B73**(2) 133–138 (2001). DOI [10.1007/s003400100618](https://doi.org/10.1007/s003400100618). [p 157]
- 302 R. W. P. Drever, J. L. Hall, F. V. Kowalski, J. Hough, G. M. Ford, A. J. Munley and H. Ward. *Laser phase and frequency stabilization using an optical resonator*. Applied Physics B **B31**(2) 97–105 (1983). DOI [10.1007/BF00702605](https://doi.org/10.1007/BF00702605). [p 158]
- 303 G. C. Bjorklund. *Frequency-modulation spectroscopy: a new method for measuring weak absorptions and dispersions*. Optics Letters **5**(1) 15–17 (1980). URL <http://www.opticsinfobase.org/abstract.cfm?id=7054>. [p 158]
- 304 G. C. Bjorklund, M. D. Levenson, W. Lenth and C. Ortiz. *Frequency modulation (FM) spectroscopy. Theory of lineshapes and signal-to-noise analysis*. Applied Physics B **B32**(3) 145–152 (1983). DOI [10.1007/BF00688820](https://doi.org/10.1007/BF00688820). [p 158]
- 305 M. D. Levenson, W. E. Moerner and D. E. Horne. *FM spectroscopy detection of stimulated Raman gain*. Optics Letters **8**(2) 108–110 (1983). URL <http://www.opticsinfobase.org/abstract.cfm?id=7922>. [p 158]
- 306 C. S. Fletcher, J. E. Lye, N. P. Robins and J. D. Close. *A self-locked magneto-optic trap*. Optics Communications **212**(1-3) 85–88 (2002). DOI [10.1016/S0030-4018\(02\)01952-1](https://doi.org/10.1016/S0030-4018(02)01952-1). [p 158]
- 307 T. P. Dinneen, C. D. Wallace and P. L. Gould. *Narrow linewidth, highly stable, tunable diode laser system*. Optics Communications **92**(4-6) 277–282 (1992). DOI [10.1016/0030-4018\(92\)90636-6](https://doi.org/10.1016/0030-4018(92)90636-6). [p 158]

- 308 Miroslaw R. Walkiewicz. *Manipulation of Atoms using Laser Light*. Ph.D. thesis, University of Melbourne, School of Physics, Victoria 3010, Australia (2000). [p 160]
- 309 R. Pallas-Areny and J. G. Webster. *AC instrumentation amplifier for bioimpedance measurements*. IEEE Transactions on Biomedical Engineering **40**(8) 830–833 (1993). DOI [10.1109/10.238470](https://doi.org/10.1109/10.238470). [p 161]
- 310 M. F. Suesserman. *Bootstrapped, AC-coupled differential amplifier*. US Patent 5300896 (1994). [p 161]
- 311 W. Whitlock. *A new balanced audio input circuit for maximum common-mode rejection in real-world environments*. In *Proceedings of the 101st Convention of the Audio Engineering Society* (1996). Available as AES Preprint 4372, and covered by US Patent 5568561., URL <http://www.jensen-transformers.com/an/ingenaes.pdf>. [p 161]
- 312 M. L. Meade. *Lock-in Amplifiers: Principles and Applications*. Peter Peregrinus on behalf of the Institution of Electrical Engineers, London, UK (1983). ISBN 090604894X. [p 161]
- 313 A. B. Carlson. *Communication Systems : An Introduction to Signals and Noise in Electrical Communication*. McGraw-Hill, 3rd edn. (1986). ISBN 007009960X. [p 162]
- 314 K. Petermann. *Laser Diode Modulation and Noise*, vol. 3 of *Advances in Optoelectronics*. Kluwer Academic Publishers, Dordrecht, The Netherlands (1988). ISBN 9027726728. [p 163]
- 315 S. Kobayashi, Y. Yamamoto, M. Ito and T. Kimura. *Direct frequency modulation in AlGaAs semiconductor lasers*. IEEE Journal of Quantum Electronics **18**(4) 582–595 (1982). DOI [10.1109/JQE.1982.1071603](https://doi.org/10.1109/JQE.1982.1071603). [pp 163 and 164]
- 316 P. Tremblay and R. Ouellet. *Frequency response of a Fabry-Perot interferometer used as a frequency discriminator (semiconductor laser application)*. In G. R. Hanes (ed.), *CPEM '90 Digest. Conference on Precision Electromagnetic Measurements, Ottawa, Ont., Canada, 11–14 June 1990*. IEEE, New York, NY, USA (1990), pp. 252–253. Also published in IEEE Transactions on Instrumentation and Measurement **40** 204–207 (1991). [p 164]
- 317 B. Bodermann, H. R. Telle and R. P. Kovacich. *Amplitude-modulation-free optoelectronic frequency control of laser diodes*. Optics Letters **25**(12) 899–901 (2000). URL <http://www.opticsinfobase.org/abstract.cfm?id=551>. [p 164]
- 318 M. Prevedelli, T. Freegarde and T. W. Hänsch. *Phase locking of grating-tuned diode lasers*. Applied Physics B **60** S241–S248 (1995). [p 164]
- 319 A. Abramovici and J. Chapsky. *Feedback Control Systems: A Fast-Track Guide for Scientists and Engineers*. Kluwer Academic Publishers, Boston, MA, USA (2000). ISBN 0792379357. [pp 165 and 166]
- 320 B. J. Lurie and P. J. Enright. *Classical Feedback Control with MATLAB*. Marcel Dekker, New York, NY, USA (2000). ISBN 0824703707. [pp 165, 166 and 167]
- 321 A. Schoof, J. Grunert, S. Ritter and A. Hemmerich. *Reducing the linewidth of a diode laser below 30 Hz by stabilization to a reference cavity with a finesse above 10<sup>5</sup>*. Optics Letters **26**(20) 1562–1564 (2001). URL <http://www.opticsinfobase.org/abstract.cfm?id=65408>. [p 165]

- 322 G. Bianchini, P. Cancio, F. Minardi, F. S. Pavone, F. Perrone, M. Prevedelli and M. Inguscio. *Wide-bandwidth frequency locking of a 1083-nm extended-cavity DBR diode laser to a high-finesse Fabry-Perot resonator*. Applied Physics B **B66**(4) 407–410 (1998). DOI [10.1007/s003400050410](https://doi.org/10.1007/s003400050410). [p 165]
- 323 L. Hilico, D. Touahri, F. Nez and A. Clairon. *Narrow-line, low-amplitude noise semiconductor laser oscillator in the 780 nm range*. Review of Scientific Instruments **65**(12) 3628–3633 (1994). DOI [10.1063/1.1144483](https://doi.org/10.1063/1.1144483). [p 165]
- 324 G. W. Neat, J. W. Melody and B. J. Lurie. *Vibration attenuation approach for spaceborne optical interferometers*. IEEE Transactions on Control Systems Technology **6**(6) 689–700 (1998). DOI [10.1109/87.726529](https://doi.org/10.1109/87.726529). [p 166]
- 325 W. Jitschin and G. Meisel. *Fast frequency control of a cw dye jet laser*. Applied Physics **19**(2) 181–184 (1979). DOI [10.1007/BF00932394](https://doi.org/10.1007/BF00932394). [p 166]
- 326 W. V. Klitzing and R. J. Butcher. *Practical issues in the development of saturation spectroscopy at ultra-high resolution*. Measurement Science & Technology **9**(3) 417–421 (1998). DOI [10.1088/0957-0233/9/3/015](https://doi.org/10.1088/0957-0233/9/3/015). [p 166]
- 327 R. Kowalski, S. Root, S. D. Gensemer and P. L. Gould. *A frequency-modulated injection-locked diode laser for two-frequency generation*. Review of Scientific Instruments **72**(6) 2532–2534 (2001). DOI [10.1063/1.1373670](https://doi.org/10.1063/1.1373670). [p 168]
- 328 Christopher J. Vale. *Atomic Beam Techniques in a Rubidium Vapour Cell*. Ph.D. thesis, Victoria University of Technology, Melbourne, Australia (1999). [p 168]
- 329 Lincoln David Turner. *The Non-linear Spectroscopy of the Potassium D<sub>2</sub> line*. Honours thesis, Flinders University, Department of Physics, Adelaide, Australia (1998). [p 168]
- 330 C. Campbell. *Fresnel diffraction of Gaussian laser beams by circular apertures*. Optical Engineering **26**(3) 270–275 (1987). [p 170]
- 331 W. Ketterle, D. S. Durfee and D. M. Stamper-Kurn. *Making, probing and understanding Bose-Einstein condensates*. In M. Inguscio, S. Stringari and C. Wieman (eds.), *Bose-Einstein condensation in atomic gases: Proceedings of the International School of Physics “Enrico Fermi”, Varenna, Italy*. IOS Press, Amsterdam (1999), vol. Course CXL, pp. 67–176. URL <http://arxiv.org/abs/cond-mat/9904034>. [pp 178, 184, 239 and 241]
- 332 A. Robert, O. Sirjean, A. Browaeys, J. Poupard, S. Nowak, D. Boiron, C. I. Westbrook and A. Aspect. *A Bose-Einstein condensate of metastable atoms*. Science **292**(5516) 461–464 (2001). DOI [10.1126/science.1060622](https://doi.org/10.1126/science.1060622). [p 178]
- 333 G. D. Domenico, G. Miletí and P. Thomann. *Pump-probe spectroscopy and velocimetry of cold atoms in a slow beam*. Physical Review A **64**(4) 043408 (pages 5) (2001). DOI [10.1103/PhysRevA.64.043408](https://doi.org/10.1103/PhysRevA.64.043408). [p 178]
- 334 N. Read and N. R. Cooper. *Free expansion of lowest-Landau-level states of trapped atoms: A wave-function microscope*. Physical Review A **68**(3) 035601 (pages 4) (2003). DOI [10.1103/PhysRevA.68.035601](https://doi.org/10.1103/PhysRevA.68.035601). [pp 178 and 183]
- 335 K. Toyoda, Y. Takahashi and T. Yabuzaki. *Magnetic resonance imaging of Bose-Einstein condensates*. Applied Physics B **B74**(2) 115–120 (2002). DOI [10.1007/s003400100775](https://doi.org/10.1007/s003400100775). [p 179]

- 336 V. Savalli, G. Z. K. Horvath, P. D. Featonby, L. Cognet, N. Westbrook, C. I. Westbrook and A. Aspect. *Optical detection of cold atoms without spontaneous emission*. Optics Letters **24**(22) 1552–1554 (1999). URL <http://www.opticsinfobase.org/abstract.cfm?id=37522>. [p 179]
- 337 J. E. Lye, B. D. Cuthbertson, H.-A. Bachor and J. D. Close. *Phase modulation spectroscopy: a non-destructive probe of Bose-Einstein condensates*. Journal of Optics B: Quantum & Semiclassical Optics **1**(4) 402–407 (1999). DOI [10.1088/1464-4266/1/4/308](https://doi.org/10.1088/1464-4266/1/4/308). [p 179]
- 338 J. E. Lye, J. J. Hope and J. D. Close. *Rapid real-time detection of cold atoms with minimal destruction*. Physical Review A **69**(2) 023601 (pages 5) (2004). DOI [10.1103/PhysRevA.69.023601](https://doi.org/10.1103/PhysRevA.69.023601). [p 179]
- 339 K. Rzążewski and R. W. Boyd. *Equivalence of interaction Hamiltonians in the electric dipole approximation*. Journal of Modern Optics **51**(8) 1137–1147 (2004). DOI [10.1080/09500340310001631635](https://doi.org/10.1080/09500340310001631635). [pp 179 and 181]
- 340 R. Loudon. *The Quantum Theory of Light*. Oxford University Press, London, 1st edn. (1973). ISBN 0198511302. The second edition [342] contains a much reduced discussion of frequency-dependent polarisability in §2.8. [pp 180, 181 and 194]
- 341 P. A. M. Dirac. *The Principles of Quantum Mechanics*. Oxford University Press, London, 4th edn. (1958). [p 180]
- 342 R. Loudon. *The Quantum Theory of Light*. Oxford University Press, London, 2nd edn. (1983). ISBN 0198511558. [pp 181 and 284]
- 343 J. A. Andersen, M. E. J. Friese, A. G. Truscott, Z. Ficek, P. D. Drummond, N. R. Heckenberg and H. Rubinsztein-Dunlop. *Light guiding light: Nonlinear refraction in rubidium vapor*. Physical Review A **63**(2) 023820 (2001). DOI [10.1103/PhysRevA.63.023820](https://doi.org/10.1103/PhysRevA.63.023820). [p 181]
- 344 N. Bloembergen and Y. R. Shen. *Quantum-theoretical comparison of nonlinear susceptibilities in parametric media, lasers and Raman lasers*. Physical Review **133**(1A) A37 (1964). DOI [10.1103/PhysRev.133.A37](https://doi.org/10.1103/PhysRev.133.A37). [p 181]
- 345 A. S. Parkins and D. F. Walls. *The physics of trapped dilute-gas Bose-Einstein condensates*. Physics Reports **303**(1) 1–80 (1998). DOI [10.1016/S0370-1573\(98\)00014-3](https://doi.org/10.1016/S0370-1573(98)00014-3). [p 182]
- 346 O. Morice, Y. Castin and J. Dalibard. *Refractive index of a dilute Bose gas*. Physical Review A **51**(5) 3896–3901 (1995). DOI [10.1103/PhysRevA.51.3896](https://doi.org/10.1103/PhysRevA.51.3896). [p 182]
- 347 J. Javanainen and J. Ruostekoski. *Off-resonance light scattering from low-temperature Bose and Fermi gases*. Physical Review A **52**(4) 3033–3046 (1995). DOI [10.1103/PhysRevA.52.3033](https://doi.org/10.1103/PhysRevA.52.3033). [p 182]
- 348 J. Javanainen, J. Ruostekoski, B. Vestergaard and M. R. Francis. *One-dimensional modeling of light propagation in dense and degenerate samples*. Physical Review A **59**(1) 649–666 (1999). DOI [10.1103/PhysRevA.59.649](https://doi.org/10.1103/PhysRevA.59.649). [p 182]
- 349 L. V. Hau, B. D. Busch, Chien Liu, Z. Dutton, M. M. Burns and J. A. Golovchenko. *Near-resonant spatial images of confined Bose-Einstein condensates in a 4-Dee magnetic bottle*. Physical Review A **58**(1) R54–R57 (1998). DOI [10.1103/PhysRevA.58.R54](https://doi.org/10.1103/PhysRevA.58.R54). [p 183]

- 350 D. G. Fried, T. C. Killian, L. Willmann, D. Landhuis, S. C. Moss, D. Kleppner and T. J. Greytak. *Bose-Einstein condensation of atomic hydrogen*. Physical Review Letters **81**(18) 3811–3814 (1998). DOI [10.1103/PhysRevLett.81.3811](https://doi.org/10.1103/PhysRevLett.81.3811). [p 183]
- 351 A. F. Molisch and B. P. Oehry. *Radiation Trapping in Atomic Vapours*. Oxford University Press, London (1999). ISBN 0198538669. [p 184]
- 352 J. Dziarmaga and K. Sacha. *Bose-Einstein-condensate heating by atomic losses*. Physical Review A **68**(4) 043607 (pages 5) (2003). DOI [10.1103/PhysRevA.68.043607](https://doi.org/10.1103/PhysRevA.68.043607). [p 184]
- 353 M. R. Andrews, D. M. Kurn, H.-J. Miesner, D. S. Durfee, C. G. Townsend, S. Inouye and W. Ketterle. *Propagation of sound in a Bose-Einstein condensate*. Physical Review Letters **79**(4) 553–556 (1997). DOI [10.1103/PhysRevLett.79.553](https://doi.org/10.1103/PhysRevLett.79.553). [pp 185, 186 and 242]
- 354 M. R. Andrews, M.-O. Mewes, N. J. V. Druten, D. S. Durfee, D. M. Kurn and W. Ketterle. *Direct, nondestructive observation of a Bose condensate*. Science **273**(5271) 84–87 (1996). [pp 187, 189 and 238]
- 355 H. D. Politzer. *Bose-stimulated scattering off a cold atom trap*. Physical Review A **55**(2) 1140–1146 (1997). DOI [10.1103/PhysRevA.55.1140](https://doi.org/10.1103/PhysRevA.55.1140). [p 188]
- 356 S. Inouye, A. P. Chikkatur, D. M. Stamper-Kurn, J. Stenger, D. E. Pritchard and W. Ketterle. *Superradiant Rayleigh scattering from a Bose-Einstein condensate*. Science **285**(5427) 571–574 (1999). DOI [10.1126/science.285.5427.571](https://doi.org/10.1126/science.285.5427.571). [p 188]
- 357 S. Inouye, R. F. Low, S. Gupta, T. Pfau, A. Gorlitz, T. L. Gustavson, D. E. Pritchard and W. Ketterle. *Amplification of light and atoms in a Bose-Einstein condensate*. Physical Review Letters **85**(20) 4225–4228 (2000). DOI [10.1103/PhysRevLett.85.4225](https://doi.org/10.1103/PhysRevLett.85.4225). [p 188]
- 358 O. E. Mustecaplioglu and L. You. *Superradiant light scattering from trapped Bose-Einstein condensates*. Physical Review A **62**(6) 063615 (2000). DOI [10.1103/PhysRevA.62.063615](https://doi.org/10.1103/PhysRevA.62.063615). [p 188]
- 359 M. G. Moore and P. Meystre. *Theory of superradiant scattering of laser light from Bose-Einstein condensates*. Physical Review Letters **83**(25) 5202–5205 (1999). DOI [10.1103/PhysRevLett.83.5202](https://doi.org/10.1103/PhysRevLett.83.5202). [p 188]
- 360 D. Schneble, Y. Torii, M. Boyd, E. W. Streed, D. E. Pritchard and W. Ketterle. *The onset of matter-wave amplification in a superradiant Bose-Einstein condensate*. Science **300**(5618) 475–478 (2003). DOI [10.1126/science.1083171](https://doi.org/10.1126/science.1083171). [p 188]
- 361 U. Leonhardt, T. Kiss and P. Piwnicki. *Quantum backaction of optical observations on Bose-Einstein condensates*. European Physical Journal D **7**(3) 413–423 (1999). DOI [10.1007/s100530050585](https://doi.org/10.1007/s100530050585). [p 189]
- 362 W. Ketterle. *Comment on Quantum backaction of optical observations on Bose-Einstein condensates by U. Leonhardt, T. Kiss, and P. Piwnicki*. European Physical Journal D **12**(1) 123 (2000). DOI [10.1007/s100530070047](https://doi.org/10.1007/s100530070047). [p 189]
- 363 U. Leonhardt, T. Kiss and P. Piwnicki. *Reply to the comment on Quantum backaction of optical observations on Bose-Einstein condensates*. European Physical Journal D **12**(1) 124 (2000). DOI [10.1007/s100530070048](https://doi.org/10.1007/s100530070048). [p 189]

- 364 V. B. Braginsky and F. Y. Khalili. *Quantum Measurement*. Cambridge University Press, Cambridge, UK (1992). ISBN 052141928X. [p 189]
- 365 D. A. R. Dalvit, J. Dziarmaga and R. Onofrio. *Measurement-induced squeezing of a Bose-Einstein condensate*. Physical Review A **65**(3) 033620 (2002). DOI [10.1103/PhysRevA.65.033620](https://doi.org/10.1103/PhysRevA.65.033620). [p 189]
- 366 F. Strauch, V. Gomer, H. Schadwinkel, B. Ueberholz, D. Haubrich and D. Meschede. *Diffraction by cold atoms*. Optics Communications **145**(1-6) 57–63 (1998). DOI [10.1016/S0030-4018\(97\)00470-7](https://doi.org/10.1016/S0030-4018(97)00470-7). [p 191]
- 367 D. A. Steck. *Rubidium 87 D-line data, revision 1.6*. Web document LA-UR-03-8638, Los Alamos National Laboratory, Theoretical Division T-8 (2001). URL <http://steck.us/alkalidata>. [pp 192, 194 and 195]
- 368 I. I. Sobelman. *Atomic Spectra and Radiative Transitions*, vol. 1. Springer-Verlag, Berlin (1979). ISBN 3540090827. Translation of *Vvedenie v teoriyu atomnykh spectrov* [Introduction to the theory of atomic spectra], Nauka, Moscow (1977). [pp 193 and 194]
- 369 A. R. Edmonds. *Angular Momentum in Quantum Mechanics*. Princeton University Press, Princeton, NJ, USA, 2nd edn. (1960). ISBN 0691025894. [p 196]
- 370 V. Gomer and D. Meschede. *A single trapped atom: light-matter interaction at the microscopic level*. Annalen der Physik **10**(1-2) 9–18 (2001). DOI [10.1002/1521-3889\(200102\)10:1/2<9::AID-ANDP9>3.0.CO;2-#](https://doi.org/10.1002/1521-3889(200102)10:1/2<9::AID-ANDP9>3.0.CO;2-#). [p 196]
- 371 J. W. Cooley and J. W. Tukey. *An algorithm for the machine calculation of complex Fourier series*. Mathematics of Computation **19** 297–301 (1965). [pp 209 and 314]
- 372 M. Frigo and S. G. Johnson. *FFTW: An adaptive software architecture for the FFT*. In *Proceedings of the IEEE International Conference on Acoustics, Speech, and Signal Processing (ICASSP)*. Seattle, WA, USA (1998), vol. 3, pp. 1381–1384. The FFTW library and documentation are available online at <http://www.fftw.org/>,. URL <http://www.fftw.org/fftw-paper-icassp.pdf>. [p 210]
- 373 A. Reigber. *FFTW for IDL*. Web document, Epsilon.Nought: Radar Remote Sensing (2003). URL [http://epsilon.nought.de/idl\\_fftw.html](http://epsilon.nought.de/idl_fftw.html). [p 210]
- 374 D. J. Bernstein. *djbfft*. Web document (1999). URL <http://cr.yp.to/djbfft.html>. [p 210]
- 375 H. V. Sorensen, D. L. Jones, M. T. Heideman and C. S. Burrus. *Real-valued fast Fourier transform algorithms*. IEEE Transactions on Acoustics, Speech, & Signal Processing **35**(6) 849–863 (1987). DOI [10.1109/TASSP.1987.1165220](https://doi.org/10.1109/TASSP.1987.1165220). [p 210]
- 376 I. S. Uzun, A. Amira and A. Bouridane. *FPGA implementations of fast Fourier transforms for real-time signal and image processing*. In *Proceedings of the IEEE Conference on Field-Programmable Technology (FPT)*. IEEE (2003). URL <http://www.celoxica.com/techlib/files/CEL-Wo402101462-250.pdf>. [p 210]
- 377 A. Benkrid, K. Benkrid and D. Crookes. *Design and implementation of a generic 2D orthogonal discrete wavelet transform on FPGA*. In *Proceedings of the 11th Annual IEEE Symposium on Field-Programmable Custom Computing Machines*. IEEE, Napa, CA, USA (2003), pp. 162–172. [p 210]

- 378 J. L. Devore. *Probability and Statistics for Engineering and the Sciences*. Brooks/Cole, Pacific Grove, CA, USA, 3rd edn. (1991). ISBN 0534143520. [p 216]
- 379 L. D. Turner, K. F. E. M. Domen and R. E. Scholten. *Diffraction-contrast imaging of cold atoms*. Submitted to Physical Review Letters (2005). arXiv:physics/0501057, URL <http://arxiv.org/abs/physics/0501057>. [pp 224 and 257]
- 380 E. R. I. Abraham and E. A. Cornell. *Teflon feedthrough for coupling optical fibers into ultrahigh vacuum systems*. Applied Optics 37(10) 1762–1763 (1998). URL <http://www.opticsinfobase.org/abstract.cfm?id=43646>. [p 225]
- 381 A. J. den Dekker and A. van den Bos. *Resolution: a survey*. Journal of the Optical Society of America A 14(3) 547–557 (1997). URL <http://www.opticsinfobase.org/abstract.cfm?id=68810>. [p 230]
- 382 P. Hariharan. *Optical Holography: Principles, Techniques and Applications*. Cambridge University Press, Cambridge, UK (1984). ISBN 0521243483. [p 231]
- 383 E. Abbe. *Beitrage zur theorie des mikroskops und der mikroskopischen wahrnehmung [Contributions to the theory of the microscope and microscopic observation]*. Archiv für mikroskopische Anatomie und Entwicklungsmechanik 9 413–468 (1873). [p 232]
- 384 A. J. Walton. *The Abbé theory of imaging: an alternative derivation of the resolution limit*. European Journal of Physics 7(1) 62–63 (1986). DOI [10.1088/0143-0807/7/1/112](https://doi.org/10.1088/0143-0807/7/1/112). [pp 232 and 233]
- 385 W. T. Cathey. *Optical Information Processing and Holography*. John Wiley & Sons, New York (1974). ISBN 0471140783. [p 232]
- 386 S. Herman. *Quasigeometric approach to the Fourier analysis of imaging lenses*. Journal of the Optical Society of America 61(10) 1428–1429 (1971). [p 232]
- 387 W. T. Cathey. *Angular spectrum and coherent imaging*. Journal of the Optical Society of America 64(11) 1503–1506 (1974). URL <http://www.opticsinfobase.org/abstract.cfm?id=55518>. [p 233]
- 388 D. Slepian and H. Pollak. *Prolate spheroidal wave functions, Fourier analysis and uncertainty – I*. Bell System Technical Journal 40(1) 43–64 (1961). [p 233]
- 389 H. J. Landau and H. Pollak. *Prolate spheroidal wave functions, Fourier analysis and uncertainty – II*. Bell System Technical Journal 40(11) 65–84 (1961). [p 233]
- 390 D. Slepian and H. Pollak. *Prolate spheroidal wave functions, Fourier analysis and uncertainty – III: The dimension of essentially time-and band-limited signals*. Bell System Technical Journal 41(7) 1295–1336 (1962). [p 233]
- 391 D. Slepian. *Prolate spheroidal wave functions, Fourier analysis and uncertainty – IV: Extensions to many dimensions; generalized prolate spheroidal functions*. Bell System Technical Journal 43(11) 3009–3058 (1964). [p 233]
- 392 D. Slepian. *Prolate spheroidal wave functions, Fourier analysis and uncertainty – V: The discrete case*. Bell System Technical Journal 57(3) 1371–1430 (1978). [p 233]

- 393 F. Gori and R. Grella. *The converging prolate spheroidal functions and their use in Fresnel optics*. Optics Communications **45**(1) 5–10 (1983). DOI [10.1016/0030-4018\(83\)90398-X](https://doi.org/10.1016/0030-4018(83)90398-X). [p 233]
- 394 M. Bertero and E. R. Pike. *Resolution in diffraction-limited imaging, a singular value analysis. I. The case of coherent illumination*. Optica Acta **29**(6) 727–746 (1982). [p 233]
- 395 A. Thaning, P. Martinsson, M. Karelín and A. T. Friberg. *Limits of diffractive optics by communication modes*. Journal of Optics A: Pure & Applied Optics **5**(3) 153–158 (2003). DOI [10.1088/1464-4258/5/3/301](https://doi.org/10.1088/1464-4258/5/3/301). [p 233]
- 396 A. VanderLugt. *Optimum sampling of Fresnel transforms*. Applied Optics **29**(23) 3352–3361 (1990). URL <http://www.opticsinfobase.org/abstract.cfm?id=37791>. [p 233]
- 397 A. Stern and B. Javidi. *Sampling in the light of Wigner distribution*. Journal of the Optical Society of America A **21**(3) 360–366 (2004). DOI [10.1364/JOSAA.21.000360](https://doi.org/10.1364/JOSAA.21.000360). [p 233]
- 398 A. W. Lohmann, M. E. Testorf and J. Ojeda-Castañeda. *Holography and the Wigner function*. In H. J. Caulfield (ed.), *Holography: A tribute to Yuri Denisyuk and Emmett Leith* (2002), vol. 4737 of *Proceedings of the SPIE*, pp. 77–88. DOI [10.1117/12.474960](https://doi.org/10.1117/12.474960). [p 233]
- 399 A. W. Lohmann, R. G. Dorsch, D. Mendlovic, Z. Zalevsky and C. Ferreira. *Space-bandwidth product of optical signals and systems*. Journal of the Optical Society of America A **13**(3) 470–473 (1996). URL <http://www.opticsinfobase.org/abstract.cfm?id=17375>. [p 233]
- 400 Michael Robin Matthews. *Two-component Bose-Einstein condensation*. Ph.D. thesis, University of Colorado, JILA, Boulder CO, USA (1999). URL [http://jila.ww.colorado.edu/pubs/thesis/matthews/matthews\\_thesis.pdf](http://jila.ww.colorado.edu/pubs/thesis/matthews/matthews_thesis.pdf). [pp 237, 241 and 242]
- 401 Jason Remington Ensher. *The first experiments with Bose-Einstein condensation of <sup>87</sup>Rb*. Ph.D. thesis, University of Colorado, JILA, Boulder CO, USA (1998). URL [http://jila.ww.colorado.edu/pubs/thesis/ensher/ensher\\_thesis.pdf](http://jila.ww.colorado.edu/pubs/thesis/ensher/ensher_thesis.pdf). [p 237]
- 402 A. Toepler. *Beobachtungen nach Einer Neuen Optischen Methode – Ein Beitrag zur Experimentalphysik [Observations According to a New Optical Method – A Contribution to Experimental Physics]*. M. Cohen & Son, Bonn (1864). [p 238]
- 403 J. Gluckstad and P. C. Mogensen. *Optimal phase contrast in common-path interferometry*. Applied Optics **40**(2) 268–282 (2001). URL <http://www.opticsinfobase.org/abstract.cfm?id=62826>. [pp 239 and 241]
- 404 F. Zernike. *How I discovered phase contrast*. Science **121**(3141) 345–349 (1955). Modified excerpts from the Nobel lecture <http://nobelprize.org/physics/laurates/1953/zernike-lecture.pdf>. [p 239]
- 405 F. Zernike. *Phase-contrast, a new method for microscopic observation of transparent objects. Parts I and II*. Physica (Utrecht) **9** 686–698, 974–986 (1942). [p 239]
- 406 F. Zernike. *Das phasenkontrastverfahren bei der mikroskopischen beobachtung [Phase-contrast methods in microscopic observations]*. Zeitschrift für Technische Physik **16** 454–457 (1935). [p 239]

- 407 C. S. Anderson. *Fringe visibility, irradiance, and accuracy in common path interferometers for visualization of phase disturbances.* Applied Optics **34**(32) 7474–7485 (1995). URL <http://www.opticsinfobase.org/abstract.cfm?id=45515>. [p 241]
- 408 M. R. Andrews, C. G. Townsend, H.-J. Miesner, D. S. Durfee, D. M. Kurn and W. Ketterle. *Observation of interference between two Bose condensates.* Science **275**(5300) 637–641 (1997). DOI [10.1126/science.275.5300.637](https://doi.org/10.1126/science.275.5300.637). [p 241]
- 409 H.-J. Miesner, D. M. Stamper-Kurn, M. R. Andrews, D. S. Durfee, S. Inouye and W. Ketterle. *Bosonic stimulation in the formation of a Bose-Einstein condensate.* Science **279**(5353) 1005–1007 (1998). DOI [10.1126/science.279.5353.1005](https://doi.org/10.1126/science.279.5353.1005). [p 242]
- 410 S. Inouye, M. R. Andrews, J. Stenger, H.-J. Miesner, D. M. Stamper-Kurn and W. Ketterle. *Observation of Feshbach resonances in a Bose-Einstein condensate.* Nature (London) **392**(6672) 151–154 (1998). DOI [10.1038/32354](https://doi.org/10.1038/32354). [p 242]
- 411 D. M. Stamper-Kurn, H.-J. Miesner, S. Inouye, M. R. Andrews and W. Ketterle. *Collisionless and hydrodynamic excitations of a Bose-Einstein condensate.* Physical Review Letters **81**(3) 500–503 (1998). DOI [10.1103/PhysRevLett.81.500](https://doi.org/10.1103/PhysRevLett.81.500). [p 242]
- 412 R. Onofrio, D. S. Durfee, C. Raman, M. Kohl, C. E. Kuklewicz and W. Ketterle. *Surface excitations of a Bose-Einstein condensate.* Physical Review Letters **84**(5) 810–813 (2000). DOI [10.1103/PhysRevLett.84.810](https://doi.org/10.1103/PhysRevLett.84.810). [p 242]
- 413 R. Onofrio, C. Raman, J. M. Vogels, J. R. Abo-Shaeer, A. P. Chikkatur and W. Ketterle. *Observation of superfluid flow in a Bose-Einstein condensed gas.* Physical Review Letters **85**(11) 2228–2231 (2000). DOI [10.1103/PhysRevLett.85.2228](https://doi.org/10.1103/PhysRevLett.85.2228). [p 242]
- 414 C. Raman, J. R. Abo-Shaeer, J. M. Vogels, K. Xu and W. Ketterle. *Vortex nucleation in a stirred Bose-Einstein condensate.* Physical Review Letters **87**(21) 210402 (2001). DOI [10.1103/PhysRevLett.87.210402](https://doi.org/10.1103/PhysRevLett.87.210402). [p 242]
- 415 M. R. Matthews, B. P. Anderson, P. C. Haljan, D. S. Hall, M. J. Holland, J. E. Williams, C. E. Wieman and E. A. Cornell. *Watching a superfluid untwist itself: recurrence of Rabi oscillations in a Bose-Einstein condensate.* Physical Review Letters **83**(17) 3358–3361 (1999). DOI [10.1103/PhysRevLett.83.3358](https://doi.org/10.1103/PhysRevLett.83.3358). [p 242]
- 416 M. R. Matthews, B. P. Anderson, P. C. Haljan, D. S. Hall, C. E. Wieman and E. A. Cornell. *Vortices in a Bose-Einstein condensate.* Physical Review Letters **83**(13) 2498–2501 (1999). DOI [10.1103/PhysRevLett.83.2498](https://doi.org/10.1103/PhysRevLett.83.2498). [p 242]
- 417 P. C. Haljan, I. Coddington, P. Engels and E. A. Cornell. *Driving Bose-Einstein-condensate vorticity with a rotating normal cloud.* Physical Review Letters **87**(21) 210403 (2001). DOI [10.1103/PhysRevLett.87.210403](https://doi.org/10.1103/PhysRevLett.87.210403). [p 242]
- 418 B. P. Anderson, P. C. Haljan, C. E. Weiman and E. A. Cornell. *Vortex precession in Bose-Einstein condensates: observations with filled and empty cores.* Physical Review Letters **85**(14) 2857–2860 (2000). DOI [10.1103/PhysRevLett.85.2857](https://doi.org/10.1103/PhysRevLett.85.2857). [p 242]
- 419 P. Engels, I. Coddington, P. C. Haljan and E. A. Cornell. *Nonequilibrium effects of anisotropic compression applied to vortex lattices in Bose-Einstein condensates.* Physical Review Letters **89**(10) 100403 (2002). DOI [10.1103/PhysRevLett.89.100403](https://doi.org/10.1103/PhysRevLett.89.100403). [p 242]

- 420 I. Coddington, P. C. Haljan, P. Engels, V. Schweikhard, S. Tung and E. A. Cornell. *Experimental studies of equilibrium vortex properties in a Bose-condensed gas*. Physical Review A **70** (2004). DOI [10.1103/PhysRevA.70.063607](https://doi.org/10.1103/PhysRevA.70.063607). [p 242]
- 421 J. M. Gerton, D. Strekalov, I. Prodan and R. G. Hulet. *Direct observation of growth and collapse of a Bose-Einstein condensate with attractive interactions*. Nature (London) **408**(6813) 692–695 (2000). DOI [10.1038/35047030](https://doi.org/10.1038/35047030). [pp 242 and 251]
- 422 M. D. I. Castillo, D. Sanchez de la Llave, R. R. Garcia, L. I. Olivos-Perez, L. A. Gonzalez and M. Rodriguez-Ortiz. *Real-time self-induced nonlinear optical Zernike-type filter in a bacteriorhodopsin film*. Optical Engineering **40**(11) 2367–2368 (2001). DOI [10.1117/1.1412425](https://doi.org/10.1117/1.1412425). [p 242]
- 423 K. Komorowska, A. Miniewicz, J. Parka and F. Kajzar. *Self-induced nonlinear Zernike filter realized with optically addressed liquid crystal spatial light modulator*. Journal of Applied Physics **92**(10) 5635–5641 (2002). DOI [10.1063/1.1515949](https://doi.org/10.1063/1.1515949). [p 242]
- 424 Junmin Liu, Jingjun Xu, Guangyin Zhang and Simin Liu. *Phase contrast using photorefractive LiNbO<sub>3</sub>:Fe crystals*. Applied Optics **34**(22) 4972–4975 (1995). URL <http://www.opticsinfobase.org/abstract.cfm?id=46187>. [p 242]
- 425 S. Kadlecak, J. Sebby, R. Newell and T. G. Walker. *Nondestructive spatial heterodyne imaging of cold atoms*. Optics Letters **26**(3) 137–139 (2001). URL <http://www.opticsinfobase.org/abstract.cfm?id=63027>. [pp 242, 244 and 245]
- 426 R. G. Racca and J. M. Dewey. *Time smear effects in spatial frequency multiplexed holography*. Applied Optics **28**(17) 3652–3656 (1989). URL <http://www.opticsinfobase.org/abstract.cfm?id=32746>. [p 245]
- 427 Zhiwen Liu, M. Centurion, G. Panotopoulos, J. Hong and D. Psaltis. *Holographic recording of fast events on a CCD camera*. Optics Letters **27**(1) 22–24 (2002). URL <http://www.opticsinfobase.org/abstract.cfm?id=67266>. [p 245]
- 428 J. E. Lye, J. J. Hope and J. D. Close. *Nondestructive dynamic detectors for Bose-Einstein condensates*. Physical Review A **67**(4) 043609 (pages 13) (2003). DOI [10.1103/PhysRevA.67.043609](https://doi.org/10.1103/PhysRevA.67.043609). [pp 247, 248 and 251]
- 429 J. J. Hope and J. D. Close. *Limit to non-destructive optical detection of atoms*. Physical Review Letters **93** (2004). DOI [10.1103/PhysRevLett.93.180402](https://doi.org/10.1103/PhysRevLett.93.180402). [pp 247 and 251]
- 430 Y. Jiang, O. Jedrkiewicz, S. Minardi, P. D. Trapani, A. Mosset, E. Lantz and F. Devaux. *Retrieval of spatial shot-noise in the full dynamic range of calibrated CCD cameras*. European Physical Journal D **22**(3) 521–526 (2003). DOI [10.1140/epjd/e2003-00002-4](https://doi.org/10.1140/epjd/e2003-00002-4). [p 249]
- 431 H. M. Ozaktas, B. Barshan, D. Mendlovic and L. Onural. *Convolution, filtering, and multiplexing in fractional Fourier domains and their relation to chirp and wavelet transforms*. Journal of the Optical Society of America A **11**(2) 547–559 (1994). URL <http://www.opticsinfobase.org/abstract.cfm?id=614>. [p 250]
- 432 L. Stankovic, S. Stankovic and I. Djurovic. *Space/spatial-frequency analysis based filtering*. IEEE Transactions on Signal Processing **48**(8) 2343–2352 (2000). DOI [10.1109/78.852015](https://doi.org/10.1109/78.852015). [p 250]

- 433 C. A. Sackett, C. C. Bradley, M. Welling and R. G. Hulet. *Bose-Einstein condensation of lithium*. Applied Physics B **B65**(4-5) 433–440 (1997). DOI [10.1007/s003400050293](https://doi.org/10.1007/s003400050293). [pp 250 and 251]
- 434 E. Arimondo. *Coherent population trapping in laser spectroscopy*. Progress in Optics **35** 257–354 (1995). [p 251]
- 435 R. Folman, P. Krueger, J. Schmiedmayer, J. Denschlag and C. Henkel. *Microscopic atom optics: from wires to an atom chip*. In B. Bederson and H. Walther (eds.), *Advances in Atomic, Molecular and Optical Physics*, Academic Press, San Diego, vol. 48, pp. 263–355 (2002). ISBN 012003848X. [pp 252 and 257]
- 436 M. Vengalattore, R. S. Conroy, W. Rooijakkers and M. Prentiss. *Ferromagnets for integrated atom optics*. Journal of Applied Physics **95**(8) 4404–4407 (2004). DOI [10.1063/1.1667598](https://doi.org/10.1063/1.1667598). [p 252]
- 437 J.-P. Guigay, R. H. Wade and C. Delpha. *Optical diffraction of Lorentz microscope images*. In *Proceedings of the 25th Anniversary meeting of EMAG*. Electron Microscopy and Analysis Group, Institute of Physics (1971), pp. 238–239. ISBN 0854981004. [p 256]
- 438 H. M. Ozaktas, Z. Zalevsky and M. A. Kutay. *The Fractional Fourier Transform with Applications in Optics and Signal Processing*. John Wiley & Sons, New York (2001). ISBN 0471963461. [p 261]
- 439 H. J. Metcalf and P. van der Straten. *Laser cooling and trapping*. In M. Bass, J. M. Enoch, E. van Strykland and W. L. Wolfe (eds.), *Handbook of Optics*, McGraw-Hill, New York, vol. III (2001). ISBN 0071354085. URL <http://www.phys.uu.nl/~straten/preprint/handpubl.pdf>. [p 277]
- 440 O. Wiener. *Stehende lichtwellen und die schwingungsrichtung polarisierten lichtes [Standing lightwaves and the direction of polarised light]*. Annalen der Physik (Leipzig) **40** 203–243 (1890). In German. [p 301]
- 441 Y. A. Kravtsov and Y. I. Orlov. *Geometrical Optics of Inhomogeneous Media*. Springer-Verlag, Berlin (1990). ISBN 3540519440/0387519440. Translation of *Geometricheskaja optika neodnorodnykh sred*. [p 303]
- 442 D. Hilbert. *Begründung der elementaren strahlungstheorie [Fundamental radiation theory]*. Physikalische Zeitschrift **13** 1056–1064 (1912). In German. [p 304]
- 443 I. E. Arsaev and B. E. Kinber. *Geometrical optics approach in the study of the propagation of waves in nonuniform absorbing media*. Radiophysics and Quantum Electronics **11** 781–786 (1968). DOI [10.1007/BF01080823](https://doi.org/10.1007/BF01080823). Translation of Izvestiya Vysshikh Uchebnykh Zavedenii Radiofizika (USSR), vol. 11(9), pp. 1377–87 (1968). [p 304]
- 444 J. C. van den Berg (ed.). *Wavelets in Physics*. Cambridge University Press, Cambridge, UK (1999). ISBN 0521593115. [pp 307 and 308]
- 445 B. B. Hubbard. *The World According to Wavelets: The story of a mathematical technique in the making*. A. K. Peters, Wellesley, MA, USA, 2nd edn. (1998). ISBN 1568810725. [pp 307, 314 and 315]

- 446 M. Unser and Wavelet Digest Steering Committee. *The Wavelet Digest*. Website and e-mail newsletter, Swiss Federal Institute of Technology Lausanne EPFL (1992–).  
URL <http://www.wavelet.org/>. [p 307]

# Author index to references

In this thesis, references are numbered in citation order. Following is an index giving the reference numbers for all authors cited. The pages on which a given author is cited may be found first by looking up the reference number in this index, and then following the back-references given in the desired citation.

- |  |  |  |
|--|--|--|
| Abbe, E. 383                           | Babic, V. M. 18  | Boiron, D. 332                                     |
| Abgrall, M. 299                        | Bachor, H.-A. 337                                      | Born, M. 19  |
| Abo-Shaeer, J. R. 413, 414             | Bacry, H. 65   | Borrmann, S. 77                                    |
| Abraham, E. R. I. 380                  | Bajt, S. 98  | Boshier, M. G. 264                                 |
| Abramovici, A. 319                     | Balboa, R. M. 180                                      | Boucher, R. H. 111                                 |
| Adams, C. S. 255, 294                  | Banerjee, A. 262                                       | Bouridane, A. 376                                  |
| Addiss, R. R. 251                      | Banham, M. R. 166                                      | Boyd, M. 360                                       |
| Adrian, M. 146                         | Barakat, R. 107  | Boyd, R. W. 339                                    |
| Allard, F. 299                         | Baraniuk, R. G. G. 190, 196,<br>197, 199–204, 216, 220 | Bracewell, R. N. 28                                |
| Allman, B. E. 99, 100                  | Barshan, B. 431  | Bradley, C. C. 4, 433                              |
| Almeida, J. B. 69                      | Barty, A. 98, 99, 104                                  | Bragg, W. L. 74                                    |
| Alonso, M. A. 44, 68                   | Baruchel, J. 133                                       | Braginsky, V. B. 364                               |
| Alquaddoomi, O. 78                     | Batar, A. 245  | Brennen, G. K. 5                                   |
| Amira, A. 376                          | Bauschke, H. H. 121, 122                               | Breton, M. 285                                     |
| Andersen, J. A. 343                    | Beheshti, S. 206                                       | Browaeys, A. 332                                   |
| Anderson, B. P. 415, 416, 418          | Beijerinck, H. C. W. 241                               | Bryngdahl, O. 79                                   |
| Anderson, C. S. 407                    | Ben-Yuan Gu 115  | Buldyrev, V. S. 18                                 |
| Anderson, M. H. 3, 244                 | Benkrid, A. 377  | Burns, M. M. 349                                   |
| Andrews, H. C. 165                     | Benkrid, K. 377  | Burrus, C. S. 375                                  |
| Andrews, M. R. 2, 353, 354,<br>408–411 | Bernardo, L. M. 33                                     | Busch, B. D. 349                                   |
| Anon. 161                              | Bernstein, D. J. 374                                   | Busch, H. C. 291                                   |
| Arif, M. 100                           | Berry, M. V. 57  | Butcher, R. J. 326                                 |
| Arimondo, E. 434                       | Bertero, M. 394  | Cable, A. 1  |
| Arndt, R. 297                          | Berthoud, P. 246                                       | Cadilhac, M. 65                                    |
| Arnold, A. S. 264                      | Beverini, N. 301                                       | Campbell, C. 330                                   |
| Arsaev, I. E. 443                      | Bianchini, G. 322                                      | Campbell, J. C. 281                                |
| Arsenin, V. Y. 172                     | Bjorklund, G. C. 303, 304                              | Cancio, P. 322                                     |
| Asakura, T. 126                        | Bleloch, A. L. 132                                     | Candès, E. J. 186, 208, 222,<br>223, 225, 226, 230 |
| Asatryan, A. A. 20, 44                 | Bloch, D. 288  | Carazo, J. M. 156, 157                             |
| Aspect, A. 332, 336                    | Bloembergen, N. 344                                    | Carlson, A. B. 313                                 |
| Aucouturier, E. 248                    | Bodermann, B. 317                                      | Castillo, M. D. I. 422                             |

- Castin, Y. 346  
 Cathey, W. T. 385, 387  
 Centurion, M. 427  
 Chamberland, M. 300  
 Chambolle, A. 210  
 Chang, J. J. 146  
 Chang Jae Lee 249  
 Chapsky, J. 319  
 Charalambous, P. 108  
 Chen, Q. 106  
 Cheng, J. 173  
 Chien Liu 349  
 Chikkatur, A. P. 356, 413  
 Chin, R. T. 182  
 Choi, H. 196, 197, 199–203,  
     216  
 Choi, K. 284  
 Chu, S. 1, 238  
 Cip, O. 274  
 Clairon, A. 323  
 Cloetens, P. 133, 134  
 Close, J. D. 296, 306, 337,  
     338, 428, 429  
 Coddington, I. 417, 419, 420  
 Cognet, L. 336  
 Cohen, D. 158  
 Coifman, R. R. 183, 209  
 Colton, I. 101  
 Combettes, P. L. 121, 122  
 Conroy, R. S. 236, 436  
 Conway, J. F. 145  
 Cooley, J. W. 371  
 Cooper, N. R. 334  
 Cornejo-Rodríguez, A. 97  
 Cornell, E. A. 3, 244, 380,  
     415–420  
 Corwin, K. L. 244, 290  
 Courant, R. 164  
 Cowley, J. M. 40, 58  
 Cox, S. G. 255, 294  
 Crookes, D. 377  
 Cuneo, C. J. 286  
 Cuthbertson, B. D. 337  
 Cyr, N. 285, 300  
 Dahleh, M. A. 206  
 Dalibard, J. 346  
 Dalvit, D. A. R. 365  
 Dandliker, R. 277  
 Danielson, P. 252  
 Das, D. 262  
 Daubechies, I. 192  
 David, T. J. 163  
 Davis, G. M. 187  
 Davis, J. C. 175  
 Davis, K. B. 2  
 Davis, T. J. 22, 50  
 de Jonge, N. 128  
 de Rivaz, P. 213  
 Delpha, C. 437  
 DeMille, D. 255  
 Demoli, N. 91  
 den Dekker, A. J. 381  
 Denschlag, J. 435  
 Deutsch, I. H. 5  
 Devaney, A. J. 90, 117  
 Devaux, F. 430  
 Devore, J. L. 378  
 DeVore, R. A. 194  
 Dewey, J. M. 426  
 Dimarcq, N. 248  
 Dinneen, T. P. 307  
 Dirac, P. A. M. 341  
 Djurovic, I. 432  
 Do-Young Jeong 293  
 Domen, K. F. E. M. 379  
 Domenico, G. D. 333  
 Donoho, D. L. 184–186, 193,  
     205, 208, 209, 211, 218, 219,  
     221–227, 230, 232, 233  
 Dorsch, R. G. 399  
 Dragoman, D. 67  
 Dragotti, P. L. 214  
 Drever, R. W. P. 302  
 Drummond, P. D. 343  
 Druten, N. J. V. 354  
 Dubochet, J. 146  
 Ducloy, M. 288  
 Duncan, M. L. 227  
 Duniway Stockroom  
     Corporation 257  
 Durand, S. 215  
 Durfee, D. S. 2, 331, 353, 354,  
     408, 409, 412  
 Dutton, Z. 349  
 Dziarmaga, J. 352, 365  
 Edmonds, A. R. 369  
 Engels, P. 417, 419, 420  
 Enright, P. J. 320  
 Ensher, J. R. 3, 401  
 Epstein, R. J. 290  
 Erickson, H. P. 55, 150  
 Ertmer, W. 239  
 Esslinger, T. 267  
 Featonby, P. D. 336  
 Feiock, F. D. 37  
 Fernández-Guasti, M. 97  
 Fernandez, J. J. 157  
 Ferreira, C. 33, 399  
 Fessler, H. 82  
 Ficek, Z. 343  
 Figueiredo, M. A. T. 217  
 Finn, R. 158  
 Flannery, B. P. 174  
 Flesia, A. G. 232, 233  
 Fletcher, C. S. 306  
 Flowers, G. 256  
 Folman, R. 435  
 Forbes, G. W. 20, 39, 44, 68  
 Ford, G. M. 302  
 Fortagh, J. 259  
 Fox, P. J. 101, 103  
 Fox, R. W. 280  
 Francis, M. R. 348  
 Frank, J. 152  
 Freegarde, T. 318  
 Fretel, E. 246  
 Friberg, A. T. 395  
 Fried, D. G. 350  
 Friese, M. E. J. 343  
 Frigo, M. 372  
 Frigo, S. P. 99  
 Froment, J. 215  
 Froning, P. 82  
 Gabor, D. 70, 73, 191  
 Galatsanos, N. P. 176  
 Gao, D. 43, 50  
 Garcia, J. 33  
 Garcia, N. 131  
 Garcia, R. R. 422  
 Gaskill, J. D. 34  
 Gensemer, S. D. 327  
 George, N. 112  
 Gerchberg, R. W. 105, 123  
 Gerton, J. M. 421

- Ghael, S. P. 204  
 Gilbert, S. 256  
 Gleeson, H. F. 272  
 Gluckstad, J. 403  
 Golovchenko, J. A. 349  
 Gomer, V. 366, 370  
 Gonzalez, L. A. 422  
 Goodman, J. W. 23  
 Gori, F. 62, 393  
 Gorlitz, A. 357  
 Goss, W. P. 73  
 Gould, P. L. 307, 327  
 Gowen, B. 158  
 Grabowski, A. 245  
 Graef, M. D. 95  
 Granados-Agustín, F. 97  
 Gray, M. B. 296  
 Green, H. S. 14  
 Grella, R. 393  
 Greytak, T. J. 350  
 Griffin, P. F. 255, 294  
 Groetsch, C. W. 7  
 Grossmann, A. 259  
 Grünert, J. 254, 321  
 Grzywacz, N. M. 180  
 Gu, M. 170  
 Guangyin Zhang 424  
 Guigay, J.-P. 45–47, 134, 437  
 Gullikson, E. M. 175  
 Gupta, S. 357  
 Gureyev, T. E. 10, 50, 120,  
     159, 162, 163  
 Gustavson, T. L. 357  
 Hahn, M. 142  
 Halioua, M. 138–140  
 Haljan, P. C. 415–420  
 Hall, D. S. 415, 416  
 Hall, J. L. 273, 302  
 Hand, C. F. 290  
 Hänsch, T. W. 318  
 Hanssen, K.-J. 54, 137  
 Hariharan, P. 382  
 Hau, L. V. 349  
 Haubrich, D. 242, 260, 366  
 Hawthorn, C. J. 265  
 Heckenberg, N. R. 298, 343  
 Hegerl, R. 147  
 Heideman, M. T. 375  
 Hemmerich, A. 267, 321  
 Henke, B. L. 175  
 Henkel, C. 435  
 Herman, S. 386  
 Hignette, O. 134  
 Hilbert, D. 164, 442  
 Hilico, L. 323  
 Hillery, A. D. 182  
 Ho Seong Lee 292  
 Holland, M. J. 415  
 Hollberg, L. W. 263, 280  
 Homo, J. C. 146  
 Honda, T. 125  
 Hong, J. 427  
 Hongjie Xu 87  
 Hope, J. J. 338, 428, 429  
 Hori, H. 287  
 Horikoshi, G. 253  
 Horne, D. E. 305  
 Horvath, G. Z. K. 336  
 Hough, J. 302  
 Howells, M. R. 106  
 Howie, A. 132  
 Hua Deng 289  
 Hubbard, B. B. 445  
 Hughes, I. G. 294  
 Hulet, R. G. 4, 421, 433  
 Hunt, B. R. 165  
 Huo, X. 218, 221, 232  
 Hwang, W. L. 234  
 Hyuck Cho 292  
 Iannelli, J. 283  
 Ikonen, E. 268  
 Inguscio, M. 322  
 Inouye, S. 353, 356, 357,  
     409–411  
 International Organisation  
     for Standardisation 228  
 Isaacson, M. 106  
 Ishimaru, H. 253  
 Ito, A. 125  
 Ito, M. 315  
 Jackson, J. D. 11  
 Jacobson, D. L. 100  
 Jaenicke, R. 77  
 Jahnens, B. 52  
 James, E. M. 132  
 Javanainen, J. 347, 348  
 Javid, B. 397  
 Jawerth, B. 194  
 Jedlicka, P. 274  
 Jedrzejewicz, O. 430  
 Jia, C. L. 52  
 Jiang, Y. 430  
 Jianwei Miao 108  
 Jianwen Chen 87  
 Jiménez, J. L. 97  
 Jingjun Xu 424  
 Jitschin, W. 325  
 Johnson, S. G. 372  
 Johnstone, I. M. 205  
 Jones, D. I. G. 271  
 Jones, D. L. 375  
 Joyeux, D. 114, 116  
 Jun Zhu 152  
 Jung, E. C. 293  
 Junmin Liu 424  
 Juptner, W. P. O. 71  
 Kadlec, S. 425  
 Kajzar, F. 423  
 Kalifa, J. 189  
 Karelina, M. 395  
 Kasevich, M. 250  
 Katsaggelos, A. K. 166, 176,  
     177  
 Katz, J. 78  
 Ketterle, W. 2, 331, 353, 354,  
     356, 357, 360, 362, 408–414  
 Khalili, F. Y. 364  
 Killian, T. C. 350  
 Kimura, T. 315  
 Kinber, B. E. 443  
 King, B. 83  
 Kingsbury, N. 212, 213  
 Kinoshita, K. 125  
 Kirkland, E. J. 143  
 Kirz, J. 108  
 Kiss, T. 361, 363  
 Kitching, J. 276, 283  
 Klein, S. 57  
 Kleinz, J. 147  
 Kleppner, D. 350  
 Klitzing, W. V. 326  
 Klug, A. 150, 151  
 Knops, R. M. S. 241  
 Kobayashi, S. 315

- Kocatepe, M. 92  
 Kodama, I. 125  
 Kohl, M. 412  
 Komorowska, K. 423  
 Konig, W. 267  
 Koolen, A. E. A. 241  
 Koren, G. 114, 116  
 Korevaar, E. 284  
 Kuroogi, M. 287  
 Kovacich, R. P. 275, 317  
 Kowalski, F. V. 302  
 Kowalski, R. 327  
 Kozuma, M. 287  
 Kravtsov, Y. A. 20, 441  
 Krueger, P. 435  
 Kubler, O. 141, 142  
 Kuga, T. 295  
 Kuklewicz, C. E. 412  
 Kurn, D. M. 2, 353, 354, 408  
 Kutay, M. A. 27, 438  
 Kwang-Hoon Ko 293  
 Lakshminarayanan, V. 69  
 Lalor, É. 26  
 Lamy, Y. 128  
 Landau, H. J. 389  
 Landhuis, D. 350  
 Langmore, J. P. 148, 149  
 Lantz, E. 430  
 Laurent, P. 299  
 Lazar, J. 266, 274  
 Lee, W. D. 281  
 Leith, E. N. 75, 80  
 Lenth, W. 304  
 Lentzen, M. 52  
 Leonhardt, U. 361, 363  
 Lepault, J. 146  
 Levenson, M. D. 304, 305  
 Levesque, M. 300  
 Libbrecht, K. G. 273  
 Lindquist, K. 261  
 Lison, F. 242  
 Liu, G. 113  
 Lohmann, A. W. 72, 79, 169,  
     398, 399  
 Loudon, R. 340, 342  
 Low, R. F. 245, 357  
 Lu, Z. T. 244  
 Lucier, B. J. 194, 198, 210  
 Ludvigsen, H. 268  
 Ludwig, W. 133, 134  
 Luiten, A. N. 275  
 Luke, D. R. 121, 122  
 Lurie, B. J. 320, 324  
 Lye, J. E. 306, 337, 338, 428  
 Maccioni, E. 301  
 Mackin, T. R. 101  
 Mahajan, V. N. 35, 36  
 Maki, J. J. 240, 286  
 Maksimovic, I. 299  
 Maleki, M. H. 90, 117  
 Malkiel, E. 78  
 Mallat, S. 49, 189, 234  
 Mandel, L. 13  
 Mandelbrot, B. B. 179  
 Marathay, A. S. 15, 16, 30  
 Marinho, F. 33  
 Marsili, P. 301  
 Martinsson, P. 395  
 Mas, D. 33  
 Matadeen, R. 158  
 Matsumura, T. 125  
 Matthews, M. R. 3, 400, 415,  
     416  
 Mayer, S. K. 240  
 Mayo, S. C. 50, 159, 163  
 McCartney, M. 98  
 McDowall, A. W. 146  
 McFerran, J. J. 275  
 McIntyre, D. H. 240, 286  
 McMahon, P. J. 99, 100  
 McNulty, I. 99  
 Meade, M. L. 312  
 Meisel, G. 325  
 Melmed, A. J. 130  
 Melody, J. W. 324  
 Menders, J. 284  
 Mendlovic, D. 169, 399, 431  
 Menzel, E. 51  
 Meschede, D. 242, 260, 279,  
     366, 370  
 Mestrovic, J. 91  
 Metcalf, H. J. 247, 279, 439  
 Mewes, M.-O. 2, 354  
 Meyer, F. G. 183  
 Meystre, P. 359  
 Michaud, A. 300  
 Miesner, H.-J. 353, 408–411  
 Miletí, G. 333  
 Miller, P. R. 50, 159  
 Miller, R. J. 272  
 Minardi, F. 322  
 Minardi, S. 430  
 Miniewicz, A. 423  
 Misell, D. L. 109, 110, 144  
 Mishina, T. 81  
 Moerner, W. E. 305  
 Mogensen, P. C. 403  
 Moler, K. A. 238  
 Molisch, A. F. 351  
 Monroe, C. 243  
 Moodie, A. F. 58  
 Moon Gi Kang 177  
 Moon, H. S. 293  
 Moore, M. G. 359  
 Morgenstern, B. 54  
 Morice, O. 346  
 Morton, G. A. 129  
 Moss, S. C. 350  
 Mosset, A. 430  
 Mukae, T. 295  
 Mukunda, N. 66  
 Munley, A. J. 302  
 Munson, D. C. 160  
 Murtagh, F. 231  
 Mustecaplioglu, O. E. 358  
 Nabiev, R. 278  
 Nam-Yong Lee 198  
 Nan-Xian Chen 115  
 Natarajan, V. 258, 262  
 Nazarathy, M. 64  
 Neat, G. W. 324  
 Neelamani, R. 181, 199–202,  
     207  
 Neifeld, M. A. 83  
 Nellessen, J. 239  
 Newell, R. 425  
 Newsam, G. 107  
 Newton, I. 6  
 Nez, F. 323  
 Nguyen, M. K. 231  
 Nieto-Vesperinas, M. 21  
 Nilsson, O. 269  
 Noble, A. 250  
 Nosratinia, A. 187

- Nowak, R. D. 190, 217  
Nowak, S. 332  
Nugent, K. A. 94, 96,  
98–102, 104  
Oates, C. W. 280  
Oehry, B. P. 351  
Ohtsu, M. 287  
Ohyama, N. 125  
Ojeda-Castañeda, J. 398  
Okano, F. 81  
Olivos-Perez, L. I. 422  
Onofrio, R. 365, 412, 413  
Onural, L. 32, 92, 124, 431  
Oosterkamp, T. H. 128  
Orlov, Y. I. 441  
Orlova, E. V. 158  
Ortiz, C. 304  
Ouellet, R. 316  
Ovchinnikov, Y. B. 245  
Ozaktas, H. M. 27, 431, 438  
Ozgen, M. T. 127, 235  
Paganin, D. 50, 93, 94, 96,  
98, 99, 102, 104, 159, 162  
Pallas-Areny, R. 309  
Panepucci, R. R. 106  
Panotopoulos, G. 427  
Pape, T. 158  
Papoulis, A. 41, 42, 48  
Parka, J. 423  
Parkins, A. S. 345  
Parrent, G. B. 15  
Parry, D. J. 50  
Patwardhan, A. 158  
Pavone, F. S. 322  
Pearman, C. P. 294  
Pedrini, G. 82  
Penczek, P. A. 152  
Pensak, L. 251  
Perrone, F. 322  
Petermann, K. 314  
Pfau, T. 245, 357  
Pietilainen, A. 268  
Pike, E. R. 394  
Piwnicki, P. 361, 363  
Pogany, A. 43, 50, 162, 163  
Polack, F. 114, 116  
Politzer, H. D. 355  
Pollak, H. 388–390  
Poupard, J. 332  
Prentiss, M. 1, 236, 436  
Press, W. H. 174  
Prevedelli, M. 318, 322  
Pritchard, D. E. 1, 356, 357,  
360  
Prodan, I. 421  
Psaltis, D. 427  
Qian, W. 130  
Raab, E. 1  
Racca, R. G. 426  
Radermacher, M. 153  
Raman, C. 412–414  
Ramberg, E. G. 129  
Rapol, U. D. 258  
Raveh, I. 169  
Read, N. 334  
Reichelt, A. 59  
Reigber, A. 373  
Renn, M. J. 244  
Retsch, C. C. 99  
Ricci, L. 267  
Riis, E. 238, 255  
Ritter, S. 321  
Robert, A. 332  
Roberts, A. 104  
Robins, N. P. 296, 306  
Robinson, H. 243  
Rodriguez-Ortiz, M. 422  
Rogers, G. L. 74, 84–86  
Rolleston, R. 112  
Romberg, J. 220  
Rooijakkers, W. 236, 436  
Root, S. 327  
Rosenblatt, M. 188  
Rowland, T. 195  
Rubinstein-Dunlop, H.  
298, 343  
Ruffini, A. 301  
Ruostekoski, J. 347, 348  
Ruzicka, B. 266, 274  
Rzążewski, K. 339  
Sacha, K. 352  
Sackett, C. A. 4, 433  
Saito, S. 269  
Sakai, I. 253  
Saleh, B. E. A. 17  
Salvade, Y. 277  
Sanchez de la Llave, D. 422  
Sang Eon Park 292  
Sanjurjo, J. R. 156  
Sasabe, H. 155  
Savalli, V. 336  
Saxton, W. O. 105, 123  
Sayeed, A. M. 204  
Sayre, D. 108  
Schadwinkel, H. 260, 366  
Schatz, M. 158  
Scherzer, O. 53  
Schiske, P. 89, 135  
Schlenker, M. 133, 134  
Schmidt, R. 158  
Schmiedmayer, J. 435  
Schnars, U. 71  
Schneble, D. 360  
Scholten, R. E. 101, 265, 379  
Schoof, A. 321  
Schoots, K. 128  
Schoser, J. 245  
Schröder, R. 152  
Schuh, P. 242  
Schultz, P. 146  
Schweikhard, V. 245, 420  
Scott, N. J. 251  
Scott, P. D. 113, 124  
Searcy, P. 284  
Sebby, J. 425  
Semet, V. 131  
Seredysnki, J. 142  
Shaddock, D. A. 296  
Shamir, J. 64  
Shen, Y. R. 344  
Sheppard, C. J. R. 170  
Sherman, G. C. 31  
Shevy, Y. 276, 283, 289  
Shiddiq, M. 291  
Shinohara, K. 125  
Silva, N. J. 240  
Simin Liu 424  
Simon, R. 66  
Singer, W. 60  
Sirjean, O. 332  
Slagmolen, B. J. J. 296  
Slepian, D. 388, 390–392  
Smith, D. A. 294  
Smith, M. F. 148, 149

- Sobelman, I. I. 368  
 Songcan Lai 83  
 Soontaranon, S. 126  
 Sorbothane Inc. 270  
 Sorensen, H. V. 375  
 Sorrentino, F. 301  
 Sorzana, C. O. S. 157  
 Southwell, W. H. 38  
 Sovic, I. 91  
 Spence, J. C. H. 106, 130  
 Stamper-Kurn, D. M. 331, 356, 409–411  
 Stankovic, L. 432  
 Stankovic, S. 432  
 Starck, J.-L. 208, 229–231  
 Stark, H. 158  
 Steck, D. A. 367  
 Stenger, J. 356, 410  
 Stephens, M. 261  
 Stern, A. 397  
 Steven, A. C. 145  
 Stevenson, A. W. 50  
 Storck, E. 59  
 Stoschek, A. 211  
 Strauch, F. 260, 366  
 Streed, E. W. 360  
 Strekalov, D. 421  
 Strohben, J. W. 12  
 Stroke, G. W. 138–140  
 Suesserman, M. F. 310  
 Sukenik, C. I. 291  
 Swann, W. 243  
 Swanson, T. B. 240  
 Tadmor, Y. 178  
 Taeg Yong Kwon 292  
 Takahashi, Y. 335  
 Talbot, W. H. F. 8  
 Talvitie, H. 268  
 Tang Chao 178  
 Teague, M. R. 61  
 Teich, M. C. 17  
 Telle, H. R. 317  
 Testorf, M. E. 398  
 Tetu, M. 285, 300  
 Teukolsky, S. A. 174  
 Thaning, A. 395  
 Theriault, S. 285, 300  
 Thomann, P. 246, 333  
 Thon, F. 56, 140  
 Thust, A. 52  
 Tikhonov, A. N. 171, 172  
 Tiller, J. B. 99  
 Tillmann, K. 52  
 Tiqiao Xiao 87  
 Tiziani, H. J. 60, 82  
 Toepler, A. 402  
 Tolhurst, D. J. 178  
 Tollett, J. J. 4  
 Torii, Y. 295, 360  
 Touahri, D. 323  
 Townsend, C. G. 353, 408  
 Toyoda, K. 335  
 Toyoshima, C. 154, 155  
 Trapani, P. D. 430  
 Tremblay, P. 300, 316  
 Truscott, A. G. 298, 343  
 Tukey, J. W. 371  
 Tuncer, T. 235  
 Tung, S. 420  
 Turner, L. D. 101, 329, 379  
 Tyler, C. W. 180  
 Typke, D. 147, 153  
 Ueberholz, B. 260, 366  
 Umeki, T. 295  
 Unser, M. 446  
 Unwin, N. 154  
 Upatnieks, J. 75, 80  
 Urban, K. 52  
 Uzun, I. S. 376  
 Vahala, K. 278  
 Valdez, E. C. 282  
 Vale, C. J. 328  
 Valentini, C. 248  
 van den Bos, A. 381  
 van der Straten, P. 247, 439  
 van Druten, N. J. 2  
 van Dyck, D. 133  
 van Heel, M. 158  
 van Landuyt, J. 133  
 van Leeuwen, K. A. H. 241  
 VanderLugt, A. 63, 396  
 Velazquez-Muriel, J. A. 157  
 Vengalattore, M. 236, 436  
 Vestergaard, B. 348  
 Vetterli, M. 214  
 Vetterling, W. T. 174  
 Vikram, C. S. 76  
 Vincent, R. 118, 119  
 Vogel, C. R. 168  
 Vogels, J. M. 413, 414  
 Volkov, V. V. 95  
 Vossing, H.-J. 77  
 Vu Thien Binh 131  
 Vuletic, V. 267  
 Wade, R. H. 136, 437  
 Wakin, M. 220  
 Walker, T. G. 425  
 Walkiewicz, M. R. 308  
 Wall, M. 98  
 Wallace, C. D. 307  
 Walls, D. F. 345  
 Walton, A. J. 384  
 Wanninger, P. 282  
 Ward, H. 302  
 Wasan, A. 258  
 Wavelet Digest Steering Committee 446  
 Weber, K. P. 265  
 Webster, J. G. 309  
 Weidemuller, M. 267  
 Weierstall, U. 106  
 Weiman, C. E. 418  
 Weiss, D. S. 238  
 Weisstein, E. W. 24, 25, 195  
 Welling, M. 433  
 Wen-Xiang Cong 115  
 Werner, J. 239  
 Werner, S. A. 100  
 Westbrook, C. I. 332, 336  
 Westbrook, N. 336  
 Weyers, S. 248  
 Weyl, H. 29  
 Whitlock, W. 311  
 Widjaja, J. 126  
 Wieman, C. E. 3, 243, 244, 256, 261, 263, 290, 415, 416  
 Wiener, N. 167  
 Wiener, O. 440  
 Wilkins, S. W. 43, 50, 159, 162, 163  
 Willasch, D. 140  
 Williams, J. E. 415  
 Willmann, L. 350  
 Wilson, J. S. 264

- Wolf, E. 13, 14, 19  
Wolf, K. B. 68  
Wolff, U. 59  
Wynands, R. 260
- Xiao, Y. 236  
Xu, K. 414
- Yabuzaki, T. 335  
Yada, K. 125  
Yamaguchi, M. 125  
Yamamoto, M. 173  
Yamamoto, Y. 269, 315  
Yariv, A. 276, 278, 283  
Yingji Zhang 87  
Yonekura, K. 155  
Yoshikawa, Y. 295  
You, L. 358  
Yu, T. 211  
Yuxin Wang 99  
Yuyama, I. 81
- Zabler, S. 134  
Zalevsky, Z. 169, 399, 438  
Zernike, F. 404–406  
Zhang, X. 88  
Zhang, Y. 88  
Zheng-Tian Lu 290  
Zhiwen Liu 427  
Zhizhan Xu 87  
Zhua, Y. 95  
Zi Dong Liu 288  
Zimmermann, C. 259, 267



## Appendix A

# Intensity: the result of optical measurement

An optical detector converts energy from the electromagnetic field incident on its area into some other form: chemical potential for a photoplate, a current from a photodiode. Hence the intensity is identified with an energy flux with units of power per unit area. The Maxwell equations lead directly to a continuity equation relating the rate of change of electromagnetic energy inside a volume to the flux of electromagnetic energy through its surface [21, p 5–6]. The energy flux vector so derived,  $\mathbf{S} = c/4\pi \mathbf{E} \times \mathbf{H}$  is the *Poynting vector*. Many authors, including Born & Wolf [19, p 10] and Nieto-Vesperinas [21, p 6], have appropriated the time-averaged magnitude of the Poynting vector as the intensity  $I$ , writing  $I = |\langle \mathbf{S} \rangle|$ , where  $\langle \dots \rangle$  indicates a time average over a period much longer than one optical cycle. Marathay [16, pp 278–285] has pointed out that in general, this intensity is *not* what is measured by photodetectors.

The Poynting vector of a *plane wave* is oriented along the direction of propagation and has magnitude  $|\mathbf{S}| = c/8\pi \sqrt{\epsilon/\mu} \mathbf{E} \cdot \mathbf{E}$ . It is common practice in the optics literature to define intensity as the magnitude of the Poynting vector, but then to use this plane-wave expression to calculate it, not only for a single plane wave, but for arbitrary fields. Marathay considered two plane waves incident at 45 degrees to a detector, both of wavelength  $\lambda$  but with perpendicular wavevectors, and polarisations in the plane of incidence. The Poynting vector  $\mathbf{S}$  predicts  $\lambda/2$  fringes while  $\mathbf{E} \cdot \mathbf{E}$  predicts the absence of fringes. The experiment was first performed by Wiener in 1890 [440].<sup>1</sup> No fringes were observed. The Wiener experiment also confirms

---

<sup>1</sup> Born and Wolf [19, pp 311–313] review this experiment conducted with photographic film as the de-

the insensitivity of standard optical detectors to magnetic fields.

It is thus an matter of experimental fact that the intensity is, in general, *not* the magnitude of the Poynting vector. It is quite remarkable that this is so rarely recognised. Of course, this has little bearing on the validity of most of the literature, which *uses* the form  $I \propto \langle \mathbf{E} \cdot \mathbf{E} \rangle$  and only errs in *deriving* it from the false premise  $I = |\langle \mathbf{S} \rangle|$ .

Finally, note that semi-classical [13, §9.3] and fully quantised [13, §14.5] treatments of photodetection yields probabilities proportional to  $\mathbf{A} \cdot \mathbf{A}$  for coherent fields, where  $\mathbf{A}$  is the *vector potential* of classical electrodynamics. In the Coulomb gauge and in the absence of free charges the detection probability is proportional to  $\mathbf{E} \cdot \mathbf{E}$ , confirming the classical result.<sup>2</sup> In light of this discussion, we assume in this thesis that the intensity measured by photodetectors is given by

$$I = \sqrt{\frac{\epsilon}{\mu}} \langle \mathbf{E} \cdot \mathbf{E} \rangle \quad (\text{A.1})$$

where  $\epsilon$  is the dielectric permittivity and  $\mu$  the magnetic permeability. As we are only concerned with intensity ratios in this thesis, we discard the dimensional constants, and write

$$I \equiv \langle \mathbf{E} \cdot \mathbf{E} \rangle = \langle |\mathbf{E}|^2 \rangle. \quad (\text{A.2})$$

---

tector, and reference others confirming the result for other types of detector.

<sup>2</sup> Assuming free charges is particularly questionable when considering the coupling of the incident field to the single electron photodetector! A quantum treatment of Wiener's experiment does not seem to have been attempted.

## Appendix B

# Rays in absorbing media

Kravtsov and Orlov's book briefly discusses the problem of rays in absorbing media, and we follow their treatment here [441, §2.3.7]. As the refractive index enters the wave equation as  $n^2$ , we work with the real and imaginary parts of  $n^2 = \epsilon = \epsilon_r + i\epsilon_i$ . Our global assumption that the deviation of refractive index from unity is small,  $|n - 1| \ll 1$ , ensures that  $\epsilon_i \ll \epsilon_r$ . Expanding  $n = n_r + in_i = \sqrt{\epsilon}$  about  $\epsilon_r$  yields to first order

$$n_r = \sqrt{\epsilon_r}, \quad n_i = \frac{\epsilon_i}{2\sqrt{\epsilon_r}}. \quad (\text{B.1})$$

The separation of  $\epsilon$  into a real component and a much smaller imaginary component is reminiscent of the first two terms of the asymptotic expansion (2.12). The artifice employed by Kravtsov and Orlov is to make this similarity explicit, writing  $\epsilon_i = \kappa/k$  so that the separation of  $\epsilon$  may be included in (2.13, 2.15), which to first order become<sup>1</sup>

$$(\nabla S)^2 = \epsilon_r, \quad (\text{B.2})$$

$$2(\nabla A_0 \nabla S) + A_0 \nabla^2 S + k\epsilon_i A_0 = 0. \quad (\text{B.3})$$

It may be seen immediately that the eikonal equation is that of the equivalent non-absorbing medium; to first order, rays follow the same paths as in the absence of absorption. The absorption term  $\epsilon_i$  manifest itself in the transport equation. In our summary of ray optics, we have not discussed the evolution of amplitude along a ray. It suffices to note that by transforming into local ray coordinates, the transport equation reduces to a first-order ordinary differential equation [441, §2.3.1] with

---

<sup>1</sup> Note that the equivalent equation (2.3.35) in Reference [441] erroneously has  $\nabla S$  in place of  $\nabla^2 S$ .

solution:

$$\begin{aligned} A(P_2) &= A(P_1) \exp \left( -\frac{k}{2} \int_{P_1}^{P_2} \frac{\nabla^2 S}{\sqrt{\epsilon_r}} + \frac{\epsilon_i}{\sqrt{\epsilon_r}} ds \right) \\ &= \frac{A(P_1)}{\sqrt{\mathcal{J}}} \exp \left( -\frac{k}{2} \frac{\epsilon_i}{\sqrt{\epsilon_r}} ds \right). \end{aligned} \quad (\text{B.4})$$

Following Kravtsov, we have written the amplitude change due to ray propagation in terms of the *ray divergence*  $\mathcal{J}$ . We are not concerned with the form of  $\mathcal{J}$ , merely that it separates from the factor involving  $\epsilon_i$ . The expressions for the evolution along a ray of the amplitude (B.4) and eikonal (2.17), let us write the wavefunction (2.12) to first order along a ray between points  $P_1$  and  $P_2$  as:<sup>2</sup>

$$\begin{aligned} f(P_2) &= A(P_2) \exp(ikS(P_2)) \\ &= \frac{A(P_1)}{\sqrt{\mathcal{J}}} \exp \left( -\frac{k}{2} \int_{P_1}^{P_2} \frac{\epsilon_i}{\sqrt{\epsilon_r}} ds \right) \exp \left( ikS(P_1) + ik \int_{P_1}^{P_2} \sqrt{\epsilon_r} ds \right) \\ &= \frac{A(P_1)}{\sqrt{\mathcal{J}}} \exp \left( ikS(P_1) + ik \int_{P_1}^{P_2} \sqrt{\epsilon_r} + i \frac{\epsilon_i}{2\sqrt{\epsilon_r}} ds \right) \end{aligned}$$

and then using (B.1),

$$= \frac{A(P_1)}{\sqrt{\mathcal{J}}} \exp \left( ikS(P_1) + ik \int_{P_1}^{P_2} n ds \right). \quad (\text{B.5})$$

where  $n$  in the final line is the *complex* refractive index  $n = n_r + in_i$ . Hence weak absorption may be accounted for by substituting the complex refractive index for the real refractive index in the standard expression for optical path-length. This result was obtained from Fermat's principle by David Hilbert in 1912 [442].

Second-order corrections to this result were considered by Arsaev and Kinber [443], who showed that ray deviation due to absorption is in direction  $\nabla(\epsilon_i/\epsilon_r)$ .

---

<sup>2</sup> Kravtsov does not complete the derivation, one must substitute his equation (2.2.14) into (2.3.39).

## Appendix C

# Origin of the twin-image in Gabor in-line holography

The reconstruction of the wavefield may be understood by decomposing the original wavefield incident on a thin photoplate into a reference wave  $F$  corresponding to the illumination in the absence of the object, and a scattered wave  $f$  [23, §9.2–3]. The irradiance at the plate is then

$$\begin{aligned} I(\mathbf{x}) &= |F(\mathbf{x}) + f(\mathbf{x})|^2 \\ &= |F(\mathbf{x})|^2 + |f(\mathbf{x})|^2 + f(\mathbf{x})F^*(\mathbf{x}) + F(\mathbf{x})f^*(\mathbf{x}). \end{aligned} \quad (\text{C.1})$$

If the object is weakly absorbing, then the *autocorrelation term*  $|f(\mathbf{x})|^2$  may be neglected. Assume that after processing, the photoplate is a positive with amplitude transmittance proportional to the incident irradiance, that is, the aperture function of the photoplate is  $q = \beta I$ .<sup>1</sup> Illuminating the developed plate with the same source results in a reconstructed wavefield  $f_r$  after the plate given by

$$\begin{aligned} f_r(\mathbf{x}) &= F(\mathbf{x})q(\mathbf{x}) \\ &= \beta F(\mathbf{x}) (|F(\mathbf{x})|^2 + f(\mathbf{x})F^*(\mathbf{x}) + F(\mathbf{x})f^*(\mathbf{x})) \\ &= \beta |F(\mathbf{x})|^2 F(\mathbf{x}) + \beta |F(\mathbf{x})|^2 f(\mathbf{x}) + \beta F^2(\mathbf{x})f^*(\mathbf{x}) \end{aligned} \quad (\text{C.2})$$

where  $\beta$  is the response constant of the plate. Note that the first two terms are, up to a constant, the original wavefield  $F + f$  that was initially incident on the plate.

---

<sup>1</sup> See Born and Wolf [19, §8.10.1] for the full glory of the chemical information processing possible with the Hurter-Driffield photographic response curve. Note that the plate shifts phase as well as absorbs, and indeed phase holograms can yield *more* efficient reconstructions.

The third term is, however, of the same magnitude and involves the *conjugate* of the scattered field. It can be shown [23, §9.2.5] that the conjugate term corresponds to the formation of a *real* image after the photoplate.

An optical system focused on the virtual image corresponding to the  $f(\mathbf{x})$  term will see an out-of-focus copy superimposed. An optical system focused on the real image, or for that matter a photodetector placed in the real-image plane, similarly registers an image of the object with a diffracted version of the virtual image superimposed. If the optical system renders phase-contrast, the phase-shifts in the real-image plane are seen to be reversed, as is the parallax; this is known as a *pseudoscopic* image. The impossibility of separating these two superposed images at the reconstruction stage is known as the *twin-image problem*.

## Appendix D

# Wavelets in ten minutes

In less than two decades, wavelet analysis has revolutionised signal processing. Wavelets have also found application across the landscape of modern physics from electromagnetic propagation to Hartree-Fock calculations of atomic states [444]. However, while wavelet techniques are now indispensable in signal processing, they are still unfamiliar to most physicists. This Appendix gives the shallowest of reviews of what wavelets are, hinting at the connection between wavelet transforms and space-frequency analysis.

There are many books and review articles on wavelets, although most address specific mathematics or engineering audiences. The collection *Wavelets in Physics* provides a good introduction and references selected for a physics audience [444]. Although mine is a physics thesis, my use of wavelets is mostly for their image analysis properties and these are best explained in the comprehensive but clear treatise of Mallat [49]. The introduction is particularly concise and available online (see references). Much of this Appendix is based on Mallat's discussions, with many of the figures adapted with permission from his book. I have eschewed references to the primary literature; Mallat and others give thorough reviews. The historical development is readably presented in the popular summary by Hubbard [445]. The *Wavelet Digest* [446] is a monthly e-mail newsletter published since 1992; its website links to new books and articles as they appear.

### D.1 What is a wavelet?

A wavelet  $\psi$  is a function localised in both in location and in frequency. It must have zero mean, that is  $\int_{-\infty}^{\infty} \psi(x) dx = 0$ , and so must go to zero at the extremes

and have at least one zero-crossing. To ensure localisation in frequency, the Fourier transform  $\tilde{\psi}(u)$  must fall off rapidly enough that

$$\int_{-\infty}^{\infty} \frac{|\tilde{\psi}(u)|^2}{|u|} du < \infty, \quad (\text{D.1})$$

which in practice is satisfied if  $\psi$  is continuously differentiable ( $C^1$ ). It is easy to ‘draw’ a wavelet: starting off at zero, or on a zero-asymptote, draw as many wiggles as desired without taking the pen off the paper, before returning or asymptoting back to zero. As long as the areas above and below the axis are equal, you have drawn an admissible wavelet.

A simple closed-form wavelet is the *Mexican-hat* wavelet depicted in Figure D.1, it is the second derivative of the Gaussian given by

$$\psi(x) = \frac{2}{\pi^{1/4}\sqrt{3}} (x^2 - 1) \exp\left(-\frac{x^2}{2}\right). \quad (\text{D.2})$$

We can make a family of atoms  $\psi_{u,s}$  with different centres and spreads by translating the wavelet by  $u$  and dilating (scaling) it by  $s$ :

$$\psi_{u,s}(x) = \frac{1}{\sqrt{s}} \psi\left(\frac{x-u}{s}\right), \quad (\text{D.3})$$

the factor ensures that the family remains normalised with  $\|\psi_{u,s}\| = 1$ .

## D.2 The Continuous Wavelet Transform

The *wavelet transform*  $\mathcal{W}f(u,s)$  of a function  $f$  is just the correlation, or inner product, of  $f$  with the scaled and dilated wavelet, that is

$$\mathcal{W}f(u,s) = \int_{-\infty}^{\infty} f(x) \psi_{u,s}^*(x) dx. \quad (\text{D.4})$$

An example function  $f$  consisting of a piecewise smooth section and a very unsmooth section is shown in Figure D.2 above its wavelet transform  $\mathcal{W}f(u,s)$ . Such continuous wavelet transforms are useful in transient characterisation or edge-detection, and have been used in the analysis of physical systems [444]. It clearly results in a two-dimensional representation of a one-dimensional function, however. The question arises: can we find a sampling of the translation/dilation space with lower – or even zero – redundancy?

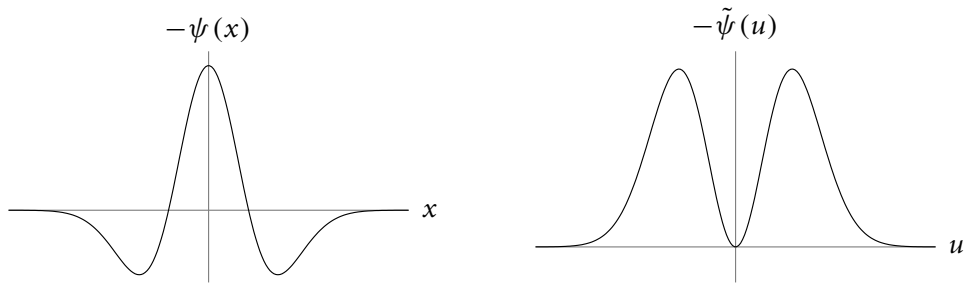


FIGURE D.1 **A closed-form wavelet.** The Mexican-hat wavelet (D.2) and its Fourier transform.

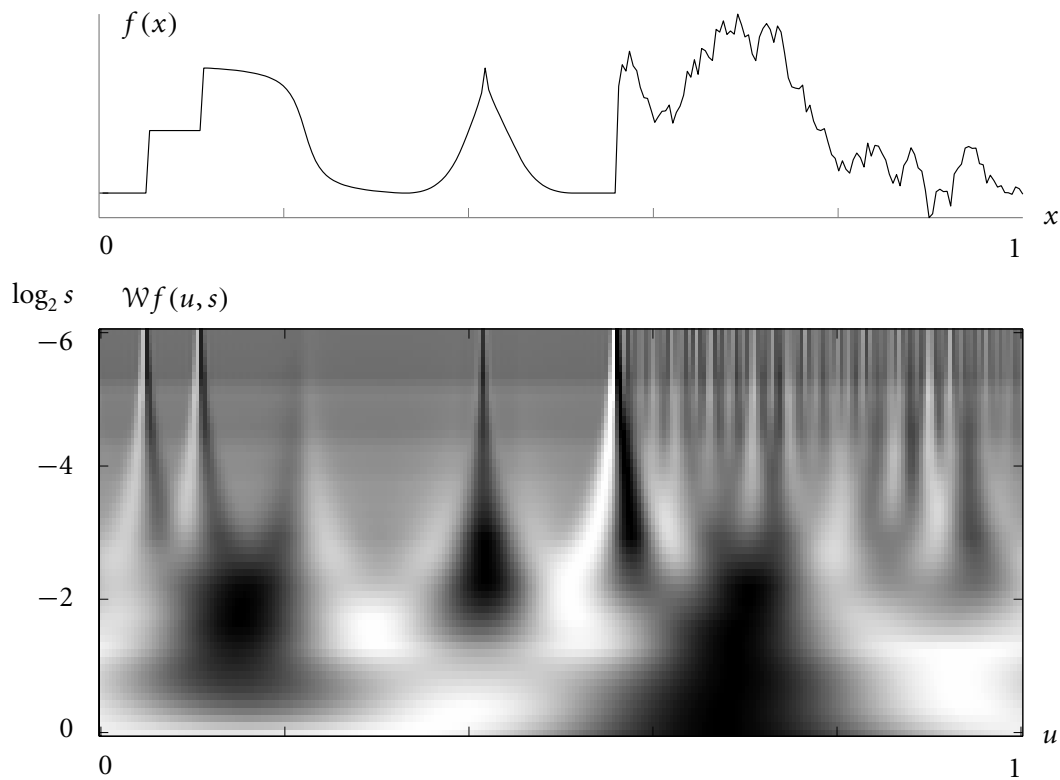


FIGURE D.2 **The wavelet transform of an unsmooth function.** An unsmooth function  $f$  (above) and its continuous wavelet transform  $\mathcal{W}f(u, s)$ , computed using the Mexican-hat wavelet (D.2). Adapted from p 81 of Reference 49.

At fine scales, near the top of the wavelet transform plot, the value of the transform differs from zero (mid-grey) only in the immediate vicinity of singularities: sharp wavelets are enlisted only near sharp edges. If we could sample this plane efficiently we might need only a few wavelets from each scale, even for signals containing singularities.

### D.3 Discrete sets of wavelets

The transition from the continuous *Fourier* transform to the discrete transform is straightforward: frequency space is sampled on an even grid. A general sampling of the wavelet transform is a much more complicated exercise [49, §5], but for our purposes a *dyadic* sampling suffices. We sample the scale variable by octaves  $s = 2^j$  using twice the number of translations  $u = 2^j n$  each time the scale is halved. Our family of atoms derived from the wavelet  $\psi(x)$  is now

$$\psi_{j,n}(x) = \frac{1}{\sqrt{2^j}} \psi\left(\frac{x - 2^j n}{2^j}\right) \quad \text{where } j, n \text{ are integers.} \quad (\text{D.5})$$

This sampling is depicted on the space-frequency plot Figure D.3, each box centre is a sampling point. The well-known Uncertainty principle demands that the more localised the wavelet in space, the more spread out in frequency. The *Heisenberg boxes* have fixed area corresponding to the space-frequency product. With only a rescaling of the frequency axis to become a scale axis, we can imagine that overlaying this sampling grid on the continuous transform plot Figure D.2 might yield an economic sampled representation of  $f(x)$ . Only a few fine-scale wavelets in the upper region of the plot would differ significantly from zero.

Dyadic sampling of the space-frequency plane may be compared to the simple rectangular grid of the windowed Fourier transform [49, §4.2], or to the grid-less but quadratic Wigner distribution or ambiguity function discussed in §2.6 [49, §4.5].

### D.4 Wavelet bases

Unfortunately, ‘drawing’ a wavelet  $\psi(x)$  and then scaling and translating it according to (D.5) to form a set  $\{\psi_{j,n}(x)\}$  does not usually make a basis, orthonormal or otherwise. The set of dilates and translates of the nice, smooth, easy-to-write-down

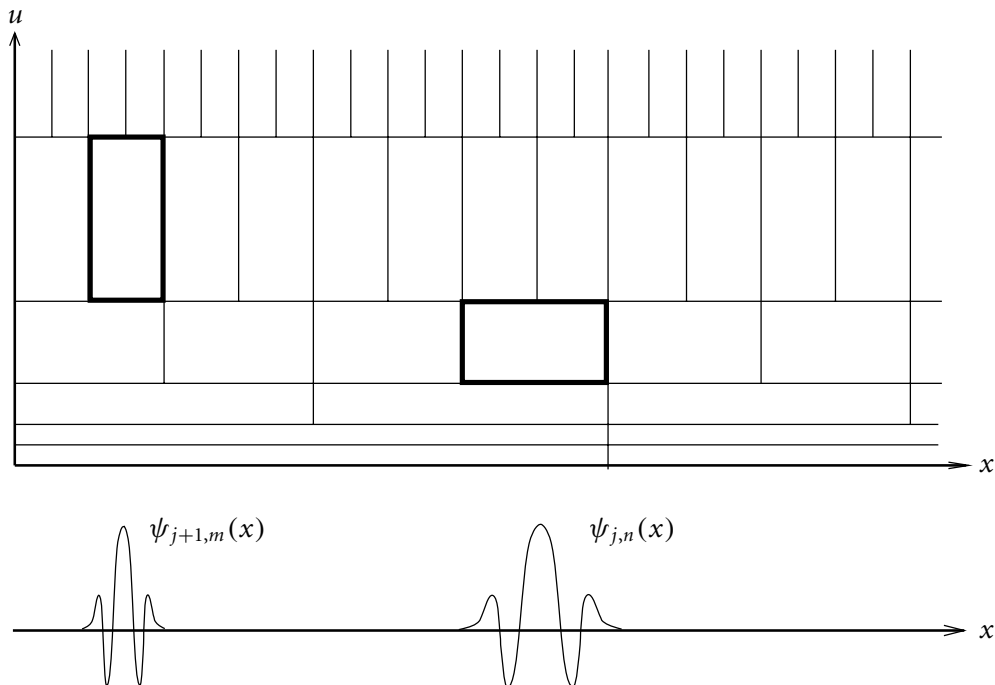


FIGURE D.3 **Space-frequency tiling by dyadic sampling of wavelets.** The wavelet shown at left has half the width of the one at right, and so has  $j$ -index higher by one and has twice the frequency spread. Adapted from p 10 of Reference 49.

Mexican-hat wavelet does *not* make a basis, for example. One wavelet that *does* generate a basis has been known since 1910: the *Haar wavelet* shown in Figure D.4.<sup>1</sup> On inspection the three example wavelets shown are clearly orthonormal. The Haar basis is, however, very bad at approximating smoothly varying functions; consider that even  $f(x) = x$  is approximated by a very inefficient staircase.

As is the wont of mathematicians, Yves Meyer was not satisfied with the non-discovery of any orthonormal wavelets smoother than the Haar wavelet, and sat down to prove there exists no smoother wavelet that generates an orthonormal basis. He failed spectacularly, discovering in 1985 an eponymous family of very smooth ( $C^\infty$ ) orthonormal wavelets, and arguably creating the field of wavelet analysis in the process.

A plethora of orthogonal wavelets ensued, culminating in the construction of a family of near-optimal orthogonal wavelets by Ingrid Daubechies in 1988. Like the Haar wavelets, Daubechies' wavelets are compactly-supported<sup>2</sup> but, unlike the

<sup>1</sup> Note that the Haar wavelet is clearly *not* continuously differentiable. It is not even continuous. Being  $C^1$  was only a sufficient condition: the Haar wavelet *does* satisfy the admissibility criterion (D.1).

<sup>2</sup> Exactly zero outside a finite range (the ‘support’).

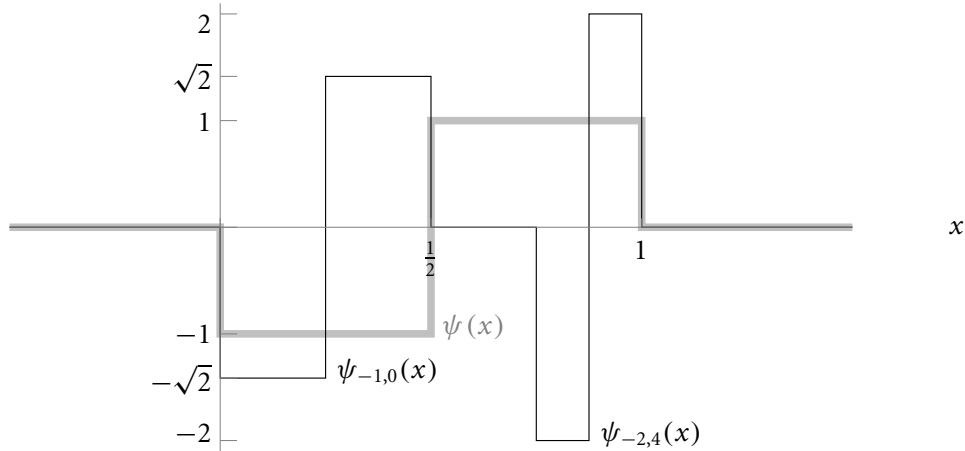


FIGURE D.4 **Three dilations and scalings of the Haar wavelet.** The Haar mother wavelet is shown in grey. Finer scale wavelets always fall within one constant section of a coarser wavelet and so are orthogonal.

Haar wavelets, may be made as smooth as one desires. A few examples from the Daubechies family are shown in Figure D.5; note that as the wavelet becomes smooth, its support spreads out. The family *includes* the Haar wavelet as Daubechies-1, having the narrowest support but the least smoothness.

Daubechies wavelets are strange-looking functions. You certainly can't tell by looking at them that they are orthonormal to their own dyadic dilates and translates. You may not be surprised that they lack a closed-form representation. Indeed, the Haar wavelet is the only known orthogonal wavelet that may be written down in closed form. Some orthogonal wavelets have piecewise-vanilla forms in the Fourier representation, but Daubechies wavelets must be generated by a recursive process. This absence of reassuring formulae for wavelets may have led some non-mathematicians to think of wavelets as being of only numerical significance. In fact, the mathematical foundation of *multiresolution analysis* firmly anchors wavelet methods to the bedrock of modern applied mathematics.<sup>3</sup>

---

<sup>3</sup> Unfortunately any remotely proper discussion of the provenance of orthogonal wavelets must consider scaling functions and multiresolution analysis. See §7 of Reference 49.

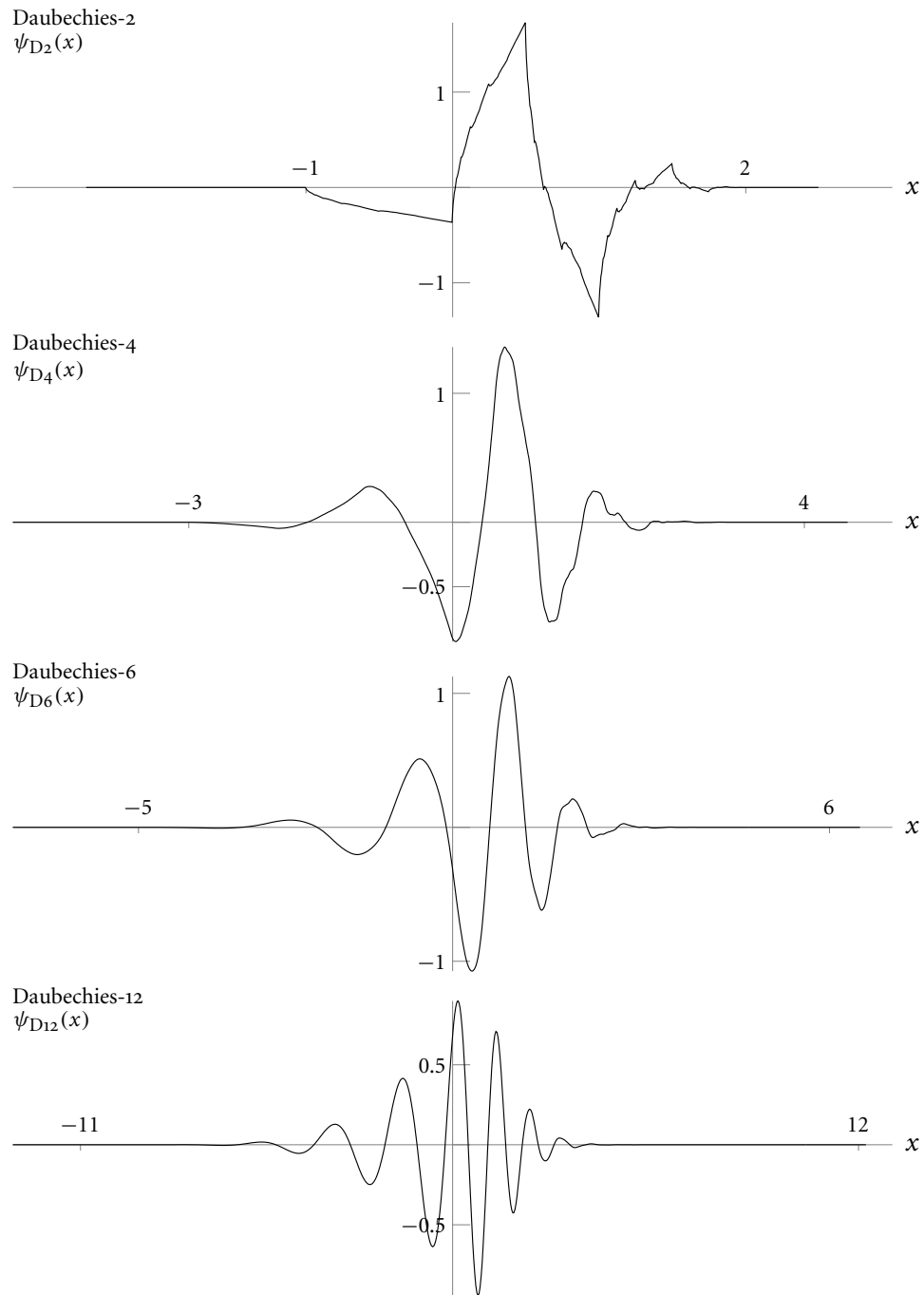


**FIGURE D.5 Four Daubechies wavelets.** Ticks on the  $x$ -axis show the compact support of the wavelet. Higher-order Daubechies wavelets are genuinely smoother (it is not an artefact of the plot resolution), but have wider support. The Daubechies-2 and -6 wavelets are used in the forward algorithm described in §3.6.

## D.5 Choosing a wavelet

Wavelets have been described as furnishing the analyst with ‘an embarrassment of riches’.<sup>4</sup> Our images are finite, encouraging us to choose wavelets of compact support. Both Daubechies-2 and Daubechies-12 wavelets plotted on the page before have compact support, but have dramatically different trade-offs between smoothness and length of support. A signal singularity will interact with a greater number of wavelets if the wavelets have long support, but such wavelets will be smoother and better represent the non-singular portions of the signal.

It has been suggested [445, p 246] by Rioul that in image processing work, wavelets that are once or twice continuously differentiable are sufficient. The great frequency localisation available with higher-order wavelets is useful in audio compression but irrelevant to broadly non-harmonic signals such as real-world images. These heuristics suggest the Daubechies-4 wavelet would be a good choice, if we had to choose a single wavelet basis for image processing. The wavelet-Wiener filter used in the forward algorithm requires *two* bases. Using Daubechies-2 and Daubechies-6 wavelets allows sufficient independence of the power spectra to make the two basis approach worthwhile, but does not stray too far from our smoothness ideal.

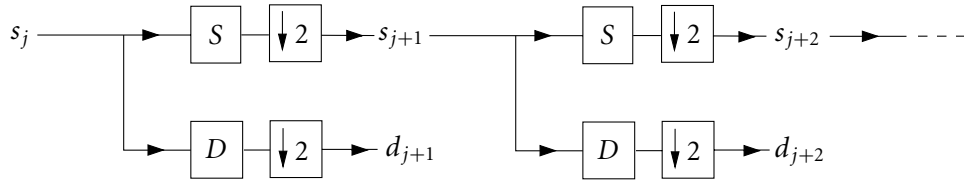
A number of adaptive algorithms are able to choose the *best basis* from a dictionary of orthogonal bases [445, pp 96–108] [49, §9.4]. Going beyond orthogonal bases, the *multiwavelet* approach fineses the trade-off between smoothness and support at the expense of a more complicated algorithm. In our application, these enhancements likely offer only incremental benefit. Dramatic improvements over the demonstrated forward performance would likely require the use of new geometric multiresolution frames such as the curvelets discussed in §3.7.4.

## D.6 The Discrete Wavelet Transform

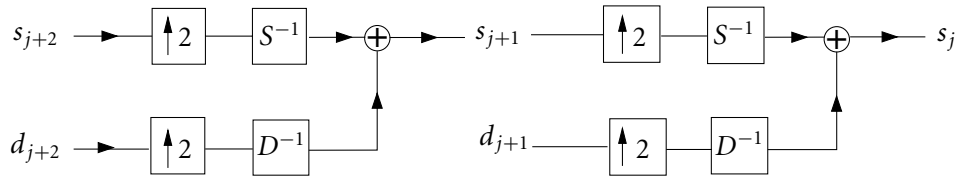
The (re)discovery of the FFT by Cooley and Tukey [371] transformed Fourier analysis from a mathematical abstraction to an essential tool of science and engineering. Mallat’s discovery of the *Discrete Wavelet Transform (DWT)* is having a similar effect on wavelet analysis. Mallat’s discussion [49, §7.3] is rigourous but opaque; in

---

<sup>4</sup> See §16 of Reference 445. This chapter, entitled ‘Which Wavelet?’, provides a clear and equation-free overview of wavelet choice.



A A forward DWT is computed with a cascade of filterings into smooth  $s$  and detail  $d$  components, followed by a factor 2 subsampling (discarding every second sample). Detail components are accumulated and the process is repeated on the smooth component.



B An inverse DWT reconstructs each progressively finer level of approximation  $s_j$  by inserting zeros between samples of each approximation and each detail set  $d_j$  (ie. factor 2 upsampling) and filtering and adding the output.

FIGURE D.6 The Discrete Wavelet Transform. Adapted from p 257 of Reference 49.

preference, see §13.10 of Reference 174<sup>5</sup> and pp 44–47 and §8 of Reference 445.

While the Cooley-Tukey algorithm decimates in space, the DWT decimates in *scale*. Beginning with the original array  $s_0$  of  $N$  sampled data, two filters are applied: a *smoothing* filter  $S$  and a *detail* filter  $D$ . The detail filter captures the finest textures  $d_1$  in the sampled data and these are stored. The output of the smoothing filter  $s_1$  is then filtered again, capturing detail  $d_2$  on a coarser scale and appending this information to the store. Eventually the signal has been smoothed away completely and we are left with only detail  $\{d_1, d_2, \dots, d_n\}$  at progressively coarser scales.

It should be no surprise that the smoothed signal  $s_1$  may be represented by fewer than  $N$  samples. In fact, the DWT *throws away* every second sample in the output of both  $S$  and  $D$  filters. Hence the first smoothed signal  $s_1$  contains  $N/2$  samples as does the first detail signal  $d_1$ . After the second filtering stage,  $s_2$  and  $d_2$  contain only  $N/4$  samples. The algorithm iterates more and more rapidly through its shrinking signal  $s_j$  until only two samples remain in  $s_n$ . We have, however, been

<sup>5</sup> *Numerical Recipes* provides a review of wavelets opposite to this Appendix: it begins with the discrete transform as a linear algebraic process and ultimately the Daubechies wavelets emerge rather naturally from the matrix algebra.

accumulating the details  $d_j$  of length  $N, N/2, N/4, \dots, 2$  and so the length of this output signal  $\{d_1, d_2, \dots, d_n, s_n\}$  is just  $N$ , the length of the input signal.

This output signal, composed of evenly-spaced spatial samples at dyadically finer scales, is the DWT of the input. The devil is in the only detail, the choice of the filters  $S$  and  $D$ . Not only must the information content of the signal be split between the smoothed and detailed channels without loss, this must be done so that the *subsampling* – the deletion of every second sample – does not result in any loss of information either. Pairs of filters which can do this are known as *conjugate mirror filters* and were invented by engineers some time before orthogonal wavelets were discovered.

Mallat showed that for every orthogonal wavelet there is a pair of mirror filters. The Daubechies-2 wavelet has corresponding filters which are merely discrete convolutions with a particular *four* element vector. Daubechies- $p$  wavelets are convolutions with vectors of length  $2p$ . Consequently, the DWT is *fast*, taking the same number of operations as a moving average over  $p$  points. In other words it is an  $O(N)$  algorithm, even faster than the FFT which is  $O(N \log N)$ .

Finally, the *inverse DWT* sketched in Figure D.6B begins with the two-element smoothest approximation and progressively pads out and reinserts the detail. Finer and finer scale approximations result until the original signal is reconstructed.

## D.7 Wavelets in two dimensions

In this thesis, our signals are images, and our wavelets must be two-dimensional. Getting a two dimensional wavelet basis is as simple as multiplying two one-dimensional bases:

$$\{\psi_{j_x,n}(x)\psi_{j_y,m}(y)\} \quad \text{with } j_x, j_y, n, m \text{ integers.} \quad (\text{D.6})$$

This basis doesn't sit well with our concept of resolution, however. The elements having  $j_x$  and  $j_y$  differing by more than one or two have shapes highly elongated along the  $x$ - or  $y$ -axes. We would prefer to have *one* scale which we bisect to attain finer and finer resolution, rather than having two 'resolutions' defined along the two axes.

A proper discussion of this concept of resolution in separable bases requires an understanding of the role of scaling functions in multiresolution analysis [49, §7.7]. Instead, we jump straight to the discrete two-dimensional wavelet transform,

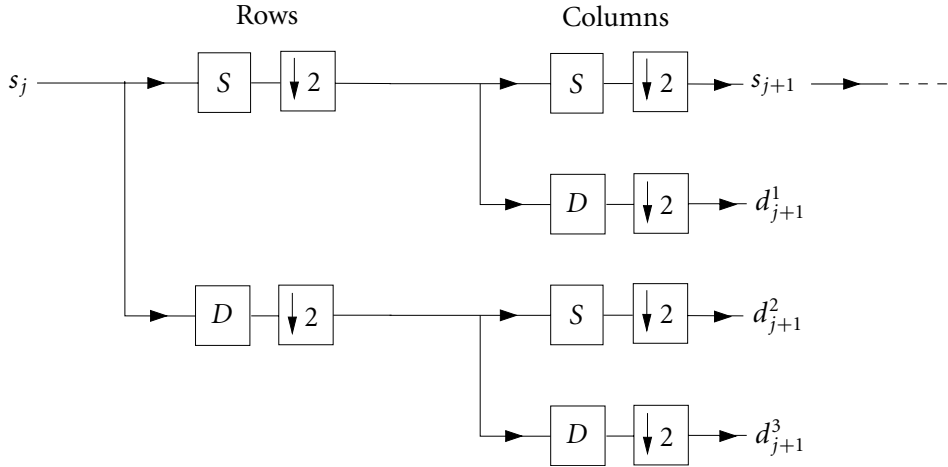


FIGURE D.7 **The 2D Discrete Wavelet Transform.**  $S$  and  $D$  are conjugate mirror filters operating on one-dimensional row or column components, identical to the filters of Figure D.6A. Adapted from p 312 of Reference 49.

depicted in Figure D.7.

Exactly the same conjugate mirror filters are used, now acting on the rows or columns of the image. We extract first the row detail, subsample and then pass it off to a second pair of the same filters but this time operating on columns. The  $S$  subfilter output is smoothed over columns but contains row details; we'll call it  $d_1^2$ . The  $D$  subfilter output contains both row and column detail; call it  $d_1^3$ . Returning to the output of the first filter pair, we now take the row smooth component and extract column detail; this is  $d_1^1$ . Finally, the smooth output of the column filter acting on the smooth output of the row filter is, indeed, an overall smoothing of the image. This is  $s_1$ , and is passed on to the next iteration of the algorithm. At each scale  $j$ , we produce *three* detail subimages  $d_j^1$ ,  $d_j^2$  and  $d_j^3$ , corresponding to column-detail, row-detail and block-detail.

For an  $N \times N$  pixel input image  $s_0$ , the three sets of detail data  $d_1^k$  are each  $\frac{1}{2}N \times \frac{1}{2}N$  pixels, the next three sets  $\frac{1}{4}N \times \frac{1}{4}N$  and so on. We can arrange these in a nested tiling of subimages Figure D.8; it is clear that the transformed output is an  $N \times N$  pixel image. Fine detail in the image is encoded in the  $d_1^j$  subimages; they show the enlistment of the finest scale wavelets near image edges. Progressively coarser details are encoded in the smaller subimages nested towards the top-left. Wavelet coefficients  $d_j^k[n, m]$  are still parameterised by four integers, but these are now the translation coordinates  $n$  and  $m$ , the row/column/block index  $k$  and a *single* dyadic scale index  $j$ .

$s_3$	$d_3^2$		
$d_3^1$	$d_3^3$	$d_2^2$	
		$d_1^2$	
	$d_2^1$	$d_2^3$	
	$d_1^1$		$d_1^3$

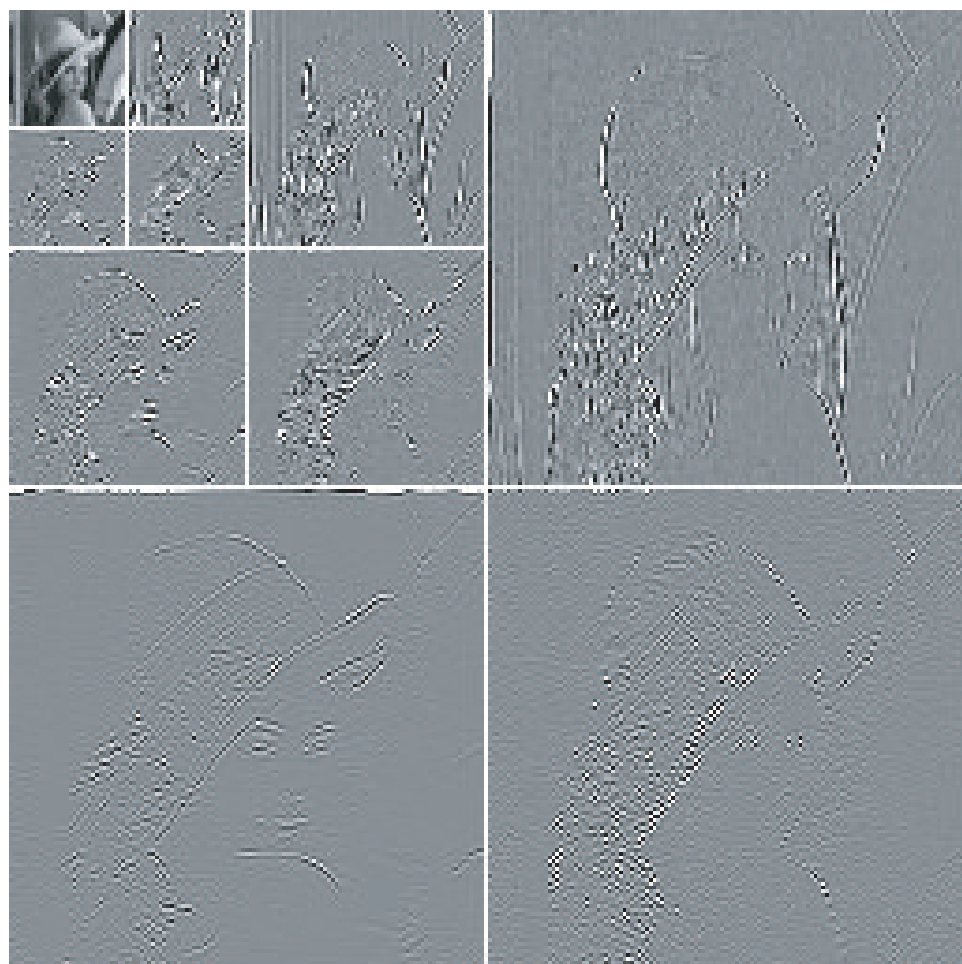


FIGURE D.8 Separable two-dimensional DWT of *Lena*.

— 0 +

The image actually shows the output of a DWT algorithm terminated after the first three filter/subsample iterations. A complete DWT would run until only the  $2 \times 2$  pixel  $s_n$  subimage remained in the top-left corner. Adapted from p 310 of Reference 49.

Figure 3.15 demonstrated that *Lena* could be reconstructed with low distortion from a relatively small number of significant wavelet coefficients, at least in comparison to a Fourier reconstruction. This efficiency is also displayed by the *Lena* DWT on the facing page: large areas of small wavelet coefficients are visible as the mid-grey regions.

Again, the transform is efficient, especially as the eight notionally distinct 1D convolution operations factor into the six filtering steps shown in Figure D.7. For a  $K$ -element filter ( $K = 4$  for Daubechies-2 wavelets) the full 2D DWT is complete in fewer than  $\frac{8}{3}KN^2$  operations [49, p 312]. The inverse transform reverses the filtering and upsamples, in exact analogy with the one-dimensional case [49, Figure 7.27].

Note that the `forward` algorithm actually uses a *redundant DWT* [49, §5.4] so that the retrieval performance is shift-invariant. Performance decreases to be of the same  $N \log N$  order as the `FFT`, although other shift-invariant transforms mentioned in §3.7.2 may be more efficient.



## Appendix E

# Power dissipated in anti-Helmholtz coils

It is readily shown with the Biot-Savart law that the magnetic field due to a loop centred on the origin of radius  $r$  carrying current  $NI$  is axial and has value [11, ??]

$$B_z = \frac{\mu_0 NI}{2} \frac{r^2}{(r^2 + z^2)^{3/2}}. \quad (\text{E.1})$$

The field gradient  $\partial B / \partial z$  due to an anti-Helmholtz coil pair, spaced by  $r$  is then

$$\left. \frac{\partial B_z}{\partial z} \right|_{z=0} = -\frac{3\mu_0 NI}{2r^2} \left(\frac{4}{5}\right)^{5/2} = 1.079 \frac{NI \text{ (amp)}}{r^2 \text{ (cm}^2\text{)}} \text{ G/cm} \quad (\text{E.2})$$

where  $NI$  is in amperes and  $r$  in centimetres. The number of turns  $N$  of wire of radius  $w$  which fit into the coil former of cross-sectional area  $A$  depicted in Figure E is

$$N = \frac{A}{4w^2}, \quad (\text{E.3})$$

assuming square packing. Ignoring the enamel thickness, the resistance  $R$  of the coils is

$$R = \frac{\rho l}{\pi w^2} \quad (\text{E.4})$$

where  $\rho$  is the resistivity and the total length of wire is

$$l = 2\pi r N \quad (\text{E.5})$$

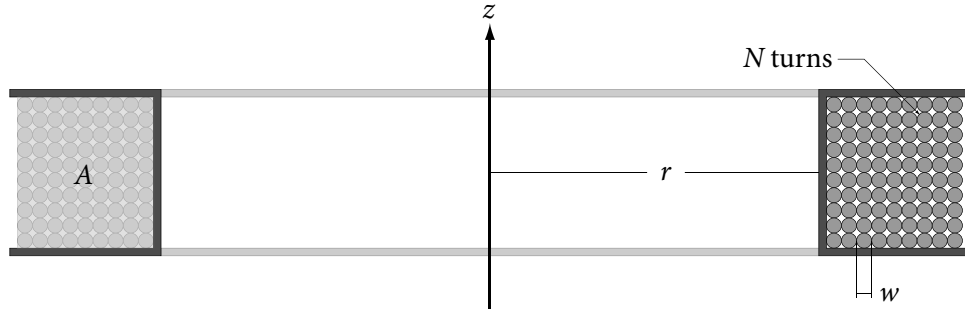


FIGURE E.1 Geometry of a single coil former.

when the coil depth is much smaller than its radius. The Joule heating  $P$  is given by

$$P = RI^2 = \frac{\rho 2\pi r N}{\pi w^2} \left( \frac{1}{0.859 \mu_0 N} \frac{\partial B}{\partial z} r^2 \right)^2 \quad (\text{E.6})$$

where we have used (E.4) and (E.5) to find the resistance and (E.2) to find the current. Using (E.3) this simplifies to

$$= \frac{2.72\rho}{\mu_0^2 A} \left( \frac{\partial B}{\partial z} \right)^2 r^5. \quad (\text{E.7})$$

The heat load does *not* depend on the  $w$ , the thickness of wire used, which may then be chosen to provide an appropriate resistive load for the power supply in use. Dissipated heat may be reduced by increasing the coil area, although this increases the expense and there are typically quite stringent mounting constraints. The sensitive dependence on the radius  $r$  is the rather surprising result of this Appendix.

## Appendix F

# Noninterferometric phase imaging of a neutral atomic beam

This Appendix is a facsimile of the paper

P. J. Fox, T. R. Mackin, L. D. Turner, I. Colton, K. A. Nugent and  
R. E. Scholten.

*Noninterferometric phase imaging of a neutral atomic beam.*

Journal of the Optical Society of America B **19**(8) 1773–1776  
(2002 Aug).

The paper describes non-interferometric measurements of the generalised phase of a rubidium atomic beam. The Transport-of-Intensity equation (3.1) is trivially solved in one dimension. Assuming a pure-phase object, it is possible to retrieve the phase-shift from a single beam profile. In this experiment the phase-shift was induced in the atomic beam by a strong off-resonant traveling laser beam orthogonal to the beam direction.

My contribution was primarily to the data analysis. In conjunction with Imogen Colton, I also estimated the ultimate sensitivity of this non-interferometric phase measurement and compared it to existing atom interferometers. Achieving TIE sensitivity comparable with traditional atom interferometers seemed prohibitively difficult. As a consequence of this analysis, I decided to explore non-interferometric *optical* measurement of laser-cooled atoms: in some senses an inversion of the work described in this paper.

## Noninterferometric phase imaging of a neutral atomic beam

P. J. Fox, T. R. Mackin, L. D. Turner, I. Colton, K. A. Nugent, and R. E. Scholten

*School of Physics, University of Melbourne, Victoria 3010, Australia*

Received February 28, 2002; revised manuscript received May 3, 2002

We demonstrate quantitative phase imaging of a neutral atomic beam by using a noninterferometric technique. A collimated thermal atomic beam is phase shifted by an off-resonant traveling laser beam with both a Gaussian and a  $\text{TEM}_{01}$  profile and with both red and blue detuning of as much as 50 GHz. Phase variations of more than 1000 rad were recovered from velocity-selective measurements of the propagation of the atomic beam and were found to be in quantitative agreement with theoretical predictions based on independently measured phase object intensity profiles and detunings. © 2002 Optical Society of America

*OCIS codes:* 100.5070, 120.3180, 120.5050, 260.3160, 350.5030.

### 1. INTRODUCTION

The measurement of the phase of a wave field has been at the heart of many advances in physics and is the basis of many important applications. Measuring phase with atomic matter waves offers advances in both fundamental and applied precision experiments<sup>1</sup>; for example, neutral-atom interferometry has been used to measure rotation, gravity, and gravitational gradients with remarkable precision.<sup>2,3</sup>

Phase is traditionally measured by interferometry and indeed is often defined in terms of interference. Phase can more generally be defined in terms of the propagation direction of the wave field, which can be determined noninterferometrically.<sup>4,5</sup> The noninterferometric approach was initially developed for applications in adaptive optics and has now been demonstrated for visible microscopy, x rays, electrons, and neutrons.<sup>6</sup> The technique inherently determines both intensity and phase simultaneously, and it directly measures the phase rather than its cosine. It does not require beam splitters or mirrors and places minimal constraints on the temporal coherence of the wave field. These factors are particularly valuable for matter wave phase measurements and allow us to demonstrate the approach with a simple collimated thermal rubidium beam.

### 2. DEFINING PHASE

For an arbitrary matter wave, the time-averaged probability current is an average of momentum vector  $\mathbf{p}$  over the Wigner distribution  $W(\mathbf{r}, \mathbf{p})$ :

$$\mathbf{j}(\mathbf{r}) = \frac{1}{m} \int \mathbf{p} W(\mathbf{r}, \mathbf{p}) d\mathbf{p}, \quad (1)$$

where  $m$  is the atomic mass and  $\mathbf{r}$  is position. We can define a function  $\Phi$  such that

$$\mathbf{j}(\mathbf{r}) = \frac{1}{m} \rho(\mathbf{r}) \nabla \Phi(\mathbf{r}), \quad (2)$$

where  $\rho(\mathbf{r})$  is the probability density. We refer to  $\Phi$  as the generalized phase. For a stationary scalar wave field in the coherent limit, that is, when the wave function can be written as<sup>7</sup>  $\psi(\mathbf{r}) = \sqrt{\rho(\mathbf{r})} \exp iS(\mathbf{r})/\hbar$ , the probability current reduces to  $\mathbf{j}(\mathbf{r}) = \rho(\mathbf{r}) \nabla S(\mathbf{r})/m$ , where  $S$  is the conventional phase. In this limit the generalized phase and the conventional phase are the same, but the generalized phase remains well defined for partially coherent fields. This is particularly important for a noncoherent field such as the thermal atom source used in our experiments and permits phase measurement in circumstances in which interferometric recovery would not be possible. Measurements of the generalized phase are equivalent to measurements of the interferometric phase in cases when interferometry is possible. For a polychromatic wave, the generalized phase measurement yields the same result as interferometry at the average wavelength.<sup>4</sup>

In free space, in the absence of sources or sinks, conservation of probability implies that  $\nabla \cdot \mathbf{j}(\mathbf{r}) = 0$ . In the paraxial approximation, where the  $z$  derivative of the phase is constant ( $\partial\Phi/\partial z \approx k$  and  $\partial^2\Phi/\partial z^2 \approx 0$ ), this conservation of probability may be written as the paraxial transport-of-intensity equation (TIE; Ref. 8):

$$\frac{\partial \rho(\mathbf{r}_\perp)}{\partial z} = -\frac{\hbar}{p} \nabla_\perp \cdot [\rho(\mathbf{r}_\perp) \nabla_\perp \Phi(\mathbf{r}_\perp)], \quad (3)$$

where  $\mathbf{r}_\perp$  is the two-dimensional position vector in the plane normal to the propagation axis and  $p = \hbar k$  the atomic momentum. The TIE is derived from the parabolic wave equation, which is satisfied by the conventional Fresnel diffraction result but with broader applicability.<sup>8</sup> Experimentally, the probability distribution is measured at two planes separated by  $\Delta z$  and the derivative is calculated numerically. If the field is free of singularities, sources, or sinks, then a unique solution for phase exists<sup>9</sup> and can be readily obtained by Fourier techniques.<sup>5</sup>

In the experiments discussed here, we measured the probability density by using fluorescence imaging in one

dimension only. The solution of the TIE was then obtained by twice integrating along  $x$ .

### 3. APPARATUS

Our experimental arrangement for measuring atomic matter wave phase is shown in Fig. 1. A rubidium beam was produced with a recirculating thermal source<sup>10</sup> and collimated in one dimension (along  $x$ ) by polarization gradient ( $\text{lin} \times \text{lin}$ ) laser cooling.<sup>11</sup> The residual transverse velocity distribution is  $\Delta v \approx 6v_r$  (FWHM), where  $v_r = 6 \text{ mm/s}$  is the single-photon recoil velocity for Rb.

The atoms were then influenced by the phase object, an off-resonant traveling wave laser beam propagating along  $\hat{y}$ . The probability density of the phase-shifted matter wave was determined by velocity-selective fluorescence imaging. The fluorescence probe laser was incident at  $9^\circ$  to the atomic beam and was detuned from resonance by being locked to the first crossover peak 60.35 MHz below the desired  $F = 3 \rightarrow F' = 4$  transition of  $^{87}\text{Rb}$ . The selected longitudinal velocity group was then approximately  $v = 300 \pm 15 \text{ m/s}$  (atomic de Broglie wavelength,  $\lambda_{\text{dB}} = 0.016 \text{ nm}$ ), where the width is determined by the geometry and the saturated probe laser linewidth. The fluorescence was imaged by use of a cooled CCD camera with a 16-bit dynamic range and a spatial resolution in the image plane of  $6.43 \pm 0.05 \mu\text{m}$ .

To measure the longitudinal derivative, probability distributions are needed in two planes separated along propagation axis  $\hat{z}$ . Initial measurements were made with two fluorescence probes separated by approximately 6 mm. The small separation distance allowed both probes to be imaged on the same CCD frame, but the difference between the two closely spaced images did not have an adequate signal-to-noise ratio for accurate phase recovery. A much larger effective separation was achieved with a single fixed CCD imaging system and a single fluorescence probe. Two images were acquired, at 10 cm from the nominal phase object location, with the phase object on and off. The image with the phase object off is equivalent to a fluorescence profile taken immediately after the phase object, with two provisos: First, the unperturbed atomic beam profile should not change between the phase object's location and the fluorescence probe. We satisfy this condition by ensuring that the

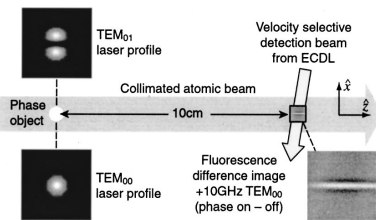


Fig. 1. Experimental setup. The probability density of the atomic beam is modified by interaction with an off-resonant laser beam. Measurement of the fluorescence profile with the phase object on and off determines the evolution of the atomic beam. Images were taken with a CCD camera oriented along  $\hat{y}$ . ECDL, external-cavity diode laser.

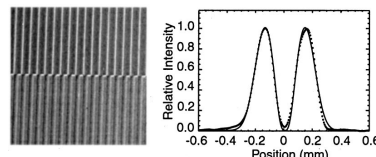


Fig. 2. Scanning-electron micrograph of the diffraction mask used to generate the  $\text{TEM}_{01}$  mode pattern, fabricated from a microscope overslip by excimer-laser ablation, and the measured (dotted curve) and calculated (solid curve) profiles along  $x$ . Grating spacing,  $20 \mu\text{m}$ .

atomic beam does not diverge significantly (e.g., by no more than one imaging pixel width) over the separation between effective imaging planes. For our divergence of  $\pm 6v_r/v$  the maximum separation distance was  $\Delta z = 10 \text{ cm}$ .

The object-on-object-off method also assumes that the phase object is nonabsorbing. Using measurements in two separated planes, we determined both the phase and the probability distribution simultaneously and unambiguously. With only one measurement plane, the effects of absorption cannot be distinguished from gradients in the phase. Optical pumping produces an effect equivalent to absorption, for example, by transferring atoms from the  $^{87}\text{Rb } F = 3$  to the  $F = 2$  hyperfine ground state, where they are not detected. To minimize this effect we pumped the atoms back into the  $F = 3$  ground state with a low-intensity (2 mW, Gaussian profile, 1-mm waist diameter) repumping beam tuned to the  $F = 2 \rightarrow F' = 3$  transition.

### 4. PHASE OBJECTS

The phase object is a traveling wave laser beam propagating in the  $\hat{y}$  direction, interacting with the atoms by means of the dipole potential. Spontaneous emission is effectively isotropic and hence is neglected. For a laser beam with intensity profile  $I(x, z) = I_0 G(x, z)$ , the dipole potential is<sup>12</sup>

$$U(x, z) = \frac{\hbar \delta}{2} \ln \left[ 1 + \frac{I_0}{I_s} \frac{\Gamma^2}{(\Gamma^2 + 4\delta^2)} G(x, z) \right], \quad (4)$$

where  $\delta = \omega - \omega_0$  is the detuning of the laser frequency from resonance,  $I_s$  is the saturation intensity for the atomic transition, and  $\Gamma$  is the transition linewidth.

The phase object intensity profiles are

$$G_{00}(x, z) = \exp \left[ -2 \left( \frac{x^2}{\sigma_x^2} + \frac{z^2}{\sigma_z^2} \right) \right] \quad (5)$$

and  $G_{01}(x, z) = (x^2/\sigma_x^2) G_{00}(x, z)$ , where  $\sigma_{x,z}$  are the characteristic  $1/e^2$  beam widths. For the Gaussian phase object, a 500-mW 780-nm single-mode Ti:sapphire laser beam was focused at the atomic beam by an  $f = 300 \text{ mm}$  focal-length lens. The measured beam waist was  $\sigma_x = 200 \mu\text{m}$ .

The  $\text{TEM}_{01}$  beam was generated with a binary diffractive phase mask (Fig. 2) fabricated from a glass substrate by excimer laser ablation.<sup>13</sup> Approximately 8% (40 mW) of the Ti:sapphire beam was diffracted into the first-order

Fox *et al.*

Vol. 19, No. 8/August 2002/J. Opt. Soc. Am. B 1775

$\text{TEM}_{01}$  beam, focused with the  $f = 300 \text{ mm}$  lens to a measured beam waist of  $\sigma_x = 485 \mu\text{m}$  and oriented such that the dark band in the mode was along the atomic beam axis.

## 5. RESULTS

The atomic probability distribution and the longitudinal derivative were found from the sum and the difference of phase-on and phase-off image averages. The phase was then calculated by integration along  $x$ . Figure 3 shows the results for the 40-mW  $\text{TEM}_{01}$  phase object in comparison with theoretical phase profiles calculated from the projected dipole potential. The agreement is generally good across the range of detunings. The phase-retrieval algorithm successfully determined the sign and spatial structure of the phase shift for variations in phase of nearly 200 rad. Note that the asymmetry in the profile is due partly to asymmetries in the laser mode that were not taken into account with the theoretical profiles.

At smaller detunings ( $\pm 1 \text{ GHz}$ ) the recovered phase profiles show significant distortions at the profile edges. The distortions result from relatively noisy data at these detunings, which are particularly significant in regions where the phase gradient is small. We could avoid these low-spatial-frequency artifacts by collecting additional data and ensuring that the result had converged.

Figure 4 shows the recovered and the calculated phase profiles for the 500-mW Gaussian profile phase object. The agreement is excellent for negative detunings, in this case for phase variations of more than 1000 rad. The agreement is also good for large positive detunings,  $\delta = +20, 50 \text{ GHz}$ . Discrepancies occur at smaller positive detunings as a result of optical pumping losses. With the phase-on/phase-off method, optical pumping removes detectable atoms from the center of the atomic beam, increasing the apparent phase gradient and the integrated phase shift. The saturated linewidth is approximately 6 GHz for the beam intensity used with the Gaussian phase object; hence there is significant overlap with both hyper-

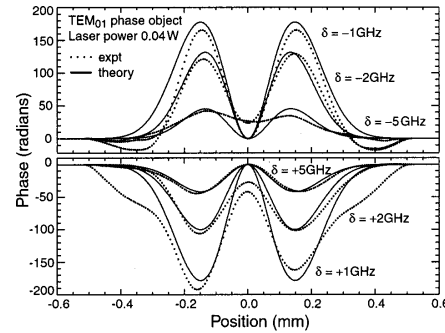


Fig. 3. Retrieved phase at  $\lambda_{\text{dB}} = 0.016 \text{ nm}$  for  $\text{TEM}_{01}$  phase objects. Results at small detunings show low-spatial-frequency artifacts induced by noise in regions of small phase gradients. The statistical uncertainty in the original fluorescence images is 0.3%.

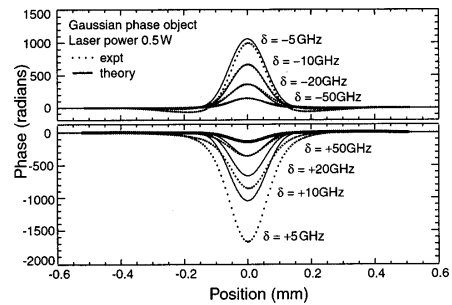


Fig. 4. Retrieved phase at  $\lambda_{\text{dB}} = 0.016 \text{ nm}$  for Gaussian phase objects. The discrepancy at small positive detunings is due to optical pumping losses into the undetected hyperfine ground state.

fine ground states (3-GHz splitting) for smaller detunings. This effect increases the phase shift but was neglected in the calculated phase.

The results in Figs. 3 and 4 indicate that the phase of an incoherent atomic beam can be determined noninterferometrically, quantitatively, and with detailed spatial structure over a range of at least 1000 rad. Problems with optical pumping losses at small detunings could be alleviated by use of increased power in the repump laser or by the use of  $^{87}\text{Rb}$ , which has a larger ground-state hyperfine separation, but a true separated-beam measurement should provide a direct measurement of the losses and an unambiguous determination of the phase profile.

Even for large phase shifts, interferometry demands sufficient stability and coherence to measure phase variations of less than one fringe. With our noninterferometric approach the necessary experimental precision is determined by the final desired phase resolution, which might be many wavelengths. The minimum phase resolvable with our noninterferometric method is approximately  $\Delta\Phi = k\Delta\theta$ , where  $\Delta\theta$  is the imaging resolution. With slow atoms (20 m/s), a phase-shift resolution of the order of  $10^{-15} \text{ m}$  is feasible. Further research will develop the technique with slow atoms and for retrieving phase in two dimensions, where interferometry is particularly difficult and the phase-recovery algorithm is inherently more stable.

## ACKNOWLEDGMENTS

We thank E. Harvey for collaboration in fabricating phase masks and D. Paganin and A. Barty for helpful discussions.

R. Scholten's email address is r.scholten@physics.unimelb.edu.au.

## REFERENCES

1. P. R. Berman, ed., *Atom Interferometry* (Academic, San Diego, Calif., 1997).
2. T. L. Gustavson, A. Landragin, and M. A. Kasevich, "Rotation sensing with a dual atom-interferometer Sagnac gyroscope," *Class. Quantum Grav.* **17**, 2385–2398 (2000).

3. A. Peters, K. Y. Chung, and S. Chu, "Measurement of gravitational acceleration by dropping atoms," *Nature* **400**, 849–852 (1999).
4. K. A. Nugent and D. Paganin, "Matter-wave phase measurement: a noninterferometric approach," *Phys. Rev. A* **61**, 063614 (2000).
5. D. Paganin and K. A. Nugent, "Noninterferometric phase imaging with partially coherent light," *Phys. Rev. Lett.* **80**, 2586–2589 (1998).
6. K. A. Nugent, D. Paganin, and T. E. Gureyev, "A phase odyssey," *Phys. Today* **54**(8), 27–32 (2001).
7. A. Messiah, *Quantum Mechanics* (North-Holland, Amsterdam, 1961), Vol. 1, p. 222.
8. M. R. Teague, "Deterministic phase retrieval: a Green's function solution," *J. Opt. Soc. Am. A* **73**, 1434–1441 (1983).
9. T. E. Gureyev, A. Roberts, and K. A. Nugent, "Partially coherent fields, the transport-of-intensity equation, and phase uniqueness," *J. Opt. Soc. Am. A* **12**, 1942–1946 (1995).
10. M. R. Walkiewicz, P. J. Fox, and R. E. Scholten, "Candlestick rubidium beam source," *Rev. Sci. Instrum.* **71**, 3342–3344 (2000).
11. R. E. Scholten, R. Gupta, J. J. McClelland, R. J. Celotta, M. S. Levenson, and M. G. Vangel, "Laser collimation of a chromium beam," *Phys. Rev. A* **55**, 1331–1338 (1997).
12. J. P. Gordon and A. Ashkin, "Motion of atoms in a radiation trap," *Phys. Rev. A* **21**, 1606–1617 (1980).
13. E. C. Harvey, J. P. Hayes, B. C. Dempster, T. R. Mackin, and R. E. Scholten, "Excimer laser ablation used for the fabrication of micro-optic phase and diffraction elements," in *Micro-Opto-Electro-Mechanical Systems*, R. R. Syms, ed., Proc. SPIE **4075**, 152–158 (2000).



## Appendix G

# Frequency noise characterisation of narrow linewidth diode lasers

This Appendix is a facsimile of the paper

L. D. Turner, K. P. Weber, C. J. Hawthorn and R. E. Scholten.

*Frequency noise characterisation of narrow linewidth diode lasers.*

Optics Communications **201**(4–6) 391–397 (2002 Jan).

This paper describes the use of a single-chip phase-locked loop circuit to demodulate the beat-note between two external-cavity diode lasers (ECDLS). Frequency analysis of the demodulated signal gives a direct measurement of the optical frequency noise of the lasers. This technique enabled us to identify and eliminate individual noise sources affecting our lasers as well as measuring the coloured noise spectrum, a necessary step in designing the laser servo (see §4.6).

I designed, tested and calibrated the FM-demodulator circuit and obtained and analysed most of the data presented in the paper.



ELSEVIER

15 January 2002

Optics Communications 201 (2002) 391–397

OPTICS  
COMMUNICATIONS[www.elsevier.com/locate/optcom](http://www.elsevier.com/locate/optcom)

## Frequency noise characterisation of narrow linewidth diode lasers

L.D. Turner, K.P. Weber, C.J. Hawthorn, R.E. Scholten\*

*School of Physics, University of Melbourne, Parkville, Vic. 3010, Australia*

Received 4 October 2001; received in revised form 4 October 2001; accepted 15 November 2001

---

### Abstract

We examine several approaches to laser frequency noise measurement in the frequency and time domains. Commonly employed methods such as optical frequency discrimination and the Allan variance are found to be complex, expensive, time-consuming, or incomplete. We describe a practical method of demodulating a laser beat note to measure a frequency noise spectrum, using a phase-locked loop frequency discriminator based on a single low-cost integrated circuit. This method measures the frequency noise spectrum of a laser directly and in detail and is insensitive to intensity fluctuations. The advantages of this scheme are demonstrated through measurement of the frequency noise spectrum for two external cavity diode lasers (ECDL), clearly distinguishing several common noise sources. These are isolated and removed, reducing the individual laser rms linewidth from 2 MHz to 450 kHz. The spectrum is used to calculate the Allan variance, which shows almost none of the important information. © 2002 Elsevier Science B.V. All rights reserved.

PACS: 42.55.-f; 42.55.Px; 42.60.Mi; 42.60.-v

Keywords: Diode lasers; Frequency noise; Frequency discrimination

---

### 1. Introduction

Narrow linewidth and highly stable lasers are critically important in fields as diverse as optical communications, laser cooling and atomic frequency standards. When designing a laser sys-

tem, the identification and removal of frequency noise sources is crucial to narrowing the linewidth. Accurate measurement of the laser frequency stability is also often required as an experimental parameter.

External cavity diode lasers (ECDLs) are a common example of such narrow linewidth lasers [1]. ECDLs use semiconductor diode lasers in an external cavity with dispersive feedback, often from a diffraction grating. The linewidth is greatly reduced with respect to the diode alone, and the laser can be tuned through the broad gain curve of the diode.

---

\* Corresponding author. Tel.: +61-3-8344-5457; fax: +61-3-9347-4783.

E-mail address: r.scholten@physics.unimelb.edu.au (R.E. Scholten).

ECDLs exhibit varying forms of frequency noise from environmental, fundamental, and artificial sources. Environmental noise includes 50 or 60 Hz power-line-induced noise, and acoustically coupled noise, in particular at frequencies corresponding to mechanical resonances. Fundamental noise is typically dominated by white phase noise at high frequencies and flicker frequency noise (also known as  $1/f$  noise or pink noise) at low frequencies [2]. The flicker frequency noise is often the dominant component of the linewidth, and so it is common practice to stabilise the laser to an external frequency reference, for example a Fabry–Perot etalon or sub-Doppler atomic resonance. The feedback systems usually rely on dithering the laser frequency [3] or the reference frequency [4], but in both cases it is common to find significant noise at the dither frequency, thus introducing an artificial source of frequency noise.

## 2. Measurement of laser frequency noise

Laser frequency noise may be measured directly at the optical frequency, or by heterodyning to a reference laser.

### 2.1. Optical frequency discrimination

Direct optical measurements use an optical frequency discriminator to convert frequency modulation to intensity modulation. Common examples are transmission at the side of a Fabry–Perot etalon fringe [5], or the side of an atomic absorption resonance [6], either Doppler-broadened or sub-Doppler. These can be convenient and low cost, but high frequency resolution, signal to noise ratio, and stability are more difficult to achieve. In addition, such optical frequency discriminators typically do not distinguish between frequency and intensity fluctuations. This lack of distinction between the two types of fluctuations is particularly important when analysing the frequency noise of diode lasers, because fluctuations in the injection current affect both frequency and output power.

### 2.2. Radio frequency discrimination

Laser frequency noise can also be measured by heterodyning two lasers, for example by superimposing the two beams on a fast photodiode (PD) to produce a radio frequency (rf) beat note at the difference frequency. Frequency fluctuations apparent in the beat note are the combination of the individual frequency fluctuations of the lasers. A single laser can also be superimposed with itself via a fiber delay loop [7], but such self-homodyne systems are ill-suited to measuring laser noise at low frequencies, since impractically long delays are required.

The heterodyne method is very commonly used to obtain a measure of the linewidth of a laser. The beat note is analysed with an rf spectrum analyser and the width of the spectral peak at the beat frequency, averaged over some measurement time, is taken as the combined laser linewidth. Unfortunately this provides very little information on the composition, and hence sources, of the frequency noise [2].

## 3. Analysis of radio frequency spectra

Frequency noise analysis of the beat signal can provide this information, either in the frequency domain or in the time domain. The beat note signal produced by lasers with frequency difference  $v_0$  has voltage

$$V(t) = V_0(t) \sin[2\pi v_0 t + \phi(t)], \quad (1)$$

where  $V_0(t)$  describes amplitude fluctuations of the two lasers and  $\phi(t)$  is the difference of the individual phases. The instantaneous beat frequency is

$$v(t) = v_0 + \frac{1}{2\pi} \frac{d\phi(t)}{dt} = v_0 + \Delta v(t) \quad (2)$$

with frequency fluctuations  $\Delta v(t) \ll v_0$ .

### 3.1. Time domain frequency analysis

The time domain parameters are variances of multiple measurements of the instantaneous frequency  $v(t)$  each of period  $\tau$ . The standard measure is the Allan variance, the zero dead-time two-sample deviation over a given time period  $\tau$ :

$$\sigma^2(\tau) = \frac{1}{2} \langle [v_\tau(t) - v_\tau(t + \tau)]^2 \rangle, \quad (3)$$

where the brackets  $\langle \rangle$  denote time averaging. The measurement of an Allan variance requires two frequency counters, a pulse sequencer, and a computer with data acquisition system to calculate the variance at each time interval [8].

### 3.2. Frequency domain analysis

The fundamental parameter in the frequency domain is the frequency noise power spectral density, measured in Hz<sup>2</sup>/Hz, given by

$$S_{\Delta\nu}(f) = 2 \int_0^\infty \langle \Delta\nu(t) \Delta\nu(t + \tau) \rangle \exp(-i2\pi f \tau) d\tau, \quad (4)$$

where  $f$  is termed the Fourier frequency. The root mean square (rms) linewidth  $\Delta\nu_{\text{rms}}$  is then

$$\Delta\nu_{\text{rms}}^2 = \int_0^\infty S_{\Delta\nu}(f) df. \quad (5)$$

The beat note linewidth measured on an rf spectrum analyser is not simply related to the rms linewidth. If the frequency noise spectrum is a delta function, the rf beat spectrum will be approximately rectangular with width of  $L = 2\sqrt{2}\Delta\nu_{\text{rms}}$ . If the rf beat spectrum is Gaussian, the full width at half maximum (FWHM) will be  $2.35\Delta\nu_{\text{rms}}$  [9].

The Allan variance may be determined from the frequency noise spectrum  $S_{\Delta\nu}$  by the integral [10]

$$\sigma^2(\tau) = 2 \int_0^\infty S_{\Delta\nu}(f) \frac{\sin^4(\pi f \tau)}{(\pi f \tau)^2} df \quad (6)$$

but in general the frequency noise spectrum cannot be determined from the Allan variance [11]. The frequency noise spectrum is therefore preferable to the Allan variance.

## 4. Experiment

### 4.1. Phase-locked loop frequency discriminator

The frequency noise spectrum may be recovered directly from the beat signal with a frequency

discriminator which outputs a voltage proportional to  $\Delta\nu(t)$ , with minimal dependence on amplitude fluctuations  $V_0(t)$ . The power spectral density of this voltage, for example acquired with an audio frequency spectrum analyser, is  $S_{\Delta\nu}$ .

Previous experiments using discriminators have required complex rf electronics [12] and suffered from poor spectral resolution [13]. We describe a simple frequency discriminator and its application to ECDLs, and demonstrate the increased information over the rf beat spectrum alone and over Allan variance measurements.

We use a single chip phase-locked loop (Philips SA568), which consists of a local voltage controlled oscillator phase-locked to the input signal with a phase detector and feedback loop. The feedback voltage depends on the frequency of the input signal. Unlike previously employed discriminators, this frequency discriminator operates across a broad range of beat note frequencies from 40 to 110 MHz, tracks frequency deviations of up to 10 MHz, and is insensitive to amplitude modulation (20 dB rejection).

Fig. 1 is a schematic of our apparatus. The single frequency output beams from two ECDLs [14] are superimposed on a New Focus 1621 photodetector. The beat signal was amplified by 32dB with a wideband MMIC (Agilent MSA-0886) and fed directly into the SA568. Our circuit

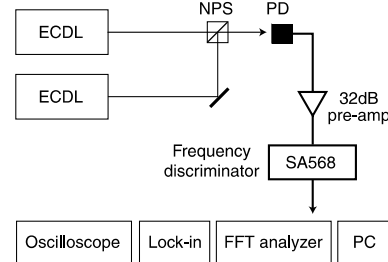


Fig. 1. Two external cavity diode lasers (ECDLs), locked to saturated absorption resonances, were superimposed with a non-polarising beamsplitter (NPS) onto a fast photodiode (PD). The heterodyne signal was pre-amplified and analysed with a frequency discriminator (Philips SA568) and the frequency spectrum acquired with any one of the audio frequency spectrum analysers shown.

uses only a few associated passive components, as specified in the Agilent and Philips datasheets. For normal laboratory use, the frequency discriminator output spectrum can be acquired with an oscilloscope with FFT capability, a lock-in amplifier, or the audio digitiser of a personal computer sound card. For the high-resolution results presented here, we used an SRS760 FFT audio frequency spectrum analyser.

#### 4.2. External cavity diode lasers

The ECDL are based on the Littrow configuration design of Arnold et al. [15] (Fig. 2). Each consists of a Sanyo DL-7140-201 laser diode and aspheric collimating lens ( $f = 4.5 \text{ mm}$ , 0.55NA, Thorlabs C230TM-B) mounted in a collimation tube (Thorlabs LT230P5-B) fixed to a modified mirror mount (Newport U100-P). A  $10 \text{ k}\Omega$  thermistor sensor and Peltier thermoelectric cooler (Melcor CP1.4-71-045L,  $30 \times 30 \times 3.3 \text{ mm}^3$ ) are used to stabilise the diode temperature. A gold-

coated diffraction grating provides wavelength-selective feedback. We use Richardson Grating Laboratory 3301FL-330H gratings with 1800 lines/mm on a  $15 \times 15 \times 3 \text{ mm}^3$  substrate, with a typical diffraction efficiency of about 15%. Up to 80% of the intra-cavity power is directly reflected to form the output beam. The grating is attached to the front face of the modified U100-P, which provides vertical and horizontal grating adjustment. A 1 mm thick PZT piezoelectric transducer disk under the grating is used to modify the cavity length for fine frequency tuning. The output beam is reflected from a mirror attached to the grating arm. The double reflection from grating and mirror maintains a fixed output beam direction as the grating angle and lasing wavelength is adjusted [14]. The output power is typically 40 mW at 780 nm, and the wavelength can be tuned discontinuously over a 10 nm range by rotation of the grating alone, and over a wider range with suitable temperature adjustment.

The lasers also have a stacked piezoelectric transducer (Tokin AE0203D04) which drives the grating-mirror pivot arm. This stack alters the grating angle and the cavity length, allowing electronic wavelength adjustment of 20 GHz over the 100 V range of the stack. This allows greater scanning range and much safer voltages compared to the original design [15].

Each laser is mounted to a heavy (5 kg) metal base to provide inertial and thermal damping. The base is isolated from the optical bench with viscoelastic polymer (Sorbothane) at the corners and enclosed with an aluminum cover, which is also isolated from the laser by strips of Sorbothane. The laser and saturated absorption optics are covered with an acrylic enclosure. The aluminum cover and acrylic enclosure shield the lasers from air currents, improve temperature stability, and suppress acoustic vibrations.

The laser frequencies were stabilised to two saturated absorption peaks in a rubidium vapour cell using ac (heterodyne) locking [3]. The laser frequencies were initially dithered at 23 and 29 kHz by modulation of the piezo disk voltage. The saturated absorption signals are detected with silicon photodetectors (Burr-Brown OPT210) and a home-made lock-in amplifier. One laser was

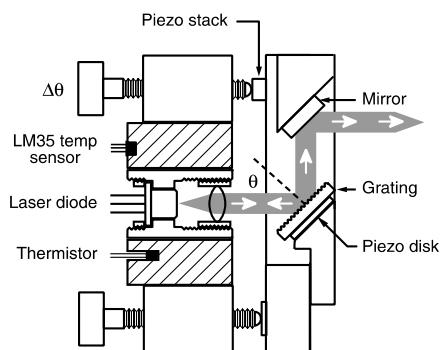


Fig. 2. External cavity diode laser design, based on [15]. An AlGaAs laser diode, aspheric collimation lens, and diffraction grating in a Littrow configuration, are mounted in a kinematic mirror mount. A thermistor temperature sensor is used for feedback to stabilise the laser temperature with a thermoelectric cooler (not shown). An LM35 semiconductor sensor provides a separate temperature readout. The mirror maintains a fixed output beam direction as the grating angle is adjusted [14]. A piezoelectric stack is used to adjust the grating angle and hence wavelength (20 GHz/100 V) and a piezo disk adjusts the cavity length for frequency locking feedback.

locked to the Rb<sup>85</sup> 5S<sub>1/2</sub>(F = 2) → 5P<sub>3/2</sub>(F' = 3) hyperfine transition and the other to the Rb<sup>85</sup> 5S<sub>1/2</sub>(F = 2) → 5<sup>2</sup>P<sub>3/2</sub>(F' = 2, 3) crossover, separated by 60.35 MHz.

#### 4.3. Frequency noise spectra

The rf beat between the two lasers was measured with an rf spectrum analyser (Fig. 3), and with our phase-locked loop frequency discriminator (Fig. 4). Once the SA568 internal oscillator frequency was set to within a few MHz of the beat frequency, no further adjustments were necessary. The SA568 output was analysed with the FFT spectrum analyser to produce the frequency noise spectra shown in Fig. 4.

The modulator voltage output per unit frequency deviation input was calibrated by the Bessel null method [16] in which absolute frequency deviations are measured by viewing carrier suppression on an rf spectrum analyser. This calibration is not required for general application, where only the relative contribution of frequency

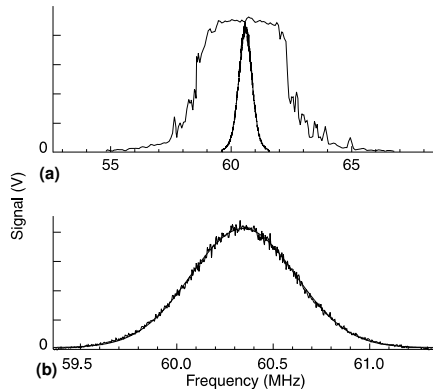


Fig. 3. (a) Beatnote spectra for two ECDLs locked to Rb transitions at 780 nm, separated by 60.3 MHz, before and after noise minimisation modifications. (b) Detail of the beatnote spectrum after noise minimisation modifications, taken with 3 kHz resolution bandwidth, averaged over 64 sweeps of 2 s each. The close agreement with a Gaussian fit (smooth curve) indicates that the deviations in laser frequency are large compared to the frequencies of modulation [9].

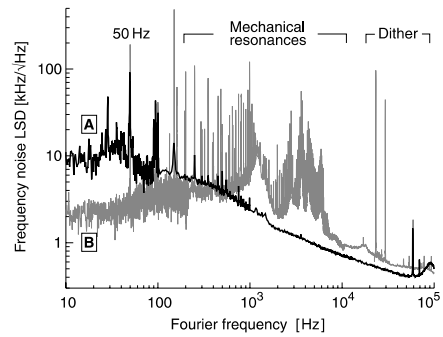


Fig. 4. Frequency noise linear spectral density (the square-root of the power spectral density  $S_{Av}(f)$ ) of ECDL beat note, before (B) and after (A) noise minimisation modifications.

noise sources in a laser system is needed. Even if absolute quantitation is desirable, the rf spectrum analyser is necessary only for a once-off calibration.

The detail evident in the spectra of Fig. 4 immediately illustrates the power of this method. The prominent peaks at 50 and 150 Hz in spectrum (B) are power-line harmonics which are evident up to 6 kHz. The sharp resonance at 990 Hz is due to a turbo-pump on the same optical bench as the experiment. The broad resonance around 1100 Hz is an acoustic mode of the aluminum laser enclosure, while the series of resonances between 2 and 7 kHz are mechanical modes of the mirror mount on which the laser diode and grating are fixed. Peaks due to the dither imposed on the lasers are clearly resolved at 23 and 29 kHz. The overall  $1/f$  character is apparent above the bandwidth limit of our control loop ( $f > 2$  kHz).

Integrating frequency noise spectrum B using Eq. (5), we find  $\Delta v_{rms} = 1.05$  MHz. The rf beat spectrum (Fig. 3(a)) is approximately rectangular, hence we expect a FWHM linewidth of  $L = 2\sqrt{2}\Delta v_{rms} = 2.97$  MHz, which is consistent with the measured results. This corresponds to individual laser linewidths of 2 MHz.

Similarly, the relative contribution of the dither and the mechanical modes may be assessed by integrating over the appropriate range of Fourier frequencies. The two dither contributions are 0.6

and  $0.15 \text{ MHz}^2$ , and the total contribution of mechanical modes and power harmonics for both lasers was  $0.2 \text{ MHz}^2$ . The square root of the sum of these almost completely accounts for the total rms linewidth.

#### 4.4. Allan variance

Fig. 5 shows the Allan variance of the beat note calculated using Eq. (6). Very little spectral detail is evident. The oscillations at  $\tau > 10 \text{ ms}$  are due to the 50 and 150 Hz harmonics of the power line. Oscillations due to the dither for  $\tau$  between 10 and 100  $\mu\text{s}$  are barely discernible. The resolution of subtle fluctuations due to the dither would require prohibitively large numbers of frequency counts at every delay. The region between 0.1 and 10 ms corresponds to the mechanical modes. Here the Allan variance is amorphous, showing none of the rich structure of Fig. 4. Due to the need to make a large number of counts for every period, determining an Allan variance spectrum is a laborious process, especially for long periods (low frequencies). In contrast, a frequency noise spectrum such as Fig. 4 may be obtained in seconds.

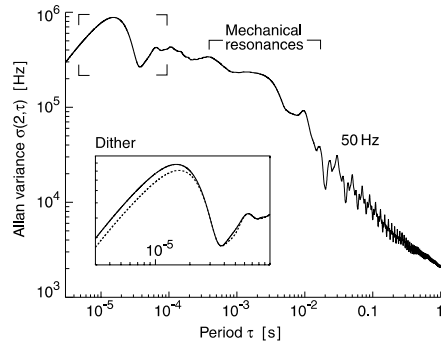


Fig. 5. Allan variance calculated from frequency noise data in Fig. 4. The inset shows an expanded view with an added curve (dashed) calculated from a frequency noise spectrum from which the higher frequency dither peak has been deleted (—). The two variances are almost indistinguishable, whereas in Fig. 4 the dither peaks are clearly resolved.

#### 4.5. Distinguishing and eliminating noise sources

The rf beat spectrum of Fig. 3 is a useful measure of laser performance, but provides little insight into the sources of laser noise. In contrast, the detailed laser frequency noise spectrum of Fig. 4 allows identification of the primary sources of laser noise, such as the power-line harmonics, turbo-pump, dither modulation, and mechanical noise. By distinguishing these separate components, it was possible to systematically reduce each noise source.

The power-line harmonics were minimised by careful elimination of ground loops. Changes to the ground circuits produced changes in the laser frequency noise which were readily apparent in real time from the demodulated spectrum.

The turbo-pump-induced noise was only a small contribution to the total laser linewidth, but was nevertheless eliminated by relocating the lasers to a separate optical table.

The dither modulation frequency noise, caused by modulation of the cavity length via the piezo disk, was reduced by locking to a modulation of the atomic reference frequency rather than the laser [4]. The atomic absorption resonance frequency was modulated by the Zeeman effect, using solenoid coils around our vapour cells. The locking electronics did not completely demodulate the dither frequencies, and hence produced small modulations of the lasers as seen from the peaks in the final laser noise spectrum, at the new dither frequencies of 57 and 68 kHz.

The mechanical noise was investigated by systematically modifying various components of the laser, for example by adding small masses or inelastic damping to the grating, the mirror mount arm, and the retaining springs of the mirror mount. These changes produced frequency shifts of different noise peaks which allowed identification of the mechanical noise sources. Through these explorations, it became apparent that the grating arm and associated retaining springs of the mirror mount were the primary source.

The lasers were initially stabilised by feedback to the piezo stack, which tunes the laser by rotation of the grating, causing a frequency shift of 200 MHz/V. The stack was driven by a high-voltage

(150 V) amplifier with a gain of 10, leading to a net amplification of 2 MHz/mV from the feedback circuit. Thus, the initial laser linewidth of 2 MHz is consistent with just 1 mV of noise in the feedback circuit.

The stack-induced mechanical noise was minimised by connecting the high-voltage feedback to the piezo disk rather than the stack. This reduced the laser linewidth to 400 kHz, but unfortunately also reduced the scanning range of the laser to approximately 1.3 GHz. A regulated and filtered variable dc supply was applied to the stack to allow laser frequency offset adjustment and hence recover the broad tuning range, with only a small penalty in the linewidth.

The final rf beat and frequency noise spectra are shown in Figs. 3 and 4. From the rf beat spectrum, the combined FWHM linewidth has been reduced from 3 MHz to 640 kHz, consistent with individual laser linewidth reductions from 2 MHz to 450 kHz. Integrating the frequency noise spectrum (Eq. (5)), we find  $\Delta\nu_{\text{rms}} = 540$  kHz corresponding to a FWHM linewidth of 635 kHz, in excellent agreement with the rf width.

The final linear spectral density noise of Fig. 4 has increased by approximately 5 dB at low frequencies, but is substantially smaller over most of the spectral range. The increased noise at low frequencies is due to a limitation of the simple feedback servo circuit which used only an integrator, leading to excessive gain at low frequencies. While a more complex circuit could reduce this noise, we expect that even if the noise in this band was completely eliminated, each laser linewidth would be reduced by just 70 kHz.

## 5. Conclusion

These results show that phase-locked loop frequency discrimination provides an unambiguous and high-resolution frequency noise spectrum using common laboratory test equipment. The frequency discriminator separates frequency noise from intensity noise, which is particularly valuable in characterising diode laser systems. In contrast

with Allan variance analysis, electronic, mechanical and acoustic noise sources may be clearly identified and observed in real time. The method is applicable to lasers stabilised by electronic and by optical means and is capable of analysing lasers with linewidths from 10 MHz down to a few kHz.

## Acknowledgements

We would like to thank Zivko Jovanovski for his expert construction and testing of the radio frequency electronics. This work was supported by the Australian Research Council and conducted with the assistance of the Australian Postgraduate Award scheme (LDT, KPW, CJH).

## References

- [1] C.E. Wieman, L. Hollberg, Rev. Sci. Instrum. 62 (1991) 1.
- [2] Y. Salvadé, R. Dändliker, J. Opt. Soc. Am. A 17 (2000) 927.
- [3] A. Hemmerich, D.H. McIntyre, J.D. Schropp, D. Meschede, T.W. Hansch, Opt. Commun. 75 (1990) 118.
- [4] T.P. Dinneen, Ch.D. Wallace, P.L. Gould, Opt. Commun. 92 (1992) 277.
- [5] M. Kourogi, M. Ohtsu, Opt. Commun. 81 (1991) 204.
- [6] A.P. Willis, A.I. Ferguson, D.M. Kane, Opt. Commun. 122 (1995) 31.
- [7] H. Ludvigsen, M. Tossavainen, M. Kaivola, Opt. Commun. 155 (1998) 180.
- [8] S. Kunze, S. Wolf, G. Rempe, Opt. Commun. 128 (1996) 296.
- [9] D.S. Elliott, R. Roy, S.J. Smith, Phys. Rev. A 26 (1982) 12.
- [10] J. Rutman, F.L. Walls, Proc. IEEE 79 (1991) 952.
- [11] C.A. Greenhall, Does Allan variance determine the spectrum?, in: IEEE International Frequency Control Symposium, Institute of Electrical and Electronics Engineers, New York, 1997.
- [12] C.-C. Chen, M.Z. Win, IEEE Photon. Technol. Lett. 2 (1990) 772.
- [13] K.R. Manes, A.E. Siegman, Phys. Rev. A 4 (1971) 373.
- [14] C.J. Hawthorn, K.P. Weber, R.E. Scholten, Rev. Sci. Instrum. 72 (2001) 4477.
- [15] A.S. Arnold, J.S. Wilson, M.G. Boshier, Rev. Sci. Instrum. 69 (1998) 1236.
- [16] M. Schwartz, Information Transmission, Modulation, and Noise, McGraw-Hill, New York, 1990.

## Appendix H

# Off-resonant defocus-contrast imaging of cold atoms

This Appendix is a facsimile of the paper

L. D. Turner, K. P. Weber, D. Paganin and R. E. Scholten.

*Off-resonant defocus-contrast imaging of cold atoms.*

Optics Letters **29**(3) 232–234 (2004 Feb).

This paper presents results from the first series of experiments with defocus-contrast imaging. Images were taken by Karl Weber during 2002 July. In late 2002 and early 2003 I processed these images with the TIE-based retrieval algorithm (derived by David Paganin and co-workers and described in §3.3). This paper presents this TIE-based work.

While writing this paper I became aware of the contrast-transfer formalism, but did not obtain retrievals using CTF-deconvolution until after this paper was submitted. A comparison of the TIE-retrievals used in this paper with CTF-retrievals from the same data was give on p 213.

232 OPTICS LETTERS / Vol. 29, No. 3 / February 1, 2004

## Off-resonant defocus-contrast imaging of cold atoms

Lincoln D. Turner, Karl P. Weber, David Paganin,\* and Robert E. Scholten

School of Physics, University of Melbourne, Victoria 3010, Australia

Received June 16, 2003

We demonstrate the retrieval of column-density images of cold atoms, using a noninterferometric phase-recovery technique based on a single off-resonant and defocused intensity image. The quantitative column density is retrieved via Fourier inversion and remains robust with respect to detuning and defocus. The technique offers excellent prospects for simple, nondestructive imaging of atoms in magnetic and optical traps and condensates. © 2004 Optical Society of America

OCIS codes: 100.5070, 120.5050, 350.5030.

Optical imaging provides a powerful diagnostic method for a diverse range of experiments involving cold atoms. On-resonant absorption imaging is predominant, despite its limited dynamic range and recoil heating. Off-resonant phase-imaging techniques have allowed nondestructive and quantitative imaging of Bose-Einstein condensates<sup>1,2</sup> (BECs), but conventional approaches require precisely aligned phase plates or interferometers. We describe how one may exploit Fresnel diffraction of an off-resonant probe beam to observe weakly absorbing cold atoms in phase contrast, using a standard absorption imaging configuration modified only by a small defocus of the imaging lens.

Off-resonant imaging relies on rendering phase shifts into intensity variations measurable with a CCD detector. Interferometry is the classic approach, for example, in the recent implementation of off-axis digital holography,<sup>3</sup> but it is awkward to construct and align an interferometer around a cold atom sample. The Zernike phase-contrast technique<sup>4</sup> forms a common-path interferometer in which the background unscattered wave serves as the interferometric reference. A  $\pi/2$  phase plate inserted in the Fourier plane of an image relay system shifts the phase of the unscattered probe wave so that it interferes with the field retarded by the atoms to produce a phase-contrast image. Difficulties associated with precise fabrication of the phase plate and exacting alignment requirements have impeded the application of the Zernike method to atom imaging.<sup>1</sup>

The Zernike phase plate produces an intensity signal that is approximately linear in the phase shift for small phase shifts. A phase-contrast signal is also produced through Fresnel diffraction. The effect is familiar in optical microscopy, where dark and bright contours appear at the edges of a transparent object (e.g., a cell, an optical fiber) at the slightest defocus. The diffracted intensity image can be compared to a calculated diffraction pattern and hence used to fit the atom column density.<sup>5</sup> Absorption and phase-shift information can also be retrieved directly from the Fresnel diffraction pattern by inverse methods. In particular, a solution was recently derived for the special case of x-ray imaging of homogeneous samples, where absorption and phase retardation are both functions only of the object thickness.<sup>6</sup> Here we outline this result as applied to the retrieval of a

column-density image of cold atomic gas from a single defocus-contrast image.

A probe beam propagates through the atom cloud and diffracts in the free space beyond (Fig. 1). The probe beam is described as a scalar plane wave of complex amplitude  $U_{\text{in}}$  propagating along the  $z$  axis, incident on an object with a spatial distribution of complex refractive index  $n(\mathbf{r}, z)$ . For an optically thin object, the amplitude over the exit plane is

$$U(\mathbf{r}, z = 0) = U_{\text{in}} \exp \left\{ ik_0 \int [n(\mathbf{r}, z) - 1] dz \right\}, \quad (1)$$

where  $k_0 = 2\pi/\lambda_0$  is the wave number for vacuum probe wavelength  $\lambda_0$  and  $\mathbf{r} = (x, y)$  are the transverse coordinates.

The complex refractive index for a sample of two-level atoms with number density  $\rho(\mathbf{r}, z)$  can be written as<sup>7</sup>

$$n(\mathbf{r}, z) = 1 + \frac{3\lambda_0\rho(\mathbf{r}, z)}{2k_0^2} \left( \frac{i - 2\delta}{1 + 4\delta^2} \right), \quad (2)$$

$$= 1 + \rho(\mathbf{r}, z) (n_r + in_i). \quad (3)$$

$n_r$  and  $n_i$  are the real and the imaginary refractive-index components normalized to the atomic density and relative to vacuum, and  $\delta$  is the detuning in full linewidths; it follows that  $n_r/n_i = -2\delta$ . We wish to measure the integrated column density of the sample,  $\rho(\mathbf{r}) = \int \rho(\mathbf{r}, z) dz$ . The intensity  $I$  and phase  $\phi$  of the field at the exit plane are

$$I(\mathbf{r}, z = 0) = |U(\mathbf{r}, z = 0)|^2 = I_{\text{in}} \exp[-2k_0 n_r \rho(\mathbf{r})], \quad (4)$$

$$\phi(\mathbf{r}, z = 0) = k_0 n_r \rho(\mathbf{r}), \quad (5)$$

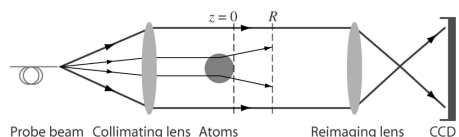


Fig. 1. Schematic of the imaging configuration. A cloud of  $^{85}\text{Rb}$  atoms was illuminated with a fiber-coupled and collimated laser beam detuned from resonance. A lens reimaged the light from a plane at defocus distance  $R$  onto a CCD. Rays illustrate the antilensing for above-resonance illumination.

where  $I_{\text{in}} = |U_{\text{in}}|^2$ . Equation (4) is the familiar Beer-Lambert law, the basis of absorption imaging.

The paraxial wave equation implies a continuity equation, known as the transport-of-intensity equation<sup>8</sup>

$$\nabla_{\perp} \cdot [I(\mathbf{r}, z) \nabla_{\perp} \phi(\mathbf{r}, z)] = -k_0 \frac{\partial}{\partial z} I(\mathbf{r}, z), \quad (6)$$

where  $\nabla_{\perp}$  is the gradient operator in the transverse plane. Substituting from Eqs. (4) and (5) and evaluating at the plane  $z = 0$ , this may be written in terms of  $\rho(\mathbf{r})$  as

$$\frac{n_r}{2k_0 n_i} I_{\text{in}} \nabla_{\perp}^2 \exp[-2k_0 n_i \rho(\mathbf{r})] = \frac{\partial}{\partial z} I(\mathbf{r}, z = 0). \quad (7)$$

We approximate the intensity derivative  $\partial I(\mathbf{r}, z = 0)/\partial z$  as the finite difference  $[I(\mathbf{r}, z = R) - I(\mathbf{r}, z = 0)]/R$ , where  $I(\mathbf{r}, z = 0)$  is given by Eq. (4), so

$$\left(1 - \frac{R\delta}{k_0}\right) \nabla_{\perp}^2 \exp[-2k_0 n_i \rho(\mathbf{r})] = \frac{I(\mathbf{r}, z = R)}{I_{\text{in}}}. \quad (8)$$

Equation (8) may be inverted in Fourier space, such that the Laplacian  $\nabla_{\perp}^2$  becomes a multiplication by  $-|\mathbf{k}|^2$ , where  $\mathbf{k} = (k_x, k_y)$  is the spatial frequency vector in the transverse plane. The column density is then recovered by deconvolution:

$$\exp[-2k_0 n_i \rho(\mathbf{r})] = \mathcal{F}^{-1} \left\{ \frac{\mathcal{F}\{I(\mathbf{r}, z = R)/I_{\text{in}}\}}{1 + \frac{R\delta}{k_0} |\mathbf{k}|^2} \right\}. \quad (9)$$

That is, to find the column density, the defocused image is Fourier transformed, the Fourier coefficients are reweighted, and the inverse Fourier transform is taken. The result is a synthetic in-focus absorption image, which is then converted to a column density  $\rho(\mathbf{r})$  by taking the logarithm; setting  $R = 0$  recovers the Beer-Lambert case. Provided that the product  $R\delta$  is positive, the denominator is greater than unity and the deconvolution is a well-posed inverse problem.

Figure 1 depicts our apparatus. A sample of cold atoms was generated by a conventional magneto-optical trap<sup>9</sup> (MOT) with a getter source. The trap accumulated  $6 \times 10^5$   $^{85}\text{Rb}$  atoms in a nearly Gaussian cloud of FWHM  $230 \pm 9 \mu\text{m}$  at a peak density of  $3.9 \pm 0.4 \times 10^{16} \text{ m}^{-3}$ . An imaging laser of 0.5-MHz linewidth was detuned between  $\pm 5$  linewidths  $\Gamma$  from the  $^{85}\text{Rb}$   $5S_{1/2}(F=3) \rightarrow 5P_{3/2}(F=4)$  resonance. The cw probe beam was fiber coupled, linearly polarized, and collimated before passing through the MOT with irradiance of  $10 \mu\text{W cm}^{-2}$ . The diffracted beam was attenuated by neutral-density filters to reduce the fluorescence contribution and imaged with a 35-mm camera lens (200 mm Micro-Nikkor) onto a CCD (Roper VersArray 1300F, 20- $\mu\text{m}$  square pixels) with a magnification of 1.8. A standard absorption imaging configuration has been altered only by allowing the lens and CCD assembly to translate an adjustable distance  $R$  along a rail so that an image of the diffraction pattern at distance  $R$  beyond the object was produced on the detector.

We emphasize that the lens serves only to reimaging and magnify the intensity pattern from one focal plane

to the other. Identical images could have been acquired without imaging optics, had it been possible to place the bare CCD detector at defocus distance  $R$  from the MOT (inside the vacuum chamber in our setup).

We acquired four images at each detuning and defocus:  $I_{\text{abs}}$  with the MOT and probe beam on,  $I_{\text{fluoro}}$  with the MOT on and probe off,  $I_{\text{bright}}$  with the MOT off and probe on, and  $I_{\text{dark}}$  with both off. The normalized absorption ratio image,

$$\frac{I(\mathbf{r}, z = R)}{I_{\text{in}}} = \frac{I_{\text{abs}} - I_{\text{fluoro}}}{I_{\text{bright}} - I_{\text{dark}}}, \quad (10)$$

includes a correction for fluorescence that would not be required if imaging a nondissipative object such as a BEC. The fluorescence blurred rapidly with defocus and added only a low-level featureless background to the defocused images.

Figure 2 shows a typical defocused image, normalized as above, taken at a detuning  $\delta = +3\Gamma$  and a defocus  $R = 30 \text{ mm}$ . Blue detuning yields a refractive index with the real component less than unity, and so the probe beam is antifocused, darkening the center and forming a bright ring around the edges. Red detuned ( $\delta < 0$ ) images yield a more familiar focusing effect, brightening the middle of the image. However, this is where residual absorption is strongest and the effects tend to cancel, causing a loss of contrast related to the singularity in Eq. (9) for negative  $R\delta$ . If the residual object absorption is significant and red detuning is desired, the lens should be defocused by  $-R$ , i.e., toward the atom cloud, to ensure positive  $R\delta$ . The line profile in Fig. 2 shows the extent of the defocus contrast enhancement, comparing focused and defocused images taken at the same detuning. The in-focus absorption contrast of 6% increased to 30% when the image was defocused by 30 mm.

We processed the in-focus image  $I(\mathbf{r}, z = 0)/I_{\text{in}}$  (not shown) following Eq. (4) and the normalized defocus image of Fig. 2,  $I(\mathbf{r}, z = R)/I_{\text{in}}$ , following Eq. (9). Using fast Fourier transforms, we obtained full retrieval of a  $512 \times 512$  pixel image in less than 1 s on a 1-GHz Pentium processor.

Figure 3 shows the column-density image retrieved from the defocused image and a central line profile compared with the same line retrieved from the in-focus image. The improvement in the signal-to-noise ratio (SNR) is not unexpected given the higher contrast shown by Fig. 2. Users of laser imaging

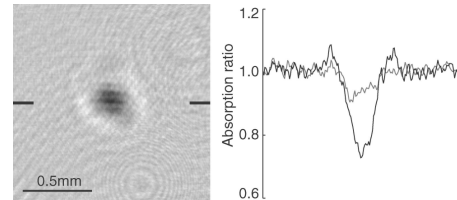


Fig. 2. Defocused image for detuning  $\delta = +3\Gamma$  and defocus  $R = 30 \text{ mm}$ . Line profiles (three-pixel rows averaged) are shown for the defocus image and (gray curve) for a conventional in-focus absorption image at the same detuning.

234 OPTICS LETTERS / Vol. 29, No. 3 / February 1, 2004

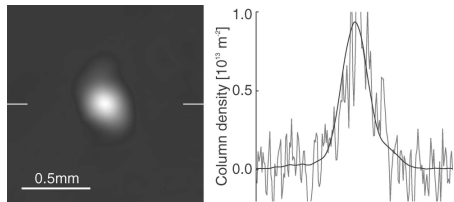


Fig. 3. Column-density gray-scale image retrieved from the defocus image of Fig. 2. Line profiles (single pixel row) are shown for the column density derived from our method compared with that retrieved from conventional in-focus absorption imaging at the same detuning (gray curve).

systems will have noted the remarkable ease with which vacuum windows and lenses align themselves as unwanted interferometers. The resulting spurious fringes are typically at a higher spatial frequency than the majority of structure in the object. The retrieval is biased against high spatial frequencies, rolling off as  $|\mathbf{k}|^{-2}$  for large  $|\mathbf{k}|$ . We found that this inherent denoising successfully suppressed the effects of unintended interference in our imaging system.

We obtained column densities from contrast images at detunings from 0 to  $+5\Gamma$  and defocusing ranging from 10 to 40 mm. We also took an in-focus image at each detuning and retrieved the column density with the standard absorption imaging method. As the density of our MOT was relatively low, absorption at  $+5\Gamma$  was only 2%, yielding a unity SNR for standard absorption imaging at this extreme detuning. Column densities retrieved from absorption and defocus-contrast images showed good agreement, with the central column density being  $9.4 \pm 0.7 \times 10^{12} \text{ m}^{-2}$ . Absorption imaging is very sensitive to small errors in focus. As little as 0.5-mm defocus of our imaging system caused a 20% error in the column density retrieved with standard in-focus absorption imaging, whereas the same error in  $R = 20 \text{ mm}$  caused negligible error in our defocus-contrast image. Consequently, the peak column densities measured by absorption imaging show greater scatter than the defocus-contrast measurements, which exhibit only small shot-to-shot variation consistent with MOT fluctuations detectable from fluorescence images.

The optimal defocus distance depends on the size and structure of the object being imaged. At zero defocus, there is only residual absorption contrast. The contrast increases linearly with defocus until the finite-difference approximation of the intensity derivative used to obtain Eq. (8) no longer holds. This transition from single fringe contrast to holographic contrast nominally occurs at defocus  $R_{\max} = 2\pi^2/\lambda|\mathbf{k}|^2$ . Therefore, at any defocus distance  $R$  there is an object structure scale  $\sqrt{\pi 2\lambda R}$  that is optimally diffracted.<sup>10</sup> Much smaller structures in the object will be in holographic contrast and will be

suppressed by the filter, while much larger structures will show only absorption contrast with little additional defocus contrast.

Of previously reported methods for off-resonant imaging, the Zernike phase-contrast technique is most similar to our defocus-contrast approach. Both our method and the Zernike method are bright-field techniques and so have a SNR superior to those of dark-field methods in the presence of technical noise. Residual absorption by the atom cloud introduces inaccuracies in the Zernike contrast but increases the signal for defocus contrast. The Zernike method has enabled many sequential nondestructive images of a BEC to be taken.<sup>1</sup> Our technique yields lower contrast for all but the optimal spatial frequency component of an image. Equivalently, our technique is somewhat more destructive for the same SNR. Nevertheless, we expect that several sequential nondestructive images of a BEC could be obtained with our method, using only conventional absorption imaging optics.

Our results demonstrate a quantitative off-resonant imaging technique based on defocus contrast. The method uses a standard absorption imaging apparatus but retrieves quantitative column-density images calibrated by knowing defocus distance  $R$  and probe detuning  $\delta$ . We expect that the great simplicity of the technique will lead to the wider use of nonresonant imaging in cold atom research.

This work was supported by the Commonwealth Department of Education, Science and Training Innovation Access Programme and by Australian Research Council grant DP0208799. R. E. Scholten's e-mail address is r.scholten@physics.unimelb.edu.au.

\*Present address, School of Physics and Materials Engineering, Monash University, Victoria 3800, Australia.

## References

1. M. R. Andrews, M.-O. Mewes, N. J. van Druten, D. S. Durfee, D. M. Kurn, and W. Ketterle, *Science* **273**, 84 (1996).
2. M. R. Andrews, D. M. Kurn, H.-J. Miesner, D. S. Durfee, C. G. Townsend, S. Inouye, and W. Ketterle, *Phys. Rev. Lett.* **79**, 553 (1997).
3. S. Kadlecak, J. Sebby, R. Newell, and T. G. Walker, *Opt. Lett.* **26**, 137 (2000).
4. F. Zernike, *Physica* **9**, 686 (1942).
5. F. Strauch, V. Gomer, H. Schadwinkel, B. Ueberholz, D. Haubrich, and D. Meschede, *Opt. Commun.* **145**, 57 (1998).
6. D. Paganin, S. C. Mayo, T. E. Gureyev, P. R. Miller, and S. W. Wilkins, *J. Microsc. (Oxford)* **206**, 33 (2002).
7. W. Demtröder, *Laser Spectroscopy*, 2nd ed. (Springer-Verlag, Berlin, 1981).
8. M. R. Teague, *J. Opt. Soc. Am.* **73**, 1434 (1983).
9. E. L. Raab, M. Prentiss, A. Cable, S. Chu, and D. E. Pritchard, *Phys. Rev. Lett.* **59**, 2631 (1987).
10. A. Pogany, D. Gao, and S. W. Wilkins, *Rev. Sci. Instrum.* **68**, 2774 (1997).

## Appendix I

### X-ray phase imaging: Demonstration of extended conditions with homogeneous objects

This Appendix is a facsimile of the paper

L. D. Turner, B. B. Dhal, J. P. Hayes, A. P. Mancuso, K. A. Nugent,  
D. Paterson, R. E. Scholten, C. Q. Tran and A. G. Peele.

*X-ray phase imaging: Demonstration of extended conditions with homogeneous objects.*

Optics Express 12(13) 2960–2965 (2004 Jun).

This paper presents results of diffraction-contrast imaging with monochromatic x-rays. X-ray applications of DCI have not been included in this thesis. In this experiment, x-rays from a synchrotron were focused with a zone-plate to form an effective point-source. The diverging beam then passed through a test object fabricated in polymer by laser ablation. A CCD detector measured the Fresnel diffraction pattern. Retrievals of the object thickness with CTF and TIE retrieval methods were compared with direct thickness measurements performed with an atomic force microscope.

My contribution was the derivation of the monomorphous CTF, and the retrieval algorithm. This paper presents an abbreviated form of the derivation of Section 2.5. Andrew Peele fabricated the test object, coordinated the experiments and processed the data. The paper was written primarily by Andrew Peele and secondarily by me.

## X-ray phase imaging: Demonstration of extended conditions with homogeneous objects

L. D. Turner,<sup>1</sup> B. B. Dhal,<sup>1</sup> J. P. Hayes,<sup>2</sup> A. P. Mancuso,<sup>1</sup> K. A. Nugent,<sup>1</sup>  
D. Paterson,<sup>3</sup> R. E. Scholten,<sup>1</sup> C. Q. Tran<sup>1</sup> and A. G. Peele<sup>1,4</sup>

<sup>1</sup> School of Physics, University of Melbourne, Victoria 3010, Australia

<sup>2</sup> Industrial Research Institute Swinburne, Swinburne University of Technology, Hawthorn 3122, Australia

<sup>3</sup> Advanced Photon Source, Argonne National Laboratory, 9700 S. Cass Avenue, Argonne, Illinois 60439, USA

<sup>4</sup> Now at Department of Physics, Latrobe University, Victoria 3086, Australia

[a.peele@latrobe.edu.au](mailto:a.peele@latrobe.edu.au)

**Abstract:** We discuss contrast formation in a propagating x-ray beam. We consider the validity conditions for linear relations based on the transport-of-intensity equation (TIE) and on contrast transfer functions (CTFs). From a single diffracted image, we recover the thickness of a homogeneous object which has substantial absorption and a phase-shift of  $-0.37$  radian.

© 2004 Optical Society of America

**OCIS codes:** (340.7480) X-rays; (340.7440) X-ray imaging; (340.7460) X-ray microscopy

### References and links

1. G. Schmahl, D. Rudolph and P. Guttmann, "Phase contrast x-ray microscopy – experiments at the BESSY storage ring," in *X-ray Microscopy II*, D. Sayre, M. Howells, J. Kirz and H. Rarback, eds., Vol 56 in Springer Series in Optical Sciences (Springer-Verlag, Berlin, 1988), pp. 228–232.
2. D. Sayre and H. N. Chapman, "X-ray microscopy," *Acta Cryst. A* **51**, 237–252 (1995).
3. K. A. Nugent, T. E. Gureyev, D. F. Cookson, D. Paganin and Z. Barnea, "Quantitative phase imaging using hard x rays," *Phys. Rev. Lett.* **77**, 2961–2964 (1996).
4. A. Pogany, D. Gao and S. W. Wilkins, "Contrast and resolution in imaging with a microfocus x-ray source," *Rev. Sci. Instrum.* **68**, 2774–2782 (1997).
5. U. Bonse and M. Hart, "An x-ray interferometer," *Appl. Phys. Lett.* **6**, 155–157 (1965).
6. A. Momose, T. Takeda and Y. Itai, "Phase-contrast x-ray computed tomography for observing biological specimens and organic materials," *Rev. Sci. Instrum.* **66**, 1434–1436 (1995).
7. Y. Kohmura, H. Takano, Y. Suzuki and T. Ishikawa, "Shearing x-ray interferometer with an x-ray prism and its improvement," in *Proc. 7th Intern. Conf. on X-ray Microscopy*, D. Joyeux, F. Polack, eds., J. de Physique IV, Vol 104, J. Susini (EDP Sciences, Les Ulis, 2003), pp. 571–574.
8. T. Wilhein, B. Kaulich, E. Di Fabrizio, F. Romanato, M. Altissimo, J. Susini, B. Fayard, U. Neuhäusler, S. Cabrini and F. Polack, "Differential interference contrast x-ray microscopy with twin zone plates at ESRF beamline ID21," in *Proc. 7th Intern. Conf. on X-ray microscopy, ibid.*
9. E. M. Di Fabrizio, D. Cojoc, S. Cabrini, B. Kaulich, J. Susini, P. Facci and T. Wilhein, "Diffractive optical elements for differential interference contrast x-ray microscopy," *Opt. Express* **11**, 2278–2288 (2003), <http://www.opticsexpress.org/abstract.cfm?URI=OPEX-11-19-2278>.
10. E. Forster, K. Goetz and P. Zaumseil, "Double crystal diffractometry for the characterization of targets for laser fusion experiments," *Krist. Tech.* **15**, 937–945 (1980).
11. J. R. Palmer and G. R. Morrison, "Differential phase contrast imaging in the scanning transmission x-ray microscope," in *Short Wavelength Coherent Radiation*, P. H. Bucksbaum and N. M. Ceglio, eds., Vol. 11 of OSA Proceedings Series (Optical Society of America, Washington, D. C., 1991), pp. 141–145.
12. C. Jacobsen, M. Howells, J. Kirz and S. Rothman, "X-ray holographic microscopy using photoresists," *J. Opt. Soc. Am. A* **7**, 1847–1861 (1990).
13. L. J. Allen, W. McBride and M. P. Oxley, "Exit wave reconstruction using soft x-rays," *Opt. Commun.* **233**, 77–82 (2004).
14. M. R. Teague, "Deterministic phase retrieval: Greens function solution," *J. Opt. Soc. Am. A* **73**, 1434–41 (1983).
15. D. Paganin and K. A. Nugent, "Noninterferometric phase imaging with partially coherent light," *Phys. Rev. Lett.* **80**, 2586–2589 (1998).

16. T. E. Gureyev, A. Pogany, D. M. Paganin and S. W. Wilkins, "Linear algorithms for phase retrieval in the Fresnel region," *Opt. Commun.* **231**, 53–70 (2004).
17. X. Wu and H. Li, "A general theoretical formalism for x-ray phase contrast imaging," *J. X-ray Sci. Tech.* **11**, 33–42 (2003).
18. J.-P. Guigay, R. H. Wade and C. Delpha, "Optical diffraction of Lorentz microscope images," in *Proceedings of the 25th meeting of the Electron Microscopy and Analysis Group*, W. C. Nixon, ed. (The Institute of Physics, London, 1971), pp. 238–239.
19. J.-P. Guigay, "Fourier transform analysis of Fresnel diffraction patterns," *Optik* **49**, 121–125 (1977).
20. D. Paganin, S. C. Mayo, T. E. Gureyev, P. R. Miller and S. W. Wilkins, "Simultaneous phase and amplitude extraction from a single defocused image of a homogeneous object," *J. Microsc* **206**, 33–40 (2001).
21. P. Cloetens, W. Ludwig, J. Baruchel, D. Van Dyck, J. Van Landuyt, J.-P. Guigay and M. Schlenker, "Holotomography: Quantitative phase tomography with micrometer resolution using hard synchrotron radiation x-rays," *Appl. Phys. Lett.* **75**, 2912–2914 (1999).
22. M. H. Maleki and A. J. Devaney, "Noniterative reconstruction of complex-valued objects from two intensity measurements," *Opt. Eng.* **33**, 3243–3253 (1994).
23. A. N. Tikhonov and V. Y. Arsenin, "Solutions of Ill-posed Problems" (V. H. Winston, Washington D.C., 1977).
24. E. C. Harvey and P. T. Rumsby, "Fabrication techniques and their application to produce novel micromachined structures and devices using excimer laser projection," in *Micromachining and Microfabrication Process Technology III*, S. Chang and S. W. Pang, eds., Proc. SPIE **3223**, 26–33 (1997).
25. L. D. Turner, K. P. Weber, D. Paganin and R. E. Scholten, "Off-resonant defocus-contrast imaging of cold atoms," *Opt. Lett.* **29**, 232–234 (2004).
26. L. D. Turner, K. F. E. M. Domen, W. Rooijakkers and R. E. Scholten, School of Physics, University of Melbourne 3010, Australia are preparing a manuscript to be called "Holographic imaging of cold atoms".
27. M. Centurion, Y. Pu, Z. Liu, D. Psaltis and T. W. Hänsch, "Holographic recording of laser-induced plasma," *Opt. Lett.* **29**, 772–774 (2004).

## 1. Introduction

Absorption contrast has been the principal imaging mode for x-rays for over 100 years, nonetheless there has been considerable development recently in implementing phase contrast techniques. Phase contrast can be strong when absorption contrast is minimal; for instance for low-Z materials or for high energy x-rays [1, 2, 3]. Phase contrast can also be used without delivering a high dose to the sample [2]. And certain phase methods require no additional optics leading to source-limited, rather than optics-limited, resolution [4].

Demonstrated methods for obtaining the phase from an x-ray wavefield are now legion. Interferometric methods include the use of Bonse and Hart [5] type interferometers [6], shearing interferometers [7], differential interference contrast arrangements using two zone plates [8] or diffractive optical elements [9]. Zernike phase contrast [1] has also been demonstrated. Other methods include refraction measurement using crystal diffraction [10], and segmented detectors [11]. Propagation-based methods have also been developed and involve recovery of the object phase and/or amplitude from one or more measurements of the object diffraction pattern. Methods include in-line holography [12], iterative schemes [13] and approaches based on solution of the equations governing the propagation of the wavefield [14, 15, 3].

In this paper we consider aspects of the latter method. Here the Fresnel integral describing the diffracted intensity is linearized allowing a straightforward retrieval of object phase and transmission. A first order Taylor expansion obtains the transport of intensity equation (TIE) solution [16, 3]. Alternatively a Born-type approximation [17, 16] gives a solution identical in form to that derived by Guigay [18, 19] in the context of electron microscopy. We will refer to this as the contrast transfer function (CTF) solution. Both the TIE and the CTF solution can be further simplified under the assumption of a homogeneous object [20, 16]. This permits the thickness distribution of an object to be retrieved from a *single* diffracted image.

In the TIE it is the first-order Taylor expansion that restricts the validity of the solution. Other than a requirement for paraxiality, there is no limitation on the magnitude of the phase or the absorption. On the other hand, the Born-type approximation previously used in deriving the CTF method can be quite restrictive. Guigay showed [19] that a less restrictive requirement applies for a pure phase object. Like the TIE condition, this condition depends on the feature

sizes present as well as the wavelength and propagation distance.

Here we show that the Fresnel-diffracted intensity can be linearized at a later stage of the derivation. As a consequence we find that the less restrictive phase condition extends to weakly-absorbing objects. In Section 2 we outline the derivations of the TIE and the CTF solutions and their validity conditions and show how the assumption of a homogeneous object allows retrieval of the object thickness from a single diffracted image. In Section 3 we present experimental results demonstrating quantitative thickness retrieval under our derived validity conditions.

## 2. Derivations

### 2.1. TIE and CTF

We begin with the Fourier transform,  $\mathcal{F}[\cdot]$ , of the intensity  $I(\mathbf{r}, z)$  obtained under Fresnel diffraction of an object-plane wavefield  $f(\mathbf{r}) = f(\mathbf{r}, z=0)$  with wavelength  $\lambda$  [18]:

$$\mathcal{F}[I(\mathbf{r}, z)] = \int_{-\infty}^{+\infty} f^*(\mathbf{r} + \lambda z \mathbf{u}/2) f(\mathbf{r} - \lambda z \mathbf{u}/2) \exp(-2\pi i \mathbf{r} \cdot \mathbf{u}) d\mathbf{r}. \quad (1)$$

The transverse spatial coordinates and their corresponding Fourier conjugates are given by  $\mathbf{r}$  and  $\mathbf{u}$  respectively. To obtain the TIE solution we Taylor expand the wavefield to first order,

$$f(\mathbf{r} + \lambda z \mathbf{u}/2) = f(\mathbf{r}) + \frac{1}{2} \lambda z \mathbf{u} \cdot \nabla f(\mathbf{r}), \quad (2)$$

where  $\nabla$  is the gradient operator in the transverse plane. Substituting into Eq. (1) gives

$$\nabla \cdot (I(\mathbf{r}, z) \nabla \phi(\mathbf{r}, z)) = -\frac{2\pi}{\lambda} \frac{\partial}{\partial z} I(\mathbf{r}, z), \quad (3)$$

where  $\phi$  is the phase of the wavefunction  $f$ . The validity condition for the TIE solution is therefore that the higher order Taylor expansion terms can be disregarded:

$$\left| \sum_{j=2}^{\infty} \frac{1}{j!} \left( \frac{1}{2} \lambda z \mathbf{u} \cdot \nabla \right)^j f(\mathbf{r}) \right| \ll 1. \quad (4)$$

This condition can always be satisfied by choosing a sufficiently small propagation distance, while requiring no approximation regarding the magnitude of the amplitude or phase.

The previous approach to obtain the CTF solution was to write the object wavefunction in terms of its absorption  $\mu$  and phase  $\phi$  components such that:

$$f(\mathbf{r}) = f_0 \exp(-\mu(\mathbf{r}) + i\phi(\mathbf{r})), \quad (5)$$

where  $I_0 = |f_0|^2$  is the intensity of the plane wavefield incident on the object. Then the Born-type approximation of  $\mu \ll 1$  and  $|\phi| \ll 1$  was made so that

$$f(\mathbf{r}) = f_0 (1 - \mu(\mathbf{r}) + i\phi(\mathbf{r})). \quad (6)$$

Substituting Eq. (6) into Eq. (1) and retaining  $\mu$  and  $\phi$  to first order, obtained Guigay's result

$$\mathcal{F}[I(\mathbf{r}, z)] = I_0 (\delta(\mathbf{u}) - 2 \cos(\pi \lambda z u^2) \mathcal{F}[\mu(\mathbf{r})] + 2 \sin(\pi \lambda z u^2) \mathcal{F}[\phi(\mathbf{r})]) \quad (7)$$

in which  $\delta(\mathbf{u})$  denotes the Dirac delta distribution. When the object is pure phase ( $\mu = 0$ ), Guigay [19] also showed, by substituting Eq. (5) into Eq. (1), that the corresponding form of Eq. (7) can be obtained if, for all  $\mathbf{r}$ ,

$$|\phi(\mathbf{r} + \lambda z \mathbf{u}/2) - \phi(\mathbf{r} - \lambda z \mathbf{u}/2)| \ll 1. \quad (8)$$

This is sometimes referred to as the slowly-varying phase condition. It should be noted that the displacement vector  $\lambda z \mathbf{u}$ , over which points in the phase should be similar, is a function of propagation distance  $z$  and of spatial frequency  $\mathbf{u}$ .

## 2.2. TIE for a homogeneous object

Consider the case of an optically thin and homogeneous object for which

$$\mu(\mathbf{r}) = k\beta T(\mathbf{r}) \quad \text{and} \quad \phi(\mathbf{r}) = -k\delta T(\mathbf{r}), \quad (9)$$

where  $k = 2\pi/\lambda$ , the refractive index is  $n = 1 - \delta + i\beta$  and  $T$  is the thickness of the object. We substitute into Eq. (1), re-factor and make a first-order Taylor expansion of  $T$  yielding

$$\mathcal{F}[I(\mathbf{r}, z)] = I_0 \int_{-\infty}^{+\infty} \exp(-2k\beta T(\mathbf{r})) \exp(-ik\delta\lambda z \mathbf{u} \cdot \nabla T(\mathbf{r})) \exp(-2\pi i \mathbf{r} \cdot \mathbf{u}) d\mathbf{r}. \quad (10)$$

If we assume that  $|\lambda z u \cdot \nabla \phi(r)| \ll 1$  then we can expand the second exponential to first order,

$$\mathcal{F}[I(\mathbf{r}, z)] = I_0 \int_{-\infty}^{+\infty} \exp(-2k\beta T(\mathbf{r})) (1 - ik\delta\lambda z \mathbf{u} \cdot \nabla T(\mathbf{r})) \exp(-2\pi i \mathbf{r} \cdot \mathbf{u}) d\mathbf{r} \quad (11)$$

and then applying the Fourier derivative theorem  $\mathcal{F}[\nabla f(\mathbf{r})] = 2\pi i \mathbf{u} \mathcal{F}[f(\mathbf{r})]$  we obtain:

$$\mathcal{F}[I(\mathbf{r}, z)] = I_0 \mathcal{F}[\exp(-2k\beta T(\mathbf{r}))] \left( 1 + \frac{\delta}{\beta} \lambda z u^2 \right). \quad (12)$$

This may be solved for the thickness  $T$ :

$$T(\mathbf{r}) = -\frac{1}{2k\beta} \ln \mathcal{F}^{-1} \left[ \frac{\beta}{\beta + \delta \pi \lambda z u^2} \mathcal{F} \left[ \frac{I(\mathbf{r}, z)}{I_0} \right] \right]. \quad (13)$$

The validity condition on the thickness  $T$  is similar to that for the TIE in Eq. (4).

## 2.3. Derivation of extended validity CTF solution

Here we begin by substituting Eq. (5) into Eq. (1):

$$\begin{aligned} \mathcal{F}[I(\mathbf{r}, z)] &= I_0 \int_{-\infty}^{+\infty} \exp(-\mu(\mathbf{r} + \lambda z \mathbf{u}/2) - \mu(\mathbf{r} - \lambda z \mathbf{u}/2) + i(\phi(\mathbf{r} - \lambda z \mathbf{u}/2) - \phi(\mathbf{r} + \lambda z \mathbf{u}/2))) \\ &\quad \times \exp(-2\pi i \mathbf{r} \cdot \mathbf{u}) d\mathbf{r}. \end{aligned} \quad (14)$$

Assuming both real and imaginary parts of the exponential are small, we expand, noting the Fourier transforms:

$$\begin{aligned} \mathcal{F}[I(\mathbf{r}, z)] / I_0 &= \delta(\mathbf{u}) - \mathcal{F}[\mu(\mathbf{r} + \lambda z \mathbf{u}/2) + \mu(\mathbf{r} - \lambda z \mathbf{u}/2)] \\ &\quad + i \mathcal{F}[\phi(\mathbf{r} - \lambda z \mathbf{u}/2) - \phi(\mathbf{r} + \lambda z \mathbf{u}/2)]. \end{aligned} \quad (15)$$

Applying the Fourier shift theorem  $\mathcal{F}[f(\mathbf{r} - \mathbf{a})] = \exp(-2\pi i \mathbf{a} \cdot \mathbf{u}) \mathcal{F}[f(\mathbf{r})]$  to each term and rearranging recovers Eq. (7). If the object is homogeneous then, substituting Eq. (9), we can retrieve the thickness  $T$  from a single diffracted image:

$$T(\mathbf{r}) = \mathcal{F}^{-1} \left[ \frac{1}{-2k(\delta \sin(\pi \lambda z u^2) + \beta \cos(\pi \lambda z u^2))} \mathcal{F} \left[ \frac{I(\mathbf{r}, z)}{I_0} - 1 \right] \right]. \quad (16)$$

The linearizing assumption made in obtaining Eq. (15) is that

$$2\mu(\mathbf{r}) \ll 1 \quad \text{and} \quad |\phi(\mathbf{r} + \lambda z \mathbf{u}/2) - \phi(\mathbf{r} - \lambda z \mathbf{u}/2)| \ll 1. \quad (17)$$

These conditions on the validity of Eq. (7) are much less stringent than previously realised. While the object must be weakly absorbing it need not be non-absorbing, which is less restrictive than the pure phase assumption made by Guigay. Furthermore, the weak phase condition required in the Born-type approach is here relaxed to the slowly-varying condition Eq. (8).

Assuming object homogeneity allows us to incorporate the effect of object absorption. Consequently the contrast transfer function, which is the denominator term of Eq. (16), is non-zero at  $u = 0$ . Nulls in the CTF at frequencies above  $u = 1/\sqrt{2\lambda z}$  may be avoided by incorporating additional images at different propagation distances [21, 22], or simply by Tikhonov regularisation [23]. We find that Tikhonov regularisation leaves only minor artefacts at high frequencies whereas assuming a pure phase object introduces intractable low-frequency instability.

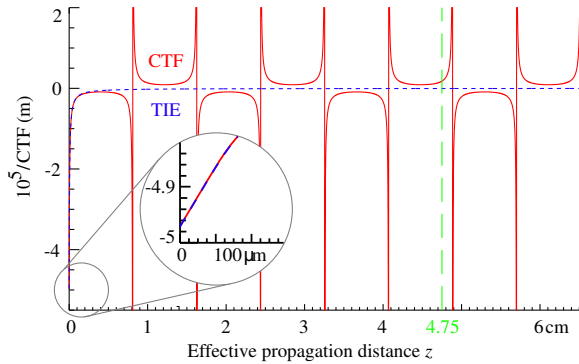


Fig. 1. Inverse of the contrast transfer functions for the TIE (blue dotted line) and CTF (red line) forms calculated for an infinite grid with spatial feature size of  $1.9\text{ }\mu\text{m}$  and the experimental conditions. The green dashed line is at the experimental distance. The embedded movie shows the inverse CTFs as shown here with a slider indicating the  $z$  position corresponding to diffraction distance. Also shown in the movie is a plot of an input amplitude (green) and the amplitude retrieved using either the CTF (red) or TIE (blue) methods for the indicated propagation distance. The CTF method correctly accounts for the contrast reversals that arise on propagation. The TIE method should only be applied for  $z$  closer than the first contrast reversal; it may retrieve *inverted* amplitudes if applied at greater  $z$ .

### 3. Experimental results

Laser ablation [24] was used to etch a grid of lines in a polyimide film (composition  $\text{C}_{22}\text{H}_{10}\text{N}_2\text{O}_4$  and density  $1.45\text{ g cm}^{-3}$ ). The lines were measured by atomic force microscope (AFM) to be approximately  $1.9\text{ }\mu\text{m}$  apart and  $90\text{ nm}$  high and were superimposed on an  $80\text{ }\mu\text{m}$  square of  $650\text{ nm}$  in height.

The experiments were performed at a wavelength of  $0.436\text{ nm}$  and with  $z = 0.0475\text{ m}$ , where  $z$  is as defined above. Through the thickest part of the object the transmission  $\exp(-2\mu)$  is 98.7% and the phase-shift  $\phi$  is  $-0.37$  radian. Accordingly, neither the Born-type approximation nor the phase-only requirement are met. However, for most positions and spatial frequencies the slowly-varying phase condition Eq. (8) is obeyed.

Figure 1 shows a plot of the inverse of the contrast transfer function from the CTF solution Eq. (16) for the  $1.9\text{ }\mu\text{m}$  grid features. A contrast transfer function can also be defined, in the weak absorption limit, for the TIE solution Eq. (13) and its inverse is also shown in Fig. 1. Inspection shows that the TIE solution should yield grid features reversed in contrast compared to the CTF solution. No contrast reversal is expected for the  $80\text{ }\mu\text{m}$  square.

The experiments were performed at beamline 2-ID-B at the Advanced Photon Source. A beam of  $2844\text{ eV}$  ( $\Delta E/E \simeq 10^{-3}$ ) x-rays with FWHM size  $1.5 \times 0.5\text{ mm}$  illuminated a  $160\text{ }\mu\text{m}$  diameter gold zone plate with an outer zone width of  $50\text{ nm}$ . The focal length was  $18.4\text{ mm}$  and a  $10\text{ }\mu\text{m}$  diameter order sorting aperture was placed at a distance of  $17.2\text{ mm}$  from the zone plate. A  $30\text{ }\mu\text{m}$  wide gold beamstop blocked the zero order beam. This zone plate configuration provided a point source of illumination at a distance of  $R_1 = 54.7\text{ mm}$  from the object. After passing through the object the beam was allowed to propagate through a He-filled flight tube a distance of  $R_2 = 363\text{ mm}$  onto a crystal scintillator which was imaged through a  $20\times$  objective by a CCD camera with  $13.5\text{ }\mu\text{m}$  pixels. This expanding beam mode is analyzed using the parallel beam mode derivations described above using the conversion [4]

$$I_{R_1}(\mathbf{r}, R_2) = \frac{1}{M^2} I_\infty \left( \frac{\mathbf{r}}{M}, \frac{R_2}{M} \right), \quad (18)$$

where  $M = (R_1 + R_2)/R_1$  is the magnification,  $I_{R_1}(\mathbf{r}, R_2)$  is the expanding beam diffraction-

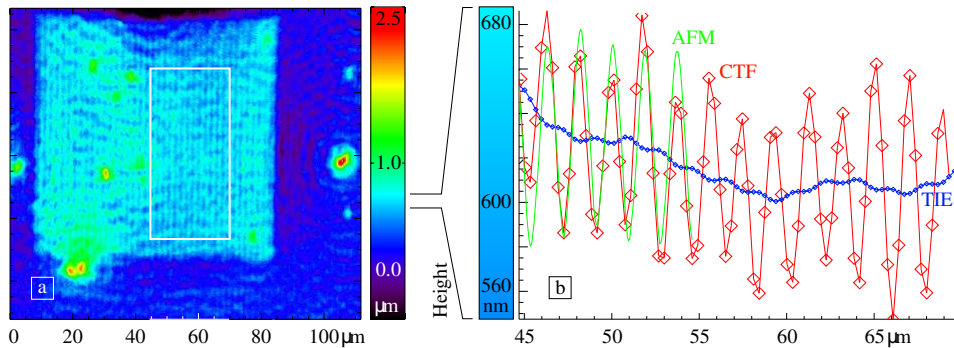


Fig. 2. (a) CTF-retrieved thickness map for the square with grid lines.(b) Column-average of retrieved thickness for the grid pattern in the region shown in (a) for the TIE solution (blue) and the CTF solution (red). The AFM result (green) shows excellent agreement. AFM measurements also confirm the presence of grid lines outside the square. These are not a retrieval artefact, unlike the circular fringes around the contaminant at centre right. The contaminating material presumably violates the assumption of an homogeneous object.

pattern due to a point source a distance  $R_1$  behind the object and  $I_\infty$  is parallel beam diffraction-pattern. The object thickness map was retrieved from the measured diffraction pattern using both the CTF solution Eq. (16) with Tikhonov regularization, and the TIE solution Eq. (13), and is shown in Fig. 2(a). We line average the essentially one-dimensional image in the region outlined in white. Both CTF and TIE methods retrieve the mean height of the  $80\text{ }\mu\text{m}$  square as  $610 \pm 50\text{ nm}$ , concurring with the AFM result of  $650\text{ nm}$ . However, the TIE retrieval grossly underestimates the height of the grid pattern and, as predicted in Fig 1, reverses the contrast (Fig. 2(b)). As expected from the validity conditions for Eq. (16), the CTF retrieval of the grid pattern (Fig. 2(b)) is in excellent agreement with the AFM measurement of  $90\text{ nm}$ .

#### 4. Conclusions

We have explored the validity conditions for the linear CTF expression relating object phase-shift and absorption to the contrast of the Fresnel diffraction-pattern. The linear expression is found *not* to be restricted to weakly phase-shifting objects: it applies to a substantially wider class of objects which show weak absorption and slowly-varying phase.

If an object is made of one material with known complex refractive index, the CTF expression may be inverted to retrieve the object thickness from a single diffracted image. We demonstrated an example where the CTF solution could correctly retrieve thickness features of a weakly-absorbing object with large, but slowly-varying, phase-shift. Thickness features at two well-separated spatial frequencies were retrieved by the CTF solution while the TIE retrieval was valid only at the lower spatial frequency. These results augur well for wider applications of the CTF technique such as imaging cold atom clouds [25, 26] and plasmas [27].

#### Acknowledgments

The authors acknowledge Australian Research Council Fellowships (LDT, APM: Australian Postgraduate Awards, AGP: QEII Fellowship, KAN: Federation Fellowship). This work was supported by the Australian Synchrotron Research Program, which is funded by the Commonwealth of Australia under the Major National Research Facilities Program. Use of the Advanced Photon Source was supported by the U.S. D.O.E., Basic Energy Sciences, Office of Science under Contract No. W-31-109-Eng-38. We thank A. Cimmino for providing the AFM results, D. Paganin for useful discussions and an anonymous referee for insightful comments.



## Colophon

« THIS THESIS WAS typeset using the  $\text{\LaTeX} 2\epsilon$  computer typesetting system. Source was prepared in the GNU emacs editor using the `AUC\TeX` package. The PDF was created with GNU ghostscript and the `latex` package `hyperref`. The text font is Adobe Minion. Minion is integrated with the Y&Y MathTime fonts for typesetting formulae using the `mathpmnt` package.

« I HAVE used text figures for page numbers and to number equations, figures and the like, while using lining figures for all scientific quantities.

« GRAPHS were generated in the Interactive Data Language (IDL) with routines written by the author. Illustrations were drawn in Adobe Illustrator cs, with some technical drawings originally prepared in Autodesk AutoCAD. Th bibliography was compiled with Bib $\text{\TeX}$  with extra data extracted from the IEE INSPEC database by a perl script written by the author.

« IN designing this thesis, I have been influenced by Robert Bringhurst's book *The Elements of Typographic Style* and Edward Tufte's *The Visual Display of Quantitative Information*. ♡

# University Library



MINERVA  
ACCESS

A gateway to Melbourne's research publications

Minerva Access is the Institutional Repository of The University of Melbourne

**Author/s:**

TURNER, LINCOLN DAVID

**Title:**

Holographic imaging of cold atoms

**Date:**

2004-08

**Citation:**

Turner, L. D. (2004). Holographic imaging of cold atoms. PhD thesis, School of Physics, The University of Melbourne.

**Publication Status:**

Published

**Persistent Link:**

<http://hdl.handle.net/11343/38894>

**File Description:**

Holographic imaging of cold atoms

**Terms and Conditions:**

Terms and Conditions: Copyright in works deposited in Minerva Access is retained by the copyright owner. The work may not be altered without permission from the copyright owner. Readers may only download, print and save electronic copies of whole works for their own personal non-commercial use. Any use that exceeds these limits requires permission from the copyright owner. Attribution is essential when quoting or paraphrasing from these works.